To my wife Algun and our families

for their continuos support and encouragement

CMOS and SOI CMOS FET-based Gas Sensors

by

James A. Covington

School of Engineering

University of Warwick

A thesis submitted to the University of Warwick

for the degree of Doctor of Philosophy

September 2001

Contents

List of Figures

List of Tables

Summary

In recent years, there has been considerable interest in the use of gas/vapour monitors and electronic nose instruments by the environmental, automotive and medical industries. These applications require low cost and low power sensors with high yield and high reproducibility, with an annual prospective market of 1 million pounds. Present device and sensor technologies suffer a major limitation, their incompatibility with a standard silicon CMOS process. These technologies have either operating/annealing temperatures unsuited for MOSFET operation or an inappropriate sensing mechanism. The aim of this research is the development of CMOS compatible gas/vapour sensors, with a low cost of fabrication, high device repeatability and, in the future, transducer sensor amalgamation. Two novel approaches have been applied, utilising bulk CMOS and SOI BiCMOS. The bulk CMOS designs use a MOSFET sensing structure, with an active polymeric gate material, operating at low temperatures (< 100 ^{o}C), based on an array device of four elements, with channel lengths of 10 μm or 5 μm. The SOI designs exploit a MOSFET heater with a chemoresistive or chemFET sensing structure, on a thin membrane formed by the epi-taxial layer. By applying SOI technology, the first use in gas sensor applications, operating temperatures of up to 300 ^{o}C can be achieved at a power cost of only 35 mW (simulated). Full characterisation of the bulk CMOS chemFET sensors has been performed using electrochemically deposited (e.g. poly(pyrrole)/BSA)) and composite polymers (e.g. poly(9-vinylcarbazole)) to ethanol and toluene vapour in air. In addition, environmental factors (humidity and temperature) on the response and baseline were investigated. This was carried out using a newly developed flow injection analysis test station, which conditions the test vapour to precise analyte (< 15 PPM of toluene) and water concentrations at a fixed temperature (RT to 105 ^{o}C ±0.1), with the sensor characterised by either I-V or constant current instrumentation. *N*-channel chemFET sensors operated at constant current (10 μA) with electrochemically deposited and composite polymers showed sensitivities of up to 1.1 μV/PPM and 4.0 μV/PPM to toluene vapour and to 1.1 μV/PPM and 0.4 μV/PPM for ethanol vapour, respectively, with detection limits of <20 PPM and <100 PPM to toluene and <20 PPM and 10+ PPM to ethanol vapour (limited by baseline noise), respectively. These responses followed either a power law (composite polymers) or a modified Langmuir isotherm model (electrochemically deposited polymers) with analyte concentration. It is proposed that this reaction-rate limited response is due to an alteration in polymers work function by either a partial charge transfer from the analyte or a swelling effect (polymer expansion). Increasing humidity caused, in nearly all cases a reduction in relative baseline, possible by dipole formation at the gate oxide surface. For the response, increasing humidity had no effect on sensors with composite polymers and an increase for sensors with electrochemically-deposited polymers. Higher temperatures caused a reduction in baseline signal, by a thermal expansion of the polymer, and a reduction in response explained by the analyte boiling point model describing a reduction in the bulk solubility of the polymer. Electrical and thermal characterisation of the SOI heaters, fabricated by the MATRA process, has been performed. I-V measurements show a reduction in drain current for a MOSFET after back-etching, by a degradation of the carrier mobility. Dynamic measurement showed a two stage thermal response (dual exponential), as the membrane reaching equilibrium (100-200 ms) followed by the bulk (1-2 s). A temperature coefficient of 8 mW/^{o}C was measured, this was significantly higher than expected from simulations, explained by the membrane being only partially formed. Diode and resistive temperature sensors showed detection limits under 0.1 ^{o}C and shown to measure a modulated heater output of less than 1 ^{o}C at frequencies higher than 10 Hz. The principal research objectives have been achieved, although further work on the SOI device is required. The results and theories presented in this study should provide a useful contribution to this research area.

Acknowledgements

I would like to thank my academic supervisor Prof. Julian Gardner for generously allowing me the opportunity of studying in this field, and for his constant guidance and support during my PhD. I would also like to acknowledge the Engineering and Physical Science Research Council (EPSRC) for their financial support during three years of this study. I am also grateful to all of my friends a colleagues for their constant support and encouragement during the course of this study. For practical work associated with my PhD. I would particularly like to thank the members of the *Sensors Research Laboratory, School of Engineering, University of Warwick***,** including, Mr F. T. Courtney for his assistance in mechanical matters and to Mr G. Searle, Mr S. M. Lee, Mr I. Griffiths, Mr P. Boilet, Mr R. Folland and to Dr M.V. Cole for their help in technical matters. Also Mr D. Chrastina, from the *Department of Physics, University of Warwick,* with his assistance with certain equipment and the members of the *Optical Engineering Laboratory, School of Engineering, University of Warwick.*

I would also like to acknowledge Prof. P. N. Bartlett for his assistance in modelling and C. Seng for the deposition of electrochemically grown conducting polymers, from the *Department of Chemistry, University of Southampton UK* and Dr J. Li of *Cyrano Sciences, USA* for the deposition of composite polymers. Also Prof. N. F. de Rooji, Mr D. Braind, and the other members of the fabrication laboratory of the *Insitutute of Microtechnology University of Neuchatel, Switzerland* for the fabrication of devices.

Furthermore, I would like to acknowledge Dr F. Udrea, Mr C.C. Lu, Dr D. Setaidi and Dr D. Togaru from the *Department of Engineering, University of Cambridge, UK* with whom I worked in close collaboration in a part of this research. Also Dr G. Ensell, and the other members of the *Southampton University Microtecnology Centre, UK* for assistance in the fabrication of devices.

Lastly, I would like to acknowledge Dr J.V. Hatfield from the *Department of Electrical and Electronic Engineering, UMIST, Manchester, UK,* with whom I worked in collaboration for some of this study, including donation some of several the devices used in this work.

Declaration

The work described in this thesis is entirely original and my own, except where otherwise indicated.

Parts of this work have been presented at international conferences and published in the scientific literature listed below:

1. Journal Papers /Books

[1] J.V. Hatfield, J.A. Covington, J.W. Gardner, GasFETs incorporating conducting polymers as gate materials, *Sensors and Actuators B,* 65 (1-3) (2000) pp. 253-256.

[2] J.A. Covington, J.W. Gardner, C. Toh, P.N. Bartlett and D. Briand, The Characterisation of an Electrodeposited Conducting polymer FET Array for Vapour Sensing, Published in Electronic Noses and Olfaction 2000 (Ed. J.W. Gardern, K.C. Persaud), IoP, 2000, pp. 35-42.

[3] J.A Covington, J.W. Gardner, D. Briand, A polymer gate FET sensor array for detecting organic vapours, *Sensors and Actuators B,* 77 (1-2) (2001) pp. 155-162.

[4] F. Udrea, J.W. Gardner, D. Setiadi, J.A. Covington, T. Dogaru, C.C. Lu, W.I. Milne, Design and simulations of a new class of SOI CMOS micro hot-plate gas sensors, *Sensors and Actuators B: Chemical, 78 (*1-3) (2001) pp. 180-190.

2. Conference Papers

[1] J.V. Hatfield, J.A. Covington, J.W. Gardner, GasFETs incorporating conducting polymers as gate materials, *Technical Digest of the Seventh International Meeting on Chemical Sensors*, (1998), *Beijing*, pp. 707-709.

[2] J. A. Covington, J.W. Gardner, J.V. Hatfield, Conducting polymer FET devices for vapour sensing, *Proc. Of SPIE Smart Electronics and MEMS* (1999), pp. 296-307.

[3] D. Setiadi, F. Udrea, W.I. Milne, J.A. Covington, 3D Numerical Simulation of Novel SOI MOSFET Based Gas Sensors, *Proceedings of ECS Chemical Sensors* (1999), *Hawii*, pp. 416-419

[3] J.A Covington, J.W. Gardner, D. Briand, A polymer gate FET sensor array for detecting organic vapours, *8th International Conference on Chemical Sensors,* (oral presentation given) (2000), *Basel,* pp. 166.

[4] J.A. Covington, J.W. Gardner, C. Toh, P.N. Bartlett and D. Briand, The Characterisation of an Electrodeposited Conducting polymer FET Array for Vapour Sensing, *International Symposium on Electronic Noses*, (oral presentation), (2000), *Brighton*, pp. 29-30.

[5] F. Udrea, D. Setiadi, J.W. Gardner, J.A. Covington, C.C. Lu, A novel class of smart gas sensors using CMOS micro-heaters embedded in an SOI membrane. *Eurosensors XIV* (2000), *Copenhagen*, pp 707-710.

[6] M. Cole, J.W. Gardner, J.A. Covington, D. Fife, J.W. Brignell, P.N. Bartlett, Active bridge polymeric resistive device for vapour sensing, *Eurosensors XIV* (2000) *Copenhagen*, pp. 895-898.

[7] C.C. Lu, D. Setiadi, F. Udrea, W.I. Milne, J.A. Covington, J.W. Gardner, 3D Thermo-electro -mechanical simulations of gas sensors based on SOI membranes, *Modeling and Simulation of Microsystems* (2000) *San Diego*, pp. 297-300.

[8] J.W. Gardner, J.A. Covington, F. Udrea, T. Dogaru, C-C Lu, W.I. Milne, SOI-based Micro-hotplate Microcalorimeter Gas Sensor with Integrated BiCMOS Transducer, *Transducer 01 & Eurosensors XV*, (2001) *Munich*, pp. 1688-1691.

[9] C.C. Lu, F. Udrea, J.W. Gardner, D. Setiadi, T. Dogaru, T.H. Tsai, J.A. Covington, Design and Coupled-Effect Simulations of CMOS Micro Gas-Sensors Built on SOI Thin Membranes, *Design, Test Integration and Packaging of MEMS/MOEMS*, *Proc. of SPIE*, Vol. 4408 (2001), pp. 86-95.

Selected Abbreviations and Acronyms

TERM	DEFINITION
ADC	Analogue to Digital Converter
AFM	Atomic Force Microscope
ASIC	Application Specific Integrated Circuit
ANN	Artificial Neural Network
BAW	Bulk Acoustic Wave
BiCMOS	Bipolar Complementary Metal Oxide Semiconductor
BSA	Butane Sulfonate Acid
CCM	Constant Current Measurement
CMOS	Complementary Metal Oxide Semiconductor
CVD	Chemical Vapour Deposition
DAC	Digital to Analogue Converter
DAQ	Data Acquisition
DIO	Digital Input/Output
DSA	Decane Sulfonate Acid
EMC	Electromagnet Compatibility
IC	Integrated Circuit
I.D.	Inner Diameter
IVC	Current-Voltage Characterisation
LED	Light Emitting Diode
LPCVD	Low Pressure Chemical Vapour Deposition
MFC	Mass Flow Controller
MFM	Mass Flow Meter
MOS	Metal Oxide Semiconductor
MOSFET	Metal Oxide Semiconductor Field Effect Transistor
O.D.	Outside Diameter
PARC	Pattern Recognition
PBT	Poly(bithiophene)
P.C	Personal Computer
PCB	Printed Circuit Board
PPY	Poly(pyrrole)
R.H.	Relative Humidity

R.T	Room Temperature
SAD	Sensor Array Device
SAW	Surface Acoustic Wave
SCE	Saturated Calomel Electrode
SEM	Scanning Electron Microscope
SOI	Silicon-On-Insulator
SPCO	Single Pole Change Over
SRL	Sensors Research Laboratory
TBATFB	Tetrabutyammonium Tetrafluoroborate
TTL	Transistor–Transistor Logic
UV	Ultra–Violet
VI	Virtual Instrument
VOC	Volatile Organic Compound

Symbol Reference

TERM	DEFINITION
A	Area
A	Constant
A	Absorbed species
a	Temperature dependent constant
a	Diameter of the active area of a membrane
A_d	Area of a diode
a_E	Polymer – ethanol dependence constant
Al	Aluminium
a_w	Polymer – water dependence constant
Au	Gold
B	Constant
C	Constant
C	Analyte concentration
c	Diffusion rate of hydrogen from metal surface to the metal – silicon oxide interface
C'	Constant
c_1	Absorption/disassociation rate of hydrogen
C_A	Concentration of an analyte outside the polymer
C_E	Concentration of ethanol
C_h	Concentration of water
$c_{i,gas}$	Concentration of solvent molecules in the carrier gas
$c_{i,poly}$	Concentration of solvent molecules within a polymer
C_p	Concentration of an analyte within a polymer
C_o	MOSFET gate oxide capacitance
C_{OX}	MOSFET gate oxide capacitance
C_T	Concentration of toluene
C_{VAP}	Concentration of vapour
C_W	Concentration of water
D	Flexural rigidity
d	Diffusion rate of hydrogen from metal – silicon oxide interface to the metal surface

d	Effective charge separation
d_1	De-absorption/associate rate of hydrogen
d_s	De-absorption rate
E	Young's modulus
e	Elementary charge
E_{fc}	Fermi level of the substrate
E_g	Energy bandgap of silicon
E_m	Fermi level of the gate material
E_t	Activation energy
E_{vac}	Vacuum energy level
F	Hydrogen molecular flux
f	Total packing fraction of carbon to polymer
f_C	Fractional coverage
F_i	Number of unoccupied absorption sites at the gate – silicon oxide interface
F_e	Number of absorbed sites at the gate – silicon dioxide interface
G	Device conductance
g_m	Transconductance of a MOSFET
G_0	Initial device conductance
h	Thickness of a membrane
H_a	Hydrogen atoms at the catalytic metal (gate) surface of a gasFET
H_a	Heat loss by conduction and convection to the surrounding air
H_i	Hydrogen atoms at the catalytic metal (gate) silicon dioxide interface of a gasFET
$H_{i,o}$	Initial heat of absorption
H_m	Heat loss by conduction through a membrane
H_r	Heat loss by radiation
H_T	Total heat loss from a membrane
i	Number of molecules
I_C	Collector current

I_D	Diode current
I_{DS}	Drain – source current
$I_{DS(0)}$	Initial drain – source current
Ir	Iridium
I_S	Diode saturation current
I_{Sensor}	Current through the sensor
J	Current density
k	Boltzmann's constant
k'	Temperature dependent constant
k_1	Forward reaction rate
k_{-1}	Backward reaction rate
k_2	Reaction rate
k_E	Binding coefficient of ethanol
k_f	Forward reaction rate
k_b	Backward reaction rate
K_h	Binding coefficient of water
K_o	Dielectric constant of silicon dioxide
k_p	Partition coefficient for a polymer
$k_{p,g}$	Ratio of solvent within a polymer to the solvent in the same volume outside the polymer
$k_{p,w}$	Water – polymer partition coefficient
K_s	Dielectric constant of silicon
k_T	Binding coefficient of toluene
k_W	Binding coefficient of water
L	MOSFET channel length
L	Length of a square membrane
M_1	Molecular weight of a stationary phase polymer
m	Oxidation states for a metal oxide
m	Thickness of a membrane
n	n doping level
n'	Carrier concentration
N_a	Number of acceptor atoms
n_e	Number of hydrogen atoms absorbed at the surface of the

	gate
$N(E_F)$	Density of states at the Fermi level
n_h	Number of hydrogen atoms per unit area at the metal – silicon oxide interface
n_i	Intrinsic carrier density
n_O	Number of absorbed oxygen atoms
$n_{O,H}$	Number of absorbed OH groups
n_s	Number of absorbed hydrogen atoms
N_s	Number of Absorption sites
O	Oxygen atoms
O_a	Disassociated oxygen atoms on a catalytic metal surface
P	Partial pressure
p	p doping level
p_2	Saturated vapour pressure of a solute vapour
P_{AIR}	Partial pressure of air
P_C	Temperature dependent constant
P_{CO}	Partial pressure of carbon monoxide
Pd	Palladium
P_{H2}	Partial pressure of hydrogen
P_{O2}	Partial pressure of oxygen
Pt	Platinum
q	Electron charge
q	Load pressure
Q	Dipole charge
Q_B	Bulk charge of a MOSFET
Q_o	Charge at zero gate voltage, due to trapped charges in the gate oxide
R	Electrical resistance
R	Gas constant
r^2	Correlation coefficient
R_0	Initial resistance before exposure to an analyte
r_0	Radius
R_{FB}	Feed back resistance

R_{SCALE}	Value of the scaling resistor
R_{Sensor}	Resistance of the sensor
S_e	Sensitivity coefficient to ethanol
Si	Silicon
SiO_2	Silicon dioxide
S_H	Initial sticking coefficient of hydrogen absorption
S_h	Sensitivity coefficient to water
T	Temperature
t	Time
t	Trouton's constant
T_b	Boiling point of an analyte
Ti	Titanium
T_0	Initial or room temperature
t_{BULK}	Time for the bulk to reach equilibrium
t_{MEM}	Time for the membrane to reach equilibrium
t_{on}	Time to reach steady state
t_{SWITCH}	Switching time of a MOSFET
t_{TOTAL}	Time to reach equilibrium
u	Distance across a membrane
v_c	Volume fraction of carbon black in the composite
V_{BE}	Base- emitter voltage
V_D	Diode voltage
V_{DS}	Drain – source voltage
V_{FB}	MOSFET flat band voltage
V_G	Gate voltage
V_{go}	Bandgap voltage of silicon at absolute zero
V_{GDS}	Gate/drain – source voltage
$V_{GDS(0)}$	Initial gate/drain – source voltage
V_{GS}	Gate – source voltage
V_{OUT}	Output voltage
V_T	MOSFET threshold voltage
V_{TH}	Thermal voltage
V_{THRES}	MOSFET threshold voltage

V_{T0}	Initial MOSFET threshold voltage before exposure to a react analyte
V_S	Source voltage
W	MOSFET channel width
X	Combustible species
x_o	Thickness of the gate oxide
Z	Co-ordination number for a composite polymer
Γ	Number of binding sites within a polymer
α	Spatial content of the localised wavefunction
α	Constant
α_e	Ethanol sensitivity term
β	Constant
ε_o	Permittivity in a vacuum
ΔV_{TMAX}	Maximum shift in threshold voltage
ϕ_b	Potential barrier height
ϕ_C	Work function of carbon
ϕ_f	Difference between the Fermi level and the intrinsic fermi level
ϕ_m	Work function of the gate material
ϕ_{ms}	Difference in work function between the metal and the semiconductor
ϕ_{mso}	Difference in work function between the metal and the semiconductor before formation of a dipole layer by exposure to hydrogen
ϕ_{PC}	Work function of a polymer
ϕ_{PC}	Average work function of a composite polymer
ϕ_{ps}	Difference in work function between the polymer and the semiconductor
ϕ_s	Work function of silicon
ϕ_{si}	MOSFET surface potential (at oxide/silicon interface)
ϕ_T	Thermal voltage (kT/q)
γ	Constant

γ_2	Vapour activity coefficient
η	Coverage of the active area of a micro-hot plate
φ	Applied gate voltage
κ	Thermal conductivity
θ	Coverage of hydrogen at the gate – silicon dioxide interface
θ_e	Proportion of occupied sites by ethanol
θ_h'	Occupancy of water molecules on the absorption sites of a conducting polymer
θ_t	Fraction of occupied sites at time t
μ_n	Carrier mobility n-doped
μ_0	Carrier mobility at room temperature
μ_p	Carrier mobility p-doped
ρ_c	Resistivity of carbon
ρ_m	Resistivity of the polymer matrix
σ	Electrical conductivity
σ	Standard deviation
σ_1	Principal plane stress
σ_1	Density of a stationary phase polymer
σ_2	Principal plane stress
σ_i	Charge concentration by a dipole layer at the metal silicon dioxide interface
σ_{MAX}	Maximum stress on a membrane
τ	Time constant
τ_1	Time constant
τ_2	Time constant
τ_{ON}	Time constant for response
τ_{OFF}	Time constant for recovery
τ_{OFFSET}	Time constant as time goes to infinity
υ	Poisson’s ratio
Ψ	Electroresistive potential

{ }	Unoccupied site

CHAPTER 1

Introduction

The purpose of this chapter is to introduce the concept of an electronic nose, discussing the technology, current devices, applications and their limitations. Next, the aims and objectives of the research undertaken are presented. Lastly, an outline of the thesis is given.

1.1 Electronic Noses

The development of the electronic nose instrument can be regarded as a simple yet crude replication of the human olfactory system. The human olfactory system had been considered, until recently, the only way to distinguish complex odours from, for example food or beverages. Not surprisingly, this technique is still used for odour discrimination, due to its simplicity and sensitivity. The architecture of the electronic nose can be paralleled to the mammalian olfactory system and segregated into three distinct components: detection, signal processing and identification/recognition. Here a brief history and overview of the electronic nose instrument is given, with the similarities between the mammalian olfactory system and the electronic nose emphasised.

1.2 The concept of electronic noses

The term ‘electronic nose’ was first used, amongst others, by Persuad *et al.* in 1985 [1.1], though early research by Hartman in 1954, using an electrochemical sensor, could be considered the first experimental instrument [1.2]. Ten years later Hartman in collaboration with Wilkens introduced the concept of the odour sensor [1.3]. Stetter

proposed an array of gas sensors with partially overlapping sensitivities, in the 1980s, that could be used to detect complex odours [1.4]. Since then, advancements in gas sensor technologies, pattern recognition techniques and neural networks have led to the rapid development of many gas mixture and odour analysis systems.

The term ‘electronic nose’ was defined by Gardner and Bartlett in 1994 [1.5] as ‘an instrument, which comprises of an array of electronic sensors with partial specificity and an appropriate pattern recognition system, capable of recognising simple or complex odours’. This electronic nose instrument can be divided into an odour delivery system, a detection stage of gas sensors, a number of signal processing steps, (including analogue to digital converters) and a pattern recognition action to identify the odour. A schematic of a typical electronic nose instrument is given in figure 1.1. Also included is the basic structure of the mammalian olfactory system for comparison [1.6]. The components of this electronic nose instrument and the mammalian olfactory system are described in the following sections.

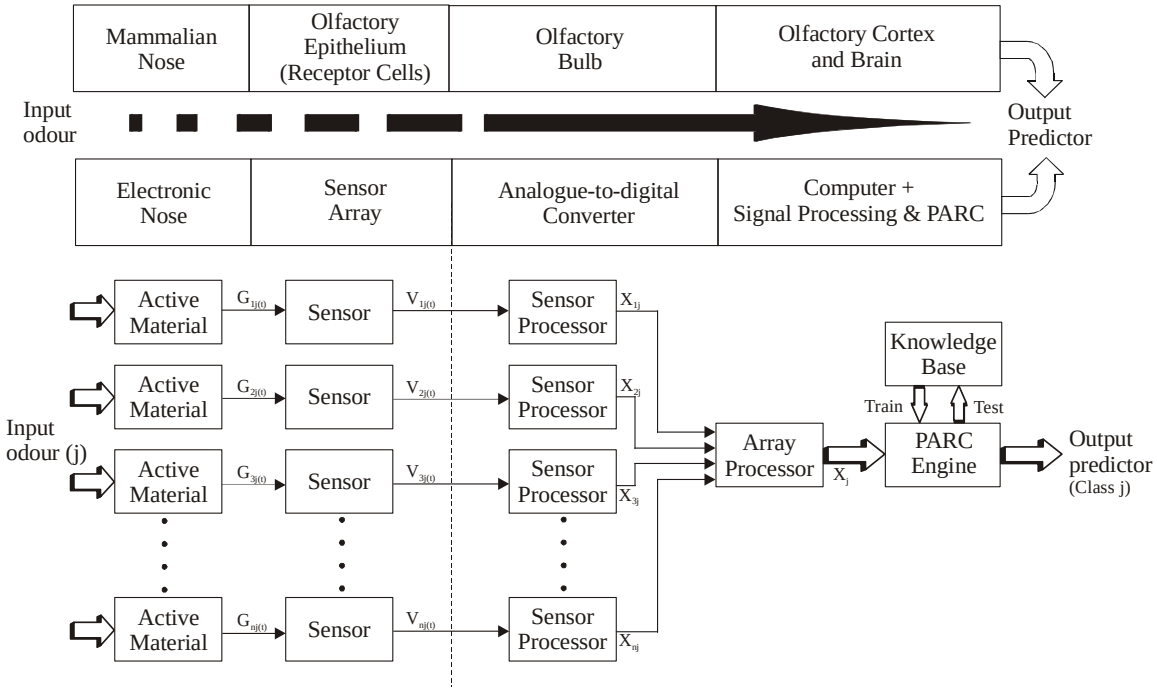

Figure 1.1: A simplified schematic of an electronic nose instrument and biological olfactory system.

1.2.1 Mammalian olfactory system

The mammalian olfactory system is capable of identifying complex odours, which are delivered through the nasal passages to the olfactory epithelium. This epithelium is composed of three types of cells, receptor, supporting and basal cells [1.7-1.9]. Odours diffuse through layers of mucus and bind with proteins that are sensitive to that

molecule, on the receptor cells. The number of different olfactory binding proteins is relatively small (hundreds) when compared to the number of receptor cells (100 million), though each receptor cell has an overlapping sensitivity to many different odorants. Various biochemical transduction processes convert the molecular signals to spiking voltage potentials that are transmitted to the brain from the olfactory system via relay stations within the olfactory bulb. This olfactory bulb is composed of higher level cells, namely the glomeruli node, mitral cells and granular layer. These cells compress and transmit information to the olfactory cortex and to the brain. It is believed that considerable processing occurs within the granular layer to improve the signal-to-noise ratio and to amplify the signal, resulting in higher sensitivity and selectivity.

The last stage is the olfactory cortex and brain. Here Haberly has suggested, that the olfactory cortex operates as a content–addressable memory, where a pattern of input signals, from an odour, stimulates a previous memory of that odour [1.10]. So the information is stored as a unified sensing experience with memories such as names, places and feelings.

1.2.2 Gas sensors

The gas sensor is crudely equivalent to the receptor cell and glomeri performing the signal measurement role for an electronic nose. Regardless of the sensor output, i.e. an electrical signal, such as resistance, voltage or frequency, or other form depending on the sensor technology, the basic function of the sensor is the same: to convert a chemical input into a useable measurand [1.11]. An ideal gas sensor would have a number of generic characteristics independent of any particular sensor technology [1.12]. An clear requirement is that the sensor responds to the input chemical with a wide sensitivity range from very low concentrations to the saturation level of that chemical in any defined environment. In addition, this response would be linear with concentration. Some gas sensors do saturate at some value (below vapour saturation level) and are non-linear with concentration, generally with a greater response at low chemical concentrations with the lowest detection level determined by the baseline noise of the instrument.

Another important characteristic is the sensors response time. In an ideal case this would be rapid (< 10 s), though in certain applications longer response times are acceptable. The recovery time is also a factor as this defines the sampling rate of an

instrument made of these sensors. Any response should be repeatable and return to its initial value once the odour is removed, over a period of years or the lifetime of the sensor. Unfortunately in practice, sensors suffer from baseline drift and variations in sensitivity, depending on the environmental conditions and the age of the sensor. True sensor drift, ignoring environmental conditions (e.g. temperature, humidity and flow rate), is normally a slow reaction due to the chemical ageing of the sensing material by a change in its morphology. In addition, the sensitivity can be effected by poisoning of the chemical binding sites, reducing the magnitude of the response. In biological systems, this problem is eradicated by averaging over a large number of cells that are continually replaced (20 day cycle). Careful conditioning of both the sensors and the input can minimise these effects.

Many different gas sensor technologies are presently used in electronic nose instruments, summarised in table 1.1.

Sensor Technology	**Description**
Acoustic wave [1.13, 1.14]	Bulk Acoustic Wave (BAW) sensors are typically a single quartz crystal with an external polymer film. These operate via a change in resonant frequency, by an increase in mass as the vapour binds to the polymer (assuming visoelastic effects are negligible). Surface Acoustic Wave (SAW) sensors are based on piezoelectric materials using surface waves in a delay or resonator configuration. In a delay system a second set of electrodes are used to receive the launched wave. In a resonator, a single electrode is used as a receiver and a transmitter. Both are effected by changes in surface film (usually polymer) by predominantly a mass sensitivity (again assuming visoelastic effects are negligible). Both operate at room temperature.
Conducting polymer [1.15]	These sensors use electrically conducting polymers, normally as a chemoresistor, deposited between two electrodes (usually gold). Sensing mechanism is a change in conductance brought by exposure to an organic vapour. Sensors operate around room temperature.

Electrochemical [1.16]	Based on the oxidation or reduction of an analyte on the catalytic surface of the sensor. The sensing electrode is typically a precious metal coated with carbon. The analyte reacts at the boundary between the gas, solid electrode and liquid electrode. Two other electrodes (reference and counter) lie within an electrolyte solution in the bulk of the device. These sensors normally operate at room temperature and are sensitive to a number of toxic gases.
Field-Effect [1.17]	These sensors appear in two configurations, a Metal Insulator Semiconductor Capacitor or MISCAP and the more popular MIS Field Effect Transistor or MISFET. Both use catalytic metals (e.g. Pd) as the gate electrode. These devices operate via a change in surface potential at the insulator layer usually by a change in work function between the metal and the semiconductor. This shift in work function is due to the formation of a hydrogen dipole layer at the metal-insulator interface. Hydrogen in produced on the catalytic surface of the sensor through the breakdown of hydrogen containing molecules. The sensors operates between 100-250 ^{o}C depending on gas or vapour to be detected.
Fibre-optic [1.18]	Here a fibre optic cable is used to guide light to and from a gas sensitive layer. Detection is achieved by measuring the optical path length (swelling), luminescence, absorption, fluorescence or reflectance of the light. Sensing materials can be dyed to fluoresce in the presence of certain analytes.
Metal-oxide [1.19]	These are the most popular types of sensor, utilising SnO_2 or ZnO, though other materials are available. This material is normally doped with a catalyst (e.g. Pd) to reduce the sensitivity. Typically, a Taguchi configuration is used, with a Pt heater coil in a ceramic tube, coated with sintered metal oxide. The sensor operates via a change in conductance, through an increase in carrier concentration and in potential barrier between grains of the metal-oxide. Sensors operate between 300 – 550 ^{o}C depending on the target gas.
Pellistor [1.20]	Pellistors are high temperature devices (≈ 500^{o}C), utilising a Pt

	heater coil, coated in a porous alumina containing particles of catalytic metals such as Pt, Pd or Pt/Pd composite. The Pt coil operates as a heater and a temperature sensor. As the combustible species react on the catalyst they release heat, measured by a change in resistance of the Pt coil.

Table 1.1: Popular gas sensor technologies.

All of these sensors respond to a broad range of chemicals, gases and odours, though posses little or no integration with any associated control and measurement electronics and generally have a high cost of fabrication. This extra cost is not significant in an expensive desktop instrument (£30,000 – 150,000), though for a low-cost handheld unit (< £5,000) it is an issue. The control and measurement electronics are based on standard silicon technology used for the fabrication of nearly all integrated circuits. The combination of a sensor with control electronics on a single silicon die, is an attractive proposal, resulting in a sensor with improved sensitivity, due to the lower signal-to-noise ratio and lower cost by using standard CMOS technology. Some attempts in device integration have resulted in sensors fabricated by a non-standard CMOS process [1.21] or with the drive electronics integrated into a single discrete IC separated from the sensor (ASIC design) [1.22, 1.23]. Many of the sensor technologies, described earlier, are either incompatible with CMOS due to the sensing mechanism (e.g. electrochemical cells), or operate significantly above the maximum working temperature of bulk CMOS electronics (e.g. 300 ^{o}C to 550 ^{o}C of metal oxides).

1.2.3 Signal processing, identification and recognition

In all electronic nose instruments, there are tools available to condition the input signals prior to recognition, similar to the actions of the olfactory bulb [1.24, 1.25]. These signal processing techniques are there to remove (or reduce) noise and baseline drift from the signal. The most popular algorithms are difference, averaging, normalising, relative signal, linearisation and autoscaling. These mechanisms can be tailored to the specific sensor or transduction mechanism. For example, the difference measurement is used by many researchers for a response to air followed by a test sample and may remove some of the baseline drift (i.e. common additive errors). More

recently, dynamic information combined with the more traditional static information has been used to improve selectivity of many sensors.

These algorithms pre-process the information before recognition or identification is performed. This stage is equivalent to the olfactory cortex of the brain in the mammalian system. The processed information is fed into a pattern recognition (PARC) engine, which performs the identification or odour discrimination. There are two traditional methods for odour recognition based on classical PARC and artificial neural networks (ANN) [1.26,1.27]. Classical PARC is a statistical method based on the application of probability. Here each odour is represented as a set of multi-components, for which there are many recognition algorithms. Artificial neural networks are described as a number of parallel distributed processing elements that store experiential knowledge and makes use of it. This is achieved through a learning or training process by strengthening interconnections in the network, known as synaptic weights. These ANNs have a number of advantages over the classical PARC method, firstly they are usually more accurate because they can deal with highly non-linear responses. Furthermore, they have a greater tolerance to drift and noise, though it is difficult to optimise the size and shape of the network and to find an appropriate training method.

1.2.4 Smart gas sensors

Gardner [1.28] has defined the term smart sensor as requiring three features:

- Perform a logical function
- Communicate with one or more devices
- Make a decision using crisp or fuzzy data

This definition is one of many reported and what is classified as a smart sensor is still a matter of debate. The first requirement is to perform a logical function, which would require the integration of some type of processing unit or an ASIC design. The second requirement is to communicate with other devices, this can be thought of in two ways, either it passes information to a secondary unit or information is passed to itself altering its behaviour. This could be thought of as a feedback control system, though any sensor that can adapt or warn the user about environmental conditions requires some decision making mechanism, for example a temperature sensor for detecting over heating.

It can be considered the long term goal of many electronic nose researchers to develop the smart gas sensor. Such a device would integrate the transducer circuitry with the sensor allowing some on-board decision making process. In addition, this circuitry could be used to compensate for temperature, humidity and drift over the life time of the sensor, as well as having some discriminatory hardware/software for the identification of complex odours. Such research may culminate in the 'nose on a chip', though this goal is still some way off and as yet there are no gas sensors that can be considered as truly smart.

1.3 Commercial electronic noses

Many commercial electronic nose companies have appeared as off-shoots of university research (e.g. Neotronics Scientific, Alpha MOS, Osmetech from Warwick, Southampton, UMIST Universities). This university research, combined with the many commercial applications has led to improvements in both sensor technologies and pattern recognition techniques. These instruments should not be confused with sensors or sensor systems which detect only simple single chemicals, but are designed to measure and quantify chemical signals from complex odours, where there may be over a thousand different chemical components.

There are a number of different sensor technologies available to the electronic nose engineer, described earlier, though no two instruments are based on exactly the same technology as over two hundred patents cover this field. Some commercial electronic nose instruments are listed in table 1.2.

Product name	Supplier	Sensor type	No. of sensors
αFox 3000/4000/5000 αCentauri αPrometheus	Alpha MOS France	Metal oxide resistors, SAW, Conducting polymer resistors (includes mass spectrometer)	6/12/18
3320 VOCmeter	AppliedSensor (use to be Nordic sensors and Lennartz Electronics)	MOSFET, IR CO_2 sensor, Metal oxide resistors	15
Osmetech Microbial Analyser	Osmetech, UK	Conducting polymer resistors	32
BH 114	Bloodhound sensors Ltd, UK	Metal oxide resistors	14
Cyrano 320	Cyrano Sciences inc. USA	Carbon black composite polymer resistors	32
eNOSE 5000	Marconi, UK	Metal oxide resistive, BAW, SAW, Conducting polymer resistors	12
MOSES II	Lennartz Electronics GSG, Germany	Quartz microbalance, Metal oxide resistors Calorimeters Electrochemical sensors	24
Olfactometer	HKR Sensor Systems GmBH, Germany	Quartz microbalance	6
Scentinel	Mastiff Electronics Ltd, UK	Conducting polymer resistors	16

Table 1.2: Commercially available electronic nose instruments.

The cost of these commercial products is still very high (usually £30,000 to £150,000), and there is no generic system which results in each instrument being tailored to the

specific application. Furthermore, these instruments are large, bulky, with high power consumption and are designed specifically for a laboratory environment where factors such as temperature and humidity can be controlled. More recently, there has been the development of a portable, low cost electronic nose instrument by Cyrano Sciences (Cyrano A320) based on resistive conducting polymer sensors costing under 8,000 Euros. This is the first generic hand held instrument designed for multiple applications outside the laboratory.

1.3.1 Applications of electronic noses

The first two major applications for electronic nose instruments was in the food and beverages industries [1.29]. The use of electronic nose instruments within the food industry has varied from assessing the freshness of seafood products (fish, oysters, squid etc.) [1.30, 1.31], through to the maturity of cheeses. The other main market has been in the beverages industry, where electronic nose instruments are used for assessing the quality of lagers, beers and spirits [1.32]. Since then there has been similar applications in the perfume, packaging and pharmaceutical industries [1.33].

New markets for these instruments are now appearing in environmental monitoring and medical diagnostics. In both of these applications electronic nose instruments are being used to monitor the release of chemicals by bacteria from either an environmental source, such as cyanobacteria in ponds or streams, or in medical applications such as *E. coli* [1.34, 1.35].

Lastly, and prospectively the most lucrative market for electronic nose instruments/gas monitors is in the automotive industry. Here companies are interested in monitoring the air quality within the cabin of the car. Clearly, present electronic nose instruments are both too bulky and expensive for the mass market, where car companies are looking for a 1 million sensor yield a year at a cost of much less than 50 Euros. The solution to this problem is the development of a smart gas sensor, possible employing CMOS technology, to create a small, integrated sensor with a high yield, good repeatability and most importantly at a low cost. These companies have strict requirements of what they expect from these instruments. A typical specification for such an electronic nose/gas monitor is given in table 1.3 [1.36].

Power, signal and environmental conditions	Requirement	**Target gases**	Concentration
Supply voltage	5 volts	O_2	-
Signal levels	0.5 – 4.5 volts	CO	0 – 300 PPM
Temperature (storage)	-40 to +55 ^oC	NOx NO	0 – 250 PPM
		NO2	0 – 100 PPM
Temperature (operating)	0 to 55 ^oC	n-pentane	0 – 100 PPM
Humidity	15-98 % r.h.	n-hexane	50 PPM
Lifetime	10 years	Benzene	0 – 100 PPM
Response time	< 0.5 seconds	Toluene	0 – 500 PPM
Relaxation time	20 seconds	Xylene	0 – 1000 PPM
Size	$6 \times 6 \times 6$ cm^3	Trimethyl-benzene	0 – 100 PPM
Calibration	At factory	VOC (human origin)	-

Table 1.3: A typical specification for a cabin monitor for the automotive industry

It may be many years before any electronic nose instrument is able to fulfil these requirements as no device or sensing material has, at present, these characteristics.

1.4 Aims of the project

As stated earlier, two of the major problems with many gas sensor technologies is the high cost of fabrication and the inability to integrate control and processing circuitry with the sensor. Such a combination could lead to a low cost, reproducible sensor for the hand-held electronic nose and automotive markets. Hence, the aims of this project are to look at possible sensor technologies that are CMOS compatible and, in the future, could allow circuit integration, assisting in the development of the first fully integrated smart sensor and 'nose on a chip'. This work will centre on the detection (sensor) part of the electronic nose instrument. The base technology will be either standard bulk CMOS technology or silicon-on-insulator (SOI) CMOS technology. This SOI technology has been chosen for a number of reasons, though most significantly transistors formed in SOI technology can operate at significantly higher temperatures than in bulk CMOS. Sensor structures formed in these technologies will use a number of different sensing materials which are compatible and appropriate to the operational

temperature. Lastly, sensor structures will be pre-dominantly based on the MOSFET, due to its supremacy in VLSI design. The bulk CMOS devices will use a MOSFET sensing structure and the SOI devices will rely on a MOSFET heater with an additional sensing structure (either a chemoresistor or a MOSFET) on a thin membrane. Hence, the main objectives of the research may be summarised as:

- The design and development of novel CMOS compatible gas/vapour sensors, employing field effect transistors (FETs), using either bulk CMOS for room temperature operation (< 100 ^{o}C) or SOI CMOS for high temperature operation (30-300 ^{o}C).
- The static and dynamic characterisation of novel room temperature (< 100^{o}C) chemical FET (chemFET) sensors with conducting polymer films. Their response to analyte concentration and the effect of environmental factors (water concentration and temperature) on the response and the baseline.
- The development of new empirical and theoretical models for room temperature chemFET sensors for the response, to analyte concentration, water concentration and temperature under static conditions.
- Modelling and electro-thermal characterisation of SOI based sensors, utilising MOSFET heaters on a SOI membrane, with either a resistive or chemFET sensing structure with an appropriate vapour sensitive film.

1.5 Outline of thesis

The thesis describes the design, development and evaluation of some CMOS compatible gas/vapour sensors. The first chapter reviews the mammalian olfactory system, present electronic nose instruments and their applications. Also included are the aims and objectives of this thesis.

Chapter 2 further reviews many of the background technologies used in the project. This includes the operation and history of high and room temperature MOS and FET based sensors. In addition, by a discussion on conducting polymer resistive sensors, with a brief description of the sensing mechanisms involved.

Chapters 3 and 4 cover new research into the design and development of these CMOS compatible gas/vapour sensors. This includes the rules and concepts that should be followed to produce a useable design, concluding in the realisation of these sensors.

Included are thermal and mechanical simulations of these novel heater structures based on SOI technology. Chapter 4 discusses the different methods for active material deposition. This describes the conducting polymers used in this research; the electrochemically deposited, composite and chemically pre-pared/electrochemically doped polymers, covering the material structures and thickness measurements.

Chapter 5 covers the design and development of a new chemical test station and associated electronics. The test station is designed to produce specific concentrations of an analyte at a fixed temperature and humidity and measure the response of the sensors with a custom built electronic interface. This dynamic test station is used in the collection of all the data used in this thesis.

Chapter 6 and 7 discusses the dynamic and static responses of these new room temperature polymer based FET sensors, showing typical results to two analytes. Also described are the effects of temperature and humidity on both the response and the baseline, the first full characterisation of many of these types of sensor. Included, are discussions of the operation on these sensors and how this relates to the interactions between the analyte, vapour sensitive material and the device. From these discussions and results, models have been produced to describe the effect of analyte, humidity and temperature on the response and the baseline.

Chapter 8 describes the evaluation of these new SOI CMOS sensors. Thermal and electrical profiling of the MOSFET heaters is performed, investigating both the power consumption and the effect of temperature on the FET heaters and temperature sensors. Lastly, a brief description of these devices as vapour sensors, including their response to two analytes.

Chapter 9 concludes this research discussing the results and how these have fulfilled the aims of the project. Lastly in further work, the latest developments from the research are presented and possible advancements for electronic nose instruments proposed.

1.6 References

1.1 K. C. Persaud and P. Pelosi, An approach to an electronic nose, Artificial Internal Organs, 31 (1985), 297-300.

1.2 J. D. Hartman, A possible objective method for the rapid estimation of flavours in vegetables, Proc. Am. Soc. Hort. Sci., 64 (1954), 335.

1.3 W. F. Wilkens and J. D. Hartman, An electronic analog for the olfactory processes, Ann. NY Acad Sci., 118 (1964), 608.

1.4 S. Zaromb and J. R. Stetter. Theoretical basis for identification and measurement of air contaminants using an array of sensors having partially overlapping sensitivities, Sensors and Actuators, 6 (1984), 225-243.

1.5 J. W. Gardner, P. N. Bartlett, A brief history of electronic noses, Sensors and Actuators B, 18-19, (1994), 211-220.

1.6 J. W. Gardner and P. N. Bartlett, Intelligent ChemSADs for artificial odour-sensing of coffees and larger beers, *Olfaction and Taste XI*, (1994), 690-693.

1.7 J. L. Davis and H. Eichenbaum, Olfaction, The MIT Press (1991).

1.8 S. Firestein and G. M Shepherd, Olfactory receptors share antagonist homology with other g-protein receptors, J. Physiol., 430 (1991), 135-158.

1.9 H. B. Barlow, J. D. Mollon, The Senses, Cambridge University Press (1982).

1.10 L.B. Haberly, Neural circuits in olfactory cortex: anatomy and functional implications, *Chem. Sens*, **10**, (1985), 219-238.

1.11 J. W. Gardner and P. N. Bartlett, Electronic Noses: Principles and Applications, Oxford University Press (1999), 67-72.

1.12 A. C. Pike, *PhD Thesis*, University of Warwick, Coventry, CV4 7AL, UK, 1996.

1.13 D. A. Buttry and M. D. Ward, Measurement of interfacial processes at electrode surface with the electrochemical quartz crystal microbalance, Chem. Rev. 92 (1992), 1355-1379.

1.14 J. W. Grate, S. J. Martin and R. M. White, Acoustic wave microsensors: Part1 & 2, Anal. Chem., 65 (1993), 940A-948A & 987A-996A.

1.15 P. N. Bartlett and J. W. Gardner, Odour sensors for an electronic nose, In *Sensors and Sensory Systems for electronic noses*, (ed. J. W. Gardner and P. N. Bartlett) NATO ASI Series, Vol. 212, 1992, 31-51.

1.16 B. S. Hobbs, A. D. S. Tantrum and R. Chan-Henry, Liquid electrolyte fuel cells. In *Techniques and mechanisms in gas sensing* (ed. P. T. Moseley, J. O. W. Morris and D. E. Williams), 1991, Adam Hilger, Bristol, 161-188.

1.17 I. Lundström, Hydrogen sensitive MOS structures, Sensors and Actuators, **1**, (1981), 403-426.

1.18 T. A. Dickinson, D. R. Walt, J. White and J. S. Kauer, A chemical-detecting system based on a cross-reactive optical sensor, Nature, **382**, (1996), 697-700.

1.19 P. T. Moseley, A. M. Stoneham and D. E. Williams, Oxide semiconductors: patterns of gas response behaviour depending on material type. In *Techniques and mechanisms of gas sensing*, ((ed. P. T. Moseley, J. O. W. Morris and D. E. Williams), 1991, Adam Hilger, Bristol, 108-138.

1.20 E. Jones, The pellistor catalytic gas sensor, In *Techniques and mechanisms of gas sensing*, ((ed. P. T. Moseley, J. O. W. Morris and D. E. Williams), 1991, Adam Hilger, Bristol, 17-31.

1.21 J. W. Gardner, A. Pike, N. F. de Rooji, M. Koudelka-Hep, P. A. Clerc and A. Hierlemann, Integrated array sensor for detecting organic materials, *Sensors and Actuators*, B, **26-27**, (1995), 135-167.

1.22 M. Cole, J. W. Gardner, P. Scivier and J. E. Brignell, Characterisation of a current chip for an array of six resistive microbridges. *Proc. Eurosensors XII*, Southampton, 1998.

1.23 P. I. Neaves and J. V. Hatfield, A new generation of integrated electronic noses, *Sensors and Actuators*, B, **26-27**, (1995) 223-231.

1.24 J. W. Gardner and P. N. Bartlett, Electronic Noses: Principles and Applications, Oxford University Press (1999), 117-138.

1.25 H. Bates, W. Göpel and J. Hesse, Sensors Update, VCH, Vol. 2 Weinheim, (1996).

1.26 J. W. Gardner, Detection of vapours and odours from a multisensor array using pattern recognition. Part 1: Principal components and cluster analysis, *Sensors and Actuators* B, 4 (1991), 109-116.

1.27 S. Haykin, Neural Networks. A comprehensive foundation, Macmillan Publishing, 1994.

1.28 J. W. Gardner, Microsensors: principles and applications, John Wiley & Sons (1994), 269-278.

1.29 P. N. Bartlett, J. M. Elliott and J. W. Gardner, Electronic noses and their application is the food industry, *Food Technology*, Vol. 51, No. 12, (1997), 44-48.

1.30 R. Olafsson, E. Martinsdottir, G. Olafdottir, S. I. Sigfusson and J. W. Gardner, Monitoring the fish freshness using tin oxide sensors, In Sensors and Sensory Systems for electronic noses, (ed. J. W. Gardner and P. N. Bartlett) NATO ASI Series, Vol. 212, 1992, 257-272.

1.31 M. Schweizer-Berberich, S. Vaihinger and W. Göpel, Characterisation of food freshness with sensor arrays, *Sensors and Actuators* B, 18-19, (1994), 282-290.

1.32 T. C. Pearce J. W. Gardner, S. Freil, P. N. Bartlett and N. Blair, Electronic nose for monitoring the flavours of beers, *Analyst*, 118 (1993), 371-377.

1.33 H. Ulmer, J. Mitrovics, G. Noetzel, U. Weimar and W. Göpel, Odours and flavours identified with hybrid modular sensor systems, *Sensors and Actuators B*, **43**, (1997), 413-422.

1.34 J. W. Gardner, M. Craven, C. Dow and E. L. Hines, The prediction of bacteria type and culture growth phase by an electronic nose with a multi-layer perceptron network, *Meas. Sci. Technology*, 9, (1998), 120-127.

1.35 H. W. Shin, E. Llobet, J. W. Gardner, E. L. Hines and C. S. Dow, The classification of the strain and growth phase of cyanobacteria in potable water using an electronic nose system, *IEE – Sci. Meas. Technol.*

1.36 Electronic Chemical Imaging for Automotive Applications, CIA, CAA Cabin air analyser specification, 1996.

CHAPTER 2

MOS processes, materials and resistive sensor technologies employing catalytic metals and conducting polymers

2.1 Introduction

At present there are many types of gas and chemical sensor based on a range of operating principles. This chapter gives a brief introduction into a number of these technologies, covering recent research and accepted theories relevant to this work. These discussions are separated into three main device/sensor types, FETs, MOS capacitors and discrete resistive devices utilising catalytic metals, conducting polymers and metal oxide sensing films.

2.2 GasFET and MIS capacitor devices.

Silicon based semiconductor gas sensors have been of interest to researchers, since they was first reported by Lundström and co-workers in 1975 [2.1,2.2]. Here a MOSFET with a palladium gate electrode was used to sense hydrogen gas and since then many other materials and gases have been investigated. The main focus of his research has been the development of gas sensitive Metal Insulator Semiconductor Field Effect Transistors (MISFETs, GasFETs or chemical FETs, (ChemFETs)) and MIS capacitors (MISCAPs)).

Lundström and co-workers have developed a theory for the operation of these gasFETs and MIS capacitors in both an inert atmosphere and in the presence of oxygen

(covered in review articles [2.3,2.4,2.5,2.6]). Experiments have shown that this sensitivity to hydrogen can be measured over a dynamic pressure range of 14 orders of magnitude without the sensor saturating.

The basic theory regarding a GasFET or MIS capacitor with a Pd electrode (or similar catalytic metal, such as Pt) sensitivity to hydrogen is by a modulation in the flat band potential. Such devices are shown schematically in figure 2.1. Here a standard, *n*-type MOSFET with a *n*-diffused source and drain in a lightly *p*-doped substrate and MOS capacitor is shown.

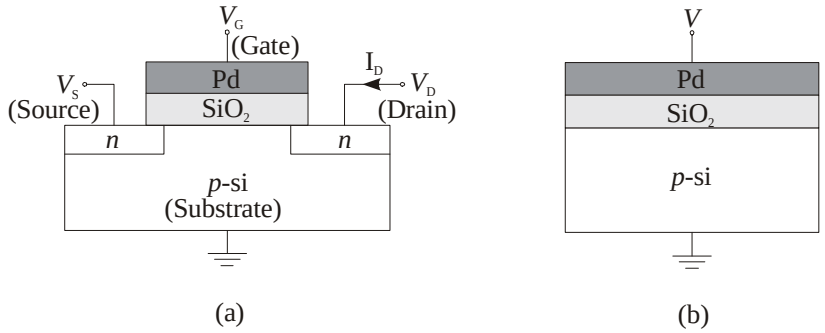

Figure 2.1: Schematic of (a) GasFET and (b) MISCAP.

If we consider a GasFET with a thick Pd-gate film (≈ 100nm), hydrogen gas molecules are absorbed at the surface of the palladium by disassociating into atomic hydrogen. These atoms diffuse through the metal and absorb on the inner surface of the gate-insulator junction where they become polarised as shown in figure 2.2.

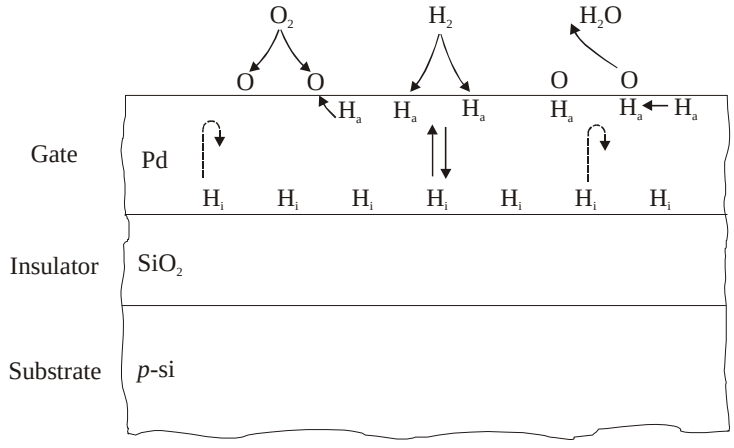

Figure 2.2: Dipole formation in a Pd-MOS device.

The resulting dipole layer is in equilibrium with the outer layer of chemisorbed hydrogen and hence in phase with the gas. The dipole layer produces an abrupt rise in the surface potential at the metal-oxide interface. This voltage subtracts from the gate

voltage already applied, shifting the I-V characteristics of the FET device to the left. In the presence of oxygen (or other oxidising gases) further chemical reactions take place on the surface of the catalyst. Water molecules are formed, reducing the number of hydrogen atoms available at the Pd-insulator surface. When the hydrogen is removed from the ambient atmosphere, the atomic hydrogen within the MOSFET recombine into hydrogen molecules, which desorb from the surface. If the atmosphere contains oxygen then this recombination is dominated by the production of water. Once the hydrogen has been removed from the metal/insulator interface the potential between the Pd and the insulator returns to its initial level. This shows that the reaction is totally reversible, though the recovery rate can be very slow and may take a number of hours. The reaction described above occurs at room temperature though to increase the speed of the response and to rapidly remove water molecules from the metal surface, the sensors are normally operated of 150 ^{o}C to 200 ^{o}C.

The gasFET response is either measured as a shift in gate-source voltage (V_{GS}) or drain-source current (I_{DS}), and it has been shown that this response is related to a shift in the threshold voltage. This shift in threshold voltage is usually defined as:

$$V_T = V_{T0} - \Delta V \qquad (2.1)$$

where V_{T0} is the initial threshold voltage and ΔV is the potential produced by the formation of the dipole layer. To investigate which terms could be affected by exposure to a gas or vapour it is useful to define that parameters that make up the threshold voltage. This threshold voltage can be described as [2.7]:

$$V_T = V_{FB} + \phi_{si} - \frac{Q_B}{C_o} = \phi_{ms} + \phi_{si} - \frac{Q_o}{C_o} - \frac{Q_B}{C_o} \qquad (2.2)$$

where V_{FB} is the flat band voltage, ϕ_{si} is the surface potential, ϕ_{ms} is the difference in work function between the metal and the semiconductor, Q_B is the bulk charge, C_o is the oxide capacitance and Q_o is the charge at a zero gate voltage. Some of these terms can be further defined and shown to be constant. The oxide capacitance C_o can be expanded to:

$$C_o = \frac{K_o \varepsilon_o}{x_o} \qquad (2.3)$$

where K_o is the dielectric constant, ε_o is the permittivity in a vacuum and x_o is the thickness of the gate oxide per unit area. The bulk charge term can be further expanded and has been shown to equal:

$$Q_b = -qN_a\sqrt{\frac{2K_s\phi_{si}}{qN_a}} \quad (2.4)$$

where K_s is the dielectric constant for silicon, q is the electron charge and N_a is the density of acceptor atoms. Under strong inversion this can be re-written (for an external applied voltage φ), as:

$$Q_b = -\left[2qK_s\varepsilon_o N_a\left(\varphi - \phi_{si}\right)\right]^{1/2} \quad (2.5)$$

Note that φ is the voltage for a *n*-inversion with respect to the *p*-substrate. In addition, the work function of silicon can be further defined and shown to be dependent only on the thermal voltage and the difference between the fermi level and the midband gap energy, defined as:

$$\phi_{si} = 2\phi_f + 6\phi_T \quad (2.6)$$

where ϕ_T is thermal voltage and ϕ_f is defined as:

$$\phi_f = \phi_T \ln\frac{N_a}{n_i} \quad (2.7)$$

where n_i is the intrinsic carrier density. Though this term is temperature dependent the thermal voltage and doping levels are not effected by any exposure to gases or vapours. Furthermore, the parameters in expressions (2.3) and (2.5) these values are device specific and cannot be altered by exposure of a active gas or vapour. The last term is the difference in work function between the metal and the semiconductor expressed as:

$$\phi_{ms} = \phi_m - \phi_s = \left(E_{vac} - E_m\right) - \left(E_{vac} - E_{fc}\right) \quad (2.8)$$

where E_{vac} is the vacuum energy level, E_{fc} is the Fermi level of the substrate and E_m is the Fermi level of the gate material. It is this term which can be altered by the formation of a dipole layer and so the shift in work function can be defined as:

$$\phi_{ms} = \phi_{ms0} - q\Delta V \quad (2.9)$$

Hence in the presence of this dipole layer it is the barrier height at the metal-insulator layer that is changed, given by:

$$\Delta V = n_h\frac{p}{\varepsilon_O} = n_i\frac{Qd}{\varepsilon_O} = \frac{\sigma_i d}{\varepsilon_O} \quad (2.10)$$

where n_h is the number of hydrogen atoms per unit area at the inner surface and p is the effective dipole moment when absorbed, Q is the dipole charge, σ_i the charge concentration and d the effective charge separation. The chemical reactions that occur by the absorption of hydrogen can be stated as:

$$H_2 \underset{d_1}{\overset{c_1}{\Leftrightarrow}} 2H_a \qquad \text{and} \qquad O_2 \Leftrightarrow 2O_a$$

$$4H_a + O_2 \rightarrow 2H_2O \tag{2.11}$$

The production of water has more steps than shown here, through the absorption of OH groups. This H_a term defines the hydrogen concentration at the surface of the gate material and c_1 and d_1 are the absorption/disassociation and de-absorption/association reaction rates. The hydrogen at H_a diffuses into the metal/insulator interface, but remains in equilibrium with the hydrogen concentration at the surface, thus:

$$H_a \underset{d_1}{\overset{c_1}{\Leftrightarrow}} H_i \tag{2.12}$$

where H_i is the concentration of hydrogen at the metal/insulator.

Above we have described this response in terms of the number of atoms at the interface. This can be related to the oxygen and hydrogen concentrations in ambient atmosphere, so:

$$c_1 P_{H_2} F_e^2 = d_1 n_e^2 + f\left(P_{O_2}\right) n_e^2 \tag{2.13}$$

where P_{H_2} and P_{O_2} are the partial pressures of H_2 and O_2 and n_e is the number of hydrogen atoms absorbed at the surface of the gate. Lastly, the term F_e defines the number of unabsorbed sites containing neither H_2, O_2 nor H_2O. From equation (2.13), we can see that the left hand side is the probability of a hydrogen molecule finding an unoccupied site, being absorbed and disassociating into two hydrogen atoms. The right hand side of the equation is the probability of two hydrogen atoms recombining into a water molecule. The function $f(P_o)$ depends on the reactions which control the formation of water. If we use this equation as being analogous to the conditions on the metal/insulator interface we get:

$$c n_e F_i = d n_i F_e \tag{2.14}$$

where F_i is the number of unoccupied absorption sites at this interface and n_i is the number of atoms at the interface. From the assumptions used for equation (2.14) we can state that:

$$\frac{n_i}{F_i} = \frac{\Delta V}{\Delta V_{TMAX} - \Delta V} \tag{2.15}$$

In addition, we know that sites at this interface can either be unoccupied or occupied thus combining equation (2.14) and (2.15), we get:

$$\frac{\Delta V}{\Delta V_{TMAX} - \Delta V} = \frac{c}{d}\sqrt{\frac{c_1 P_{H_2}}{f(P_{O_2}) + d_1}} \qquad (2.16)$$

This equation fits the experimental results to a high degree of confidence, with a maximum shift in the threshold voltage of around 0.5 volts. The $f(P_O)$ function is defined as $k_1 P_{O_2}$ for temperatures below 50 ^oC, otherwise $k_1\sqrt{P_{O_2}}$, where k_1 is a constant rate parameter.

Experiments have shown that this model is only a simplified version of the true response. By using UHV (Ultra High Vacuum) over a large pressure range it has been shown that the absorption of hydrogen at the interface leads to a Temkin-like isotherm [2.8]:

$$\theta = a\left[\frac{1}{2}\ln\left(\frac{P_{H_2}}{P_C}\right) + \ln\left(\frac{1-\theta}{\theta}\right)\right] \qquad (2.17)$$

where a and P_C are temperature dependent constants and θ is the coverage of hydrogen at the Pd-SiO_2 interface. This in practice means that $\theta \approx \ln P_{H_2}$. More recently measurements by Fogelberg et al.[2.9] have shown that the dipole moment associated with the absorption of hydrogen atoms is quite large (2 dB). This is significantly greater than would be expected for a simple dipole moment model on the surface or partially inside the metal at the metal-insulator interface. Thus the hydrogen atom must absorb into the oxide side of the interface. A more realistic model, assumes that absorbed hydrogen atoms behave as laterally mobile dipoles, and thus the mean charge distribution can be treated as two homogenous charged sheets. When a new dipole is formed at the interface, it will experience a repulsive electrostatic force from the presence of existing dipoles. Thus the work in forming a new dipole will reduce the heat of absorption, equalling:

$$\Delta H_i = \Delta H_{i,O} - q\Delta V = \Delta H_O - q\left(\frac{pn_i}{\varepsilon_O}\right) \qquad (2.18)$$

where $\Delta H_{i,O}$ is the initial heat of absorption with a value of 0.86 eV/hydrogen atom, thus the absorption energy decreases with hydrogen concentration. When the hydrogen coverage is high, the heat of absorption falls to the level of the bulk Pd ($\Delta H_i \approx 0.1$ eV/Atom) and hydrogen will accumulate in the bulk. This will cause expansion of the

Pd lattice (described as blistering), which will inhibit the operation of the sensor. A practical limit for hydrogen surface density has been measured at $1 \times 10^{18}\,m^{-2}$.

The coupling between the surface and the interface is also more complex than described earlier, where earlier it was assumed that the diffusion through the metal is so quick that the surface and interface are in equilibrium. However, under transient conditions where the interface goes towards almost complete hydrogen saturation, then extremely long time constants appear. The energy barrier can account for these time constants for a hydrogen atom entering the interface state. Furthermore, it has been shown that the chemistry on the metal surface can be contrary from the model shown in figure 2.1 [2.10]. This describes a situation where hydrogen molecules are disassociating on an empty surface. Also that hydrogen atoms are not blocked by oxygen or OH groups. This revised model can more accurately describe the behaviour of the Pd-SiO_2-Si structure with and without ambient oxygen. The coverage of hydrogen at the surface for Pd and Pt can be modelled by:

$$\frac{dn_s}{dt} = 2FS_H \frac{N_s - n_s}{N_s} - d_s \frac{n_s^2}{N_s} - \frac{dn_i}{dt} \qquad (2.19)$$

where n_s is the number of absorbed hydrogen atoms, N_s the number of absorption sites, F is the hydrogen molecular flux (which is proportional to the hydrogen pressure P_{H_2}), S_H is the initial sticking coefficient for hydrogen absorption and d_s is the desorp-absorption rate. This expression is for hydrogen in a vacuum or inert gas, in the presence of oxygen, becomes:

$$\frac{dn_s}{dt} = 2FS_H \frac{N_s - 4n_O - 4n_{OH} - n_s}{N_s} - d_s \frac{n_s^2}{N_s} - r_{OH} \frac{n_O n_s}{N_s} - r_{H_2O} \frac{n_{OH} n_s}{N_s} - \frac{dn_i}{dt} \qquad (2.20)$$

where n_{OH} and n_O is the number of absorbed atoms. It is interesting to note that one oxygen atoms blocks four hydrogen absorption sites.

Sensitivity to ammonia and improved sensitivity to hydrocarbons, has been reported with thin gates using the catalytic metals Pd, Pt, and Ir [2.11]. These gates are made so thin as to be discontinuous and so porous (gap sizes 1-10 nm), though still electrically continuous. This response is due to the absorbed vapour causing an electrical polarisation on the surface of this thin metal gate. Such an occurrence happens with thick films though the metal between the surface and the insulator removes the effect. Initially, it was thought that a capacitive coupling of the metal film

to the insulator surface explained this phenomenon, though recent work indicates that charges/dipoles on the insulator surface may give the most significant contribution.

Work by Popova et al. used sintered SnO_2 as the gate material of gasFETs for the detection of ammonia [2.12, 2.13]. It was found that a major limitation of these devices was a significant humidity dependence. A suggested model was based on the lateral transportation of NH_3^+ and OH^- ions along the gate surface with applied gate/channel and source/drain field. This weakens the bonds between the absorbed ions and the SnO_2 surface. Due to the strong non-uniformity of the channel, in the saturated regime, the positive and negative ions are redistributed causing a variation in the gate voltage.

Dobos et al. used carbon monoxide to test the porosity of the palladium gate. He showed that performing an oxidation/reduction treatment caused the gate electrode to be porous and allow the CO to effect the flat band voltage by the formation of dipole moments [2.14]. Further work by Dobos and co-workers [2.15] used a patterning technique to etch holes through the catalytic gate down to the insulator. These devices showed a response to CO explained using a theory similar to Lundström for hydrogen, where CO is absorbed on the palladium surface near the insulator. Thus the shift in threshold voltage was equated to:

$$\frac{1}{\Delta V_T} = \frac{1}{\Delta V_{max}} \frac{k_{-1}}{k_1} \frac{1}{P_{co}} + \frac{1}{\Delta V_{max}} \qquad (2.21)$$

where k_1 and k_{-1} are the forward and backward reaction rates, P_{co} is the partial pressure of CO. The ΔV_{max} calculated at 0.9 volts at 180^{o}C, with a ΔV of 10 mV at a pressure of 13.3 Pa of CO. Later papers explained the response by a reaction mechanism, where CO reacts with the oxygen and is removed as CO_2. This reduction in oxygen results in a decrease of the threshold voltage. A similar effect has been observed with NO [2.16]. Here, it was shown that above 473 K the NO dissociates into atomic nitrogen and oxygen on the catalyst surface. An explanation for the observed sensitivity is that the atomic nitrogen desorbs as N_2O with the remaining oxygen atoms combining with previously absorbed hydrogen atoms, removing them from the surface of the Pd gate. As the concentration of hydrogen at the surface and the metal-insulator interface remains constant, hence hydrogen on the insulator surface is removed, decreasing the dipole moment. As the NO or CO is removed, the hydrogen on the insulator surface returns to its previous level. Clearly, these responses only occur in a low oxygen

background where the partial pressure of hydrogen dominates and so have limited practical application outside the automotive industry for exhaust monitoring.

One limitation of catalytic gasFET sensors is the baseline drift, caused by an instability in the threshold voltage. Two causes are sodium ion contamination and hydrogen induced drift (HID). Sodium ion contamination occurs with all MOS transistors. Here, sodium ions within the insulator drift across the oxide (under the influence of an electric field), altering the main device characteristics. Minimising the applied field and using high quality fabrication procedures limits this effect (high quality fabrication refers to modern equipment in a low contaminated clean room, which leads to low sodium contamination and low number of trapped charges). Even with this contamination reduced to a minimum, these sensors are not stable enough for continuous measurement, as even trace quantities of hydrogen can cause a variation in the sensor baseline. This reaction is reversible, though it can, in some cases, have very long recovery periods (of up to hours) once the hydrogen in removed. By changing the materials used in the fabrication of the device this effect can be reduced. For example, it has been reported that by placing a layer of aluminium between the catalytic metal and the SiO_2 gate reduces this effect. Also by changing the insulating material to SiN_4, Si_3N_4 or Ta_2O_5 a similar reduction in the drift was discovered [2.17]. Nylander et al. concluded that a large proportion of this drift is due to the flat band voltage of the device and was related to the SiO_2 insulator and not the metal [2.18]. Two problems associated with these methods of reducing the drift, is that by changing the gate insulator or adding an aluminium layer, the adhesion of the catalytic metal to the gate insulator is reduced. This increases the complexity of the device and therefore the unit cost. A further limitation of present gasFET technology is the maximum operating temperature (max 250 ^{o}C before instability) that limits the range of chemicals that can be detected, as different chemicals breakdown at different temperatures. In addition, these high operating temperatures reduce the life span of these sensors, through thermal stresses and have a high power consumption, as an external heater is usually required on either the underside of the device or the package. Efforts to create sensors on membranes with an integrated heater have only been partially successful [2.19]. Lastly, the operating temperature and fabrication process (i.e. the use of a catalytic gate) is not CMOS compatible, requiring external discrete circuitry and a specialised fabrication

process, which further increases the unit cost of the final sensor, though these sensors are used in an electronic nose instrument (AppliedSensor, 3320).

2.3 Polymer based FET sensors

There has been only limited research on the application of conducting polymers as the gate material of FET chemical sensors. These sensors usually operate at room temperature and so have a low power consumption, with a wide sensitivity range due to the many available polymers. The first reported work using a polymer based FET sensor was by Josowicz & Janata in 1986 [2.25]. Here a suspended gate FET (SGFET) was fabricated with an electropolymerised polypyrrolle film deposited onto a Pt gate electrode. With SGFETs the gate consists of a metal mesh suspended around 100 nm above the insulator surface. The gas or vapour can now interact on both the inner and outer surface of the gate. It was shown that the deposition of these polymers shifted the previous threshold voltage by –70 to –380 mV depending on the polymer. Josowicz & Janata stipulated that exposure to alcohols brought about a change in the work function of the electronic conductor adjacent to the gate insulator. These devices were operated at constant current and showed a response to methanol, ethanol, i-propanol and i-butanol at a concentration of 5 μL/min giving a maximum shift in threshold voltage to methanol of 65 mV. These results showed a positive shift in threshold voltage when exposed to a vapour, suggesting that the electrons within the polypyrrole have become more tightly bound or that alcohols absorb on the polypyrrole through the –OH groups or both. Later SGFETs, using laser induced polymer deposition techniques, were fabricated by Papez et al. [2.26]. Here polypyridine films were deposited through the irradiation of pyridine and SF_6 with a focused ion beam to a thickness between 10-20 nm. These devices were tested to ethanol and ammonia (polar molecules), which produced a high irreversible change in gate voltage (≈ -500 mV) and with propylamine (non-polar) which produced a positive reversible shift. The devices exhibited an almost linear dependence to concentration throughout the test range (38 – 1150 PPM). The main problem associated with this type of sensor is the complexity of the fabrication process and the number of steps required to a) produce the suspended gate structure and b) deposit the gas sensitive layer on the active side of the gate. Additionally these sensors typically suffer from poor repeatability and significant drift. The costs and non-

standard (non-CMOS) fabrication process has made these sensors unpopular for electronic nose instruments.

Further research into conducting polymer FET sensors followed a number of years later. Barker et al. fabricated a multi-sized array of four *p*-type enhanced FET sensors, all with the same channel dimensions but with varying gap sizes etched into the insulator layer [2.27]. Polyaniline was spun coated over the device, which was patterned using a photolithography method with the excess polymer removed using nitric acid. Capacitance-voltage (CV) measurements showed an increase in the capacitance when compared with a simple air-gap, due to the polymers lower resistance, allowing a partial charging of the gate. CV measurement provides useful information about the doping profile of the gate oxide. These instruments measure the capacitance between the gate and the substrate for a sweep in the gate voltage. High frequency (100 kHz – 1 MHz) CV techniques measure only the oxide capacitor in the accumulation mode. Low frequency (< 20 Hz) or quasi-static (mHz) techniques measure the operation of the oxide over the entire operating range. Information extracted of the SiO_2/Si interface state densities together with their distribution in the band gap and the determination of fixed oxide charges provides useful information for the understanding of MOS degradation phenomena and oxide breakdown. Increasing temperature caused a rise in the threshold voltage (0.6 V increase for 30^{o}C) with polymer deposition when compared to a solid gate test structure. Lastly, these devices were tested to 8 PPM of NO_2. This produced an increase in drain current when compared to a baseline of nitrogen, though tests were not performed in ambient conditions, were the effects of humidity can be examined and so is not a true representation of how the sensors will perform in a non-defined environment.

Hatfield et al. has developed a technique where a base conducting polymer layer is deposited from pyrrole vapour [2.28]. The resulting polypyrrole film is defined using standard photolithography techniques and etched using oxygen plasma etcher. This device originated as a *p*-type enhanced ISFET (Ion-Sensitive FET used in liquid to detect certain ions and pH level [2.29]), with two gateless FETs on which the polymer is deposited and one reference FET with an aluminium gate. Results showed a change in the I-V characteristics of the sensor when tested to ethyl ethanoate and n-Butyl acetate, with an increase in drain current corresponding to an increase in concentration.

Further experiments showed a shift in threshold voltage of 17 mV to 500 PPM of methanol and 24 mV to 500 PPM of ethyl ethanoate.

Domansky, Li, Josowicz used a similar technique to fabricate both Polyaniline and composite polyaniline/polyaniline/palladium chemFETs [2.30]. The addition of Pd was used to increase the selectivity and permit analysis of complex gas mixtures by a single sensor. The first polyaniline film was spun coated onto the device, with the second layer electrochemically grown on top using a normal three-electrode electrochemical cell. Finally, this second film was doped with palladium ions. These composite sensors showed a response to hydrogen that the a sensor with only a polyaniline layer could not detect. Furthermore, both composite and single layer devices showed a sensitivity to ammonia. The response to hydrogen was explained by a modulation of the palladiums work function. Further work combined standard chemFETs and SGFETs with composite polymer/Pd materials, electrochemically grown polyaniline layers and single palladium layers to create an array of four devices, for the detection of hydrogen and ammonia [2.31]. It was shown that the composite chemFETs were very sensitive to hydrogen, with a relatively logarithmic response, between –128 mV/dec. to –143 mV/dec. at an operating temperature of 90^{o}C. Furthermore, the ammonia sensors made of both the single polymer and composite layers showed a response of –21 to –22mV/dec. and –34 to –35 mV/dec. respectively, with only a negligible dependence to humidity concentration. Clearly, understanding the chemical reactions occurring within the sensor and active films will be difficult, as both materials will react differently to gases/vapours and to each other. Also the 90 ^{o}C operating temperature will require high power and again the SGFET design is complex and non-CMOS compatible.

Meister et al. used an electrochemical deposition technique to grow polypyrrole between two gate contacts 20 μm apart, over the gate oxide, to a thickness of 500 nm [2.32]. Here Meister stated that the response of the sensor was due to a shift in the threshold voltage brought about by a modulation of the work function between the polymer and the insulator. Operating the chemFET at constant current and with a NoPcTS-doped polypyrrole film, the gate voltage decreased from 0.54 volts to 0.51 volts under the influence of 40 PPM of dimethyl methyphophonate (DMMP). Furthermore, a CuPcTS-CIO_4 doped film, showed a sensitivity to $NO_\times$ of 180 mV for 18 PPM of $NO_\times$ in the opposite direction. This was explained by the absorbed $NO_\times$ gas

behaving as an electron acceptor increasing in work function, and DMMP acting as an electron donor decreasing the work function.

Meijerink et al., with conducting polymers, poly(pyrrole)/BSA (butane sulphonic acid) and poly(pyrrole)/TEATFB (tetraethylammonium tetrafluoroborate) carried out similar work [2.33]. These devices had channel dimension of 15 × 500 μm (channel length to width) and were exposed to different concentrations of isopropanol. The BSA doped poly(pyrrole) device showed a shift in threshold voltage of 3.5 mV for 1.68 mol/L of analyte and –22 mV at the same concentration for TEATFB doped poly(pyrrole).

In summary, though some research has been performed on FET sensors employing conducting polymer films there are still a number of gaps. Firstly, no researcher has reported a full device characterisation to analyte concentration, humidity and temperature, both on the response and on the baseline. In addition, many of the sensor structures are highly complex (e.g. SGFETs), which significantly increases the unit cost of the final product.

2.4 Resistive conducting polymer sensors

There has been considerable research in the development of resistive sensors utilising conducting polymers as gas/vapour sensors. This is only a very small part of the total work into these materials, which is dominated by research on polymers as ionic conductors (for fuel cells and batteries). For the purposes of this review these materials have been segregated into three polymer types: electrochemical deposited polymers, multi-deposited polymers and carbon black composite polymers.

2.4.1 Electrochemically deposited conducting polymers

The first use of electrochemically deposited polymer films for resistive gas sensors was performed by Lundström et al. in 1983 and later by Miasik et al. [2.34, 2.35]. Here these sensors were tested to ammonia and hydrogen sulphide showing a significant, though irreversible reaction. Later work by Bartlett et al. and Persaud et al. showed that these electrochemically deposited conducting polymers respond in a rapid reversible way to a range of organic vapours (such as methanol and isopropanol) at room temperature [2.36, 2.37]. These sensors are usually operated as a chemoresistor, where the polymer is deposited between two electrodes. This room temperature, hence low

power operation, with the ease of deposition and the many available polymers (hence sensitivities), make these films ideal for electronic noses, and many of the early electronic nose instruments were based on these sensors.

A common feature of these polymers is the presence of a conjugated π-electron system that extends over the backbone [2.38, 2.39]. Most commonly used polymers for gas/vapour sensing are based on the pyrrole, aniline and thiophene monomers. A typical deposition process requires the monomer to react to form an extended conjugated system. Electrochemical techniques are used to control the growth rate, and quality of the polymer. For deposition, a potential on the working electrode (where the polymer is deposited) is applied, this is either stepped to a potential or repeatedly cycled into the region where the monomer is oxidised and the polymer is formed. This occurs in a solution containing the monomer and a suitable background electrolyte. The counter-ion required to balance on the polymer chains is provided by the background electrolyte used in the solution. For the cyclic process, the growth of the polymer is observed as an increase in the area under the oxidation and reduction curve. The properties of the resulting film depend, not only the monomer, but the final potential, counter-ion and the growth conditions.

The most basic model of conduction for these polymers, is that radical cations are produced due to a charge transfer process that occurs between the polymer and the doping ions. It is thought that radical cations are delocalised π-electrons that have been removed from the polymer backbone. A single radical cation is described as a polaron and when two nearby polarons combine they produce a bipolaron. These polaron and biopolaron charge carriers can travel along the conjugated backbone. In this way the polymer film will conduct when an electric field is applied. Pfuger et al. have characterised the physical properties of these conducting films and concluded that there is a significant cross-linking between polymer chains. This limits the distance the charge carriers can travel [2.40]. Thus, the conductivity of the polymer film depends upon the chain length, the conjugated chain length (distance to a cross-link), and the interchain hopping barrier, i.e. the distance a charge carrier has to jump in order to transfer from one chain to another.

It has been proposed that there are five possible sites of interaction between the polymer and the vapour that could result in a change of conductance as shown in figure 2.3.

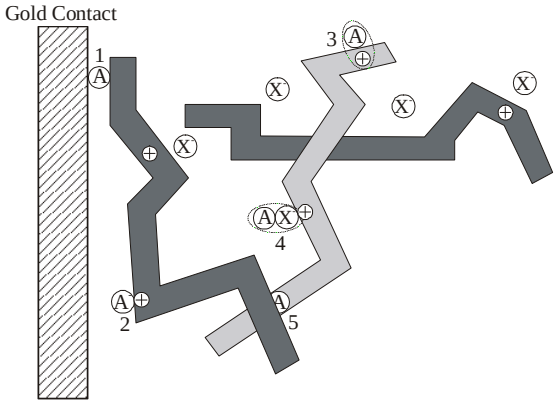

Figure 2.3: Possible interaction sites for analyte on a polymer chemoresistor.

Firstly, the response could be due to the vapour effecting the charge transfer between the polymer and the gate electrode (usually gold). Secondly, it could be through the direct generation or removal of charge carriers, by oxidation or reduction of the polymer chain. This interaction could be significant for ammonia or hydrogen sulfide, though this seems less likely for the weak interactions of organic vapours such as alcohols. Thirdly, the organic vapour could interact with the mobile charge carriers on the polymer chains and thus alter their mobility along the chain. Fourthly, the vapour could interact with the counterions X-, within the film and thus alter their mobility along the chain. Lastly, the vapour could alter the rate of interchain hopping in the material and so modulate the conductivity of the film. Though any of these interactions are possible the last three are the most likely, with the reaction probably being a combination of these three types (depending on the analyte).

Research into the effect of water concentration on the response has been sparse. Timofeeva et al. have reported the interaction of water vapour with poly(aniline) and poly(pyrrole) films [2.42]. Further work by Ingleby, Gardner and Bartlett suggested a model for the response of poly(pyrrole) and poly(aniline) [2.43] to water and ethanol vapour. They assumed that the water and ethanol are absorbed onto the same sites, i.e. a competitive binding model. They proposed that the proportion of water occupied sites (with no ethanol vapour), $\theta_h^{'}$ can be given by a standard Langmuir isotherm:

$$\theta_h^{'} = \frac{K_h C_h}{(1 + K_h C_h)} \qquad (2.22)$$

where C_h is the concentration of water and K_h is a binding coefficient, this assumes partition coefficient is 1 and dependant on the forward and backward reaction rates.

$$K_h = \frac{k_f}{k_b} \tag{2.23}$$

where k_f is the forward reaction rate and k_b in the backward reaction rate. With ethanol vapour present, (with the response also modelled to a Langmuir isotherm), the proportion of occupied sites by water and ethanol was described by:

$$\theta_h'' = \frac{K_h C_h}{(1 + K_h C_h + K_e C_e)} \quad \theta_e = \frac{K_e C_e}{(1 + K_e C_e + K_h C_h)} \tag{2.24}$$

The steady state response, in terms of device conductance, G, can now be defined by the fractional site occupancy:

$$\frac{G(\tau \rightarrow \infty) - G_0}{G_0} \approx \frac{S_h(\theta_h' - \theta_h'') - S_e\theta_e}{(1 - S_h\theta_h')} \tag{2.25}$$

where S_h and S_e are sensitivity coefficients to water and ethanol. Hence the size of the steady state response depends on the sensitivity and not the geometry. Further measurements showed that this response was absorption rate limited, i.e.:

$$\frac{G(t \gg t_{on}) - G_0}{G_0} \approx \frac{\frac{(-S_h K_h C_h - S_e K_e C_e)}{(1 + K_h C_h + K_e C_e)} + \frac{S_h K_h C_h}{(1 + K_h C_h)}}{\left[1 - \frac{S_h K_h C_h}{(1 + K_h C_h)}\right]} \tag{2.26}$$

where t is time and t_{on} is the time taken to reach a steady state. Due to the competitive nature of this model as the water concentration increases then the response to ethanol decreases. Clearly, this is a major limitation of these sensors as small shifts in environmental conditions will produce varying responses. Furthermore, it is difficult to compensate for humidity as the sensors normally used for humidity measurement are based on polymers. The response and recovery time of these sensors was shown to approximately follow a double exponential function, divided into an initial response due to exposure to or removal of ethanol, followed by a long-term response due to the vapour or drift within the polymer. This second component was found to be very long; typically 3000 seconds, using poly(pyrrole)/DSA exposed to ethanol vapour. This is another limitation, as a system containing these sensors will have a very slow sampling rate.

A number of research groups have looked into the effect of temperature on the conductivity of these polymers and have agreed that it follows a three-dimensional random hopping model based on a Mott type [2.44-2.46], given by:

$$\sigma = A\exp\left[\frac{-B}{T^{1/4}}\right] \quad (2.27)$$

where σ is the electrical conductivity, T is the temperature, A is a constant and B is given by:

$$B = 2\left(\frac{3}{2\pi}\right)^{\frac{1}{4}} \left[\frac{\alpha^3}{k_b N(E_F)}\right]^{\frac{1}{4}} \quad (2.28)$$

where α describes the spatial extent of the localised wavefunction, $N(E_F)$ is the density of states at the Fermi level and k_b is the backward reaction rate. Bartlett et al. looked at the effect of temperature on the response of the polymer films to methanol and has concluded that the constant, A, is an exponential factor. Further work by Ingleby et al. [2.47], tested polymer films at five different temperatures between 30-57 ^oC and an empirical model was suggested. A Langmuir isotherm shift in the work function, was assumed and hence, the change in conductance was described and approximated to (for a small shift in work function):

$$\frac{\Delta G}{G} \approx \exp\left[\frac{-\alpha_e K_e C_e}{kT(1 + K_e C_e)}\right] - 1 \approx \frac{-\alpha_e K_e C_e}{kT(1 + K_e C_e)} \quad (2.29)$$

For poly(aniline) the sensitivity term α_e, was shown to follow an exponential dependence, and K_e, (the binding constant) a linear dependence to temperature. Poly(pyrrole) sensors showed a significantly greater sensitivity to temperature on both the binding constant and the sensitivity term, following an exponential dependence. In both cases the increase in temperature produced a decrease in the response.

In summary, these electrochemically deposited polymers are sensitive to a broad range of gases and vapours and have a room temperature, hence low power, operation. Their main limitations are the small magnitude of the responses in comparison to other sensors types (e.g. metal oxides), which is non-linear and is significantly effected by humidity and temperature.

2.4.2 Spun or drip cast polymers

Another method of fabricating sensors, using conducting polymers, has been suggested by Persaud et al. [2.48]. Here a two-layer construction is implemented, where a chemically prepared base layer has an electrochemically deposited top layer. This two stage construction allows greater inter-electrode seperation, which improves the

robustness and the measurement of its resistance. The first level is usually spun or drip-cast onto the device and patterned using standard photolithography techniques [2.49]. An oxy-plasma etcher is then used to remove the excess polymer. This deposition technique gives accurate definition over the sensing area. The top layer is electrochemically deposited on top using a standard monomer, such as polypyrrole, poly(thiophene) or poly(aniline) with a number of different counter-ions (e.g. Cl^- & BF_4^-). Results have demonstrated, for a chemoresistor, that varying the counter-ion in a poly(pyrrole) based gas sensors can increase the sensitivity and diversity of the sensors response [2.50]. Furthermore these sensors have shown an improved discrimination, with resistances exhibiting different shifts to the same analyte depending on the counter-ion. At present there is a library of 80 different conducting polymer types, utilising different monomers and counter-ions [2.51], though at present there is little published work on the effects of humidity and temperature on the response and baseline of these sensors.

2.4.3 Carbon-black composite polymers

Carbon-black composite materials differ from those described earlier as the base polymer is non-conductive (regularly used in gas chromatography) and is made conductive by the dispersion of carbon black particles into this insulating polymer film. Resistive devices employing these composite polymers operate by a swelling effect where exposure to an organic vapour increases the resistance of the film by increasing the separation of the carbon black spheres. These composite materials are commercially used as thermister materials (e.g. carbon black/polyethylene), where thermal expansion causes an increase in resistance. Alternative applications for these materials are as pressure sensors, where the compressive stresses enhances the conduction by creating more particle to particle contacts, resulting in an overall decrease in resistance [2.52].

Lundberg and Sundqvist in 1985 accidentally discovered the chemical sensing capabilities of carbon black-filled polyethylene while examining the effects of hydrostatic pressures on these composite materials [2.53]. Here they were investigating these materials as pressure and gas transducers using electrically conducting thermoplastics manufactured by ET-Semicon®, using a PTFE/carbon black composite. It was found that these materials were sensitive to a range of chemicals is gaseous form such as butane, pentane and propane.

A few years later Ruschau et al. used carbon black composite materials with polyethylene, polyurethane and polyvinyl to create chemical sensors [2.54]. These sensors were loaded near the percolation threshold (described later), with the magnitude of the response (i.e. the swelling) depending on the solubility of the polymer and the solvent. It was shown that the response time was dependent on the polymer thickness (a log function of thickness) and the diffusion of the solvent through the polymer. Also the sensitivity to pentane, acetone, ethanol and a number of other chemicals was shown. It was found that the recovery time was significantly longer than the response time (response time 7-165 minutes depending on the solubility of the analyte).

Talik et al. looked at the use of carbon black composite materials for the detection of chlorinated hydrocarbons, using polyvinyl chloride as the polymer [2.55]. Here three methods; resistance, tensile strength and tear extensibility were used to determine the vapour concentration. It was found that only the change in conductivity gave reliable information about the concentration of the vapour. Also that the change in sample resistance was linear with concentration of CCl_4 and $CHCl_3$. Lastly, the effect of temperature was investigated on the electrical conductivity, σ, and was shown to have a temperature dependence, T, of:

$$\sigma \approx \sigma_0 \exp\left(-\frac{E_t}{kT}\right) \tag{2.30}$$

where E_t is the activation energy, k Boltzmann's constant.

Lonergan, Lewis et al. used these materials in the development of a multi-polymer sensor array for the separation of different organic vapours [2.56]. Initially the effect of carbon black to polymer mix was investigated. Clearly, the greater the carbon content the lower the resistance of the sensor. It was found that the sensors were most sensitive with a low carbon loading. A sensitivity increase of a factor of 5 was shown for a loading between 50% and 15%, though this produced sensors with very high resistances (MΩ) that makes the measurement of small variations in resistance difficult. This increase in response was due to the sensors operating near the percolation threshold. At a low carbon loading the composites are insulators, because there are no pathway of conductive particles. As the carbon black content is increased, a sharp transition occurs in which the resistivity of the composite drops sharply (up to a magnitude of 10) for very small increases in carbon black content. This transition is

described as the percolation threshold. Sensors operating in this region would be highly non-linear, though very responsive. More quantitatively, the percolation theory predicts that the resistivity of a carbon black organic polymer composite, ρ, will be given by:

$$\rho = \frac{(Z - 2)\rho_c\rho_m}{A + B + \left[(A + B)^2 + 2(Z - 2)\rho_c\rho_m\right]^{1/2}} \qquad (2.31)$$

where

$$A = \rho_c\left[-1 + (Z/2)(1 - (\nu_c/2))\right] \qquad (2.32)$$

$$B = \rho_m\left[(Z\nu_c/2f) - 1\right] \qquad (2.33)$$

and ρ_c is the resistivity of the carbon black, ρ_m is the resistivity of the polymer matrix, ν_c is the volume fraction of carbon black in the composite, Z is the co-ordination number of the carbon black particles and f is their total packing fraction $(\nu_c \leq f)$. The volume fraction of the carbon black composite at the percolation threshold, ν_p is given by $2f/Z$. Seventeen different polymers were used successfully to separate nine common organic solvents. Furthermore, from experimental results, it was shown that chemoresistors with composite polymer films respond linearly over at least a factor of 10^2 range of concentration (before the percolation threshold).

From the same research group, Doleman et al. investigated polymer blends to create detectors with additional analyte discrimination information relative to a specific sensor [2.57]. Here poly(vinyl acetate) and poly(methyl ethanoate) were mixed at various ratios of carbon black to create a number of different sensors. It was statistically shown that varying the carbon black loading ratio added diversity to sensor arrays when tested against standard fixed carbon black/polymer composite sensors.

Further research by Doleman et al. compared carbon black composite sensors to bulk conducting organic polymer and tin oxide sensors [2.58]. Here fourteen carbon black sensors were compared to eight tin oxide sensors and 12 bulk organic conducting polymer sensors in resolving nineteen test solvents. Results showed that tin oxide had the fastest response time, achieving steady state in 7 seconds, compared to carbon black composites and bulk organic polymers that varied widely from 20 – 200 seconds depending on the polymer and the film thickness. Furthermore, the magnitude of the tin oxide sensors response was around 10 times greater than that of the carbon black composites sensors and 15 times greater that the bulk organic polymer sensors. In these tests using organic vapours it was found that the resolving power of the carbon black

composite sensor arrays was significantly better than the tin oxide and bulk conducting polymer array, though the bias of this research was to prove the effectiveness of these composite polymers.

Research into these materials as gas sensors has been at constant humidity and temperature. Full characterisations of these environmental factors has not been fully reported by researchers and both of these parameters may be a limitation, for example carbon black composites can be used as humidity detectors. These sensors are now used in a commercially available electronic nose instrument, the Cyrano A320.

2.5 Metal oxide sensing films

By far the most researched material for gas sensing and the most commonly used in electronic noses is metal oxides, of which tin oxide (SnO_2) is the most popular. These materials are now widely commercially available as single devices or in arrays [2.59, 2.60]. Their popularity is due to their rapid and large responses to many gases and vapours. The metal oxide films are normally doped with a small quantity of Pd, Pt or Au and operated in a resistive configuration. The choice of temperature and catalyst can alter the sensitivity, although in all cases the resulting sensor is still sensitive to a wide range of combustible gases. The simplest sensor (known as the Taguchi-type) uses a Pt heater coil within a ceramic tube. The SnO_2 (or alternative metal oxide) is deposited over this ceramic tube and the gas is sensed as a change in conductivity brought about by combustion reactions occurring within lattice oxygen species on the surface SnO_2. The basic reactions can be described by:

$$\frac{m}{2}O_2 \;+\; \{vacant\ \ site\} \;+\; e^- \;\xrightarrow{k_1}\; \{O_m^-\} \tag{2.36}$$

$$X \;+\; \{O_m^-\} \;\xrightarrow{k_2}\; \{XO_m\} \;+\; e^- \tag{2.37}$$

$$(XO_m) \;\rightarrow\; further\ \ reaction \tag{2.38}$$

where the expressions in the curly brackets are surface effects, X is the combustible species and O_m^- is the oxygen species with an oxidation state (m = ½, 1, 2) depending on operating temperature and catalyst doping. Furthermore, the concentration of oxygen will depend upon the two reaction rates (k_1 and k_2), as the concentration of combustible species increases, the steady state concentration of O_m^- will decrease. From the above expressions we can see that the combustible gases will increase the

carrier concentration *n*', then the electrical conductivity of the material can be described as:

$$\sigma = \mu_n e n' \quad (2.39)$$

where μ_n is the carrier mobility and *e* is the elementary charge. Hence, the change in conductivity can now be coupled to the reaction kinetics by:

$$\Delta\sigma = \mu_n e \Delta n' \propto [X]^r \text{ ; Where } 0.5 < r < 1 \quad (2.40)$$

The variation in carrier mobility is a significant effect though it does not account for the magnitude of the observed response. Thus the conductance must include a concentration mobility term arising from the granular structure into which the gas can diffuse, reacting with individual granules. Then the carrier mobility is a function of the potential barrier between contacting grains by a hopping model. Hence the conductance (*G*) can now be modelled simply as a function of the potential barrier height ϕ_b:

$$G = G_0 \exp\left(-\frac{\phi_b}{kT}\right) \quad (2.41)$$

where G_0 is a temperature dependant constant. This change in the barrier height can be related to the initial and final carrier concentration in the gas by:

$$\Delta\phi_b \approx \ln\left(1 + \frac{\Delta n'}{n'}\right) \quad (2.42)$$

These expressions of the carrier concentration and potential barrier can be related back to the chemical reactions, hence:

$$\Delta G \propto \frac{k_1}{k_2}[X]^r \quad (2.43)$$

where k_1 and k_2 are the reactions rates from earlier. Thus the sensitivity and selectivity of these materials is then a function of k_1/k_2.

The main limitation of these sensors is the high operating temperature and so high power consumption. Furthermore, these sensors normally respond to broad range of different combustible gases though some selectivity is achievable by using different materials and operating temperatures. In addition, these sensors suffer from poisoning and require re-calibration regularly, are labour intensive in their fabrication and suffer from batch-to-batch variations, though these sensors are very popular for electronic nose instruments.

2.6 Conclusions

In this chapter a number of sensor technologies and materials have been described which are relevant to this study. The two main limiting factors, with nearly all of these sensor technologies, is the high operating temperature and the complex/non-standard fabrication process. This makes many of these technologies incompatible with the CMOS control circuitry and their non-standard manufacture makes the cost too high for a portable electronic nose instrument which is why many of the more complex devices (e.g. SGFETs) are not commercially available. Research on CMOS compatible devices has been very limited and those technologies that could be adapted to use standard CMOS have not been fully investigated or characterised. It is some of these deficiencies that is hoped to be covered in this study.

2.7 References

2.1 I. Lundström, M.S. Shivaraman, C.M. Svensson, L. Lundvist, Hydrogen sensitive MOS field effect transistor, *Appl. Phys. Lett.,* 26, (1975), 55-57.

2.2 I. Lundström, M.S. Shivaraman, C.M. Svensson, A hydrogen sensitive Pd-gate MOS transistor, *J. Appl. Phys.,* 46, (1975), 3876-3881.

2.3 I. Lundström, M. Armgarth, L.G. Petersson, Physics with catalytic gate chemical sensors, *CRC Critical Rev. Solid State Mater. Sci,* 15, (1985), 201-278.

2.4 A. Spetz, F. Winquist, H. Sundgren, I. Lundström, Field Effect gas sensors, in G. Sberveglieri, (ed.), *Gas Sensors*, Kluwer, Dordrecht, 1992, Vol. 1, 734-737.

2.5 I. Lundström, Field effect chemical sensors, W. Gopel, J. Hesse, J.N Zemel (eds.), *Sensors: A Comprehensive Survey*, VCH, Weinheim, Vol. 1, 1991, 467-529.

2.6 L-G Ekedahl, M. Eriksson, I. Lundström, Hydrogen sensing mechanisms of metal-insulator interfaces, *Accounts of Chemical Research,* Vol. 31, No. 5 (1998), 249-256.

2.7 E. S. Yang, *Microelectronics Devices*, McGraw-Hill, 1988, 229-253.

2.8 I. Lundström, Why bother about gas-sensitive field-effect devices, *Sensors and actuators A*, **56**, (1996), 75-82.

2.9 J. Fogelberg, M. Eriksson, H. Dannetun, L.-G. Petersson, Kinetic modelling of hydrogen adsorption absorption in thin-films on hydrogen-sensitive field effect devices – observation of large hydrogen-induced dipoles at the Pd-SiO_2 interface, *J. of Appl. Phys.,* Vol. 78 (1995), 988-996.

2.10 L. G. Petersson, H. M. Dannetun, J. Fogelberg, I. Lundström, Hydrogen absorption states at the external and internal palladium surfaces of a palladium-silicon-dioxide-silicon structure, *J. Appl. Phys.*, 68, (1985), 404-413.

2.11 F. Winquist, A. Spetz, M. Armgarth, C. Nylander, I. Lundström, Modified palladium metal-oxide semiconductor structures with increased ammonia gas sensitivity, *Appl. Phys. Lett.* **43**, (1983) 839-841.

2.12 S. K. Andreev, L. I. Popova, V. K. Gueorguiev, N. S. Soyanov, Modelling the gas-sensing behaviour of SnO_2-gate FETs, *Sensors and Actuators B*, **18-19** (1994), 540-542.

2.13 S.K. Andreev, L.I. Popova, V.K. Gueorguiev, G.D. Beshkov, Characteristics and gas-sensing behaviour of a tin-oxide-gate FET, *Sensors and Actuators B*, **8** (1992), 89-91.

2.14 K. Dobos, R. Strotman and G. Zimmer, Performance of carbon monoxide sensitive MOSFETs with metal-oxide semiconductor gates, *Sensors and Actuators*, **4**, (1983), 593-598.

2.15 K. Dobos and G. Zimmer, *IEEE Trans. Electr. Dev.* **ED-32**, (1985), 1165-1169.

2.16 J. Fogelberg, H. Dannetun, I. Lundström, L-G. Petersson, A hydrogen sensitive palladium device as sensor for dissociating NO in H_2-atmosphere, *Vacuum*, Vol. 41, No. 1-3 (1990), 705-708.

2.17 M. Armgarth, C. Nylander, C. Svensson and I. Lundström, Hydrogen-induced oxide surface charging in palladium-gate metal oxide-semiconductor devices, *J. Appl. Phys.*, Vol. 56, 10 (1984), 2956-2963.

2.18 A. Spetz, M. Armgarth, I. Lundström, Hydrogen and ammonia response of metal-oxide silicon dioxide-silicon structures with thin platinum gates, *J. Appl. Phys.*,**64**, (1988), 1274-1283.

2.19 D. Braind, B. Schoot, N.F. de Rooji, H Sundgren, I. LundströmA low power micromachined MOSFET gas sensor, *J. of Micromechanical Systems*, Vol. 9, No. 3 (2000), 303-308.

2.20 H. Svenningstorp, P. Tobias, I. Lundström, P. Salomosson, P. Martensson, L-G Ekedahl, A. Spetz, Influence of catalytic reactivity on the response of metal-oxide-silicon carbide sensor to exhaust gases, *Sensors and Actuators B*, **57**, (1999), 159-165.

2.21 A. Arbab, A. Spetz, I. Lundström, Gas sensors for high temperature operation based on metal oxide silicon carbide (MOSiC) devices, *Sensors and Actuators B*, **15-16**, (1993), 19-23.

2.22 A. Baranzahi, A. Spetz, R. Johannsson, G. Hamrefors, I. Lundström, Influence of the interaction between molecules on the response of a metal-oxide-silicon carbide, MOSiC, sensor. *Proceedings of Eurosensors IX*, (1995), 722-725.

2.23 S. Nakagomi, P. Tobias, A. Baranzahi, I. Lundström, P. Martensson, A. Spetz, Influence of carbon monoxide, water and oxygen on high temperature catalytic metal-oxide-silicon carbide structures, *Sensors and Actuators B*, **45**, (1997), 183-191.

2.24 A. Baranzahi, A.L. Spetz, M. Galvmo, C. Carlsson, J. Nytomt, P. Salomonsson, E. Jobson, B. Haggendal, P. Martensson, I. Lundström, Response of metal-oxide-silicon carbide sensors to simulated and real exhaust gases, *Sensors and Actuators*, B, **43**, (1997) 52-59.

2.25 M. Josowicz, J. Janata, Suspended gate field effect transistor modified with polypyrrole as an alcohol sensor, *Anal. Chem.*, **58**, (1986), 514-557.

2.26 V. Papez, S. Brodska, Deposition of the chemically sensitive polymer layer on SGFET gate by laser-induced chemical vapour polymerisation, *Sensors and Actuators B*, **40**, (1997), 143-145.

2.27 P.S. Barker, A.P. Mankman, M.C. Petty, R. Pride, A polyaniline/silicon hybrid field effect transistor humidity sensor, *IEE Proc. Circuits Devices Syst.*, **144**, No. 2, (1997), 111-116.

2.28 J.V. Hatfield, K.S. Chai, A conducting polymer gasFET, Proceedings Eurosensors XI, (1997), 739-742.

2.29 A. Garde, J. Alderman and W. Lane, Development of a pH-sensitive ISFET suitable for fabrication in a volume production environment, *Sensors and Actuators B*, **27**, (1995), 341-344.

2.30 K. Domansky, J. Li, J. Janata, Selective doping of chemically sensitive layers on a multisensing chip, *J. Electrochemical Soc.*, Vol. 144, No. 4 (1997), L75-L78.

2.31 K. Domansky, D.L. Baldwin, J.W. Grate, T.B. Hall, J. Li, M. Josowicz, J, Janata, Development and calibration of field-effect transistor-based sensor array for measurement of hydrogen and ammonia gas mixtures in humid air, *Anal Chem.*, **70**, (1998), 473-481.

2.32 V. Meister, K. Potje-Kamloth, Polymer-oxide-silicon-field-effect-transistor (POSFET) as sensor for gases and vapours, *Chemical Sensors III*, (1997).

2.33 M.G.H. Meijerink, M. Koudelka-Hep, N.F. Rooij, D.J. Strike, J. Hendrikse, W. Olthuis and P. Bergeveld, Gas-dependent field effect transistor with an electrodeposited conducting polymer gate contact, *Electrochemical and Solid-State Letters*, **2**, (1999), 138-139.

2.34 C. Nylander M. Armgrath and I. Lundström, Ammonia detector based on conducting polymers, *Anal. Chem. Symp. Series*, 17, (1983), 203-207.

2.35 J. J. Miasik, A. Hooper and B. C. Tofield, Conducting polymer gas sensor, *J. Chem. Soc.*, Faraday Trans. 1, 82, (1986), 1117-1126.

2.36 K. C. Persaud and P. Pelosi. Sensor arrays using conducting polymers, *In Sensors and Sensory Systems for electronic noses*, (ed. J. W. Gardner and P. N. Bartlett) NATO ASI Series, Vol. 212, 1992, 237-256.

2.37 P. N. Bartlett, P. Archer and S. K. Linh-Chung, Conducting polymer gas sensors: Part I & II, *Sensors and Actuators* (1989), 125-150.

2.38 J.W. Gardner, P.N. Bartlett, K.F.E. Pratt, Modelling of gas-sensitive conducting polymer devices, *IEE Proc.-Circuits Devices Syst.* Vol. 142, No. 5, (1995), 321-333.

2.39 J. W. Gardner, P. N. Bartlett, Electronic Noses: Principles and Applications, Oxford University Press, 1999. 78-88.

2.40 J. C. Scott, P. Pfluger, M. T. Kroudbi and C. B. Street, Electron spin resonance studies of pyrrole polymers, *Phys. Rev. b. Condens. Matt.*, 28, (1983), 2140-2145.

2.41 P.N. Bartlett, S.K. Ling-Chung, Conducting Polymer gas sensors. Part III Results for four different polymers and five different vapours, *Sensors and Actuators*, **19**, (1989), 287-292

2.42 O.N. Timofeeva, B.Z. Lubentsov, Y.Z. Sudakova, D.N. Chernyshov, M.L. Khidekel, Conducting polymer interaction with gaseous substances I, Water, *Synthetic metals*, **40**, (1991), 111-116.

2.43 P. Ingleby, J.W. Gardner, P.N. Bartlett, Effect of micro-electrode geometry on response of thin-film poly(pyrrole) and poly(aniline) chemoresistive sensors, *Sensors and Actuators **B***, 57 (1999), 17-27.

2.44 J.P. Paraneix, M. El Kadiri, H. Kuzmany, M. Mehring, S. Roth (eds.) *Springer series in solid state sciences,* Springer, Germany 1987, 23-26.

2.45 Y. Shen, K. Carneiro, C. Jacobson, R. Qian, J. Qui, Characterisation of the transport properties of conducting polymer films, *Synthetic Metals*, **18**, (1987), 77-83.

2.46 N.F. Mott, E.A. Davies, *Electronic processes in non-crystalline materials*, Clarendon Press, Oxford, 1979.

2.47 P. Ingleby, *PhD Thesis*, University of Warwick, Coventry, CV4 7AL, UK (1999).

2.48 K. C. Pesaud and P. Pelosi, Semiconducting organic polymers for gas sensing, European Patent EP 0 766 818, 1988

2.49 J. V. Hatfield, P. Neaves, P. J. Hicks, K. Persaud and T. Travers, Towards an integrated electronic nose using conducting polymer sensors, *Sensors and Actuators B*, 18-19, (1994), 221-228.

2.50 T. M. Hawkins and P. J. Travers, Counter-ion influence on the response of conducting polymer gas sensors, (Accepted for publication Sensors and Actuators), 2001.

2.51 A. N. Chaudry, T. M. Hawkins and P. J. Travers, A method for selecting an optimum sensor array,. *Sensors and actuators B,* 69, (2000), 236-242.

2.52 T. Oka, S. Yoshikawa, R.E. Newnham, J. Runt, A. Amin, Composite pressure sensors, presented *at the Annual Meet. American Ceramic Society, Cincinatti* (1988).

2.53 B. Lundberg, B. Sundqvist, Resistivity of a composite conducting polymer as a function of temperature, pressures and enviroment: Application as a pressure and gas concentration transducer, *J. Apps, Phys,* **60**, No. 3, (1986), 1074-1079.

2.54 G.R. Ruscau, R.E. Newnham, J. Runt, B.E. Smith, 0-3 Ceramin/Polymer Composite Chemical Sensors, *Sensors and Actuators,* **20**, (1989), 269-275.

2.55 P. Talik, M. Zamkowska-Wacawek, W. Wacawek, Sensing properties of the CB-PCV composites for clorinated hydrocarbon vapours, *J. of Mater. Sci.,* **27**, (1992), 6807-6810.

2.56 M. C. Lonergan, E. J. Severin, B. J. Doleman, S. A. Beaber, R. H. Grubbs, N.S. Lewis, Array-based vapor sensing using chemically sensitive carbon-black-polymer resistors, *Chem. Mater.,* **8**, (1996), 2298-2313.

2.57 B. J. Doleman, R. D. Sanner, E. J. Severin, R. H. Grubbs, N. S. Lewis, Use of compatible polymer blends to fabricate arrays of carbon black-polymer composite vapor detectors, *Anal. Chem,* **70**, (1998), 2560-2564.

2.58 B. J. Doleman, M. C. Lonergan, E. J. Severin, T. P. Vaid, N.S. Lewis, Quantative Study of the Resolving Power of Arrays of Carbon Black-Polymer Composites in Various Vapor-Sensing Tasks, *Anal. Chem.*,**70**, (1998), 4177-4190.

2.59 K. Ihokura, J. Watson, The Stannic Oxide Gas Sensor, CRC Press Inc., Florida, 1994.

2.60 J. W. Gardner, Microsensors: Principles and Applications, Wiley, 1994, 228-232.

2.61 B. J. Baliga (ed.), Epitaxial silicon technology, Academic Press London (1986), 134-147.

2.62 S. A. Campbell, H. J. Lewerenz, Semiconductor Micromachining: Volume 2 Techniques and Industrial Applications, Wiley (1998), 153-183.

2.63 P. Corcoran, PhD Thesis, University of Warwick, Coventry, CV4 7AL, UK, 1991.

2.64 J.W. Gardner, A. Pike, N. F. Rooij, M. Koudelka-Hep, P. A. Clerc, A. Hierlemann, W. Gopel, Integrated chemical sensor array for detecting organic solvents, *Sensors and Actuators B*, **26**, (1995), 135-139.

2.65 F. Udrea, J. W. Gardner, UK and World patent application BG2321336A and WO98/32009.

2.66 J. W. Gardner, F. Udrea, W.I. Milne, Numerical simulation of a new generation of high-temperature micropower and odour sensors based on SOI technology, *Proc. Of SPIE Smart Electronics and MEMs, Vol. 3673*, (1999), 104-112.

CHAPTER 3

Design of CMOS compatible devices for gas sensing

3.1 Introduction

There are, at present, several types of gas sensor technologies based on a number of different operating principles. A limitation of these sensors is the difficulty in amalgamating the gas sensitive materials with modern VLSI IC design. Here we investigate a number of these technologies that could be integrated with the control electronics inheriting many of the advantages of modern CMOS, such as low cost and high device reproducibility.

A suitable CMOS compatible device is the MOSFET, due to its dominance in the IC industry, its well-known operation, simple construction and ease of integration. Other CMOS devices utilising materials such as aluminium and polysilicon are possible though suffer from certain limitations.

Here two CMOS compatible designs are investigated. Firstly, a room temperature ($T < 100\ ^{o}C$) bulk CMOS chemFET device that could employ a conducting polymer film as the active (gate) material. Secondly, a high temperature ($T < 300\ ^{o}C$) device based on SOI CMOS, employing a MOSFET heater with either a resistive or chemFET sensing device suitable for conducting polymers, catalytic metals or metal oxides.

3.1.1 MOS technology

The development of the vacuum tube in 1906 and the invention of the transistor in 1947 have opened up the field of electronic circuit design, leading to the development of the first integrated circuit in 1958 [3.1]. These early integrated circuits, based on bipolar technology have now been superseded by the MOSFET. At present, the MOSFET is the dominant device used in VLSI (Very Large Scale Integration) and has overshadowed the other technologies for a number of reasons, though pre-dominantly due to its simple structure.

The first MOSFET was fabricated in 1960 by Kahng and Atalla [3.2]. The device had a channel length of over 20 μm and a gate oxide thickness of 100 nm. Although present day MOSFETs have been reduced in size, the choice of silicon and thermally grown silicon dioxide, used in this first MOSET, remains the most important combination. The MOS transistor is a four terminal device where lateral current flow is controlled by an externally applied vertical electric field. With no applied voltage the back-to-back *pn* junction between the drain and the source prevents current flowing. With a positive voltage on the gate in respect to the source, negative carriers provide a conduction channel between the source and the drain. Since the vertical as well as the lateral field control the current, it is known as a field effect transistor.

MOSFET technology can be subdivided into NMOS (*n*-channel MOSFET) and CMOS (complementary MOSFET), which allows both *p*-type as well as *n*-type transistors. This is achieved as either an *n*-well is formed within a *p*-substrate or a *p*-well within a *n*-substrate. Both of these technologies are popular, as NMOS requires less processing steps than CMOS and bipolar, while CMOS has lower power consumption and now dominates. In addition, these devices can be scaled smaller than other technology types, reducing the unit cost (less silicon used/more devices per wafer), the intrinsic switching time and the power consumption/switching energy of the MOSFET.

As device dimensions are scaled down, the interaction between transistors gives rise to latch-up. This latch-up is an internal feedback mechanism causing a temporary or permanent loss of circuit function. If we consider a *p*-well structure then the n^+ source, *p*-well and *n*-substrate constitute a vertical *npn* transistor, and the *p*-well, *n*-substrate and p^+ source form a lateral *pnp* transistor. The collector of each transistor drives the base of the other transistor, and so we have a positive feedback loop. When

the loop gain is greater than one, the *pnpn* device is switched to a low impedance state with large current conduction. This parasitic action interferes with CMOS circuitry and must be avoided.

3.1.2 Silicon-On-Insulator technology

Silicon-On-Insulator (SOI) has been proposed as an alternative substrate to bulk silicon, giving improved performance (speed, power consumption) and the possibility of creating completely new devices [3.3]. In simple terms an SOI wafer is made of three sections, a handle wafer, normally 300-450 μm thick, an epi-taxial layer (up to 10 μm thick) and a second thin silicon layer in which the devices are fabricated.

There are at present a number of ways of creating a SOI wafer, though the most popular and successful are based on the separation of implanted oxygen (SIMOX) or silicon direct bonding (SDB) [3.4]. In the SIMOX process, oxygen is implanted at high energy (typically 150-200 keV) with a doses of $1 - 2 \times 10^{18}$ ions/cm^2, under the surface of the wafer. Following this process the wafer is annealed close to melting point (1150^{o}C, for 3 hours), to form a buried oxide. This creates a typical SOI structure with an oxide layer 450 nm thick and a device (top) silicon layer of 150 nm thick that can be etched to produce ultra thin films.

In 1986 an alternative and simpler method of creating SOI wafers was demonstrated based on the fusion of hydrophilic silicon wafers (SDB). The bonding process is in two steps; firstly two wafers are mated in a particle free environment, both having a thermally grown oxide, and then heated to between 700-1500 ^{o}C. According to proposed mechanisms, the wafers adhere at room temperature due to hydrogen bridge bonds of chemisorbed water molecules, which react in the annealing process to form Si-O-Si bonds. Once completed the remaining device silicon is removed by either etching or polishing. Schematic representations of the SIMOX and wafer bonding processes are given in figure 3.1.

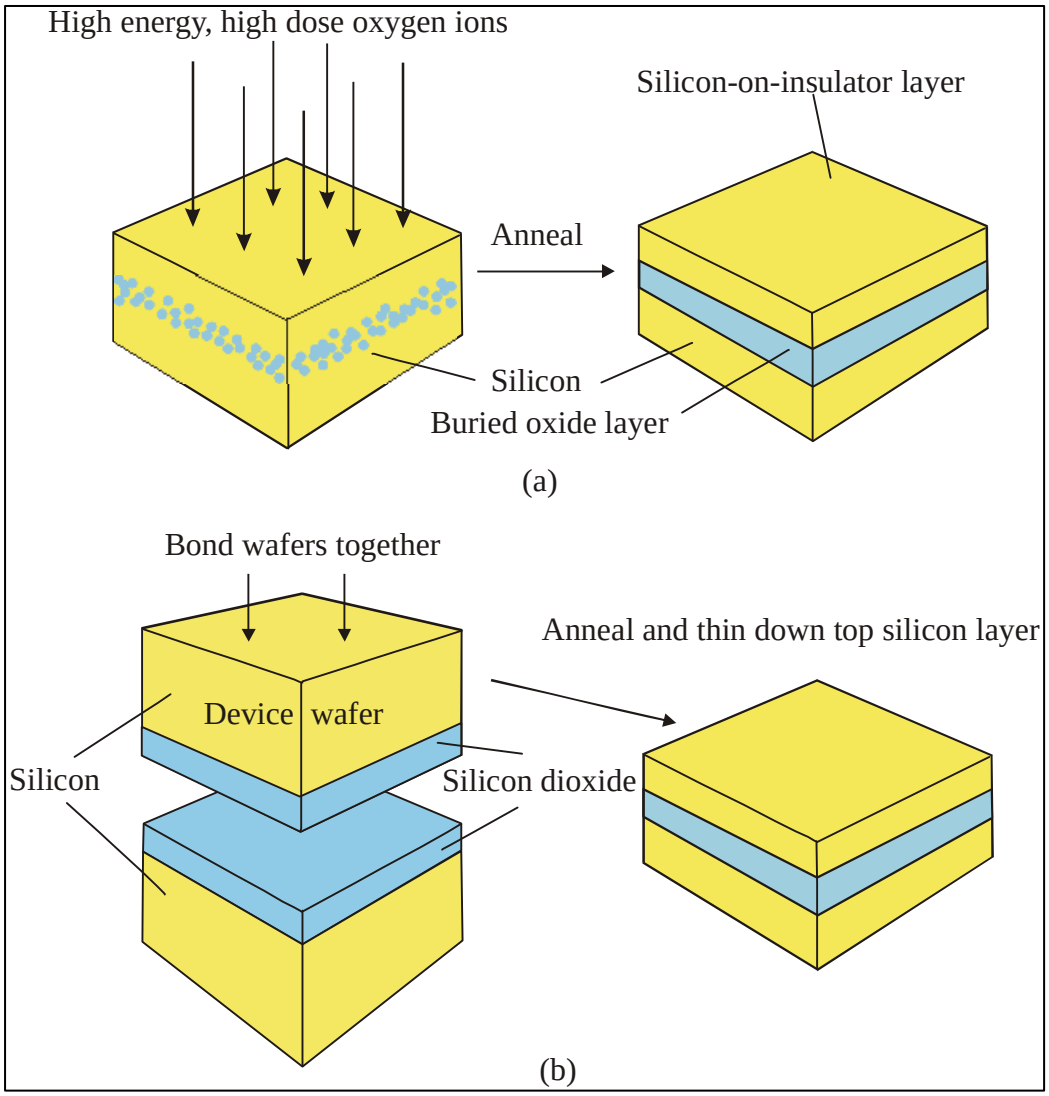

Figure 3.1: Examples of (a) SIMOX and (b) wafer bonding process in forming SOI wafers.

The fabrication of devices using SOI technology has a number of advantages over standard bulk silicon. If the SOI device silicon is thin enough then the depletion zone extends to the oxide layer and so no floating substrate is present. Hence devices using this technology have low parasitic capacitances with excellent lateral device isolation, by either oxidation of the device silicon or by narrow trenches. Furthermore, they do not exhibit kink phenomena, have a sharp sub-threshold slope, and are stable in terms of dynamic floating body effects and charge pumping phenomena. The kink phenomena occurs with devices that do not have a substrate contact, in this case a "kink" can occur at between 2 volts to 3 volts due to an accumulation of charge carriers in the source which reduces the channel resistance. Within this fully dielectrical isolated device no latch-up is possible and so no wells, well selects or guard rings are necessary. Hence SOI devices have a 20-30% high packing density. The speed of such

devices is between 50 % to 300% higher due to the smaller junction and parasitic capacitances. The increased demand for integrated power devices containing high and low power transistors is another application for SOI technology, due to the advantageous separation of the insulating oxide compared to other isolation techniques. Reduced area consumption and higher operating temperatures are feasible due to the avoidance of latch-up and leakage currents. This technology is becoming popular with IC manufactures such as Intel and IBM who are now making their next generation of processors using this technology, though at present, unit costs are 10 times higher than standard CMOS.

3.1.3 Development of resistive gas sensors utilising SOI technology

The most popular and widely available gas sensor is the resistive (Taguchi) gas sensor, as described earlier. These sensors have a good sensitivity to a range of combustible gases giving typically larger, faster responses than room temperature sensors. The main problems associated with these commercially available gas sensors is the significant power consumption (e.g. 230-760 mW) [3.5], which is unacceptable for portable gas monitors or battery powered applications. Further developments have led to commercial planar versions of these sensors (Capteur Ltd, UK), where platinum and gold is screen printed onto either side of an alumina tile, using the gold as the electrodes for the metal oxide. This has reduced fabrication variations, though the minimum feature size is still in the hundreds of micron and the power consumption is still significant at around 500 mW.

Silicon based microheaters have been suggested to both reduce feature size and power consumption, utilising either a lateral or vertical heater arrangement [3.6]. Previously, vertical heaters have been more successful due to better thermal properties and ease of mounting, where platinum (heater) layers are embedded in low stress silicon nitride. With these devices the silicon under the heater is removed to form a membrane reducing the power consumption. Though this process is based on silicon the device is still not CMOS compatible. Sensors have been developed using polysilicon as the heater, though these tend to suffer from non-linearity and poor repeatability.

Gardner and Udrea have proposed the first use of SOI technology in the design of a resistive gas sensor [3.7, 3.8]. Here the sensing structure and heater lie within the

device silicon of an SOI wafer, and the handle silicon is removed to create a membrane. The buried oxide layer acts as an etch stop and thermally isolates the sensing area reducing the power loss. Also, local oxidation provides electrical isolation for any associated electronics. This design, being CMOS compatible, allows both the sensor and the circuitry on a single chip, with only the deposition of the gas sensitive layer as a last post-processing step. The heater is a small SOI MOSFET, where the electrode and gas sensitive material are deposited on top, as shown in figure 3.2 .

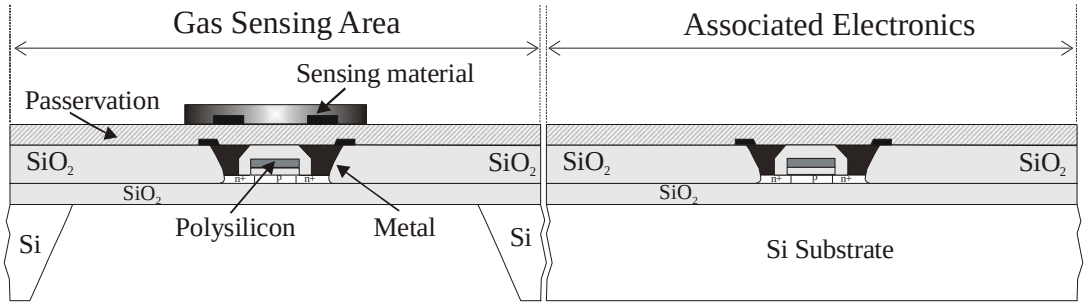

Figure 3.2: SOI sensor configuration with FET heater and associated electronics.

Also by using SOI technology both the heater and integrated circuitry should, in principle, be able to operate at significantly higher temperatures than standard CMOS. The development of these SOI gas sensors is described later in this chapter

3.2 Design of a room temperature chemFET sensor

The design and development of room temperature chemFET sensors is comparatively simple, as many of the problems associated with other higher temperature sensors (e.g. thermal losses and stresses) do not apply. The principle parameters requiring consideration in the development of these chemFET sensing structures are:

- Mode of operation
- Device dimensions
- Sensor electrode material

3.2.1 Mode of operation

Many conventional sensors are operated at either a constant voltage or constant current. The FET has a non-linear forward I-V characteristic and can be operated in three different regimes, sub-threshold ($V_{GS} < V_T$), linear ($V_{DS} < V_{GS} - V_T$) or saturated ($V_{DS} > V_{GS} - V_T$). Typically, the linear or saturated regimes are used due to the larger

signals and simpler operation. The linear regime is where the drain current (I_{DS}) varies approximately linearly with the gate (V_{GS}) and drain voltages (V_{DS}) [3.9,3.10]. The linear regime of an *n*-channel FET is given by: (the quadratic term is small and usually ignored ($V_{DS}^2 << V_{GS}V_{DS}$)):

$$I_{DS} = \frac{W}{L}\mu_n C_O\left[(V_{GS} - V_T)V_{DS} - \frac{V_{DS}^2}{2}\right] \quad 0 < V_{DS} < V_{GS}\text{-}V_T \qquad (3.1)$$

where μ_n is the effective surface mobility of the carriers in the channel, C_O is the gate capacitance per unit area, V_T is the threshold voltage, W is the channel width and L is the channel length. The response of the chemFET sensor, to an active gas or vapour, has been shown to modulate the threshold voltage [3.11, 3.12]. If we consider the linear mode of operation, the change in drain current at constant V_{GS} and V_{DS} is given by:

$$\Delta I_{DS} = -\left(\frac{W}{L}\mu_n C_O V_{DS}\right)\Delta V_T \qquad (3.2)$$

Hence it is possible to design a sensor to give an increased response due to this multiplication or gain term. Furthermore, this is a linear dependence that simplifies the measurement and post-processing steps. The easiest parameter to modify is the *W*/*L* ratio, though fabrication parameters such as the gate insulator can also be varied e.g. different thickness or an alternative material (e.g. silicon nitride). Increased response may be achieved though there are a number of drawbacks, specifically in the repeatability of the design, as any device to device variations will alter this gain factor. Also very accurate control over the applied V_{DS} will be necessary. Using constant current in the linear region is also possible, though the solution is complex, giving no advantages in either device sensitivity or post-processing.

In the saturated region, where $V_{DS} > V_{GS} - V_T$ (after pinch off), the drain current has stabilised and can now be defined by:

$$I_{DS} = \frac{W\mu_n C_O}{2L}(V_{GS} - V_T)^2 \qquad (3.3)$$

Operating the chemFET at constant current and considering only a change in the threshold voltage, before and after exposure to gas/vapour, can be equated to:

$$\Delta V_{GS} = \Delta V_T \qquad (3.4)$$

Hence, we can monitor directly any chemical interactions which effect the threshold voltage.

This has a number of advantages over operating in the constant voltage regime, specifically:

- ΔV_{GS} is now independent of W/L, μ_n, C_o and so process variations.
- Constant current circuits are easier to generate in CMOS and constant voltage circuits require external resistors.
- The linear regime may give larger responses, but the sensitivity ($\Delta V_{GS}/V_{GS}$) is the same. Furthermore I_{DS} is now independent of V_{DS}.

Clearly, this is only applicable at constant temperature, as increasing temperature will modify the transconductance of the device. Constant voltage operation in the saturated region is possible though complex with no advantages.

A further configuration is to operate the devices in pairs with one as a sensor and the second as a reference. By looking at the differential output of these devices it should be possible to isolate some of the remaining fabrication and temperature effects. This is a common strategy for several types of gas sensors e.g. a pellistor [3.13]. An example of such as configuration is shown in figure 3.3. Such a design is appealing as current sources, with the reference FET driven by a current mirror, and amplifiers are simple to design and construct in CMOS.

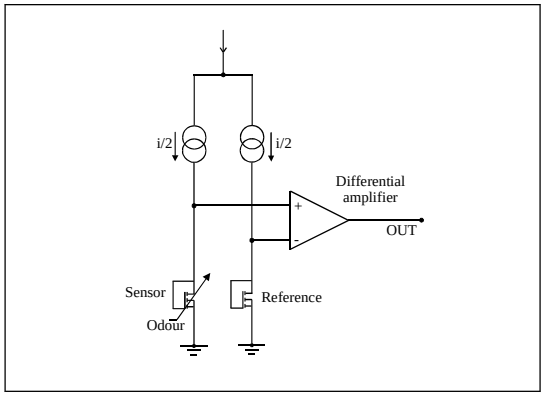

Figure 3.3: Schematic of a sensor and reference with integrated circuitry.

One of the last steps of the fabrication process, after the standard CMOS stages have been completed, is the opening of the gate. Generally in chemFET sensors the gas sensitive material is deposited in contact with the gate insulator material (usually oxide) [3.14,3.15]. For room temperature chemFET sensors employing conducting polymer films either a slot is removed in the gate exposing part of the gate insulator or the whole

of the gate is removed with separate electrodes for electrical contact. These electrodes also assist in the deposition process. Opening of the electrodes can be done in two ways, either by fabricating the device as normal and then etching through the later deposited layers to expose the gate and subsequently the gate oxide or by leaving holes as these layers as they are deposited. Though the second method seems easier, the processes involved after the deposition of the gate can attack this gate material and subsequently the gate oxide.

3.2.2 Dimension and configuration of the gate structure

As stated earlier, it is possible to operate a FET sensor at constant current where the response is measured as a shift in threshold voltage and is independent of gate area and channel dimensions. Hence, smaller devices can be formed that are less expensive and gives the possibility of creating sensor arrays, at a practical cost. Another factor controlling the dimension of the gate, and so the device, is the gas sensitive material. Certain polymers can limit the size of the slot or the distance between electrodes. For example electrochemically deposited conducting polymers can be grown across a gap of up to 50 μm, though other polymers can be deposited across much larger gaps, limited only by the gate resistance. We can summarise some of the different methods polymer deposition, as:

1. Electrochemically (1-step process), which needs channel length < 50 μm.
2. Chemically deposition of electro-active base polymers followed by electrochemistry (no gap limit).
3. Spray coating of polymer composite (1 or 2 step process, with no gap limit).

Each method has a different demand on the design, though the spray coating is the simplest. This is dealt with in more detail in chapter 4. Furthermore the gate material and/or sensing electrodes have to be exposed through the fabrication process or as a post-processing step. Hence the layout of the gate will have to encompass design rules to give adequate space for these post-CMOS processing steps without effecting the rest of the FET device, i.e. interference between devices/sensors.

3.2.3 Sensor electrode material

Similarly to the dimensions of the device, the gate material has to be chosen to be compatible with the sensing material. For example electrochemically grown conducting polymers cannot be deposited on Al due to its low work function. Furthermore, it is difficult to electrochemically grow on *p*-type polysilicon, as the solvent has to be appropriate to the side reactions that occur at the silicon surface in aqueous solution at high potential and at the same time for the polymerisation process. Deposition on *n*-type polysilicon is further complicated as UV illumination is also required to generate holes for the reaction, and as yet this has not been fully tested. Also, the resistance of the electrode structure in the deposition process is important as the IR drop over the electrode maybe significant in comparison to the resistance of the electrolyte used in the deposition process. Another limitation of Al is its instability with long term exposure to an ambient atmosphere in which its conducting properties degrade. These limitations of Al are problematic, as it is the dominant metal used in the CMOS process. It is possible to use Al as the sensor electrode/gate electrode for polymer deposition methods 2 and 3, though long term stability is an issue. Typically, materials such as Au are used in many room temperature resistive gas sensors, as it does not suffer from these constraints, though polysilicon in certain circumstances can also be used.

3.3 Final room temperature chemFET sensor design

The main room temperature chemFET sensor used in this research was designed and fabricated in collaboration between the Institute of Microtechnology, University of Neuchatel, Switzerland and the University of Warwick. These devices were originally designed on a European project and are being used in a number of research applications [3.16].

Here an array device was designed consisting of four enhanced *n*-type MOSFET sensors. The silicon substrate was *n*-type lightly doped, with the devices constructed within a *p*-well, reducing the interference from one sensor to the next. The devices have a common gate and drain and so operate in the saturated region. Two channel dimensions were used, 385 μm × 10 μm (channel width/length (W/L) = 38.5) and 105 μm × 5 μm (W/L = 21). The channel is meandered to reduce the overall size of the sensor and to improve electrical connectivity to the active polymer materials. The

total area of the sensor array is 624 μm × 495 μm (10 μm channel length) and 483 μm × 282 μm (5 μm channel length). Also included is a *pn*-diode to monitor the temperature of the substrate. In this application the tracks used to connect the drain, source and gate are Al, though the sensing electrode (i.e. the gate of the FET sensor) is Au. Etching through the silicon nitride passivation layer and subsequent oxide layers opened up this gold gate electrode. For the sensor FETs the gold is also etched exposing the gate oxide, as illustrated in figure 3.4. This shows a side and top view of an individual sensor, emphasising the common gate and drain and showing the active polymer material in contact with the gate oxide. This opening is 2 μm larger than the channel to ensure that in fabrication any misalignment between the source/drain mask and the gold/gate etching mask does not result in the gold electrode covering any of the channel. This feature is also employed with the 5 μm channel length sensor array.

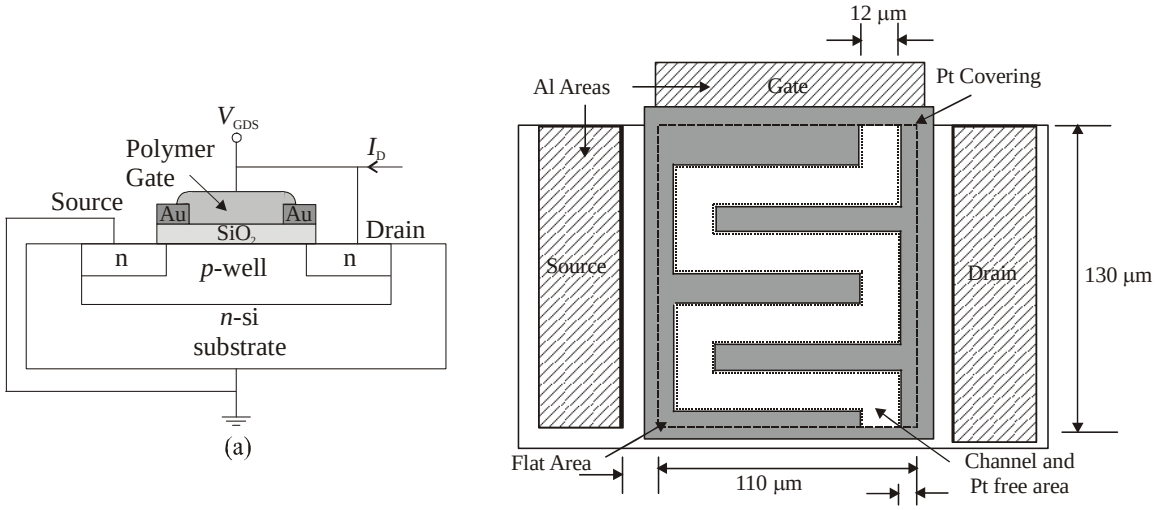

Figure 3.4: Schematic overview of a single chemFET device with channel dimensions of 385 μm × 10 μm.

A drawing of the complete device, with a 10 μm channel length, is shown in figure 3.5. The final device with 4 mm × 4 mm in size with pads (300 μm × 300 μm) for electrical connection to the sensors. Four different combinations of solid gate (channel covered by gold) and open gate (channel oxide exposed) were produced, as detailed in table 3.1. These combinations of open and closed gate are there to create chemFET arrays with references, either one reference for the rest of the array or one reference per chemFET. By using these references, information regarding the FET itself can be gathered and gives the possibility of taking a differential output removing some of the fabrication

variables. An added option is to have four open chemFET sensors giving the possibility of having multi-polymer arrays.

Though these sensors are not completely CMOS compatible, as gold is used as the gate, the remainder of the process is. This gold gate structure allows the evaluation of a range of conducing polymers. Furthermore, it can simply be replaced with polysilicon for a standard process.

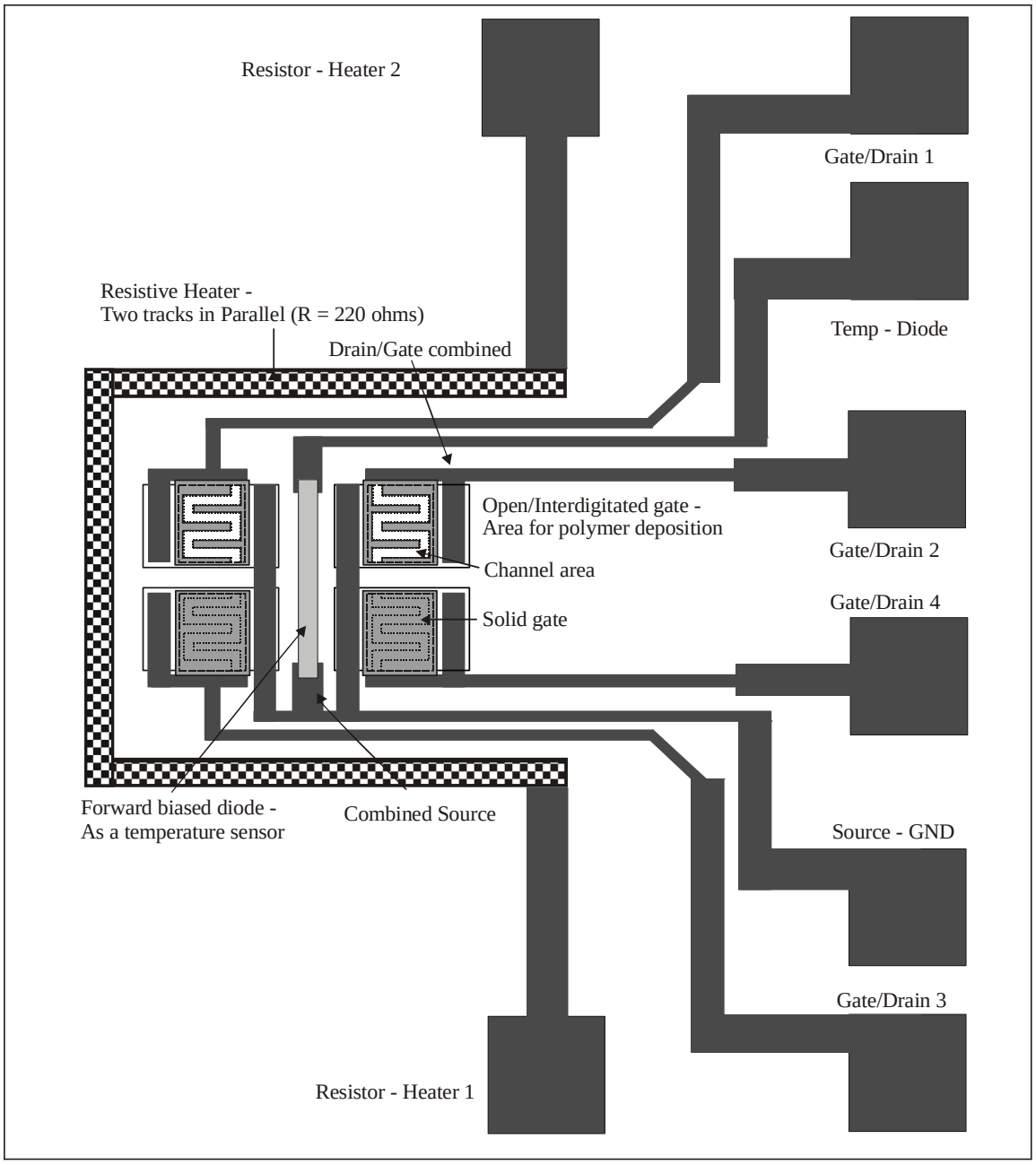

Figure 3.5: Drawing of final chemFET sensor array.

Configuration	Description
4 Open gates	Used for multi-polymer arrays, for up to 4 different polymers
3 Open gates 1 Closed gate	Multi-polymer array of up to 3 different polymers, with 1 reference FET.
2 Open gates 2 Closed gates	Two chemFET sensors each with references.
4 Closed gates	Device testing

Table 3.1: Room temperature chemFET sensors, open and closed gate combinations.

3.3.1 Fabrication process

These sensors were fabricated, using an 8 mask process. A summary of the fabrication steps is given in figure 3.6, with a list of design parameters given in table 3.2.

Parameter	Value	**Parameter**	Value
Channel length & Channel width	385 × 10 μm 105 × 5 μm	Depth of doping	1.5 μm
Silicon wafer	330 μm, *p*-doped	Thickness of gate oxide	80 nm
P-well doping	20 kΩ/sq.	Thickness of Au/Ti	1200/300 nm
Depth of *P*-well	4 μm	Thickness of Al	4.5 μm
Source/drain doping	20 Ω/sq.	Thickness of SiN_x passivation	2 μm

Table 3.2: Room temperature chemFET device fabrication parameters.

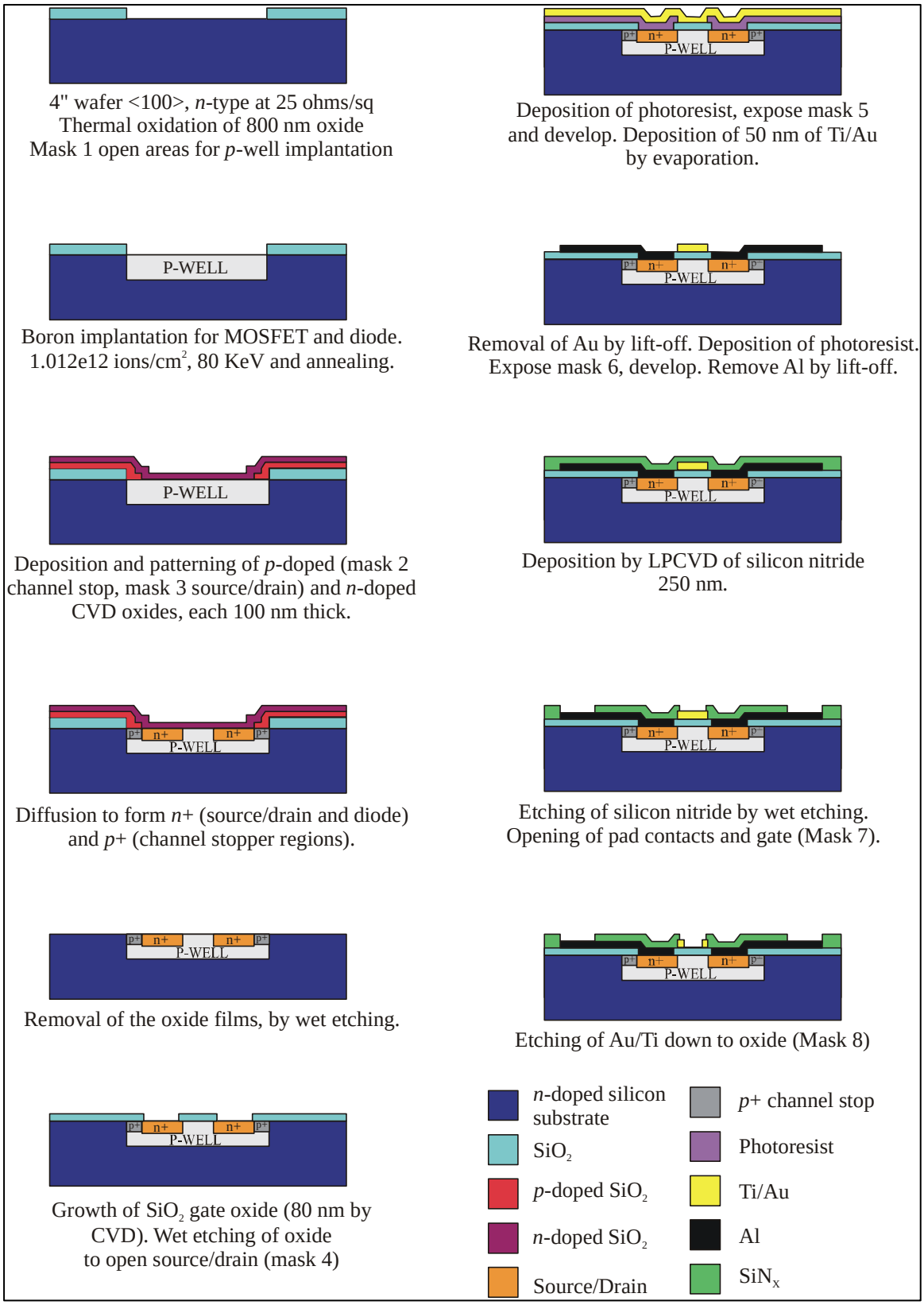

Figure 3.6: Fabrication process for the room temperature chemFET sensor.

3.4 Design of gas sensors using SOI technology

This section describes the design of a number of SOI based heaters and gas sensors. This work is in collaboration with the University of Cambridge and funded by the EPSRC, grant no. GR/L92426.

The design is based on a micro-hotplate with a MOSFET heater and a chemoresistive, microcalorimeter or chemFET sensor structure. Also included are temperature sensors to monitor the membrane and to give a feedback signal to any control electronics. By using this technology the sensors and heater are fully compatible with the drive/measurement electronics, giving the possibility of circuit integration.

The final layout will depend, to an extent, on the fabrication facilities. Two different foundries were used for this project. Firstly, the Temic Matra MHS 0.8 μm BiCMOS SOI process, through Europractice. This is a facility that allows European Universities to purchase small areas of a wafer at a fraction of the cost the entire wafer. This allows rapid design and development of new devices at a low cost. A limitation of this method of device fabrication is that the process is inflexible and cannot be altered to improve the design. The second fabrication facility is the Southampton University Microtechnology Centre (SUMC). Here as part of the EPSRC project, two fabrication runs are available. This process can be tailored to the design needs (e.g. different wafer thickness), though the complexity of the design has to be kept low due to the limited resolution (3 μm gate dimensions) and lack of integrated devices.

3.4.1 Design of a micro-hot plate

A method of reducing the power consumption of a high temperature heater/sensor is to form a micro-hot plate. Here the heater structure is fabricated on a thin membrane, where the handle silicon is removed, thus reducing the mass and surface of the heated area, and so significantly reducing the power consumption [3.18]. SOI wafers are ideal for micro-hot plates as the embedded insulating layer behaves both as an etch stop, to assist in fabrication, and an insulating layer to reduce power consumption. Ideally this power consumption should not exceed 100 mW for battery powered instruments. For SOI technology the depth of the insulating oxide layer and device silicon defines the thickness of the membrane. The SIMOX process forms very thin SOI layers (<1 μm),

while SDB layered wafers (Unibond) are usually thicker (1-10 μm) [3.19]. As a general rule the thinner the membrane the lower the power consumption, though this causes an increase in the mechanical stresses which could result in membrane failure.

Figure 3.7 shows the basic design of a micro-hot plate containing an active area comprising of a MOSFET heater and sensor electrodes. These structures are situated in the centre of a thin membrane, which is supported by an outer frame of silicon. The thermal isolation of the buried insulator is further improved by LOCOS (local oxidation of silicon) that consumes the remaining silicon. Two possible heater/sensor configurations exist, either a vertical or lateral arrangement. In a lateral configuration the sensor electrodes and heater are in the same plane, this solution though simpler, can consume more silicon and increases the power consumption of the heater. A vertical arrangement, as in figure 3.7, shows the heater and sensing electrodes on different planes.

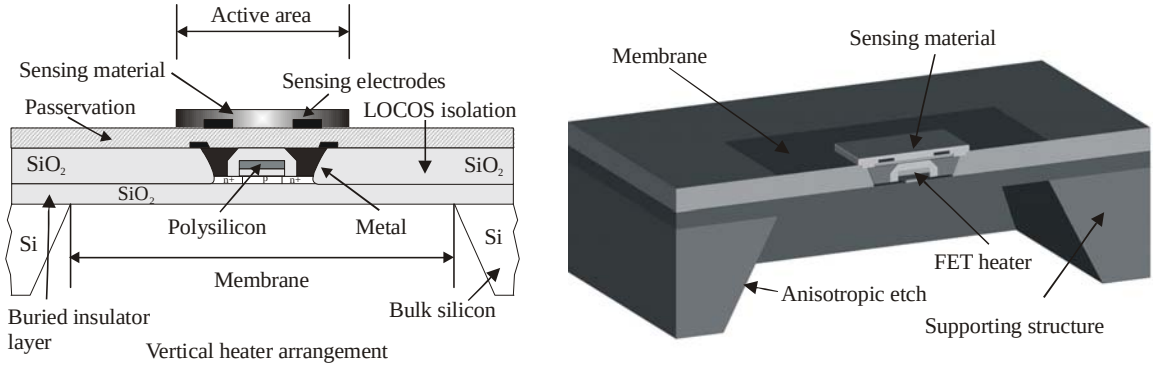

Figure 3.7: SOI micro-hot plate.

This configuration is usually smaller and has reduced power consumption, though this design may cause a greater temperature fluctuations around the perimeter of the heater/sensor.

Thermal losses from a micro-hot plate occur by three mechanisms, conduction through the membrane (H_m), conduction and convection to the surrounding air (H_a) and radiation (H_r) [3.20]. Thus the total heat loss (H_T) can be expressed as:

$$H_T = H_m + H_a + H_r \qquad (3.5)$$

A number of models have been formed to help in the design of an ideal micro-hot plate. Research by Dibbern [3.21] has modelled the power loss by these three mechanisms and has formed a simplified expression of H_T (in mW), as:

$$H_T = H_m + (0.33\Delta T + 10)A \qquad (3.6)$$

where ΔT is the temperature difference between the heater and the ambient atmosphere. Here the heat losses H_a and H_r are assumed to be proportional to the heater area A (mm^2), hence they are only dependent on device geometry. Thus the thermal loss by radiation at 300 ^oC is roughly 10 mW/mm^2. The contribution of conduction can be evaluated according to:

$$H_m \approx \frac{2\pi\kappa m\Delta T}{\ln\left(\frac{u}{a}\right)} \tag{3.9}$$

where m is the thickness of the membrane, κ is the membrane thermal conductivity, ΔT is the temperature difference between the active area and the silicon substrate, u is the distance across the membrane and a is the diameter of the active area. This equation defines the heat loss for a circular membrane though a square membrane has been found to give a similar result. Hence, the thermal loss by conduction depends only on the geometry of the membrane/heater and the thermal conductivity of its components.

From experimentation its has been shown that a minimum ratio of active area to membrane of 1:3 is required for mechanical stability, i.e. the thermal gradient to the silicon frame ($T = T_0$) should not cause excessive thermal or mechanical stress. An active area of 150 μm × 150 μm with a membrane of 500 μm × 500 μm has been chosen to give adequate space for the heater/electrode structures within the design rules and for the deposition of active material.

3.5 Design of a MOSFET heater

The MOSFET heater is proposed here as an alternative to a simple resistive structure for a number of reasons. Firstly, since the design should be CMOS compatible, platinum or other similar materials are impractical. Polysilicon heaters have been previously used though they tend to suffer from variable sheet resistance, poor long-term stability and require heavy doping that can induce stress in the membrane.

A heater is described by a length L, width W, and thickness t. For a MOSFET heater it is the channel of the device, formed beneath the gate, that becomes the heater. The heater thickness is the channel depth and so depends upon the region of operation (linear or saturated) the depth of the diffusion and the applied voltage. Clearly, the heater itself will only cover a fraction (coverage $\eta < 1$) of the active area (area covering the heater and sensor), since a proportion must be given over to the drain/source etc.

The actual drain voltage across the device should be calculated as the polysilicon/aluminium tracks may lead to a significant voltage drop. Thus the channel resistance of the MOSFET must exceed the track resistance and so the drain voltage must surpass the IR drop, i.e.:

$$V_{DS} \quad >> \quad i_{DS} R_{track}$$

The length, and so the resistance of the gate track is irrelevant, as there is no current flowing. Hence, it is important to balance the coverage/no. of FETs to the resistance of the connecting wires. Work with resistive heaters has shown that the optimum design should have a small number of parallel heaters (4 to 10) [3.21].

Initially many different MOSFET heater designs were considered of which three final configurations were used, namely:

- Interdigitated
- Interdigitated with gap
- Square

These designs are covered in the following sections.

3.5.1 Interdigitated heater structures

The interdigitated heater design, as the name suggests, consists of a number of FETs connected in parallel. Here two designs have been created with either a fully interdigitated design or an interdigitated design with a gap. In the interdigitated design, 6 MOSFETs are laid out in parallel with a common gate, source and drain. Each of these MOSFETs have identical channel dimension of 132 μm × 12 μm, giving a *W*/*L* ratio of 66 (*W*/*L* of 11 per arm, thus total *W*/*L* of 66, η = 0.35), as shown in figure 3.8. With this design it is not possible to have a temperature sensor inside the heater structure and instead it is placed on the outside (though on the membrane) requiring external temperature measurement to calibrate the temperature sensors and the heater.

The interdigitated heater with gap design is in many ways similar to the first. It contains 4 MOSFETs though with a 20 μm gap in between two pairs of 2 MOSFETs for a temperature sensor, as shown in figure 3.8. The channel dimensions remain constant at 132 μm × 12 μm, though the *W*/*L* ratio is now reduced to 44 (η = 0.28). A possible variation on this design is to increase the number of MOSFET arms from 4 to 6, with each arm 132 μm × 9 μm giving a new *W*/*L* ratio of 88 (η = 0.32). Both of these

designs have been implemented in the Matra SOI process. This will investigate the effect of FET numbers and coverage on the efficiency of the heater (power consumption) and give an indication on how the design can be optimised for the best performance. Furthermore, this variation in *W/L* will alter the transconductance term of the device. Hence we can investigate how the device parameters can be used to set the operating voltage of the device. For the SUMC process only the interdigitated with gap design is used with channel dimensions of 128 μm × 8 μm (4 MOSFETs, *W/L* = 64, η = 0.18).

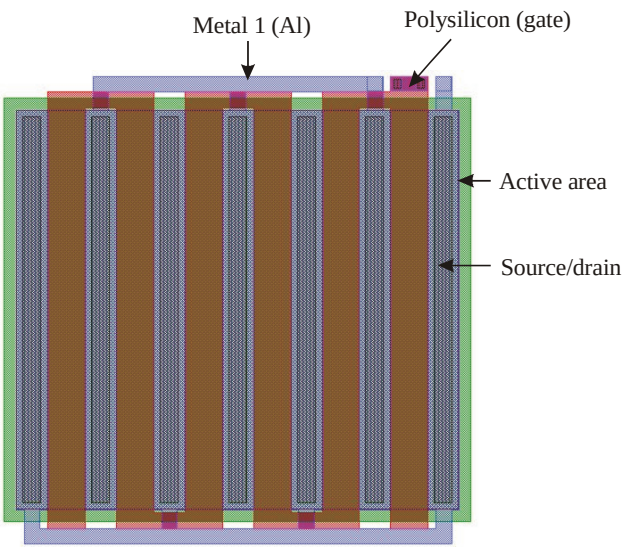

Iterdigitated design with five or six FETs in parallel.

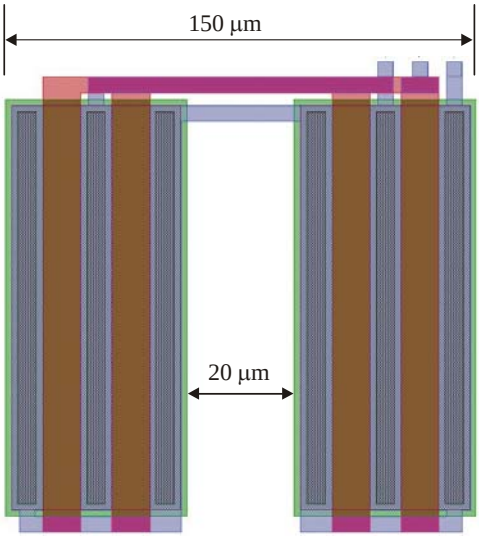

Interdigitated design with gap for temperature sensor. Here four or six FETs are used in parallel

Figure 3.8: Interdigitated heater designs.

To evaluate the effectiveness of the heater area one device with an increased active area is included (area 300 μm × 300 μm, channel dimensions 280 μm × 25 μm, *W/L* = 44, η = 0.28, sensing electrode size remains constant, Matra only). This design should reduce the temperature variations within the sensing area, but will significantly increase the mechanical stresses as the membrane to heater ratio will be 5:3. Tracks to the heater are aluminium in all cases with an on-membrane width of 10 μm and off membrane width of 15 μm with a maximum resistance of 1.2 Ω at room temperature.

3.5.2 Square heater structure

A further design has been included based on a square shaped heater, as shown in figure 3.9. Here a single lateral FET heater is laid out in a square, surrounding a central area (82 μm × 82 μm) inside which a temperature or chemical sensor can be placed. Two

heater configurations were used, initially with a FET heater of channel dimensions 480 μm × 12 μm (W/L = 40, η = 0.26), secondly with smaller channel dimensions of 425 μm × 12 μm (W/L = 35.4, η = 0.23, both SUMC only). These reduced dimensions were required to fit the tracks of a lateral placed chemical sensor.

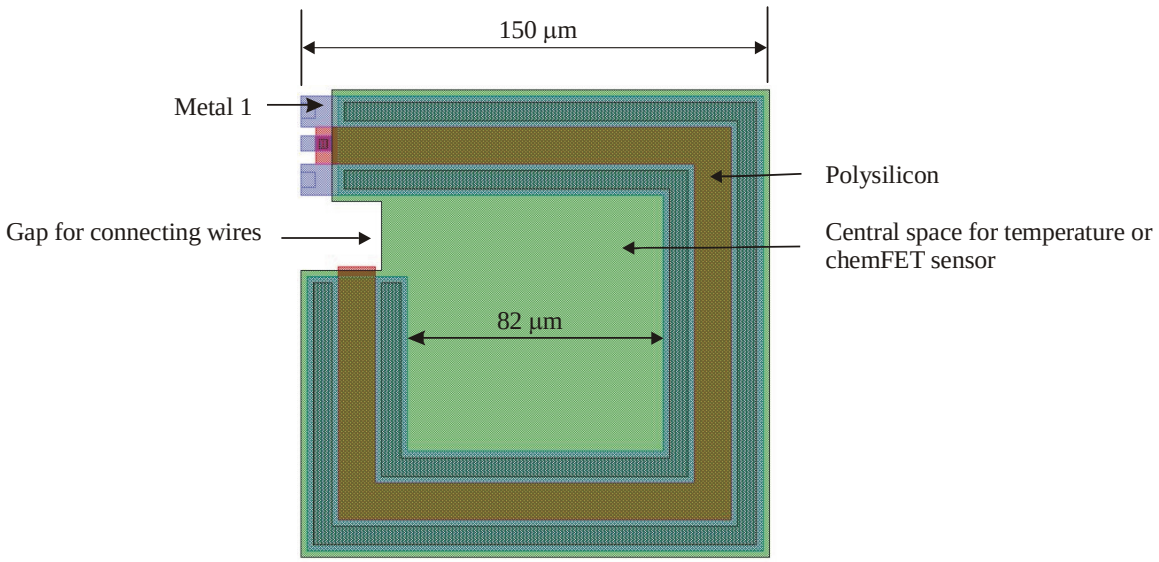

Figure 3.9: Square FET heater design.

3.5.3 Electro-thermal simulations of the MOSFET heater structure

Simulations of the MOSFET heater structures were carried out at in collaboration with University of Cambridge. These simulations were used to evaluate the effectiveness of the heater structures before fabrication.

Initial studies was carried out with the MEDICI-AVANT and ISE-INSPEC simulators. These programs perform a 2D electro-thermal simulation of the device that takes into account the full current-lattice temperature equations and the degradation of the MOSFET channel mobility with temperature. Figure 3.10a shows the forward I-V characteristics of an *n*-type MOSFET in a common source/drain configuration lying on a thin SOI membrane. At a low gate voltage (V_{GS} < 3 V) the MOSFET behaves normally as the drain voltage is increased. At a higher gate voltage (V_{GS} > 5 V), hence elevated power, the parasitic *npn* turns on which leads to a significant increase in current.

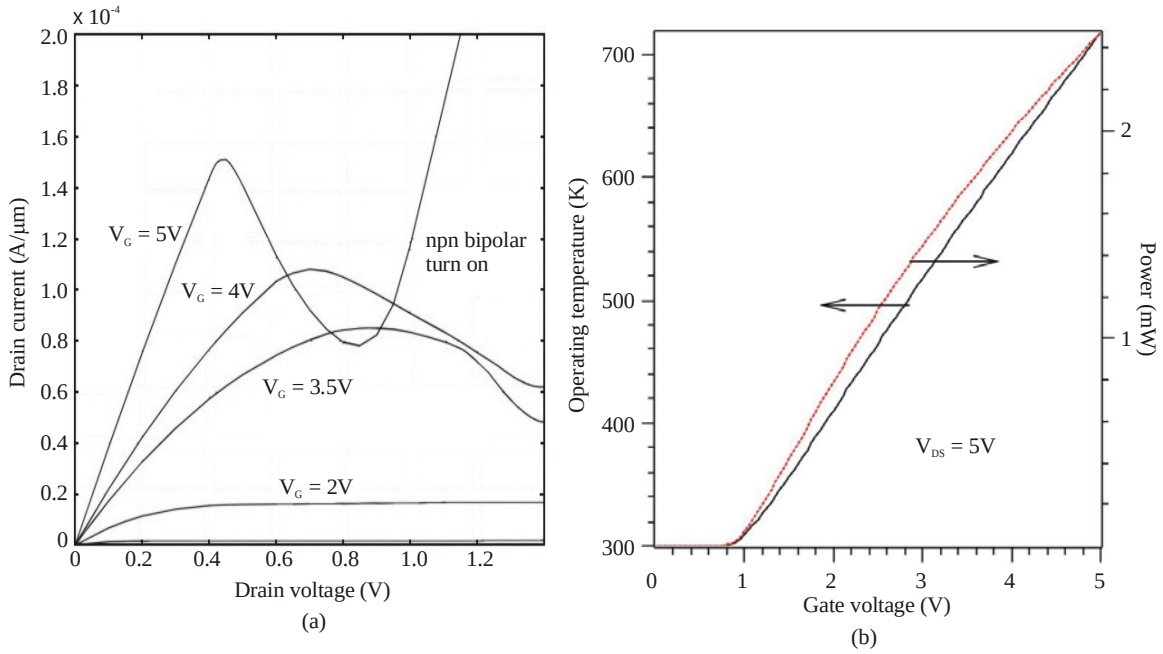

Figure 3.10: (a) I-V characteristics of a *n*-type SOI FET heater and (b) lattice temperature.

Figure 3.10b shows the lattice temperature and power consumption as a function of V_{GS} (at fixed V_{DS} = 5 V). The lattice temperature increases almost linearly with applied gate voltage, once the threshold voltage has been achieved (0.7 V). Hence a power consumption of 2.5 mW leads to a lattice temperature of 400 ^{o}C. These simulations show that the lattice temperature can be linearly controlled via the gate voltage. It should be noted that these results are for a single MOSFET in 2D, a typical heater will have a number of these devices, hence the 3D result will be different (lower lattice temperature for the same power consumption).

3D electro-thermal simulations can be used to calculate the heat loss through the membrane and to the air from the self-heating effects of the MOSFET. A Joule heating term is used to enhance the heat transfer equation, while the electro-resistive equation has a temperature-dependent electrical conductivity term, as described by [3.22]:

$$\vec{\nabla}.\left(\kappa(T)\vec{\nabla}T\right) + \frac{\vec{J}^{2}}{\sigma(T)} = 0 \qquad (3.10)$$

$$\vec{\nabla}.\left(\sigma(T)\ \vec{\nabla}\ \Psi\right) = 0 \qquad (3.11)$$

where, σ is the electrical conductivity, Ψ is electroresistive potential, κ is the thermal conductivity, T is the temperature and $\vec{J} = \sigma\vec{\nabla}\Psi$ denotes the current density. Typical values from the Matra process were used, given in table 3.6 and the physical

constants in table 3.3 [3.23]. A number of further boundary conditions were used: (a) the temperature along the surfaces of the wafer are at ambient, (b) on the upper and lower surfaces of the membrane heat is dissipated through convective loss to the air, and (c) radiation losses are neglected.

Material	Thermal conductivity W/m K	Specific Heat J/Kg K	Density Kg/m^3
Tin Oxide	35	896	7267
Silicon	157	700	2330
Silicon oxide	1.2	730	2270
Polysilicon (*n*-type)	28	750	2330
Silicon nitride	19	750	3440
Aluminium	236	904	2699

Table 3.3: Physical properties of the materials used in the SOI heater simulations.

A temperature profile of an SOI membrane is shown in figure 3.12, for an input power of 35 mW with an interdigitated FET heater design of 6 MOSFETs in parallel. It is of interest to note that the bulk silicon remains at ambient temperature, due to the LOCOS isolation and hence any further circuitry would be able to operate as normal. It can also be seen that the maximum temperature variation between the core of the heater and the sensing material is 27 K, with only a 4 K variation over the sensing element, at a mean temperature of 725 K. This maximum operating temperature of 352 ^{o}C is above the temperature at which the MOSFETs performance will significantly degrade, and shows that the 3D electro-thermal simulator does not account for these factors.

To compare the effectiveness of all the heater designs, two further simulations were performed, for the interdigitated with gap (25 μm) and square heater structures, as shown in figure 3.12 (power consumption 35 mW). The gap structure has a thermal variation of only 7 K over the heater area, which shows that the gap does not significantly effect the thermal profile, though later simulation (not shown here) with a 70 μm gap did indeed cause significant thermal variation. The square heater design also showed good thermal stability over the sensing area. The asymmetrical thermal profile of these simulations can be accounted for by the metal connections to the heater.

Clearly, these will conduct heat more efficiently than the silicon, causing the shift in thermal profile.

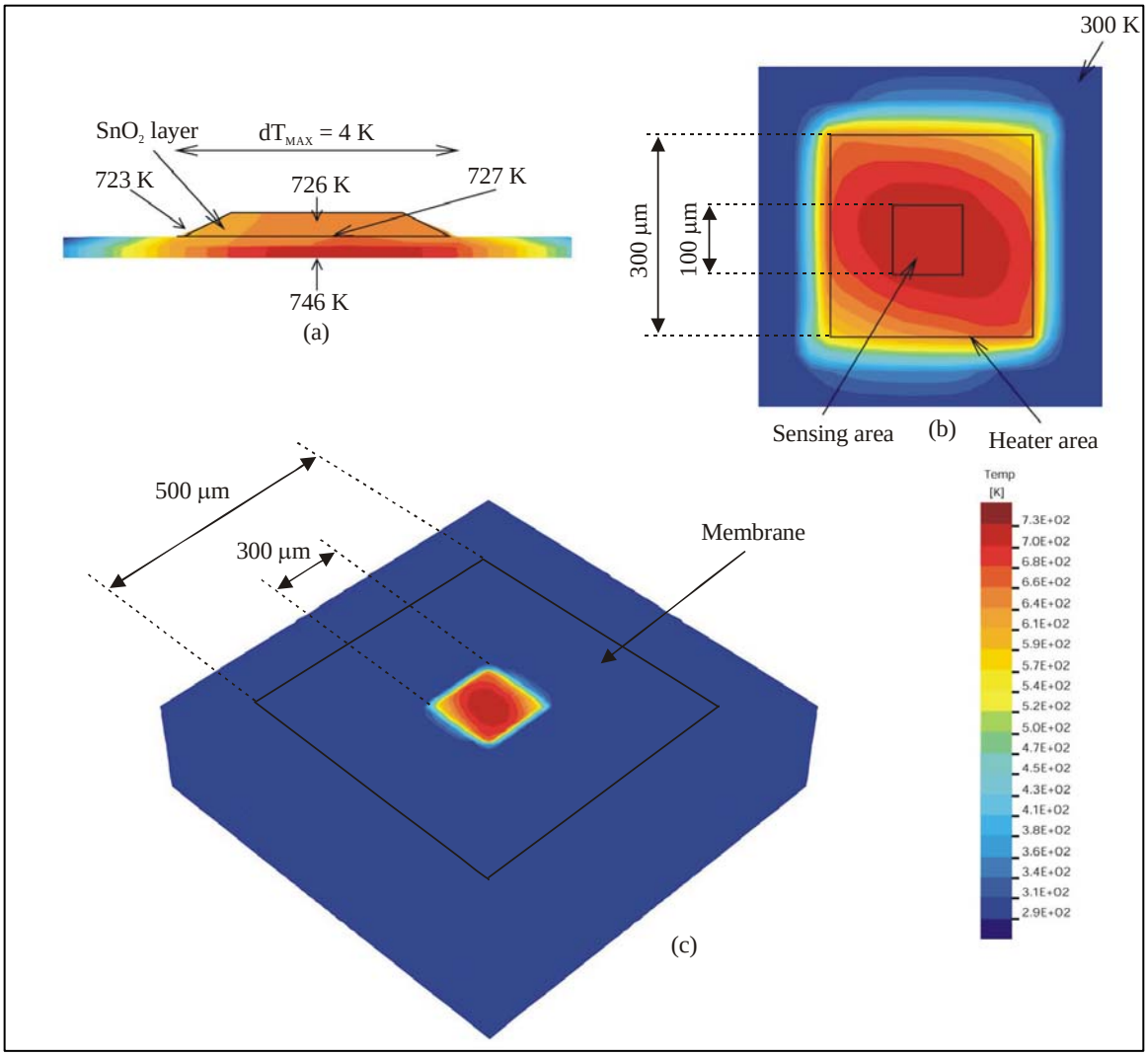

Figure 3.11: 3D Thermo-simulation of a FET heater on a SOI Membrane.

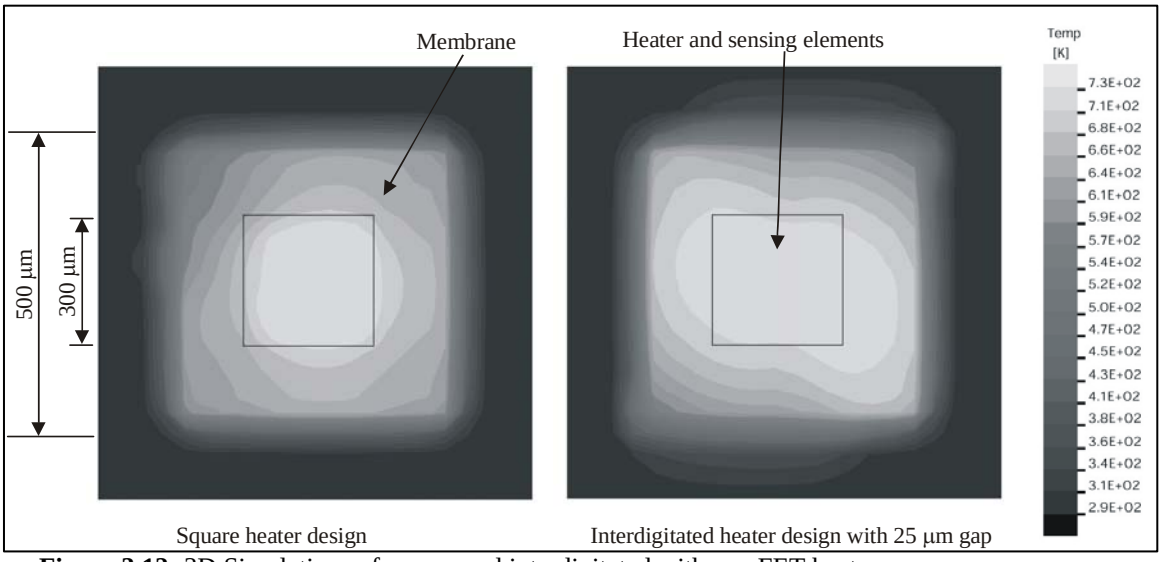

Figure 3.12: 3D Simulations of square and interdigitated with gap FET heaters.

3.5.4 Thermo-mechanical simulation of heater structures

In addition to the electro-thermal simulations, further thermo-mechanical simulations were performed using the SOLIDIS-ISE simulator. Clearly, the thickness of the SOI membrane will have repercussions on the manufacturing yield. Furthermore, high mechanical stresses will reduce the operational lifespan of these devices, where rupturing of the membrane can occur especially at an elevated temperature. It is well known that SiO_2 is more brittle, and so mechanically less suitable than Si. Hence a thick membrane has a greater mechanical stability, though unfortunately significantly increased heat loss and so power consumption.

These mechanical simulations have been based on classic thin-plate theory [3.23], where the in plane principle stresses (σ_1 and σ_2) can be obtained from:

$$\sigma_1 = \frac{Eu^2}{3(1-\upsilon^2)}\left(\frac{l}{h}\right)^2 \quad \text{and} \quad \sigma_2 = \frac{q}{2}\left(\frac{l}{h}\right)^2 \psi_1(u)$$

where

$$\psi_1(u) - \frac{3(u - \tanh u)}{u^2 \tanh u} \quad \text{and} \quad u^2 = \frac{l^2 S}{4D}$$

where l is the length of a square membrane, h is the thickness, q is the load pressure and S is a parameter from experimental data. We can calculate the flexural regidity of a thin plate (D) from:

$$D = \frac{-Eh^3}{12(1-\upsilon^2)}$$

where E is Young's modulus and υ is Poisson's ratio, thus:

$$\sigma_{MAX} = \sigma_1 + \sigma_2$$

It should be noted that the maximum stress (σ_{MAX}) is a function of the load pressure and the aspect ratio l/h. By changing the load pressure, the maximum stress can be calculated for a number of different l/h values.

The device simulated device has a 500 μm × 500 μm SOI membrane consisting of Si and SiO_2 layers. These have a thickness ratio of 1:2, chosen to optimise heat transfer and mechanical characteristics. For the 3D simulation a square membrane has been defined and a number of boundary conditions set. Specifically, the edges of the

membrane are clamped, and thus displacement is zero, the temperature along the silicon substrate base is at ambient and free convective exchange with the surrounding ambient atmosphere can occur. A table of simulation parameters is given in table 3.4 Below:

Physical parameter	Si	SiO_2
Young's modulus (E, Gpa)	190	73
Poisson's ratio (ν)	0.22	0.15
Thermal conductivity (k, $Wm^{-1}\ ^oC^{-1}$)	157	1.4
Thermal expansion coefficient (α, K^{-1})	2.33e-6	0.55e-6

Table 3.4: The physical constants used by the SOLIDIS-ISE simulator [3.24].

Figure 3.13 shows the resulting upward deformation (-Z direction) of the membrane at 400 ^oC. Also compressive stresses in the active silicon layer and tensile stress in the buried oxide layer have also been observed, as shown in figure 7.14. The resultant maximum stress is highly temperature dependent, e.g. at room temperature the maximum stress is 65 MPa and increases to 255 MPa at 700 K.

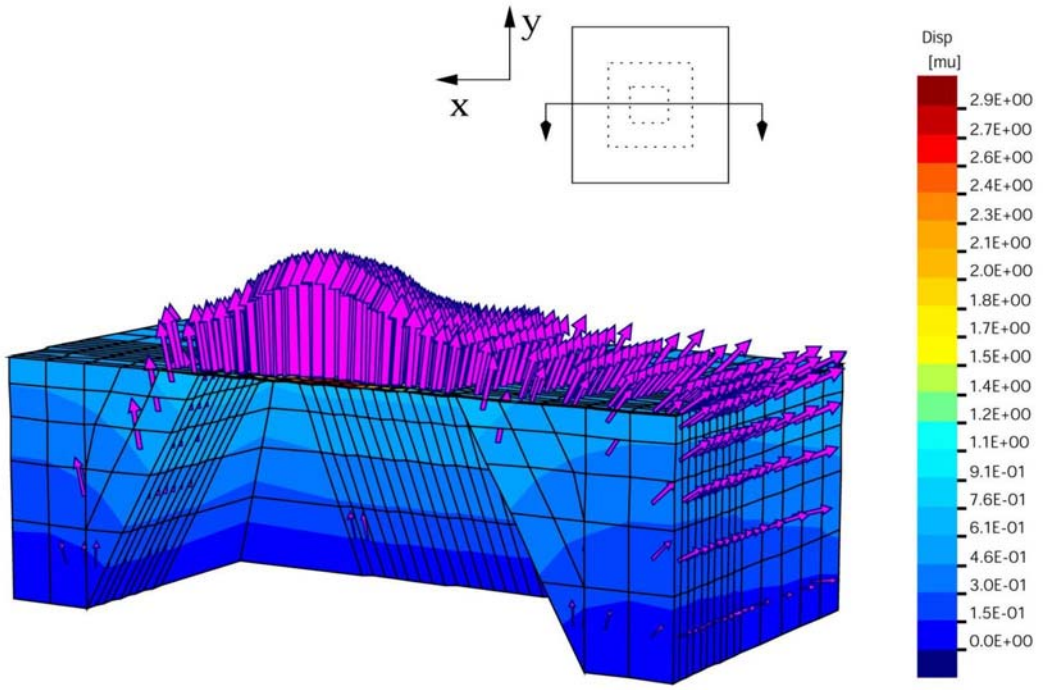

Figure 3.13: Mechanical simulation of a SOI membrane showing upward deformation of membrane.

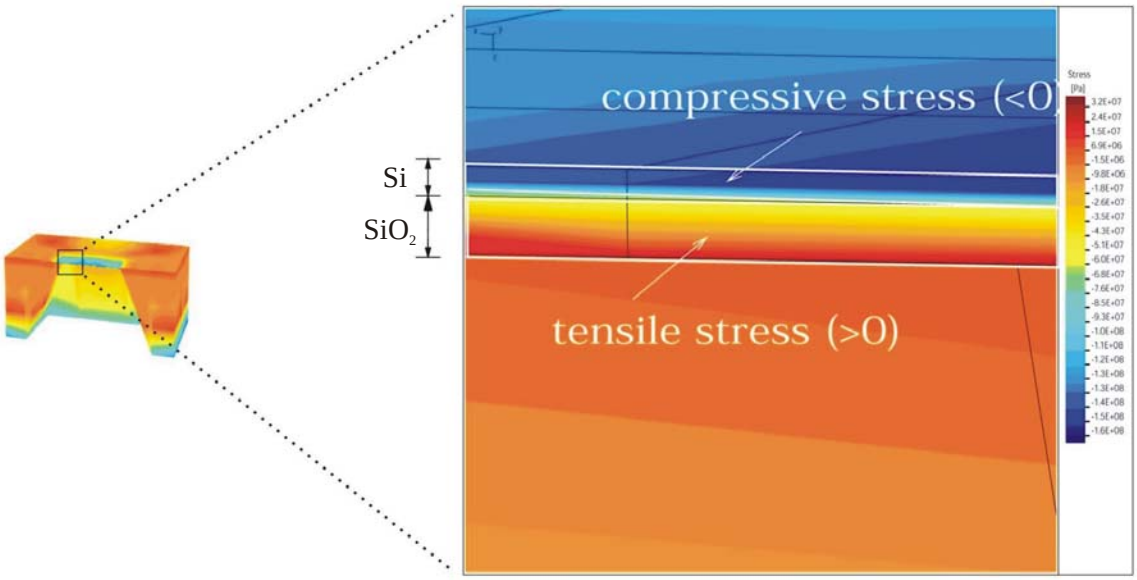

Figure 3.14: mechanical simulation of tensile stress within the buried oxide layer.

From both these thermal and mechanical simulations a set of criteria can be defined to maximise the performance of a MOSFET heater and so should have:

1. Low maximum stress in both Si and SiO_2 membrane layers, in particularly in the active area (central part of the membrane)
2. Uniform temperature distribution over the sensing element
3. Low power consumption (relatively small heating area and thin membrane)

Using these criteria a number of simulations have been performed to evaluate different sensor designs. Table 3.5 summarises these results. Design A has the best mechanical stability but the highest power consumption and worst temperature variation over the membrane. Design B has lower power consumption and the temperature variation is reduced, though stresses are increased. Design D and E show further reductions in power consumption and temperature variations, though at the cost of significantly increasing the stresses. Design C showed instability in the simulations.

Square SOI membranes l (length of membrane) = 500 μm	A l/h = 100	B l/h = 150	C l/h = 200	D l/h = 250	E l/h = 300
Maximum stress (MPa)	-220	-228	-235	-240	-255
Maximum deflection (μm)	2.6	2.8	2.9	3.1	3.2
Maximum relative temperature elevation (%)	97.4	97.8	98.2	98.6	98.8
Power consumption (mW)	53	44	39	36	34

Table 3.5: Evaluation of SOI heater structures with different membrane dimensions.

Three different wafers were used in this project. The Matra process used (SIMOX) wafers with 400 nm of buried oxide and 1200 nm of device silicon giving a *l*/*h* of 312 for a 500 μm membrane. The SUMC process used both SIMOX and UNIBOND wafers with 200 nm and 1500 nm buried oxide and 400 nm and 3000 nm device silicon respectively. This gives *l*/*h* ratio for a 500 μm membrane of 833 and 111, with the first two SIMOX wafers being above a class E and the UNIBOND wafer being between class A and B.

3.6 SOI sensor structures

A number of different sensor structures can be integrated with these MOSFET heaters. Clearly, the chemoresistor is the most straightforward, where the sensing mechanism is a change in conductance of a gas sensitive film. A set of electrodes are deposited directly over the heater, insulated by a silicon dioxide layer, with gas sensitive material added as a post-processing step. A second possibility is a micro-calorimeter; such sensors when exposed to a combusting gas, react, increasing the temperature of the active material and hence of the membrane. Normally, with microcalorimeters, the heater is also used as a temperature sensor, though in this application a separate temperature sensor will be used. The last option is a chemFET sensor, where the sensing structure sits laterally to the heater. By operating at temperatures up to 300 ^{o}C a number of materials, such as conducting polymers, catalytic metals and metal oxides are available to the designer.

3.6.1 Chemoresistive electrodes

The chemoresistor is the simplest of the sensor structures and the easiest to fit within the limitations of the design rules. Aluminium or gold electrodes are used to give an electrical contact to the gas sensitive material and, where required, to assist in the deposition process. When designing this structure an important consideration is the separation and length of the electrodes, i.e. the aspect ratio (length of channel / width of channel). By having a high aspect ratio the resistance of the material can be reduced and clearly it is easier to measure small changes in resistance when the initial value is low. For metal oxides (especially SnO_2) a minimum aspect ratio is typically quoted at 50 [3.25] with the most efficient electrode design being the interdigitated configuration.

Using the Matra SOI BiCMOS process a number of limitations on the dimensions and spacing of the electrodes were imposed. Adhering to these rules a 3 arm interdigitated electrode structure of aluminium was produced. Each arm was 51.5 μm wide and 150 μm long, giving a total electrode length of 300 μm and a spacing of 21.5 μm, (aspect ratio of 13.95). The SUMC process allowed increased flexibility in the design, here 11 gold arms were used with each arm 7 μm wide and 136 μm long, giving an aspect ratio of 212. Figure 3.15 shows both electrode structures.

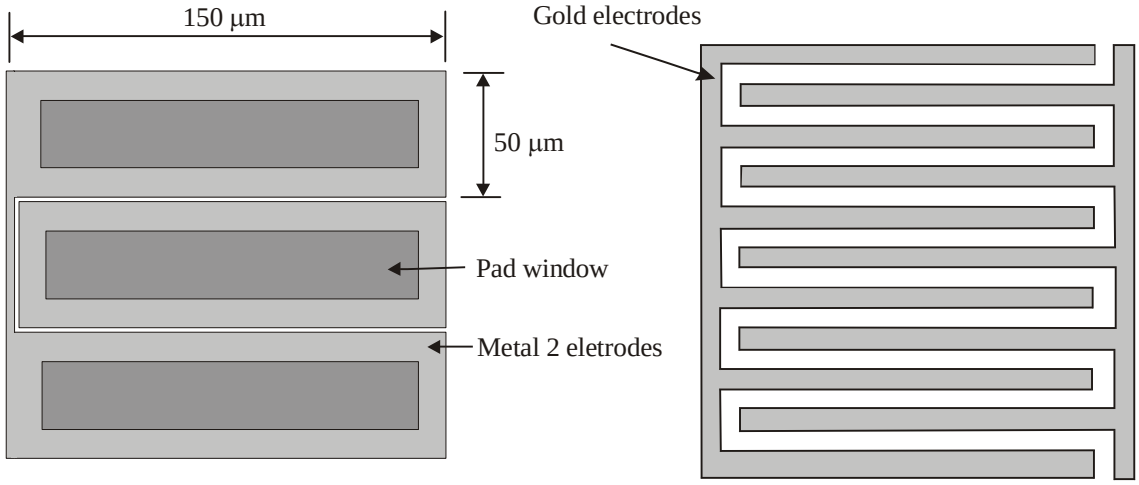

Figure 3.15: Electrode structures for Matra and SUMC processes.

This design can also be used for the microcalorimeter sensor, where the electrode structure is left to assist in the deposition process.

3.5.2 The chemFET sensor

The chemFET sensor structure is designed to lie laterally to the MOSFET heater, which surrounds the sensor. Two chemFETs were designed with channel dimensions of 180 μm × 50 μm and 150 μm × 40 μm. As with the room temperature chemFETs, a section of the (polysilicon) gate is removed, exposing the gate oxide. Two gap sizes were used removing a slot in the gate of 30 μm (wide gate FET, or WGFET) or 15 μm (narrow gate FET or NGFET). This leaves a strip of gate material on either side of the slot for electrical contact to the gas sensitive material. The variation in gap size is due to different gas sensitive materials requiring closer electrodes for deposition, whilst other materials that can span much larger gaps. By using different gate openings the gas sensitive film will be in contact with a greater area of gate oxide. As a result it is possible to investigate if this increased area generates larger responses and so we maybe able to calculate an optimum device size. The chemFET sensor structures are shown in figure 3.16.

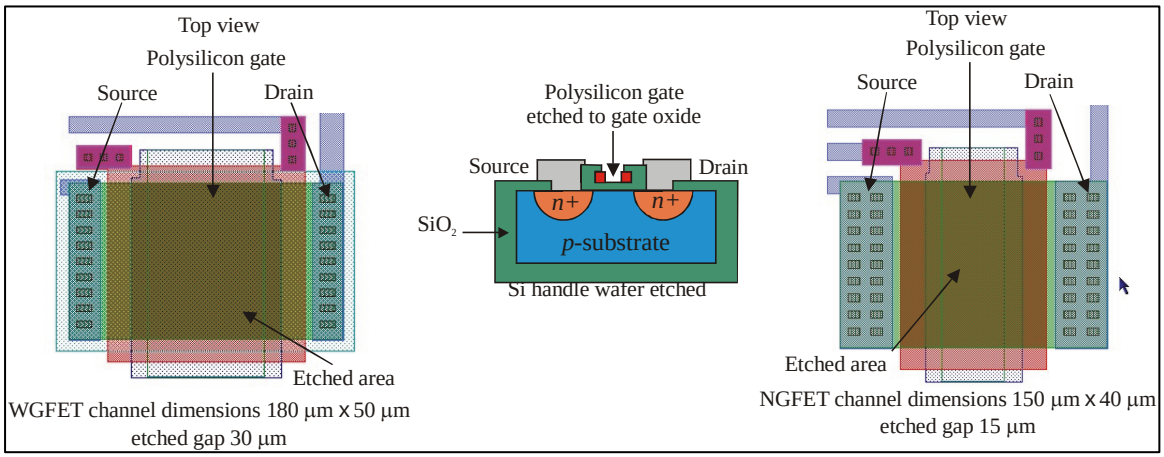

Figure 3.16: SOI chemFET sensor structures.

3.5.3 Temperature sensors

These sensors monitor the temperature of the membrane and could give a feedback signal to any control circuitry, or act as the measurement sensor for a micro-calorimeter. A number of different temperature sensors were implemented in these designs, namely:

- Spreading resistor
- *pn* junction (forward bias) diode
- Bipolar transistors (*p*-*n*-*p*)

The spreading resistor is the simplest of these structures. Its components are the *p* substrate with a *p*+ contact point, as shown in figure 3.17 (the *p* and *p*+ can be replaced with *n* and *n*+ depending on the process and the initial doping of the wafer) [3.26]. The resistance of the sensor and the effect of temperature can be calculated from:

$$R \approx \frac{\rho}{2\pi r_o} \tag{3.12}$$

$$\rho = \frac{1}{q(n\mu_n + p\mu_p)} \tag{3.13}$$

where ρ is the resistively, r_o is the radius of the spreading resistor and μ the carrier mobility is given by (for *n* and *p* doping):

$$\mu_n = 1415\left[\frac{T}{300}\right]^{-2.4}, \qquad \mu_p = 471\left[\frac{T}{300}\right]^{-2.4} \tag{3.14}$$

$$n \approx N \tag{3.15}$$

where *N* is the doping concentration and *T* is the absolute temperature (K). Three different configurations of spreading resistors were used, based on a circular, square or channel design. The circular design is not fully compatible with all layout packages as a circle is not a standard shape and for this reason the square design was also implemented. In addition, the single channel device was used to reduce the size of the sensor, and to minimise the effect on the LOCOS isolation. With the circular and square designs the two contacts are a centre point and the external perimeter of the circle or square. The dimensions/diameters were 100 μm and 200 μm and the channel design has two contact points 175 μm apart. Typical resistances at room temperature, 100 ^{o}C, 200 ^{o}C and 300 ^{o}C are given in table 3.6. These assume that the main temperature variation is due to a change in the majority mobility carrier.

Dimensions	Room temp.	100^{o}C	200^{o}C	300^{o}C
Circular - 100 μm	250 Ω	420 Ω	740 Ω	1170 Ω (3.4 Ω/^{o}C)
Circular - 200 μm	125 Ω	210 Ω	370 Ω	585 Ω (1.8 Ω/^{o}C)
Channel – 175 μm (1.5 μm silicon depth)	115 kΩ	136 kΩ	166 kΩ	200 kΩ (300 Ω/^{o}C)

Table 3.6: Typical resistance values for spreading resistors over the operating temperature range.

A schematic of a spreading resistor and some example structures are shown in figure 3.17.

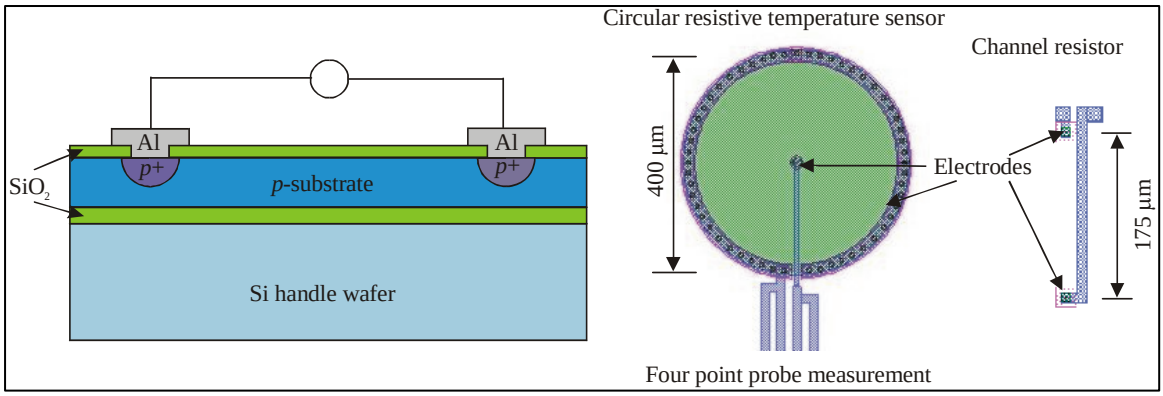

Figure 3.17: Layout of a spreading and a channel resistive temperature sensors.

The second type of temperature sensor was the *pn* junction diode. The temperature behaviour of a forward biased *pn* junction diode is given by:

$$I_D = I_S\left(e^{\frac{V_D}{V_{TH}}} - 1\right) \tag{3.16}$$

$$V_D = V_{TH}\ln\left(\frac{I_D}{I_S} + 1\right) \tag{3.17}$$

where I_D is the diode current, V_D is the potential drop over the diode, I_S is the Reverse bias saturation current, V_D diode voltage and V_{TH} thermal voltage (kT/q). The temperature behaviour of the saturation current I_S is:

$$I_S = AT^{\beta}e^{-\frac{V_{go}}{V_{TH}}} \tag{3.18}$$

where A and β are (temperature independent) material parameters, T is the temperature, and V_{go} is the bandgap voltage of silicon at absolute zero (approximately 1.205 V). These devices when operated as temperature sensors are usually driven at constant current with a temperature sensitivity of approximately -1.7 mV/^{o}C to -3.0 mV/^{o}C.

Two different diode configurations were used, in either a lateral or vertical arrangement. In the vertical arrangement a *p*-doped section is formed by using either the initial doping of the silicon substrate or by forming a *p*-well. On top of this a *n*-doped section is implanted, creating the diode structure. In the lateral arrangement *n* and *p* doped regions are implanted next to each other. This design is significantly smaller as electrical contact to the two different doped regions is simpler. These

different designs and configurations are shown in figure 3.18 with table 3.7 showing typical I_O values for the different diodes (assuming 1.5 μm of device silicon).

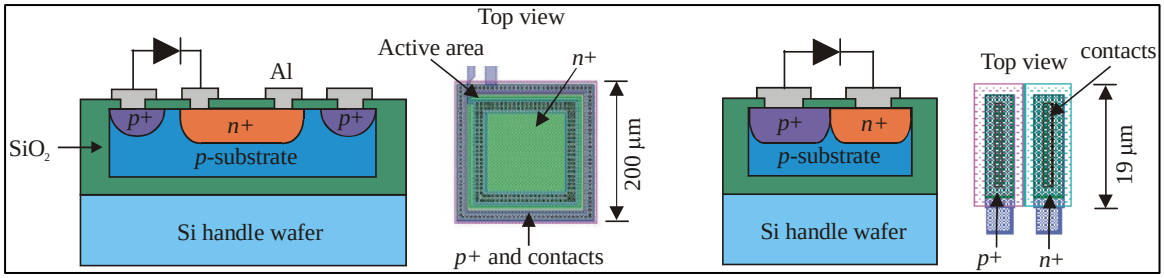

Figure 3.18: Diode temperature sensors.

Horizontal Diode	I_o (A)	Vertical Diode	I_o (A)
Area: 36 μm × 36 μm	3.0×10^{-29}	Area: 1.5 μm × 19 μm	6.5×10^{-29}
Area: 158 μm × 158 μm	5.7×10^{-28}	Area: 1.5 μm × 93 μm	3.2×10^{-28}

Table 3.7: Typical diode saturation values.

The last temperature sensors investigated were the bipolar transistors. There are two ways to implement a bipolar transistor; the first uses a CMOS vertical bipolar transistor (CVBT) with the substrate as the collector, a separate well as the base and a diffusion contact as the emitter. Because the CVBT will have a common collector in the substrate, the application of this device is strictly limited to a common collector configuration. The other possibility is to make a second diffusion in the well (separated by the gate) that will be used as a collector. This structure is actually an annular MOS transistor, which is operated in the bipolar mode, with a gate voltage negative enough to prevent the formation of a surface channel. The internal *p*+ diffusion acts as an emitter, the surrounding *p*+ diffusion as a lateral collector, the substrate as a common vertical collector and the *n*-well as the base. These temperature sensors could only be implemented in the Matra fabrication run as the SUMC run does not contain *n* or *p* wells. It is assumed that that the collector-base voltage of the bipolar transistor is biased at zero volts. This is desirable because the base-collector voltage effects the base width modulation and therefore the base emitter voltage [3.27, 3.28]. In this case it holds that:

$$I_C = I_S\left(e^{\frac{qV_{BE}}{kT}}\right) \qquad (3.19)$$

where I_C is the collector current, I_S is the saturation current, which is proportional to the emitter area and depends on the doping profile, T is the absolute temperature, k is Boltzmann's constant and q the electron charge. The saturation current I_S strongly depends on temperature and when this is taken into account, the above equation becomes:

$$I_C = C' T^{\lambda} \left(e^{\frac{qV_{BE} - V_{go}}{kT}} \right) \qquad (3.20)$$

where V_{go} is the extrapolated band-gap voltage at 0 K; λ is weakly related to the doping level and C' is a constant. The structure of two bipolar temperature sensor is shown in figure 3.19

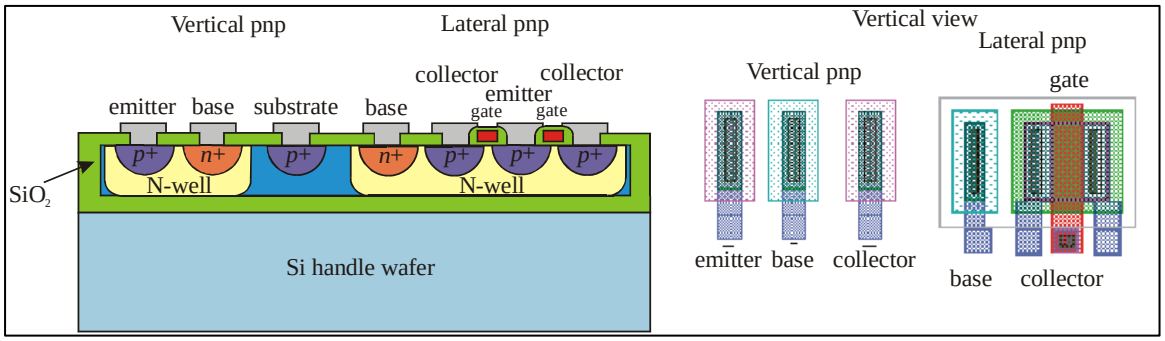

Figure 3.19 Bipolar temperature sensors (Matra only).

3.7 Cell dimensions and final layout

As stated earlier, two different fabrication processes were used in the manufacture of the SOI heater/sensor designs, Matra (Europractice) and SUMC. Table 3.8 gives the typical thickness of these processes. As can be seen the SUMC process has more than one value for certain parameters, this is due to different SOI wafers being used in the fabrication process.

Description	Matra	SUMC	Description	Matra	SUMC
Epi-layer	1200 nm	1500 or 280 nm	Metal 1	740 nm	1 µm
SOI Substrate	400 nm	3000 or 400 nm	Metal 2	1050 nm (Al)	340 nm (Ti/Au)
Gate Oxide	17.5 nm	40 nm	Passivation	1.8 µm	1 µm
Oxide Metal to Poly	700 nm	600 nm	Substrate	475 µm	525 µm

Oxide Metal 1 to 2	1.2 1 μm	N/A	Polysilicon	500 nm	400 nm

Table 3.8: Material thickness values for Matra and SUMC processes.

The final Matra design covers an area of 4 mm × 5 mm containing five membranes, of which four are used as chemoresistive gas sensors. The design consists of four different heater/sensor structures with the fifth being off membrane for comparison. Each membrane is 500 μm × 500 μm in size, with a 1.2 mm × 1.2 mm (defined area on lower side) etched area (assuming an anisotropic etch using KOH) leaving 0.5 mm from the membrane to the edges and 0.6/1.6 mm gap between the membranes. Cell 1 contains an interdigitated MOSFET heater with gap, a central diode temperature sensor and two further diode and resistive temperature sensors outside the heater. Cell 2 contains a similar structure, with a larger heater area (300 μm × 300 μm). Cell 3 has an interdigitated MOSFET heater with gap utilising a different *W*/*L* ratio (6 MOSFET arms instead of 4), a channel resistive temperature sensor within the heater structure, and a further two resistive and bipolar sensors on the membrane. Cell 4 and Cell 5 (off membrane heater) contain interdigitated heaters without gaps with bipolar temperature sensors. The final layout of the Matra design is shown in figure 3.20.

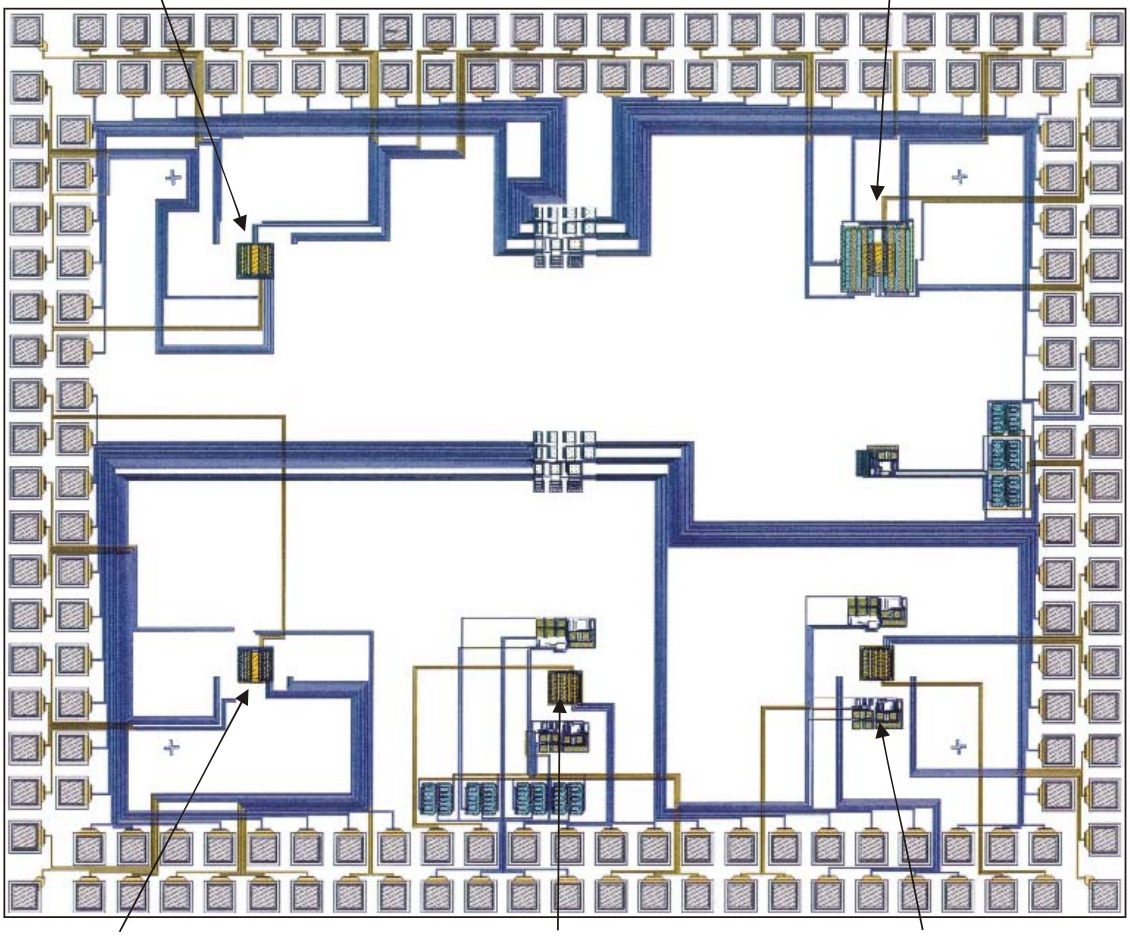

Figure 3.20: Final design for Matra process.

Figure 3.20 also contains a number of other structures located in the centre top of the chip. These are power devices are used on another project and their inclusion was done to spread the cost of manufacture.

3.7.1 SUMC final layout

The designs for the SUMC fabrication process were fitted within a 5 mm × 5 mm frame used by SUMC. The frame contains a number of test cells and alignment marks that are used to evaluate the wafers whilst being processed. These structures consume a small amount of silicon leaving a working area of 4550 μm × 4400 μm. Each cell consists of two 500 μm × 500 μm membranes with a 1.2 mm × 1.2 mm back etched area (as before created by an anisotropic etch using KOH). This will give the cell side legs of 1.9 mm, upper and lower legs of 1 mm and a leg between two membranes of 0.6 mm. The wafer is covered in repeated designs consisting of these 5 mm × 5 mm cells in a 2 × 2 format, thus the repeated structure is 10 mm × 10 mm as is shown in figure 3.21. In addition, two bulk wafers were included in the fabrication run, as a process check, and to compare the effectiveness of the SOI wafers. These devices can also be used for room temperature chemFETs employing a polysilicon gate, with a heater. Even with the bulk silicon remaining a suitable package should permit the heaters to be used to elevate the temperature of the sensors just above ambient, at a reasonable power cost.

For the SUMC fabrication run, Cell 1 contains two different heater structures (interdigitated and square), with diode and resistive temperature sensors both on and off the membrane, operating as chemoresistors. Cell 2 contains two interdigitated heaters with gap (30 μm) operating as either chemoresistors or microcalorimeters. Here the microcalorimeters can be run as a pair with one as a sensor and the other as a reference, using the diode temperature sensors to monitor the membrane. By using a separate temperature sensor an increase in sensitivity maybe achieved. Also included are repeats of these structure off membrane for comparison, with further diode and resistive temperature sensors to monitor the bulk. The remaining two cells contain square heaters with chemFETs, one as a sensor with the polysilicon removed exposing the gate oxide, and the second as a reference with the polysilicon remaining. Cell 3 contains chemFETs with the NGFETs and Cell 4 has the WGFETs. Repeats of the heater and sensor structures have been included off membrane, to investigate how the membrane effects the operation of the FETs. Also added are a number of diode temperature sensors on and off membrane as shown figure 3.21.

Cell 1: Chemorestive

Off membrane sensors:
3 Resistive (100, 150 and 200 μm)
1 Diode (vertical)

Square heater
Channel resistor/diode
temperature sensors

Interdigitated heater
Channel resistor/diode
temperature sensors

Cell 2: Chemorestive/Microcalorimeter

Off membrane sensors:
1 Resistive (100 μm)
1 Diode (vertical)

Repeated structure
off membrane

Au pads

Membrane

Interdigitated with gap heater
2 diode temperature sensors

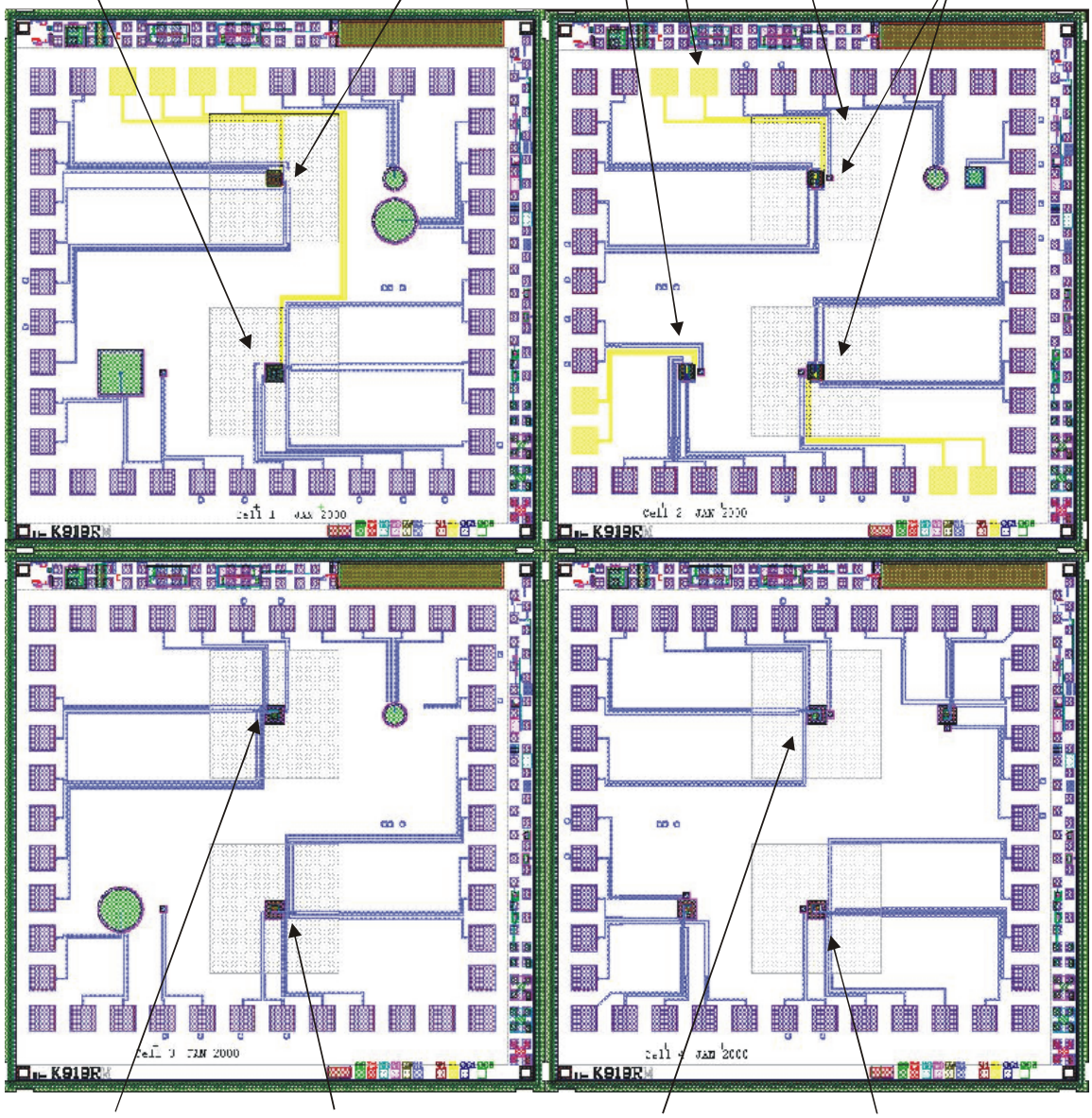

Square heater
diode temperaure sensor
Ref. chemFET sensor

Square heater
diode temperaure sensor
Narrow gate chemFET sensor

Off membrane sensors:
2 Resistive (100 and 200 μm)
21 Diode

Cell 3: Narrowgate ChemFET sensor

Square heater
diode temperaure sensor
Ref. chemFET sensor

Square heater
diode temperaure sensor
Wide gate chemFET sensor

Off membrane sensors:
2 Repeated FET heaters and
sensors for comparison

Cell 4: Wide gate ChemFET sensor

Figure 3.21: Final design for SUMC process.

3.8 Conclusions

In this chapter we have investigated a number of CMOS compatible designs employing MOSFET devices. This has covered many of the design considerations for room temperature chemFET sensors and high temperature MOSFET heaters/sensors as well as secondary structures such as temperature sensors. These structures, being CMOS compatible, should allow the integration of the heater control and measurement electronics onto the device.

The room temperature devices were fabricated at the Institute of Microtechnology, Switzerland. An array of four *n*-type enhanced FETs with gold electrodes has been designed with channel dimensions of 385 μm × 10 μm and 105 μm × 5 μm in bulk silicon. Secondly, higher temperature SOI devices will be fabricated through Europractice and SUMC. These devices employ SOI technology utilising the self-heating effects of a MOSFET to raise the temperature of a thin SOI membrane. This should give excellent control over the operating temperature as well as having lower power consumption. Here both vertical and lateral heater arrangements have been implemented. In the vertical arrangement an interdigitiated MOSFET heater of 4 or 6 transistors in parallel with and without gaps is used employing a chemoresistive or a mirocalorimetric sensors. Secondly, a lateral square heater with a central chemFET sensor with a partially removed polysilicon gate. *W*/*L* ratios and coverage values of the heater have been modified to investigate how this effects the operating point and power consumption of this heater/sensor configuration. Electro-thermal simulations have performed and have shown that operating temperatures of 300 ^{o}C are possible for only a 35 mW power consumption.

3.9 References

3.1 J. S. Kilby, Invention of the integrated circuits, *IEEE Trans. Electron Devices*, ED-23, (1976), 648

3.2 D. Kahng, A historical perspective on the development of MOS transistors and related devices, *IEEE Trans. Electron Devices*, ED-23, (1976), 655

3.3 B. J. Baliga (ed.), Epitaxial silicon technology, Academic Press London (1986), 134-147.

3.4 S. A. Campbell, H. J. Lewerenz, Semiconductor Micromachining: Volume 2 Techniques and Industrial Applications, Wiley (1998), 153-183.

3.5 P. Corcoran, PhD Thesis, University of Warwick, Coventry, CV4 7AL, UK, 1991.

3.6 J. W. Gardner, A. Pike, N. F. Rooij, M. Koudelka-Hep, P. A. Clerc, A. Hierlemann, W. Gopel, Integrated chemical sensor array for detecting organic solvents, *Sensors and Actuators B*, **26**, (1995), 135-139.

3.7 F. Udrea, J. W. Gardner, UK and World patent application BG2321336A and WO98/32009.

3.8 J. W. Gardner, F. Udrea, W. I. Milne, Numerical simulation of a new generation of high-temperature micropower and odour sensors based on SOI technology, *Proc. Of SPIE Smart Electronics and MEMs, Vol. 3673*, (1999), 104-112.

3.9 S. M. Sze, *Semiconductor Devices: Physics and Technology*, Wiley, 1985, 159-222.

3.10 E. S. Yang, *Microelectronic Devices*, McGraw-Hill, 1988, 229-253.

3.11 I. Lundstrom, M. Armgarth, A. Spetz, F. Winquist, Gas sensors based on catalytic metal-gate field effect devices, *Sensors and Actuators*, **10** (1986) 399-420.

3.12 M. G. H. Meijerink, M. Koudelka-Hep, N. F. de Rooij, D. J. Strike, J. Hendrikse, W. Olthuis, P. Bergveld, *Electrochemical and Solid-State Letters*, **2** (3), (1999) 138-139.

3.13 J. W. Gardner, *Microsensors: Principles and applications*, Wiley, 1994.

3.14 J. V. Hatfield, K. S. Chai, A conducting polymer GasFET, *Eurosensors XI*, Warsaw, Poland (1997), 739-742.

3.15 K. Domansky, J. Li, J. Janata, Selective doping of chemically sensitive layers on a multisensing chip. *Journal of Electro. Soc*., (1997) L76-L78.

3.16 D. Briand, B. van der Schoot, H. Sungren, I. Lundstr✱m, N. F. de Rooij, A low-power micromachined MOSFET gas sensors, *Tech. Digest of Transducers '99*, Sendai, Japan (1999) 938-941.

3.17 J. W. Gardner, P. N. Bartlett, *Electronic Noses: Principles and applications*, Oxford University Press, 1999.

3.18 J. W. Gardner, H. V. Shurman, P. Corcoran, Integrated tin oxide odour sensors, *Sensors and Actuators B*, **4** (1991), 117-121.

3.19 S. A. Campbell, H. Lewerenz, *Semiconductor micromachining, Vol.2: Techniques and industrial applications*, Wiley, 1998.

3.20 A. Pike, J. W. Gardner, Thermal modelling and characterisation of micropower chemoresistive silicon sensor, *Sensors and Actuators B*, 45 (1997), 19-26.

3.21 U. Dibbern, A substrate for thin-film gas sensors in microelectronic technology, *Sensors and Actuators B*, **2** (1990), 63-70.

3.22 J. W. Gardner, F. Udrea, B. Milne, Numerical simulation of a high-temperature, micropower gas and odour sensors based on SOI technology, *Proc. of SPIE Smart Electronics and MEMS*, 1-5 March, 1999.

3.23 S. Timoshenko, S. Woinowski-Krieger, Theory of plates and shells, McGraw Hill, 1959.

3.24 S. Astie, A.M. Gue, E. Scheid, L. Lescouzeres, A. Cassagnes, Optimization of an integrated SnO_2 gas sensor using a FEM simulator, *Sensors and Actuators A*, 69 (1998), 205-211.

3.25 J. P. Collinge, *Silicon of insulator technology*, Kluwar Academic Publisher, 1991.

3.26 A. Pike, *PhD Thesis*, 1996, University of Warwick, Coventry, CV4 7AL

3.27 Semiconductor Sensor, Philips data book. Vol. SC17, 1993.

3.28 K. S. Szajda, C. G. Sodini, F. H. Bowman, A low noise, high resolution silicon temperature sensor, *IEEE Journal of Solid-State Circuits*, vol. 31, **9**, (1996) 1308-1313.

3.29 A. Kolling, S. Koomen, P. Bergveld, E. Seevinck, 2-Lead multiplex system for sensor array applications, *Sensors and Actuators*, **17**, (3-4), (1989) 623-628.

CHAPTER 4

Device fabrication and deposition of vapour sensitive layers

4.1 Introduction

In the previous chapter the design of bulk CMOS and SOI CMOS compatible devices was covered. Clearly, once the standard fabrication procedures are completed then post-processing techniques can be applied to convert the device into a sensor, predominately by the deposition of a gas sensitive layer. It is this active material which defines the gas/vapour sensing properties of the final sensor. Here the final fabricated devices are described, covering the main sensor types; the room temperature chemFET sensors, including the devices made in collaboration with IMT and those donated by UMIST, and the SOI device, fabricated through Europractice. Three types of polymer deposition techniques are described and compared, the chemically prepared/electrochemically doped polymers, composite polymers and electrochemically grown polymers. This is the first time composite polymers and poly(bithiophene)/TBATFB have been used on FET devices.

In addition, these active polymer materials have been characterised by SEM and AFM, including film thickness measurements by vertical scanning interferometry to create 3D profiles of the polymers. This is one of the first applications of this method to determine the polymer thickness by a non-contact means.

Lastly a chemoresistive device and a Kelvin probe substrate are described. These devices are used to benchmark the chemFET sensors and to make Kelvin probe

measurements to determine the work functions of the electrochemically deposited and composite polymers.

4.2 Device realisation

Initial experiments were performed with sensors donated by Dr J. V. Hatfield of UMIST, UK, supplied by the National Microelectronics Research Centre, University College, Cork, Ireland. These ChemFET sensors are modified Ion Sensitive FETs (ISFETs) [4.1,4.2], originally designed to measure the pH of liquids. These devices contain two gate-less PMOS devices, with a polymer film added as a post-processing step. The channel dimensions were 600 μm × 20 μm (channel width/length), with the gate oxide composed of 70 nm of thermal grown oxide on a *n*-type <100> wafer, with 30 nm of Si_3N_4 deposited by LPCVD. The device also contains a standard FET with an aluminium gate for reference purposes. Between the two gate-less FET devices an aluminium pad was deposited for electrical contact to the polymer regions. A schematic and photograph of the device after polymer deposition in given in figure 4.1.

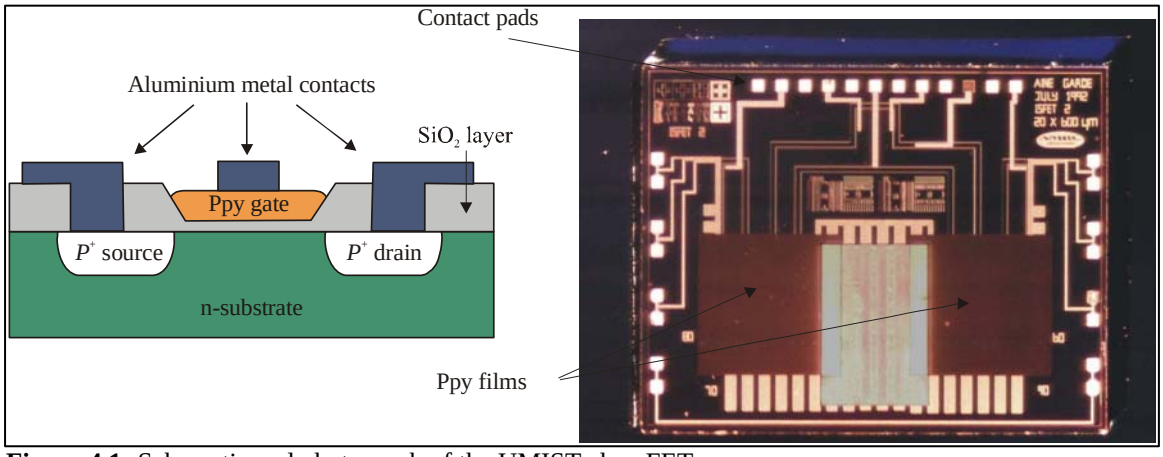

Figure 4.1: Schematic and photograph of the UMIST chemFET sensor

The substrate contact was made through the base of the device as the polymer deposition process damaged the top surface connection. The device was glued into a standard 14 pin DIL package (Spectrum Semiconductors, USA, part no. CSB1410B) using silver epoxy (Conductive epoxy, Circuit Works Corp., USA) and the remaining connections wire bonded onto the pads.

4.2.1 ChemFET array device

The second and most commonly used device was fabricated by the Institute of Microtechnology, University of Neuchatel, Switzerland. The final design covered an area of 4 mm × 4 mm, including sensing area, pads and heater. A resistive heater was also included by the *p*-doping of silicon, with a typical resistance of 220 Ω. Figure 4.2 shows a photograph of the final device before polymer deposition.

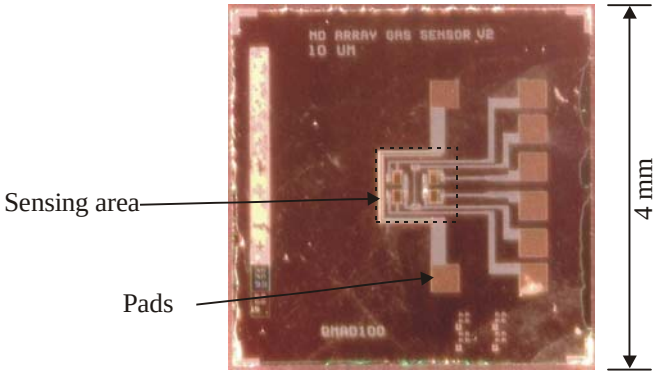

Figure 4.2: Photograph of fabricated chemFET sensor.

The sensing area can be seen more clearly in figure 4.3. Here a standard device is shown with channel dimensions of 385 μm × 10 μm with 2 closed / solid gates and 2 open / exposed channels where the gold electrode has been removed revealing the gate oxide. Using these dimensions the gold etching process clearly defines this channel region. The smaller device (channel dimensions 105 μm × 5 μm) gave inferior definition as the gold in-between the meandered arms was removed. It was found this did not effect the operation of the FET as a sensor. Also included in the design was a *pn*-thermodiode as shown in figure 4.3a. This could be also used to monitor the temperature of the silicon substrate, though was not applied here as the test equipment has accurate external temperature control (±0.1 ^{o}C). The device was mounted in the standard 14-pin DIL package (Spectrum Semiconductors, USA), used for the UMIST sensors, as shown in figure 4.3b.

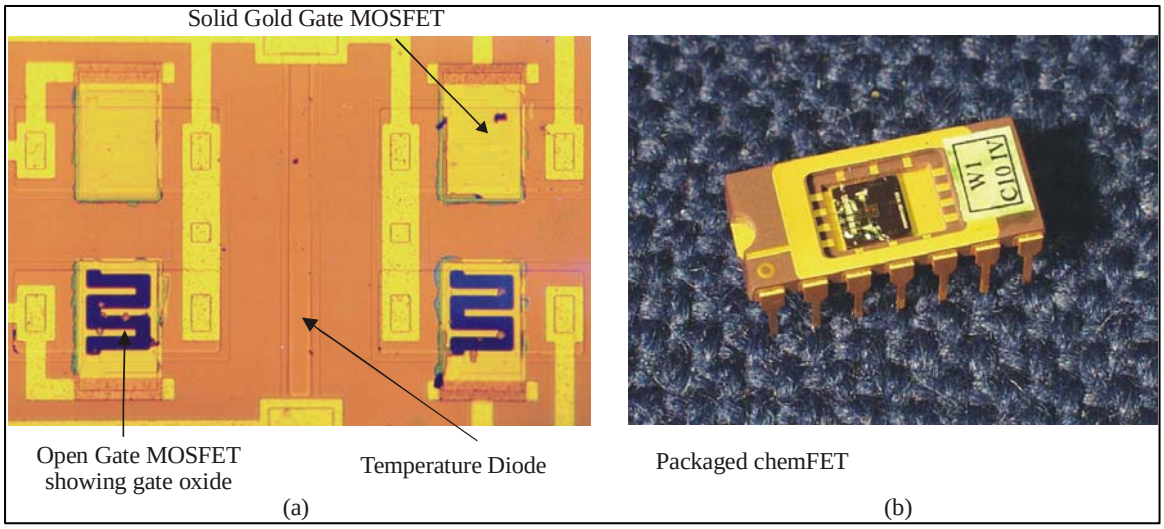

Figure 4.3: (a) Photograph of the sensing area and (b) photograph of the packaged device.

4.3 Deposition of polymer sensing materials

By using a simple room temperature chemFET design a number of different active polymer materials can be deposited and compared. In total three different types of polymer were used, chemically prepared/electrochemically doped polymers, carbon black composite polymers and electrochemically grown polymers.

4.3.1 Spun-coated polymers

Researchers at UMIST have developed a technique by which the chemically prepared conducting polymer, poly(pyrrole), can be deposited using a chemical vapour deposition technique (CVD). The resulting poly(pyrrole) film can be defined using standard photolithography techniques etched using a plasma etcher. This film is then electrochemically doped to produce the final gas sensitive layer. By using this technique it is possible to deposit these types of polymer on almost any substrate and can be accurately defined by modern lithography and etching processes. The sensor material is normally deposited whilst the devices are still as a wafer and diced into individual sensors after post-processing, though this process can be used on individual devices. A scanning electron microscope (SEM) photograph of this polymer is shown in figure 4.4.

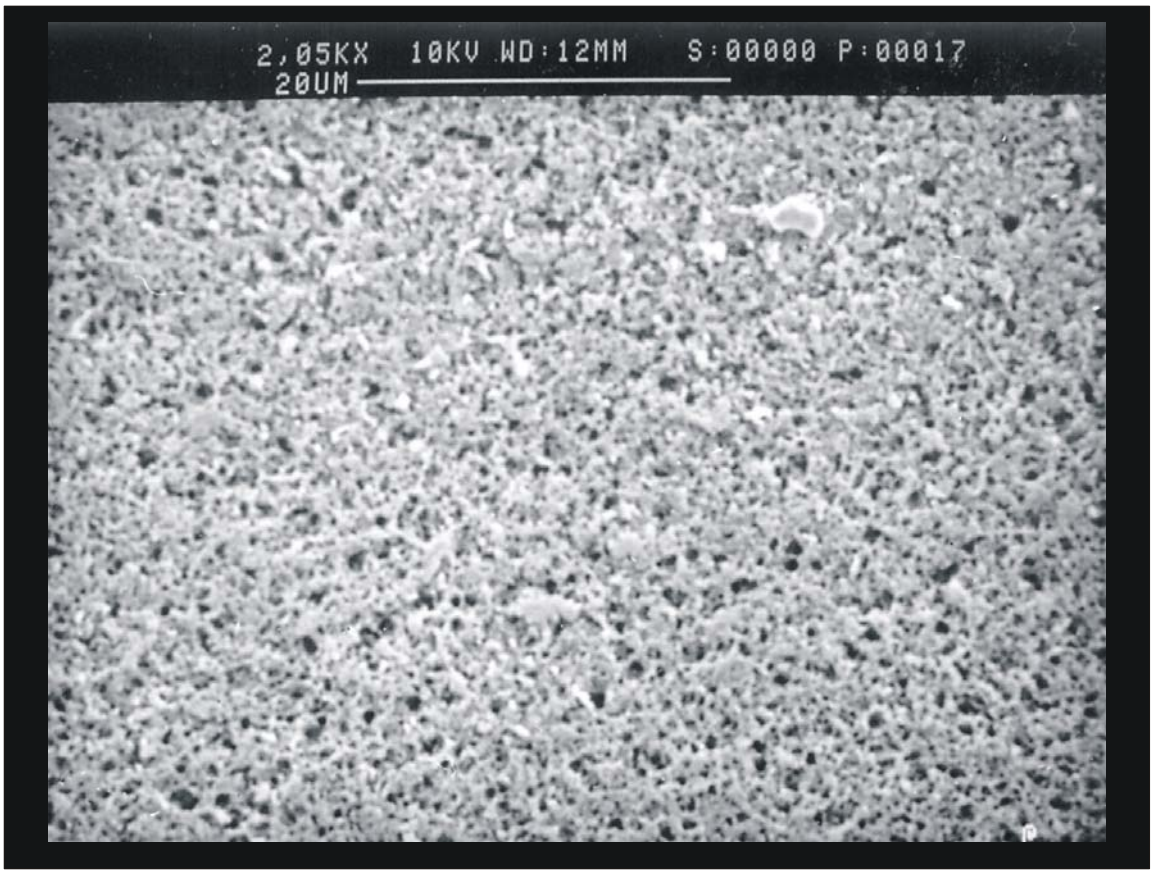

Figure 4.4: SEM of chemically prepared, CVD deposited poly(pyrrole).

This polymer shows a very porous structure that should allow the analyte to diffuse rapidly through the film and possibly give quicker, larger responses due to the higher surface area for the analyte to react with in comparison to, for example, poly(pyrrole)/BSA electrochemically deposited.

4.3.2 Carbon-black composite polymers

Carbon-black composite polymers are a combination of carbon black spheres and insulating polymer, where the carbon black endows electrical properties to the composite material. Three different types of composite polymer were used in these experiments:

- Poly(ethylene-co-vinyl acetate) with 66:33 ethylene to vinyl acetate by % weight.
- Poly(styrene-co-butadiene) AB block copolymer with 30% of styrene.
- Poly(9-vinylcarbazole)

The deposition of these polymers was initially performed by Cyrano Sciences (USA) and later replicated at the University of Warwick using the same polymers. These

composite materials have been previously used [4.3,4.4]. The polymer was dissolved in toluene at a 0.5% loading by weight of total solids to toluene and stirred continuously for a minimum of 24 hours. The polymer / toluene was mixed with a 20% loading, by weight, of carbon black (Black Pearls 2000, Cabot, USA) to polymer and stirred for 30 minutes before deposition. The Cyrano Sciences deposition was carried out using a BioDot XYZ Platform (BIODOT, Irvine, CA). This combines motion control with an AirJet 2000^{TM} dispenser. The polymer was deposited from a height of 125 mm at a temperature of 21^{o}C and humidity of 50 % r.h. (relative humidity), and an air pressure of 10 PSI, with the solution continuously stirred within the sprayer as deposition occurred. This technique produced a circular coating typically 1 mm to 1.5 mm in diameter, over the centre of the device. The number of passes/sprays controlled the thickness of the film. This value was modified to 4, 6 and 9 passes to investigate the effect of film thickness on the magnitude of the response. For these later experiments the composite mixture was altered to contain a 0.625 % loading of solids (0.250 % polymer to 0.375 % carbon black by volume) to toluene (for poly(styrene-co-butadiene) only). Here the carbon and polymer were separately dissolved in toluene and then combined for deposition. The first atomic force microscope (AFM) plot of these composite materials, is shown in figure 4.5 (Q-Scope^{TM} 788, Quesant Instrument Corp., USA) This shows a typical sphere size of around 100 nm, with multi-contacts between carbon spheres.

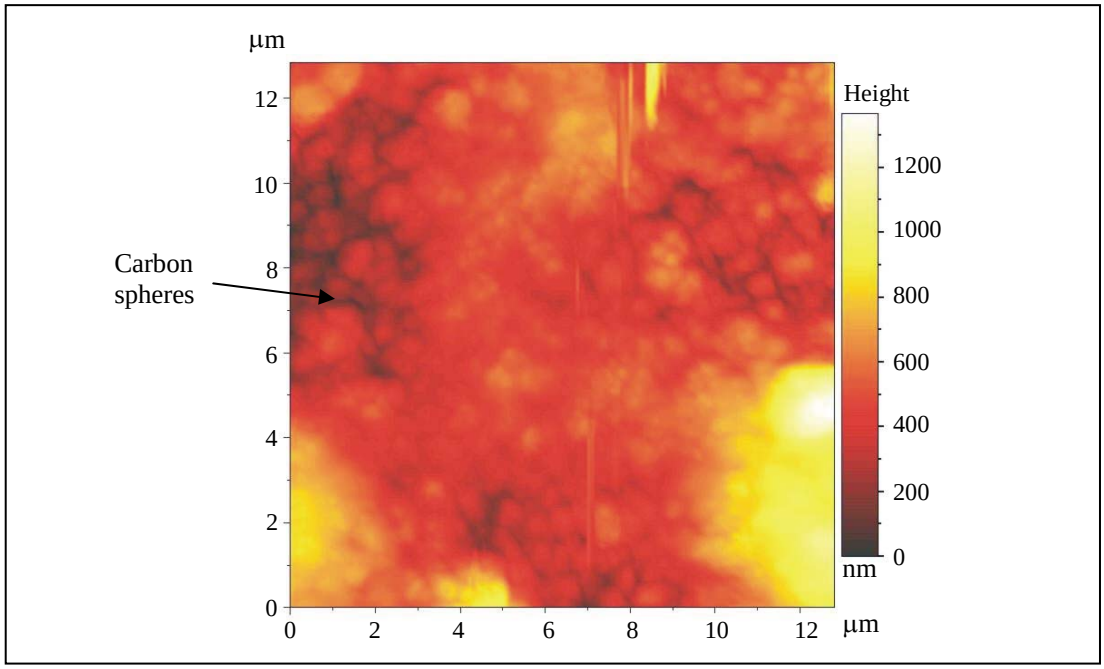

Figure 4.5: AFM plot of composite polymer material.

The second deposition process was carried out at the University of Warwick, with the assistance of Mr S. Horton a 3rd year project student. This system combined a standard liquid dispenser (RS Components, No. 552-179) with an airbrush (Student-plus ISB550, Revell, USA). The liquid dispenser, in normal operation, is used to send a pulse of air into a syringe, containing liquid, depositing the liquid onto a substrate. In this configuration the pneumatic pulse is used, through the airbrush to deposit the composite polymer. This is a significantly cheaper deposition method to the BioDOT system. The airbrush is held a distance of 50-55 mm above the sensor, sprayed at temperature of 25 ^{o}C, and a pressure of 15 PSI for 500 ms, with the composite material held in a chamber within the airbrush. The target sensor fits within a mechanical mask (made at Warwick University), which both supports the device and defines the region for polymer deposition. The mask allows a 0.8 mm, circular coating of polymer over the sensor area. As before the thickness of the polymer is defined by the number of sprays. A photograph of the dispensing system is shown in figure 4.6.

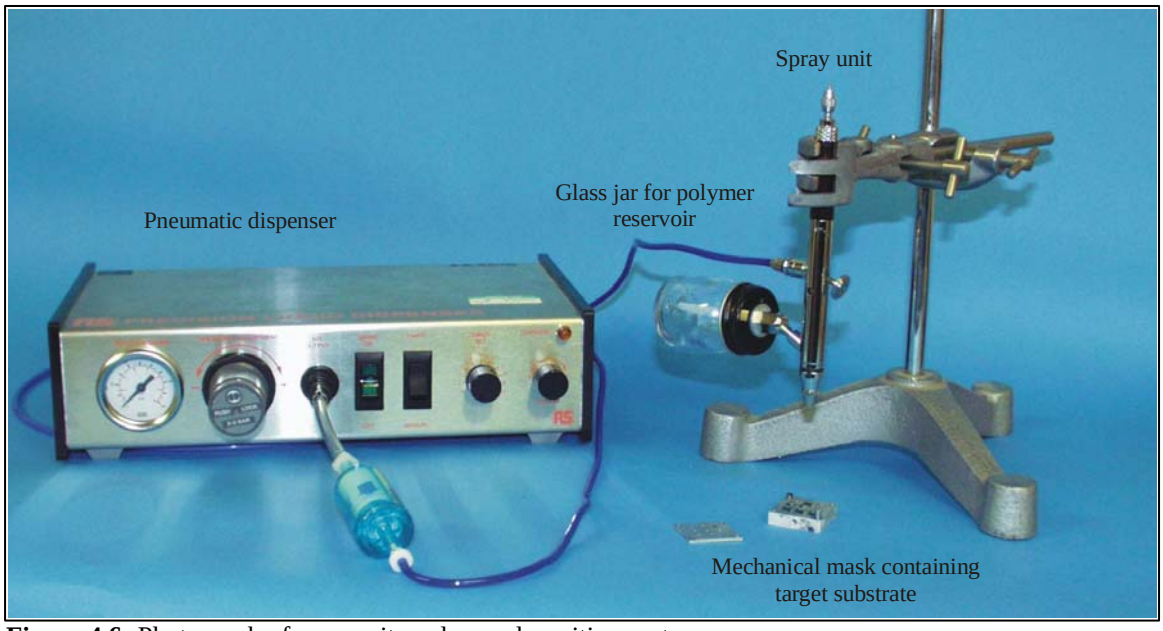

Figure 4.6: Photograph of composite polymer deposition system.

Here poly(9-vinylcarbazole) was used and sprayed 30, 40 or 50 times onto the chemFET sensor to create a range of thicknesses. As before, this was used to investigate how film thickness effects the magnitude of the response.

4.3.3 Electrochemically prepared polymers

The electrochemically grown films were deposited by Mr Chee-Seng Toh, under the supervision of Prof. P. N. Bartlett at the Department of Chemistry, University of Southampton, UK. Two different polymers were used in these experiments:

- Poly(pyrrole)/Butanesulphonic acid (BSA)
- Poly(bithiophene)/Tetrabutylammonium tetrafluoroborate (TBATFB)

For electrochemical deposition the monomer is first dissolved in an appropriate solvent, where this solvent significantly effects the electrical conductivity of the final polymer. The deposition technique has been previously shown to produce reliable, repeatable devices [4.5,4.6]. This deposition technique begins with the generation of radical cation, formed by oxidation on the surface of the electrode. This radical can react with a second radical to form a dimer, or with the neutal monomer followed by subsequent oxidation to give a dimer. The resulting polymer is deposited on the working electrode.

For deposition all aqueous solutions were freshly prepared using water purified by a Whatman RO 50 and a Whatman ‘still plus’ system. Pyrrole (Aldrich, 99%) was

filtered through a Brockmann Grade 1 aluminium oxide (BDH) column before each use. Tetrabutylammonium tetrafluoroborate or TBATFB (Fluka, >99%) was dried under vacuum at 120 ^{0}C in the presence of molecular sieves (Aldrich, 4A). Acetonitrile (Aldrich, HPLC grade) was dried using molecular sieves. Sulphuric acid (BDH, AnalaR grade, >98%), 2,2'-bithiophene (Aldrich, 97%) and 1-butanesulphonic acid, sodium salt (Aldrich, 98%) were used as received.

These polymers were deposited using the microdeposition technique, in which a luggin capillary and counter wire are combined into a single structure, as shown in figure 4.7. This configuration permits autocorrection for most of the iR(solution) drops between the working and counter electrode, and allows control over the potential of the working electrode. The luggin capillary is a commonly used tool which acts as an extension of the reference electrode, as current flows within the luggin capillary is zero, so the potential at the tip of the capillary equals that at the reference electrode. The purpose of the luggin capillary is to minimise uncompensated iR drop between reference and working electrode. In this case, it is also used to confine the solution to a very small volume, while ensuring conductivity between the 3 electrodes. The luggin capillary was filled with 1 mol dm^{-3} sulphuric acid and connected to a double-frit SCE reference electrode. The FET device was mounted onto a microstage (Microcontrole). A column of electrolyte solution from the luggin capillary was positioned over the centre sensing area of the FET device using the xyz translator of the microstage. To minimise the effects of vibration the apparatus was assembled on a Newport anti-vibration microboard. This 'solution column' structure was maintained by its own surface tension and by an adjoining arm of the luggin capillary that controlled the height of the electrolyte solution above the device. The potential was cycled on the working electrode (FET gate) to clean the area before polymer deposition. For electrodeposition, the monomer/salt solutions replaced the sulphuric acid as the electrolyte and salt bridge solutions.

A single 20 ml droplet of electrolyte was positioned between the reference and the counter electrode and the working electrode. The reference electrode was connected to the electrolyte droplet by an aqueous bridge solution of similar composition as the electrolyte solution. The polypyrrole polymer was deposited from aqueous solution containing 0.3 mol dm^{-3} pyrrole and 0.10 mol dm^{-3} BSA. Electrodeposition of polypyrrole was carried out using potential step from 0 V to 0.85 V (vs. SCE) (portable

potentiostat, Oxford Electrodes). The films were then washed with purified water and air-dried.

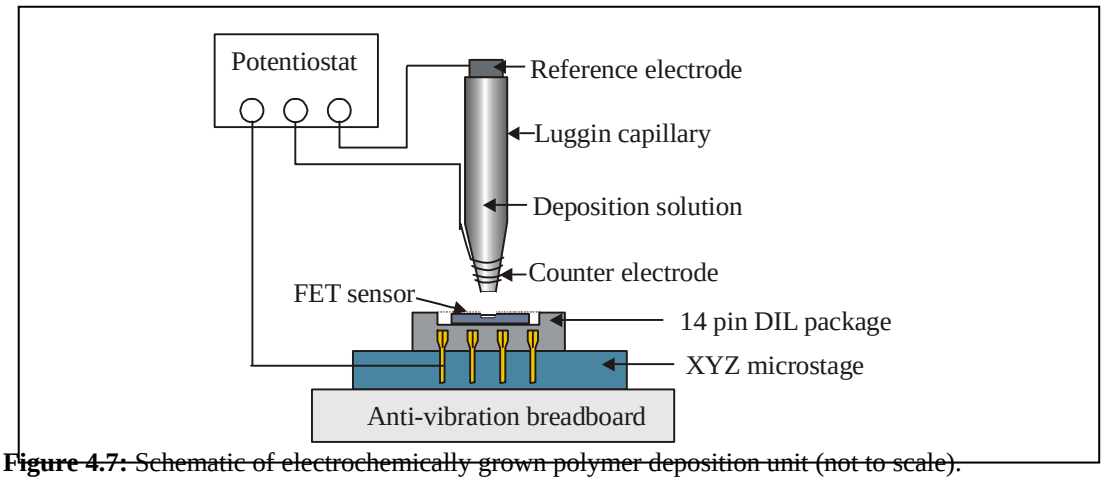

Figure 4.7: Schematic of electrochemically grown polymer deposition unit (not to scale).

Poly(bithiophene) was deposited from an acetonitrile solution containing 0.04 mol dm^{-3} 2,2'-bithiophene and 0.10 mol dm^{-3} TBATFB. A $Ag/AgNO_3$ reference electrode replaced the double-frit SCE as the reference electrode. Electrodeposition of poly(bithiophene) was carried out using potential step from 0 V to 0.85 V for 1 s, followed by potential step to 0.815 V (vs. $Ag/AgNO_3$). The films were then washed with acetonitrile and air-dried. In both cases the charge passed controlled the thickness of the polymer film. For the multi-polymer and single polymer arrays the deposition was inhibited on the remaining gates by applying a negative potential (typically –1 volt). Further details can be obtained elsewhere of this deposition process [4.7,4.8]. Typical transient potential steps obtained from the deposition of poly(pyrrole)/BSA and poly(bithiophene)/TBATFB is shown in figure 4.8.

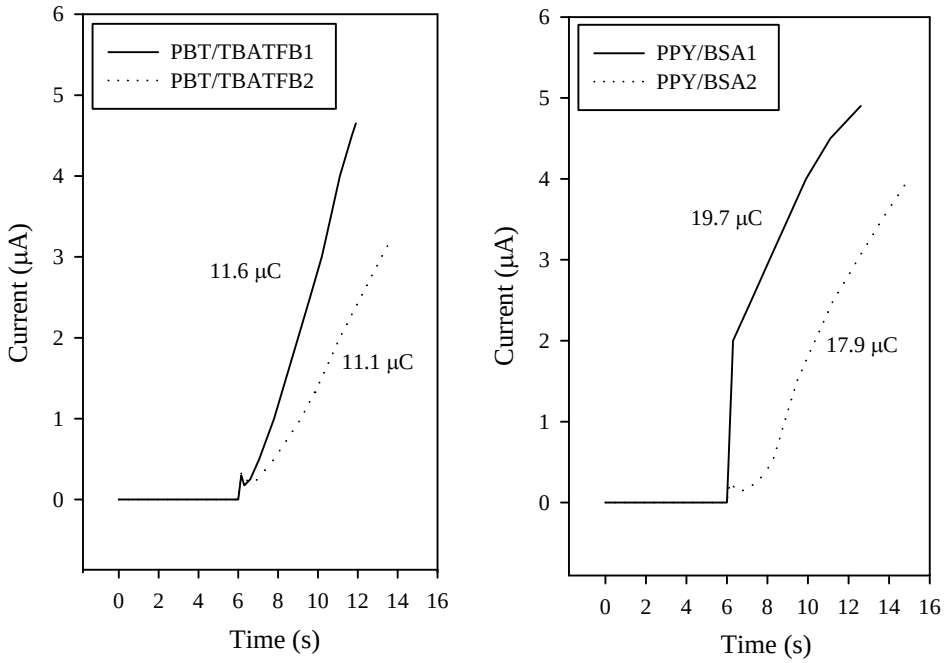

Figure 4.8: Potential growth transients for poly(pyrrole)/BSA (PPY/BSA) and poly(bithiophene)/TBATFB (PBT/TBATFB).

SEM (scanning electron microscope) plots of poly(pyrrole)/BSA and poly(bithiophene)/TBATFB are shown in figure 4.9.

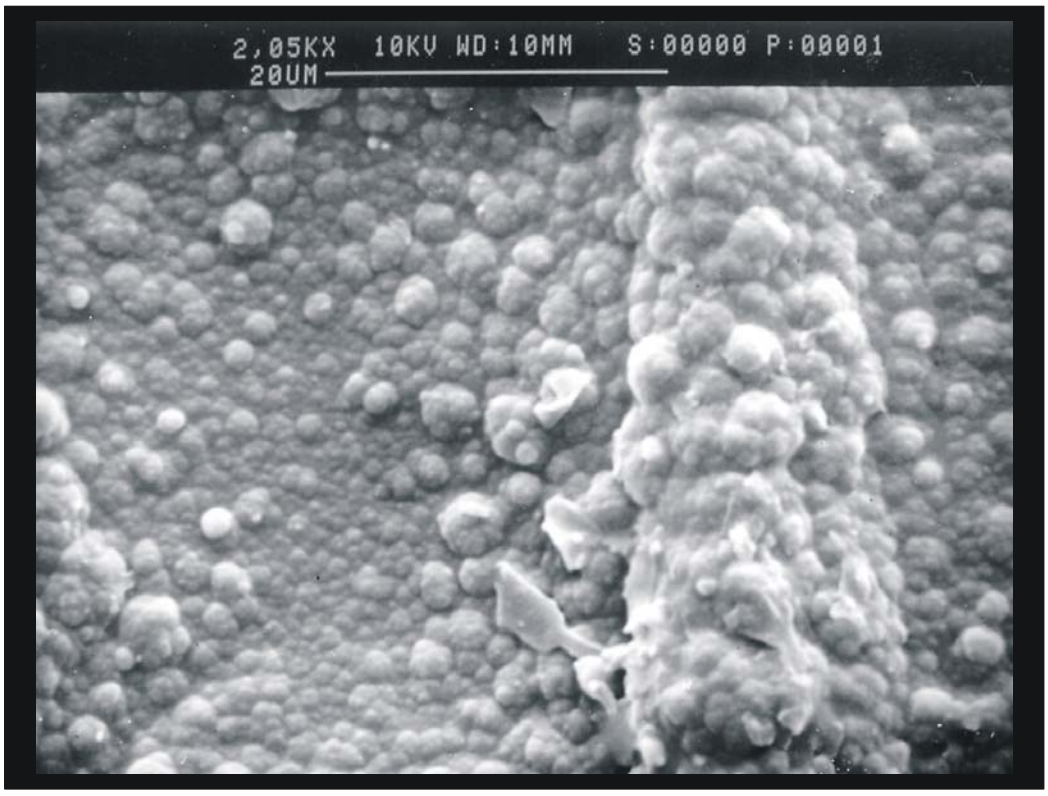

(a)

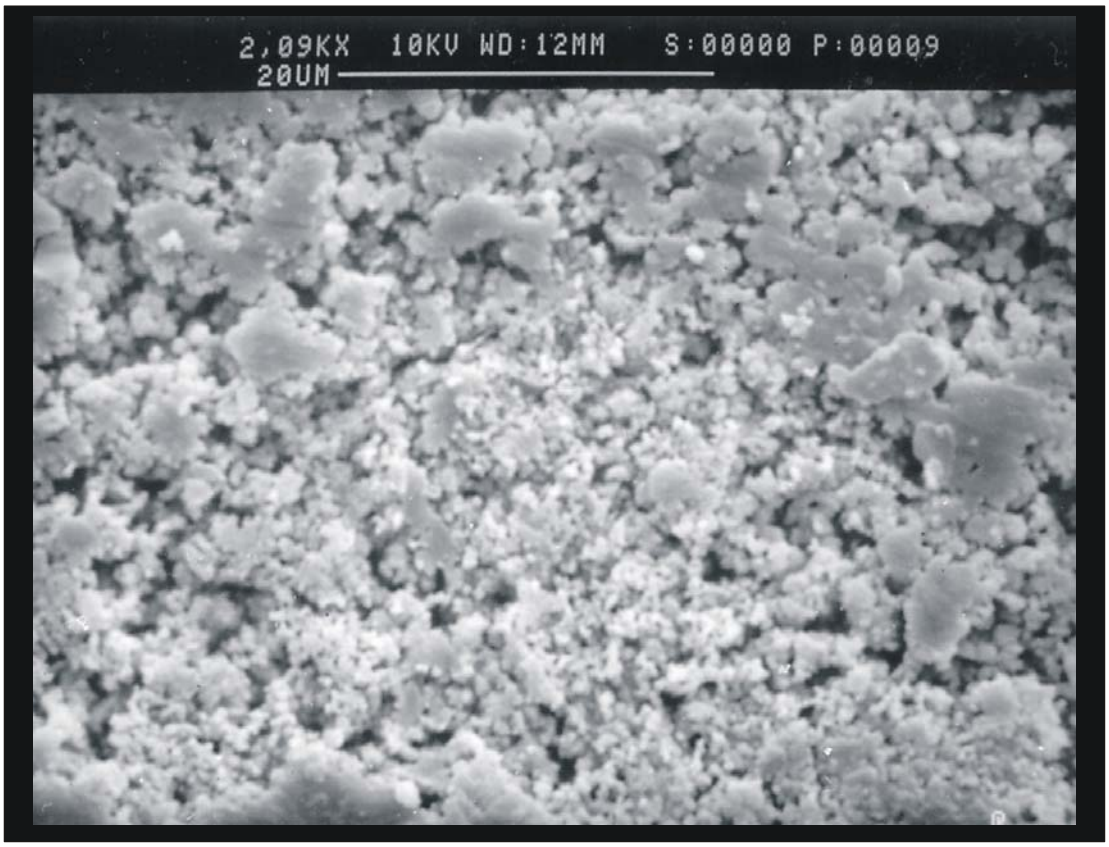

(b)

Figure 4.9: SEM plots of (a) poly(pyrrole)/BSA and (b) poly(bithiophene)/TBATFB

Poly(pyrrole)/BSA shows a typical circular structure and poly(bithiophene)/TBATFB a more honeycomb structure. From these SEMs we would expect poly(bithiophene)/TBATFB to respond more rapidly than the poly(pyrrole)/BSA as its more porous structure would allow a reactive gas/vapour to diffuse in more rapidly.

The polymers were grown in two configurations, initially only one polymer was deposited per device. Here chemFET arrays with two open gates and two closed gates were used for comparison. When two different polymers were grown per device, the four open gate configuration was implemented to ensure at least one operational sensor of each polymer. By using this deposition technique polymer growth only occurs where a potential is applied, hence accurate control over the deposition process can be achieved. This definition is significantly improved over the carbon black composite polymers, where the polymer is spread over a wide area though the actual deposition itself is more time consuming. Also for the composite deposition process the separation between devices has to be significant, as the minimum deposition area is generally a circular coating 0.5 mm in diameter. Figure 4.10 shows an array device with

electrochemically deposited polymers and demonstrates the accuracy of the deposition process.

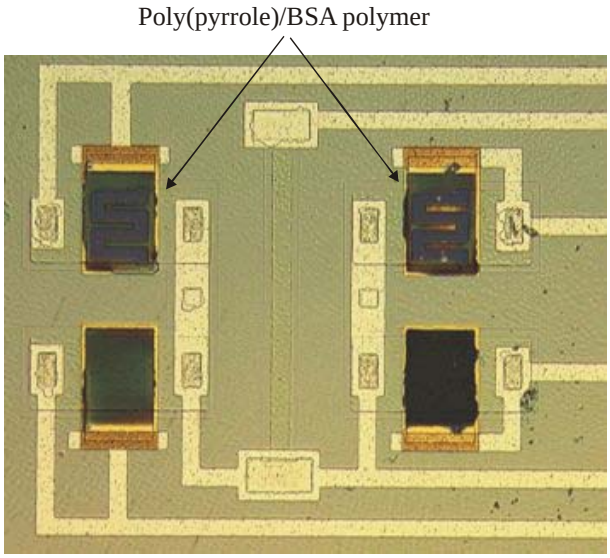

Figure 4.10: Photograph of electrochemically grown conducting polymers after deposition.

A comparison of the ease of deposition and definition of these polymers is given in table 4.1.

Polymer	**Description**
CP	Good definition defined by accuracy of lithography process and etching. Also reasonable repeatability in film thickness due to spinning/drip-cast process.
CM	Poor definition due to spraying process. Can be improved by masking, though physical limitations apply. May have non-linearity over sensing area due to spraying system.
ECP	High accuracy on deposition defined by areas of conduction. This process allows multi-polymer arrays within a small area. Under the right circumstances can produce highly repeatable film thickness by controlling growth rates.
	Substrates
CP	Process allows deposition on most substrates
CM	Process allows deposition on most substrates
ECP	Limited range of materials, popular CMOS layers such as Al and *n*-doped polysilicon cannot be used.

	Chemicals
CP	Simple chemical preparation though some batch-to-batch variation.
CM	Simple chemical preparation though some batch-to-batch variation.
ECP	Electrochemical deposition gives good repeatability in chemical composition, once earlier steps have been completed.
	Deposition time
CP	Long deposition time due to multi-step process, though only limited chemical preparation required.
CM	Rapid deposition (< 60 mins), chemical preparation 24-48 hours.
ECP	Both long sample and chemical preparation time. Rapid chemical deposition.

Table 4.1: A comparison of different deposition techniques for conducting polymers (CP = chemically prepared, CM = composite materials, ECP = Electrochemically prepared).

4.4 Thickness profiling of conducting polymer films

An important parameter that may control the magnitude of any response is the thickness of the polymer film. Profiling of the polymer films was performed using the Wyko^{TM} NT-2000 interferometer. This instrument uses phase shifting and vertical scanning interferometry to create a three dimensional surface profile of the polymer. The instrument has a vertical measurement range of 0.1 nm to 150 μm and a field of view up to 8 mm. This is the first reported use of this method of film measurement has been used to create 3D profiles of polymer films. Also, as this technique is non-contact, unlike other stylus based profiling methods that can cause errors due to the softness of the material. In a number of cases these results were verified using the Nanostep 2010 (Rank-Taylor Hobson, UK).

4.4.1 Thickness profiles of Spun-coated/drip-cast polymers

The poly(pyrrole) films used for the UMIST devices were measured at a typical thickness of 3.9 μm ±0.5 μm. A 3D plot of one of these deposited polymer films is shown in figure 4.11. As can be seen there are a number of high points within the film. These maybe anomalies due to the difficulties involved in reflecting light off a black-matt surface or surface contamination.

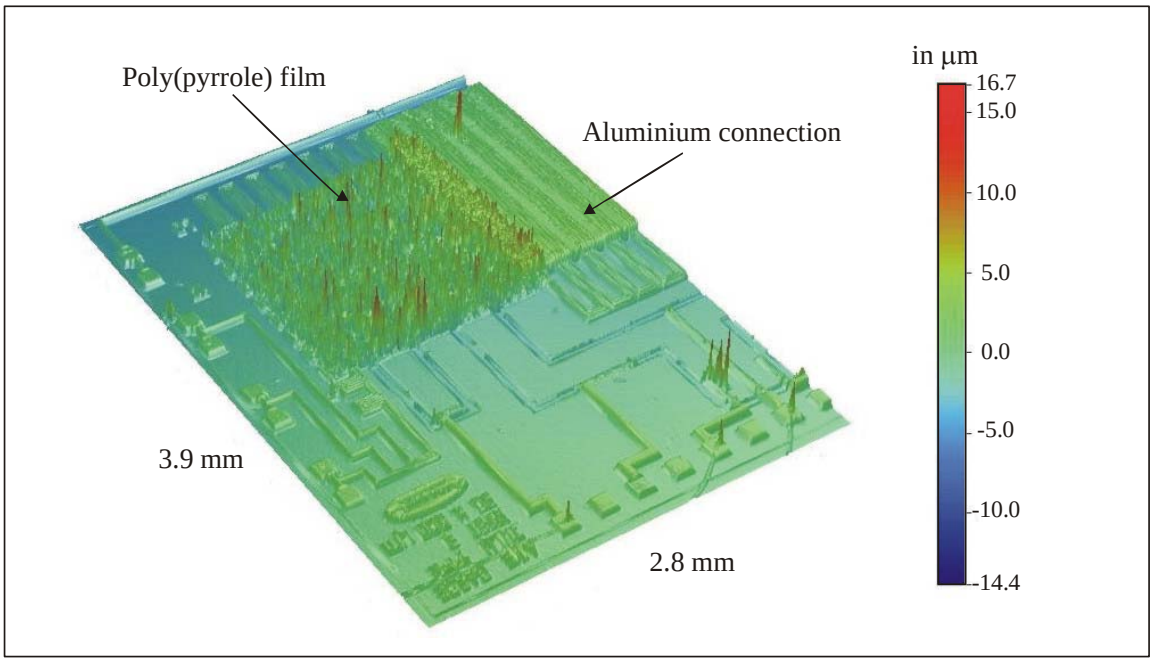

Figure 4.11: 3D profile of poly(pyrrole) deposited by CVD.

4.4.2 Thickness profiles of composite polymers

The composite polymers were deposited using two methods, with a range of different thickness values as shown in table 4.2.

Polymer	Max. thickness of polymer (μm)
poly(styrene-co-butadiene) – 15 sprays*	2.5 ± 0.20
poly(styrene-co-butadiene) – 9 sprays*	2.1 ± 0.51
poly(styrene-co-butadiene) – 6 sprays*	1.4 ± 0.23
Poly(ethylene-co-vinyl acetate) – 4 sprays	0.5 ± 0.05
Poly(styrene-co-butadiene) – 15 sprays	3.7 ± 0.25
poly(9-vinylcarbazole) – 15 sprays	1.9 ± 0.15

Table 4.2: Thickness measurement for composite polymer deposited by Cyrano Sciences Inc. USA.

A 3D profile of poly(styrene-co-butadiene), by the Wyko™ instrument is shown in figure 4.12, for a device of channel dimensions 385 μm × 10 μm. The variation in the film thickness, within the sensing area, is clearly shown to be marginal (≈ 10%)

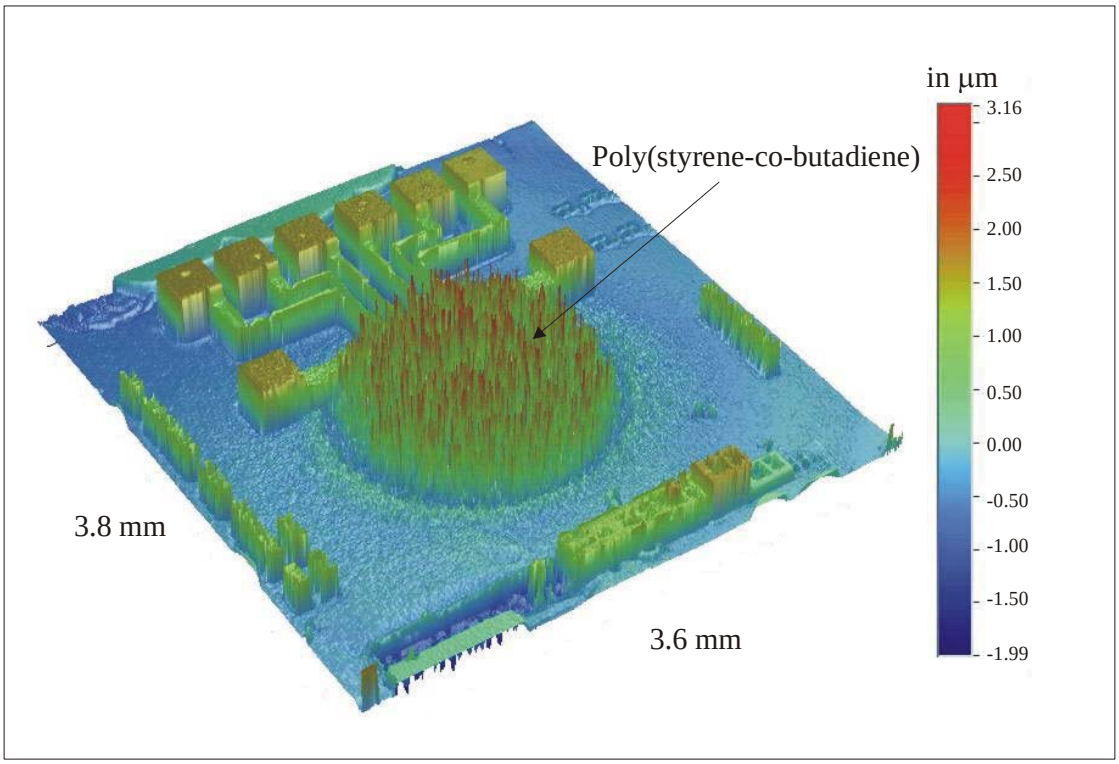

Figure 4.12: 3D profile of poly(styrene-co-butadiene).

The variable thickness measurements, from the Warwick sprayed sensors are given in table 4.3. This shows that the Warwick deposition technique applies much thinner coatings per pass that the Cyrano system.

	No. of sprays		
Polymer	30	40	50
poly(9-vinylcarbazole)	0.5μm ± 0.1	0.9 μm ± 0.2	1.3 μm ± 0.2

Table 4.3: Thickness measurements for composite polymers deposited at Warwick University.

4.4.3 Thickness profiles of electrochemically deposited polymers

The electrochemical deposition process was found to be inferior in controlling the thickness of the polymer film. Here the variation in polymer thickness was significant, as shown in table 4.4.

Sample	Av. PPY/BSA	Max. PPY/BSA	Av. PBT/TBATFB	Max. PBT/TBATFB
1.	0.45 μm	0.6 μm	0.3 μm	1.6 μm
2.	0.15 μm	0.8 μm	0.3 μm	2.4 μm
3.	0.3 μm	3.9 μm	3.3 μm	6.2 μm
4.	0.8 μm	4.1 μm	3.6 μm	5.4 μm
5.	1.8 μm	5.3 μm	2.4 μm	5.0 μm
6.	2.0 μm	8.0 μm	1.3 μm	3.7 μm
Av.	1.0 μm	3.4 μm	1.1 μm	2.5 μm
St. Dev.	1.2 μm	2.8 μm	1.3 μm	2.1 μm

Table 4.4: Thickness measurements for electrochemically deposited polymers, with average and maximum measured thickness.

This wide variation in polymer thickness maybe due the size of the gap between the gate electrodes and the difficulties involved in growing across the SiO_2 layer. A 3D profile of an electrochemically grown polymer array is shown in figure 4.13. Here the polymer has been overgrown to emphasis the definition of this process and shows a device with channel dimensions of 105 μm × 5 μm and the range of thicknesses possible.

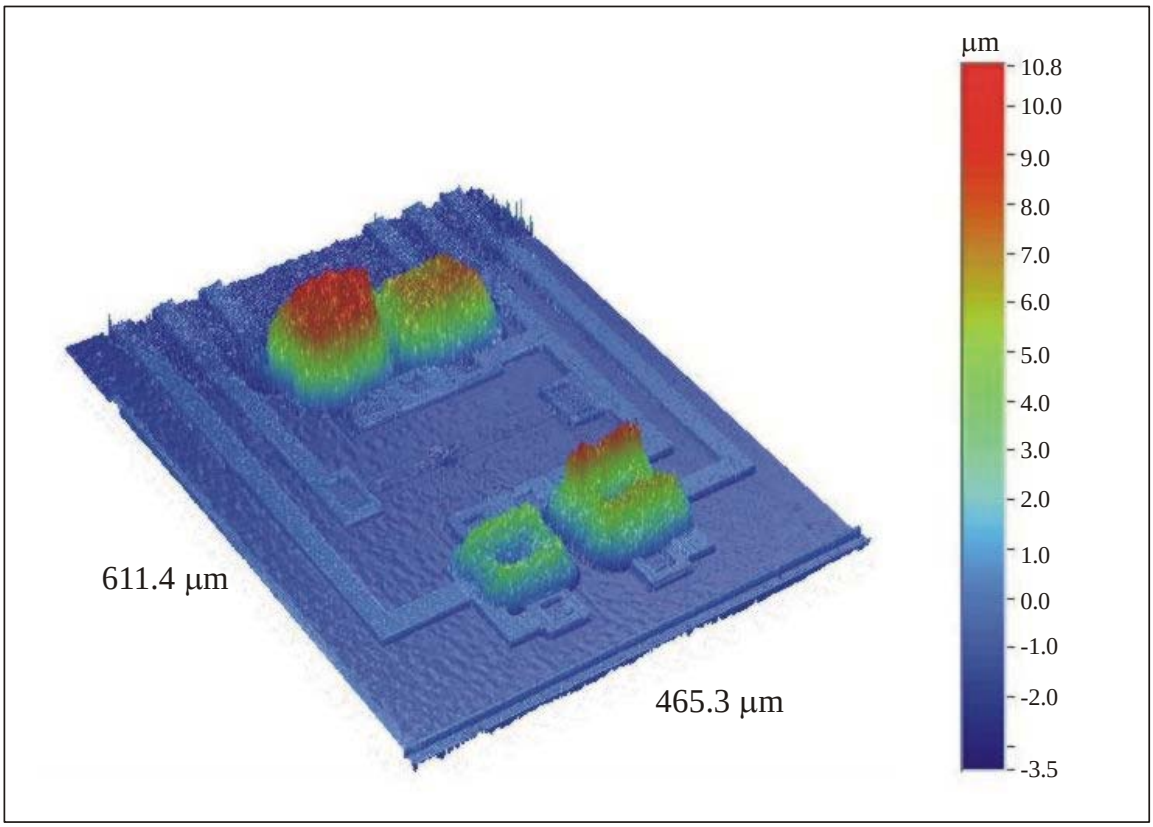

Figure 4.13: 3D profile of poly(pyrrole)/BSA.

4.5 Realisation of the SOI heater/sensor

In the previous chapter a number of SOI designs were described. Due to delays in the production of masks and the processing itself, many of the designs had not been fabricated by the end of this research period (over two years since the completion of the designs). Within the allocated time only one type of device was fabricated, through Europractice, using the Matra 0.8 μm BiCMOS process. Here the silicon substrate contains four different heater/sensor combinations with an Al electrode structure. A photograph of the fabricated device is shown in figure 4.14, with a magnified section of one sensor, before the deposition of gas sensitive material.

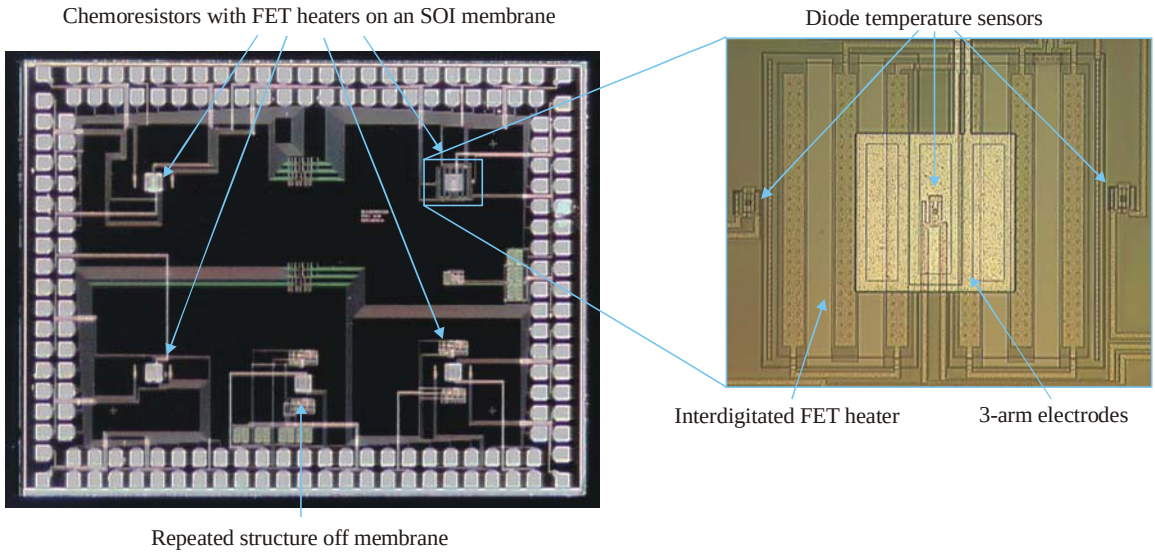

Figure 4.14: Photograph of fabricated SOI device.

Two post-processing steps were required to complete the sensor, the removal of the handle silicon and deposition of the gas sensitive layer. Once completed the sensor was packaged in a 120-pin PGA package (Spectrum semiconductors, CPG12022).

4.5.1 Back-etching of SOI sensor array

The back etching of the SOI device was performed both at the University of Warwick and University of Southampton. The removal of the handle silicon on the Matra devices was carried out at Warwick University. A number of different methods for back etching were attempted, using silicon nitride, chrome and SU-8 (a photo curable polymer based photoresist) to define the etching region. All of these materials were only partially successful, as a mask, as the devices are small and so difficult to seal. A poor seal results in the etchant (KOH) attaching the circuit side. In addition, the surface roughness of the back-side made adhesion to the handle silicon problematic. Polishing was also attempted on the back and again this was only partially successful. The final system used mixed mechanical and chemical procedures. The devices were machined using high speed diamond tipped drill bits (0.6 mm or 1.0 mm diameter). Holes were machined to leave 100 μm of handle and device silicon. A high melting point wax was then used to adhere the device to a glass slide and a metal mechanical mask was attached to the back of the device, also by wax. The device was then placed in a dri-block heater at 70 ^{o}C for 30 minutes to stabilise and a 22% concentration of KOH (Aldrich) was then pipetted on to the device for typically 30 minutes. This procedure

was repeated until the membrane was formed. This removed the remainder of the handle silicon to the buried oxide layer. The device was then heated to 110 ^{o}C to remove the device from the glass slide and the wax dispersed in semiconductor grade acetone. A photograph of a back-etched device is shown in figure 4.15.

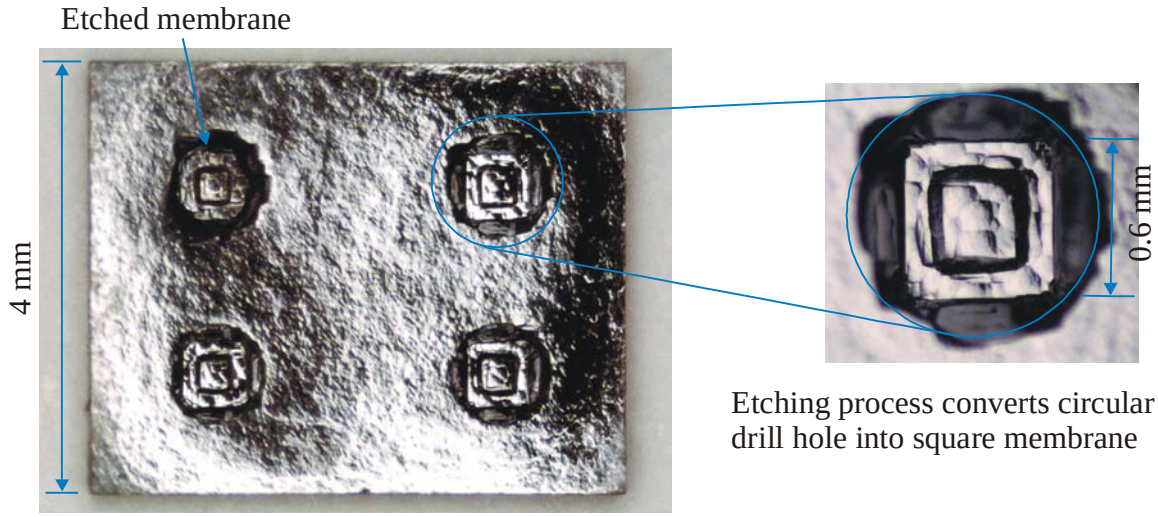

Figure 4.15: Photograph of the underside of a SOI device, with zoomed in section after removal of most of the handle silicon.

The Southampton system etchs one wafer at a time, which is clearly more efficient. Here an etching rig, developed at Warwick University, initially by Dr H. W. Shin [4.10] and later modified by Warwick and Southampton Universities is being used to etch the devices. The back of the wafer is cleaned and polished to remove any residue and surface roughness. Then a 1.5 μm silicon nitride film is deposited on the back by LPCVD, patterned using a contact mask and etched. The wafer is then fitted into a jig, as shown in figure 4.16 and placed in a 30% concentration of KOH etchant, at 70 ^{o}C for 13 hours. Before exposure to the etchant the jig is placed in hot water to allow the PTFE to expand sealing around the wafer. When 20 μm of the handle silicon is left the wafer is removed from the etchant, cleaned and placed in a reactive-ion-etcher to slowly remove the remaining silicon.

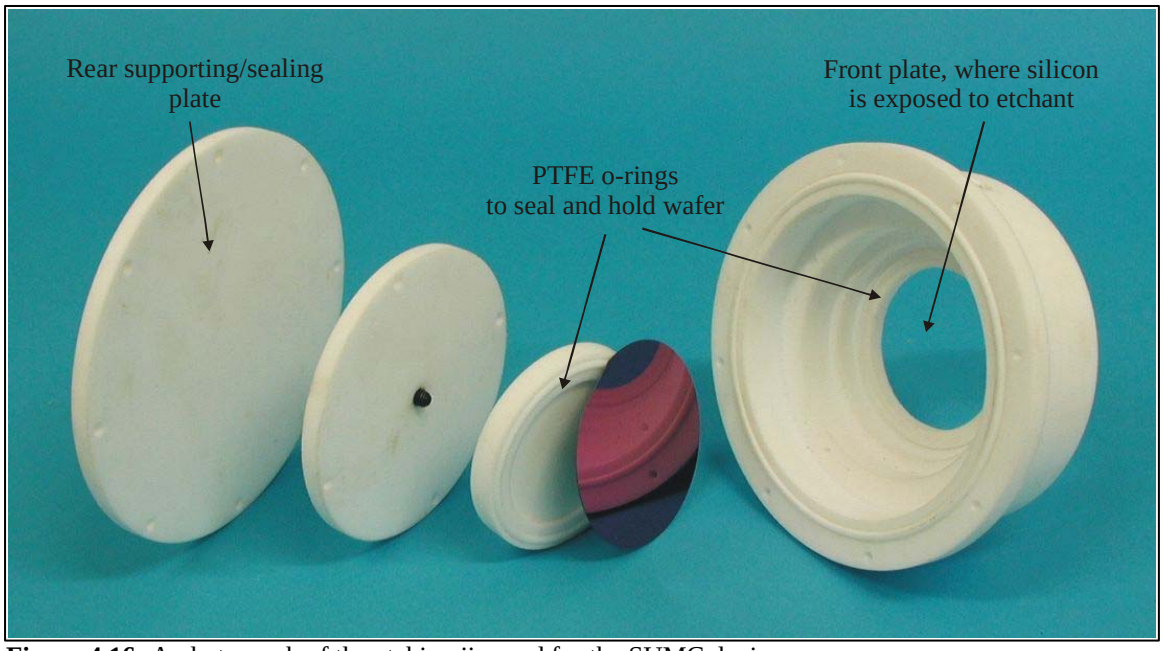

Figure 4.16: A photograph of the etching jig used for the SUMC devices

4.6 Additional devices for resistive and work function measurements

Two additional devices, designed as the University of Warwick, were used within the scope of this research. The first is a simple resistive device and would be used to compare and benchmark the composite polymer chemFET sensors to a standard chemoresistor, giving additional information about the sensing mechanisms of these composite polymers. The second device will be used to perform the first workfunction measurements on the composite polymers and repeating some previous work on electrochemically deposited polymers [4.11], using a Kelvin probe.

4.6.1 Resistive sensor

The resistive sensor (SRL127) was designed by Dr A. Pike [4.12], for the characterisation of conducting polymers or metal oxides. The SRL127 utilises standard silicon processing techniques in its fabrication. On a silicon substrate 200 nm of silicon nitride is deposited, on which 10 nm of titanium and 250 nm of gold is further added, (titanium used as an adhesion promoter). The gold is masked and etched leaving the device elements. Finally a further silicon nitride layer is deposited, as a passivation layer over the device, this is patterned and etched, opening the sensing area and bond pads with the final device roughly 4 mm × 4 mm in size. The device elements compose of two types of structures, the sensing electrodes and the heater structure. The sensing electrodes are separated by a gap of 50 μm between which the active material is

deposited. The heating element surrounds this centre sensing structure and can be used to elevate the temperature of the active film. To reduce the power consumption of the heater the silicon substrate can be back etched to create a thin membrane under the device elements. Figure 4.17 shows the structure of this sensor with a photograph of a fabricated device.

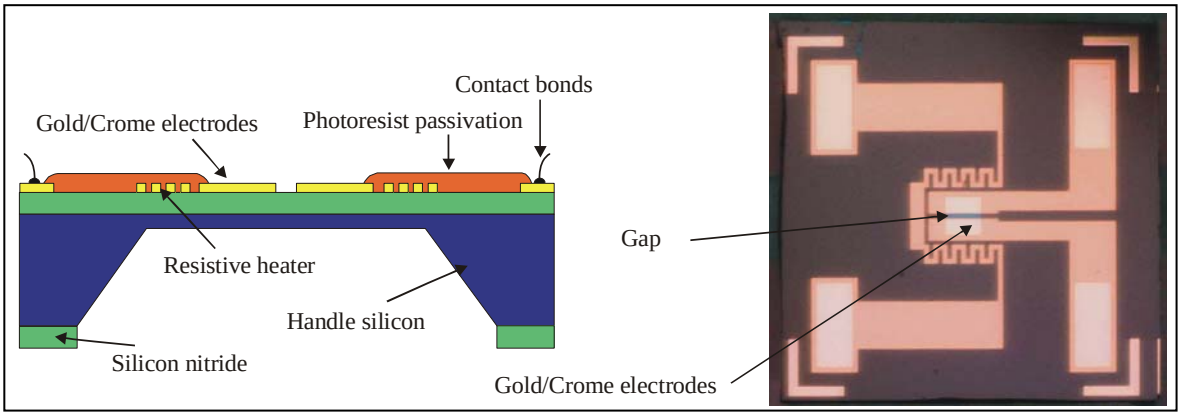

Figure 4.17: Schematic and photograph of SL127

Polymer deposition onto this chemoresistive structure was performed by Cyrano sciences using poly(styrene-co-butadiene) to similar thicknesses,. This resistive structure was placed and bonded within the standard 14-pin DIL package, used earlier, for ease of connection to the test equipment.

4.6.2 Polymer substrate

To assist in the investigation of these polymers, a further structure (SRL170) was designed to interface with a Kelvin probe. The Kelvin probe is a non-contact, non-destructive vibrating capacitor device used to measure the work function difference, or for non-metals, the surface potential, between a conducting specimen and a vibrating tip. The Kelvin method was first postulated by the Lord Kelvin, in 1861 [6.13]. The work function is the least amount of energy required to remove an electron from the surface of a conducting material, to a point just outside the metal with zero kinetic energy [6.14]. The traditional Kelvin Probe method consists of a flat circular electrode (termed the reference electrode) suspended above and parallel to a stationary electrode (the specimen), to create a simple capacitor. If an external electrical contact is made between the two electrodes their fermi levels equalise and the resulting flow of charge produces a potential gradient, termed the contact potential, between the plates. The two surfaces become equally and oppositely charged. The inclusion of a variable “backing

potential" in the external circuit, permits biasing of one electrode with respect to the other. At the unique point where the (average) electric field between the plates vanishes, which results in a null output signal, the work function difference between two surfaces can be found by measuring the flow of charge.

The device is composed of a silicon substrate 4 mm × 4 mm, on which a 200 nm silicon oxide layer is thermally grown. Above this, a Pt (200 nm) layer and a silicon nitride passivation layer are deposited. This silicon nitride is patterned and etched to expose four bond pads (300 μm × 300 μm) and a central opening (2.5 mm × 2.5 mm), for contact to the polymer. This device was fabricated at the Institute of Microtechnology, University of Neuchatel, Switzerland. The structure and a photograph of this device is given in figure 4.18.

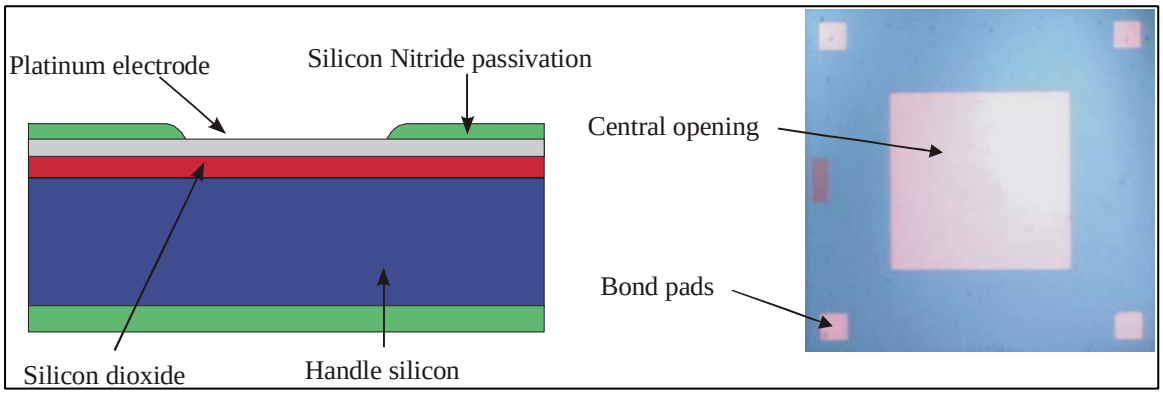

Figure 4.18: Schematic and photograph of SRL170.

For electrochemical deposition this structure is attached to a PCB mount. This mount uses a standard 0.1" pitch, which interfaces readily with the Kelvin probe. This device was used for both electrochemically grown and composite polymers.

4.7 Conclusions

Here the sensors used in this research have been described. This has included the room temperature chemFET sensors, donated by Dr J.V. Hatfield of UMIST, and the collaborative sensor array with the Institute of Microtechnology, University of Neuchatel. Also reported has been the final SOI device, fabricated through Europractice with the post-processing steps (back-etching and deposition of an active sensing layer).

A number deposition techniques have been described and compared. It has been shown that the composite polymers are both easier to create and to deposit, though do

not have the accuracy of deposition of the chemically prepared and electrochemically grown polymers, with which multi-polymer arrays can be formed. In addition, SEM and AFM measurements have been carried out to examine the structure of the polymers. In addition, thickness profiling by vertical phase shifting interferometry has been performed, which shows that all the polymers are less than 10 μm thick, with good linearity over the sensing area for the chemically prepared and composite polymers. This is the first time an AFM and vertical scanning interferometry techniques have been applied to composite polymers and chemFET sensors. Also a number of different polymer thicknesses has been deposited between 0.5 μm – 2.5 μm, to investigate how thickness can influence the magnitude of the response.

Lastly, structures for resistive and Kelvin probe measurements have been described, these will be used to compare and benchmark the chemFET sensors response (see chapter 6).

4.8 References

4.1 Garde, J. Alderman and W. Lane, Development of a pH-sensitive ISFET suitable for fabrication in a volume production environment, *Sensors and Actuators B,* 26-27, (1995) 341-344.

4.2 J. V. Hatfield, K. S. Chai, A conducting polymer GasFET, *Proceedings of Eurosensors IX*, (1997), 739-742.

4.3 M. C. Lonergan, E. J. Severin, B. J. Doleman, S. A. Beaber, R. H. Grubbs, N.S. Lewis, Array-Based Vapor Sensing Using Chemically Sensitive Carbon-Black-Polymer Resistors, *Chem. Mater.*, **8**, (1996), 2298-2313.

4.4 B. J. Doleman, R. D. Sanner, E. J. Severin, R. H. Grubbs, N. S. Lewis, Use of Compatible Polymer Blends to Fabricate Arrays of Carbon Black-Polymer Composite Vapor Detectors, *Anal. Chem*, **70**, (1998), 2560-2564.

4.5 P. N. Bartlett, J. W. Gardner, R. G. Whitaker, Electrical deposition of conducting poylerms and electrical devices, *Sensors and Actuators* , 19, (125-140), 125-140.

4.6 P. N. Bartlett, P. B. M. Archer, S. K. Ling-Chung, Conducting polymer gas sensors Part 1: Fabrication and Characterisation, *Sensors and Actuators***, 19**, (1989), 125-140.

4.7 P. N. Bartlett, J. M. Elliott, J. W. Gardner, Integrated sensor arrays for the dynamic measurement of food flavour release, *Measurement and Control*, Vol. 30 (1997), 273-279.

4.8 P. N. Bartlett, J. W. Gardner, J. M. Elliott, A. Duke, C. Beriet, Patent Application, Great Britain, (1995), No. 9514754.2.

4.9 S. M. Sze, *VLSI Technology*, McGraw-Hill, 1988.

4.10 H. W. Shin, *PhD Thesis*, 1999, University of Warwick, Coventry, CV4 7AL, UK.

4.11 J. Janata, M. Josowicz, Chemical modulation of work function as a transduction mechanism for chemical sensors, *Acc. Chem. Res.*,31 ,(1998), 241-248.

4.12 C. Pike, *PhD Thesis*, 1996, University of Warwick, Coventry, CV4 7AL, UK.

4.13 Lord Kelvin, Phil.Mag., 46 (1898), 82.

4.14 I.D.Baikie, P.J.Estrup, Low Cost PC Based Scanning Kelvin Probe Rec. Sci. Instrum.,69, (1998), 3902-3908.

CHAPTER 5

Flow injection analysis test station and measurement instrumentation

5.1 Introduction

An important factor when characterising any type of chemical sensor is the ambient conditions in which it is placed. Many types of gas sensor, including those based on conducting polymers, not only demonstrate a response to a variety of gases and vapours, but to the test conditions. The development of any model, which describes a sensors response at different concentrations of a particular reactive agent, would therefore require accurate control over other environmental conditions within the test chamber. These environmental conditions cover the ambient temperature, absolute water concentration and gas flow-rate (in clean air). To perform sensor characterisation, a Flow Injection Analysis (FIA) test station has been constructed, the aim of which is to create controlled conditions that mimic those encountered in the atmosphere. This system delivers a range of almost any concentrations a volatile organic compound (VOC) to the parts per million level, whilst maintaining environmental conditions.

The basic configuration of this test station was first developed for the analysis of beers and was later adapted to characterise discrete conducting polymer sensors [5.1-5.3]. The present system is a major re-design and re-development of these earlier test stations though the basic concept is still the same [5.4]. A number of other systems have been developed with similar characteristics to control analyte, temperature and

humidity levels. The main difference between these systems is simply in the type of sensor that is characterised [5.5-5.9].

The development of any measurement system, for gas/vapour sensors, will depend upon how the response of the sensor is attained and the total number of sensors. For *n*-channel common source chemFET sensors there are three possible measurands, the I-V characteristics, I_{DS} with constant V_{GS}/V_{DS} or V_{DS} with constant I_{DS}. At present there are few instruments commercially available that could perform these tasks for a large number of sensors, over an extended test period. This has led to the development of two instruments. The first to measure the I-V characteristics or the shift in I_{DS} at constant V_{GS}/V_{DS}, and the second to measure the change in V_{GS} at constant current to various concentrations of analyte, both are described later in this chapter.

5.2. Flow injection analysis test station

The purpose of the FIA test station is to deliver a controlled range of analyte concentrations to a number of sensors, whist maintaining the temperature of the sensors and the water content of the headspace. An important capability of this system is the automation of the chemical hardware by a computer. This will allow various test conditions to be created over long periods, with repeatability, without the requirement of user interaction.

The FIA rig can be separated into three distinct components, the chemical hardware, the interface electronics and the software control program run on a standard desktop PC. A schematic overview of this system is shown in figure 5.1.

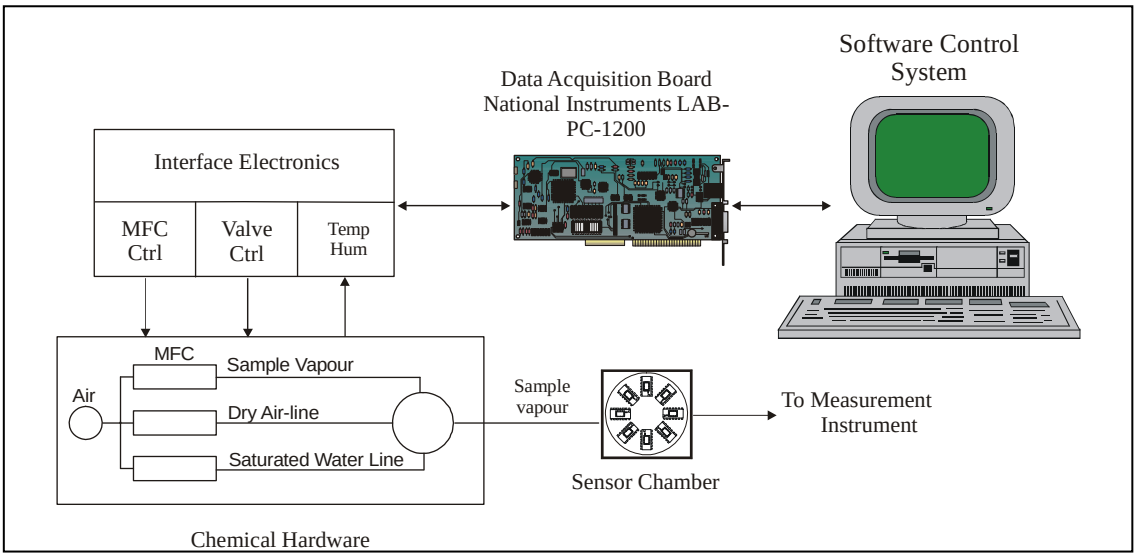

Figure 5.1: Schematic overview of FIA test station.

The chemical hardware covers the mechanical parts of the test station, tubing, mixing chambers etc. The interface electronics, as the name suggests, converts signals from the software control program into chemical hardware inputs. The control program is used to activate system inputs and to monitor system outputs, interfaced to the chemical hardware by the electronic interface and National Instruments, LAB-PC-1200 data acquisition card, within the PC.

The software control program has been custom written in a high level programming language LabVIEW^{TM} for Windows, version 5.0, by National Instruments. This gives direct control over the National Instruments data acquisition card and allows real-time control over the sampling system.

5.3. Chemical hardware

A schematic of the chemical hardware is given in figure 5.2, with the elements shown in BS 2917/ISO 1219 standard where possible. A key to the system is given in table 5.1. A volatile organic compound, under use, is placed in a sample vessel, siting within a chilled re-circulator bath. A carrier gas is bubbled through the solution, adding analyte. The concentration of the vapour is controlled by two factors, the flow-rate through the sample vessel and the temperature of the analyte. By having the sample after the mass flow controller (MFC), the flow rate through the sample vessel is always known. The temperature of the analyte within the circulator bath controls the saturated

concentration of sample vapour. Two further air lines are used to produce the water and the final analyte concentration of the sample vapour. This is achieved by mixing a dry air line and a saturated water line (i.e. dry air bubbled through water). By combining these lines at different flow rates a range of water concentrations can be attained. The exact concentration of water in this dry/wet air line mix is monitored by a commercial temperature and humidity sensors, the Rotronics H103A-L5-KW1W. This reads the PPMs of water before being mixed with the sample vapour. Thus by mixing these three lines under a controlled ratio, a broad range of water and analyte concentrations can be accomplished.

The carrier gas used in these tests was dry air from a compressed cylinder (BOC). The pressure from this cylinder is controlled through a single stage regulator. The carrier gas passes though an air filter (Part No, TCFA1201035, Lee Products Ltd) to remove any contaminants, before being delivered to the MFCs. The flow rate through the MFCs (Model No. 5850 TR, Brooks Instruments) can be programmed with an input voltage (0-5 volts,) giving a maximum flow rate of 300 ml/min (accuracy 1% of FSR). The MFCs also contain an override shut off valve and flow meter to provide a feedback signal. The sample analyte sits in a circulator refrigeration bath (Life Sciences, Neslab RTE-300M). This bath controls the temperature of the analyte between –40 ^{o}C to 200 ^{o}C ±0.1 ^{o}C. Due to the small size of the bath only two analytes can be placed within it at one time. The bath is filled with a combination of ethylene glycol and water at up to a 1:1 ratio. This keeps the coolant in liquid form even at the lowest temperature. The sensors sit in a Dri-block™ heater (model DB-2D, accuracy ±0.1^{o}C), giving complete control over the temperature. From this we can evaluate how temperature effects the response or the relative baseline of the sensors.

Stainless steel tubing and compression fittings have been used throughout the test station. This ensures that the leaks are negligible and that the tubing is resistant to many of the test analytes used. Non-return valves are deployed throughout the station to protect sensitive equipment, specifically the MFCs which can be contaminated by water or sample vapour and the humidity sensor which can be poisoned by certain analytes. A mixing chamber is also included to combine the saturated sample vapour with the water vapour. This chamber sits in a second Dri-block^{TM} heater (Lab-Line Plaza) and ensures that there is a thermal gradient in the rig that eliminates any

possibility of condensation forming. A photograph of the FIA test station is shown in figure 5.3.

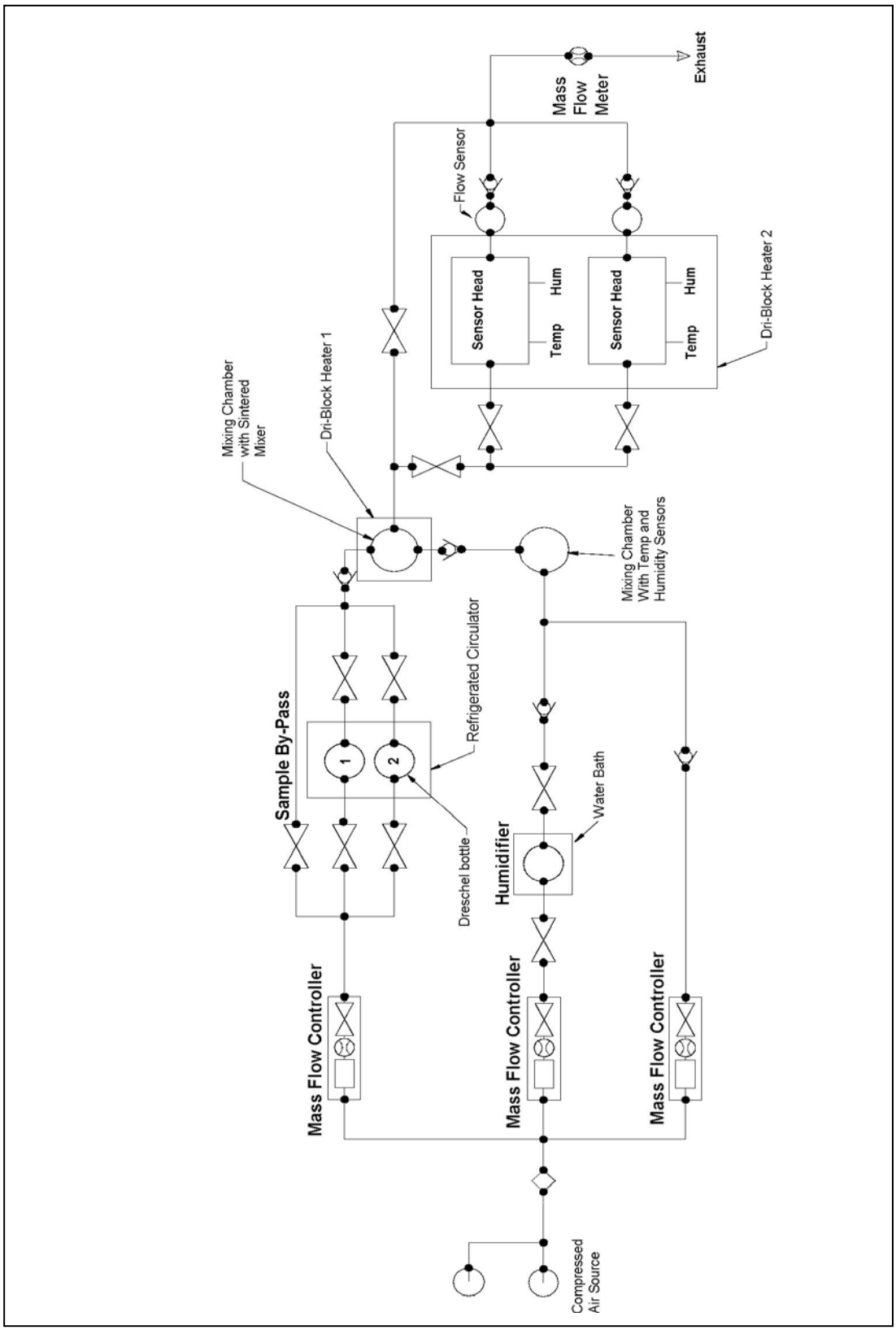

Figure 5.2: Schematic of Chemical Hardware

Symbol	Part	Supplier	Details
	Compressed Air Source, Type L Bottle	BOC Gases Ltd.	Compressed cylinder containing low grade dry air. Pressure is controlled by a single stage regulator.
	Particulate Matter Filter	Lee Products Ltd. TCFA120135A	Filters which trap particles with diameter greater than 35 μm.
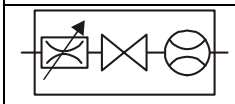	Mass Flow Controller (1, 2 and 3)	Brooks Instruments B.V.	Model TR 5850. 0 to 300 ml/min flow range. Each MFC consists of a flow controller, override valve and flow meter.
	Non–return Value	Lee Products Ltd. TKLA950113D	Used after each MFC to prevent backward flows in the system due to pressure differentials or MFC failure.
	Non-return Valve	The West Group	Viton non-return valves, resistant to sample vapours
	Solenoid Valves NC	The West Group. ET2-12H	Low power solenoid values with 5 V_{DC} switching voltage.
	Bubbler	Fisons Scientific Equipment Ltd. BTF-900-150S	250 ml Drechsel (gas washing) bottle and head with grade 1 sinter.
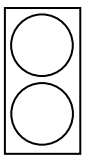	Refrigeration unit	Neslab RTE-300D	Refrigeration unit, temperature range 200^{o}C to –40^{o}C (± 0.1 ^{o}C).
	Mixing Chamber	N/A	Stainless steel mixing chamber manufactured at Warwick University to mix

			the sample vapour and the water vapour and deliver it to a single output.
	Flow Meter	Brooks Instruments B.V.	Model TR5850, to measure output flow of system
	Flow Meter	Honeywell AWM3300	Flow meter, Honeywell AWM3300.
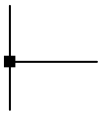	Stainless Steel 316 Tubing	Metal Supermarket	3 mm O.D. (1 mm I.D.) tubing used wherever possible within the equipment.
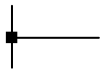	PTFE Tubing	Economatics Ltd.	3 mm O.D. (1 mm I.D.) tubing used where needed.
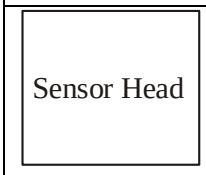	Sensor Chamber		Custom designed and manufactured sensor chamber.
	Multi-blok Heater	Cole Parmer. E-03129-02	Second heater for the mixing chamber.
	Dri–block™ heater	Techne Ltd.	Dri–block heater Model DB-2D allowing programmable temperatures to be set in a range from room temperature to 105 ºC, with long–term stability within 0.1 ºC.

Table 5.1: Chemical hardware components

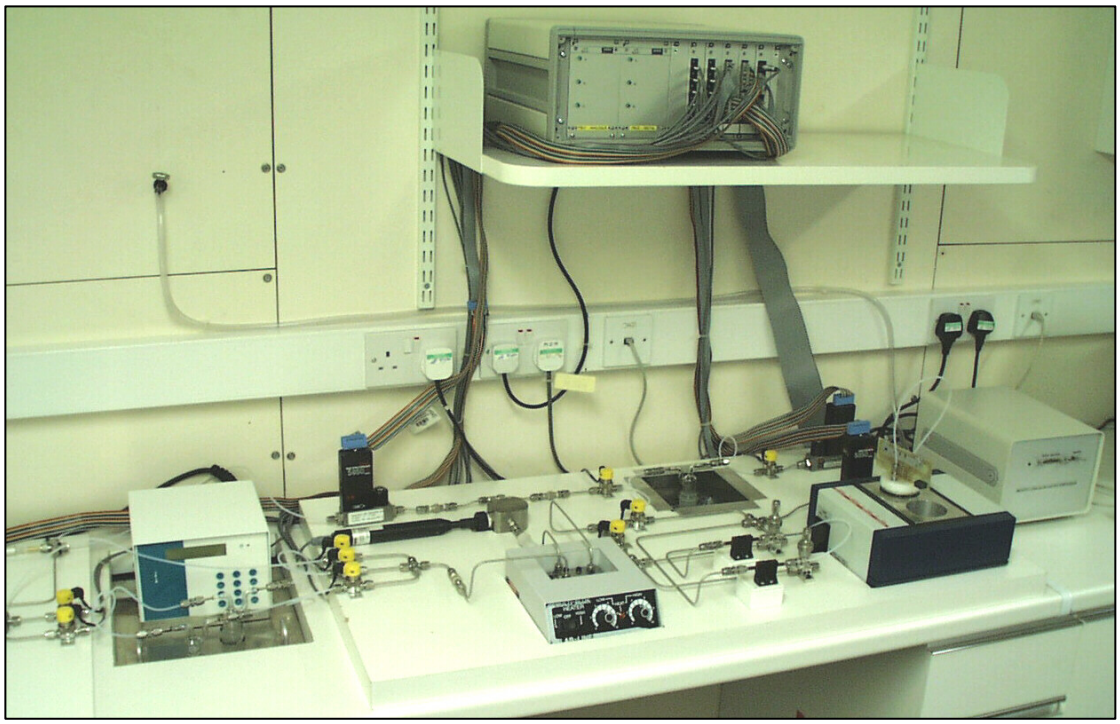

Figure 5.3: Photograph of the FIA test station

The carrier gas is bubbled through the water or analyte, held in a Drechel vessel, through a fine sinter (Grade 1). Thus we can assume that the carrier gas will become saturated and that the saturated concentration of water or analyte will be the same as that found in the static headspace. This concentration can be calculated by using Antoine vapour equation, which is only dependent on the temperature and the physical properties of the analyte, given by [5.10]:

$$\log P = A - \frac{B}{C + T} \tag{5.1}$$

where P is the partial pressure of vapour, T is the temperature (in K) of the vapour (in torr) and A, B and C are material constants. If we assume an ideal gas behaviour then we can calculate the concentration of a test sample using the partial pressure equation.

$$C_{\mathrm{VAP}} = \frac{P_{\mathrm{VAP}}}{P_{\mathrm{AIR}}} \times 10^{6} \tag{5.2}$$

where C_{VAP} is the concentration of vapour in PPM, P_{VAP} is the partial pressure of the vapour and P_{AIR} (760 torr) is assumed to be equal to atmospheric pressure. Thus by using these equations and the rig configuration almost any concentration of water or analyte (at the PPM level) can be achieved, up to the saturated vapour pressure. Typical values of certain analytes are given in table 5.2 [5.11,5.12]. Included in this table are

the minimum possible values of saturated vapour in PPM, from the cooling bath. It must be remembered that the final vapour concentrations will be significantly lower, as this air line is diluted. Also shown in table 5.2 are the lowest possible analyte concentration after dilution, where concentrations of less than 20 PPM can be achieved for these analytes at a sample flow rate of 15 ml/min. The different sample analytes, with a bypass for cleaning purposes, can be selected via solenoid valves situated on the inlet and outlet of the Dreschel vessels.

Chemical	Const. A	Const. B	Const. C	Temp. Range in degrees C	Min. Saturated / in PPM
Ethanol	8.32109	1718.10	237.52	-2 - 100	551.1 – 19.1
Toluene	6.95464	1344.500	219.48	-12 – 108	381.1 – 25.3
Water	10.12	1686.0	229.7	0.85 - 106	N/A

Table 5.2: Chemical constants, with temperature ranges, for analytes used in testing. Also minimum saturated PPM available using the refrigeration unit.

A needle valve has also been included and can be used to control the flow rate to the chamber. This is used when two sensor chambers are being operated in parallel, with a second needle valve and solenoid on the inlet to this chamber. Flow sensors (Honeywell AWM3300) are placed after the sensor chambers to regulate the flow. The outputs of these sensors are calibrated to a mass flow meter (Brooks Instruments, TR5850), where all the outlets from the sensor chambers or the sensors chamber bypass are recombined. This gives an indication of any leaks in the system. The exhaust from the system is passed to a fume cupboard for extraction.

The last component of the chemical hardware is the sensor chamber. This chamber has been specifically designed to integrate into the FIA test station and has a number of significant improvements over previous designs, namely in the reduction of dead volume. The sensor chamber is constructed out of four components and is designed to hold up to 8 14 pin DIL packages. The first component is a heat exchanger, which is a channel carved into the lower plate that contains the inlet and outlet holes (stainless steel 1/8 inch BSP compression fitting). The purpose of the heat exchanger is to elevate the temperature of the sample vapour to that of the sensors, hence removing any erroneous results by cooling effects. The second component is the centre plate,

which injects the vapour through 8, 1.0 mm holes onto the sensors. These holes are placed so the sample vapour is injected just before the sensors. Channels in this centre plate allows the sample vapour to flow over the sensors to a central, 4 mm, exhaust hole. The sensors are held in a top plate, which contain 8 14 pin-DIL holders that have been bonded into the lid with thermally conducting glue to aid heat transfer to the sensors and held by a restraining bar across the holder. The centre chamber is recessed, allowing the top plate to sit below the top of the centre plate. Temperature (LM35CAH) and humidity sensors (Panametrics MINICAP-2) have been bonded into the centre plate. This monitors the temperature of the chamber and the humidity of the exhausting gas. A PCB has been designed to fit onto the temperature and humidity sensors that contains drive circuitry for these sensors and some signal conditioning. The final part of the chamber is an interface PCB that connects the sensors within the chamber to the measurement instruments. These PCBs are designed to be plug-in so the chamber is universal to all the instruments. A schematic of the chamber is given in figure 5.4.

A modified version of this sensor chamber was fabricated for the SOI sensors. This used a similar configuration as the previous chamber, using the same lower plate and comparable centre plate with 8, 1 mm injection holes and flow channels. This centre plate was also recessed in the centre for the sensor to fit. The top plate holds a single sensor, fitted into a 128 pin DIL package bonded into the centre of this plate. A PCB then fits onto this lid to interface with the appropriate instrumentation.

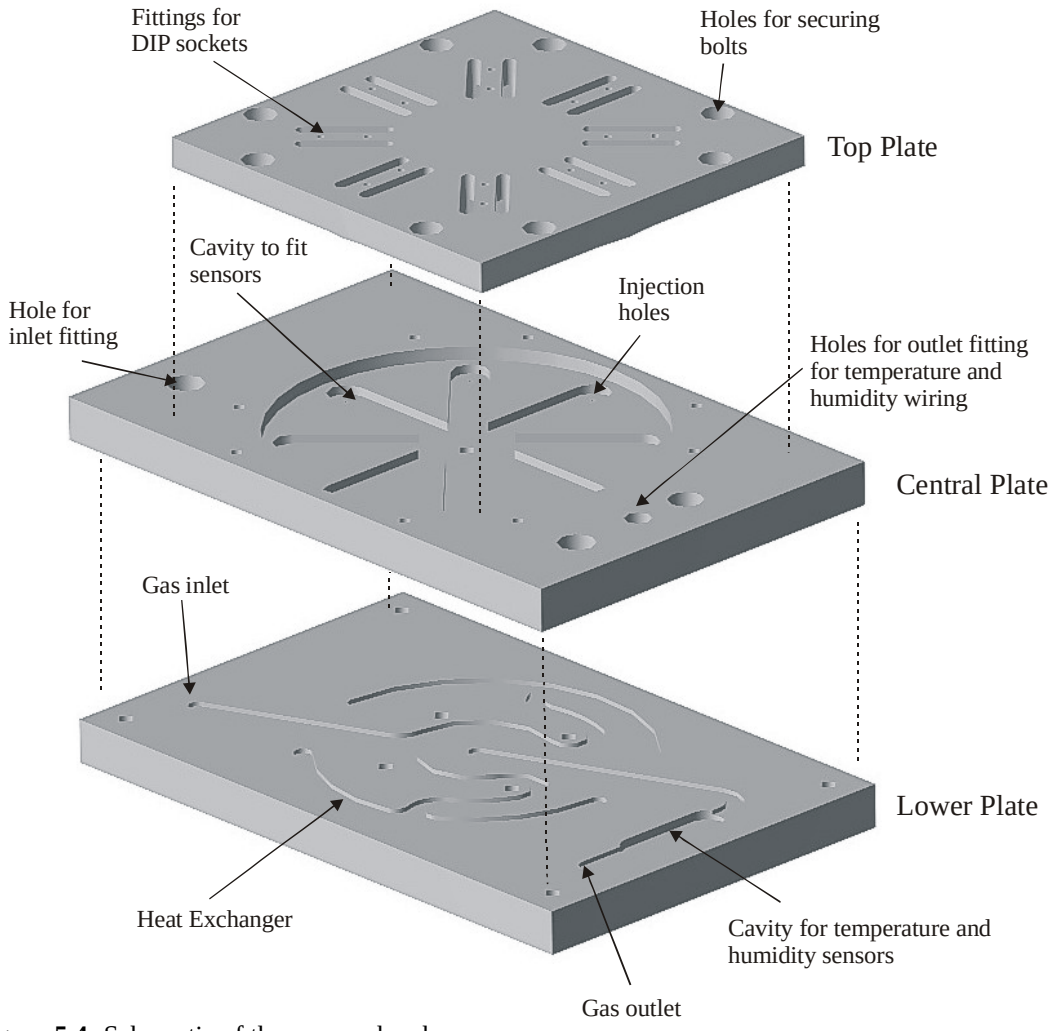

Figure 5.4: Schematic of the sensor chamber.

An important parameter for any test station is its response time. This is defined as the time taken to completely exhaust the sensor chamber and the chemical hardware. A value for this can be calculated by measuring the volume of the FIA test station. Table 5.3 shows the volume of each section of the chemical hardware and the time to exhaust. It is assumed that the flow rate through the chemical hardware is 300 ml/min. The exhaust time has also been calculated under typical test conditions, where the flow rate through each mass flow controller is 100 ml/min.

Sensor Chamber			
Description	Volume in ml	Time to exhaust (ms)	Running total (ms)
Heat Exchanger	1.591	318.4	318.4
Head Space	4.787	957.3	1275.7
Exhaust	0.752	150.4	1426.1
Volume of mixing chambers			
Humidity Holder	6.93	1390	1390
Mixing Chamber	2.51	502.5	1892.5
Volume of pipe work			
Stainless Steel	3.77	754.0	754.0
PTFE	1.18	235.6	989.6
Volume of dreschel vessels			
Tubing at 300 ml/min	2.49	497.6	497.6
Tubing at 100 ml/min	2.49	1483.5	1483.5
Bulb at 300 ml/min	8.46	1694.4	2192
Bulb at 100 ml/min	8.46	4983.5	6467.0
Total volume at 300 ml/min			
Tubing	0.99	197.8	197.8
Mixing chambers	34.9	6971.4	7169.2
Total	35.8	7169.2	7.2 sec
Total Volume in typical test conditions			
Tubing	0.99	197.8	197.8
Mixing chambers	34.9	6971.4	21490
Total	35.8	7169.2	21.5 sec

Table 5.3: Volume and exhaust times for the chemical hardware and sensor chamber.

As can be seen from table 5.3, the two important values are the exhaust time for the sensor chamber and the typical exhaust time for the complete test station. The volume of the sensor chamber is only 11.1 ml being exhausted in less than 1.5 seconds. This time is lower than the standard response time of many types of gas sensor. The compete volume of the FIA rig is 7169 ml which could be exhausted in around 21 seconds. These values are improved over previous test stations, which had significantly larger sensor chambers and rig volumes.

5.4 Electronic interface

The purpose of the electronic interface is to covert commands from the control software, via PC-based National Instruments Lab-PC-1200, to the chemical hardware. The Lab-PC-1200 card contains 2 singled ended analogue outputs, (12 bit), 8 single ended analogue inputs (12 bit) and 24 TTL digital input/output signals that are configured in banks of 8. A photograph of the interface electronics is in figure 5.3, showing 5 PCB cards fitted into a standard Eurorack system (VERO-BICC Electronics), compliant with DIN41494. The electronic interface contain one Module 1 card (for controlling of MFCs, split with two front panels), two module 2 cards to control the valves in the chemical hardware and finally a Module 3 card to interface with the humidity and flow sensors. A spare slot with the remaining control lines is also provided for future expansion. Two linear power supplies (Model No. LK35m Vero-electronics) are used, divided to supply the analogue and digital sections separately to reduce interference (switching noise, cross-talk). Lastly, for EMC and safety the case is connected to earth.

5.4.1 Electronic controller cards

The MFCs have three important features. They have remote flow programming via a 0-5 volt input, flow rate measurement and a valve override to close the valves in case of a system failure, all driven by the module 1 card.

The three MFCs of the chemical hardware are controlled by three analogue outputs. Two of these come from the Lab-PC-1200 and the third via a 12 bit serial loaded DAC on the module 1 card (AD7423AN). These control signals are passed through a 2^{nd} order lowpass filter and buffer amplifier, as shown in figure 5.5, which gives a simplified circuit diagram of the electronic interface. The system also contains a

valve overide (driven by aTLE2301-INE, 3 state output op-amp) to shut the system down in the event of a leak.

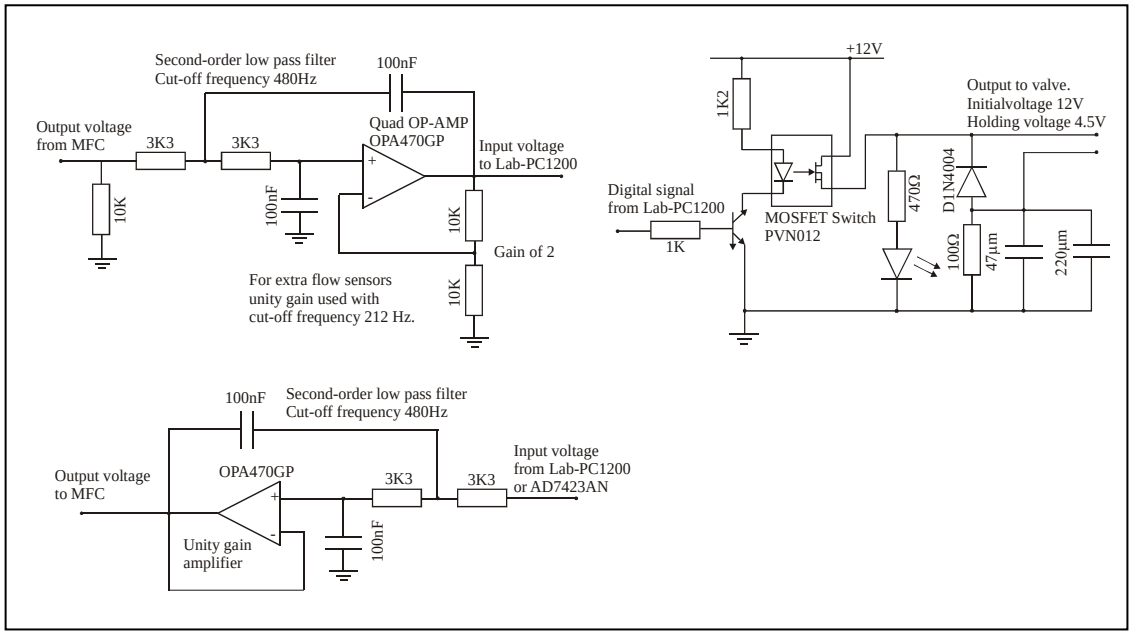

Figure 5.5: Simplified circuit diagram of MFC electronics hardware.

The module 2 card is used to control the valves of the chemical hardware. Each card can control up to 5 valves hence two are required to control the 9 valves of the system. A single digital line is used to control each valve, driving a MOSFET switch (PVN012). This semiconductor solution has been implemented over the traditional mechanical relay, due to the low power consumption of the valve (0.5 W) and the increased life span associated with no moving parts. In addition, an RC network is used to increase the life span of the valves by reducing the holding voltage to 8 volts after an initial switching voltage of 12 volts, also shown in figure 5.5.

The final card interfaces with the temperature/humidity sensor and the two Honeywell AWM3300 flow sensors. The Rotronic humidity sensor has an normalised output of 0-1 volt for humidity 0-100% r.h. and temperature 0-100^{o}C. These signals are filtered and amplified (cut-off frequency of 100 Hz, gain of 5). The flow sensors fit onto a PCB that regulates the control voltage (10 volt ±0.01, using an LT1021CN8-10 regulator) with a gain and filter circuit. A complete set of circuit diagrams is given in appendix A.

5.5 Virtual instrumentation

The software control system is written using LabVIEW^{TM} for windows, version 5.0. LabVIEW^{TM}, or Laboratory Virtual Instrument Engineering Workbench, is produced by National Instruments Inc. (USA). The package combines data acquisition, analysis, and presentation in one system. It produces a layer of software and hardware that when added to a general purpose computer, can interact with the user as though it was their own custom designed traditional electronic instrument [5.13]. The functionality and user interface can be completely customised through a high level graphical orientated software application. The LabVIEW package produces programmes called *Virtual Instruments* or *VI's*. These VI's are divided into two sections, the *Front Panel* and the *Block Diagram*. The front panel is the graphical interactive user interface that simulates the panel of a physical instrument, with controls and indicators. The front panel can contain a range of switches, buttons and dials, which graphically, have the shape and form of their physical counterparts. They are operated by the user with the mouse or keyboard. There is also a range of indicators such as graphs and sliders that show system outputs, as shown in figure 5.6. The block diagram is the VI's source code, constructed in the LabVIEW programming language 'G'. It is produced in a pictorial fashion where programming constructs are represented as graphical icons and structures. These graphical structures are connected together by wires that represent a transfer of data from one operation to another. Each indicator or control on the front panel represents a terminal on the block diagram. Data enters from an input terminal, internal operations are performed on it and an appropriate response is sent to an output terminal. The internal operations available to the programmer are very similar to those used in a standard script based language. These include arithmetic functions, comparisons, filters, strings and arrays. The language also contains logical structures such as 'FOR', 'WHILE', sequence and case loops. The sub-VI shows the hierachial structure of LabVIEW. A sub-VI is a virtual instrument that can be used in a higher level program. This allows programs to be produced in a modular structure where an application can be divided into a number of simple tasks. There is a range of built in sub-VI's that come with the package and further sub-VI's can be produced by the user and integrated into a more complex program.

5.5.1 Control software

The front panel for the software control system is shown in figure 5.6

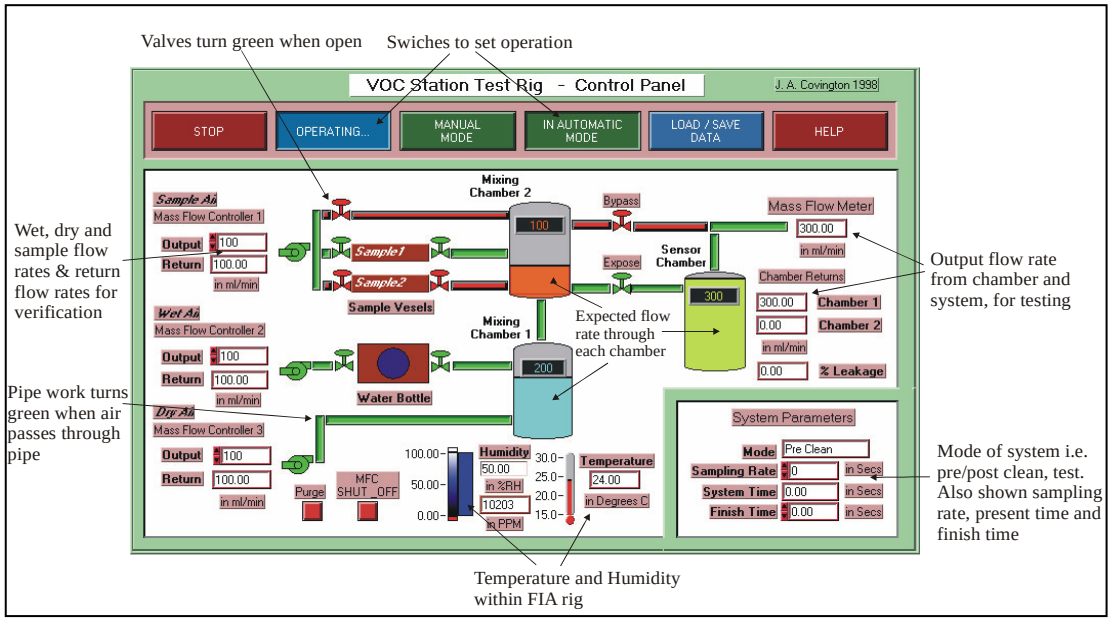

Figure 5.6: Front panel of FIA control software.

The front panel is designed to be a schematic representation of the FIA test station, showing where, at any time, sample air is flowing. At the top of the front panel are a number of control switches that allow for manual or automatic operation and a load/save switch to load control parameters and to define where the rig values (e.g. flow rate) will be stored. Also, an operation switch to activate a function and a help button. On the left hand side of the front panel are the rig inputs, specifically the three input flow rates from the mass flow controllers, including their returns. After these inputs are a series of pipe and valve indicators which represent the chemical hardware of the FIA test station. On the far right are the outputs from the flow sensors, both for sensor chamber and the mass flow meter (with the percentage leakage). Also given is the temperature (^{o}C) and humidity information (% r.h. & PPM). Lastly, on the bottom right are the system settings, showing the mode the system i.e. either pre/post clean or testing phase and the sampling rate, (rate at which information is stored), finally the present system time and finish time are displayed. The software allows both manual and automatic operation, in manual operation the valve and flow rates can be set on the front panel. In automatic mode a pre-written text file is used to control the FIA rig over a long-test period, where manual control would be difficult. Data acquired by the system can be saved to disc for later examination, to verify the flow rates, water concentration and temperature, this data is referenced to an internal clock. These automatic parameters are entered by pressing the “Load/Save” button, which initialises

a pop-up menu. This menu also includes a loading facility, for previously created text files, which contain information on the pre-clean, sample period and post-clean. The pre-clean and post-clean parameters define a period of time to purge the FIA rig of any organic vapours from a previous test.

Two programs were written to control the FIA rig. The first program operated in a similar way to earlier FIA rigs, using a text file containing the flow rates of each MFC indexed to the system time. The software calculates which valves should be open simply on the flow rates for each MFC. When testing two chemicals an extra column is added to the test file, where these columns define the sample flow rate for each analyte. As is obvious, this program has a number of limitations specifically the water concentration of the test cannot be controlled, as it will depend on the room temperature (though the relative humidity will remain constant). A second problem was the switching the flow to the sample vapour. Previously, when a sample flow is used the flow rate in the dry air line is reduced by the level required by the sample line. This causes a transient delay as the flow in the sample MFC reaches a stable value. The second program solved these problems by using a load file containing only flow rates for the sample vapour, and the required water content in PPM indexed to the system time. The program sets the flow through the water and dry air lines by using a 3D model of water content against flow rates at various temperatures. Data for this model was collected when the system was being commissioned. Clearly, any model has limitations and other variables such as water bath level will effect the water vapour concentration. For this reason a convergence routine was also used to achieve the exact water concentration. The second improvement of this program was the reduced stabilisation time. This was achieved by setting the flow rate through the sample MFC and by-passing the sample vessels whilst the baseline was being set. Once the time index has reached a defined value the flow through the MFC remains constant and valve simply switches the flow over to the sample vessel. A simplified flow diagram of the whole software system and a copy of the software is given in appendix B.

5.6 Testing protocols

The testing protocols encompass the sequence of events leading up to a test, covering leak diagnostics, pre/post cleaning of the system and all sensor testing. The sensors are

loaded into the sensor chamber and are left for a period of 24 hours in the dri-block heater to thermally equilibrate. Then the water and analyte levels are checked or, in the case of the analyte, may be replaced. The fluid level in the refrigerated cooling bath is checked and refilled if required. The temperature of the cooling bath is set and the bath is operated 1 hour before testing commences to ensure that the analyte has been chilled to the correct value.

A diagnostic check of the FIA rig is then performed, this covers the operation of the MFCs, valves, temperature and humidity system and inspects the pipework and sensor chamber for leaks. This check includes a short pre-clean, though a longer pre-clean can be programmed. This ensures the pipework, Drechel bottle head space and sensor chamber is free from contaminants and laboratory air introduced by the refilling of vessels. Once these procedures have been performed the sample and FIA rig can then be considered ready for testing. Data from the sensors is recorded to hard disc by either of the characterisation instruments, described later. This procedure can be repeated indefinitely for different sensors and analytes. A flow diagram of the testing procedure is shown in figure 5.7.

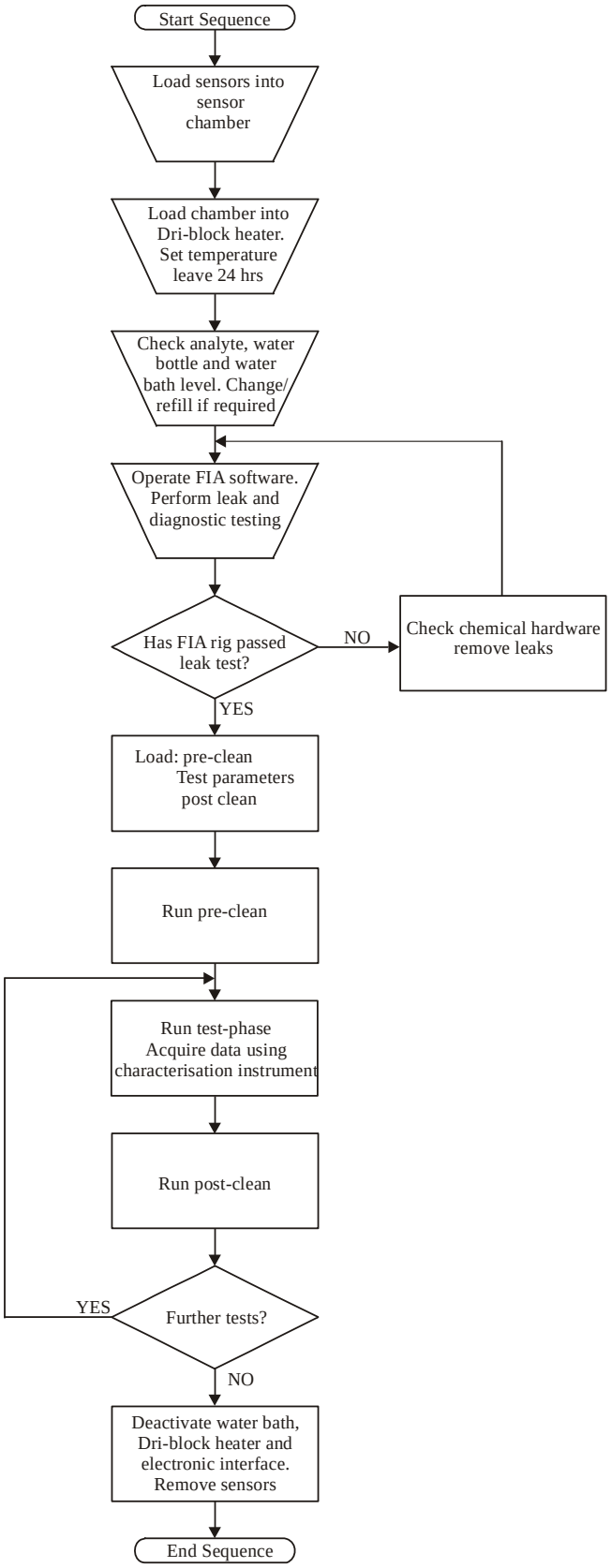

Figure 5.7: Flow diagram of testing protocols

Once the testing has finished the sensors can be removed from the sensor chamber and the rig can be cleaned to remove any trace analyte still in the pipework or the sensor chamber. This prepares the rig for the next test.

5.6.1 Leak testing diagnostics

The purpose of leak testing is to check the integrity of the chemical hardware, which could result in non-identical test conditions. This leak testing is done in manual control, performed before testing commences. In these checks the MFCs, valves, pipework, vessels and sensor chamber are verified in turn. Initially, the regulator on the gas bottle, is tested for pressure (2 bar) and remaining volume. Next each MFC is tested in turn beginning with the dry air line, as this will be mixed with the sample test line to reduce possible chemical hardware contamination.

If excess leaks are discovered any testing is postponed until the problem can be resolved. Each MFC is tested individually with the exhaust monitored by the MFM and the flow sensors of the chemical hardware. A flow rate of 300 ml/min is entered to each of the MFCs and the output of the MFM is observed to confirm they are equal. A small deviation in output to return is accepted, as the output of the MFC and MFM have a 1% error associated with them. A further 1% error is allowed as such a leak would be undetectable, giving a total allowable leak of 3% (9 ml/min). By performing these tests throughout the chemical hardware all sections can be checked, in turn, for leaks.

5.6.2 Pre/post clean and sample preparation

The pre and post clean procedures are used to remove any contaminates from the chemical hardware before and after a test. These contaminants are usually associated with a previous test or laboratory air, which may have been introduced whist the sensor were being fitted or a vessel refilled. The pre/post cleans are an automatic procedure loaded into the FIA control software, though manual operation can be performed. These are simply text files that contain flow rate and humidity information, similar to a standard test, a typical pre/post clean procedure is given in table 5.4.

	Flows rates (ml/min)				
Time (mins)	Dry	Wet	Sample	Bypass	Description
10	100	50	150	0	Clean sample vessel. Sensor chamber bypassed
10	100	50	150	0	Clean second sample vessel
10	100	50	0	150	Clean sensor chamber

Table 5.4: Pre/post clean procedure

5.7 I-V characterisation instrument

The traditional method of characterising any FET is to perform an I-V scan of the device. Such instruments do commercially exist though are expensive and usually can only scan one device at a time. For this reason an I-V characterisation instrument was designed that could interact with the FET sensors placed within the test environment of the FIA rig. The purpose of this instrument is to bias the drain and gate voltage in respect to the source and record the drain/source current, for both *n*-type or *p*-type transistors. The other requirement of the instrument, instead of characterisation, is to record results over a test period at a fixed bias. The instrument can be separated into three sections:

- Electronic interface
- Data acquisition card
- Software control system

The software control system is written in National Instruments LabVIEW^{TM} for windows, version 5.0. This control system interacts with the electronic interface via two National Instruments cards the PC-DIO-24 and the AT-MIO-XE50. The PC-DIO-24 card has 24 digital control lines that can be configured as either inputs or outputs in three banks of eight. The AT-MIO-XE50 has 16 analogue inputs (16 bit), which can be programmed to have an input range of 0 V to 5 V, 0 V to 10 V or +5 V to -5 V. A photograph of the instrument is shown in figure 5.8. The instrument is powered by a linear PSU (Coultard Lambda HDB 12/15) fitted underneath the PCB, supplying +/-15 volts and +5 volts, with a drive current of 1.8A, a line regulation of +/- 0.05% and a load regulation of +/- 0.05%.

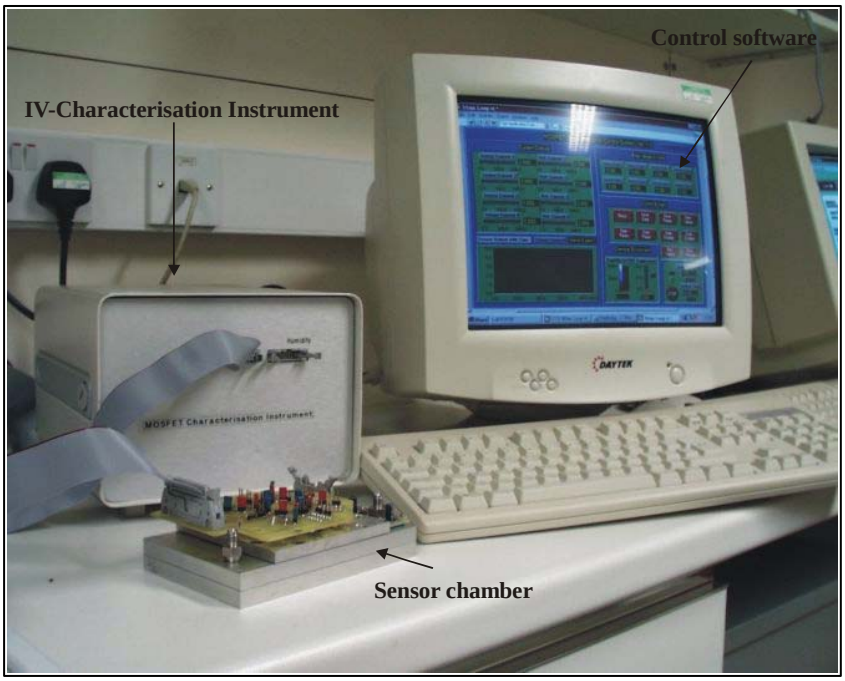

Figure 5.8: I-V characterisation instrument

5.7.1 Electronic Interface and associated hardware

The electronic interface directly interacts with the chemFET sensors. Its purpose is to produce the voltages required to bias the sensors and to convert the current through the sensors into a useable measureand. The instrument can bias up to 8 FET sensors simultaneously, usually in pairs, with each pair having a specific gate and drain voltage associated with it. These voltages are created using two quad 12-bit DACs the DAC4814 (Burr-Brown), serially programmed via the PC-DIO-24 card. The output range of the DAC is –10 to +10 volts, with a step size of 4.88 mV. These bias voltages are buffered by an ultra low noise, low offset quad amplifier, the OP-470GP (Burr-Brown). The control signals are connected to the sensors, via a 26 way IDC cable, and the PCB fitted on top of the FET sensor chamber. The source of the sensor is connected to the –ve input of a further OP-470GP op-amp. The current though the FET is converted into a output voltage using a current to voltage converter based on a op-amp with feedback resistor, where the +ve terminal is connected to the analogue ground. The output range of this circuit depends upon the value of the resistance where:

$$-V_{OUT} = R_{FB} \times I_{DS} \tag{5.3}$$

where V_{OUT} is the output voltage, R_{FB} is the value of the feedback resistor and I_{DS} is the drain/source current though the FET sensor. Any resistor can be plugged into the instrument to give a very broad current range, though a jumper selectable default

resistor is available of 10 kΩ (0.1%, 15 PPM/^{o}C), which gives a current range of ±1 mA. This output passes to both to an output stage and to the analogue inputs of the AT-MIO-16XE50. The output stage is composed of a resistor programmable amplifier the INA114AP and filter. This IC amplifies the difference between two input voltages depending on a single external resistor.

The control software scans the initial voltage from the current/voltage converter and produces an almost identical voltage via a third DAC4818AP. The output of this DAC and the current/voltage converter circuit is connected to the INA114AP and the difference of these two inputs amplified. The external resistor can be changed to set the gain, though a default gain of 200 was found to be sufficient. This output signal is filtered using a 1st order low-pass filter (1 kHz) and scanned by the analogue inputs of the AT-MIO-XE50. A simplified circuit diagram of this system is shown in figure 5.9.

The temperature and humidity sensors placed within the sensor chamber are also interfaced using this electronic card connected via a 10 way IDC lead. As most of the control electronics are integrated into the PCB fitted onto the chamber, the characterisation instrument simply buffers the input from the sensors and connects it to the analogue inputs of the AT-MIO-16XE50.

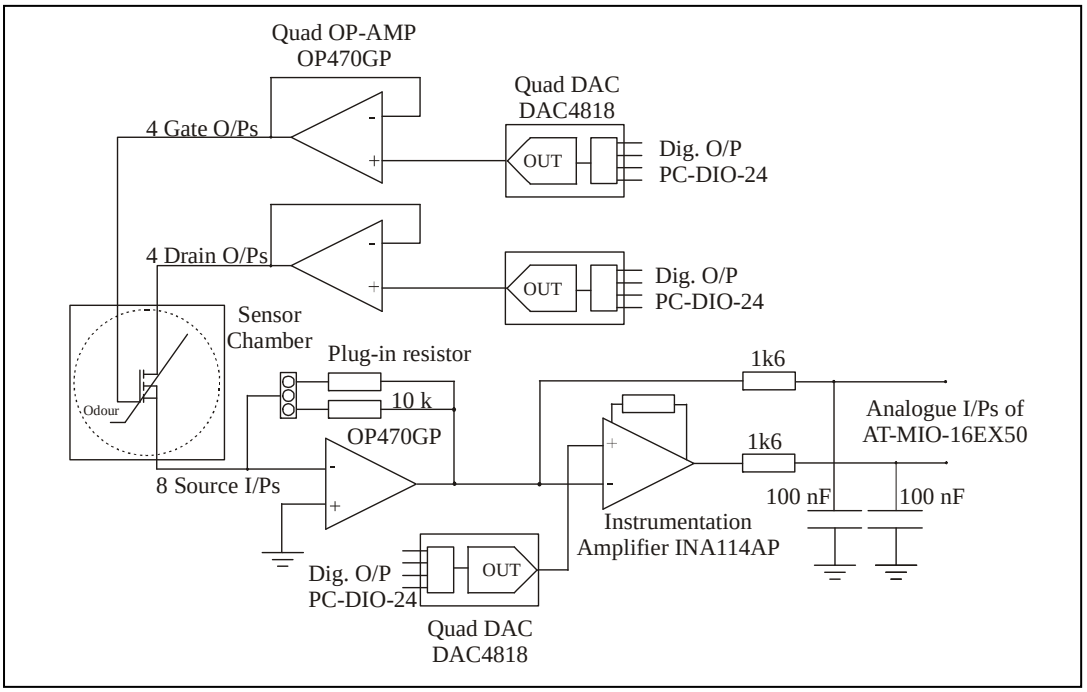

Figure 5.9: Schematic of I-V characterisation hardware.

5.7.2 Software control program for I-V instrument

The function of the software program is to control, measure and record sensor information. The control software has two main operations; the first is to perform sensor I-V characterisation; the second to record sensory information, at a fixed bias, over a test period. The program, including the front panel, is shown in appendix B. The panel is divided into two main sections, current information on the left and control features on the right. The value of the feedback resistors and the gain of the instrumentation amplifiers is entered so correct current information is relayed onto the screen. This information is logged via two pop-up menus that allows the user to enter these parameters, accessed through the “Gain” and “Resist” switches on the front panel. For a fixed bias test, drain and gate voltages for the sensors are manually entered on the front panel. A further pop-up menu is used to enter the save parameters, specifically the test length and the file name. Also a sampling rate control is available that defines the rate at which information is stored.

The IV characterisation function is more complex. This is programmed through the pop-up menus “Gate Param” and “Drain Param”. These menus allow the user to enter step information required for a characterisation. This includes the initial and final value, the number of steps, the time per run and the number of runs. The control software equally divides the characterisation range into the number of required steps. The time per run defines the length of time each characterisation will take. Clearly, for one sweep of V_{GS}, V_{DS} will have to be swept numerous times. This routine also includes a “Hysterisis” function, which performs characterisations of a FET on both ascending and descending steps, to give validity to any result. The control program takes all the results within a step level and averages them to give the final result. By using this averaging technique any random noise fluctuations are removed.

Clearly, a FET characterisation is only useful in static conditions and so an added feature was the ability to program the control software to only characterise a FET at specific times. This information is entered via a text file, indexed to the system time. A flow diagram describing the operation of the control software is given in appendix B.

5.7.3 Commissioning of I-V instrument

Commissioning of the I-V instrument is required to verify the operation of the instrument and to analyse the resolution and drift. This is to ensure that the measured output is due to a change within the sensor and not an artefact of the electronics or control system. A number of simple tests were used to verify both the operation of the instrument and to investigate the resolution and noise characteristics. Each channel was tested using a number of precision resistors (± 0.1%) at a fixed output. Further tests were performed using a standard *n*-type enhanced MOSFET the BSS88 (Infieon), to ensure its ability to characterise standard transistors.

Initial tests investigated the resolution and drift of the instrument, fixed resistor of values 1.6 kΩ, 2 kΩ, 5 kΩ and 10 kΩ (± 0.1%), were placed between the drain's and source's of the instrument, with a constant voltage output of 1 volt, a gain of 208 and the input range of the instrument set to 1 mA. Readings were taken over a 24 hour period at a sample rate of 1 results every 60 seconds. The output of the instrument for 2 resistance's is shown in figure 5.10a, over a 10,000 second period. As can be seen from this figure that the mean value of 100.0303 μA ±0.2 nA (10 kΩ) and 607.4912 μA ±0.3 nA (1.6 kΩ) was measured with a maximum variation of 0.01nA. A slight variation from ohms law calculated output would be expected as the resistance tolerance is ± 0.1%. The temperature co-efficient over the test period for these fixed resistors was measured at 1-2 nA/^{o}C. The second test was to ensure the instrument could create a step output and to look at the transient output of the instrument. The precision resistors were subjected to voltage steps of 1 to 5 volts in 0.5 volt steps, for a period of 20 seconds per step at the maximum sampling rate. The data acquisition rate is controlled by the speed of the computer running the software, and the transient response of the DACs to voltage changes. This showed that the system had a maximum sample rate of 1.25 Hz.

The concluding test was the characterisation of a standard *n*-type enhanced MOSFET, BSS88. The transistor was characterised at a current range of 1 mA, a V_{DS} sweep of 0 to 1 volts in 0.25 volt steps and V_{GS} between 0.8 volts to 1.05 volts in 0.05 volt steps. The resulting characterisation is shown in figure 5.10b. A number of devices were characterised and error bars are included for each point.

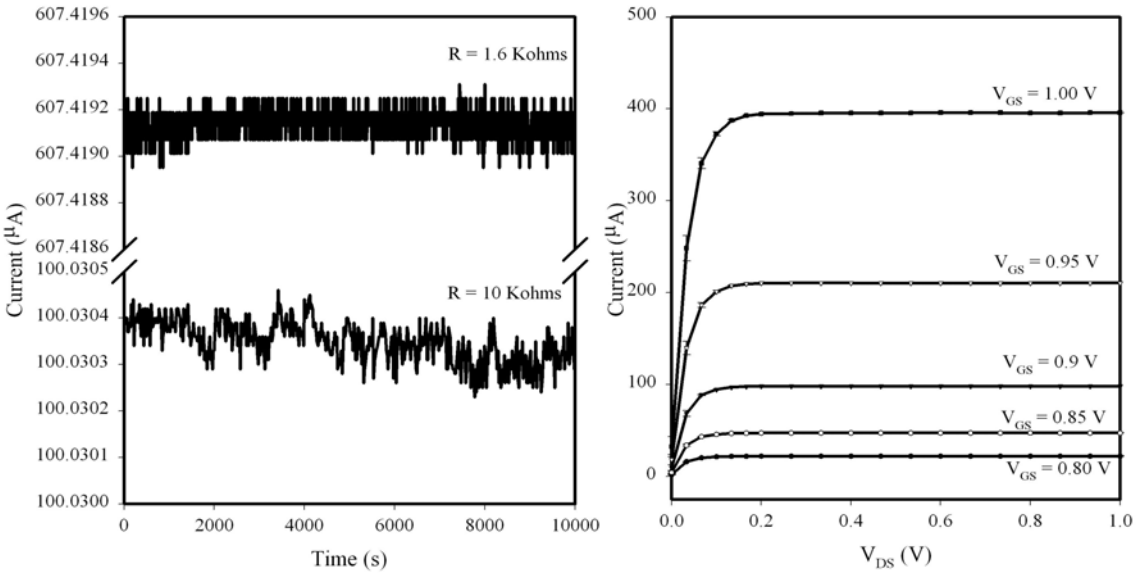

Figure 5.10: (a) Typical noise values and (b) characterisation of BSS88 transistors.

5.8 Constant current measurement instrument

To augment the I-V characterisation instrument, a further instrument was developed based on a constant current output. The instrument was designed to interface up to 32 sensors producing a constant current output and measure the voltage drop over the sensors induced by this current. Here, this first version was limited to 16 sensors. As with the other measurement tools, this instrument is based on the combination of an electronic interface, a National Instruments card and software control system, written in LabVIEW. The software control program is used to record the results from the instrument and to interface with measurement circuitry. The program interacts with the electronic instrument via 2 PC-DIO-24 National Instrument cards (described earlier). The electronic interface is housed in a euro rack. (VERO-BICC Electronics), as shown in figure 5.11, where individual boards plug into a main backplane. The instrument is powered by a single linear PSU (Model Mp. LK 35, VERO-BICC Electronics), supplying ± 12 volts and + 5 volts.

Figure 5.11: Constant current measurement instrument.

5.8.1 Electronic interface of the constant current measurement instrument

Unlike the chemical hardware and I-V characterisation instrument, the CCM instrument both measures the final output as well as setting the test conditions. The electronic interface can be broken into three basic cards:

- Constant current
- Temperature and humidity
- Backplane

The backplane is an interface connecting the PCB cards to the 2 PC-DIO-24's. Each constant current card is designed to interact with up to 8 sensors, with the instrument containing a maximum of 4 cards. The constant current card can be segregated into three sections, the constant current interface, filter and amplifier section and the measurement circuitry. A simplified circuit diagram of these sections is shown in figure 5.12. The constant current circuit shown operates by using the op-amp (quad OP470GP) as the constant current source. This occurs because of a precision diode (LT1009CZ, 2.5V ±5 mV) which restricts the voltage to 2.5 volts between one side of the scaling resistor (R_{SCALE}) and the non-inverting input of the op-amp. The magnitude of the constant current is then set by the value of the scaling resistor, defined by the equation:

$$V_{\text{Sensor}} = R_{\text{Sensor}} \times I_{\text{Sensor}} \quad (5.4)$$

$$V_{\text{Sensor}} = R_{\text{Sensor}} \times \frac{2.5}{R_{\text{SCALE}}} \quad (5.5)$$

where V_{Sensor} is the voltage drop over the sensor and R_{Sensor} is the resistance of the sensor (here the channel of the MOSFET). To allow the maximum amount of flexibility in output current, any R_{SCALE} resistor can be plugged in, though a default resistance of 100 kΩ (± 0.1%) is used to give a standard current of 10 μA that is jumper selected.

The second stage is a combination of a second order low pass filter and amplifier, using a simple resistor/capacitor/op-amp (Quad OP470GP) combination. Its purpose is to remove noise from the signal and to scale the output (V_{Sensor}) to 10 volts. The filter is set to a frequency of 160 Hz, and the amplification to a default value of two. A circuit diagram of this section is also shown in figure 5.12.

The final section of this card is the measurement electronics. This is performed by a pair of on board analogue to digital converters (ADCs), the Burr-Brown ADS1211. This IC is a 24 bit ADC based on a sigma-delta converter and can be used to scan four channels.

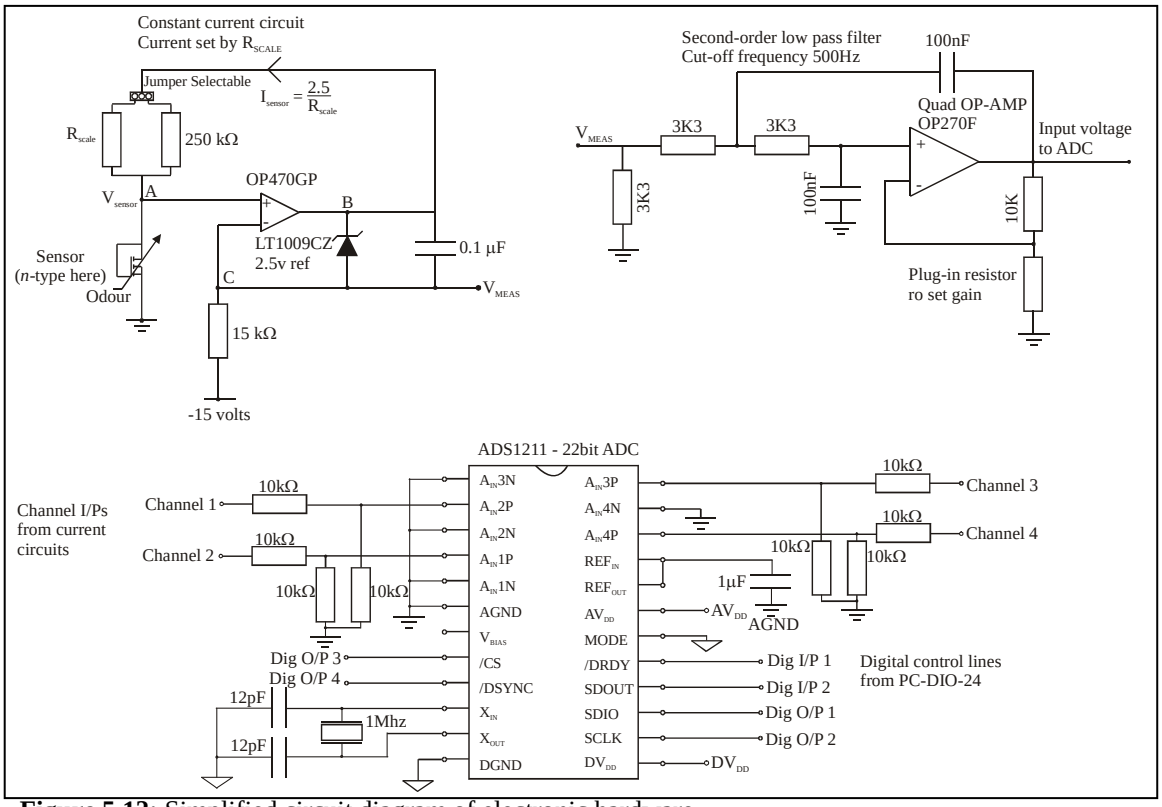

Figure 5.12: Simplified circuit diagram of electronic hardware.

The output from the ADC's can be controlled via a simple three-wire interface, connected to the PC-DIO-24 and software control system. By using on-board ADCs the sensitivity and resolution of the instrument should be improved.

The final card is the temperature and humidity interface. This consists of a 2^{nd} order low pass filter (50 Hz) and amplifier (OP270GP). The output of this circuit is read by the Crystal Technology CS5504 ADC, a dual input 20 bit ADC that also operates by a signal-delta converter. The constant current cards and temperature humidity card are interfaced to the appropriate sensors via a 10 way IDC connector.

5.8.2 Control software for constant current instrument

Unlike the previous control software this program simply has to record values from the sensors and does not have any additional control features. The complete program including the front panel and pop-up menus are given in appendix B. The front panel is divided into three main sections, firstly on the left are a number of slide bar indicator displaying the voltages across the sensors. On the bottom right is a thermometer and colour bar, which indicates the temperature and humidity within the chamber. Above these are the control parameters, specifically the present time, finish time and sample rate. A number of switches are also shown that allow the user to enter system parameters, including the gain for each sensor, save details (e.g. file name) and finish time. A last function of the control software is to interact with the ADCs within the electronic interface. A flow diagram of the software control system is included in appendix B. The software control system initialises communication with the ADCs, setting the ADC into unipolar operation, with a gain of 1, scanning channel 1. Then a sub-vi "Sensor Output" scans the /DRDY output from the ADCs, waiting for an indication that a conversion has been performed. Data is then clocked from the ADC, via the DOUT and CLK lines. As only the fourth result can be taken as a true value the first three readings are discarded. A new channel is then selected and the operation is repeated. This is performed for all 4 channels, with two ADCs working in parallel. The result from these ADCs is converted from a binary to a decimal value, scaled to take into account the gain values and the front panel is updated. A similar operation is performed on the ADCs for the temperature and humidity ADC.

5.8.3 Commissioning of constant current measurement instrument

The commissioning of CCM instrument was performed in three ways, by investigating the drift, resolution and the response time. These parameters were investigated by using eight fixed precision resistors (2 × 2 kΩ, 5.1 kΩ, 22 kΩ, 50 kΩ) of value ± 1%, with a fixed current of 10 μA. The voltage output was measured over a period of 24 hours, with a sampling rate of 1 reading every 60 seconds. The output from two resistors is shown in figure 5.13a, over 10,000 seconds. Typical measured values were 99.812 mV and 51.408 mV with sample variance of ±5 μV and ±1 μV, with similar results observed for the remaining resistors. This variation in sample variance is due to the different gains being use (10kΩ gain = 200, 5.1kΩ gain = 100). To show the time response of the instrument two resistors (2.2kΩ and 650kΩ) were switched, through an analogue multiplexer, at a frequency of 0.5 Hz, as shown in figure 5.13b. This shows that the instrument can measure rapid changes in sensor parameter up to a frequency of 2.1 Hz. The temperature dependence of the instrument was measured at an average of 100 to 200 nV/^{o}C.

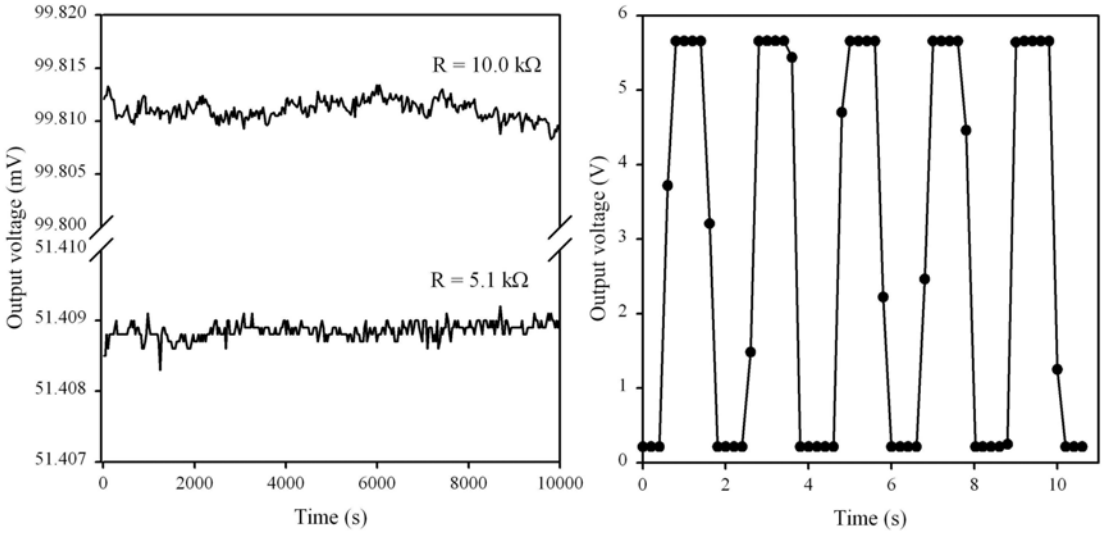

Figure 5.13: Noise and response measurements for constant current measurement instrument.

5.9 Testing protocols for I-V characterisation and constant current measurement instruments

An overview of the testing procedures used with both instruments is shown in figure 5.14. Both sequences are initialised after the sensors have been stabilised at a fixed temperature and the chemical hardware has passed leak and maintenance testing, with the characterisation instruments activated in the testing phase of the sequence. For the I-V instrument, the required current range and gain is set before testing. The software is

then activated, with the resistor, gain and test values (whether a fixed output or ramp) entered. Then save and, if required, load details are added and the save file is created. Finally data storage is activated by the “Save Data” switch.

For the CCM instrument a similar operation is required, configuring the current and gain values of the electronic interface, the activation of the software and the entering gain values. To assist in the selection of appropriate current and amplification values, the software can be activated without amplification and using the default output of 10 μA. The display then shows the output from the amplification op-amp on screen. The resistance of R_{SCALE} is usually set so the output is between 10 – 500 mV, this will depend upon the polymer and the characteristics of the sensor, e.g. channel dimensions. The gain resistor is then selected so the output is between 8 – 10 volts. Once completed the gain value can be entered in the software and the real voltage over the sensors displayed. When complete save parameters and a sampling rate is entered, the storage of results is activated by pressing of the “Save Data” switch.

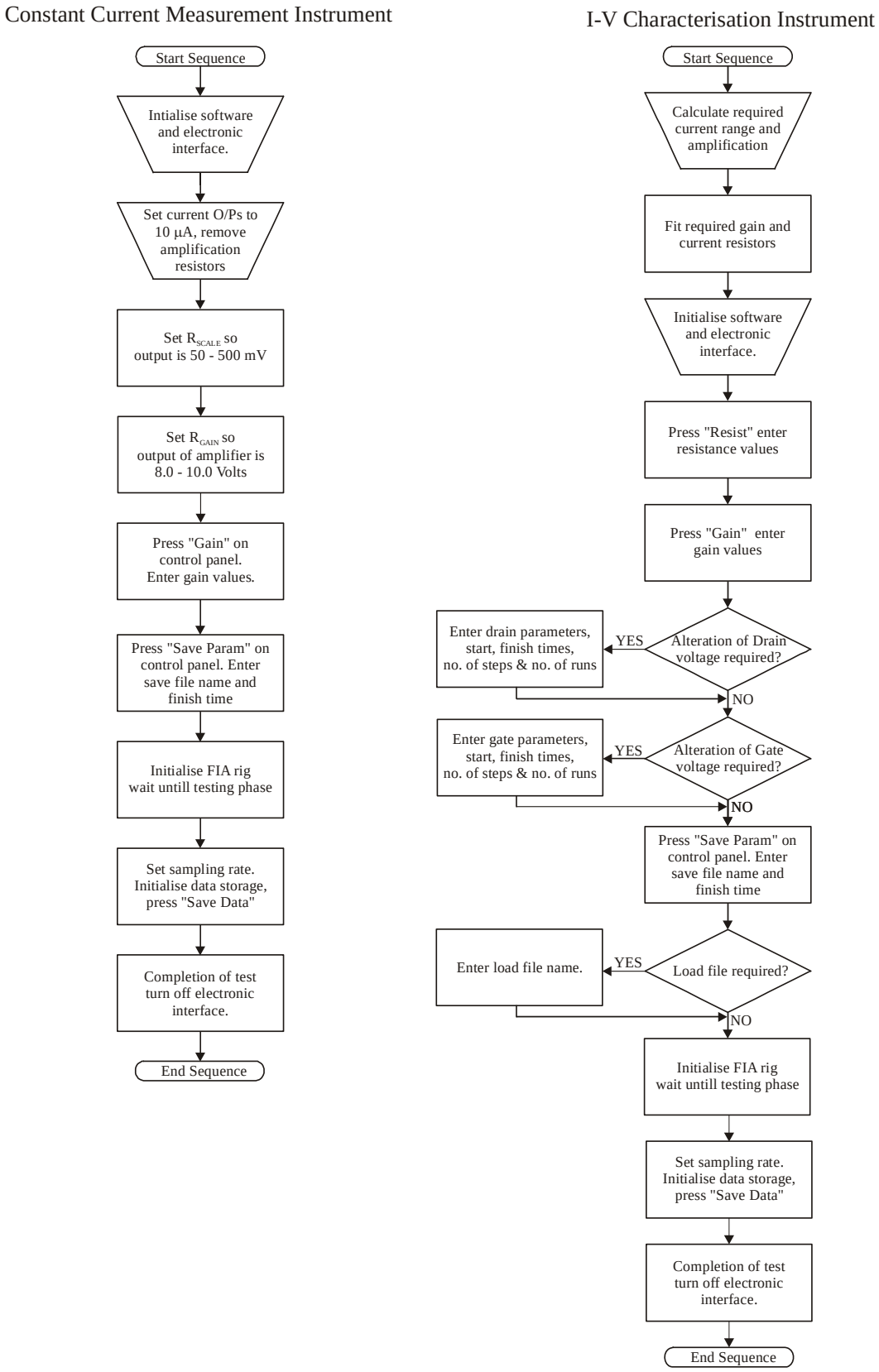

Figure 5.14: Testing protocols for I-V and constant current measurement instruments.

5.10 Conclusions

This chapter has documented the design, construction and commissioning of a flow injection analysis test station and associated electronics used for the dynamic and static testing of sensors to volatile organic compounds. A summary of the of the specification of the test station and associated measurement electronics is given in table 5.5 below:

Test station components	Value	**Measurement electronics**	Value
Flow rate per MFC	0 to 300 ml/min ± 1 % FSR	IVC Output	- 10 to + 10 volts ± 0.025 %
Flow rate of system	0 to 900 ml/min ± 3 % FSR	IVC input range*	0.1 nA – 2 mA ± 0.001 %
Chamber temperature	RT to 105 ^{o}C ± 0.1 ^{o}C	Sampling rate of IVC	1.25 Hz
Cooling bath temperature	-30 ^{o}C to +200 ^{o}C ± 0.1 ^{o}C	Temperature drift	1-2 nA/^{o}C
Min. con. Ethanol	25 PPM ± 0.1%	CCM current output range*	250 nA – 2 mA ± 0.1%
Min. con. Toluene	20 PPM ± 0.1%	CCM input range	-10 to + 10 volts ± 0.005 %
Humidity measurement	0 – 100 % RH ± 1% -40 ^{o}C to +60 ^{o}C ± 0.3 ^{o}C	CCM Sampling rate	2.1 Hz
		Temperature drift	100-200 nV/^{o}C

Table 5.5: The specification of the FIA rig and measurement electronics (* limited by drive op-amp, this can be altered to increase current range)

Details of the chemical hardware, electronic interface and custom written software control systems have been included, as well as comprehensive notes on the measurement instruments. This includes information on the commissioning, as well as testing protocols used throughout these experiments. The instruments have been shown to have a high sensitivity and good long term stability.

5.11 Reference

5.1 J. W. Gardner, T. C. Pearce, S. Friel, P. N. Bartlett and N. Blair, A multisensor system for beer flavour monitoring using an array of conducting polymers and predictive classifiers, *Sensors and Actuators*, B, **18-19** (1994), 240-243.

5.2 T. C. Pearce, *PhD Thesis*, University of Warwick, Coventry, CV4 7AL, UK (1997).

5.3 P. Ingleby, J.W. Gardner, P.N. Barlett, Effect of micro-electrode geometry on response of thin-film poly(pyrrole) and poly(aniline) chemoresistive sensors, *Sensors and Actuators*, **B**, 57 (1999), 17-27.

5.4 P. Ingleby, *PhD Thesis*, University of Warwick, Coventry, CV4 7AL, UK (1999).

5.5 M.C. Lonergan, E.J. Severin, B.J. Doleman, S.A. Beaber, R.H. Grubbs, N.S. Lewis, Array-Based Vapor Sensing Using Chemically Sensitive Carbon-Black-Polymer Resistors, *Chem. Mater.*, **8**, (1996), 2298-2313.

5.6 V. Demarne, A. Grisel, R. Sanjines and F. Lèvy, Integrated semiconductor gas sensor evaluation with an automated test system, *Sensors and Actuators*, B, **1** (1990), 87-92.

5.7 T. Nakamoto, S. Ustimo, N. Yamashita, T. Moriizumi abd Y. Sonoda, Active gas/odour sensing using automatically controlled gas blender and numerical optimisation techniques, *Sensors and Actuators*, B, **20** (1994), 131-137.

5.8 I. Harvey, G. Coles and J. Watson, The development of an environmental chamber for the characterisation of gas sensors, *Sensors and Actuators*, B, **16** (1989), 393-405.

5.9 H-E. Endreas, H. Jander and W. Götter, A test station for gas sensors, *Sensors and Actuators*, B, **23** (1995), 163-172.

5.10 N. A. Lange and J. A. Dean, *Langes Handbook of Chemistry*, McGraw Hill, London, 1985.

5.11 T. Boublik, V. Fried and E. Hala, *The Vapour Pressure Book of Pure Substances*, Elsevier Publishing, 1990.

5.12 A. M. James and M. P. Lord, *Macmillan's Chemical and Physical Data*, The Macmillian Press Ltd, London, 1992.

5.13 National Instruments, LabVIEW™ User Manual, 1995.

CHAPTER 6

Room temperature chemFET sensors employing conducting polymer films: results, theory and analysis

6.1 Introduction

The selectivity and sensitivity of any chemical sensor will be fundamentally limited by the gas sensitive material employed. Previous chapters have concentrated on the design and development of room temperature chemFET sensors, employing conducting polymer films. Though much is known of these materials its amalgamation with these FET devices is a recent innovation. Certain polymers (e.g. resistive sensors employing poly(pyrrole)/DSA [6.1]) have shown a broad range of selectivities and sensitivities to a number of organic vapours. Here, and in the next chapter, the characterisation of these room temperature chemFET sensors is performed; investigating their response to two organic vapours under different environmental conditions. Once characterised empirical and theoretical models will be developed describing the interactions between the analyte, gas sensitive material and the device parameters. This first chapter focuses on the dynamic and static response of these chemFET sensors to analyte concentration. Also investigated is the effect of film thickness on the magnitude of this response.

6.2 Response of chemFET sensors to different organic vapours

ChemFET sensors with conducting polymer films were exposed to two different analytes as described in the following sections. All of these experiments were performed at a constant temperature of 30 ^{o}C and a constant water concentration of 4500 PPM (10 % r.h. at 30 ^{o}C), unless stated. The two analytes chosen were ethanol and toluene. Because firstly, resistive sensors employing these conducting polymer films have demonstrated a rapid reversible response to one or both of these analytes [6.1,6.2,6.3]. Furthermore, ethanol is an alcohol (a polar molecule) and so may have a strong water dependency. Toluene is an aromatic (a non-polar molecule) and so has different chemical properties [6.4,6.5]. Both are volatile organic compounds and are considered as environmental pollutants. Both are clear, colourless liquids, with toluene having a sweet odour. Toluene occurs naturally in crude oil and the tolu tree. It is produced for commercial use as a by-product of the petrochemical industry from the processing of petrol and other fuels made from crude oil. Toluene is manufactured for paints, adhesives and a number of other products. The main health concern involves its effect on the brain, which causes headaches, confusion, hearing problems and memory loss. Ethanol can be fermented, but for commercial use is typically made from ethyl ethanoate or etrene. Mostly it effects health in a liquid form and may cause a burning sensation.

6.2.1 UMIST chemFET sensors employing a conducting polymer

The *p*-channel enhanced (MISFET) chemFETs donated by Dr J. V. Hatfield of UMIST were the first sensors to be tested. These sensors were used to evaluate the test equipment and for preliminary work into these sensors, for these reasons only ethanol vapour was used.

Prior to the experiments the chemFET sensors were given 24 h to equilibrate at the test chamber temperature, controlled externally by the DRI-BLOCK^{TM} heater. This was followed by 1 hour at the first water concentration to further equilibrate. The sensors were exposed to six different concentrations of ethanol vapour (2665, 3732, 5331, 11729, 17593 and 25058 PPM) for a period of 45 minutes. This was to ensure that equilibrium was achieved even if the kinetics are slower than minutes. After each exposure, the sensors were left for 45 minutes to recover and return to their initial value. The current passing through the devices was kept below 100 μA to reduce any

thermal (Joule) heating effect. The chemFET sensors were driven at a gate voltage of –0.6 V and a drain voltage of –0.5 V, for the fixed voltage run, operating in the linear region, and gate voltages of –0.4 V to –0.6 V and drain voltages of 0 V to –1 V, in –0.1 V steps, for the I-V characterisation tests. Typical I-V characteristics from a UMIST sensor is shown in figure 6.1 at a fixed gate source voltage of –0.6 V.

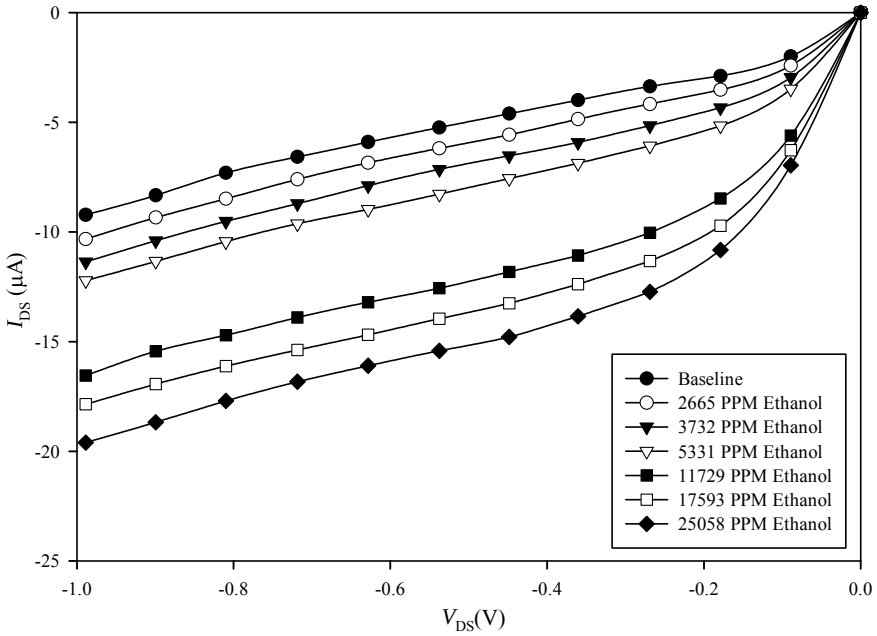

Figure 6.1: Typical shift in I-V characteristics of a *p*-channel MISFET chemFET sensor employing poly(pyrrole) to ethanol vapour in air, at a fixed gate voltage of –0.6 V.

As can be seen from figure 6.1, exposure to ethanol vapour causes an increase in the drain current of the chemFET sensor. A number of different sensors were exposed to ethanol vapour, the results of which are described later.

6.2.2 ChemFET sensors employing composite polymers

ChemFET sensors employing the polymer composite materials were tested to both ethanol and toluene vapour at different concentrations. These sensors were fabricated by IMT, as described in chapter 3, and are enhanced *n*-channel MOSFETs. The sensors were placed in a DRI-BLOCK^{TM} (DB-2D) heater for a period of 24 hours to equilibrate before testing, and operated at a constant current of 10 μA with the gate/drain-source (V_{GDS}) voltage monitored. Each sensor was exposed for 60 minutes at a constant water concentration to create a stable baseline. When this equilibrium had been achieved the sensor was exposed to a pulse of a particular analyte for a period of 25 minutes followed by 25 minutes recovery time at the initial water vapour concentration. Figure

6.2 shows the typical responses of chemFET sensors with poly(styrene-co-butadiene), poly(ethylene-co-vinyl acetate) and poly(9-vinylcarbazole) coatings as the gate to six different toluene vapour concentrations (1316, 1843, 2633, 5793, 8690 and 12378 PPM). Figure 6.4 shows the same sensors were exposed to six different concentrations of ethanol vapour (2665, 3732, 5331, 11729, 17593 and 25058 PPM), as shown in figure 6.3.

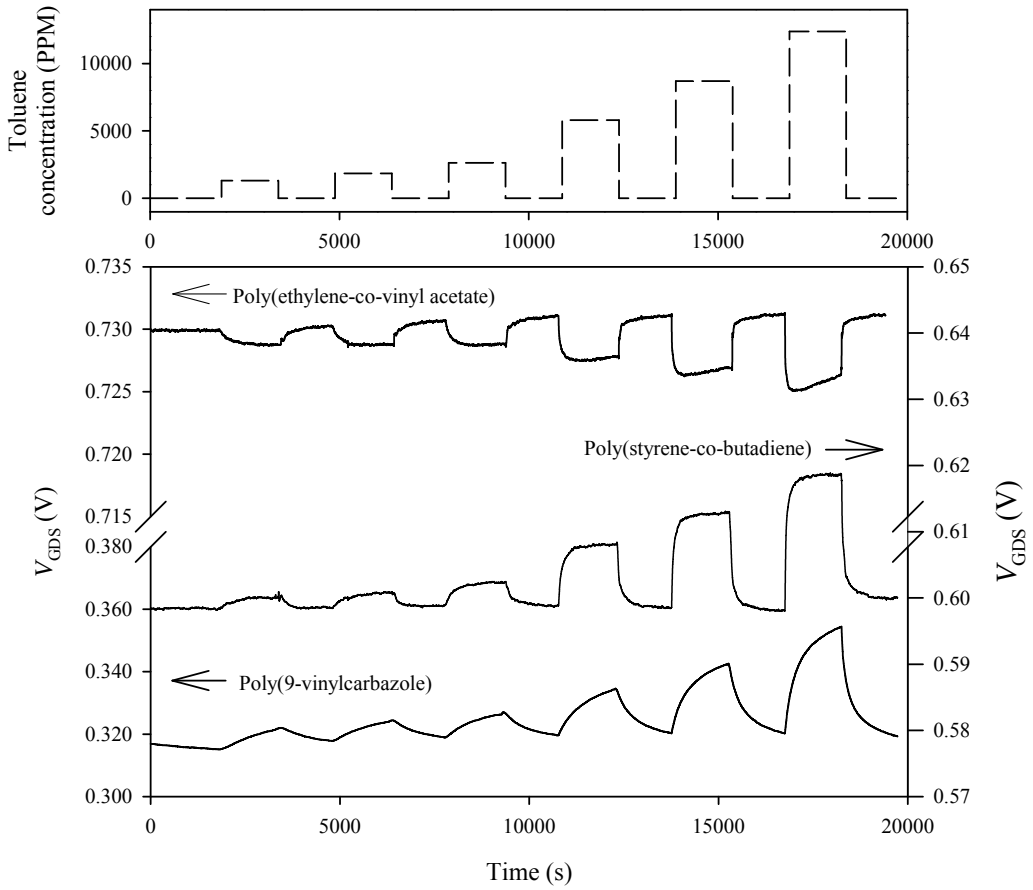

Figure 6.2: Typical responses of *n*-channel (MOSFET) chemFET sensors employing composite polymer films as the gate to toluene vapour in air.

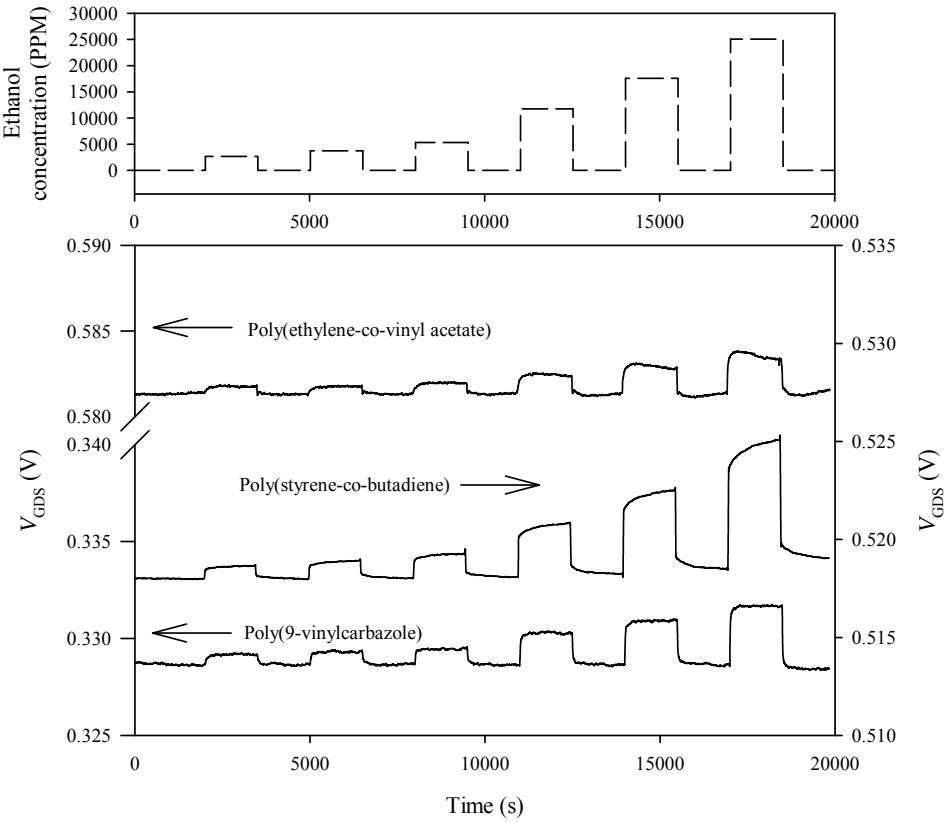

Figure 6.3: Typical responses of *n*-channel (MOSFET) chemFET sensors employing composite polymer films as the gate to ethanol vapour in air.

These results refer to the chemFET devices where the active polymer material is in direct contact with the gate oxide. Experiments with the solid gate devices showed a reduced response (typically 5% of open gate sensors). Example responses from these solid gate devices are shown in figure 6.4.

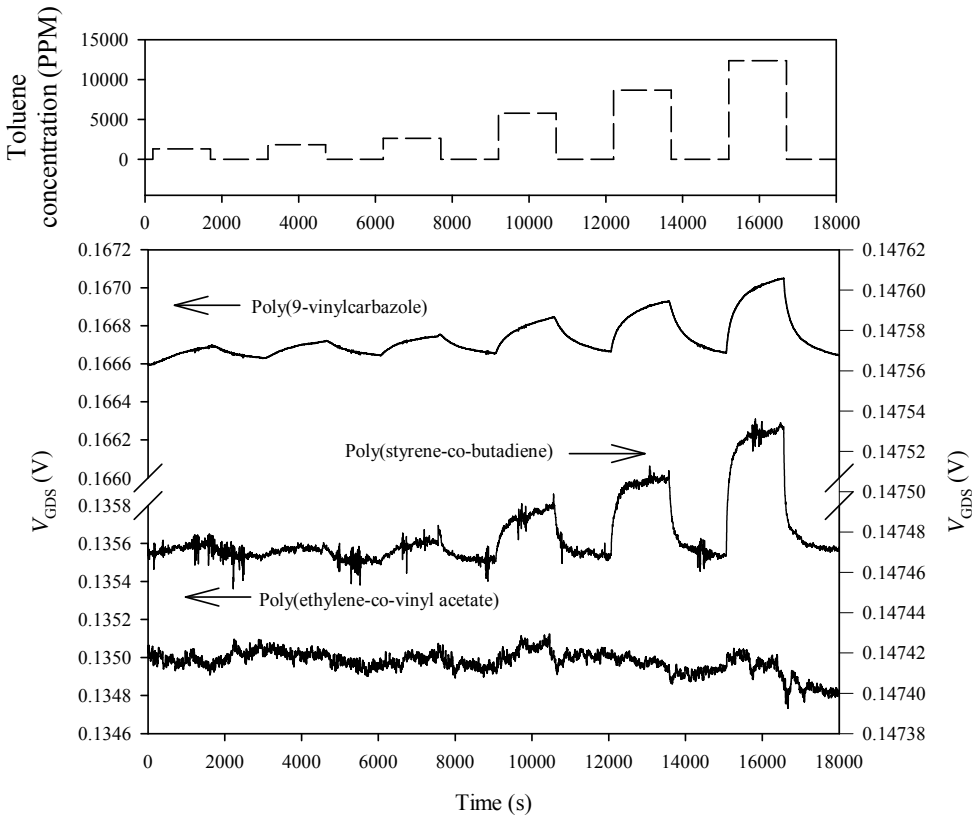

Figure 6.4: Response of *n*-channel (MOSFET) chemFET sensors employing composite polymer films deposited on to a solid gold gate to toluene vapour in air.

From figure 6.2 and figure 6.3, we can state that these chemFET sensors do have some response to these analytes. Furthermore, the response to toluene vapour is significantly greater (≈ 4 times) than to ethanol vapour, with nearly all the sensor exhibiting an increase in V_{GDS} with analyte concentration. The remaining polymer, poly(9-vinylcarbazole) shows a reversal in response sign direction between toluene and ethanol vapour, possible related to the hydrophobic nature of the polymer (discussed in chapter 7).

We would assume that the gold electrode is behaving as a barrier between the gate oxide and the polymer preventing any chemical interactions that occur in the polymer from effecting the device characteristics. Here a sensitivity has been shown, this may be due to the gold being discontinuous in places or possesses pinholes and allowing the polymer to pass though the gaps in the gold and become in contact with a small area of the gate oxide, giving this response.

6.2.3 ChemFET sensors employing electrochemically deposited polymers

The chemFET sensors employing electrochemically deposited polymer films as the gate, were tested to a similar regime as the chemFET sensors with composite polymer films and are also based on the IMT fabricated device (a *n*-channel MOSFET). The sensors were placed in a DRI-BLOCK^{TM} heater for a period of 24 hours to thermally equilibrate before testing. The sensors were driven at a constant current of 10 μA and the drain/gate voltage (V_{GDS}) monitored. The sensors were exposed to six different pulses of ethanol vapour (2665, 3732, 5331, 11729, 17593 and 25058 PPM) and toluene vapour (1316, 1843, 2633, 5793, 8690 and 12378 PPM) for 30 minutes followed by 40 minutes recovery period. Typical responses of poly(bithiophene)/TBATFB and poly(pyrrole)/BSA to ethanol and toluene vapour, in air, are shown in figure 6.5 and figure 6.6, respectively.

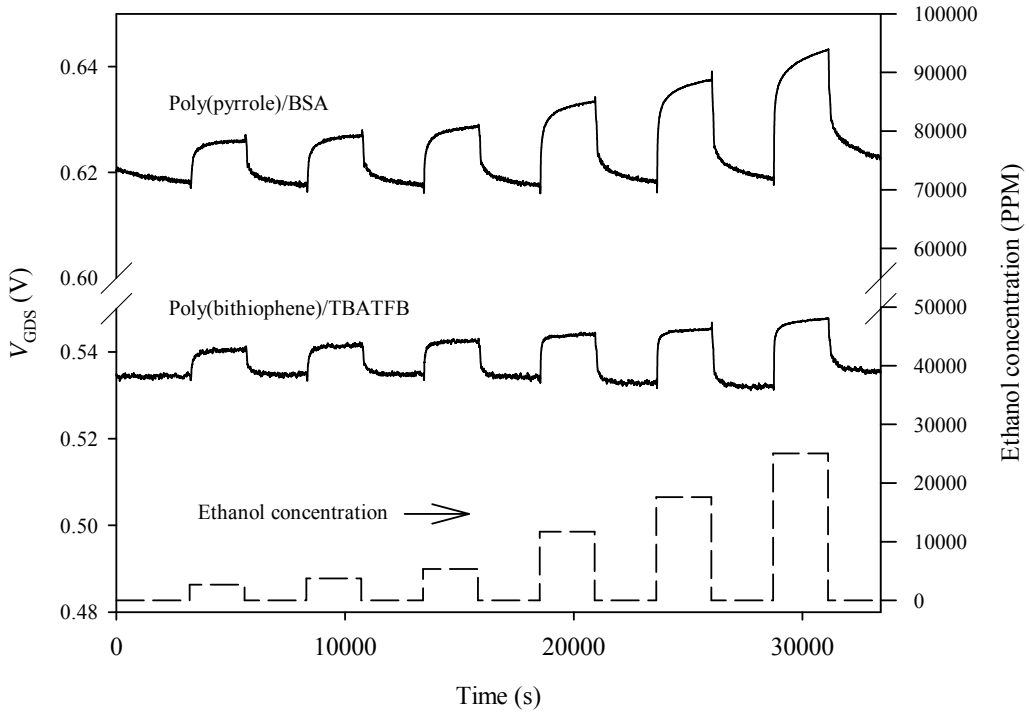

Figure 6.5: Typical responses of *n*-channel (MOSFET) chemFET sensors employing electrochemically deposited polymer films as the gate to ethanol vapour in air.

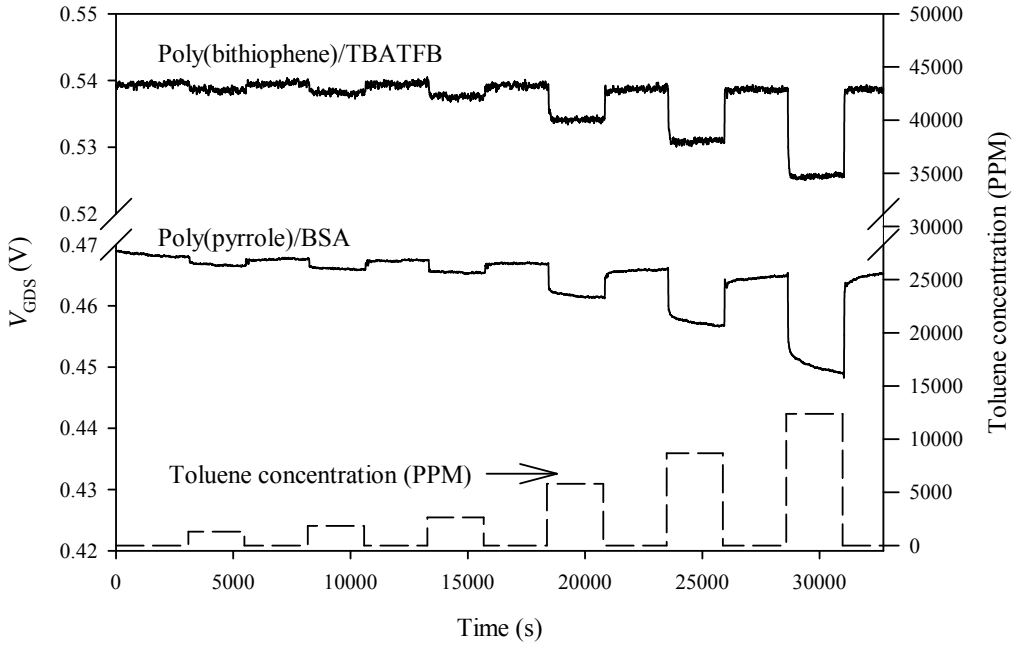

Figure 6.6: Typical responses of *n*-channel MOSFET chemFET sensors employing electrochemically deposited polymer films as the gate to toluene vapour in air.

As before these results refer to devices where the polymer is in direct contact with the gate oxide. The solid gated device showed no response to the analytes, as shown in figure 6.7.

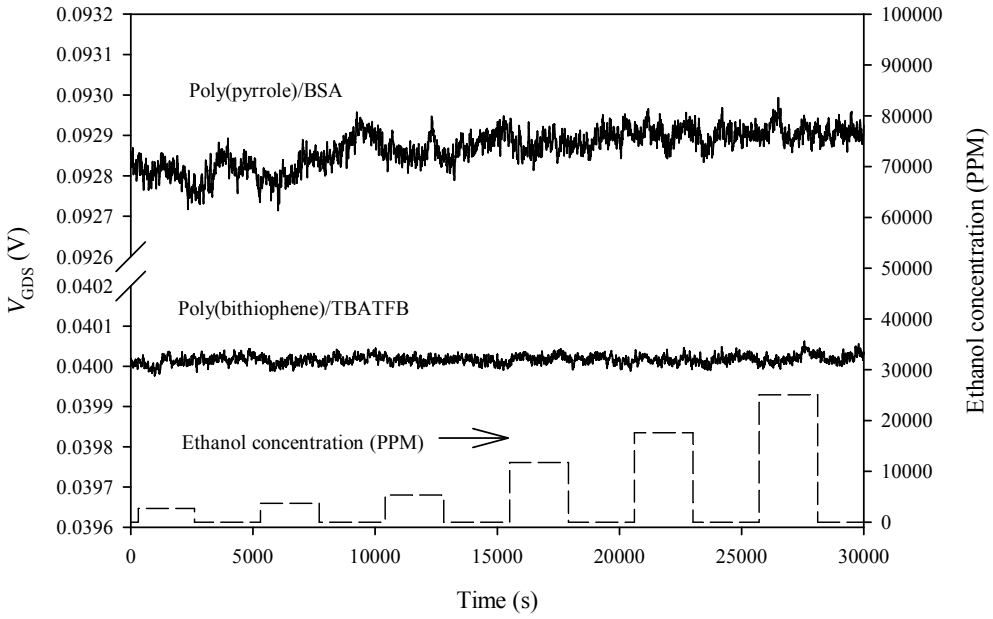

Figure 6.7: Response of *n*-channel (MOSFET) chemFET sensors employing electrochemically deposited polymer films onto a solid gold gate to ethanol vapour in air.

In this section, it has been shown that these *n*-channel chemFET sensors with composite polymer and electrochemically deposited polymer films respond to ethanol

and toluene vapour in air. The response to toluene is especially interesting, as resistive electrochemically deposited polymer sensors generally respond in a minimal small way to this analyte. Furthermore, the direction of this response varies between analytes with ethanol vapour causing a positive shift in V_{GDS} and toluene vapour a negative shift. Also *p*-channel chemFET sensors with a spun coated/electrochemically doped polymer has shown a sensitivity to ethanol vapour.

6.3 Dynamic modelling of *n*-channel (MOSFET) chemFET sensors

An important parameter for any sensor is its dynamic response. This transient response can yield further information useful in understanding the chemical and device interactions occurring within the sensor. Furthermore, it gives the response time, which defines the maximum sampling rate of any system containing these sensors. Tests have only investigated the effect of analyte concentration on the response time, which ignores variations in water concentration and temperature. From previous work using resistive electrochemically deposited conducting polymers, empirical models for the dynamic response have been reported [6.6]. These models give rise to the Langmuir isotherm, in the form of a simple adsorption – desorption reaction, described by:

$$A + \{\ \} \underset{k_b}{\overset{k_f}{\rightleftharpoons}} \{A\} \tag{6.1}$$

with k_f the forward rate constant and k_b the backwards rate constant, where A is the adsorbed species, { } represents an empty adsorption site and {A} represents an occupied site. The Langmuir isotherm describes a circumstance where there are a fixed number of evenly distributed independent absorption sites for the analyte to bind. As these sites are filled, the probability of finding an available site falls, reducing the rate of the response. Initial results used a simple first order exponential modelling function that is consistent with the kinetics of a purely reaction-rate limited response [6.7]:

$$\left(V_{GDS}(t) \;-\; V_{GDS(0)}\right) \;=\; \Delta V_{GDS}\left(1 \;-\; \exp\left(\frac{-t}{\tau_{ON}}\right)\right) \tag{6.2}$$

$$\left(V_{GDS}(t) \;-\; V_{GDS(0)}\right) \;=\; \Delta V_{GDS}\left(\exp\left(\frac{-t}{\tau_{OFF}}\right) \;-\; 1\right) \tag{6.3}$$

where $V_{GDS}(t)$ is the voltage at time t, $V_{GDS(0)}$ is the baseline value in the absence of analyte and ΔV_{GDS} is the change in drain-gate-source voltage (i.e. the static response, defined as the difference between before and after exposure to an analyte), τ_{ON} and τ_{OFF} are the time constants for the on and off responses, respectively. By examination it was found that the second order exponential expression was more consistent with the available data, i.e.:

$$V_{GDS}(t) = V_{GDS(0)} + \Delta V_{GDS(1)}\left[1 - \exp\left(\frac{-t}{\tau_{ON1}}\right)\right] + \Delta V_{GDS(2)}\left[1 - \exp\left(\frac{-t}{\tau_{ON2}}\right)\right] \quad (6.4)$$

$$t \to \infty \quad V_{GDS}(t) = V_{GDS(0)} + \Delta V_{GDS(1)} + \Delta V_{GDS(2)} \quad (6.5)$$

$$V_{GDS}(t) = V_{GDS(0)} + \Delta V_{GDS(1)} \exp\left(\frac{-t}{\tau_{OFF1}}\right) + \Delta V_{GDS(2)} \exp\left(\frac{-t}{\tau_{OFF2}}\right) \quad (6.6)$$

$$t \to \infty \quad V_{GDS}(t) = V_{GDS(0)} \quad (6.7)$$

where $\Delta V_{GDS(1)}$ and $\Delta V_{GDS(2)}$ are the two components of the response, defined by ($t = \infty$):

$$V_{GDS}(t) = V_{GDS(0)} + V_{GDS(1)} - V_{GDS(0)} + V_{GDS(2)} - V_{GDS(0)} \quad (6.8)$$

$$V_{GDS}(t) = V_{GDS(1)} - V_{GDS(2)} - V_{GDS(0)} \quad (6.9)$$

Clearly, these equations assume that the response of the sensor is a positive increase in V_{GDS}. If the opposite occurs then equation (6.4) and (6.6) are reversed. Figures 6.8 to figure 6.11 show the on and off transients for chemFET sensors employing composite polymer and electrochemically deposited polymer films, to toluene and ethanol vapour in air and include the empirical model (expression 6.4 and 6.6) to these transients. These demonstrate excellent fits with correlation coefficients of above 0.98 for both on and off transients.

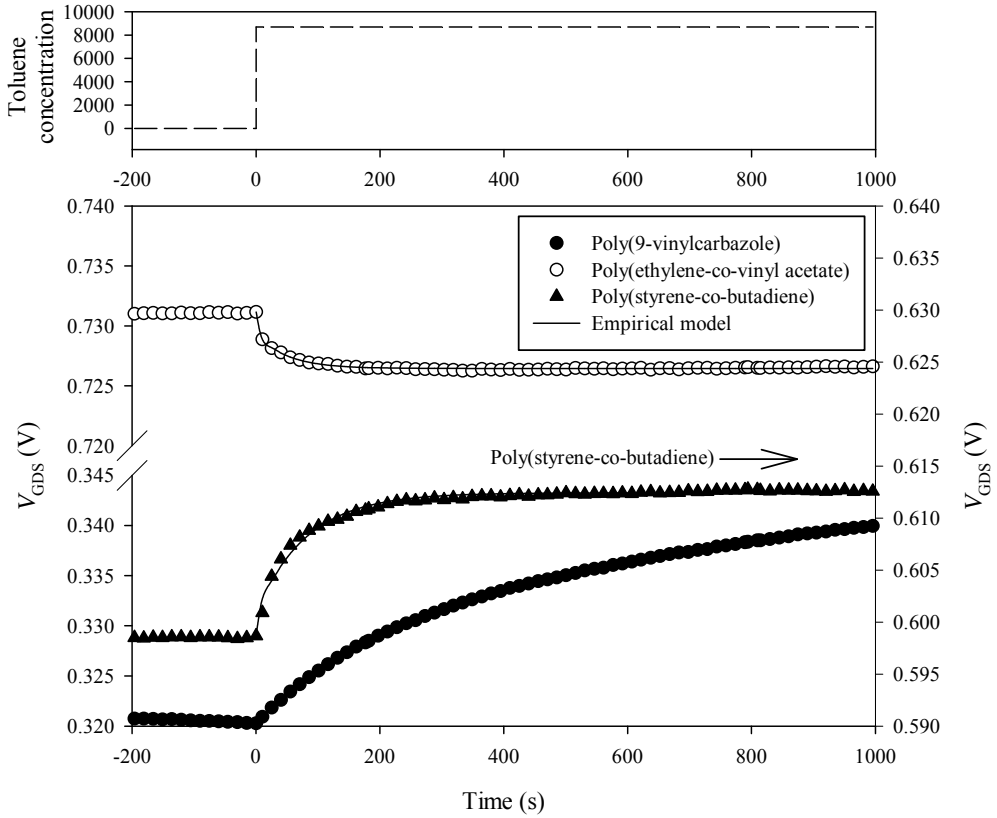

Figure 6.8: Transient response of chemFET sensors employing composite polymer films to toluene vapour in air modelled by a double exponential expression.

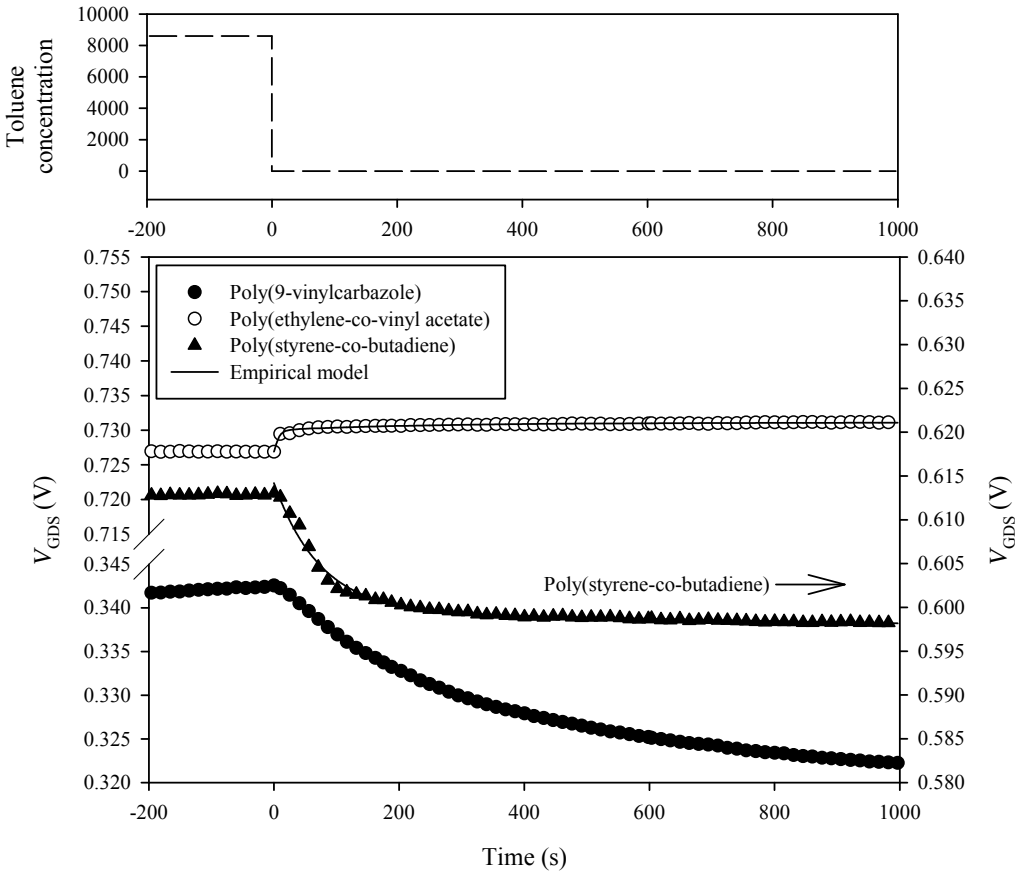

Figure 6.9: Transient recovery of chemFET sensors employing composite polymer films to toluene vapour in air, modelled by a double exponential expression.

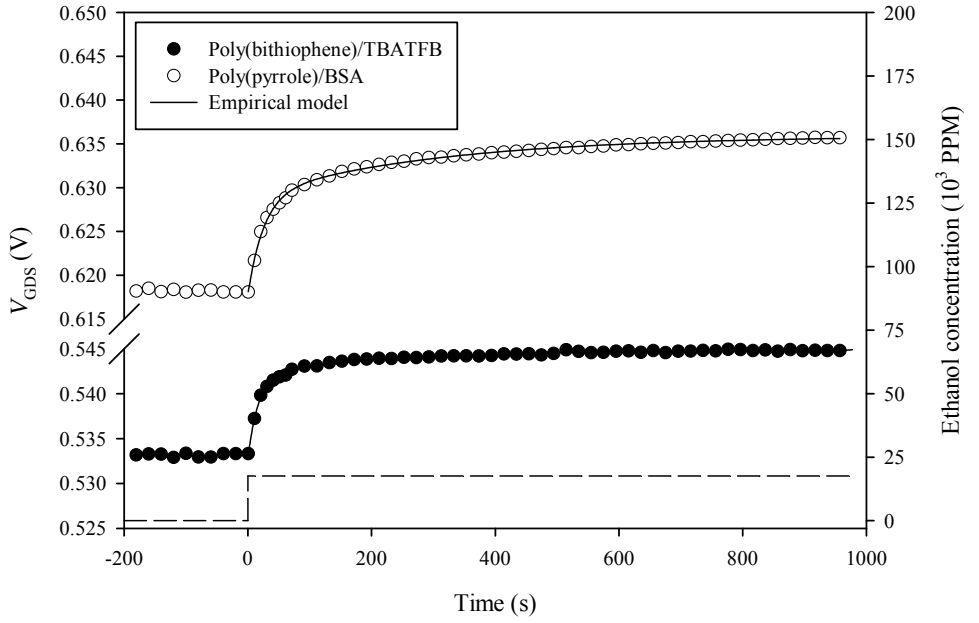

Figure 6.10: Transient response of chemFET sensors employing electrochemically deposited polymer films to ethanol vapour in air, modelled by a double exponential expression.

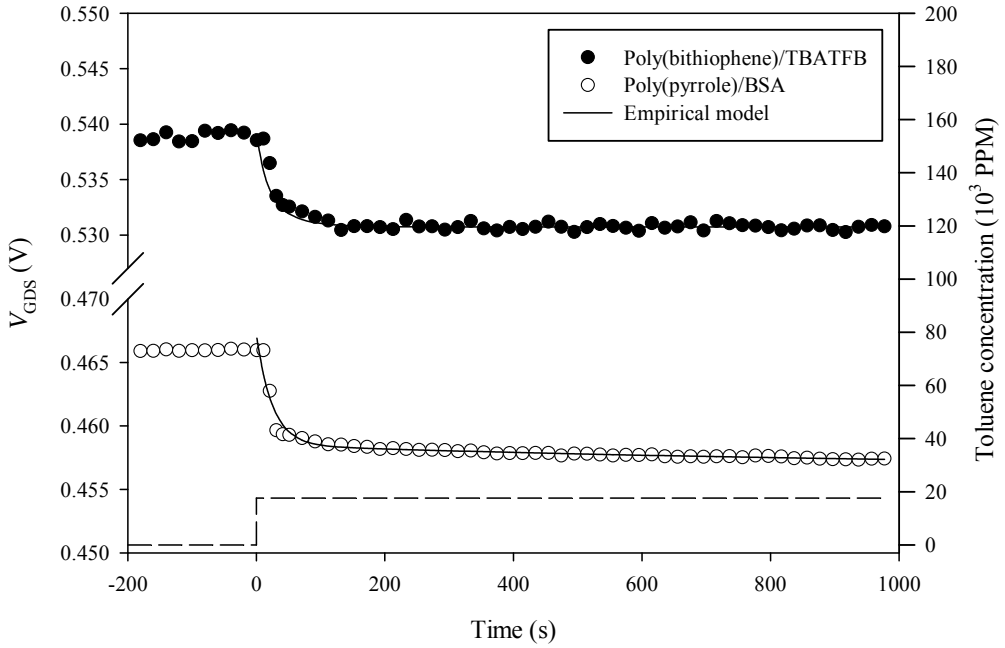

Figure 6.11: Transient recovery of chemFET sensors employing composite polymer films to ethanol vapour in air, modelled by a double exponential expression.

This double exponential expression is consistent with a dual reaction, where the first component is an initial response of the analyte and the second component is a long-term response by either the analyte or drift within the polymer. For the chemFET sensors with composite polymers it was found that the values of the second time constants (τ_{ON2} and τ_{OFF2}) were generally large, typically above 1000 seconds, and independent of analyte concentration. For the electrochemically deposited polymers the second component was also found to be concentration dependent.

If we consider expression (6.1) further, for a purely reaction rate limited response where the Langmuir isotherm dominates, the response time is defined by:

$$\theta_t = \frac{[1 - \exp(-kt)]}{(1 + K)} \tag{6.10}$$

where θ_t is the fraction of occupied sites after time t, K is the ratio of the forward and backward reaction rate constants and k is given by:

$$k = k_f C + k_b \tag{6.11}$$

The effect of the time constant predicted by expressions (6.4) and (6.6) can therefore be modelled by:

$$\tau = \frac{1}{k_f C + k_b} \tag{6.12}$$

This expression is valid for a purely reaction-rate limited response and is consistent with a non-competitive binding model where the target vapour simply fills the available sites. For a competitive reaction the analyte would not only bind to the available sites, but would compete with, for example, water vapour and this could be more consistent with the double exponential model. In these models we have assumed that this dynamic response is simply the absorption of analyte and is not significantly effected by water vapour. By observation it was found that expression (6.12) did not fit the available data, where the time value did not tend to zero as the concentration reached infinity. Hence, though the general trend is reaction-rate limited, this basic model has to be modified to:

$$\tau = \tau_{\mathrm{OFFSET}} + \frac{1}{k_{\mathrm{f}} C + k_{\mathrm{b}}} \tag{6.13}$$

where τ_{OFFSET} is the value of the time constant as the concentration tends to infinity. This τ_{OFFSET} is possible due to the test station caused by some physical component within it (e.g. the MFCs) or a chemical interaction between the polymer and the water vapour. This model is shown in figure 6.12 and figure 6.13 for the on and off transients for the chemFET sensors with composite polymer films (first component) and figure 6.14 and figure 6.15 for the on transients and figure 6.16 and figure 6.17 for the off transients for chemFET sensors with electrochemically deposited polymer films (first and second components) to toluene and ethanol vapour in air at constant water concentration and temperature (4500 PPM water and 30 ^{o}C).

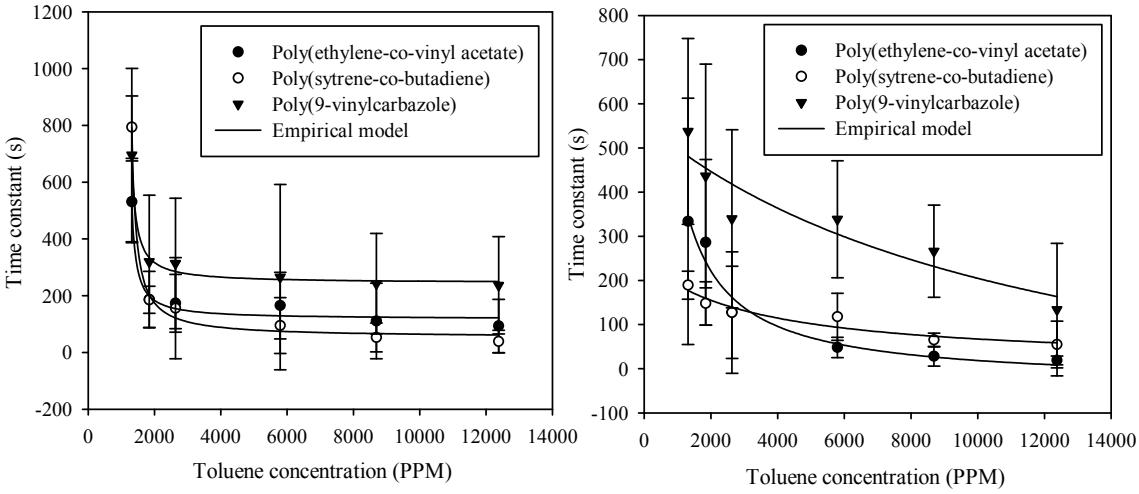

Figure 6.12: τ_{on} (left) and τ_{off} (right) transients for chemFET sensors employing composite polymer films to toluene vapour in air at 30 ^{o}C.

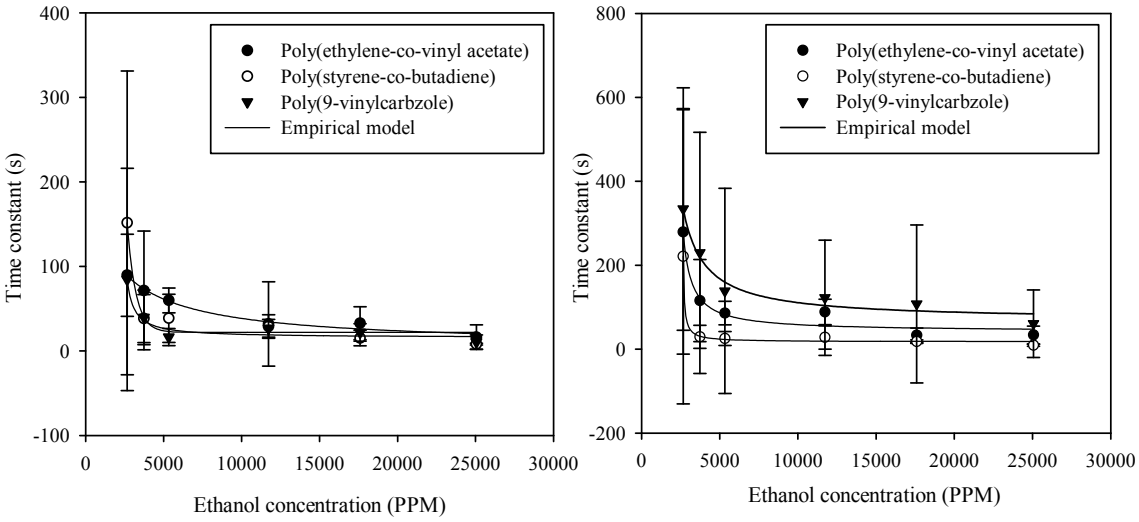

Figure 6.13: τ_{on} (left) and τ_{off} (right) transients for chemFET sensors employing composite polymer films to ethanol vapour in air at 30 ^{o}C.

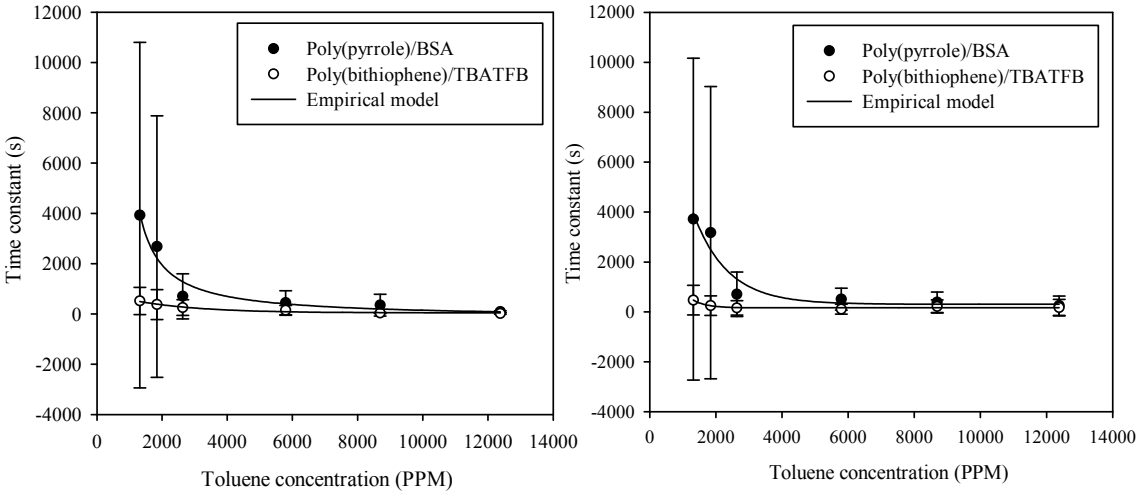

Figure 6.14: τ_{on1} (left) and τ_{on2} (right) transients for chemFET sensors employing electrochemically deposited polymer films to toluene vapour in air at 30 ^{o}C.

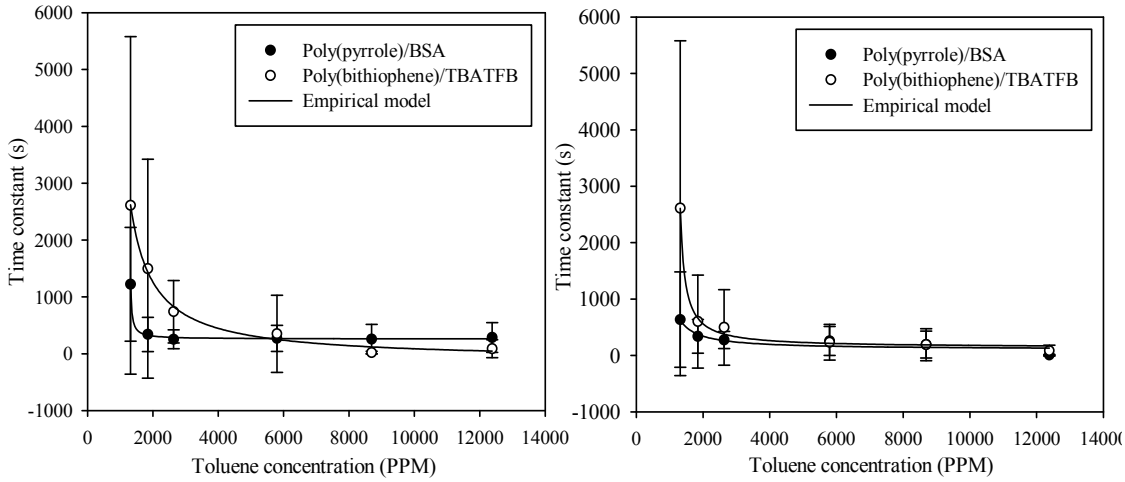

Figure 6.15: τ_{off1} (left) and τ_{off} (right) transients for chemFET sensors employing electrochemically deposited polymer films to toluene vapour in air at 30 ^{o}C.

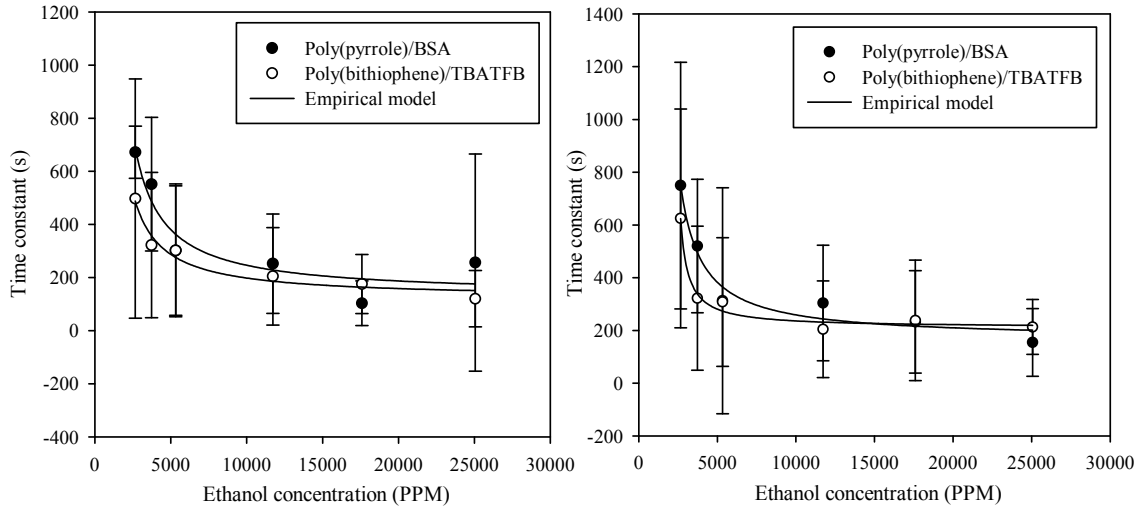

Figure 6.16: τ_{on1} (left) and τ_{on2} (right) transients for chemFET sensors employing electrochemically deposited polymer films to ethanol vapour in air at 30 ^{o}C.

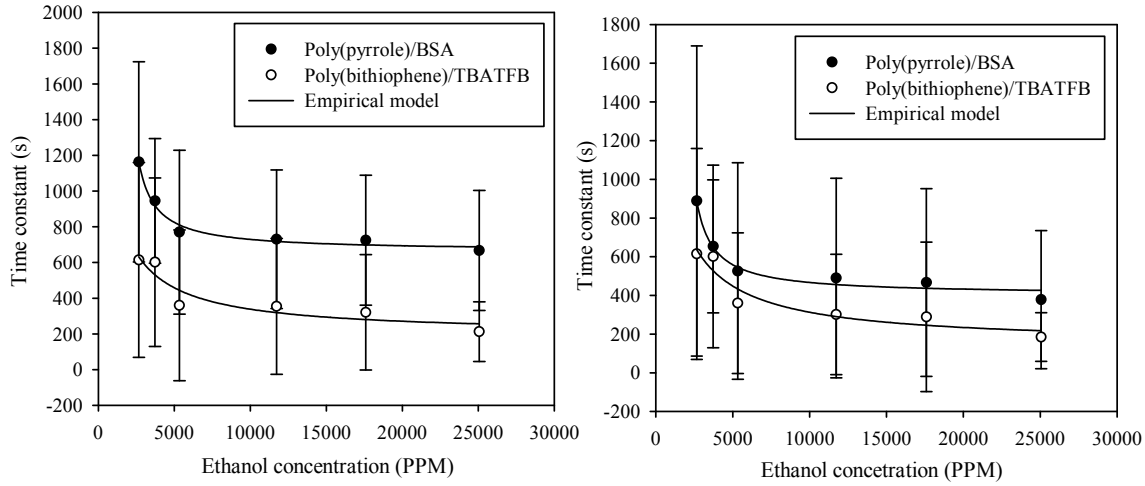

Figure 6.17: τ_{off1} (left) and τ_{off2} (right) transients for chemFET sensors employing electrochemically deposited polymer films to ethanol vapour in air at 30 ^{o}C.

Table 6.1 gives the coefficients for expression (6.13) for chemFET sensors employing both composite and electrochemically deposited polymer films to both toluene and ethanol vapour in air.

Toluene-ON	τ_{OFFSET}	$\pm\sigma\tau_{OFFSET}$	k_b	$\pm\sigma_{kb}$	k_f	$\pm\sigma_{kf}$	r^2
CP1	117.40	19.92	-2.21E-02	1.40E-02	1.86E-05	1.08E-05	0.978
CP2	53.22	19.25	-1.19E-02	4.00E-03	1.01E-05	3.08E-06	0.994
CP3	244.50	13.76	-2.01E-02	8.09E-03	1.69E-05	6.21E-06	0.991
PPY	3.27E-05	2.41E-05	-2.13E-04	2.18E-04	3.44E-07	1.82E-07	0.952
PBT	21.33	22.00	-1.31E-04	3.70E-04	1.63E-06	3.22E-07	0.992
Toluene-OFF	τ_{OFFSET}	$\pm\sigma\tau_{OFFSET}$	k_b	$\pm\sigma_{kb}$	k_f	$\pm\sigma_{kf}$	r^2
CP1	-33.91	40.40	1.32E-04	1.17E-03	1.89E-06	9.86E-07	0.964
CP2	10.91	63.57	4.24E-03	9.36E-04	1.35E-06	1.82E-06	0.916
CP3	-219.70	764.10	1.29E-03	1.10E-03	1.07E-07	3.37E-07	0.866
PPY	258.70	15.39	-3.34E-02	1.65E-02	2.62E-05	1.27E-05	0.997
PBT	-114.70	89.49	-3.29E-04	1.23E-04	5.28E-07	1.01E-07	0.993
Ethanol-ON	τ_{OFFSET}	$\pm\sigma\tau_{OFFSET}$	k_b	$\pm\sigma_{kb}$	k_f	$\pm\sigma_{kf}$	r^2
CP1	42.07	16.34	-1.65E-02	1.10E-02	7.78E-06	4.22E-06	0.96
CP2	17.40	4.55	-1.69E-01	1.26E-01	6.53E-05	4.75E-05	0.995
CP3	68.46	20.39	-3.48E-03	3.04E-03	2.71E-06	1.20E-06	0.965
PPY	132.80	85.22	-7.43E-04	1.97E-03	9.55E-07	7.94E-07	0.896
PBT	121.90	33.17	-1.03E-03	1.71E-03	1.41E-06	6.85E-07	0.961
Ethanol-OFF	τ_{OFFSET}	$\pm\sigma\tau_{OFFSET}$	k_b	$\pm\sigma_{kb}$	k_f	$\pm\sigma_{kf}$	r^2
CP1	6.16	8.82	5.30E-03	2.45E-03	2.56E-06	1.20E-06	0.98
CP2	16.47	4.28	-5.58E-02	3.44E-02	2.65E-05	1.31E-05	0.967
CP3	15.71	5.84	-7.26E-02	6.32E-02	3.27E-05	2.41E-05	0.939
PPY	663.50	27.56	-2.83E-03	1.55E-03	1.81E-06	6.07E-07	0.98
PBT	197.40	104.50	5.59E-04	1.72E-03	6.55E-07	7.55E-07	0.868

Table 6.1: Modelling coefficients for expression (6.11).

6.3.1 Response time

An important dynamic property of any sensor is its response time. This value is defined as the period from the beginning of the response to 90% of its final value and sets the sampling rate of any system containing these sensors. Table 6.2 gives the response times of the chemFET sensors employing composite and electrochemically deposited polymer films at constant water concentration and temperature (4500 PPM water, 30 ^{o}C) at fixed toluene and ethanol vapour concentration in air of 5793 PPMs and 11729 PPMs, respectively. These values have been calculated from the coefficients determined earlier and are the average values from five samples for each type of sensor.

Toluene – ON	Av. (s)	± σ (s)	**Toluene - OFF**	Av. (s)	± σ (s)
CP1	304	175	CP1	299	298
CP2	472	300	CP2	412	352
CP3	1397	993	CP3	698	383
PPY/BSA	330	257	PPY/BSA	649	403
PBT/TBATFB	251	78	PBT/TBATFB	1020	852
Ethanol - ON	Av. (s)	± σ (s)	**Ethanol - OFF**	Av. (s)	± σ (s)
CP1	237	250	CP1	360	558
CP2	212	87	CP2	145	60
CP3	136	150	CP3	2174	3393
PPY/BSA	772	845	PPY/BSA	1263	7345
PBT/TBATFB	572	366	PBT/TBATFB	1251	881

Table 6.2: Typical time responses of chemFET sensors employing composite and electrochemically deposited polymer films to toluene and ethanol vapour in air at fixed concentrations of 5793 PPMs and 11729 PPMs respectively at constant water concentration and temperature (4500 PPM, 30 ^{o}C). (CP1 – Poly(ethylene-co-vinyl acetate), CP2 – Poly(styrene-co-butadiene), CP3 – Poly(9-vinylcarbzole), PPY – Poly(pyrrole)/BSA, PBT – Poly(bithiophene)/TBATFB).

If these sensors were used in an electronic nose instrument the sample period would have to be in minutes. Though this value is high it is not completely unacceptable for certain applications. Work by other researchers [6.8] has shown that resistive devices employing composite polymer and electrochemically deposited polymer films generally show this double exponential response. The response times, for resistive sensors, to 6900 PPMs of ethanol vapour, was reported at between 100 – 200 seconds for composite polymers (e.g. poly(N-vinylpyrrolidiene) and 200 – 300 seconds for the electrochemically deposited polymers. These values are not inconsistent with previous chemosensor results. The Cyrano Sciences electronic nose instrument (A320) using resistive composite polymer sensors has reported a response and recovery time to toluene vapour at < 60 seconds and < 125 seconds [6.9] and for methanol vapour at < 50 seconds and < 80 seconds respectively, though the concentration range was not defined. These values are considerable quicker than those measured here for chemFET sensors. This may be due to a number of reasons, firstly, as a result of different polymers being tested. Secondly, the chemFET sensors may have thicker polymer films than those used for the Cyrano electronic nose, so we would expect the chemFET sensor to give slower responses. Lastly, if the response of chemFET sensors to an analyte is an interface effect, then the response only occurs once the analyte has diffused from the surface. For a resistive sensor, as soon as the analyte diffuses into the polymer a response would be measurable.

It is interesting to note that, for the chemFET sensors with electrochemically deposited films, the response times to toluene vapour are significantly faster than those for ethanol vapour. It is proposed that this could be due to the ethanol vapour being in competition with water vapour for the same sites within the polymer. Hence, the speed of the reaction is limited by the time taken for the water to de-absorb. Furthermore, the response to toluene vapour has a similar response time to the composite polymers (if not faster) possible suggesting a similar reaction mechanism. In addition, the recovery times for the composite polymers are very similar, whilst the electrochemically deposited polymers have significantly longer recovery periods.

6.4 Static modelling of chemFET sensors

Previously, we have considered the dynamic response of chemFET sensors, here the static response is investigated. This static response can be considered as the differential result of V_{GDS} from a baseline value $V_{GDS(0)}$ to a final value $V_{GDS(f)}$. As before all measurements (unless stated) were taken at a constant water concentration of 4500 PPM and constant temperature of 30 ^{o}C.

6.4.1 Static response of the UMIST sensor

The static response of the UMIST chemFET sensors to ethanol vapour is shown in figure 6.18. Here the drain current as a function of ethanol concentration, at water concentrations of 4500 and 6583 PPMs is shown. These *p*-channel (MISFET) chemFET sensors were operated at a constant gate voltage of –0.6 volts and constant drain voltage of –0.5 volts and so in the linear region, with drain current monitored.

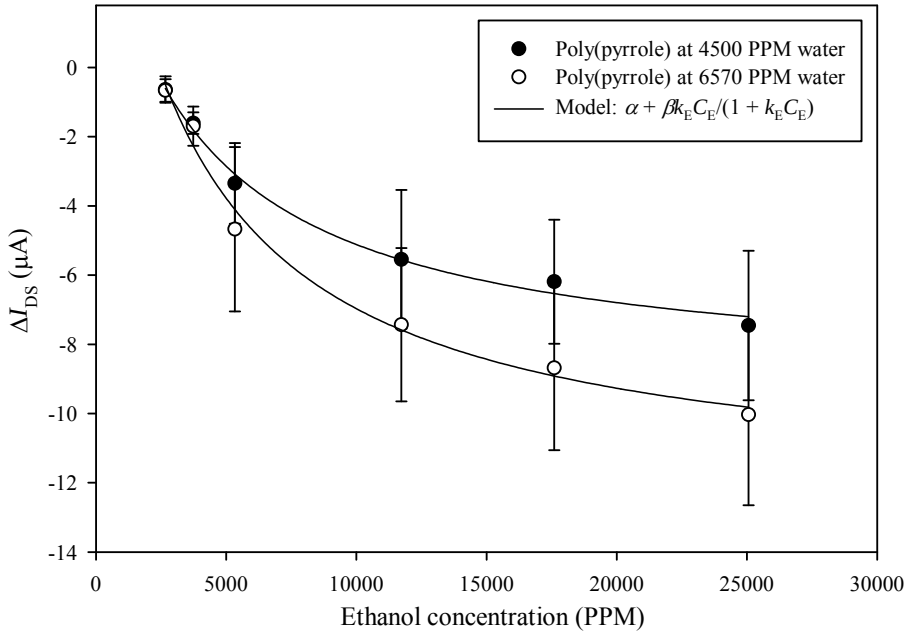

Figure 6.18: The effect of ethanol vapour in air on drain source current of UMIST chemFET sensors employing a chemically prepared polymer films.

These responses have been fitted to a Langmuir isotherm. Such a model has been applied here as resistive devices employing these conducting polymers follow this model, though this is the first time the Langmuir isotherm has been applied to conducting polymer chemFET sensors [6.10]. Hence, we can state that:

$$\Delta I_{DS} \approx \alpha + \frac{\beta k_E C_E}{(1 + k_E C_E)} \tag{6.14}$$

where C_E is the ethanol concentration, k_E is the binding coefficient and α is a device constant. Five sensors were used in these measurement and Langmuir isotherm coefficients are given in table 6.3, also included is the mean and maximum sensitivities.

4500 PPM	α (μA/PPM)	$\pm \sigma_\alpha$ (μA/PPM)	βk_E (μA/PPM)	$\pm \sigma_{\beta k E}$ (μA/PPM)	k_E (PPM^{-1})	$\pm \sigma_{kE}$ (PPM^{-1})	r^2
Sample 1	17.10	57.30	-2.93E-02	1.77E-01	1.29E-03	4.25E-03	0.943
Sample 2	69.60	287.00	-1.52E-01	1.15E+00	1.82E-03	7.60E-03	0.934
Sample 3	6.58	2.24	-3.47E-03	1.52E-03	1.79E-04	6.78E-05	0.994
Sample 4	42.30	65.10	-6.42E-02	1.75E-01	1.14E-03	1.76E-03	0.982
Sample 5	3.48	1.07	-2.02E-03	5.48E-04	1.07E-04	3.04E-05	0.99
Av.	27.80	82.60	-5.02E-02	3.01E-01	9.08E-04	2.74E-03	0.96
6750 PPM	α (μA/PPM)	$\pm \sigma_\alpha$ (μA/PPM)	βk_E (μA/PPM)	$\pm \sigma_{\beta k E}$ (μA/PPM)	k_E (PPM^{-1})	$\pm \sigma_{kE}$ (PPM^{-1})	r^2
Sample 1	15.50	91.40	-3.10E-02	3.27E-01	1.59E-03	9.32E-03	0.857
Sample 2	13.50	4.15	-1.24E-02	6.04E-03	5.51E-04	1.74E-04	0.998
Sample 3	13.80	7.82	-1.38E-02	1.30E-02	6.27E-04	3.61E-04	0.995
Sample 4	9.50	8.10	-7.16E-03	7.90E-03	3.18E-04	2.56E-04	0.981
Sample 5	33.00	107.00	-6.57E-02	3.98E-01	1.61E-03	5.25E-03	0.957

Av.	17.10	43.70	-2.60E-02	1.50E-01	9.40E-04	3.07E-03	0.958
Sensitivity	4500 PPM (nA/PPM)	± σ (nA/PPM)	6750 PPM (nA/PPM)	± σ (nA/PPM)			
Typical	-0.52	0.20	-0.40	0.12			
Max	-0.88		-0.63				

Table 6.3: Values of Langmuir isotherm coefficients for chemFET sensors with chemically prepared electrochemically doped film to ethanol vapour in air.

Also shown in figure 6.18 is the effect of water concentration on these chemFET sensors, here a reduction in the magnitude of the response to ethanol vapour was observed with increasing water concentration. It is proposed that this is due to competition between the water vapour and the ethanol vapour for the same site [6.10].

6.4.2 ChemFET sensor employing composite polymers

To further investigate the effect of analyte concentration, subsequent experiments were carried out with a wide range of ethanol and toluene concentrations for the *n*-channel (MOSFET) chemFET sensors. Specifically 470 – 19150 PPMs of toluene vapour in 957 PPM steps and 978 – 39122 PPMs of ethanol vapour in 1956 PPM steps. As before the sensors were given 24 hours to equilibrate at a temperature of 30^{o}C and 60 minutes at a fixed water concentration of 4500 PPM. The sensors were exposed to pulses of analyte for 25 minutes duration with 25 minutes recovery period. Five sensors of each type were used with the results averaged, as shown in figure 6.19 and 6.20 for toluene and ethanol vapour in air, respectively.

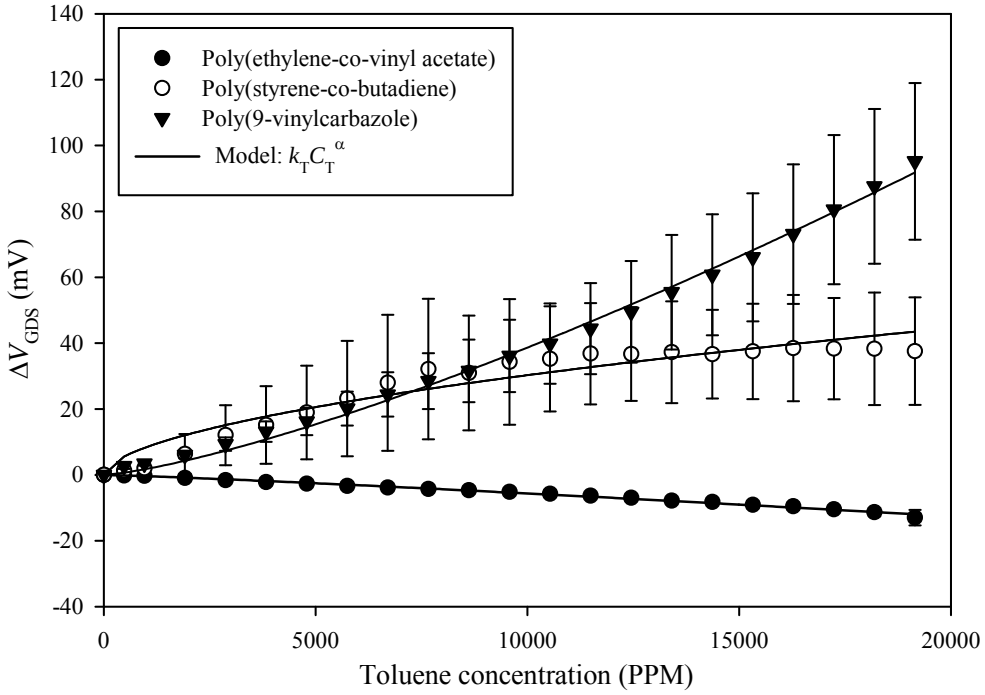

Figure 6.19: Broad range static response of chemFET sensors employing composite polymer films to toluene vapour in air.

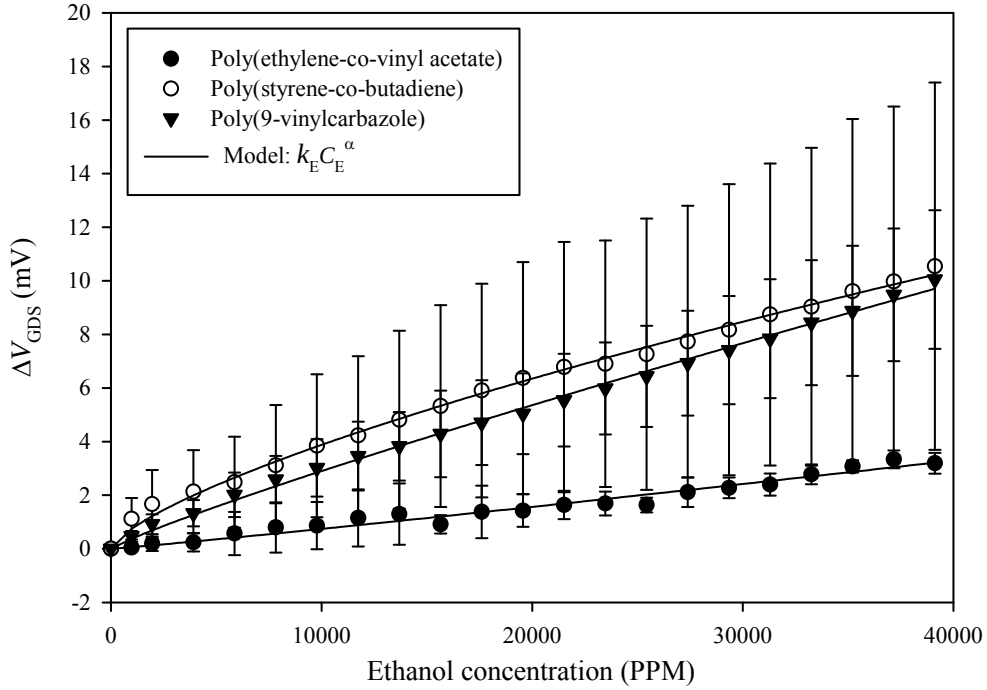

Figure 6.20: Broad range static response of chemFET sensors employing composite polymer films to ethanol vapour in air.

For display purposes, the sensors have been modelled to a power law, though for completeness we can fit these responses to a number of different models and investigate which gives the best result. Clearly, the power law is empirical and does not

account for the chemistry occurring within the polymer itself. Four different empirical models were fitted to the data, these were power law, linear with offset, linear without offset (this is a power model with $\alpha = 1$) and the Langmuir isotherm, using the following equations:

$$\Delta V_{GDS} = k_T C^{\alpha} \quad \text{(Power law)} \tag{6.15}$$

where k_T is a binding coefficient for toluene.

$$\Delta V_{GDS} = V_{GDS(0)} + k_T C_T \quad \text{(Linear with offset)} \tag{6.16}$$

$$\Delta V_{GDS} = k_T C_T \quad \text{(Linear without offset)} \tag{6.17}$$

$$\Delta V_{GDS} = \frac{\alpha k_T C_T}{1 + k_T C_T} \quad \text{(Langmuir)} \tag{6.18}$$

where α is a sensor constant. Here, k_T and C_T can be replaced with k_E and C_E for ethanol vapour. Table 6.4 and table 6.5 show the coefficients of these models for toluene and ethanol vapour. In addition, the correlation coefficients are included to show the quality of the fit.

Power	k_T (mV/PPM)	$\pm \sigma_{kT}$ (mV/PPM)	α (mV/PPM)	$\pm \sigma_{\alpha}$ (mV/PPM)	r^2
CP1-Sample 1	-1.41E-05	2.10E-05	1.39	1.51E-01	0.981
CP1-Sample 2	-2.54E-03	6.21E-04	0.85	2.57E-02	0.993
CP1-Sample 3	-2.47E-05	1.15E-05	1.34	4.82E-02	0.99
CP1-Sample 4	-9.93E-05	3.07E-05	1.18	2.74E-02	0.996
CP1-Sample 5	-2.90E-06	1.99E-06	1.56	7.09E-02	0.985
CP1-Av.	-5.35E-04	1.37E-04	1.26	6.46E-02	0.989
CP2-Sample 1	1.93E-02	1.44E-02	0.75	7.75E-02	0.922
CP2-Sample 2	5.02E-01	2.89E-01	0.48	6.14E-02	0.987
CP2-Sample 3	1.94E-04	8.59E-05	1.22	4.58E-02	0.988
CP2-Sample 4	3.05E-08	5.02E-08	2.13	1.47E-01	0.967
CP2-Sample 5	1.56E-02	4.28E-03	0.79	2.89E-02	0.989
CP2-Av.	1.30E-01	7.58E-02	1.14	8.30E-02	0.971
CP3-Sample 1	2.12E-05	1.33E-05	1.52	6.48E-02	0.986
CP3-Sample 2	5.77E-05	3.96E-05	1.44	7.03E-02	0.982
CP3-Sample 3	1.68E-04	4.09E-05	1.37	2.53E-02	0.997
CP3-Sample 4	1.55E-03	1.83E-04	1.11	1.23E-02	0.999
CP3-Sample 5	5.80E-06	5.83E-06	1.70	9.35E-02	0.977
CP3-Av.	3.60E-04	5.65E-05	1.43	5.32E-02	0.988
Linear	$V_{GDS(0)}$ (mV)	$\pm \sigma_{VGDS(0)}$ (mV/PPM)	k_T (mV/PPM)	$\pm \sigma_{kT}$ (mV/PPM)	r^2
CP1-Sample 1	0.55	0.58	-6.35E-04	5.20E-05	0.887
CP1-Sample 2	-0.44	0.18	-5.73E-04	1.64E-05	0.985
CP1-Sample 3	0.95	0.29	-7.04E-04	2.58E-05	0.975
CP1-Sample 4	0.60	0.13	-6.00E-04	1.18E-05	0.993
CP1-Sample 5	1.73	0.41	-7.63E-04	3.62E-05	0.959

CP1-Av.	0.68	0.32	-6.55E-04	2.84E-05	0.960
CP2-Sample 1	2.14	1.44	1.61E-03	1.28E-04	0.892
CP2-Sample 2	15.00	3.61	2.34E-03	3.22E-04	0.735
CP2-Sample 3	-1.20	0.61	1.63E-03	5.44E-05	0.979
CP2-Sample 4	-5.36	2.09	2.04E-03	1.86E-04	0.837
CP2-Sample 5	2.60	0.76	1.81E-03	6.78E-05	0.977
CP2-Av.	2.63	1.93	1.91E-03	1.73E-04	0.8611
CP3-Sample 1	-5.40	2.03	3.47E-03	1.81E-04	0.951
CP3-Sample 2	-5.67	2.51	4.38E-03	2.24E-04	0.952
CP3-Sample 3	-9.65	2.50	6.69E-03	2.23E-04	0.979
CP3-Sample 4	-3.28	0.47	4.72E-03	4.22E-05	0.998
CP3-Sample 5	-10.60	4.39	5.78E-03	3.92E-04	0.919
CP3-Av.	-6.92	2.38	5.01E-03	2.12E-04	0.960
Linear (no offset)	k_T (mV/PPM)	$\pm \sigma_{kT}$ (mV/PPM)	r^2		
CP1-Sample 1	-5.92E-04	2.67E-05	0.882		
CP1-Sample 2	-6.06E-04	9.37E-06	0.98		
CP1-Sample 3	-6.31E-04	1.62E-05	0.961		
CP1-Sample 4	-5.54E-04	8.57E-06	0.985		
CP1-Sample 5	-6.31E-04	2.54E-05	0.92		
CP1-Av.	-6.03E-04	1.72E-05	0.9461		
CP2-Sample 1	7.72E-04	6.80E-05	0.88		
CP2-Sample 2	3.48E-03	2.23E-04	0.495		
CP2-Sample 3	1.54E-03	3.00E-05	0.975		
CP2-Sample 4	1.63E-03	1.08E-04	0.816		
CP2-Sample 5	2.11E-03	4.35E-05	0.962		
CP2-Av.	1.86E-03	1.07E-04	0.792		
CP3-Sample 1	3.05E-03	1.06E-04	0.932		
CP3-Sample 2	3.94E-03	1.27E-04	0.94		
CP3-Sample 3	5.95E-03	1.50E-04	0.96		
CP3-Sample 4	4.47E-03	3.98E-05	0.995		
CP3-Sample 5	4.97E-03	2.25E-04	0.895		
CP3-Av.	4.48E-03	1.29E-04	0.944		
Langmuir	αk_T (mV/PPM)	$\pm \sigma_{\alpha kT}$ (mV/PPM)	k_T (mV/PPM)	$\pm \sigma_{kT}$ (mV/PPM)	r^2
CP1-Sample 1	-3.31E-04	3.51E-05	-2.86E-05	3.29E-06	0.942
CP1-Sample 2	-7.78E-04	2.28E-05	1.96E-05	2.60E-06	0.996
CP1-Sample 3	-4.39E-04	1.88E-05	-2.01E-05	1.78E-06	0.992
CP1-Sample 4	-4.47E-04	1.38E-05	-1.30E-05	1.56E-06	0.996
CP1-Sample 5	-3.82E-04	2.79E-05	-2.59E-05	2.51E-06	0.978
CP1-Av.	-4.75E-04	2.37E-05	-1.36E-05	2.35E-06	0.981
CP2-Sample 1	2.87E-03	3.53E-04	4.30E-05	1.42E-05	0.945
CP2-Sample 2	1.15E-02	1.47E-03	1.64E-04	3.19E-05	0.942
CP2-Sample 3	1.16E-03	4.15E-05	-1.66E-05	1.65E-06	0.994
CP2-Sample 4	6.33E-04	1.81E-05	-3.86E-05	5.15E-07	0.996
CP2-Sample 5	2.96E-03	1.35E-04	2.83E-05	4.51E-06	0.991
CP2-Av.	4.03E-03	4.70E-04	3.79E-05	1.21E-05	0.969
CP3-Sample 1	1.78E-03	4.19E-05	-2.73E-05	7.70E-07	0.997
CP3-Sample 2	2.40E-03	8.27E-05	-2.57E-05	1.20E-06	0.994
CP3-Sample 3	4.02E-03	5.21E-05	-2.15E-05	5.18E-07	0.999
CP3-Sample 4	3.98E-03	8.60E-05	-7.39E-06	1.23E-06	0.998
CP3-Sample 5	2.53E-03	8.81E-05	-3.17E-05	9.43E-07	0.995
CP3-Av.	2.94E-03	7.01E-05	-2.27E-05	9.32E-07	0.997

Table 6.4: Parameter fits to broad range static response of chemFET sensors employing a composite polymer film to toluene vapour in air, including the confidence interval r^2.

Power	k_T (mV/PPM)	$\pm \sigma_{kT}$ (mV/PPM)	α (mV/PPM)	$\pm \sigma_{\alpha}$ (mV/PPM)	r^2
CP1-Sample 1	2.64E-03	2.04E-03	6.74E-01	7.61E-02	0.89
CP1-Sample 2	5.66E-08	7.38E-08	1.69E+00	1.14E-01	0.967
CP1-Sample 3	5.86E-05	4.57E-05	1.03E+00	7.47E-02	0.956
CP1-Sample 4	2.12E-04	6.75E-05	9.04E-01	3.09E-02	0.99
CP1-Sample 5	5.67E-05	2.49E-05	1.05E+00	4.27E-02	0.986
CP1-Av.	7.26E-04	5.38E-04	1.07E+00	7.39E-02	0.951
CP2-Sample 1	2.37E-04	9.83E-05	8.93E-01	4.05E-02	0.982
CP2-Sample 2	1.01E-02	1.98E-03	6.98E-01	1.93E-02	0.993
CP2-Sample 3	7.80E-03	1.56E-03	6.91E-01	1.97E-02	0.992
CP2-Sample 4	4.78E-05	1.13E-05	1.15E+00	2.30E-02	0.997
CP2-Sample 5	3.60E-03	8.03E-04	7.62E-01	2.18E-02	0.992
CP2-Av.	4.53E-03	9.13E-04	8.57E-01	2.56E-02	0.991
CP3-Sample 1	2.44E-03	3.50E-04	7.79E-01	1.41E-02	0.997
CP3-Sample 2	1.63E-03	2.82E-04	8.47E-01	1.70E-02	0.997
CP3-Sample 3	7.33E-04	1.97E-04	9.04E-01	2.62E-02	0.993
CP3-Sample 4	4.05E-05	1.07E-05	1.14E+00	2.56E-02	0.996
CP3-Sample 5	1.01E-02	2.78E-03	6.22E-01	2.71E-02	0.981
CP3-Av.	2.99E-03	7.24E-04	8.57E-01	2.20E-02	0.993
Linear	$V_{GDS(0)}$ (mV)	$\pm \sigma_{VGDS(0)}$ (mV/PPM)	k_T (mV/PPM)	$\pm \sigma_{kT}$ (mV/PPM)	r^2
CP1-Sample 1	4.68E-01	1.43E-01	7.58E-05	6.25E-06	0.886
CP1-Sample 2	-3.35E-01	1.28E-01	8.03E-05	5.59E-06	0.916
CP1-Sample 3	6.03E-02	8.69E-02	7.83E-05	3.80E-06	0.957
CP1-Sample 4	1.60E-01	2.92E-02	7.33E-05	1.28E-06	0.994
CP1-Sample 5	2.22E-02	5.65E-02	8.89E-05	2.47E-06	0.985
CP1-Av.	8.82E-02	9.67E-02	7.69E-05	4.23E-06	0.938
CP2-Sample 1	1.65E-01	4.53E-02	7.30E-05	1.98E-06	0.986
CP2-Sample 2	2.22	1.85E-01	3.72E-04	8.08E-06	0.991
CP2-Sample 3	1.62	1.58E-01	2.67E-04	6.91E-06	0.987
CP2-Sample 4	-2.72E-01	1.04E-01	2.27E-04	4.57E-06	0.992
CP2-Sample 5	1.21	1.09E-01	2.69E-04	4.75E-06	0.994
CP2-Av.	9.34E-01	1.23E-01	2.35E-04	5.38E-06	0.989
CP3-Sample 1	8.39E-01	9.37E-02	2.22E-04	4.10E-06	0.994
CP3-Sample 2	8.03E-01	9.34E-02	3.09E-04	4.09E-06	0.997
CP3-Sample 3	4.85E-01	9.33E-02	2.56E-04	4.08E-06	0.995
CP3-Sample 4	-1.65E-01	8.16E-02	1.69E-04	3.57E-06	0.992
CP3-Sample 5	1.31	1.25E-01	1.60E-04	5.48E-06	0.978
CP3-Av.	6.55E-01	9.75E-02	2.23E-04	4.26E-06	0.991
Linear (no offset)	k_T (mV/PPM)	$\pm \sigma_{kT}$ (mV/PPM)	r^2		
CP1-Sample 1	9.33E-05	3.92E-06	0.821		
CP1-Sample 2	6.77E-05	3.27E-06	0.885		
CP1-Sample 3	8.06E-05	1.93E-06	0.956		
CP1-Sample 4	7.93E-05	1.03E-06	0.985		
CP1-Sample 5	8.97E-05	1.24E-06	0.985		
CP1-Av.	8.02E-05	2.54E-06	0.912		
CP2-Sample 1	7.92E-05	1.30E-06	0.966		
CP2-Sample 2	4.55E-04	1.19E-05	0.925		
CP2-Sample 3	3.28E-04	8.86E-06	0.918		
CP2-Sample 4	2.17E-04	2.67E-06	0.99		

CP2-Sample 5	3.14E-04	6.52E-06	0.956		
CP2-Av.	2.70E-04	6.18E-06	0.950		
CP3-Sample 1	2.54E-04	4.69E-06	0.966		
CP3-Sample 2	3.39E-04	4.53E-06	0.984		
CP3-Sample 3	2.74E-04	3.18E-06	0.988		
CP3-Sample 4	1.63E-04	1.97E-06	0.99		
CP3-Sample 5	2.09E-04	7.16E-06	0.853		
CP3-Av.	2.48E-04	4.31E-06	0.956		
Langmuir	αk_T (mV/PPM)	$\pm \sigma_{\alpha kT}$ (mV/PPM)	k_T (mV/PPM)	$\pm \sigma_{kT}$ (mV/PPM)	r^2
CP1-Sample 1	1.57E-04	2.65E-05	2.34E-05	1.00E-05	0.876
CP1-Sample 2	3.80E-05	3.30E-06	-1.40E-05	1.31E-06	0.967
CP1-Sample 3	7.12E-05	6.44E-06	-3.84E-06	2.50E-06	0.96
CP1-Sample 4	8.67E-05	4.41E-06	3.13E-06	1.83E-06	0.987
CP1-Sample 5	8.06E-05	3.99E-06	-3.38E-06	1.40E-06	0.988
CP1-Av.	8.81E-05	1.02E-05	2.15E-06	3.91E-06	0.948
CP2-Sample 1	8.82E-05	5.76E-06	3.80E-06	2.40E-06	0.979
CP2-Sample 2	7.20E-04	4.28E-05	1.99E-05	3.29E-06	0.983
CP2-Sample 3	5.30E-04	3.04E-05	2.12E-05	3.25E-06	0.984
CP2-Sample 4	1.79E-04	2.93E-06	-5.82E-06	4.15E-07	0.999
CP2-Sample 5	4.35E-04	2.47E-05	1.31E-05	2.69E-06	0.984
CP2-Av.	3.79E-04	2.05E-05	9.76E-06	2.34E-06	0.986
CP3-Sample 1	3.47E-04	1.39E-05	1.25E-05	1.88E-06	0.992
CP3-Sample 2	4.10E-04	1.56E-05	7.09E-06	1.54E-06	0.993
CP3-Sample 3	3.00E-04	1.34E-05	3.18E-06	1.61E-06	0.99
CP3-Sample 4	1.36E-04	3.05E-06	-5.41E-06	5.78E-07	0.998
CP3-Sample 5	3.91E-04	3.53E-05	3.00E-05	6.02E-06	0.959
CP3-Av.	3.17E-04	1.62E-05	9.48E-06	2.32E-06	0.986

Table 6.5: Parameter fits to broad range static response of chemFET sensors employing a composite polymer film to ethanol vapour in air, including the confidence interval r^2.

In both cases the power law and Langmuir isotherm models give a good fit to the available data, with the power model giving the best fit. From these results, we can calculate the sensitivity of these sensors, as given in table 6.6, including the maximum and average sensitivities.

Polymer	Tol. Max. (μV/PPM)	Tol. Typ. (μV/PPM)	Eth. Max. (μV/PPM)	Eth. Typ. (μV/PPM)
Poly(ethylene-co-vinyl acetate)	-0.68	$-0.55 \pm 6.9 \times 10^{-2}$	$+9.7 \times 10^{-2}$	$8.0 \times 10^{-2} \pm 1.4 \times 10^{-2}$
Poly(styrene-co-butadiene)	+4.2	$+3.1 \pm 0.75$	+0.55	$+0.39 \pm 0.21$
Poly(9-vinylcarbazole)	+5.0	$+4.0 \pm 0.61$	+0.47	$+0.29 \pm 6.5 \times 10^{-2}$

Table 6.6: Typical sensitivity values for chemFET sensors employing composite polymer films to toluene and ethanol vapour in air over a broad concentration range.

6.4.3 ChemFET sensors employing electrochemically deposited polymers

Further experiments were performed for chemFET sensors employing electrochemically deposited polymer films over a broad range of ethanol and toluene vapour concentrations. Here identical test conditions to the chemFET sensors with composite polymers were used, with equal response and recovery periods. Five sensors of each type were tested to ethanol and toluene vapour, with the responses averaged. Figure 6.21 and 6.22 show the static response of these sensors.

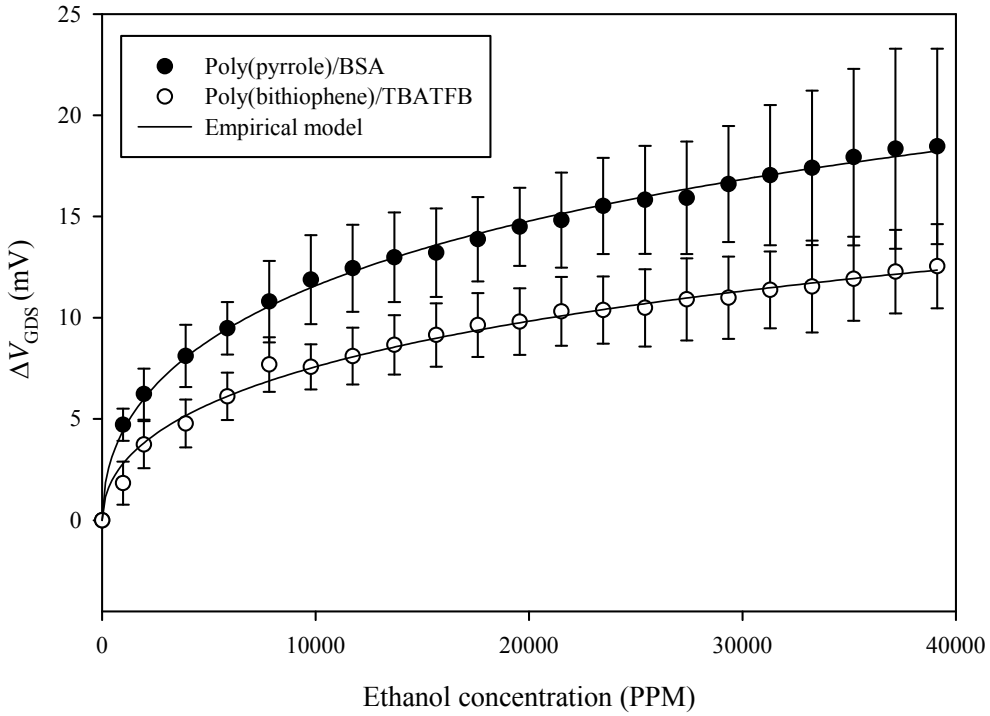

Figure 6.21: Broad range static response of chemFET sensors employing electrochemically deposited polymer films to ethanol vapour in air.

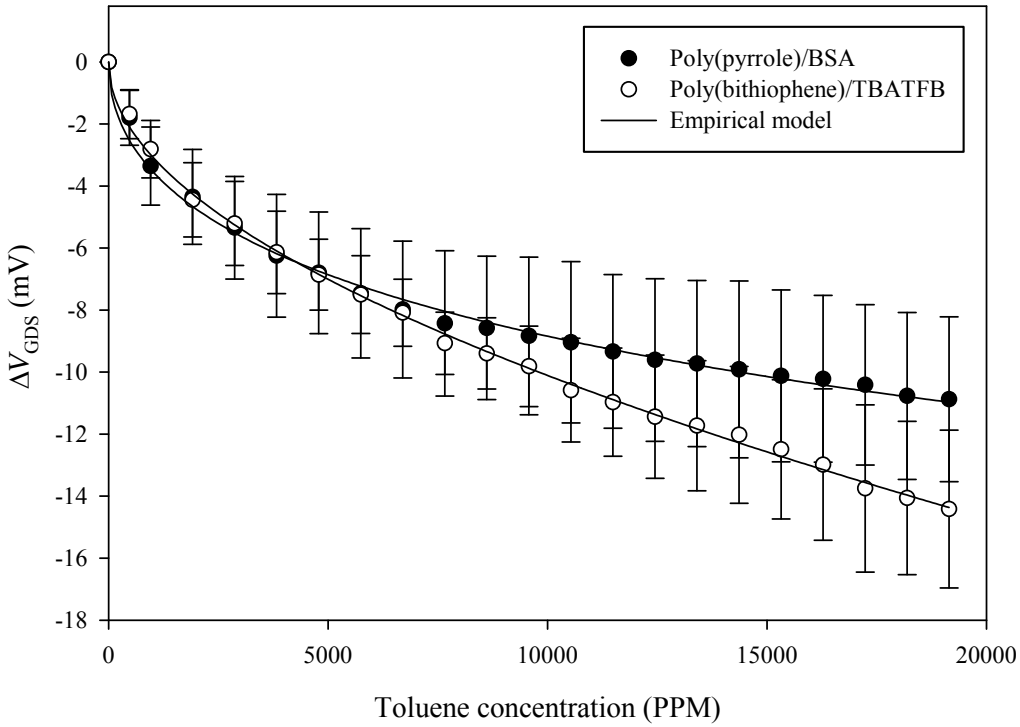

Figure 6.22: Broad range Static response of electrochemically deposited conducting polymers to toluene vapour in air, fitted to a modified Langmuir.

As before, to examine which model gives the best fit the observed data was fitted to a number of empirical models, including power law, linear, linear without offset, Langmuir isotherm and modified Langmuir isotherm. This modified Langmuir isotherm is given by:

$$\Delta V_{GDS} = \frac{\alpha k_T \sqrt{C_T}}{1 + k_T \sqrt{C_T}} \qquad (6.18)$$

This model was used in figure 6.21 and figure 6.22 (where C_T is replaced with C_E for ethanol). The coefficients for these models with standard errors and the confidence interval, r^2, is given in table 6.7 and 6.8 for ethanol and toluene vapour, respectively.

Power	k_E (mV/PPM)	$\pm \sigma_{kE}$ (mV/PPM)	α (mV/PPM)	$\pm \sigma_\alpha$ (mV/PPM)	r^2
PBT-Sample 1	0.21	4.02E-02	3.62E-01	1.91E-02	0.969
PBT-Sample 2	0.33	2.41E-02	3.59E-01	7.34E-03	0.995
PBT-Sample 3	0.28	8.07E-02	3.56E-01	2.89E-02	0.952
PBT-Sample 4	0.11	3.51E-02	4.56E-01	3.10E-02	0.964
PBT-Sample 5	0.22	3.56E-02	3.84E-01	1.63E-02	0.987
Av.	0.23	4.32E-02	3.83E-01	2.05E-02	0.973
PPY-Sample 1	1.09	1.72E-01	2.33E-01	1.58E-02	0.943
PPY-Sample 2	0.05	9.11E-03	5.87E-01	1.91E-02	0.989
PPY-Sample 3	0.48	6.15E-02	3.49E-01	1.27E-02	0.984

PPY-Sample 4	1.09	1.92E-01	2.71E-01	1.76E-02	0.949
PPY-Sample 5	0.44	3.18E-02	3.54E-01	7.25E-03	0.995
Av.	0.63	9.32E-02	3.59E-01	1.45E-02	0.972
Linear	$V_{GDS(0)}$ (mV)	$\pm \sigma_{VGDS(0)}$ (mV/PPM)	k_E (mV/PPM)	$\pm \sigma_{kE}$ (mV/PPM)	r^2
PBT-Sample 1	3.81	0.35	1.67E-04	1.54E-05	0.860
PBT-Sample 2	5.81	0.41	2.51E-04	1.80E-05	0.911
PBT-Sample 3	4.08	0.64	2.32E-04	2.86E-05	0.766
PBT-Sample 4	3.50	0.61	2.96E-04	2.71E-05	0.857
PBT-Sample 5	3.93	0.55	2.50E-04	2.46E-05	0.838
Av.	4.22	0.51	2.39E-04	2.27E-05	0.846
PPY-Sample 1	7.29	0.51	1.60E-04	2.21E-05	0.734
PPY-Sample 2	4.82	0.24	5.04E-04	1.06E-05	0.992
PPY-Sample 3	7.88	0.50	3.29E-04	2.17E-05	0.924
PPY-Sample 4	9.76	0.74	2.69E-04	3.23E-05	0.785
PPY-Sample 5	7.94	0.47	2.65E-04	2.06E-05	0.925
Av.	7.54	0.49	3.05E-04	2.14E-05	0.873
Linear (no offset)	k_E (mV/PPM)	$\pm \sigma_{kE}$ (mV/PPM)	r^2		
PBT-Sample 1	3.10E-04	2.07E-05	5.91E-03		
PBT-Sample 2	4.69E-04	3.06E-05	0		
PBT-Sample 3	3.84E-04	2.66E-05	0.281		
PBT-Sample 4	4.27E-04	2.36E-05	0.61		
PBT-Sample 5	4.08E-04	2.47E-05	0.424		
Av.	3.98E-04	2.53E-05	2.24E-01		
PPY-Sample 1	4.33E-04	3.83E-05	0		
PPY-Sample 2	6.85E-04	2.49E-05	0.812		
PPY-Sample 3	6.24E-04	4.11E-05	0		
PPY-Sample 4	6.34E-04	5.17E-05	0		
PPY-Sample 5	6.49E-04	3.88E-05	0		
Av.	5.94E-04	3.90E-05	2.03E-01		
Langmuir	αk_E (mV/PPM)	$\pm \sigma_{\alpha kE}$ (mV/PPM)	k_E (mV/PPM)	$\pm \sigma_{kE}$ (mV/PPM)	r^2
PBT-Sample 1	1.58E-03	1.34E-04	1.49E-04	1.65E-05	0.965
PBT-Sample 2	2.33E-03	2.03E-04	1.44E-04	1.66E-05	0.96
PBT-Sample 3	2.10E-03	1.82E-04	1.62E-04	1.80E-05	0.977
PBT-Sample 4	1.43E-03	1.21E-04	8.34E-05	1.06E-05	0.975
PBT-Sample 5	1.81E-03	1.10E-04	1.28E-04	1.05E-05	0.987
Av.	1.85E-03	1.50E-04	1.33E-04	1.44E-05	0.973
PPY-Sample 1	4.77E-03	3.08E-04	3.69E-04	2.74E-05	0.975
PPY-Sample 2	1.37E-03	1.21E-04	3.47E-05	6.33E-06	0.959
PPY-Sample 3	3.33E-03	4.01E-04	1.58E-04	2.46E-05	0.923
PPY-Sample 4	5.28E-03	4.66E-04	2.68E-04	2.83E-05	0.957
PPY-Sample 5	3.03E-03	3.10E-04	1.49E-04	2.00E-05	0.945
Av.	3.56E-03	3.21E-04	1.96E-04	2.13E-05	0.952
Modified Langmuir	αk_E (mV/PPM)	$\pm \sigma_{\alpha kE}$ (mV/PPM)	k_E (mV/PPM)	$\pm \sigma_{kE}$ (mV/PPM)	r^2
PBT-Sample 1	8.16E-02	4.84E-03	3.51E-03	5.92E-04	0.977
PBT-Sample 2	1.22E-01	2.74E-03	3.44E-03	2.22E-04	0.996
PBT-Sample 3	1.06E-01	9.80E-03	3.98E-03	9.67E-04	0.964
PBT-Sample 4	8.37E-02	7.09E-03	1.04E-03	6.17E-04	0.967
PBT-Sample 5	9.70E-02	4.30E-03	2.80E-03	4.09E-04	0.991
Av.	9.82E-02	5.75E-03	2.95E-03	5.61E-04	0.979

PPY-Sample 1	2.07E-01	1.09E-02	1.14E-02	9.65E-04	0.978
PPY-Sample 2	9.00E-02	2.82E-03	-1.26E-03	1.47E-04	0.993
PPY-Sample 3	1.67E-01	8.96E-03	3.71E-03	5.46E-04	0.979
PPY-Sample 4	2.47E-01	1.57E-02	8.14E-03	9.52E-04	0.97
PPY-Sample 5	1.57E-01	4.97E-03	3.55E-03	3.18E-04	0.993
Av.	1.74E-01	8.67E-03	5.10E-03	5.86E-04	0.983

Table 6.7: Parameter fits to broad range static response for chemFET sensors employing an electrochemically polymer film to ethanol vapour in air, including the confidence interval r^2.

Power	k_T (mV/PPM)	$\pm \sigma_{kT}$ (mV/PPM)	α (mV/PPM)	$\pm \sigma_{\alpha}$ (mV/PPM)	r^2
PBT-Sample 1	-1.18E-02	2.33E-03	7.47E-01	2.09E-02	0.993
PBT-Sample 2	-3.54E-01	3.12E-02	3.74E-01	9.47E-03	0.995
PBT-Sample 3	-3.65E-02	6.64E-03	6.14E-01	1.92E-02	0.992
PBT-Sample 4	-1.62E-01	3.06E-02	4.50E-01	2.02E-02	0.984
PBT-Sample 5	-7.49E-02	5.07E-03	5.33E-01	7.20E-03	0.998
Av.	-1.28E-01	1.52E-02	5.44E-01	1.54E-02	0.992
PPY-Sample 1	-4.50E-01	6.80E-02	3.50E-01	1.62E-02	0.983
PPY-Sample 2	-6.04E-01	7.08E-02	2.73E-01	1.27E-02	0.985
PPY-Sample 3	-3.88E-01	7.16E-02	3.71E-01	1.98E-02	0.978
PPY-Sample 4	-7.69E-02	1.39E-02	4.94E-01	1.92E-02	0.988
PPY-Sample 5	-8.96E-02	2.46E-02	4.53E-01	2.93E-02	0.968
Av.	-3.13E-01	4.78E-02	3.86E-01	1.87E-02	0.982
Linear	$V_{GDS(0)}$ (mV)	$\pm \sigma_{VGDS(0)}$ (mV/PPM)	k_T (mV/PPM)	$\pm \sigma_{kT}$ (mV/PPM)	r^2
PBT-Sample 1	-1.18E-02	2.33E-03	7.47E-01	2.09E-02	0.993
PBT-Sample 2	-3.54E-01	3.12E-02	3.74E-01	9.47E-03	0.995
PBT-Sample 3	-3.65E-02	6.64E-03	6.14E-01	1.92E-02	0.992
PBT-Sample 4	-1.62E-01	3.06E-02	4.50E-01	2.02E-02	0.984
PBT-Sample 5	-7.49E-02	5.07E-03	5.33E-01	7.20E-03	0.998
Av.	-1.28E-01	1.52E-02	5.44E-01	1.54E-02	0.992
PPY-Sample 1	-4.91	0.66	-5.55E-04	6.06E-05	0.807
PPY-Sample 2	-3.81	0.46	-3.09E-04	4.21E-05	0.729
PPY-Sample 3	-4.90	0.72	-5.98E-04	6.58E-05	0.805
PPY-Sample 4	-2.26	0.34	-4.48E-04	3.06E-05	0.915
PPY-Sample 5	-1.96	0.36	-3.41E-04	3.29E-05	0.843
Av.	-3.57	0.51	-4.50E-04	4.63E-05	0.822
Linear (no offset)	k_T (mV/PPM)	$\pm \sigma_{kT}$ (mV/PPM)	r^2		
PBT-Sample 1	-1.05E-03	2.30E-05	0.957		
PBT-Sample 2	-9.24E-04	5.62E-05	0.411		
PBT-Sample 3	-9.19E-04	3.17E-05	0.877		
PBT-Sample 4	-8.64E-04	4.66E-05	0.622		
PBT-Sample 5	-8.76E-04	3.66E-05	0.794		
Av.	-9.27E-04	3.88E-05	0.732		
PPY-Sample 1	-9.31E-04	6.25E-05	0.278		
PPY-Sample 2	-6.00E-04	4.72E-05	0		
PPY-Sample 3	-9.74E-04	6.39E-05	0.354		
PPY-Sample 4	-6.21E-04	2.95E-05	0.721		
PPY-Sample 5	-4.91E-04	2.76E-05	0.611		
Av.	-7.23E-04	4.61E-05	0.393		
Langmuir	αk_T	$\pm \sigma_{\alpha kT}$	k_T	$\pm \sigma_{kT}$	r^2

	(mV/PPM)	(mV/PPM)	(mV/PPM)	(mV/PPM)	
PBT-Sample 1	-1.54E-03	7.24E-05	3.19E-05	4.85E-06	0.991
PBT-Sample 2	-4.28E-03	4.51E-04	2.68E-04	3.80E-05	0.96
PBT-Sample 3	-1.84E-03	9.59E-05	7.12E-05	7.66E-06	0.989
PBT-Sample 4	-2.97E-03	1.77E-04	1.77E-04	1.56E-05	0.987
PBT-Sample 5	-2.16E-03	1.24E-04	1.05E-04	1.06E-05	0.987
Av.	-2.56E-03	1.84E-04	1.31E-04	1.53E-05	0.983
PPY-Sample 1	-4.92E-03	3.32E-04	3.17E-04	2.78E-05	0.985
PPY-Sample 2	-5.04E-03	3.46E-04	5.55E-04	4.54E-05	0.985
PPY-Sample 3	-4.64E-03	1.53E-04	2.77E-04	1.22E-05	0.996
PPY-Sample 4	-1.76E-03	1.29E-04	1.33E-04	1.58E-05	0.98
PPY-Sample 5	-1.72E-03	8.18E-05	1.82E-04	1.27E-05	0.992
Av.	-3.57E-03	1.98E-04	2.88E-04	2.16E-05	0.989
Modified Langmuir	αk_T (mV/PPM)	$\pm \sigma_{\alpha kT}$ (mV/PPM)	k_T (mV/PPM)	$\pm \sigma_{kT}$ (mV/PPM)	r^2
PBT-Sample 1	-7.58E-02	3.04E-03	-3.23E-03	2.02E-04	0.992
PBT-Sample 2	-1.58E-01	6.03E-03	4.01E-03	5.04E-04	0.993
PBT-Sample 3	-8.41E-02	3.76E-03	-1.84E-03	2.98E-04	0.99
PBT-Sample 4	-1.20E-01	6.39E-03	1.59E-03	5.63E-04	0.987
PBT-Sample 5	-9.46E-02	1.71E-03	-6.42E-04	1.45E-04	0.998
Av.	-1.06E-01	4.19E-03	-2.16E-05	3.43E-04	0.992
PPY-Sample 1	-1.80E-01	8.16E-03	-1.80E-01	8.16E-03	0.99
PPY-Sample 2	-1.62E-01	5.50E-03	1.15E-02	7.19E-04	0.995
PPY-Sample 3	-1.76E-01	9.17E-03	4.74E-03	7.28E-04	0.988
PPY-Sample 4	-7.46E-02	3.69E-03	2.47E-04	4.47E-04	0.988
PPY-Sample 5	-6.91E-02	5.41E-03	1.76E-03	8.39E-04	0.992
Av.	-1.31E-01	6.08E-03	-2.62E-02	1.90E-03	0.991

Table 6.8: Parameter fits to broad range static response for electrochemically polymer toluene, at 30°C/4500 PPM water, including the confidence interval r^2.

As before a number of these models give a good fit to the data, especially the power law, Langmuir isotherm and modified Langmuir isotherm model. Of these, the modified Langmuir model generally gave the best fit.

The maximum sensitivity and average sensitivity, of these chemFET sensors to ethanol and toluene vapour is given in table 6.9.

Polymer	Tol. Max. (μV/PPM)	Tol. Typ. (μV/PPM)	Eth. Max. (μV/PPM)	Eth. Typ. (μV/PPM)
Poly(pyrrole)/BSA	+1.11	-0.92 ± 0.16	+4.45	+1.09 ± 0.99
Poly(bithiophene)/TBATFB	-2.27	-1.03 ± 0.46	-2.93	-1.13 ± 0.40

Table 6.9: Typical sensitivity values for chemFET sensors employing composite polymer films to toluene and ethanol vapour in air.

From these results, we can see that the sensitivity of these *n*-channel MOSFET chemFET sensors with electrochemically deposited polymer films, to toluene vapour is

lower than the composite polymers, though higher for ethanol vapour. So any instrument made from these sensors would benefit from a mixture of both composite and electrochemically deposited polymers.

6.5 Modelling of chemFET response to organic vapours

To analyse these results, it is useful to examine the theoretical equations that characterise a MOSFET device. The standard equation for a standard solid metal gate *n*-channel MOSFET in the saturated regime is:

$$i_{DS} = g_m(V_{GDS} - V_T)^2 = \kappa \tag{6.19}$$

where V_{GDS} is the gate/drain voltage commoned to source, V_T is the threshold voltage, κ is a constant here and g_m is given by:

$$g_m = \mu_n C_o \frac{W}{L} = \alpha \tag{6.20}$$

where *W/L* are the channel width and length, C_o is the oxide capacitance per unit area, μ_n is the electron carrier mobility (*n*-channel) and α is a device constant. A change in i_{DS} in terms of κ may be written as:

$$\delta i_{DS} = \frac{\partial \kappa}{\partial g_m}\delta g_m + \frac{\partial \kappa}{\partial V_{GDS}}\delta V_{GDS} + \frac{\partial \kappa}{\partial V_T}\delta V_T = 0 \tag{6.21}$$

Since these chemFET sensors are operating at constant current and so V_{GDS} is measured then from equations (6.20) and (6.21):

$$\delta V_{GDS} = \delta V_T - \frac{(V_{GDS} - V_T)\delta g_m}{2g_m} \tag{6.22}$$

Thus, from this basic equation we can define the expected effect of concentration on V_{GDS} for an active sensor. As the parameter, g_m is independent of analtye concentration, then equation (6.9) simply becomes:

$$\frac{dV_{GDS}}{dC} = \frac{dV_T}{dC} \tag{6.23}$$

so the change in gate/drain voltage equals the change in threshold voltage. A similar expression can be formed for a *p*-channel MOSFET device.

6.5.1 Modelling of static responses of chemFET sensors

From the previous section, it has been shown that the response of a *n*-channel chemFET sensor with a composite polymer or electrochemically deposited polymer films, at fixed temperature and water concentration follows a power law or a modified Langmuir isotherm model. For the chemFET sensors with a composite polymer film (assuming that the threshold voltage is directly related to V_{GDS}) is a power function of concentration, then:

$$V_T = V_{T0} + k_P C_P^{\alpha} \tag{6.24}$$

and

$$\Delta V_T = \left(V_T - V_{T0}\right) = k_p C_p^{\alpha} \tag{6.25}$$

where C_p is the concentration of analyte within the polymer and k_p is the partition coefficient, with k_p a constant at a steady temperature. For the chemFET sensors employing an electrochemically deposited polymer film we can state that:

$$\Delta V_T = \frac{\alpha k_P \sqrt{C_p}}{1 + k_P \sqrt{C_p}} \tag{6.26}$$

It should be noted that these expressions are based on the concentration of an analyte within the polymer, which is a function of k_P, the ratio of analyte concentration in the carrier gas to the concentration in the polymer. McGill *et al.* [6.11] has stated that this is related to the linear solvation energy relationship which relates the logarithm of the partition coefficient (k_P) to parameters describing the properties of both the polymer (solute) and the vapour (solvent), so $k_p C_P \approx k k_p C_A$, where C_p is the analyte concentration within the polymer and C_A is the analyte concentration outside. Previous work with electrochemical deposited polymers, indicates that this shift in the threshold voltage is brought about by a modulation in the work function at the polymer/semiconductor interface, i.e. $\Delta V_T \approx \Delta\phi_{PS}$ [6.12]. It is proposed that here this shift in work function is associated with three different mechanisms. Firstly, it could be due to a partial charge transfer from the analyte to the polymer, with the polymer behaving as an acceptor (or donor) of electrons. Secondly, it could be due to a swelling effect of the polymer, where this swelling increases the average distance between the conducting carbon spheres, hence altering the average work function of the composite material or the polymer to air ratio for electrochemically deposited polymers. This swelling may be thickness dependent as the layers above the polymer/insulator

interface may restrict the swelling of the polymer. Lastly, for chemFET sensor with electrochemically deposited polymers the swelling of the polymer may cause an alteration in the band structure of the polymer, instead of the number of electrons within the bands, by modifying the interaction between polymer chain and the counter ion. Therefore, the change in response direction, for chemFET sensors with electrochemically deposited films to toluene and ethanol vapour, could be a result of one analyte behaving as a donor and the other an acceptor of electrons. Secondly, one analyte could cause an expansion and the other a contraction within the polymer. Thirdly, there maybe some different effect on the band structure within the polymer or lastly, there is some other interaction occurring between water vapour and the analyte at the gate oxide, possible with one analyte removing water vapour from this interface.

It is probable that the response is a combination of charge transfer (electronic) and swelling (mechanical) effect. With a swelling effect the shift in the composite work function $\left(\bar{\phi}_{PC}\right)$ will be a combination of the carbon sphere volume fraction f_c and the individual work functions of the carbon (ϕ_c) and the polymer (ϕ_p), hence:

$$\bar{\phi}_{PC} = f_C\phi_C + (1 - f_C)\phi_P \tag{6.27}$$

Clearly, the change in work function due to a partial charge transfer, is also a function of coverage and by combining the two effects and differentiating, as a function of concentration, we have:

$$\frac{d\bar{\phi}_{PC}}{dC} = \frac{df_C}{dC}(\phi_C - \phi_P) + (1 - f_C)\frac{d\phi_P}{dC} \tag{6.28}$$

It should be noted that if $\phi_P \approx \phi_C$, then equation (6.28) reduces to:

$$\frac{d\bar{\phi}_{PC}}{dC} \approx (1 - f_C)\frac{d\phi_{PC}}{dC} \tag{6.29}$$

where the average shift in simply reduced by a constant of $(1 - f_c)$. For the chemFET sensors with electrochemically deposited polymer films, a similar expression can be formed between the polymer and the air.

6.5.2 Work function measurements of conducting polymer materials

The work function measurements were carried out at Tor Vegata, University of Rome, Italy. By using these readings it is possible to confirm if the observed response for the chemFET sensors is due to a modulation of the work function.

Readings were attained for both the composite and the electrochemically deposited polymers. For each type of polymer the work function was measured at a temperature of 21^{o}C with the average values for each polymer given in table 6.10.

Polymer	Work function (mV)	± σ (mV)
Poly(ethylene-co-vinyl acetate)	–98.7	20.7
Poly(styrene-co-butadiene)	–46.3	11.0
Poly(9-vinylcarbazole)	130.7	36.6
Poly(pyrrole)/BSA	–93.0	6.7
Poly(bithiophene)/TBATFB	+110.6	7.0

Table 6.10: Work function measurements of polymer materials.

As well as these absolute measurements, a number of samples were exposed to ethanol vapour to measure the shift in work function, as given in table 6.11 below. Here long test periods were used, as the headspace was considerable, also the concentration of ethanol vapour was at its saturated value for the room temperature (62300 PPM at 21 ^{o}C).

Polymer	Work function before exposure (mV)	Work function on exposure (mV)	Shift in work function (mV)	period (min)
Poly(styrene-co-butadiene) Sample 1	–58	–35	+23	5
Poly(styrene-co-butadiene) Sample 2	–42	–6	+36	10
Poly(9-vinylcarbzole) Sample 1	+91	+106	+15	5
Poly(9-vinylcarbzole) Sample 2	+121	+154	+33	20
Poly(bithiophene)/TBATFB Sample 1	+122	+110	–12	5
Poly(bithiophene)/TBATFB Sample 2	+107	+70	–37	10
Poly(bithiophene)/TBATFB Sample 3	+ 103	+110	–12	15

Table 6.11: The effect of ethanol vapour in air on the work function values of three conducing polymers.

The response range for poly(styrene-co-butadiene) was between 23 mV to 36 mV which is equivalent to a 0.37 μV/PPM to 0.58 μV/PPM and for poly(9-vinylcarbazole) between 15 mV to 33 mV equivalent to 0.24 μV/PPM to 0.53 μV/PPM. These work function sensitivity values for poly(styrene-co-butadiene) are within the chemFET sensitivity range for this polymer and the poly(9-vinylcarbazole) showing a similar, though slightly higher sensitivity than the chemFET sensors, possible due to the lower test temperature. Also the direction of the shift in work function is the same as the chemFET devices employing these polymers, giving supporting evidence to the theory that the response of chemFET sensors with composite polymer films is due to a shift in the work function.

For the chemFET sensors with electrochemically deposited films poly(pyrrole)/BSA showed a shift in work function of –12 mV to –37 mV was observed, which is equivalent to –0.19 μV/PPM to –0.59 μV/PPM. These results have a very similar magnitude of sensitivity to the chemFET sensors employing the same polymer. It is interesting to note that the shift in work function is in the opposite direction to that observed for the chemFET sensors. This may be accounted for by the measurement being a comparison of polymer to air instead of polymer to silicon. In addition, it is possible that the gate oxide in the chemFET response is performing a more important role than previously thought. The use of a silicon nitride gate insulator could be used to explore this issue.

6.6 Dependence of *n*-channel chemFET sensor response to film thickness

Here the effect of modifying the film thickness on the magnitude of the response is examined. Initial tests were carried out with the poly(styrene-co-butadiene) deposited by Cyrano Sciences with three thicknesses. Further tests were carried out with poly(9-vinylcarbzole) deposited at Warwick University, as described in chapter 4, also at three thicknesses. Tests were performed using the same regime as before exposing the sensors to six different concentrations of toluene and ethanol vapour (1316, 1843, 2633, 5793, 8690 and 12378 PPMs of toluene and ethanol 2665, 3732, 5331, 11729, 17593 and 25058 PPMs of ethanol) at fixed temperature and water concentration (30 ^{o}C/4500 PPM water vapour). The sensors were stabilised at a fixed temperature for 24 hours before testing. The static results of these tests are shown in figure 6.23 for

poly(styrene-co-butadiene) and figure 6.24 for poly(9-vinylcarbzole) for toluene and ethanol vapour in air. Here all the results are fitted to a power model given in expression (6.14).

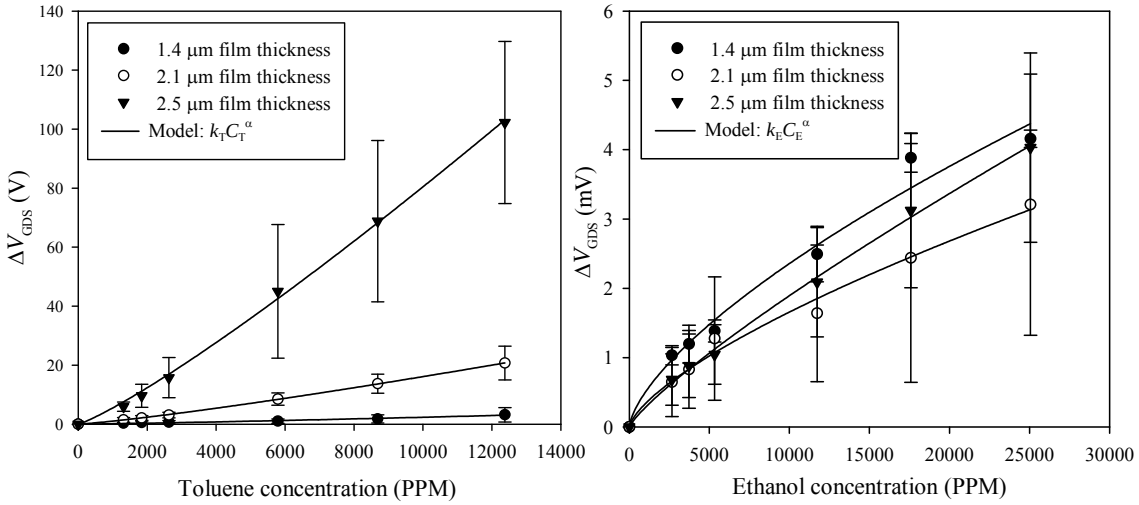

Figure 6.23: The response of chemFET sensors with three different thicknesses of poly(styrene-co-butadiene) to toluene and ethanol vapour in air.

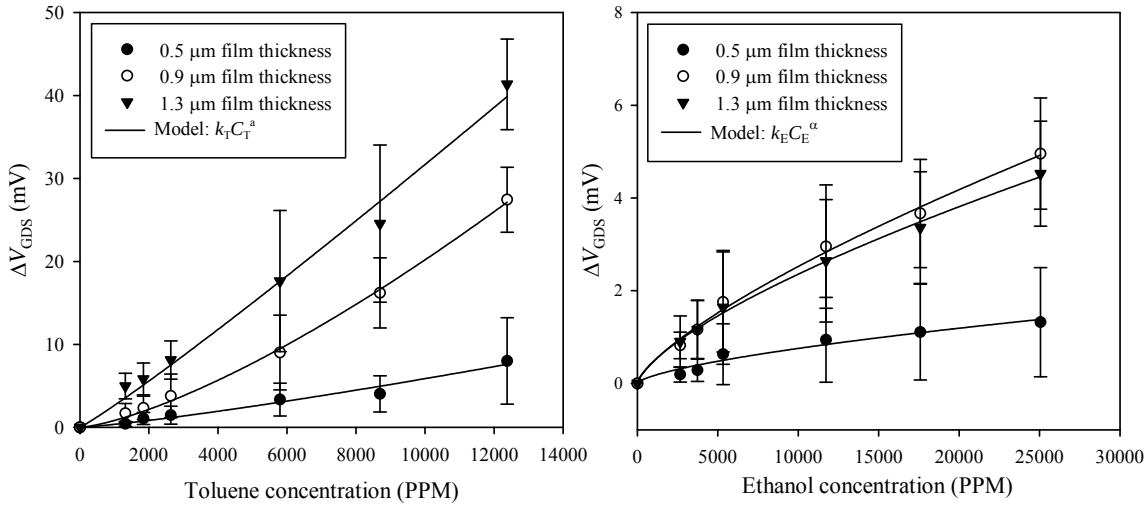

Figure 6.24: The response of chemFET sensors with three different thicknesses of poly(9-vinylcarbazole) to toluene and ethanol vapour in air.

From these tests we can state that, for poly(styrene-co-butadiene) and poly(9-vinylcarbazole) to toluene vapour in air, an increased response is observed with thicker polymer films. The same polymers to ethanol vapour shows a different effect where the response is less film dependent and once a threshold voltage has been achieved the response of the sensor remains at a similar level.

This suggests a number of possible effects are occurring, though clearly the toluene vapour response gives the impression of being a bulk effect, whilst the ethanol response may be more of an interface effect. It is proposed that for the chemFET sensors response to toluene vapour the electrical effect is more significant and so with thicker polymer films, more charge transfer occurs, increasing the shift in work function. Furthermore, as the response to low analyte concentration is non-linear it suggests that the detection limit maybe defined by the cross-linking of the polymer. This cross-linking can be thought of as bonds connecting polymer chains and so a certain analyte threshold has to be achieved (by a swelling effect) to break these cross-linking connections.

6.7 Detection limits of room temperature chemFET sensors employing conducting polymer films

A final, yet critical value for any sensor is its detection limit. UK health and safety regulations set a working limit for long term exposure to toluene vapour and ethanol vapour at 50 PPM and 1000 PPM (over 8 hours) and the short term limit at 150 PPM and 2000 PPM (< 15 minutes), respectively [6.13]. Clearly, any useful application of these sensors as vapour monitors would require a detection limit below these concentrations.

Here the chemFET sensors employing composite and electrochemically deposited polymers were tested at toluene and ethanol vapour concentrations between 52 – 523 PPMs of toluene and 87-873 PPMs of ethanol vapour in air. By using these concentrations it should be possible to estimate the detection limit of these sensors.

6.7.1 ChemFET sensors with a composite polymer gate

For the purposes of these experiments sensors with the largest responses from both the initial sensors and from the film thickness measurements were used. Results of these experiments are given in figure 6.25 for toluene and ethanol vapour in air. All these measurements were taken at a constant water concentration of 4500 PPM and constant temperature of 30 ^{o}C and the response fitted to a power model.

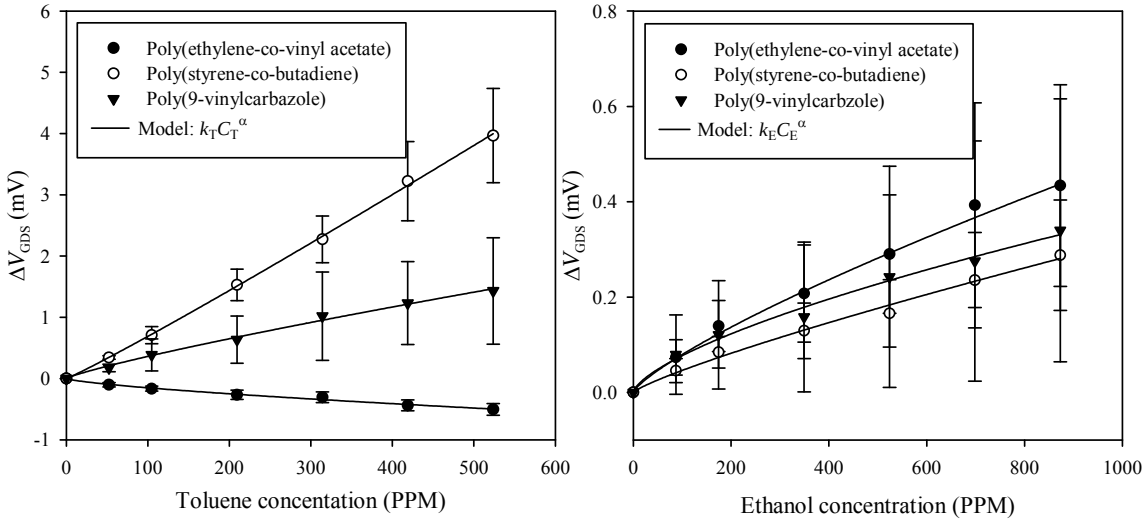

Figure 6.25: The effect of toluene and ethanol vapour in air on *n*-channel chemFET sensors employing composite polymer films at constant water concentration and temperature (4500 PPM, 30 ^{o}C).

From figure 6.25 we can estimate the detection limits of these sensors as shown in table 6.12 below.

Polymer	Toluene detection limit (PPM)	Ethanol detection limit (PPM)
Poly(ethylene-co-vinyl acetate)	10 – 20	10 – 50
Poly(styrene-co-butadiene)	< 10	10 – 50
Poly(9-vinylcarbazole)	< 10	10 – 50

Table 6.12: Detection limits for chemFET sensors employing composite polymers to toluene and ethanol vapour in air at 4500 PPM water concentration and fixed temperature 30 ^{o}C.

6.7.2 ChemFET sensors with a electrochemically deposited polymer gate

A number of chemFET sensors with electrochemically deposited polymer films were exposed to low concentrations of toluene and ethanol vapour as shown in figure 6.26. These tests were performed using the same regime as the chemFET sensors with composite polymers and the response modelled to a modified Langmuir isotherm. Table 6.13 gives the detection limits of these sensors.

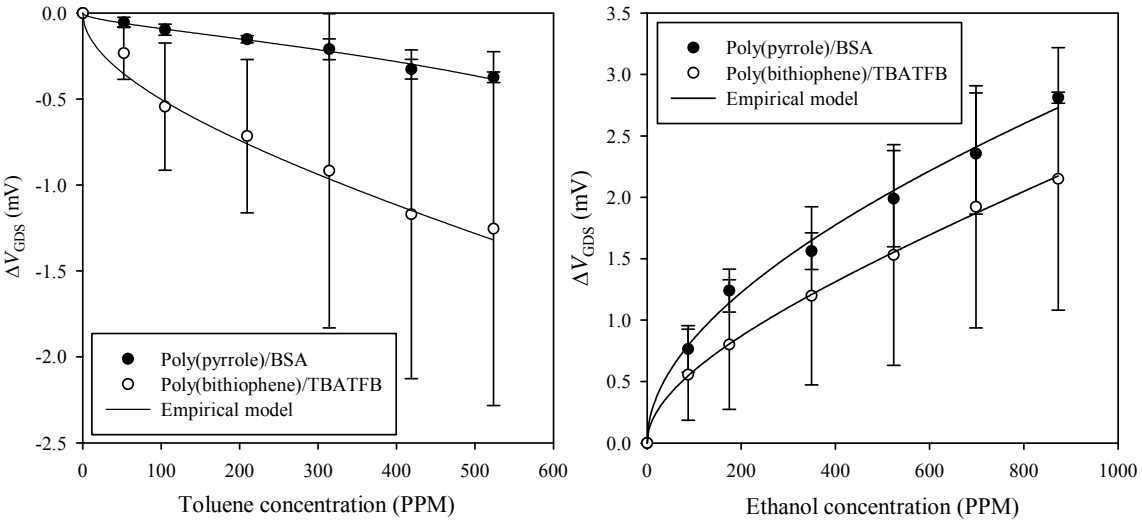

Figure 6.26: The effect of toluene vapour on chemFET sensors employing an electrochemically deposited polymer films at constant water concentration and temperature (4500 PPM, 30 ^{o}C).

Polymer	Toluene detection limit (PPM)	Ethanol detection limit (PPM)
Poly(pyrrole)/BSA	30 – 40 PPM	< 20
Poly(bithiophene)/TBATFB	10 – 20 PPM	< 20

Table 6.13: Detection limits for chemFET sensors employing electrochemically deposited polymers to toluene and ethanol vapour in air at 4500 PPM water concentration and fixed temperature 30 ^{o}C.

All of these sensors show a detection limit below the UK regulations and so could be used in a vapour monitor application.

6.8 Conclusions

In this chapter, the effect of analyte concentration on the dynamic and static response of *n*-channel (MOSFET) chemFET sensors employing composite polymer and electrochemically deposited polymer films as the gate have been investigated. In addition, the effect of ethanol concentration on the static response on *p*-channel (MISFET) chemFET sensors with chemically prepared electrochemically doped polymers has been examined. It has been found that all of these sensors respond in different degrees to the test analytes. Dynamic modelling has shown that the sensors response can be modelled to a double exponential, where the first component is dependent on analyte concentration and the second component independent (composite polymers) or also dependent on analyte concentration (electrochemical polymers). This

second component has been found to be considerably longer than the first. The response was shown to be reaction-rate limited as a function of the forward and backward reaction rates, where the time constant falls with increasing analyte concentration.

In addition, models have been developed for the effect of analyte concentration on the static response over a broad range (400 – 20000 PPMs of toluene and 300 – 40000 PPMs of ethanol vapour in air) on the sensors response and the best fitting models are summarised in table 6.14 below.

Polymer	Linear	Power	Langmuir	Modified Langmuir
Poly(pyrrole) (UMIST)			✓	
Poly(ethylene-co-vinyl acetate)		✓		
Poly(styrene-co-butadiene)		✓		
Poly(9-vinylcarbazole)		✓		
Poly(pyrrole)/BSA (SU)				✓
Poly(bithiophene)/TBATFB (SU)				✓

Table 6.14: A summary of the best fitting models for chemFET sensors employing polymer films to toluene and ethanol vapour in air (SU - deposited at Southampton University).

It is proposed that the sensors response is due to a shift in the threshold voltage, more specifically a modification of the work function between the polymer and the silicon dioxide. It is suggested that this shift in work function could be by two mechanisms, an electronic and a mechanical effect. Firstly, the electronic effect is by a partial charge transfer between the analyte and the polymer, with the analyte behaving as an acceptor or donor of electrons. Secondly, a mechanical or swelling effect within the polymer. As the analyte diffuses into the polymer it swells altering the average work function composed of the fractional coverage of polymer to carbon, for the composite polymers, or the polymer to air coverage for the electrochemical polymers. This swelling may also cause an alteration in the band structure within the polymer for the electrochemically deposited materials. It is likely that some combination of these effects is being observed.

From the broad range test results, we can calculate the typical sensitivity of the sensors. Also investigated was the detection limit of these sensors. It was found that the detection limit of many sensors was in the tens of PPM. Table 6.15 summaries the typical sensitivity of these sensors and the detection limits. Also shown in this table are the response times, defined as the length of time to reach 90 % of the final response. This sets the sampling rate limit of any system composed of these sensors.

Polymer	Toluene sensitivity (μV/PPM)	Ethanol sensitivity (μV/PPM)	Toluene detection limit (PPM)	Ethanol detection limit (PPM)
Poly(pyrrole)	-0.5 nA/PPM	0.2 nA/PPM		
Poly(ethylene-co-vinyl acetate)	-0.6 ± 0.1	$8.0 \times 10^{-2} \pm 1.4 \times 10^{-2}$	10 – 20	10 – 50
Poly(styrene-co-butadiene)	3.1 ± 0.75	0.39 ± 0.21	< 10	10 – 50
Poly(9-vinylcarbazole)	4.0 ± 0.61	$0.29 \pm 6.5 \times 10^{-2}$	< 10	10 – 50
Poly(pyrrole)/BSA	-1.03 ± 0.46	1.09 ± 0.99	10 - 20	< 20
Poly(bithiophene)/TBATFB	-1.13 ± 0.40	0.54 ± 0.41	30 - 40	< 20
Polymer	Toluene on time response	Ethanol on time response	Toluene off time response	Ethanol off time response
Poly(ethylene-co-vinyl acetate)	304 s ± 175	237 s ± 250	299 s ± 298	360 s ± 558
Poly(styrene-co-butadiene)	472 s ± 300	212 s ± 87	412 s ± 352	145 s ± 60
Poly(9-vinylcarbazole)	1397 s ± 993	136 s ± 150	698 s ± 383	2174 s ± 3393
Poly(pyrrole)/BSA	330 s ± 257	772 s ± 845	649 s ± 403	1263 s ± 7345
Poly(bithiophene)/TBATFB	251 s ± 78	572 s ± 366	1020 s ± 852	1251 s ± 881

Table 6.15: A summary of the sensitivities, detection limits and response times of chemFET sensors employing conducting polymer films.

The response time for chemFET sensors with composite materials, appears to be longer than has been previously reported by other researchers [6.8] and maybe an effect of the film thickness or of the test system, though at present there is no general agreement on the reason for the effect.

Lastly, the effect of film thickness on the magnitude of the response was investigated. These measurements were restricted to the chemFET sensors with composite polymer films, as accurate control of the thickness of the electrochemically deposited polymer films was not achieved. Here, it was shown that the sensors response increases with thicker polymer films to toluene vapour and remains similar for ethanol vapour once a threshold thickness has been achieved. This suggests a number of possible mechanisms, though the effect for toluene vapour infers that the response occurs within the bulk, whilst the ethanol response may take place at the interface. It is also proposed that in the response to toluene vapour, the electronic effect is more significant and so with thicker films, more charge transfer occurs, simply because of more polymer.

6.9 References

6.1 P.N. Bartlett, P.B.M. Archer, S.K. Ling-Chung, Conducting polymer gas sensors: Part 1 and 2, *Sensors and Actuators,* **19**, (1989), 125-150.

6.2 M.C. Lonergan, E.J. Severin, B.J. Doleman, S. A. Beaber, R. H. Grubbs, N. S. Lewis, Array-based vapour sensing using chemically sensitive carbon black-polymer resistors, *Chem. Mater.* 8, (1996), 2298-2313.

6.3 R.A. Bisell, F-B Li, P. Travers, K. Persaud, A boiling point model to describe conducting polymer gas sensor responses, Electronic Noses and Olfaction 2000 (ed. J.W. Gardner, K.C. Persaud), (2000), 23-34.

6.4 Chemical Summary for toluene, Office of pollution prevention and toxics, U.S. Environmental agency, 1994.

6.5 Chemical Summary for ethanol, Office of pollution prevention and toxics, U.S. Environmental agency, 1994.

6.6 J.W. Gardner, P.N. Bartlett, K.F.E. Pratt, Modelling of gas sensitive conducting polymer devices, *IEE Proc. Circuits, devices and systems*, 142 (1995), 321-333.

6.7 P.N. Bartlett, J.W. Gardner, Diffusion and binding molecules for sites within thin films, *Trans. Roy. Soc. London,* A, 354 (1996), 35-57.

6.8 B.J. Doleman, M.C. Lonergan, E.J. Severin, T.P. Vaid, N.S. Lewis, Quantitative study of the resolving power of arrays of carbon black-polymers in various vapour sensing roles, *Anal. Chem.*, 70, (1998), 4177-4190.

6.9 Cyrano 320 Electronic Nose leaflet, Cyrano Sciences, 2000.

6.10 P. Ingelby, PhD Thesis, University of Warwick, Coventry, CV4 7AL.

6.11 R.A. McGill, M.H. Abraham, J.W. Grate, *ChemTech,* 24 (1994), 27-37.

6.12 M.G.H. Meijerink, M. Koudelka-Hep, N.F. Rooij, D.J. Strike, J. Hendrikse, W. Olthuis and P. Bergeveld, Gas-dependent field effect transistor with an electrodeposited conducting polymer gate contact, *Electrochemical and Solid-State Letters*, **2**, (1999), 138-139.

6.13 UK Health and Safety regulations, EH40, HSE Books, HMSO, 2001.

CHAPTER 7

The effect of water concentration and temperature on static response of chemFET sensors

7.1 Introduction

Previously, in chapter 6, the effect of analyte concentration on the static and dynamic response of room temperature chemFET sensors was described. The developed models ignored the effects of temperature and water concentration, though in any practical application these factors may not be constant. This chapter describes the characterisation of chemFET sensors to temperature and water concentration and the development of models for the steady-state (i.e. static) response. These experiments were restricted to the IMT fabricated devices based on a *n*-channel MOSFET. The analytical expressions derived initially by observation are explained, where possible, by chemical interactions.

Also investigated is the effect of analyte concentration, water concentration and temperature on the static response of resistive sensors employing a composite polymer film. This may give further insights into the mechanisms involving chemFET sensors employing these composite materials.

7.2 The effect of water concentration on the static response of room temperature chemFET sensors

Here the effect of water concentration on the response of chemFET sensors employing both composite and electrochemically deposited polymer films is investigated. In both cases the sensors were placed in a DRI-BLOCK® (DB-2D) heater for a period of 24 hours to equilibrate before testing and operated at a constant current of 10 μA with the gate/drain-source (V_{GDS}) voltage monitored. Each sensor was exposed for 60 minutes to a particular water concentration to create a stable baseline, then exposed for a period of 25 minutes to a specific analyte concentration followed by a 30 minutes recovery period. The sensors were tested at six different concentrations of toluene and ethanol vapour in air (1316, 1843, 2633, 5793, 8690 and 12378 PPM of toluene and 2665, 3732, 5331, 11729, 17593 and 25058 PPM of ethanol) and at four different water vapour concentrations (3000, 4500, 6750 and 9853 PPM of water, 10-50 % r.h. and 20^{o}C).

7.2.1 ChemFET sensors employing composite polymer films as the gate

Initial tests investigated the effect of water concentration on the baseline of chemFET sensors employing composite polymer films. Here the sensors were exposed to four different water concentrations (as stated above) at 30^{o}C. Results showed a reduction in the baseline V_{GDS} value with increasing water concentration for poly(ethylene-co-butadiene) and poly(styrene-co-butadiene), though there was no observed baseline drift for poly(9-vinylcarbazole). This effect on the relative baseline (V_{GDS}) value is shown in figure 7.1 for poly(ethylene-co-vinyl acetate) and poly(styrene-co-butadiene). This shows the average shift in V_{GDS} from estimating V_{GDS} at 0 PPM water concentration and subtracting from the measured values.

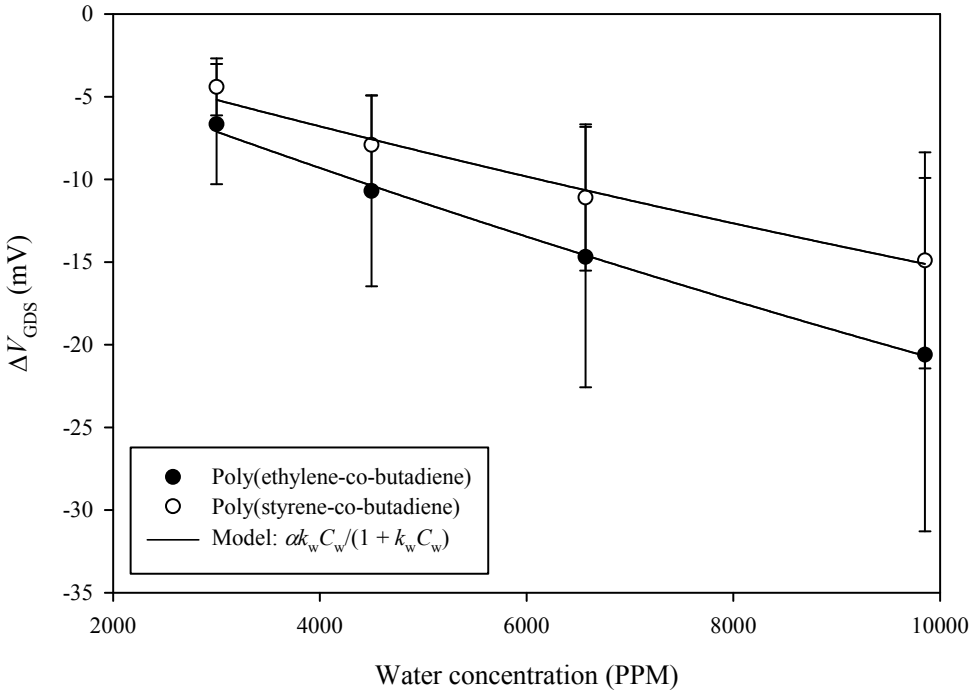

Figure 7.1: The effect of water concentration on the relative baseline of chemFET sensors employing poly(ethylene-co-vinyl acetate) and poly(styrene-co-butadiene) at 30°C.

The shift in relative baseline with water concentration has been fitted to a Langmuir isotherm, this assumes that there is a fixed number of independent absorption sites for the water molecules to bind. The shift in V_{GDS} with water concentration, at 0 PPM or constant analyte concentration, can therefore be approximated as:

$$V_{GDS} \approx V_{GDS0} + \frac{\alpha k_W C_W}{(1 + k_W C_W)} \tag{7.1}$$

where $V_{GDS(0)}$ is the baseline value at zero water concentration, C_W is the concentration of water, k_W is the binding coefficient and α is a polymer constant, hence:

$$\Delta V_{GDS} \approx \frac{\alpha k_W C_W}{(1 + k_W C_W)} \tag{7.2}$$

A possible explanation for these observed results is that the water molecules are forming a dipole layer on the surface of the gate oxide. The presence of this layer shifts the average work function, though the dipole formation will also change the capacitance. If we consider the MOSFET device, in the saturated region, then:

$$i_{DS} = aC_{ox}(V_{GDS} - V_T)^2 \tag{7.3}$$

where a is a geometric/carrier mobility constant and C_{ox} is the gate capacitance per unit area. Since this device is operated at constant current then Δi_{DS} is zero, hence:

$$\Delta i_{DS} = 2aC_{OX}(V_{GDS} - V_T)\Delta(V_{GDS} - V_T) + a\Delta C_{OX}(V_{GDS} - V_T)^2 = 0 \quad (7.4)$$

and so if ΔC_{ox} changes then:

$$\frac{\Delta C_{OX}}{C_{OX}} = \frac{2(V_{GDS} - V_T)\Delta(V_{GDS} - V_T)}{a(V_{GDS} - V_T)^2} = \frac{2\Delta(V_{GDS} - V_T)}{a(V_{GDS} - V_T)} \quad (7.5)$$

Thus V_{GDS} must shift at constant V_T. It is likely that this effect is a combination of the shift in work function and the shift in capacitance. This model is supported by the observation of a Langmuir isotherm response which suggests that as the water vapour concentration increases then the occupancy of sites at the oxide interface rises, thereby increasing the total dipole moment and so altering both the threshold voltage and the gate capacitance. This undesirable sensitivity to water vapour may be removed by using an alternative gate insulator, such as silicon nitride (though this makes the process non-standard) or by running at higher operating temperatures, (which increases the power consumption). A possible explanation for the difference in baseline dependence between poly(ethylene-co-vinyl acetate), poly(styrene-co-butadiene) and poly(9-vinlyacetate) is that the first two polymers are hydrophilic and last is hydrophobic. Though true, further work with thicker polymer films has shown a reduction or removal of this baseline dependence for poly(styrene-co-butadiene). This suggests a thickness dependence on the baseline drift, though over these test periods water vapour should still reach the polymer/oxide interface, and at present this result cannot be explained. Table 7.1 gives the coefficients for expression (7.1) for a chemFET sensors with a poly(ethylene-co-vinyl acetate) (CP1) and a poly(styrene-co-butadiene) (CP2) films.

CP1	$V_{GDS(0)}$ (V)	αk_W (mV/PPM)	$\pm \sigma_{\alpha kw}$ (mV/PPM)	k_W (PPM^{-1})	$\pm \sigma_{kw}$ (PPM^{-1})	r^2
Sample 1	8.46E-01	-4.16E-03	3.62E-04	7.72E-06	1.13E-05	0.993
Sample 2	4.60E-01	-1.71E-03	6.90E-05	1.45E-06	4.91E-06	0.998
Sample 3	5.96E-01	-2.18E-03	1.56E-04	6.41E-06	9.13E-06	0.995
Sample 4	1.13	-4.44E-03	1.51E-04	8.65E-05	7.59E-06	0.999
Sample 5	5.99E-01	-1.09E-03	8.03E-05	2.38E-06	8.63E-06	0.995
Av.	7.27E-01	-2.72E-03	1.64E-04	2.09E-05	8.30E-06	0.996
CP2	$V_{GDS(0)}$ (V)	αk_W (mV/PPM)	$\pm \sigma_{\alpha kw}$ (mV/PPM)	k_W (PPM^{-1})	$\pm \sigma_{kw}$ (PPM^{-1})	r^2
Sample 1	7.12E-01	-2.61E-03	3.71E-04	1.01E-05	1.88E-05	0.985
Sample 2	4.38E-01	-2.12E-03	1.84E-04	4.46E-06	1.09E-05	0.993
Sample 3	4.35E-01	-2.39E-03	4.68E-04	8.43E-06	2.56E-05	0.965
Sample 4	0.411	-4.56E-03	3.23E-04	1.58E-04	2.16E-05	0.993
Sample 5	0.654	-1.87E-03	6.81E-05	7.35E-06	4.69E-06	0.999
Av.	5.30E-01	-2.71E-03	2.83E-04	3.76E-05	1.63E-05	0.987

Table 7.1: Modelling coefficients fits for the effect of water concentration on the baseline of chemFET sensors employing poly(ethylene-co-vinyl acetate) and poly(styrene-co-butadiene) polymer films at 30°C.

Further tests investigated the effect of water concentration on the response. Figure 7.2 and figure 7.3, show the effect of water concentration on poly(ethylene-co-butadiene), poly(styrene-co-butadiene) and poly(9-vinylcarbazole) to toluene and ethanol vapour in air, respectively. Here the responses of 5 sensors have been averaged. Results demonstrate only a small variation in response with increasing water concentration. In figure 7.2 and figure 7.3, the sensor response, to analyte concentration, has been approximated to a power model and the effect of water concentration approximated to linear. This power law model gives the best fit to these sensor responses, as described in chapter 6. Hence the data has been fitted to:

$$\Delta V_{GDS} = k_T C_T^{\alpha} + k_W C_W \quad (7.6)$$

for toluene and

$$\Delta V_{GDS} = k_E C_E^{\alpha} + k_W C_W \quad (7.7)$$

for ethanol, where k_T, k_E and k_W are binding coefficients for toluene, ethanol and water vapour respectively. This model assumes the effects of water concentration are independent to analyte concentration and therefore would bind at different sites. Clearly, due to this minor variation in response with water concentration, the water binding coefficient is very small, as given in table 7.2 for toluene vapour and table 7.3 for ethanol vapour. Due to this small effect of water concentration, the water binding term was approximated to linear as the power model gave large fitting errors.

Furthermore, these small variations in water binding coefficient could simply be a result of temperature variations within the test chamber.

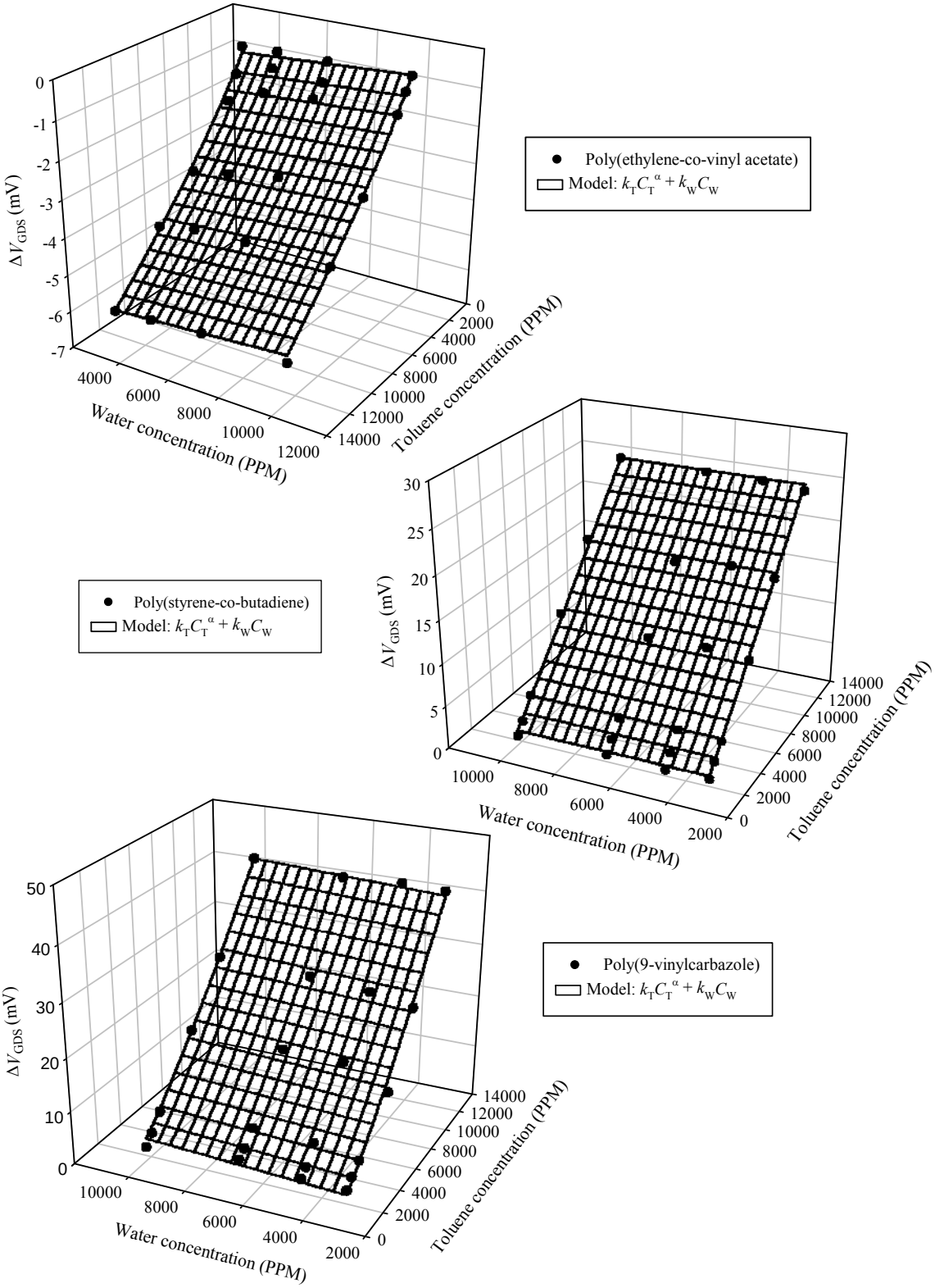

Figure 7.2: The effect of water concentration on the response of chemFET sensors employing composite polymer films to toluene vapour in air at 30°C.

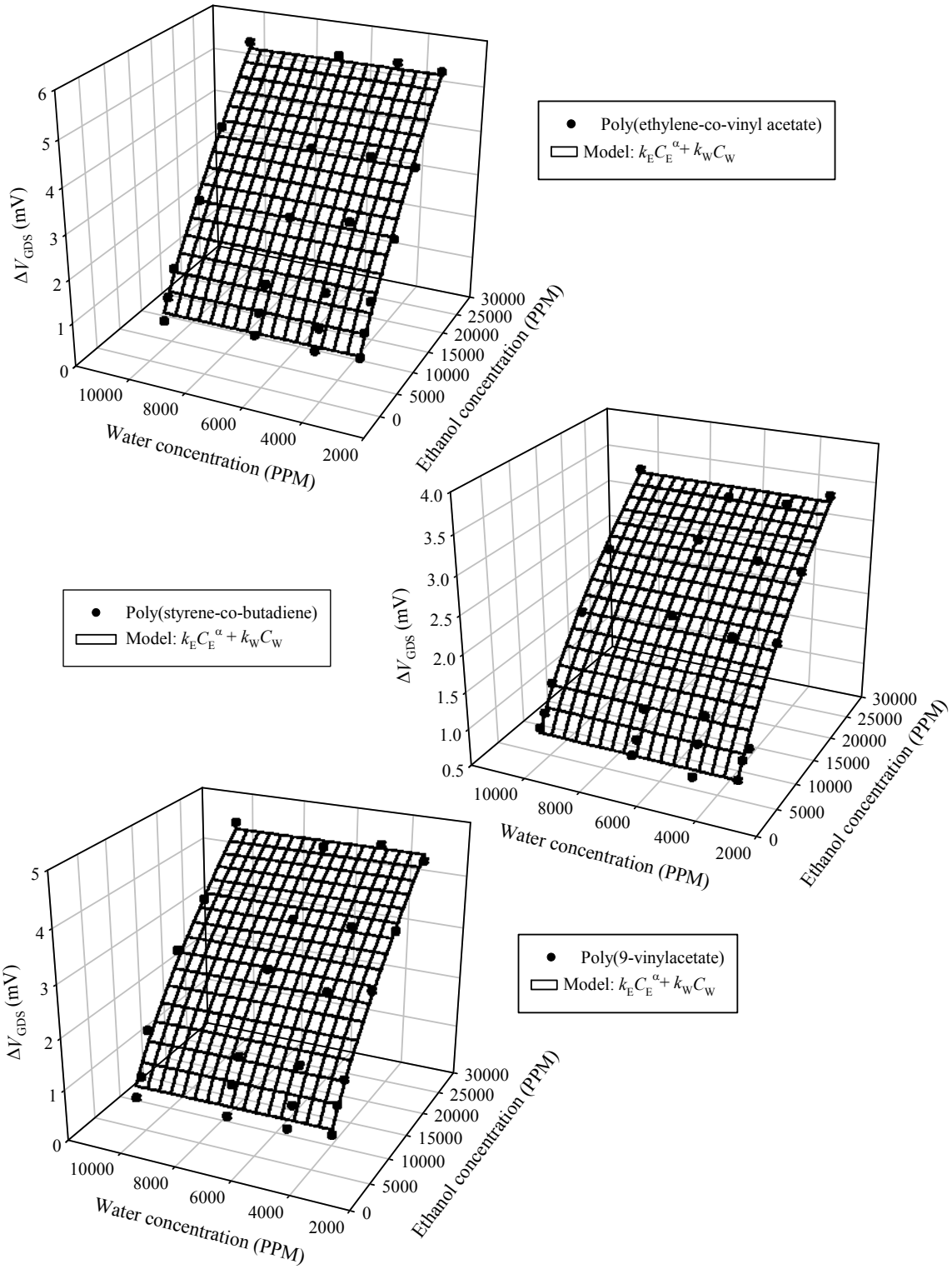

Figure 7.3: The effect of water concentration on the response of chemFET sensors employing composite polymer films to ethanol vapour in air at 30°C.

CP1	k_T (mV/PPM)	$\pm \sigma_{kT}$ (mV/PPM)	α	$\pm \sigma_\alpha$	k_W (mV/PPM)	$\pm \sigma_{kw}$ (mV/PPM)	r^2
Sample 1	-7.19E-03	2.57E-03	7.24E-01	3.71E-02	3.29E-05	2.03E-05	0.984
Sample 2	-1.58E-03	6.53E-04	8.57E-01	4.33E-02	3.78E-05	1.43E-05	0.987
Sample 3	-8.95E-03	3.78E-03	6.78E-01	4.39E-02	4.13E-05	2.11E-05	0.974
Sample 4	-2.66E-03	6.57E-04	8.28E-01	2.59E-02	1.28E-05	1.15E-05	0.995
Sample 5	-1.07E-02	4.79E-03	6.99E-01	4.64E-02	8.84E-05	3.12E-05	0.972
Av.	-6.21E-03	2.49E-03	7.57E-01	3.93E-02	4.26E-05	1.97E-05	0.982
CP2	k_T (mV/PPM)	$\pm \sigma_{kT}$ (mV/PPM)	α	$\pm \sigma_\alpha$	k_W (mV/PPM)	$\pm \sigma_{kw}$ (mV/PPM)	r^2
Sample 1	3.76E-04	1.90E-04	1.16	5.28E-02	2.99E-06	4.41E-05	0.992
Sample 2	9.55E-03	3.12E-03	0.85	3.42E-02	2.96E-05	6.50E-05	0.992
Sample 3	3.14E-03	1.86E-03	0.90	6.22E-02	-7.67E-05	5.74E-05	0.979
Sample 4	5.85E-04	3.18E-04	1.11	5.69E-02	8.72E-05	4.90E-05	0.99
Sample 5	3.04E-04	1.07E-04	1.26	3.71E-02	-6.34E-05	5.55E-05	0.997
Av.	2.79E-03	1.12E-03	1.05	4.86E-02	-4.06E-06	5.42E-05	0.990
CP3	k_T (mV/PPM)	$\pm \sigma_{kT}$ (mV/PPM)	α	$\pm \sigma_\alpha$	k_W (mV/PPM)	$\pm \sigma_{kw}$ (mV/PPM)	r^2
Sample 1	2.02E-06	2.75E-06	1.75	1.32E-01	4.15E-04	8.35E-05	0.98
Sample 2	1.02E-04	1.12E-04	1.41	1.14E-01	5.72E-04	2.10E-04	0.977
Sample 3	1.23E-04	3.22E-05	1.35	2.77E-02	1.71E-05	3.51E-05	0.998
Sample 4	1.02E-02	5.24E-03	0.85	5.42E-02	-9.03E-05	1.08E-04	0.978
Sample 5	3.38E-02	1.41E-02	0.76	4.37E-02	-1.47E-04	1.42E-04	0.98
Av.	8.85E-03	3.90E-03	1.22	7.45E-02	1.53E-04	1.16E-04	0.983

Table 7.2: Modelling coefficients for the effect of water concentration on the response of chemFET sensors employing composite polymers to toluene vapour in air (CP3 – poly(9-vinylcarbazole).

CP1	k_E (mV/PPM)	$\pm \sigma_{kE}$ (mV/PPM)	α	$\pm \sigma_\alpha$	k_W (mV/PPM)	$\pm \sigma_{kw}$ (mV/PPM)	r^2
Sample 1	4.37E-03	1.50E-03	6.96E-01	3.32E-02	2.50E-06	1.45E-05	0.985
Sample 2	1.42E-03	7.46E-04	8.14E-01	5.11E-02	5.89E-06	1.93E-05	0.979
Sample 3	1.13E-03	3.16E-04	8.47E-01	2.72E-02	-1.34E-05	1.08E-05	0.995
Sample 4	1.89E-03	6.10E-04	7.87E-01	3.13E-02	-1.32E-06	1.26E-05	0.991
Av.	2.20E-03	7.92E-04	7.86E-01	3.57E-02	-1.58E-06	1.43E-05	0.988
CP2	k_E (mV/PPM)	$\pm \sigma_{kE}$ (mV/PPM)	α	$\pm \sigma_\alpha$	k_W (mV/PPM)	$\pm \sigma_{kw}$ (mV/PPM)	r^2
Sample 1	4.12E-02	1.75E-02	4.90E-01	4.10E-02	6.43E-05	3.17E-05	0.937
Sample 2	6.46E-02	2.71E-02	4.16E-01	4.07E-02	-1.82E-05	2.71E-05	0.903
Sample 3	1.28E-02	6.55E-03	5.37E-01	4.96E-02	-5.11E-05	1.73E-05	0.931
Sample 4	1.54E-05	1.81E-05	1.11	1.03E-01	2.61E-07	5.41E-06	0.966
Sample 5	1.26E-04	8.81E-05	9.82E-01	6.85E-02	3.95E-06	9.53E-06	0.978
Av.	6.44E-03	2.35E-03	7.95E-01	6.04E-02	-1.21E-05	1.01E-05	0.966
CP3	k_E (mV/PPM)	$\pm \sigma_{kE}$ (mV/PPM)	α	$\pm \sigma_\alpha$	k_W (mV/PPM)	$\pm \sigma_{kw}$ (mV/PPM)	r^2
Sample 1	6.62E-04	2.46E-04	8.93E-01	3.62E-02	1.73E-05	1.24E-05	0.992
Sample 2	7.13E-02	2.34E-02	4.34E-01	3.19E-02	-3.31E-05	2.72E-05	0.946
Sample 3	5.18E-03	3.22E-03	6.37E-01	6.04E-02	-1.91E-05	1.94E-05	0.942
Sample 4	4.09E-04	2.00E-04	9.33E-01	4.74E-02	1.75E-05	1.41E-05	0.988
Sample 5	2.58E-02	8.52E-03	5.35E-01	3.19E-02	1.32E-06	2.21E-05	0.97
Av.	9.91E-03	3.50E-03	6.82E-01	4.10E-02	-7.69E-07	1.67E-05	0.972

Table 7.3: Modelling coefficients for the effect of water concentration on the response of chemFET sensors employing composite polymers to ethanol vapour in air

The total effect of analyte and water vapour on a chemFET sensor employing a composite polymer film can be considered as a combination of these two parameters. As no cross sensitivity term was observed and neglecting any effect of water concentration on the sensors response, we can describe the total effect as (at constant temperature):

$$V_{GDS} = V_{GDS0} + \alpha k_T C_T^{\alpha} + \frac{\beta k_W C_W}{(1 + k_W C_W)} \quad (7.8)$$

$$\Delta V_{GDS} = \alpha k_T C_T^{\alpha} + \frac{\beta k_W C_W}{(1 + k_W C_W)} \quad (7.9)$$

where k_T and C_T can be replaced with k_E and C_E for ethanol. Equations (7.8) and (7.9) only relate to poly(ethylene-co-vinyl acetate) and poly(styrene-co-butadiene) as poly(9-vinylcarbazole) is independent of water concentration and so the Langmuir isotherm term is not applicable.

7.2.2 ChemFET sensors employing electrochemically deposited polymer films as the gate

Previous work with resistive electrochemically deposited conducting polymers have shown that the magnitude of the response to ethanol vapour is related to the concentration of water molecules within this test vapour [7.1]. It has previously been shown, for resistive devices (e.g. poly(pyrrole)/DSA and poly(aniline)/DSA), that an increase in water vapour corresponds to a reduction in response at a fixed ethanol vapour concentration.

Initial work investigated the effect of water concentration on the baseline of chemFET sensors employing electrochemically deposited polymer films. The sensors were exposed to four different concentrations of water vapour (stated above). The results show a reduction in relative baseline with increasing concentration as shown in figure 7.4. Here the variation in V_{GDS} is modelled by a Langmuir isotherm and V_{GDS} taken from an initial value of 0 PPM water concentration, as with the chemFET sensors with composite polymer films. The baseline dependence could also be accounted for by the formation of a dipole layer on the gate oxide. In addition, the magnitude of this dependence is significantly greater than the composite polymer chemFET sensors. This could be due to the electrochemically deposited polymers having a more hydrophilic nature in comparison to the composite polymers, allowing additional water molecules

to reach the polymer/oxide interface or the water molecules are binding to the polymer itself, further shifting V_{GDS}.

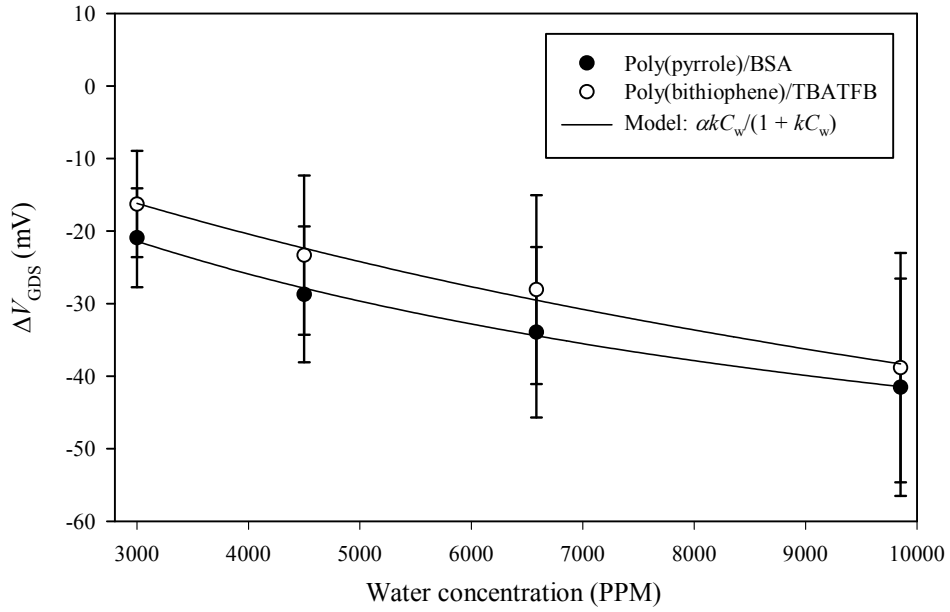

Figure 7.4: The effect of water concentration on the relative baseline of chemFET sensors employing poly(pyrrole)/BSA and poly(bithiophene)/TBATFB polymer films at 30 ^{o}C.

The modelling coefficients for these results is shown in table 7.4 below, for poly(pyrrole)/BSA (PPY) and poly(bithiophene)/TBATFB (PBT).

PPY	$V_{GDS(0)}$ (V)	αk_W (mV/PPM)	$\pm \sigma_{\alpha kw}$ (mV/PPM)	k_W (PPM^{-1})	$\pm \sigma_{kw}$ (PPM^{-1})	r^2
Sample 1	0.808	-1.01E-02	3.89E-04	1.34E-04	1.07E-05	0.998
Sample 2	0.924	-1.41E-02	6.08E-04	1.13E-04	1.09E-05	0.998
Sample 3	0.518	-8.84E-03	5.16E-04	2.39E-04	2.29E-05	0.995
Sample 4	0.649	-1.51E-02	2.16E-03	2.95E-04	6.48E-05	0.969
Sample 5	0.421	-5.90E-03	4.47E-04	6.76E-05	1.52E-05	0.993
Av.	0.635	-1.08E-02	8.24E-04	1.70E-04	2.49E-05	0.991
PBT	$V_{GDS(0)}$ (V)	αk_W (mV/PPM)	$\pm \sigma_{\alpha kw}$ (mV/PPM)	k_W (PPM^{-1})	$\pm \sigma_{kw}$ (PPM^{-1})	R^2
Sample 1	1.19	-9.73E-03	4.51E-04	5.69E-05	8.72E-06	0.997
Sample 2	0.587	-7.70E-03	4.03E-04	7.65E-05	1.11E-05	0.997
Sample 3	0.766	-2.34E-03	5.48E-05	2.84E-05	3.62E-06	0.999
Sample 4	0.642	-2.90E-03	6.42E-04	-1.23E-05	2.32E-05	0.952
Sample 5	0.380	-1.26E-02	3.11E-03	2.35E-04	9.60E-05	0.916
Av.	0.618	-7.05E-03	9.32E-04	7.69E-05	2.85E-05	0.972

Table 7.4: Modelling coefficients for the effect of water concentration on the baseline of chemFET sensors employing poly(pyrrole)\BSA and poly(bithiophene)/TBATFB polymer films at 30^{o}C.

Further experiments investigated the effect of water concentration on the response chemFET sensors exposed to ethanol and toluene vapour in air. It was found that an increase in water concentration caused an increase in the sensor response, as shown in

figures 7.5 and 7.6 for poly(pyrrole)/BSA and poly(bithiophene)/TBATFB to ethanol and toluene vapour, respectively. Clearly, this increase in response is different to that observed for resistive sensors. It is proposed that the ethanol and toluene vapour are in competition for sites with the water. As the analyte concentration increases the sites preferentially bond with the analyte over the water, with the analytes replacing the water within the polymer. As the water is removed from the polymer and so the polymer/oxide interface, the baseline V_{GDS} increases causing a distended response. Once the analyte is removed the dipole moment at the gate oxide is returned to the previous level.

Hence, we can combine the expression for the response to analyte concentration with the effect of water concentration on the baseline, using a competitive binding model (assuming a Langmuir isotherm to response for the effect of analyte concentration):

$$V_{GDS} \approx V_{GDS0} + \frac{\left(k_W C_W a_W \Gamma + k_E C_E a_E \Gamma\right)}{\left(1 + k_W C_W + k_E C_E\right)} \tag{7.10}$$

where a_W and a_E are sensitivity coefficients to water and ethanol, k_W and k_E are binding coefficients, Γ is the number of binding sites and V_{GDS0} is the baseline value at 0 PPM ethanol and water concentration. This can simply be expressed as:

$$\Delta V_{GDS} \approx \frac{\left(k_W C_W a_W \Gamma + k_E C_E a_E \Gamma\right)}{\left(1 + k_W C_W + k_E C_E\right)} \tag{7.11}$$

This expression also applies for toluene, though it is interesting to note that toluene is a non-polar molecule though still shows the same effect. Possible supporting evidence for this result could be from previous work with *p*-channel (MISFET) chemFET sensors employing spun-coated polymers. These devices have a thin silicon nitride gate insulator and showed a reduction in sensors response to ethanol vapour with increasing water concentration [7.2].

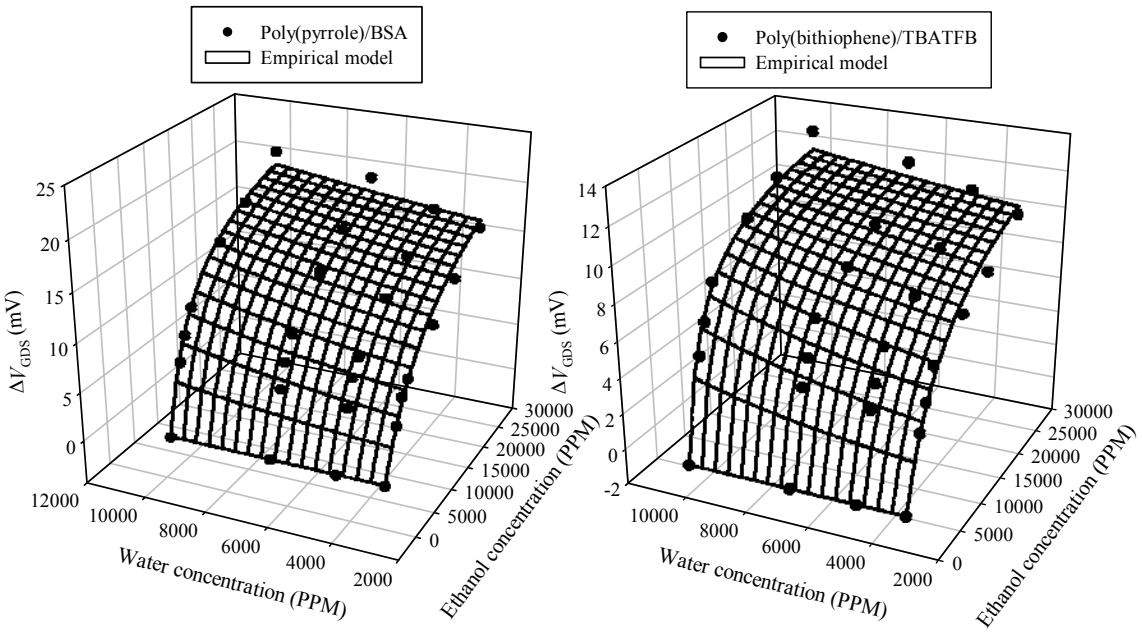

Figure 7.5: The effect of water concentration on the response of chemFET sensors employing in poly(pyrrole)/BSA and poly(bithiophene)/TBATFB polymer films to ethanol vapour in air at 30°C.

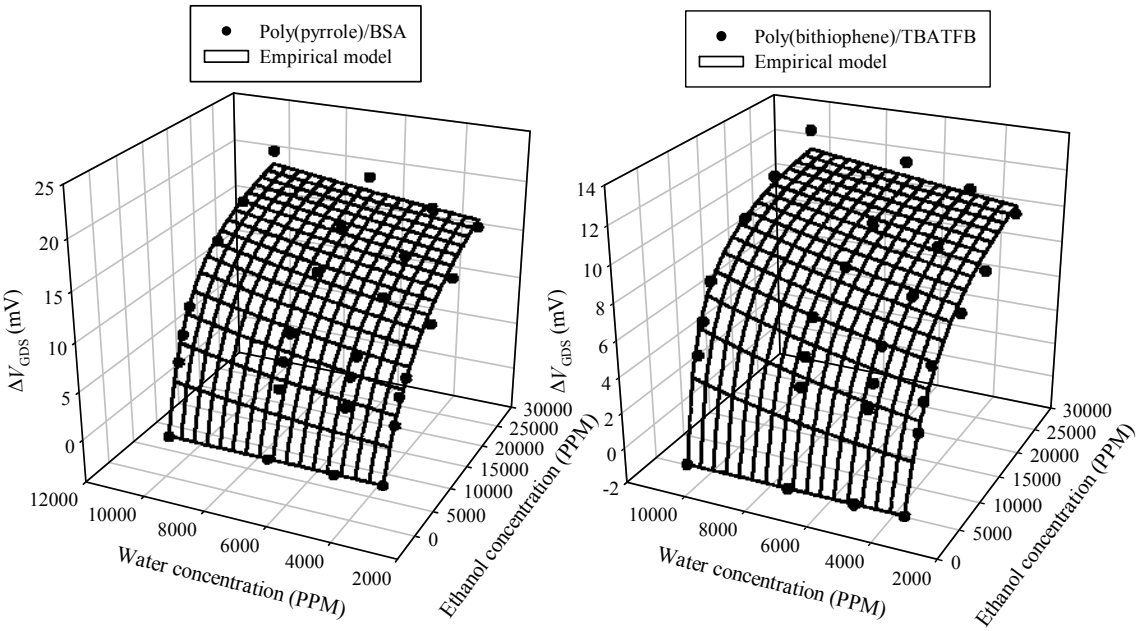

Figure 7.6: The effect of water concentration on the response of chemFET sensors employing poly(pyrrole)/BSA and poly(bithiophene)/TBATFB polymer films to toluene vapour in air at 30°C.

The modelling coefficients for expression (7.11) is given in table 7.5 and 7.6 below for ethanol and toluene vapour, respectively.

PPY	$a_E k_E \Gamma$ (mV/PPM)	$\pm\sigma_{aEkE\Gamma}$ (mV/PPM)	$a_W k_W \Gamma$ (mV/PPM)	$\pm\sigma_{aWkW\Gamma}$ (mV/PPM)	k_E (PPM^{-1})	$\pm\sigma_{kE}$ (PPM^{-1})	k_W (PPM^{-1})	$\pm\sigma_{kw}$ (PPM^{-1})	r^2
Sample 1	2.03E-03	2.07E-04	1.20E-05	4.01E-05	1.16E-04	1.48E-05	-4.21E-05	9.88E-06	0.973
Sample 2	2.52E-03	1.92E-04	2.52E-06	3.64E-05	1.03E-04	9.97E-06	-5.54E-05	6.03E-06	0.983
Sample 3	1.49E-03	1.52E-04	2.51E-05	5.61E-05	4.45E-05	7.52E-06	-5.89E-05	7.51E-06	0.962
Sample 4	2.65E-03	2.22E-04	-1.76E-05	4.32E-05	9.91E-05	1.07E-05	-5.29E-05	6.85E-06	0.98
Sample 5	1.25E-03	1.28E-04	-1.02E-05	4.12E-05	5.23E-05	8.34E-06	-5.32E-05	8.10E-06	0.967
Av.	1.98E-03	1.73E-04	2.07E-06	4.16E-05	8.21E-05	9.80E-06	-5.28E-05	7.33E-06	0.975
PBT	$a_E k_E \Gamma$ (mV/PPM)	$\pm\sigma_{aEkE\Gamma}$ (mV/PPM)	$a_W k_W \Gamma$ (mV/PPM)	$\pm\sigma_{aWkW\Gamma}$ (mV/PPM)	k_E (PPM^{-1})	$\pm\sigma_{kE}$ (PPM^{-1})	k_W (PPM^{-1})	$\pm\sigma_{kw}$ (PPM^{-1})	r^2
Sample 1	5.38E-04	5.00E-05	5.08E-06	1.35E-05	4.82E-05	6.64E-06	-7.71E-05	4.51E-06	0.963
Sample 2	2.03E-03	2.05E-04	-2.66E-06	1.88E-05	1.70E-04	2.04E-05	-6.94E-05	6.41E-06	0.971
Sample 3	1.94E-03	2.40E-04	-1.03E-05	3.77E-05	1.14E-04	1.76E-05	-6.01E-05	8.99E-06	0.955
Sample 4	2.12E-03	2.39E-04	9.52E-06	4.00E-05	1.32E-04	1.83E-05	-4.51E-05	1.06E-05	0.967
Sample 5	1.53E-03	1.24E-04	-7.04E-07	1.93E-05	1.11E-04	1.12E-05	-6.41E-05	5.46E-06	0.979
Av.	1.63E-03	1.72E-04	1.84E-07	2.59E-05	1.15E-04	1.48E-05	-6.32E-05	7.19E-06	0.967

Table 7.5: Modelling coefficients for the effect of water concentration on chemFET sensors employing poly(pyrrole)/BSA and poly(bithiophene)/TBATFB polymer films to ethanol vapour in air at 30 °C.

PPY	$a_T k_T \Gamma$ (mV/PPM)	$\pm\sigma_{aTkT\Gamma}$ (mV/PPM)	$a_W k_W \Gamma$ (mV/PPM)	$\pm\sigma_{aWkW\Gamma}$ (mV/PPM)	k_T (PPM^{-1})	$\pm\sigma_{kT}$ (PPM^{-1})	k_W (PPM^{-1})	$\pm\sigma_{kw}$ (PPM^{-1})	r^2
Sample 1	-4.37E-04	4.29E-05	-3.31E-05	2.44E-05	-3.07E-05	5.23E-06	-1.53E-05	5.38E-06	0.981
Sample 2	-4.58E-04	1.92E-05	-1.23E-05	9.96E-06	-2.40E-05	2.51E-06	-1.97E-05	2.52E-06	0.996
Sample 3	-4.44E-04	5.07E-05	-2.40E-05	3.19E-05	-2.08E-05	6.32E-06	-4.47E-05	6.64E-06	0.962
Sample 4	-4.45E-04	5.27E-05	-2.00E-05	3.29E-05	-1.99E-05	6.63E-06	-4.60E-05	6.96E-06	0.957
Sample 5	-4.52E-04	3.64E-05	-1.93E-05	2.10E-05	-2.01E-05	4.74E-06	-3.88E-05	4.79E-06	0.982
Av.	-4.47E-04	4.04E-05	-2.17E-05	2.40E-05	-2.31E-05	5.09E-06	-3.29E-05	5.26E-06	0.976
PBT	$a_T k_T \Gamma$ (mV/PPM)	$\pm\sigma$ $aTkT\Gamma$ (mV/PPM)	$a_W k_W \Gamma$ (mV/PPM)	$\pm\sigma_{aWkW\Gamma}$ (mV/PPM)	k_T (PPM^{-1})	$\pm\sigma_{kT}$ (PPM^{-1})	k_W (PPM^{-1})	$\pm\sigma_{kw}$ (PPM^{-1})	r^2
Sample 1	-5.13E-04	3.35E-05	-1.56E-05	2.04E-05	-2.81E-05	3.46E-06	-3.16E-05	3.54E-06	0.989
Sample 2	-8.30E-04	3.78E-05	-3.13E-06	1.82E-05	-1.66E-05	3.02E-06	-2.59E-05	2.94E-06	0.995
Sample 3	-4.32E-04	1.69E-05	-1.43E-07	1.03E-05	-3.26E-05	1.96E-06	-2.56E-05	2.00E-06	0.995
Sample 4	-5.81E-04	2.41E-05	-6.55E-06	1.35E-05	-2.55E-05	2.36E-06	-2.83E-05	2.36E-06	0.995
Av.	-5.89E-04	2.81E-05	-6.36E-06	1.56E-05	-2.57E-05	2.70E-06	-2.79E-05	2.71E-06	0.994

Table 7.6: Modelling coefficients for the effect of water concentration on chemFET sensors employing poly(pyrrole)/BSA and poly(bithiophene)/TBATFB polymer films to toluene vapour in air at 30 °C.

7.3 The effect of temperature on the static response of room temperature chemFET sensors

The effect of temperature on polymer based chemFET sensors has not been extensively studied by other researchers. Here we investigate the effect of temperature on the chemFET sensors employing both composite and electrochemically deposited polymer films. Four different operating temperatures (30 ^{o}C, 40 ^{o}C, 50 ^{o}C and 60 ^{o}C ± 0.1 ^{o}C), six different concentrations of ethanol and toluene vapour and four different concentrations of water vapour, in air, were used, to characterise the sensors relative baseline and response. Results of these tests are described in the following sections.

7.3.1 ChemFET sensors employing composite polymer films as the gate

Initial tests investigated the effect of temperature on the relative baseline. These experiments concerned both the solid and open gated MOSFET devices with composite polymer films. Results showed, for the solid gate MOSFET, that increasing temperature caused a rise in V_{GDS}. The open gate chemFET sensors showed the opposite effect with a decrease in $V_{GDS,}$ with increasing temperature. Figure 7.7 shows the effect of temperature on the baseline for open and closed gated devices. The solid gate results are the averaged response for all the composite polymer sensors as no pattern was discernible within the results. Both plots are the averaged results of a number of sensors taken from the extrapolated 0 ^{o}C value and show that the shift in V_{GDS} open gate devices is significant (> 150 times) in comparison to the closed gate results.

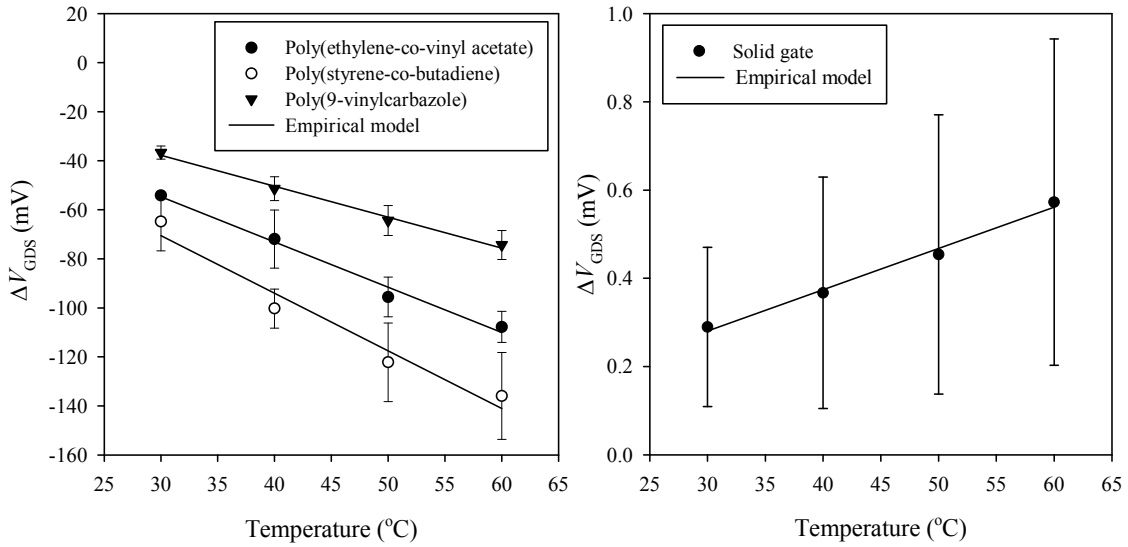

Figure 7.7: The shift in V_{GDS} for a chemFET with an open gate and solid gate to temperature between 30 – 60 °C at constant water concentration (4500 PPM).

To investigate the effects of temperature on the relative baseline it is useful to examine the equations that define the operation of a MOSFET. The standard equation for a standard solid metal gate *n*-channel MOSFET in the saturated regime is:

$$i_{DS} = g_m\left(V_{GDS} - V_T\right)^2 = \kappa \tag{7.12}$$

where V_{GDS} is the gate/drain voltage commoned to the source, V_T is the threshold voltage, κ is constant here and g_m is given by:

$$g_m = \mu_n C_{ox} \frac{W}{L} = a \tag{7.13}$$

where *W/L* are the channel width and length, μ_n is the carrier mobility and *a* is constant in our device. This effect of temperature can be investigated by solving:

$$\frac{dV_{GDS}}{dT} = \frac{dV_T}{dT} - \frac{\left(V_{GDS} - V_T\right)}{2g_m}\frac{dg_m}{dT} \tag{7.14}$$

If we first consider the effect of temperature on the baseline for a *n*-channel solid gate MOSFET, without a vapour sensitive layer, then the effect of the temperature on the threshold voltage is minimal $\left(\frac{dV_T}{dT} \approx 0\right)$ and so the temperature only effects the g_m term. Separating this term out we obtain:

$$\frac{dg_m}{dT} = \frac{W}{2L}\left[c'\frac{d\mu_n}{dT} + \mu_n\frac{dc'}{dT}\right] \tag{7.15}$$

Since the change in capacitance per unit area is weakly temperature dependant then, and using equation (7.12), then equation (7.15) reduces to:

$$\frac{dg_m}{dT} \approx \frac{g_m}{\mu_n}\frac{d\mu_n}{dT} \tag{7.16}$$

then,

$$\frac{dV_{GDS}}{dT} \approx \frac{-(V_{GDS} - V_T)}{2}\frac{d\ln\mu_n}{dT} \tag{7.17}$$

From well-known FET properties, we can state that the majority of the shift in V_{GDS} is due to a degredation in the carrier mobility (can be approximated to an exponential function) [7.3], as observed with the solid gate FETs. Hence the results have been modelled to the exponential expression:

$$\Delta V_{GDS} = \alpha \exp^{-T\beta} \tag{7.18}$$

where T is the temperature in Celsius and α and β are device parameters. The modelling coefficients for this expression to the observed results are given in table 7.7 below.

Solid gate	α (V)	$\pm \sigma_\alpha$ (V)	β ($^oC^{-1}$)	$\pm \sigma_\beta$ ($^oC^{-1}$)	r^2
Sample 1	1.00E-02	2.95E-05	1.07E-03	6.32E-05	0.993
Sample 2	1.61E-02	8.37E-05	6.86E-04	1.12E-04	0.95
Sample 3	1.47E-02	4.44E-05	9.24E-04	6.51E-05	0.99
Sample 4	6.16E-03	1.79E-05	7.59E-04	6.23E-05	0.987
Sample 5	1.29E-02	5.22E-05	1.64E-03	8.65E-05	0.994
Sample 6	7.50E-03	3.96E-05	7.09E-04	1.13E-04	0.951
Av.	1.12E-02	4.45E-05	9.63E-04	8.37E-05	0.978

Table 7.7: Modelling coefficients for the effect of temperature on the baseline of a solid gate chemFET sensor with a composite polymer coating.

Clearly, the observed decrease in baseline V_{GDS} for the open gate sensors with temperature, must be due to a different mechanism. Here the shift in V_{GDS} has been modelled to power expression, given by:

$$\Delta V_{GDS} = \alpha T^{\beta} \tag{7.19}$$

where α and β are polymer dependent components. Coefficients for this model are given in table 7.8, and for modelling purposes absolute values (without estimating at T = 0 ^oC) has been used. A possible explanation, for the observed result, is due to a thermal expansion of the carbon black/polymer composite material. This rise in temperature may cause a swelling within the polymer increasing the distance between the carbon spheres, altering the average work function of the composite polymer. Hence the swelling is related to the fractional coverage (f_C) of the device, i.e.:

$$\bar{\phi}_{PC} = f_C\phi_C + (1 - f_C)\phi_P \quad (7.20)$$

As the threshold voltage is directly related to the work function and we have observed a reduction in threshold voltage, then we have to assume a reduction in work function. Thus, if the thermal expansion of the polymer is greater than the carbon we can infer that the work function of the polymer is lower than carbon. This is shown in chapter 6 for poly(ethylene-co-vinyl acetate) and poly(styrene-co-butadiene). Alternatively the carbon expansion is greater than the polymer, and so the work function of the polymer is higher than that of carbon. A last possibility is that the increase in temperature may cause a thermal contraction within the polymer. If we assume the material is "stretched" at lower temperatures, as the temperature in increased the tension within the material is reduced and contraction occurs, bringing the carbon spheres closer together.

CP1	α (mV/^{o}C)	$\pm \sigma_\alpha$ (mV/^{o}C)	β	$\pm \sigma_\beta$	r^2
Sample 1	0.90	6.81E-02	-2.05E-01	2.02E-02	0.981
Sample 2	0.17	3.19E-03	2.84E-01	5.14E-03	0.999
Sample 3	1.16	5.52E-02	-1.03E-01	1.26E-02	0.971
Sample 4	0.77	1.20E-01	-1.61E-01	4.14E-02	0.881
Sample 5	1.18	5.84E-02	-1.05E-01	1.32E-02	0.969
Av.	0.84	6.10E-02	-5.80E-02	1.85E-02	0.960
CP2	α (mV/^{o}C)	$\pm \sigma_\alpha$ (mV/^{o}C)	β	$\pm \sigma_\beta$	r^2
Sample 1	1.24	6.71E-02	-1.01E-01	1.43E-02	0.961
Sample 2	1.41	8.42E-02	-1.34E-01	1.58E-02	0.973
Sample 3	1.26	4.34E-02	-1.74E-01	9.18E-03	0.994
Sample 4	1.20	8.14E-02	-1.62E-01	1.80E-02	0.976
Sample 5	1.19	8.30E-02	-1.57E-01	1.85E-02	0.973
Av.	1.26	7.63E-02	-1.43E-01	1.60E-02	0.980
CP3	α (mV/^{o}C)	$\pm \sigma_\alpha$ (mV/^{o}C)	β	$\pm \sigma_\beta$	r^2
Sample 1	5.21E-01	5.88E-02	-1.29E-01	3.00E-02	0.902
Sample 2	7.48E-01	2.01E-02	-1.01E-01	7.11E-03	0.99
Sample 3	7.40E-01	1.02E-02	-7.04E-02	3.66E-03	0.995
Sample 4	5.85E-01	1.54E-02	-1.57E-01	6.98E-03	0.996
Sample 5	6.32E-01	8.66E-03	-1.80E-01	3.64E-03	0.999
Av.	6.45E-01	2.26E-02	-1.27E-01	1.03E-02	0.976

Table 7.8: Modelling coefficients for the effect of temperature on the relative baseline of chemFET sensors employing composite polymer films at a fixed water concentration.

Further experiments investigated the effect of temperature on the response of chemFET sensors with composite polymer films to analyte concentration. Here an increase in temperature caused a significant reduction in response. Figure 7.8 and figure 7.9 show

the averaged effect of temperature on the chemFET sensors with composite polymer films to toluene and ethanol vapour in air, respectively.

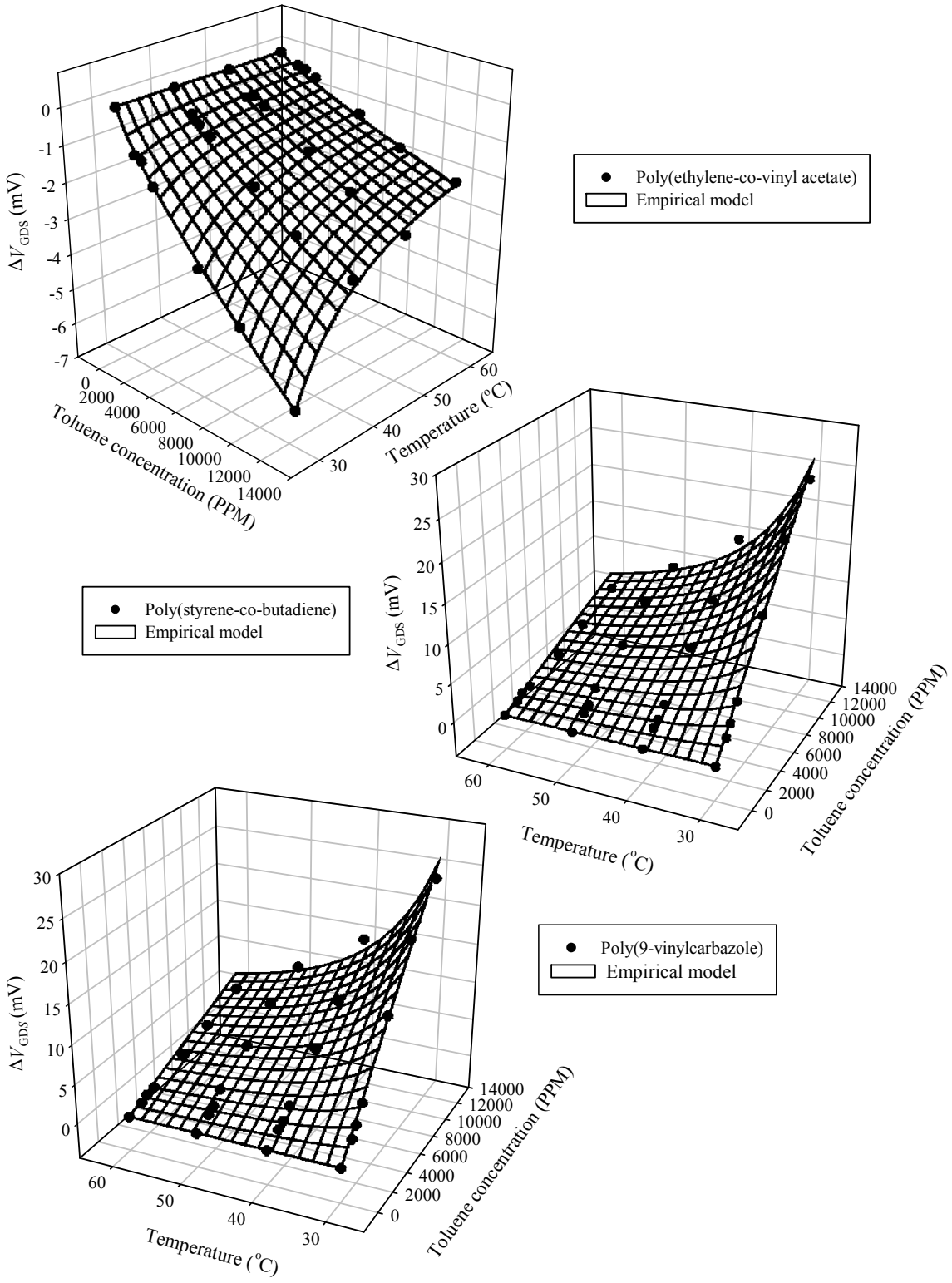

Figure 7.8: The effect of temperature on the response of chemFET sensors employing composite polymer films at a fixed water concentration of 4500 PPM to toluene vapour in air.

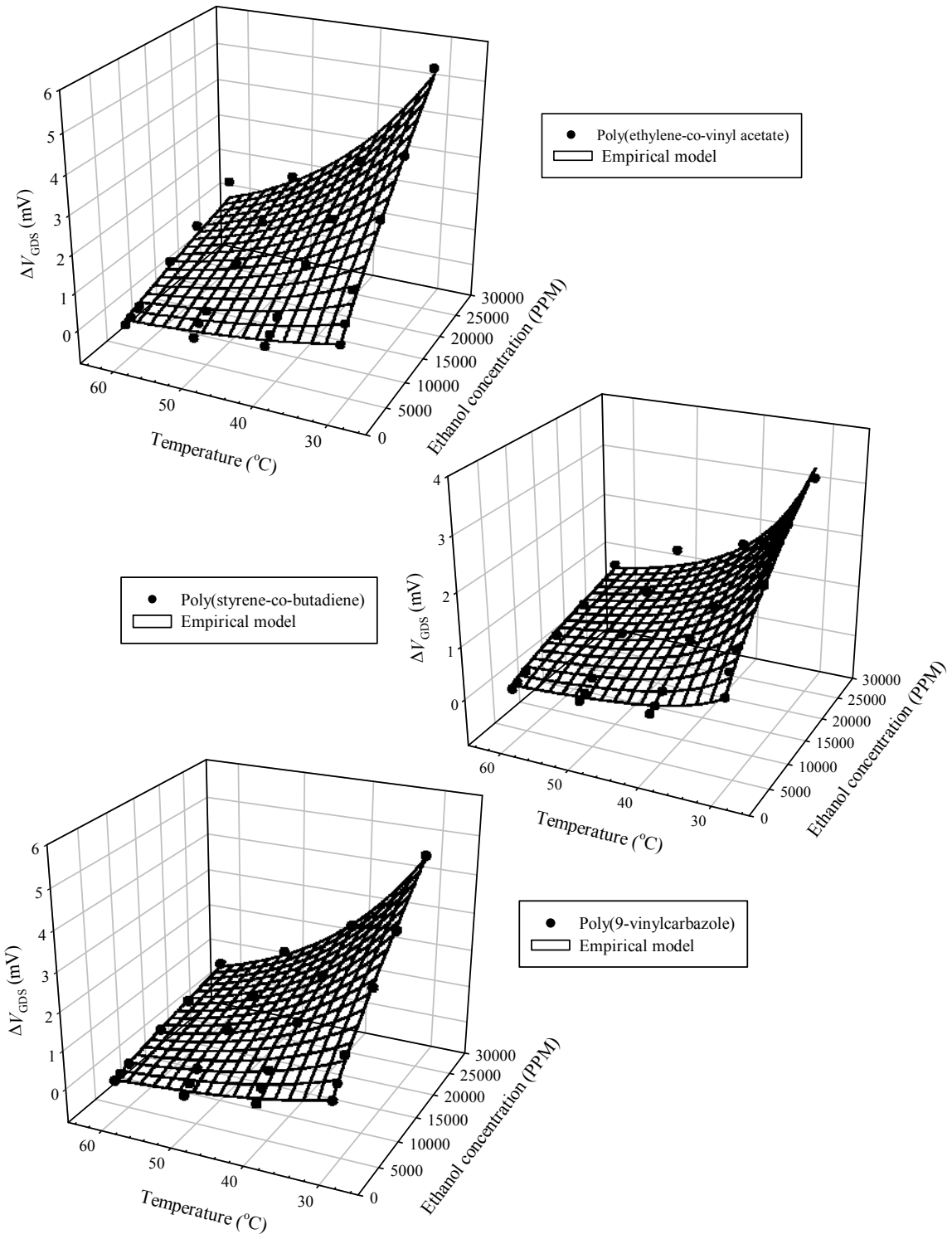

Figure 7.9: The effect of temperature on the response of chemFET sensors employing composite polymer film at a fixed water concentration of 4500 PPM to ethanol vapour in air.

A proposed mechanism, which could describe this reduction in sensor response with increasing temperature (at constant analyte concentration) is the analyte boiling point

model. [7.3]. If we consider a coefficient, $k_{p,g}$, defined as the volume of gas dissolved in 1 cm^3 at a partial pressure, c_i, for molecules i, the ratio of the concentration of the solvent in the polymer to the concentration in the same volume of gas can be expressed as:

$$k_{p,g} = \frac{c_{i,poly}}{c_{i,gas}} \tag{7.21}$$

This is more generally defined as [7.4]:

$$k_{p,g} = \frac{TR\rho_1}{\gamma_2 M_1 p_2} \tag{7.22}$$

where ρ_1 and M_1 are the density and molecular weight of the stationary phase, respectively, p_2 is the saturated vapour pressure of the solute vapour, γ_2 is the vapour activity coefficient and T is the temperature. Therefore at a given temperature $k_{p,g}$ is inversely proportional to p_2. In addition, this p_2 term can also be related to the analyte boiling point based on Trouton's rule and the Clausius-Clapeyron equation, by:

$$\log(p_2) \approx 7.7 - \frac{T_b t}{2.303RT} \tag{7.23}$$

where t is the Trouton constant for a particular vapour and R is the gas constant. Taking the logarithm equation (7.23) and combining and substituting into equation (7.22) yields:

$$\log(k_{p,g}) = \left[\log\left(\frac{RT}{\gamma_2}\right) - 7.7 + \log\left(\frac{\rho_1}{M_1}\right)\right] + \frac{T_b t}{2.303RT} \tag{7.24}$$

at a given temperature, where the term in the square brackets is simply a function of the polymer with the remaining parameter dependent on the analyte. For an ideal polymer-vapour solution the vapour activity is equal to 1, as this value falls an increased partition takes place in comparison to the volatility of the analyte. The boiling point of ethanol and toluene are 78.5 ^oC and 110.63 ^oC, respectively. The Trouton number varies between 80-120 $Jmol^{-1}K^{-1}$ depending upon the analyte involved, with values for ethanol and toluene reported of 110 $Jmol^{-1}K^{-1}$ and 120 $Jmol^{-1}K^{-1}$ [7.6], respectively, measured from experimental data. Expression (7.24) can be re-arranged to get:

$$\log(k_{p,g}) = \log\left(\frac{RT\rho_1}{\gamma_2 M_1 10^{7.7}}\right) + \frac{T_b t}{2.303RT} \tag{7.25}$$

Hence:

$$\log\left[\frac{k_{\mathrm{p,g}}}{\left(\frac{RT\rho_1}{\gamma_2 M_1 10^{7.7}}\right)}\right] = \frac{T_{\mathrm{b}}t}{2.303RT} \tag{7.26}$$

If we assume the polymer dependent temperature term is negligible in comparison to the analyte term also that the effect of temperature on the analyte term dominates over power term, then:

$$\frac{RT\rho_1}{\gamma_2 M_1 10^{7.7}} = a \tag{7.27}$$

Then we can approximate a to a constant, then:

$$\log\left(\frac{k_{\mathrm{p,g}}}{a}\right) = \frac{T_{\mathrm{b}}t}{2.303RT} \tag{7.28}$$

This shows the bulk solubility and so concentration of a solvent within a polymer reduces with increasing temperature. Hence, even if the concentration of analyte is constant, in the gas phase, the increase in temperature will reduce the vapour concentration within the polymer and so reduce the magnitude of the response. As the concentration of analyte in the vapour above the polymer is constant, then the shift in the threshold voltage can be approximated as:

$$V_{\mathrm{GDS}} \approx V_{\mathrm{GDS0}} + k' k_{\mathrm{p,g}} C_{\mathrm{g}} \tag{7.29}$$

where the shift in V_{GDS}, hence the threshold voltage, is a function of the absorbed analyte concentration (bulk solubility) and k' is the temperature dependant term. From the previous chapter the effect of analyte concentration on the response of chemFET sensors with polymer composite films was modelled as a power function, and from expression (7.28), the magnitude of the response will decrease as a power function of $1/T$. This simplified expression can now be used to model the effect of temperature on these chemFET sensors with composite polymer films, by:

$$\Delta V_{\mathrm{GDS}} \approx k' C_{\mathrm{g}}^{\alpha} 10^{\beta/\mathrm{T}} \tag{7.30}$$

where β is a vapour constant equal to:

$$\beta = \frac{T_b t}{2.303} \tag{7.31}$$

Expression (7.30) has been fitted to the observed data as shown in figure 7.8 and figure 7.9 with coefficients given in table 7.9 ad 7.10 for toluene and ethanol vapour, respectively. Here k' is replaced with the k_{T} and k_{E} for toluene and ethanol vapour.

Figure 7.10 shows a log plot of the response to toluene and ethanol vapour with temperature. Two conclusions can be drawn from these plots, initially the quality of the linear regression suggests that the log model is a good fit to the data with the analyte boiling point model being a mechanism that is consistent with the observed results. Secondly, that the gradients of the plots are similar. These comparable gradients suggest that the material variations and so temperature dependencies are small between the different polymers. Clearly, the exception to this is poly(9-vinylcarbazole) to ethanol vapour which shows a significantly different gradient to the other plots that could be related to the material polymer term being more significant.

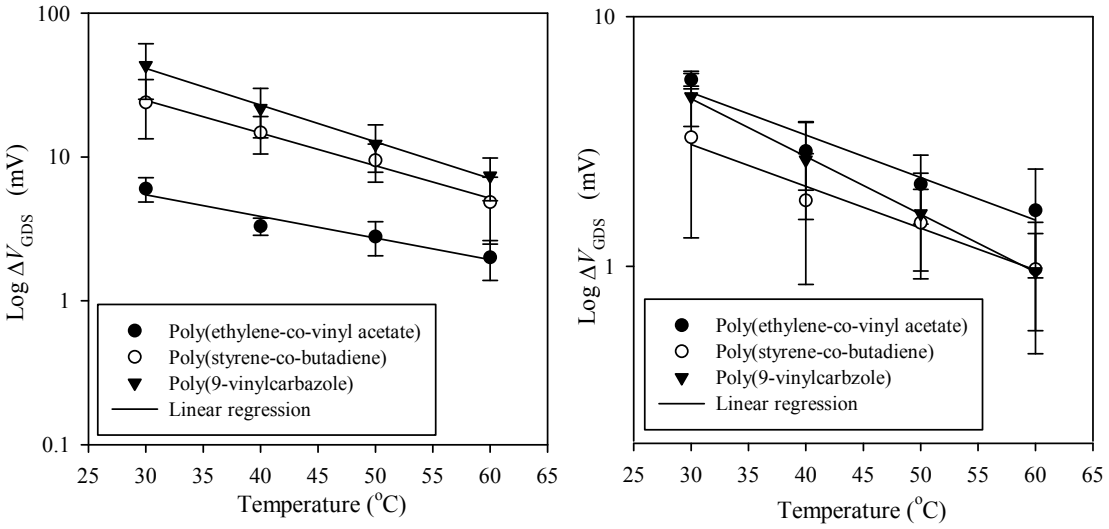

Figure 7.10: Modularised log plot of the effect of temperature on chemFET sensors employing composite polymer films at fixed toluene (left) and ethanol (right) vapour in air.

CP1	k_T (mV/PPM)	$\pm \sigma_{kT}$ (mV/PPM)	β (°C)	$\pm \sigma_\beta$ (°C)	α	$\pm \sigma_\alpha$	r^2
Sample 1	-2.47E-04	9.44E-05	31.00	1.51	0.83	4.04E-02	0.982
Sample 2	-2.53E-05	1.05E-05	30.20	1.32	1.05	4.38E-02	0.987
Sample 3	-1.49E-03	7.34E-04	14.40	1.86	0.75	5.28E-02	0.954
Sample 4	-2.77E-04	1.08E-04	31.80	1.58	0.81	4.10E-02	0.98
Sample 5	-3.11E-04	7.06E-05	27.30	0.86	0.83	2.41E-02	0.993
Av.	-4.70E-04	2.04E-04	26.90	1.43	0.85	4.04E-02	0.979
CP2	k_T (mV/PPM)	$\pm \sigma_{kT}$ (mV/PPM)	β (°C)	$\pm \sigma_\beta$ (°C)	α	$\pm \sigma_\alpha$	r^2
Sample 1	1.63E-05	1.32E-05	38.40	2.56	1.18	8.48E-02	0.967
Sample 2	9.31E-05	3.84E-05	54.00	2.16	0.91	4.15E-02	0.987
Sample 3	4.13E-04	2.81E-04	18.40	2.11	0.97	7.26E-02	0.953
Sample 4	2.83E-05	1.27E-05	42.80	1.56	1.16	4.69E-02	0.989
Sample 5	1.03E-04	5.05E-05	33.30	1.62	1.05	5.18E-02	0.982
Av.	1.31E-04	7.92E-05	37.40	2.00	1.05	5.95E-02	0.976
CP3	k_T (mV/PPM)	$\pm \sigma_{kT}$ (mV/PPM)	β (°C)	$\pm \sigma_\beta$ (°C)	α	$\pm \sigma_\alpha$	r^2

Sample 1	4.09E-05	2.52E-05	34.80	1.91	1.15	6.50E-02	0.976
Sample 2	1.17E-05	2.80E-06	61.50	1.18	1.15	2.43E-02	0.997
Sample 3	2.29E-04	9.28E-05	36.80	1.49	0.98	4.26E-02	0.986
Sample 4	1.57E-03	6.47E-04	32.00	1.72	0.78	4.34E-02	0.975
Sample 5	1.19E-03	4.44E-04	40.60	1.75	0.78	3.86E-02	0.983
Av.	6.09E-04	2.42E-04	41.20	1.61	0.97	4.28E-02	0.983

Table 7.9: Modelling coefficients for the effect of temperature on the response of chemFET sensors employing composite polymer films to toluene vapour in air at fixed water concentration, from expression (7.30).

CP1	k_E (mV/PPM)	$\pm \sigma_{kE}$ (mV/PPM)	β (°C)	$\pm \sigma_\beta$ (°C)	α	$\pm \sigma_\alpha$	r^2
Sample 1	5.29E-04	2.04E-04	20.10	1.38	7.53E-01	3.82E-02	0.977
Sample 2	1.93E-04	1.02E-04	30.70	2.02	7.80E-01	5.17E-02	0.965
Sample 3	4.32E-05	1.96E-05	37.90	1.75	8.83E-01	4.44E-02	0.982
Sample 4	1.49E-04	4.39E-05	31.30	1.12	8.01E-01	2.91E-02	0.989
Av.	2.28E-04	9.21E-05	30.00	1.56	8.04E-01	4.08E-02	0.978
CP2	k_E (mV/PPM)	$\pm \sigma_{kE}$ (mV/PPM)	β (°C)	$\pm \sigma_\beta$ (°C)	α	$\pm \sigma_\alpha$	r^2
Sample 1	1.86E-03	8.08E-04	43.10	2.54	4.81E-01	4.10E-02	0.963
Sample 2	8.77E-04	3.29E-04	30.70	1.72	5.86E-01	3.68E-02	0.972
Sample 3	1.16E-03	5.32E-04	13.50	1.74	6.66E-01	4.56E-02	0.956
Sample 4	1.11E-05	7.29E-06	14.90	1.78	1.02E+00	6.54E-02	0.964
Sample 5	7.80E-05	4.14E-05	24.30	1.79	8.43E-01	5.22E-02	0.967
Av.	5.32E-04	2.27E-04	20.90	1.76	7.79E-01	5.00E-02	0.965
CP3	k_E (mV/PPM)	$\pm \sigma_{kE}$ (mV/PPM)	β (°C)	$\pm \sigma_\beta$ (°C)	α	$\pm \sigma_\alpha$	r^2
Sample 1	8.19E-05	3.51E-05	34.90	1.64	8.38E-01	4.18E-02	0.981
Sample 2	1.65E-05	4.57E-06	53.90	1.48	7.96E-01	2.58E-02	0.993
Sample 3	1.97E-04	5.86E-05	36.70	1.31	7.19E-01	2.90E-02	0.988
Sample 4	3.64E-05	1.63E-05	36.60	1.66	8.97E-01	4.39E-02	0.98
Sample 5	1.92E-04	7.60E-05	58.10	2.71	5.81E-01	3.53E-02	0.981
Av.	1.10E-04	3.89E-05	46.30	1.79	7.48E-01	3.35E-02	9.86E-01

Table 7.10: Modelling coefficients for the effect of temperature on the response of chemFET sensors employing composite polymer films to ethanol vapour in air at fixed water concentration, from expression (7.30)..

The last measured temperature dependence is how increasing temperature effects the chemFET sensors relative baseline with water concentration. By simple observation it was found that the baseline water dependency reduced with increasing temperature. This can also explained by the boiling point model, where the temperature effects the concentration of water vapour within the polymer and so at the gate oxide. Hence, if we consider:

$$V_{GDS} = V_{GDS0} + \frac{\alpha a_W k_W k_{p,w} C_W}{1 + a_W k_W k_{p,w} C_W} \quad (7.32)$$

where $k_{p,w}$ is the partition coefficient for water and only considering the change in V_{GDS} and applying expression (7.28), we get.

$$\Delta V_{GDS} = \frac{\alpha a_W k_W 10^{\left(\frac{\beta}{T}\right)} C_W}{1 + a_W k_W 10^{\left(\frac{\beta}{T}\right)} C_W} \tag{7.33}$$

where T is the temperature in degrees Celsius. Alternatively, there may be a further effect of temperature simply on the binding coefficient between the gate oxide and water that follow similar characteristics to those observed. Figure 7.11 shows the effect of temperature on the water dependency for chemFET sensors employing poly(ethylene-co-vinyl acetate) and poly(styrene-co-butadiene) with the data fitted to equation (7.33).

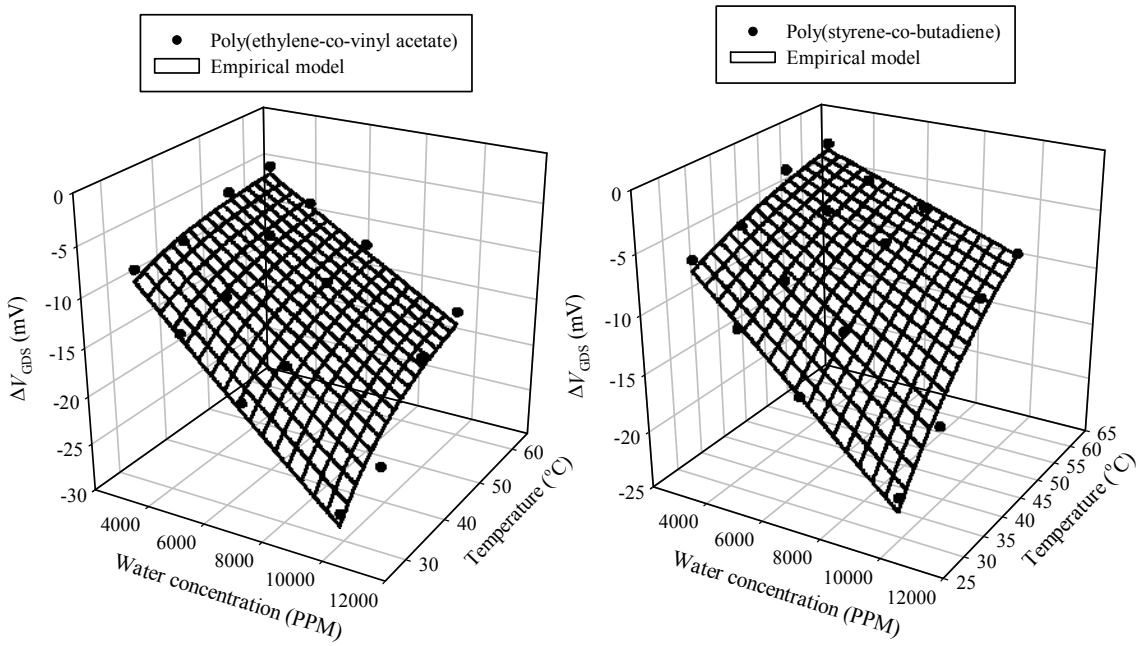

Figure 7.11: The effect of temperature on the water dependence on the relative baseline for chemFET sensors employing poly(ethylene-co-vinyl acetate) and poly(styrene-co-butadiene) polymer films.

The modelling coefficients for the effect of temperature and water concentration on the baseline are shown in table 7.11 below.

CP1	$\alpha a_w k_w$ (mV/PPM)	$\pm\sigma_{\alpha awkw}$ (mV/PPM)	$a_W k_W$ (PPM^{-1})	$\pm\sigma_{aWkW}$ (PPM^{-1})	β (°C)	$\pm\sigma_\beta$ (°C)	r^2
Sample 1	-1.30E-03	1.37E-04	3.07E-06	3.85E-06	15.90	2.08	0.965
Sample 2	-8.91E-04	8.42E-05	2.80E-06	5.25E-06	9.91	1.63	0.983
Sample 3	-8.53E-04	2.10E-04	2.07E-05	6.56E-06	25.00	5.12	0.878
Sample 4	-9.73E-04	6.84E-05	1.78E-05	5.19E-06	6.30	1.11	0.982
Sample 5	-1.05E-03	1.07E-04	9.99E-06	4.77E-06	13.10	1.87	0.965
Av.	-9.43E-04	1.17E-04	1.28E-05	5.45E-06	13.60	2.43	0.952
CP2	$\alpha a_w k_w$ (mV/PPM)	$\pm\sigma_{\alpha awkw}$ (mV/PPM)	$a_W k_W$ (PPM^{-1})	$\pm\sigma_{aWkW}$ (PPM^{-1})	β (°C)	$\pm\sigma_\beta$ (°C)	r^2
Sample 1	-7.64E-04	8.68E-05	3.40E-06	3.90E-06	16.70	2.26	0.961
Sample 2	-5.78E-04	4.92E-05	6.25E-06	2.31E-06	19.70	1.73	0.98
Sample 3	-8.68E-04	9.44E-05	3.16E-06	4.92E-06	13.10	2.04	0.958
Sample 4	-2.69E-04	4.83E-05	9.35E-06	1.68E-06	37.10	3.81	0.961
Sample 5	-1.25E-03	1.58E-04	2.68E-05	8.86E-06	8.92	2.13	0.94
Av.	-7.41E-04	8.75E-05	1.14E-05	4.44E-06	19.70	2.43	0.960

Table 7.11: Modelling coefficients for the effect of temperature on the relative baseline for chemFET sensors employing poly(ethylene-co-vinyl acetate) and poly(styrene-co-butadiene) polymer films.

It is interesting to note that both log terms for poly(ethylene-co-vinyl acetate) and poly(styrene-co-butadiene) using this expression show very similar values, suggesting that the analyte term dominates over the polymer term.

From the previous section we can now combine the effects of analyte concentration, water concentration and temperature on the response of the chemFET sensors with composite polymer films to form a final expression:

$$V_{GDS} \approx \alpha T^{-\beta} V_{GDS0} + k_T' k_{p,g} C_T + \frac{\gamma k_w' k_{p,w} C_w}{\left(1 + k_w' k_{p,w} C_w\right)} \qquad (7.34)$$

for toluene and:

$$V_{GDS} \approx \alpha T^{-\beta} V_{GDS0} + k_E' k_{p,g} C_E + \frac{\gamma k_w' k_{p,w} C_w}{\left(1 + k_w' k_{p,w} C_w\right)} \qquad (7.35)$$

for ethanol, with the water dependent term neglected for poly(9-vinylcarbazole).

7.3.2 ChemFET sensors employing electrochemically deposited polymer films as the gate

Previous studies, with resistive sensors, employing electrochemically deposited polymers have shown a reduction in sensor response with increasing temperature [7.6], as described in chapter 2.

If we first consider the shift in relative baseline with increasing temperature, for chemFET sensors with an electrochemically deposited films, with both solid and open gates we see a reduction in V_{GDS}. Here the shift in the relative baseline has been evaluated from an estimated temperature at 0 ^{o}C, as shown in figure 7.12, for the averaged response. It was found that the solid gate devices showed similar temperature dependencies to the open gate devices and have been grouped for convenience.

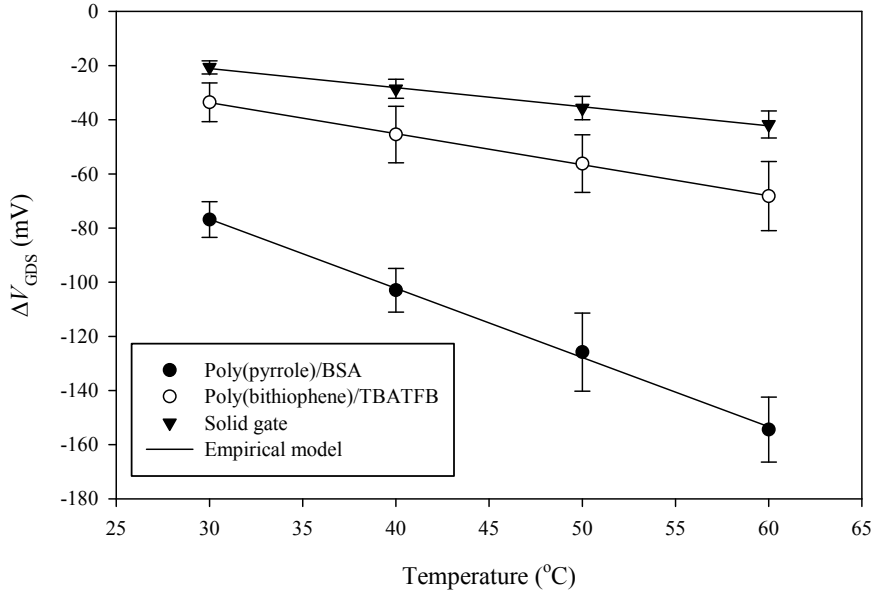

Figure 7.12: The shift in V_{GDS} for an open and solid gate chemFET sensor with electrochemically deposited polymer film to temperature at fixed water concentration.

Here all the results have been fitted to power expression (using the absolute data), given by:

$$\Delta V_{GDS} = \alpha T^{-\beta} \qquad (7.36)$$

The modelling coefficients for expression (7.36) are given in table 7.12 below.

PPY	α (mV/^{o}C)	$\pm \sigma_\alpha$ (mV/^{o}C)	β	$\pm \sigma_\beta$	r^2
Sample 1	1.25	4.46E-02	-1.39E-01	9.44E-03	0.991
Sample 2	1.44	5.55E-02	-1.44E-01	1.02E-02	0.99
Sample 3	1.06	1.63E-01	-2.20E-01	4.08E-02	0.936
Sample 4	1.24	7.53E-02	-1.60E-01	1.61E-02	0.98
Sample 5	1.30	8.76E-02	-1.50E-01	2.54E-02	0.99
Av.	1.26	8.51E-02	-1.63E-01	2.04E-02	0.977
PBT	α (mV/^{o}C)	$\pm \sigma_\alpha$ (mV/^{o}C)	β	$\pm \sigma_\beta$	r^2
Sample 1	2.46E-01	7.94E-03	1.37E-01	8.48E-03	0.992
Sample 2	9.96E-01	8.88E-03	3.74E-02	2.35E-03	0.992

Sample 3	4.14E-01	8.52E-03	7.76E-02	5.43E-03	0.99
Sample 4	5.56E-01	2.09E-02	7.51E-02	9.89E-03	0.967
Av.	9.77E-01	5.57E-02	-6.48E-02	1.48E-02	0.981
Solid gate	α (mV/^{o}C)	$\pm \sigma_{\alpha}$ (mV/^{o}C)	β	$\pm \sigma_{\beta}$	r^2
Sample 1	3.96E-01	3.37E-02	-4.28E-01	2.29E-02	0.994
Sample 2	3.49E-01	2.58E-02	-3.96E-01	1.98E-02	0.995
Sample 3	2.66E-01	2.21E-02	-3.78E-01	2.22E-02	0.993
Sample 4	3.16E-01	3.14E-02	-3.70E-01	2.66E-02	0.99
Sample 5	3.50E-01	3.49E-02	-3.97E-01	2.67E-02	0.991
Av.	3.35E-01	2.96E-02	-3.94E-01	2.36E-02	0.993

Table 7.12: Modelling coefficients for the effect of temperature on the relative baseline of chemFET sensors employing poly(pyrrole)/BSA and poly(bithiophene)/TBATFB polymer films at fixed water concentration.

The magnitude of the baseline shift is similar to the chemFET sensors with composite polymers. This effect may also be due to thermal expansion of the polymer, where this expansion alters the polymer/air ratio and so the average work function. The solid gate results are interesting as it responds in the opposite direction to the composite polymer solid gate devices, possible suggesting that either the polymer is interacting with the gold or some the polymer is contact with some of the gate oxide due to inconsistencies in the gold film.

Further experiments examined the effect of temperature on the magnitude of the response. Considering ethanol vapour first, we see a reduction in V_{GDS} with increasing temperature, as shown in figure 7.13.

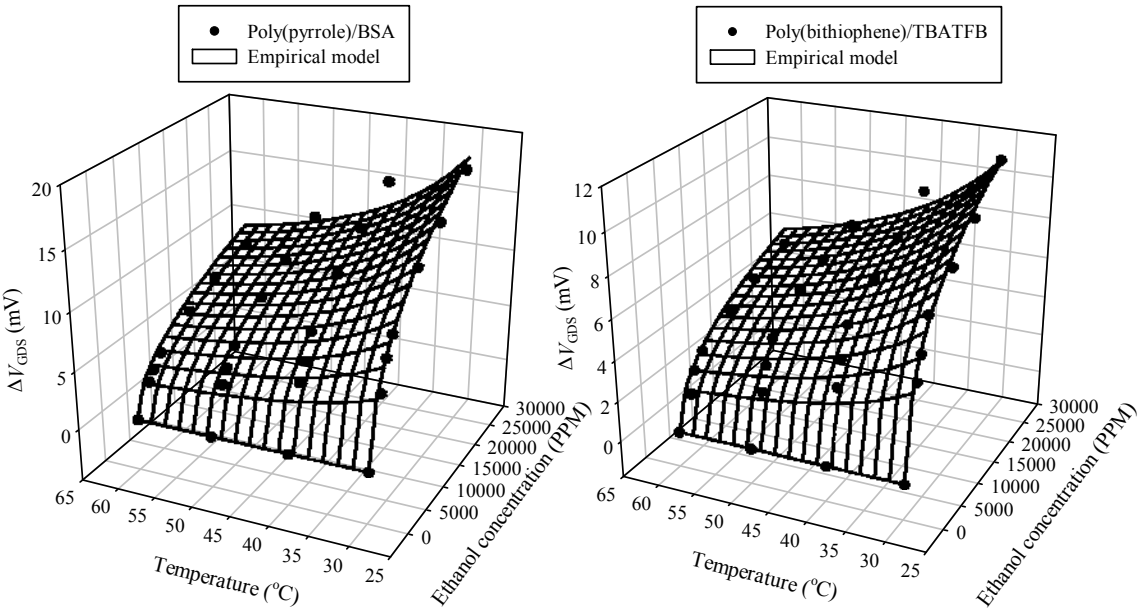

Figure 7.13: The effect of temperature chemFET sensors employing electrochemically deposited polymer films to ethanol vapour in air at fixed water concentration (4500 PPM).

For toluene, initially a similar effect was observed with a small reduction in response between 30 °C and 40 °C. Once this temperature was surpassed the response of the sensors either reduced to a negligible level or became inverted. Figures 7.14 shows the response of chemFET sensors with poly(pyrrole)/BSA and poly(bithiophene)/TBATFB at 40 °C and 50 °C.

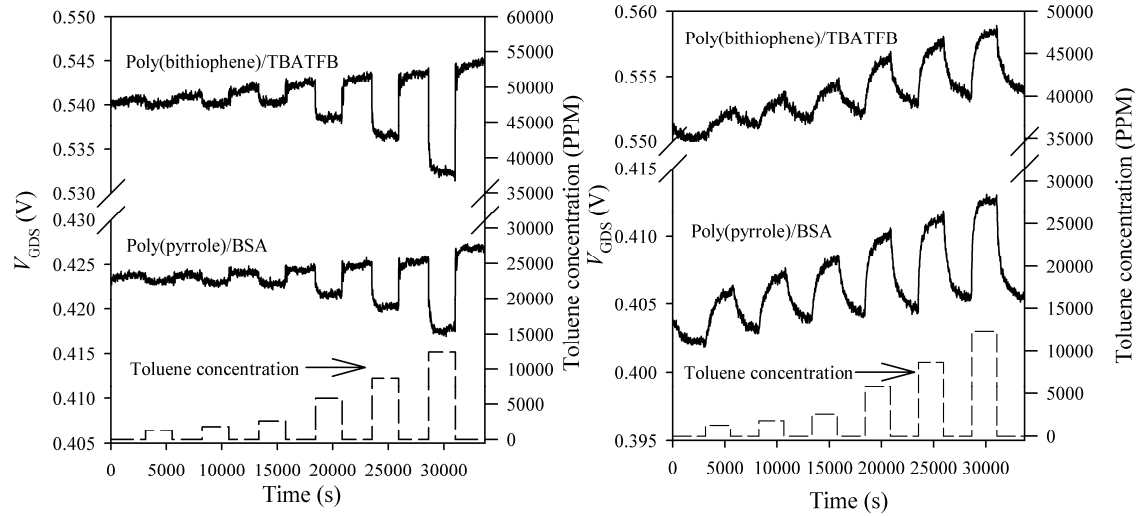

Figure 7.14: The response of chemFET sensors employing electrochemically deposited polymer films to toluene vapour in air at fixed water concentration (4500 PPM) at fixed temperature of 40°C (left) and 50°C (right).

Once the temperature was reduced it was found that this inversion of sensor response was permanent. Clearly, the increase in temperature caused some chemical reaction

within the polymer, effecting different absorption sites to the ethanol vapour, possibly due to some oxidation by the toluene vapour.

As stated earlier, an increase in temperature for electrochemically deposited polymers caused a reduction in response for a fixed ethanol concentration over the measured temperature range. As with the chemFET sensors with composite polymer films, this reduction could be explained by the analyte boiling point models. This mechanism is a simple thermodynamic effect stated in expression (7.21) to (7.31). If we assume a modified Langmuir isotherm response to ethanol concentration, then we can re-write the shift in threshold voltage to ethanol vapour as:

$$\Delta V_T = \frac{\alpha a_E k_{P,G} k_E \sqrt{C_E}}{1 + k_{P,G} k_E \sqrt{C_E}} \approx \frac{\alpha a_E 10^{\left(\frac{\beta}{T}\right)} k_E \sqrt{C_E}}{1 + a_E 10^{\left(\frac{\beta}{T}\right)} k_E \sqrt{C_E}} \qquad (7.37)$$

at constant water concentration. This is clearly a simplified solution as the interaction between the polymer and the analyte will also be temperature dependent but here it is assumed to be a negligible. Table 7.13 give the modelling coefficients for expression (7.37) for poly(pyrrole)/BSA and poly(bithiophene)/TBATFB to ethanol vapour.

PPY	$\alpha a_E k_E$ (mV/PPM)	$\pm\sigma_{\alpha aEkE}$ (mV/PPM)	$a_E k_E$ (PPM^{-1})	$\pm\sigma_{aEkE}$ (PPM^{-1})	β (^oC)	$\pm\sigma_\beta$ (^oC)	r^2
Sample 1	2.61E-02	1.78E-03	4.48E-04	1.23E-04	19.90	1.43	0.977
Sample 2	2.63E-02	3.96E-03	4.90E-04	1.53E-04	26.50	3.21	0.931
Sample 3	3.38E-02	4.51E-03	5.32E-04	2.14E-04	21.40	2.81	0.921
Sample 4	4.51E-02	5.02E-03	-7.27E-04	4.50E-04	7.67	1.79	0.919
Sample 5	3.35E-02	4.04E-03	3.99E-04	2.24E-04	19.50	2.51	0.945
Av.	3.30E-02	3.86E-03	2.28E-04	2.33E-04	19.00	2.35	0.939
PBT	$\alpha a_E k_E$ (mV/PPM)	$\pm\sigma_{\alpha aEkE}$ (mV/PPM)	$a_E k_E$ (PPM^{-1})	$\pm\sigma_{aEkE}$ (PPM^{-1})	β (^oC)	$\pm\sigma_\beta$ (^oC)	r^2
Sample 1	1.65E-02	3.18E-03	5.76E-04	4.78E-04	16.40	3.86	0.901
Sample 2	1.61E-02	1.92E-03	8.41E-04	1.29E-04	28.70	2.59	0.958
Sample 3	5.70E-02	8.26E-03	1.61E-03	5.59E-04	12.10	2.64	0.9
Sample 4	8.91E-03	1.53E-03	2.82E-04	6.58E-05	36.40	3.55	0.952
Sample 5	2.12E-02	2.43E-03	7.87E-04	1.81E-04	22.60	2.43	0.946
Av.	2.39E-02	3.46E-03	8.19E-04	2.82E-04	23.20	3.01	0.931

Table 7.13: Modelling coefficients for the effect of temperature on the response chemFET sensors employing poly(pyrrole)/BSA and poly(bithiophene)/TBATFB polymer films to ethanol vapour in air.

The log term coefficient in this expression shows a small variation between poly(pyrrole)/BSA and poly(bithiophene)/TBATFB. A possible reason for this variation is due to the material property term, though it is interesting to note that the

magnitude of this log term is similar to the composite polymers. The fit for the chemFET sensors with electrochemically deposited polymers is not as good as the composite polymers, though the general trend suggests an analyte boiling point model. It is likely that further temperature dependent mechanisms are occurring within the polymers that are not accounted for by this simple model.

The last measured parameter is the effect of temperature on the water dependence on the relative baseline for chemFET sensor with electrochemically deposited polymer films. It was found that as the temperature was increased the effect of water concentration on the baseline reduced, as observed for the chemFET sensor with, composite polymer films and was fitted to equation (7.33) as described earlier, shown in figure 7.15. Also given in table 7.14 are the coefficients for this model.

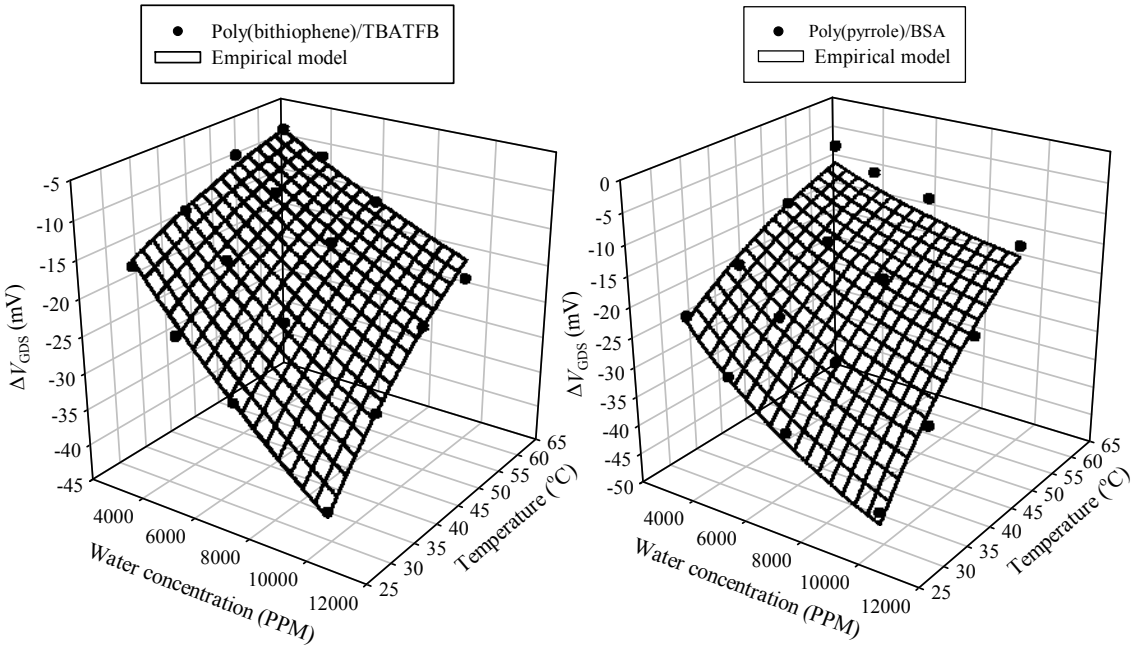

Figure 7.15: The effect of temperature on the water dependency on the baseline of chemFET sensors employing electrochemically deposited polymer films.

PPY	$\alpha a_w k_w$ (mV/PPM)	$\pm\sigma_{\alpha awkw}$ (mV/PPM)	$a_w k_w$ (PPM^{-1})	$\pm\sigma_{awkw}$ (PPM^{-1})	β (^oC)	$\pm\sigma_\beta$ (^oC)	r^2
Sample 1	-6.92E-04	8.75E-05	9.88E-06	1.29E-06	35.70	2.67	0.979
Sample 2	-1.49E-03	5.13E-04	1.52E-05	5.20E-06	34.40	7.43	0.866
Sample 3	-1.25E-06	1.53E-06	5.78E-08	8.11E-08	161.00	23.70	0.925
Sample 4	-6.43E-04	1.89E-04	1.02E-05	2.70E-06	41.20	6.34	0.924
Av.	-7.06E-04	1.98E-04	8.83E-06	2.32E-06	68.00	10.00	0.924

PBT	$\alpha a_w k_w$ (mV/PPM)	$\pm\sigma_{\alpha awkw}$ (mV/PPM)	$a_w k_w$ (PPM^{-1})	$\pm\sigma_{awkw}$ (PPM^{-1})	β (^oC)	$\pm\sigma_\beta$ (^oC)	r^2
Sample 1	-1.80E-03	1.23E-04	7.55E-06	1.79E-06	20.30	1.39	0.987
Sample 2	-7.22E-04	1.98E-04	8.91E-06	2.80E-06	33.90	5.69	0.909
Sample 3	-8.11E-04	6.65E-05	8.17E-06	3.67E-06	13.70	1.54	0.976
Sample 4	-1.19E-03	1.13E-04	1.12E-05	2.34E-06	21.90	1.93	0.978
Av.	-1.13E-03	1.25E-04	8.96E-06	2.65E-06	22.40	2.64	0.963

Table 7.14: Modelling coefficients for the effect of temperature and water concentration (3000 PPM – 9853 PPM) on the baseline for poly(pyrrole)/BSA and poly(bithiophene)/TBATFB.

Here the log term shows a significant variation between the two electrochemically deposited polymers as well as the composite polymers. This suggests that the material properties, for water dependency, are significant in comparison to the water properties or some further mechanism is occurring, possible altering the hydrophilic nature of the polymer/gate oxide interface.

We can now write the full expression for the effects of analyte concentration, water concentration and temperature on these chemFET sensors employing electrochemical polymers, as:

$$\Delta V_{GDS} \approx \alpha T^{-\beta} V_{GDS0} + \frac{\gamma\left(k_w k_{p,w} C_w + k_E k_{p,g} C_E\right)}{\left(1 + k_w k_{p,w} C_w + k_E k_{p,g} C_E\right)} \qquad (7.38)$$

Clearly, this expression is only valid for chemFET sensors to ethanol vapour as the effects of temperature for toluene vapour can produce an inversion in sensor response.

7.4 Response and comparison to chemFET sensors of resistive composite polymer sensors to analyte concentration, water concentration and temperature.

To further investigate the possible mechanisms behind chemFET sensors, a number of resistive devices were tested. Here only one polymer was used poly(styrene-co-butadiene) deposited by Cyrano Sciences (USA), based on the second recipe described in chapter 4. As this used a slightly different composite mix (0.625% solids in comparison to the original 0.5% solids) further chemFET sensors were tested, where possible, with this recipe.

7.4.1 The effect of analyte concentration on resistive sensor response

Initial tests surrounded the testing of these resistive sensors to ethanol and toluene vapour in air. In both cases sensors showed a positive shift in resistance with analyte concentration. These absolute responses are shown in figure 7.16. To calculate this resistance the sensors were operated at a constant current of 10 μA and the voltage drop over the sensors measured.

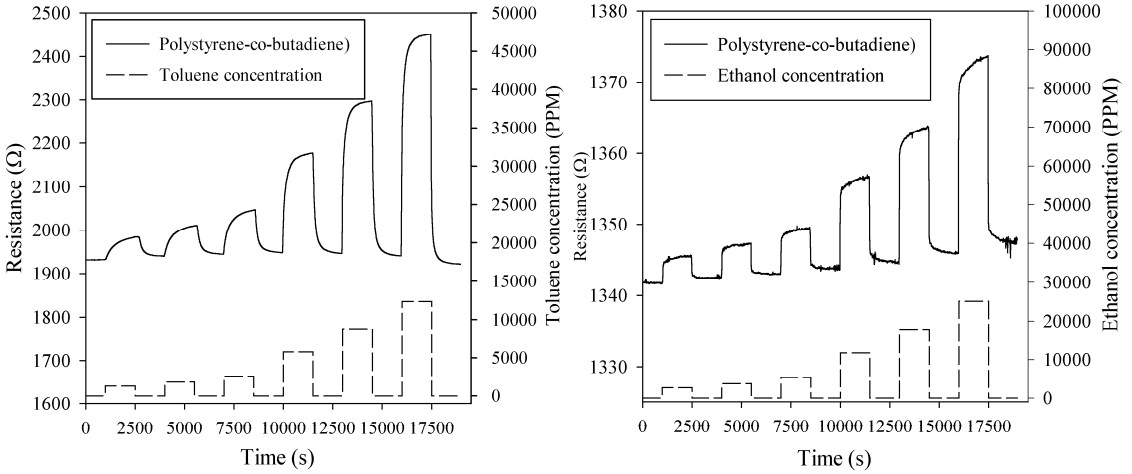

Figure 7.16: Dynamic responses of resistive composite sensors to ethanol and toluene vapour in air at constant temperature and water concentration (30 ^{o}C and 4500 PPM)

Here the effects of toluene and ethanol vapour on static response of these resistive sensors are shown in figure 7.17.

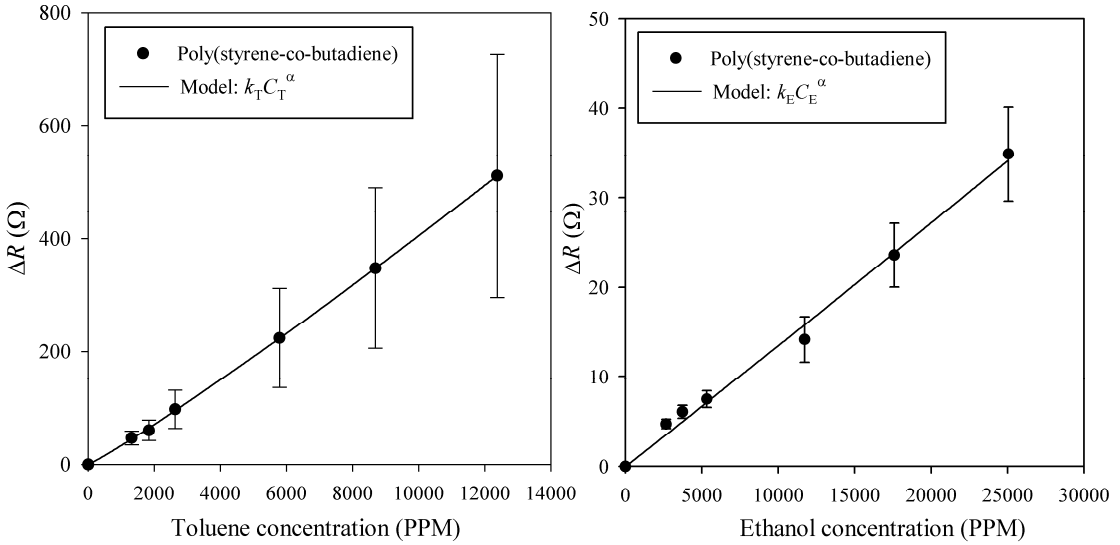

7.17: Static response of resistive devices to toluene and ethanol vapour in air at constant temperature and water concentration (30 ^{o}C and 4500 PPM)

As with the chemFET sensors employing composite polymer films the response was fitted to a power law model given by:

$$\Delta R = k_T C_T^{\alpha} \quad (7.38)$$

where R is the resistance of the sensor, k_T is a binding coefficient and C_T is the toluene concentration. A similar expression can be used for the effects of ethanol with the appropriate binding coefficient. The modelling coefficients for this expression is given in table 7.15 below.

Toluene	k_T (Ω/PPM)	$\pm\sigma_{kT}$ (Ω/PPM)	α	$\pm\sigma_\alpha$	r^2
Sample 1	1.69E-02	1.93E-03	1.08	1.24E-02	0.999
Sample 2	2.14E-02	2.35E-03	1.01	1.20E-02	0.999
Sample 3	1.01	1.20E-02	1.14	1.63E-02	0.999
Sample 4	2.21E-02	1.52E-03	1.06	7.48E-03	0.999
Sample 5	1.81E-02	1.68E-03	1.09	1.01E-02	0.999
Av.	2.17E-01	3.89E-03	1.08	1.16E-02	0.999
Ethanol	k_E (Ω/PPM)	$\pm\sigma_{kE}$ (Ω/PPM)	α	$\pm\sigma_\alpha$	r^2
Sample 1	1.80E-03	8.93E-04	9.83E-01	5.04E-02	0.995
Sample 2	1.23E-03	9.90E-04	9.87E-01	8.02E-02	0.987
Sample 3	1.95E-03	1.55E-03	9.63E-01	8.07E-02	0.986
Sample 4	1.15E-03	7.73E-04	1.03	6.79E-02	0.992
Sample 5	1.50E-03	1.01E-03	9.91E-01	6.80E-02	0.991
Av.	1.53E-03	1.04E-03	9.90E-01	6.94E-02	0.990

Table 7.15: Modelling coefficients for resistive composite polymer sensor to toluene and ethanol at fixed temperature and water concentration (30 ^oC / 4500 PPM water).

An interesting measurement is to compare the response of the resistive sensors to the chemFET sensors employing the same composite polymers. To get a fair comparison we can look at the sensitivity of each type of sensor. This sensitivity can be defined as:

$$\frac{\Delta V_{GDS}}{V_{GDS(0)}} \text{ and } \frac{\Delta R}{R_0} \quad (7.39)$$

for chemFET sensors and resistive sensors, respectively. $V_{GDS(0)}$ and R_0 are the baseline values of the sensors before exposure to a reactive analyte. Table 7.16 gives the sensitivities for resistive and chemFET sensors to toluene and ethanol vapour.

$\frac{\Delta R}{R}$ **(×10^6)**	Sample 1	Sample 2	Sample 3	Sample 4	Sample 5	Av.
Toluene sensitivity	24.09	20.70	16.68	35.96	19.23	23.33
Standard deviation	2.09	1.45	0.73	5.64	1.16	7.55
Ethanol sensitivity	1.09	1.48	1.34	1.48	1.22	1.32
Standard deviation	0.15	0.41	0.40	0.40	0.31	0.17
$\frac{\Delta V_{GDS}}{V_{GDS}}$ **(×10^6)**	Sample 1	Sample 2	Sample 3	Sample 4	Av.	
Toluene sensitivity	1.02	3.77	47.58	49.42	25.45	
Standard deviation	0.12	0.33	7.87	10.45	26.65	
Ethanol sensitivity	0.75	0.51	0.76	1.18	0.66	
Standard deviation	0.29	0.20	0.28	0.51	0.28	

Table 7.16: Sensitivity values for resistive and chemFET sensors employing poly(styrene-co-butadiene) for toluene and ethanol vapour in air

These results show a large variation in sensitivity. This is especially prominent for the chemFET sensors. It was found that, though the absolute sensor response was similar, the baseline value varied radically between 0.7 – 0.08 volts, causing large variation in sensitivities, possible due to inconsistencies within the polymer. Comparing resistive to chemFET sensors, the sensitivity was smaller for toluene vapour and greater for ethanol vapour.

7.4.2 The effect of water concentration on static sensor response of resistive devices

As with the chemFET sensors, the resistive sensors were exposed to four different water concentrations (3000, 4500, 6570, 9853 PPMs of water) using the same regime as applied to the chemFET sensors. The effect of water concentration was measured on both the baseline and on the magnitude of the response to toluene and ethanol vapour. It was found that water concentration had only a negligible effect on the baseline of these resistive sensors. This adds weight to the proposed explanation for the effect of water vapour on the baseline of the chemFET sensors as a device limitation, independent of these active material.

Furthermore, the resistive sensors showed no measurable variation in response with water concentration, as shown in figure 7.18. Here an independent model has been used where the effects of water concentration and analyte concentration are assumed to be independent (with the water term approximated to linear), as:

$$\Delta R \approx k_T C_T^{\alpha} + k_w C_w \qquad (7.40)$$

where k_T is replaced with k_E for ethanol. This shows the same characteristics as the chemFET sensors, suggesting that this is a material property. Table 7.17 gives the modelling coefficients for these resistive devices to both toluene and ethanol vapour.

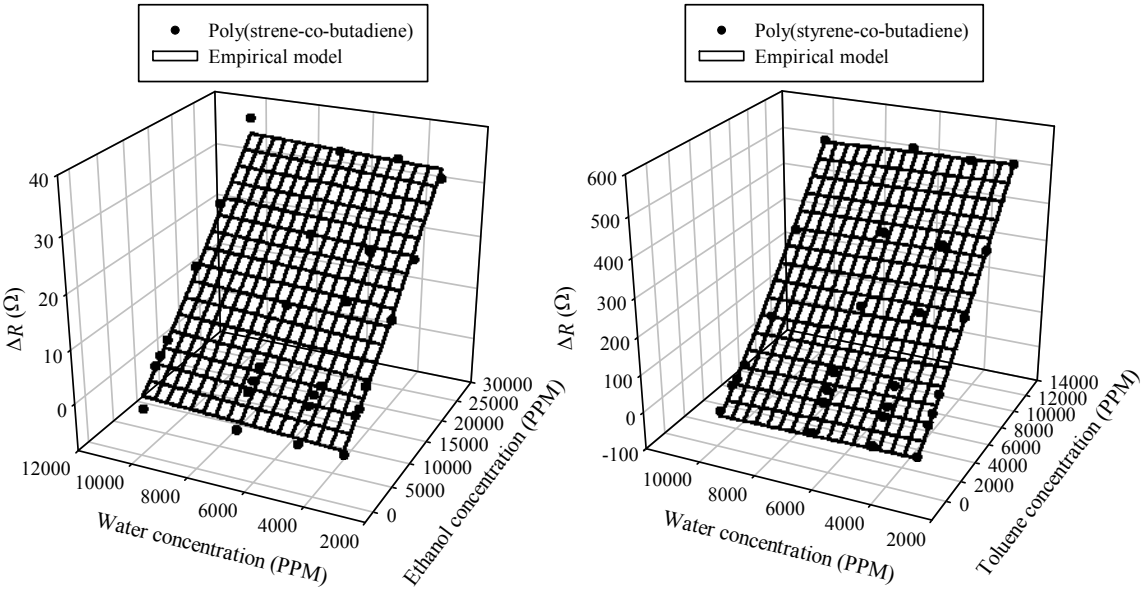

Figure 7.18: The effect of water concentration on the response of resistive composite polymer sensors at 30°C.

Toluene	a_T (Ω/PPM)	$\pm\sigma_{aT}$ (Ω/PPM)	k_T (PPM^{-1})	$\pm\sigma_{kT}$ (PPM^{-1})	k_W (PPM^{-1})	$\pm\sigma_{kW}$ (PPM^{-1})	r^2
Sample 1	3.47E-02	1.84E-02	1.01	5.61E-02	-3.62E-03	1.35E-03	0.986
Sample 2	4.28E-02	2.16E-02	0.94	5.32E-02	-2.48E-03	8.91E-04	0.985
Sample 3	1.62E-02	8.49E-03	1.15	5.47E-02	-2.31E-03	1.86E-03	0.991
Sample 4	3.02E-02	1.35E-02	1.03	4.71E-02	-2.60E-03	1.18E-03	0.991
Sample 5	2.70E-02	1.30E-02	1.05	5.10E-02	-2.79E-03	1.28E-03	0.99
Av.	3.02E-02	1.50E-02	1.04	5.24E-02	-2.76E-03	1.31E-03	0.98
Ethanol	a_E (Ω/PPM)	$\pm\sigma_{aE}$ (Ω/PPM)	k_E (PPM^{-1})	$\pm\sigma_{kE}$ (PPM^{-1})	k_W (PPM^{-1})	$\pm\sigma_{kW}$ (PPM^{-1})	r^2
Sample 1	3.62E-04	1.70E-04	1.14	4.58E-02	4.12E-04	7.01E-05	0.994
Sample 2	1.66E-04	1.04E-04	1.18	6.12E-02	3.68E-04	6.24E-05	0.99
Sample 3	2.38E-04	1.51E-04	1.17	6.20E-02	4.48E-04	8.05E-05	0.99
Sample 4	1.61E-04	7.96E-05	1.22	4.86E-02	4.65E-04	6.68E-05	0.994
Sample 5	2.22E-04	1.19E-04	1.17	5.23E-02	4.23E-04	6.83E-05	0.992
Av.	2.30E-04	1.25E-04	1.17	5.40E-02	4.23E-04	6.96E-05	0.992

Table 7.17: Modelling coefficients for the water dependency of resistive sensors employing a poly(styrene-co-butadiene) polymer films.

7.4.3 The effect of temperature on the static response of resistive composite polymer sensors

Here, as with the chemFET sensors, four operating temperatures (30°C – 60°C) were used to analyse the effect of increasing temperature on the relative baseline dependence on the sensor response. As with the previous tests identical procedures, concentrations and exposure periods were used to produce comparable results.

It was observed that increasing temperature produced a reduction in the baseline value of these resistive sensors, as shown in figure 7.19 below for ΔR/R.

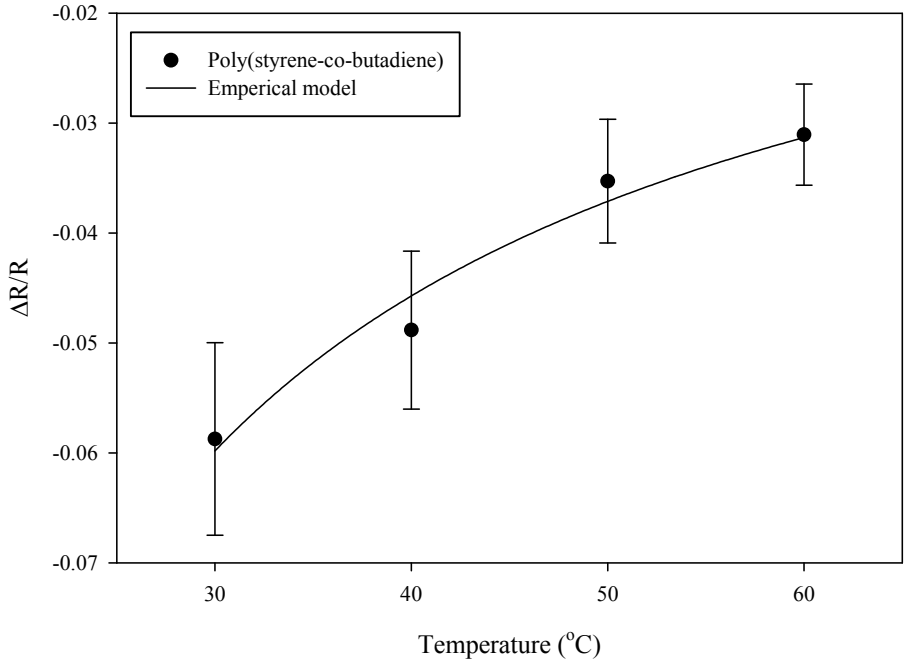

Figure 7.19: The effect of temperature on the baseline for resistive sensors at fixed water concentration (4500 PPM).

Here a power model, described earlier for the shift of a chemFET sensor with a composite polymer film, was used with the coefficient given in table 7.18 below.

Sample	α (Ω/°C)	$\pm\sigma_\alpha$ (Ω/°C)	β	$\pm\sigma_\beta$	R^2
Sample 1	-1.69	0.81	1.01	1.23E-01	0.975
Sample 2	-1.79	0.60	1.01	8.59E-02	0.987
Sample 3	-2.25	2.03	1.03	2.32E-01	0.916
Sample 4	-3.28	1.60	1.02	1.25E-01	0.975
Sample 5	-2.48	1.02	1.00	1.59E-01	0.958
Av.	-2.30	1.21	1.01	1.45E-01	0.962

Table 7.18: Modelling coefficients for the effect of temperature on the baseline for resistance composite polymer sensors.

This reduction in relative baseline, with increasing temperature, can only be realistically achieved by two mechanisms. Previous work, with resistive composite polymers has shown the same effect [7.10] and it was suggested that this was due to a 1/T dependence on the activation energy and so conductance. Alternatively, a fall in resistance could simply be due to the carbon spheres moving closer together. As the temperature increases there is either a contraction within the polymer or an expansion of the carbon spheres.

Further tests investigated the effect of temperature on the magnitude of the response. It was found, as with the chemFET sensors, that increasing temperature caused a reduction in response following a log model. Hence we can analyse this fall in response using the analyte boiling point model described earlier. Thus the sensors response can be modelled by:

$$R \approx R_0 + k_T k_{p,g} C_T^{\alpha} \tag{7.41}$$

where R_0 is the base resistance before exposure to analyte. Considering the change in resistance and substituting in equation (7.28), then:

$$\Delta R \approx k_T C_T^{\alpha} 10^{\left(\frac{\beta}{T}\right)} \tag{7.42}$$

where k_T is a binding coefficient, C_T is the concentration of toluene vapour and α is a bulk solubility constant, where k_T and C_T can be replaced with k_E and C_E for ethanol vapour. Table 7.19 gives the modelling coefficients for this expression

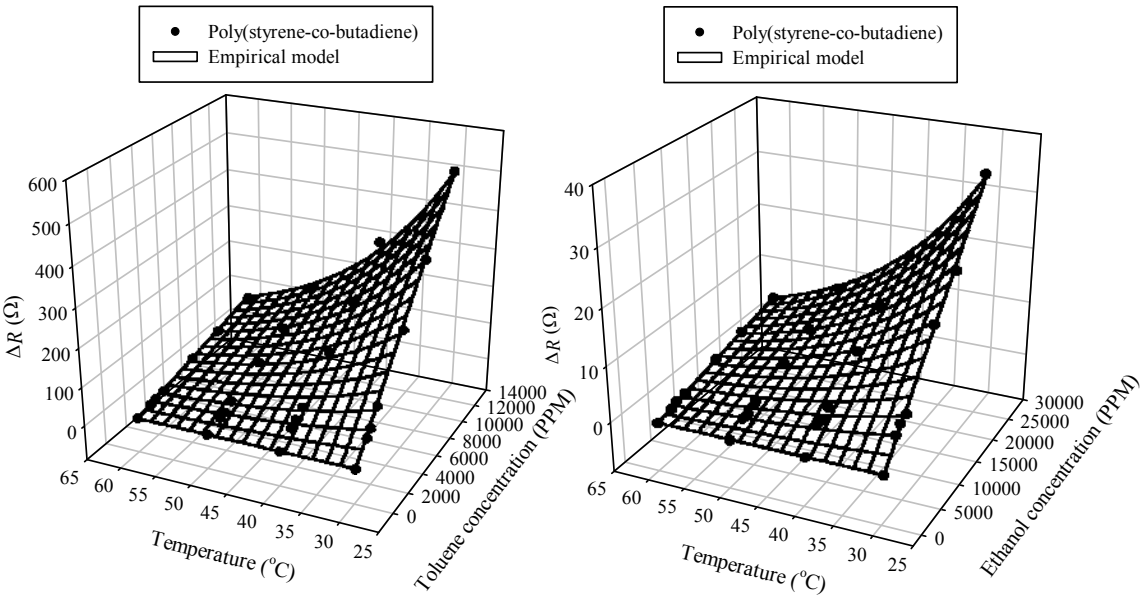

Figure 7.20: The effect of temperature on the static response of resistive composite polymers to toluene and ethanol vapour in air.

Toluene	k_T (Ω/PPM)	$\pm\sigma_{kT}$ (Ω/PPM)	α	$\pm\sigma_\alpha$	β (^oC)	$\pm\sigma_\beta$ (^oC)	r^2
Sample 1	9.98E-04	5.94E-04	37.70	2.02	1.08E+00	6.21E-02	0.977
Sample 2	1.11E-03	5.93E-04	38.10	1.98	1.01E+00	5.68E-02	0.978
Sample 3	1.10E-03	6.35E-04	37.90	1.91	1.13E+00	6.10E-02	0.98
Sample 4	1.01E-03	4.94E-04	40.80	1.78	1.06E+00	5.10E-02	0.984
Sample 5	1.27E-03	6.89E-04	37.70	1.85	1.06E+00	5.61E-02	0.98
Av.	1.10E-03	6.01E-04	38.40	1.91	1.07E+00	5.74E-02	0.98
Ethanol	k_E (Ω/PPM)	$\pm\sigma_{kE}$ (Ω/PPM)	α	$\pm\sigma_\alpha$	β (^oC)	$\pm\sigma_\beta$ (^oC)	r^2
Sample 1	1.12E-04	4.76E-05	40.10	1.57	9.54E-01	4.13E-02	0.987
Sample 2	9.50E-05	2.85E-05	33.40	1.14	8.30E-01	2.96E-02	0.99
Sample 3	2.06E-04	1.14E-04	34.50	1.94	9.25E-01	5.43E-02	0.974
Sample 4	1.09E-04	5.39E-05	38.80	1.78	9.66E-01	4.83E-02	0.982
Sample 5	1.22E-04	5.94E-05	38.30	1.75	9.48E-01	4.73E-02	0.982
Av.	1.29E-04	6.07E-05	37.00	1.64	9.25E-01	4.42E-02	0.983

Table 7.19: Modelling coefficients for the effect of temperature on the response of resistive polymer sensors to toluene and ethanol vapour in air.

The chemFET sensors, employing poly(styrene-co-butadiene), show an average Log term of 14.9 and 20.9 to toluene and ethanol vapour respectively. These values are lower than those measured for the resistive devices, though the magnitude of these responses is similar. Though the material composition is different between these two types of sensors, this may not account for this variation. It is possible that the conductivity of these materials is also be effect by temperature hence giving this distinct variation, though shows this dependence is a material, not a device limitation.

7.5 Conclusions

In this chapter we have investigated the effect of water concentration and temperature on the baseline and the response of these room temperature chemFET sensors. Table 7.20 to table 7.22 summarises the effects of water concentration and temperature on the chemFET sensors utilising composite and electrochemically deposited polymer films and the composite resistive sensors.

Polymer	$\left.\frac{\partial V_{GDS}}{\partial C_W}\right\|_{C_E}$ (μV/PPM)	Standard Deviation (μV/PPM)	$\left.\frac{\partial V_{GDS}}{\partial C_W}\right\|_{C_T}$ (μV/PPM)	Standard Deviation (μV/PPM)	$\left.\frac{\partial V_{GDS}}{\partial C_W}\right\|_{C_T=0}$ (μV/PPM)	Standard Deviation (μV/PPM)
PPY/BSA	656.2	±392.3	-447.1	±242.3	-4.2	±1.5
PBT/TBATFB	361.6	±71.5	-399.7	±69.8	-3.9	±1.6
CP1					-2.22	±1.02
CP2					-2.01	0.26

Table 7.20: Summary of the effect of water concentration on chemFET sensors employing composite and electrochemically deposited polymers at fixed temperature of 30°C (CP1 – poly(ethylene-co-vinyl acetate, CP2 – poly(styrene-co-butadiene), CP3 – poly(9-vinylcarbazole), PPY/BSA – poly(pyrrole)/BSA, PBT/TBATFB – poly(bithiophene)/TBATFB).

Polymer	$\left.\frac{\partial V_{GDS}}{\partial T}\right\|_{C_E=cons}$ (μV/°C)	Standard Deviation (μV/°C)	$\left.\frac{\partial V_{GDS}}{\partial T}\right\|_{C_T=cons}$ (μV/°C)	Standard Deviation (μV/°C)	$\left.\frac{\partial V_{GDS}}{\partial T}\right\|_{C_T=0}$ (mV/°C)	Standard Deviation (mV/°C)
PPY/BSA	27.7	±9.8			-2.6	±0.2
PBT/TBATFB	19.4	±10.8			-1.2	±0.2
ECP solid					-0.7	±0.1
CP1	5.8	±1.1	-14.3	±5.3	-3.6	±0.2
CP2	6.2	±5.0	46.0	±25.9	-4.5	±0.6
CP3	7.6	±3.9	74.2	±42.7	-1.1	±0.2
CP solid					0.0094	±0.00063

Table 7.21: Summary of the effect of temperature on chemFET sensors employing composite and electrochemically deposited films at constant water concentration (4500 PPM).

	$\left.\frac{\partial R}{\partial C_E}\right\|_{T=const}$ (Ω/PPM)	Standard Deviation (Ω/PPM)	$\left.\frac{\partial R}{\partial C_T}\right\|_{T=const}$ (Ω/PPM)	Standard Deviation (Ω/PPM)		
Resistive	1.0	±0.1	14.4	±6.0		
	$\left.\frac{\partial R}{\partial T}\right\|_{C_E=const}$ (Ω/°C)	Standard Deviation (Ω/°C)	$\left.\frac{\partial R}{\partial T}\right\|_{C_T=const}$ (Ω/°C)	Standard Deviation (Ω/°C)	$\left.\frac{\partial R}{\partial T}\right\|_{C_T=0}$ (Ω/°C)	Standard Deviation (Ω/°C)
Resistive	0.0014	±0.0002	0.037	±0.013	-2.3	±0.7

Table 7.22: Summary of the effect of analyte concentration and temperature on resistive sensors employing poly(styrene-co-butadiene).

It has been found that for chemFET sensors with the composite polymers poly(ethylene-co-vinyl acetate) and poly(styrene-co-butadiene) have a water vapour dependence on the baseline, where increasing water vapour reduces the relative

baseline. This has been found to follow a Langmuir isotherm and it has been proposed that this effect is brought about by a dipole formation on the gate oxide. Poly(9-vinylcarbzole) showed no baseline dependency. Furthermore, these composite polymers showed only a negligible shift in response with increasing water concentration. The electrochemical polymers also showed this baseline dependency to water vapour also following a Langmuir isotherm. In addition, increasing water vapour caused a rise in sensor response when exposed to ethanol and toluene vapour. It is proposed that the analyte is in competition with the water molecules where the analyte removes water molecules from the polymer and so the gate oxide causing this increase in response.

The effect of temperature was also investigated. The chemFET sensors employing composite polymers had a baseline dependency where an increase in temperature caused a reduction V_{GDS} for open gate devices and an increase for a solid gate devices. This increase in solid gate results can be accounted for by a simple degradation in the carrier mobility. It is proposed that the reduction in baseline, for open gate sensors, is caused by a thermal expansion/contraction of the composite material, altering the average work function. Increasing temperature caused a decrease in chemFET sensor response. The analyte boiling point model can account for this effect, where the concentration of analyte within the polymer is a function of temperature.

The chemFET sensors with electrochemically deposited polymer films have also shown a reduction in relative baseline with temperature for both open and solid gate devices. These effects are also be accounted for by thermal expansion. The effect of temperature on the response also showed a reduction with increasing temperature, though not as rapid as the composite polymers. The analyte boiling point model can also describe this, though this does not take into account any ion to analyte interactions within the polymer. In addition, the response of chemFET sensors with electrochemically deposited polymer films, to toluene vapour above 40 ^{o}C, showed a permanent inversion in response, possibly due to an oxidation of the active polymer film.

Lastly, resistive sensors employing poly(styrene-co-butadiene) were tested to benchmark the chemFET sensors. It was found that these sensors showed similar characteristics in sensor response modelled to a power law, no effect of water

concentration on the baseline or the response. Also, the sensors showed a similar reduction in response with increasing temperature that can be accounted for by an analyte boiling point model.

We can now ask the question, is water concentration and temperature an issue with these sensors? Firstly, the effect of water concentration on the baseline for chemFET sensors employing composite polymer films is equivalent to between 3 PPM to 0.5 PPMs of toluene vapour and 13 PPM to 5 PPMs of ethanol vapour for 1 PPM of water concentration. For chemFET sensors employing electrochemically deposited polymers this value increases to 4 PPM to 2 PPM of ethanol and toluene vapour. Also these sensors show an increase in response of equivalent to 600 PPM to 1200 PPM of ethanol for 1 PPM of water concentration. From these results we can state that water concentration is a problem with these chemFET sensors and if possible resolved through the design process. As for temperature, a 0.1 ^{o}C rise in temperature on the relative baseline for a chemFET sensors with a composite polymer film is equivalent to 30 to 150 PPM of toluene vapour and 200 to 1000 PPM of ethanol vapour. This makes the temperature control critical in any application, especially if you consider there is a logarithmic reduction in sensor response with increasing temperature of up to 7.6 $\mu V/^{o}C$. The chemFET sensors with electrochemically deposited polymers show an equally strong temperature dependence with a 0.1 ^{o}C rise in temperature equivalent to a 70 to 260 PPM of toluene vapour and 60 to 250 PPM of ethanol vapour. The effect of temperature on the response is also significant with a value up to 28 $\mu V/^{o}C$ and so we can state that through the effect of water concentration is sizeable, the effect of temperature is much more substantial.

By using these models and theories developed in this chapter, if these types of sensors were used an electronic nose instrument it may be possible compensate for the effect of water concentration and temperature. In addition, by knowing the limitations of these sensors it maybe possible to re-design the sensor to remove some of these effects, i.e. change the nature of the surface of the gate insulator material.

7.6 References

[7.1] P. Ingelby, *PhD Thesis,* 1999, University of Warwick, Coventry, CV4 7AL, UK.

[7.2] J. A. Covington, J. W. Gardner, J. V. Hatfield, Conducting polymer FET devices for vapour sensing, *Proc. Of SPIE Smart Electronics and MEMS* (1999), pp. 296-307.

[7.3] S. M. Sze, Physics of Semiconductor devices, Wiley, 1985.

[7.4] P. Talik, M. Zamkowska-Wacawek, W. Wacawek, Sensing properties of the CB-PCV composites for clorinated hydrocarbon vapours, *J. Mater. Sci.,* **27**, (1992), 6807-6810.

[7.5] H. Purnell, Gas Chromatography, John Wiley & Son, 1963.

[7.6] M. Hang, K. D. Schierbaum, G. Gauglitz. W. Göpel, Chemical sensors based upon polysiloxanes: comparison between optical, quartz microbalance, calorimetric, and capacitances, *Sensors and Actuators* **B**, 11 (1993), pp. 383-391.

[7.7] S. J. Patrash, E. T. Zellers, Characterization of polymeric surface acoustic wave sensor coatings and semiempirical models of sensor responses to organic vapours, *Anal. Chem.* 65 (1993), pp. 2055-2066.

[7.8] R. P. Schwarzenbach, P. M. Gschwend, D. M. Imboden, Environmental Organic Chemistry, John Wiley & Sons, 1993.

[7.9] CRC Handbook of Chemistry and Physics, Ed. D. R. Lide, CRC Press, 1999.

[7.10] P. Talik, M. Zamkowska-Wacawek, W. Wacawek, Sensing properties of the CB-PCV composites for clorinated hydrocarbon vapours, *J. of Mater. Sci.,* **27**, (1992), 6807-6810.

CHAPTER 8

Electrical and thermal characterisation of MOSFET heaters and gas sensors based on SOI technology

8.1 Introduction

In chapter 3 a new generation of gas sensors were proposed based on SOI technology. These designs utilise a MOSFET heater on a thin SOI membrane and have either a chemoresistive or a chemFET sensing structure. In addition, these designs are fully CMOS compatible and so further circuit integration is possible. This chapter covers the electrical and thermal analysis of these SOI MOSFET heaters, for devices with and without membranes, fabricated through Europractice using the MATRA 0.8 μm BiCMOS process. Also described is the electrical characteristics and temperature coefficients of the sensors used to monitor the output of the heaters and of the membrane. Lastly, a vapour sensitive polymer has been deposited onto the chemoresistive sensing structure of these SOI devices, to investigate the operation of the sensor element.

8.2 Electrical characterisation of SOI devices

The electrical characterisation of the SOI devices has been performed using a number of different measurement techniques. These are based on the I-V and C-V measurement of the MOSFET heaters, the I-V measurement of the temperature diodes including external heater calibration and temperature calibration of the spreading resistors. This

electrical characterisation is covered in the following sections. In all cases these measurements were performed for devices without membranes.

8.2.1 I-V and C-V characterisation before SOI membrane formation

As stated in chapter 4, only three of the four MOSFET heaters operated correctly (fourth being a short circuit). To evaluate the operation of these heaters the FETs were characterised before the formation of a membrane using a HP4145 semiconductor parameter analyser. This instrument is specifically designed to characterise electrically sensitive semiconductor devices and was used extensively with these SOI MOSFET heaters. The instrument has the facility to limit the currents involved to protect the device under test, while the high input impedance (at least 10^{12} Ω) ensures that the measured values are correct. The instrument can supply a drain current of up to 100 mA, which is sufficient in this application.

The MOSFETs were characterised in the subthreshold and linear region at a V_{DS} of 0.4 volts to 1.0 volts in 10 mV steps and at a V_{GS} of 20 mV to 100 mV in 20 mV steps, with I_{DS} measured. For the saturated region tests the devices were operated V_{DS} of 0 volts to 1.5 volts in 20 mV steps and at V_{GS} of 0.5 volts to 1.25 volts in 250 mV steps. The results of these experiments are shown in figure 8.1 for the transistors described in table 8.1. The outcome of these tests show that the variation in I-V curve is consistent with the different channel dimensions and that the start of the linear region is approximately 0.7 volts (V_{GS}). These are the expected results for a device fabricated in standard CMOS produced by the MATRA process.

Device	Description	Channel dimensions	W/L ratio
FET1	Interdigitated with gap FET heater	6 off 132 μm × 9 μm	88
FET2	Interdigitated FET heater	6 off 132 μm × 12 μm	66
FET3	Interdigitated with gap FET heater	4 off 132 μm × 12 μm	44

Table 8.1: MOSFET heater characteristics.

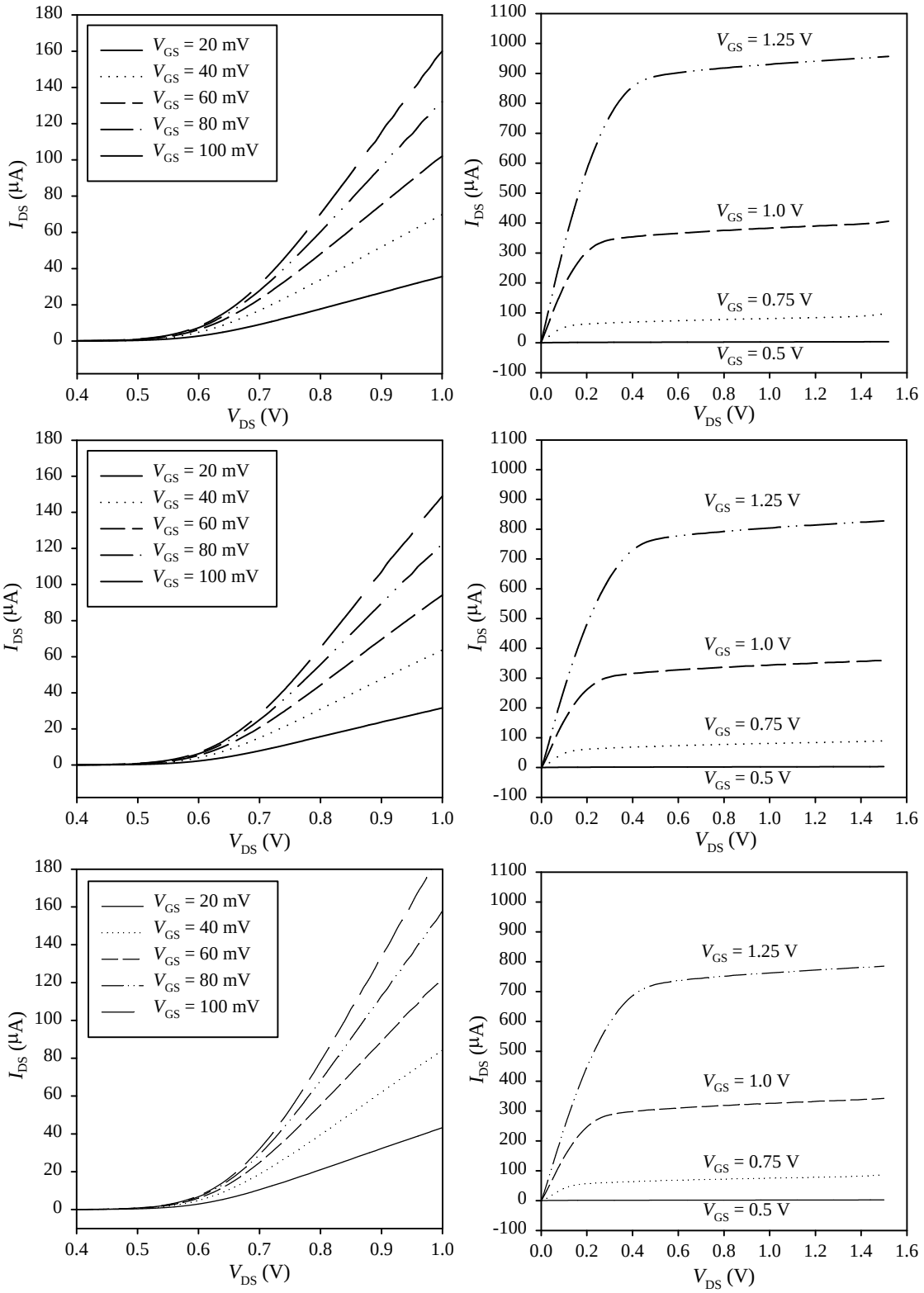

Figure 8.1: MOSFET characteristics in the subthreshold, linear and saturated regions for FET1, FET2 and FET3.

Following these I-V characterisations, C-V analysis was performed. C-V analysis is used to measure the quality of the gate oxide and the oxide capacitance (here the oxide thickness is 17.5 nm). Both high frequency (100 kHz) and quasistatic (< mHz) analysis was used. High frequency (100 kHz – 1 MHz) C-V techniques measure only the oxide capacitor in the accumulation mode [8.1]. Low frequency (< 20 Hz) or quasistatic (mHz) techniques measure the capacitance of the gate oxide over the entire operating range. A typical C-V analysis of FET design 2 is shown in figure 8.2 for a gate voltage sweep of –5 volts to + 5 volts in 200 mV steps. These measurements were taken using the Keithley 590 100 kHz C-V analyser and the Keithley 595 Quasistatic C-V meter.

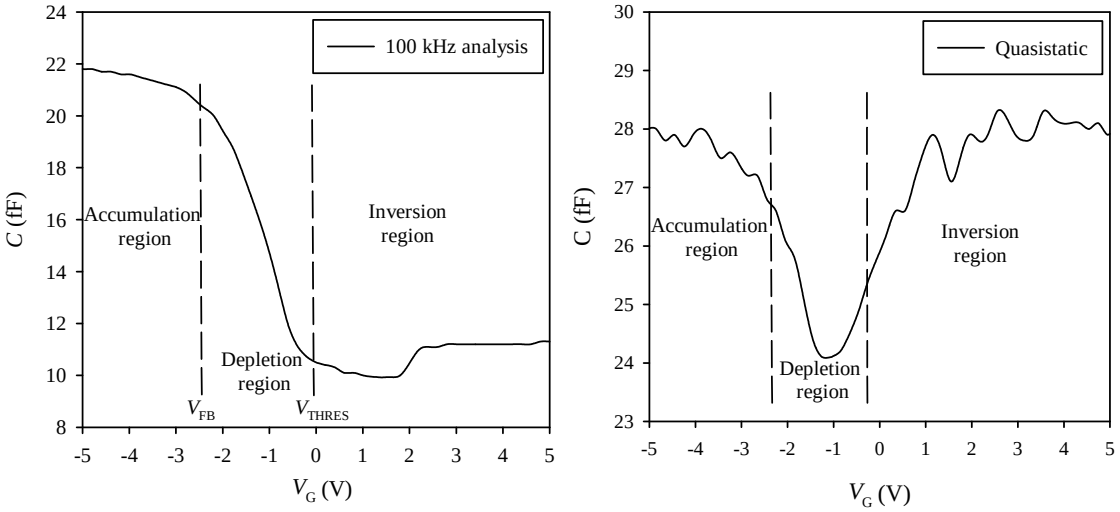

Figure 8.2: C-V analysis of the gate oxide of the MOSFET heaters.

These results are consistent with a transistor with these characteristics with a maximum a gate capacitance of 28 fF and prove the operation of the MOSFETs before the formation of a membrane.

8.2.2 Characterisation of the diode and resistive temperature sensors

To monitor the temperature of the MOSFET heaters and of the membrane a number of temperature sensors based on diodes and spreading resistors were included in the design. Two slightly different diode designs were implemented and the typical I-V characteristics of these sensors are shown in figure 8.3. Here the devices were tested between 0 volts and 2 volts in 10 mV steps and the diode current measured. To characterise the devices as temperature sensors, the diodes were operated at a constant current and the voltage monitored. This is the normal regime for these devices as the

output voltage is then linearly dependent on temperature [8.2]. The sensors were externally heated between 30 ^{o}C and 70 ^{o}C in 10 ^{o}C steps, as shown in figure 8.3, with the effect of temperature fitted to a linear regression from an initial value at 0 ^{o}C. The temperature of the devices was externally controlled by a DRI-BLOCK^{TM} heater, to a resolution of ± 0.1 ^{o}C.

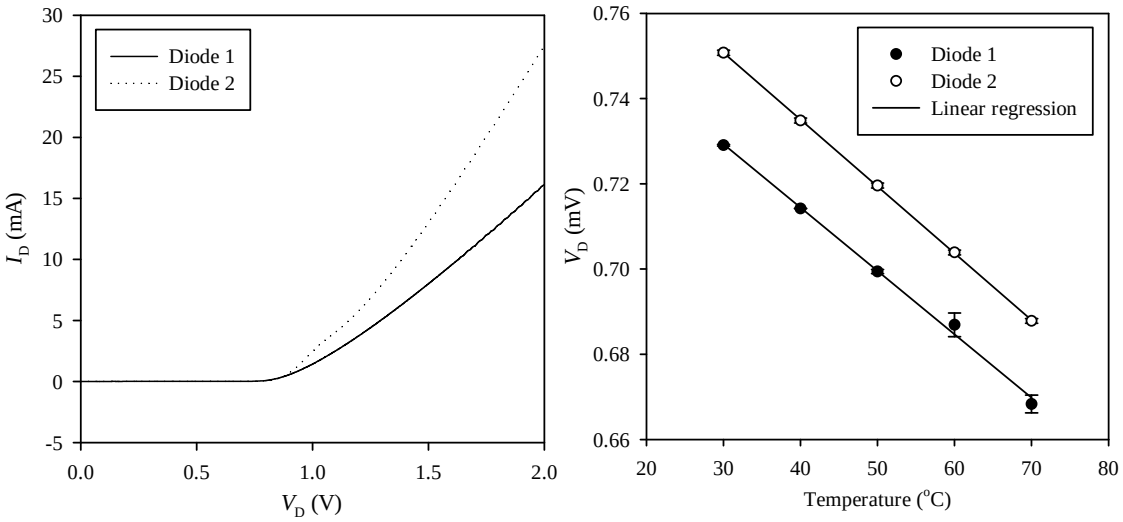

Figure 8.3: Forward I-V characteristics for the temperature diodes and the effect of temperature on the diodes operated at a constant current of 10 μA.

The I-V characteristics of an ideal diode is defined as [8.3]:

$$I = A_d I_S \left(\exp^{\frac{qV}{kmT}} - 1 \right) \qquad (8.1)$$

where A_d is the area of the diode, I_S is the saturation current, q is the electron charge, k is Boltzmann's constant, T is the temperature (in Kelvin) and m is an idealality constant between 1 and 2 (approximated to 2 for a *pn* junction diode). Expression (8.1) can be fitted to the diode data to show how ideal the diodes are behaving. Table 8.2 gives the modelling parameters for expression (8.1).

Diode	A_dI_s (mA)	$\pm \sigma_{AdIs}$ (mA)	q/mkT	$\pm \sigma_{q/mkT}$	r^2
Diode 1	0.4698	0.0349	1.838	0.0403	0.97
Diode 2	0.6780	0.0485	1.919	0.0389	0.98

Table 8.2: Diode coefficients for expression (8.1).

The results show that the diodes have similar characteristics to the ideal case, with a high correlation coefficient. With idealality (m) values of 1.8 to 1.9. This equation only

gives a qualitative solution as the generation or recombination of carriers within the depletion layer are ignored.

The second type of temperature sensor was based on a channel spreading resistor. This device is constructed as two contact points 175 μm apart with the 'body' as a channel within the LOCOS isolation. As the MOSFETs are *n*-channel then the channel is made of the *p*-substrate. The spreading resistors were tested at a constant current of 10 μA and the voltage monitored. Figure 8.4 shows the effect of temperature on these resistive devices, for a temperature range of 30 ^{o}C to 70 ^{o}C (again using a DRI-BLOCK^{TM} heater).

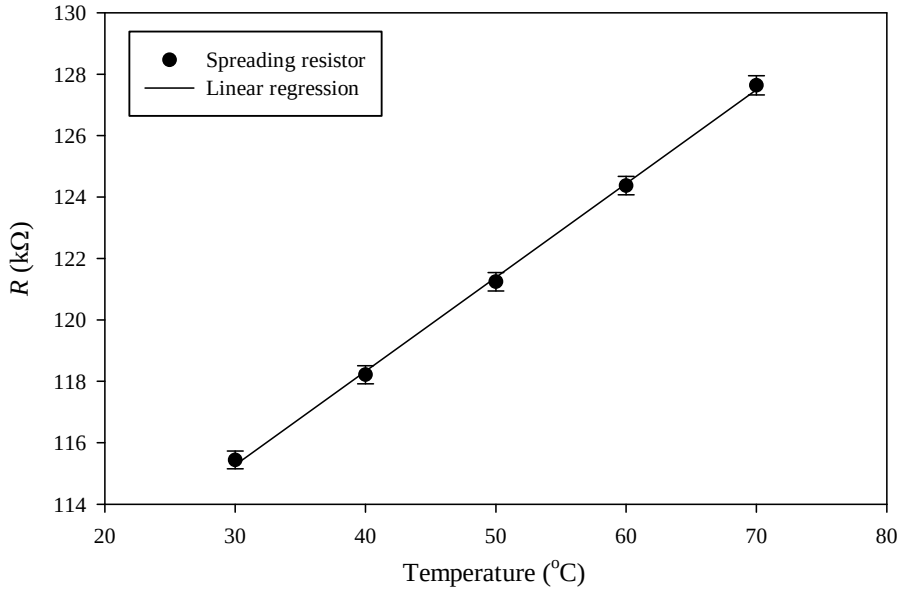

Figure 8.4: The effect of temperature on the resistance of a spreading resistor.

From these results we can calculate the temperature coefficients of these sensors as given in table 8.3. A limitation of the spreading resistor is its high resistance value. Clearly it will be difficult to measure small changes in temperature when its initial resistance is high. Table 8.2 also gives the typical baseline values at room temperature (at a constant current of 10 μA).

Sensors	Initial value (RT = 30 ^{o}C)	Standard deviation	Temperature coefficient	Standard deviation
Diode 1	0.751 V	± 0.6 mV	-1.57 mV/^{o}C	± 7 μV/^{o}C

Diode 2	0.729 V	± 0.2 mV	-1.49 mV/^{o}C	± 49 μV/^{o}C
Resistor	115.4 kΩ	± 291 Ω	305 Ω/^{o}C	± 5 Ω

Table 8.3: Summary of temperature sensors characteristics.

The variation in initial value for the different diodes is a result of dissimilar *pn* junction dimensions, though the temperature coefficients are comparable. Any variation could simply be a result of the fabrication process. Also this value is below the ideal temperature coefficient for a diode reported at -2.1 mV/^{o}C, this could also be due to variations in fabrication resulting from irregularities in the depletion zone between the *n* and *p* regions or in the doping of these regions [8.2].

Lastly the noise and the detection limit (i.e. the resolution) was investigated. Here the diode and the spreading resistor sensors were driven at a constant current of 10 μA at a temperature of 70 ^{o}C for 10,000 seconds. Results of these experiments are shown in figure 8.5.

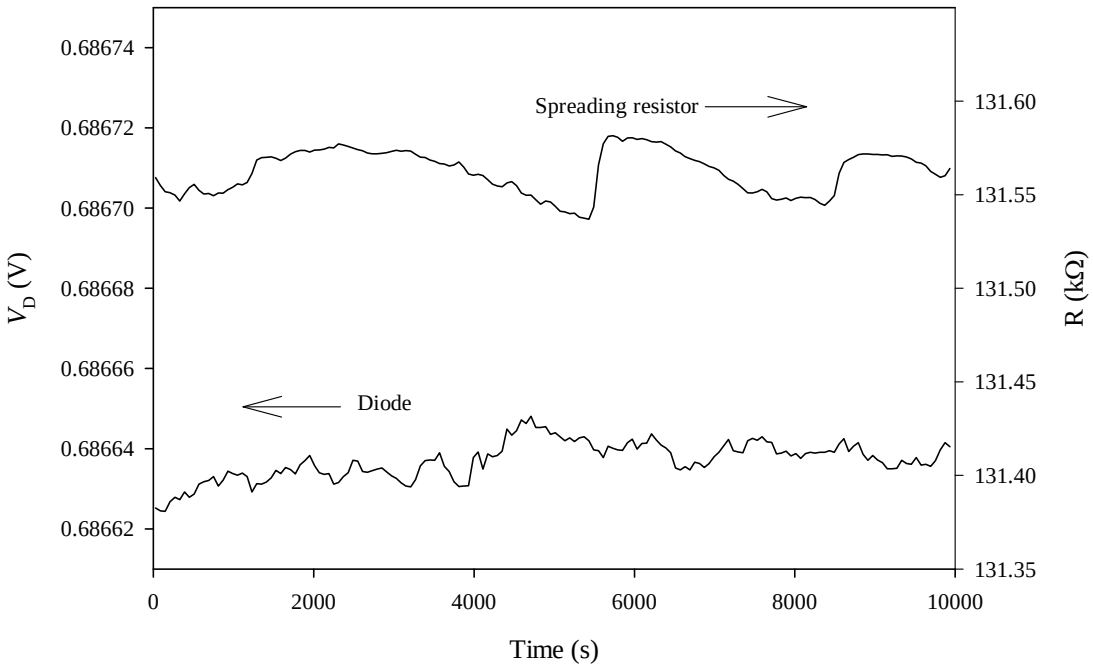

Figure 8.5: Long term measurement of the temperature sensors.

By observation and using the temperature coefficients from table 8.3 we can state that the variation in output value is equivalent to ±0.1 ^{o}C. This would be expected as the DRI-BLOCK^{TM} heater used to control the temperature has a ±0.1 ^{o}C resolution. From

these experiments, for a calibrated temperature sensor, a resolution of less than 0.01 ^{o}C could be achieved.

8.3 Thermal characterisation of SOI devices

To quantify the effectiveness of the MOSFET heaters, dynamic and static thermal characterisations have been performed. Firstly, the I-V characteristics of the MOSFET heaters with and without membranes were measured, including an analysis of the settling time. Secondly, temperature measurements, using the diode and spreading resistor sensors were carried out. This gives an indication of the membrane temperature and the effect of modulating the heater output on the membrane temperature. Lastly, thermal imaging of the devices was carried out to give an indication of the thermal profile of the SOI structure.

8.3.1 I-V analysis of the MOSFET heater after membrane formation

To investigate the performance of the MOSFET heaters, I-V characterisations were performed for devices with and without membranes. This analysis focused on the linear and saturated regions of operation, as the subthreshold region does not supply sufficient current to heat the membrane. FETs 1 and 2 were tested with V_{DS} between 0 to 6 volts in 0.1 volt steps and V_{GS} between 1 to 5 volts in 1 volt steps, with the drain current measured. Results from these experiments are shown in figure 8.6 and figure 8.7. These figures show an example of each transistor with and without a membrane. Figure 8.8 shows the I-V characteristics for transistor 3, here a comparison between a MOSFET on a membrane and the reference off the membrane, though on the same silicon die, is shown. This comparison should be more accurate than the other results, as the fabrication process will be identical for both devices. To attempt to amplify the differences this devices was characterised over a larger range with V_{GS} of 2 volts to 7 volts, with the same drain voltages.

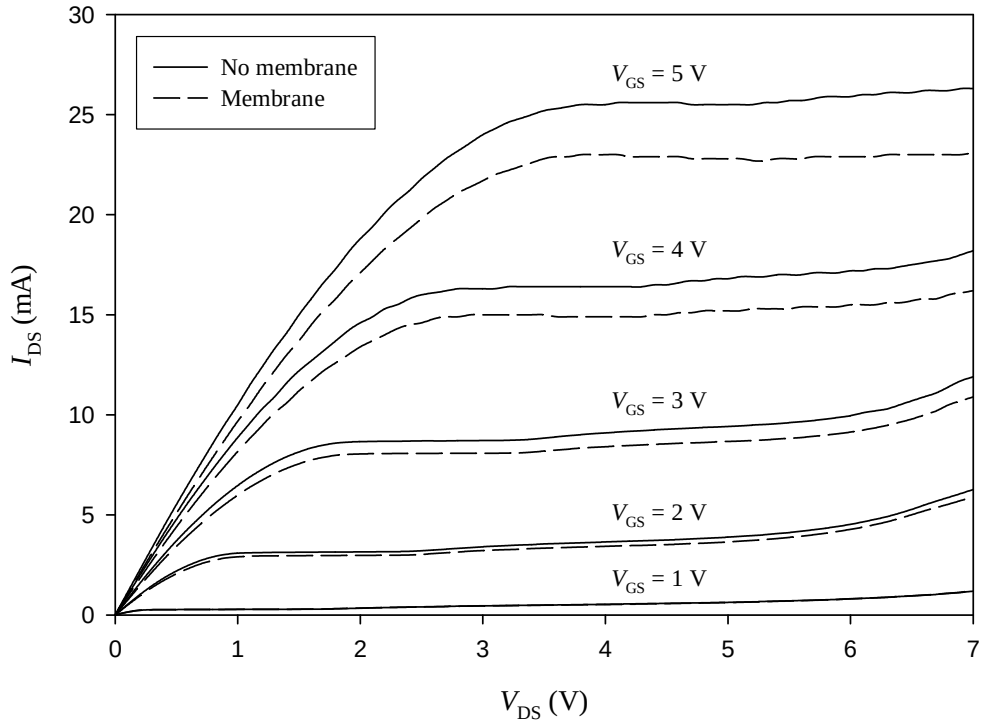

Figure 8.6: The I-V characteristics of FET 1 for devices with and without a membrane

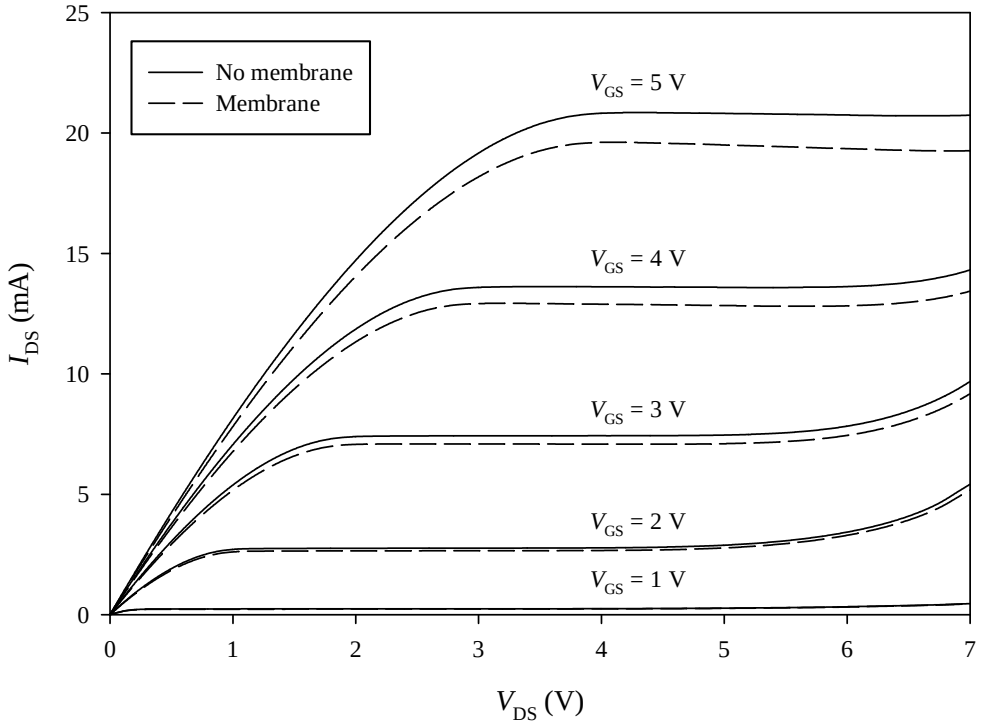

Figure 8.7: The I-V characteristics of FET 2 for devices with and without a membrane.

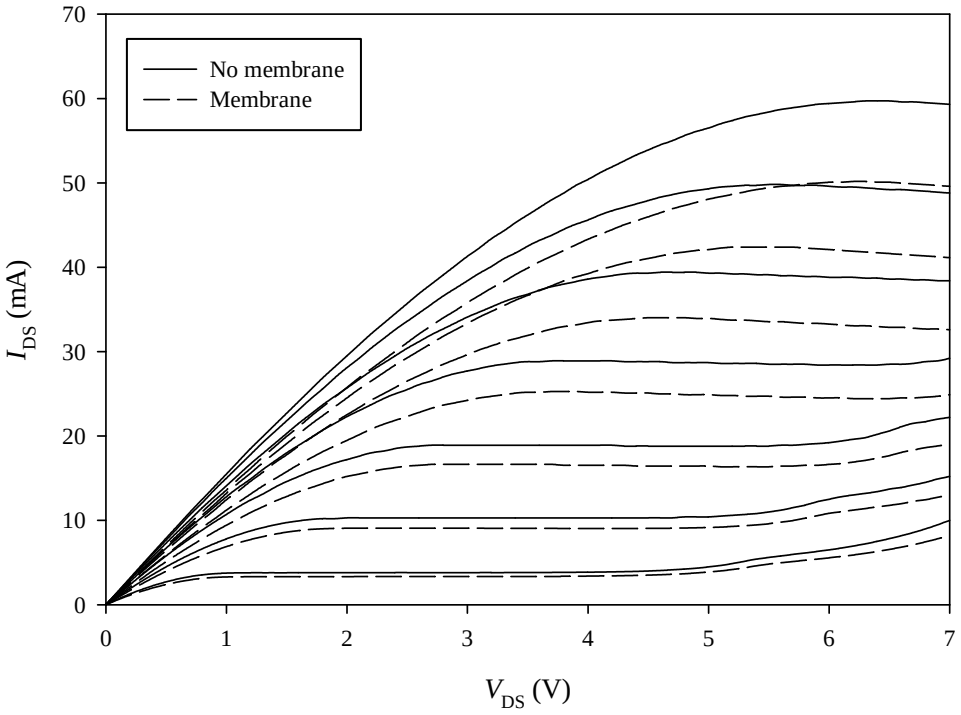

Figure 8.8: The I-V characteristics of FET 3 for devices with and without a membrane

Figure 8.6 to figure 8.8 shows there is a reduction in I_{DS} with V_{GS} and V_{DS} for transistors with a membrane compared to transistors without a membrane. This is not unexpected as MOSFET theory predicts that device parameters and performance are effected by temperature, especially the carrier mobility and threshold voltage [8.4]. The effect of temperature on the effective carrier mobility (μ) can be defined by:

$$\mu = \mu_0 \left(\frac{T}{T_0} \right)^{-m} \tag{8.2}$$

where m is a value between 0.5 and 2 depending the material properties of the material [8.3], T is the temperature, T_0 the initial (room) temperature and μ_0 is the effective carrier mobility at room temperature (in K). This expression applies above room temperature and when the gate is biased under strong inversion. The temperature dependence of the threshold voltage can be examined by investigating its components given by (under weak inversion) [8.5,8.6]:

$$V_T = \phi_{ms} - \frac{Q_o}{C_o} + 2\phi_{si} + \frac{\sqrt{4K_s \varepsilon_0 q N_a \phi_{si}}}{C_o} \tag{8.3}$$

where ϕ_{ms} is the difference in work function between the metal and the semiconductor, Q_o is the charge due to a zero gate voltage, C_0 is the oxide capacitance, K_s is the

dielectric constant for silicon, ϕ_{si} is the surface potential and N_a is the density of acceptor atoms. The work function and the fixed oxide charges are independent of temperature and so differentiating expression (8.3) in respect to temperature, we get:

$$\frac{dV_T}{dT} = \frac{dQ_b}{dT}\left(2 + \frac{1}{C_o}\sqrt{\frac{K_s \varepsilon_0 N_a Q_b}{C_o}}\right) \tag{8.4}$$

where

$$\frac{dQ_b}{dT} = \pm\frac{1}{T}\left[\frac{E_g(T=0)}{2q} - |Q_b(T)|\right] \tag{8.5}$$

From expressions and experimental data it has been shown that the threshold voltage has an approximately linear dependence to temperature. This is prominent in the linear region, as in the saturated region the degradation in the carrier mobility dominates and it is this effect which is being demonstrated in figure 8.6 to figure 8.8.

An interesting result observed in the characterisation of these MOSFETs, is that as V_{DS} approaches 5 volts a second increase in current occurs. This arises with transistors with and without membranes and so must be a MOSFET characteristic not a result of the membrane formation. Furthermore, this characteristic is suppressed as the gate voltage is increased. This rise in conduction can be explained by reverse breakdown of the *pn* diode structure at the drain. This explanation is supported by the fact that as the gate voltage increases the effect is reduced, which is a characteristic of this reverse breakdown. This reverse breakdown can be described by a Zener or avalanche effect. Zener breakdown occurs when the depletion region formed at the interface between the *n*+ doping and the *p* substrate (for a *n*-channel device) is very thin and the electric field is high. In this case electrons enter the depletion layer by a quantum-mechanical tunnelling. If the doping densities on either side of the junction area are greater than 10^{18} cm^{-3} then the critical field strength can be achieved with a reverse bias of less than 6 volts. The avalanche breakdown process occurs due to impact ionisation, where a hole collides with the crystal lattice and ionises an atom to generate an electron-hole pair. This extra hole now travels with the original hole, continuing to gain kinetic energy causing further collisions within the lattice and an avalanche multiplication arises. The probability of a collision is dependent on the electric field strength and so threshold has to be achieved before a breakdown transpires. This breakdown is inversely proportional to the impurity concentration at

the lightly doped side. Experimental results show that avalanche breakdown can occur at reverse voltages less than 10 volts for doping levels higher than 10^{17} cm^{-3}.

To further investigate the characteristics of the SOI MOSFET heaters a dynamic characterisation has been performed. This investigates the length of time taken to reach equilibrium and will help to give a further insight into the thermal mechanism occurring. Two of the MOSFET heaters were pulsed from an initial drain and gate voltage of 0 volts to a final voltage of 5 volts and the drain current measured every 10 ms. As before these measurements were taken using the HP4145 semiconductor analyser. Results from these experiments demonstrate that this pulse input causes a double exponential fall in current with time, as shown in figure 8.9.

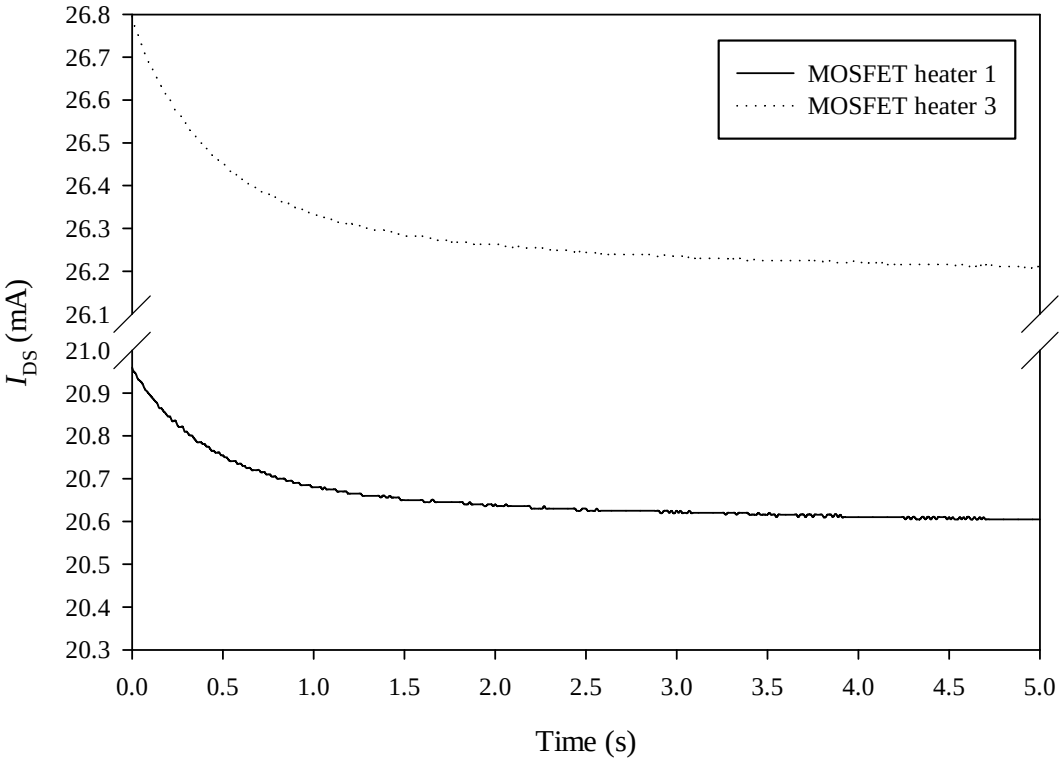

Figure 8.9: Dynamic characteristics of two MOSFET heaters

We can state that this time response will be composed of three components:

$$t_{TOTAL} = t_{SWITCH} + t_{MEM} + t_{BULK} \quad (8.6)$$

where t_{TOTAL} is the time taken for the device reach equilibrium, t_{SWITCH} is the electrical switching time of the MOSFET, t_{MEM} is the time constant for the membrane to be heated and t_{BULK} is the time taken for the remaining silicon (the bulk) to reach equilibrium. The MOSFET switching time constant can be calculated from the gate capacitance and the channel resistance. From C-V analysis the gate capacitance was

measured at 28 fF and if we assume a typical channel resistance of 100 Ω, then the switching time constant would be approximately 3 pico seconds. This is significantly faster the sample rate and so since:

$$t_{SWITCH} \ll t_{MEM} + t_{BULK} \tag{8.7}$$

then:

$$t_{TOTAL} \approx t_{MEM} + t_{BULK} \tag{8.8}$$

As shown in figure 8.9 the remaining components of expression (8.6) follow a double exponential and so the output can be described as:

$$I_{DS} = I_{DS(0)} + \alpha \exp^{-\tau_1 t} + \beta \exp^{-\tau_2 t} \tag{8.9}$$

where $I_{DS(0)}$ is the initial current value (after MOSFET switching), α and β are heater constant dependent on V_{GS} and V_{DS}, t is time and τ_1 and τ_2 are time constants relating to the membrane and the bulk. Typical values for these time constant if given in table 8.4.

Time constant	Value (s)	Standard deviation (s)
τ_1	0.238	± 0.037
τ_2	2.26	± 0.056

Table 8.4: Typical time constants of the MOSFET heaters.

These constants show that the time for the membrane to reach an equilibrium is quick, in the hundreds of milliseconds, whilst the time for the bulk to reach equilibrium is much longer, in the seconds.

The static MOSFET characteristics differ in a number of ways from the simulations described in chapter 3. The main difference being that the membrane temperature of 300 ^{o}C was not achieved and the power consumption was significantly higher. The reason for these results is that the membrane was not completely formed underneath the heater. It was found whilst back-etching that the back of the wafer was not smooth as so the back etching process resulted in a small area of the buried oxide layer being exposed whilst other areas still had silicon remaining. Since the oxide is very thin (400 nm) it was decided to stop etching when part of membrane was formed, as KOH will etch the oxide, though slowly, and if the oxide was penetrated the KOH would rapidly consume the device silicon. In addition, the mechanical procedure could well have induced stress into the membrane, which could have resulted in membrane

failure. Also, any misalignment between the etched area and the heater could have resulted in increased power consumption, as the membrane to heater ratio would be lower. The only way of discovering if these results can be improved is to characterise the SUMC SOI device once they are completed.

Two limitations that have been emphasised in these experiments, is the operating point of the device and the coverage. To get significantly elevated temperatures the heaters were driven at reasonable high voltages, which a) causes reverse breakdown and b) are outside the normal 0 to 5 volt operating range of standard CMOS. This situation can be remedied by altering the W/L ratio and by having MOSFETs with longer channel widths and/or shorter channel lengths, this will alter transconductance term of the device and give higher drain currents at the same V_{GS} and V_{DS} input. Secondly, the physical size of the heater is small when compared to the whole active area and so the coverage is low (under 40 %). Clearly, if this could be improved then the efficiency would be increased (less temperature variations over the active area, possible less power required). This can only be achieved by reducing the dimensions of the drain and source and expanding the area covered by the channel.

8.3.2 Temperature measurements of the MOSFET heaters and membrane

To get an indication of the membrane temperature the MOSFET heaters were operated at a fixed drain voltage of 7.5 volts and the gate voltage was varied between 2 to 8 volts in 0.5 volt steps. The temperature sensors were operated at a constant current of 10 μA and the voltage across the device measured. A measurement was taken for each gate voltage and so we can plot the power supplied to the heater as a function of temperature. As there is no gas sensitive material on the device the temperature sensors will not be able to give a true temperature measurement, as cooling will occur between the heater and the sensors. Figure 8.10 shows the temperature reading from the diode as a function of the input power to the MOSFET heater.

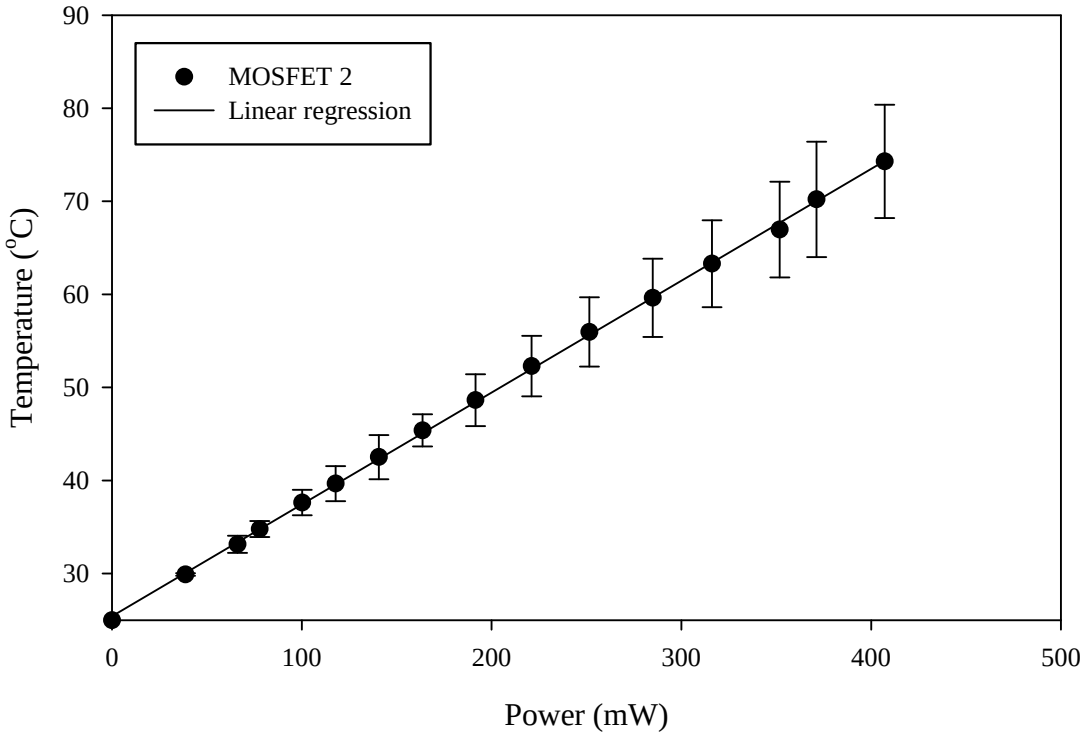

Figure 8.10: Temperature measurement of the membrane.

This power consumption is high with an average temperature coefficient of 8 mW/°C and is significantly higher than the simulated results described in chapter 3. It is proposed this is due to the membrane not being completely formed.

In addition to the tests performed above, the MOSFET heaters were modulated and the temperature sensors monitored to get further information, about the dynamic characteristics of the heater/membrane. A MOSFET heater (FET 2) was driven at a fixed drain voltage of 7 volts and the gate voltage pulsed at 0 to 5 volts at a number of different frequencies (0.4 Hz, 20 Hz and 100 Hz). A central diode temperature sensor was operated at a constant current of 10 μA and the voltage drop monitored with a Tektronix TDS210 oscilloscope. The on screen data was downloaded, via the GPIB port, to a PC and the resulting plots are shown in figure 8.11. Also measured was the output of the diode temperature sensor with the input to the gate modulated with a small square wave input of 380 mV at a fixed gate bias of 3.18 volts. The frequency of the square wave was set to 0.1 Hz, 1 Hz and 10 Hz as shown in figure 8.12.

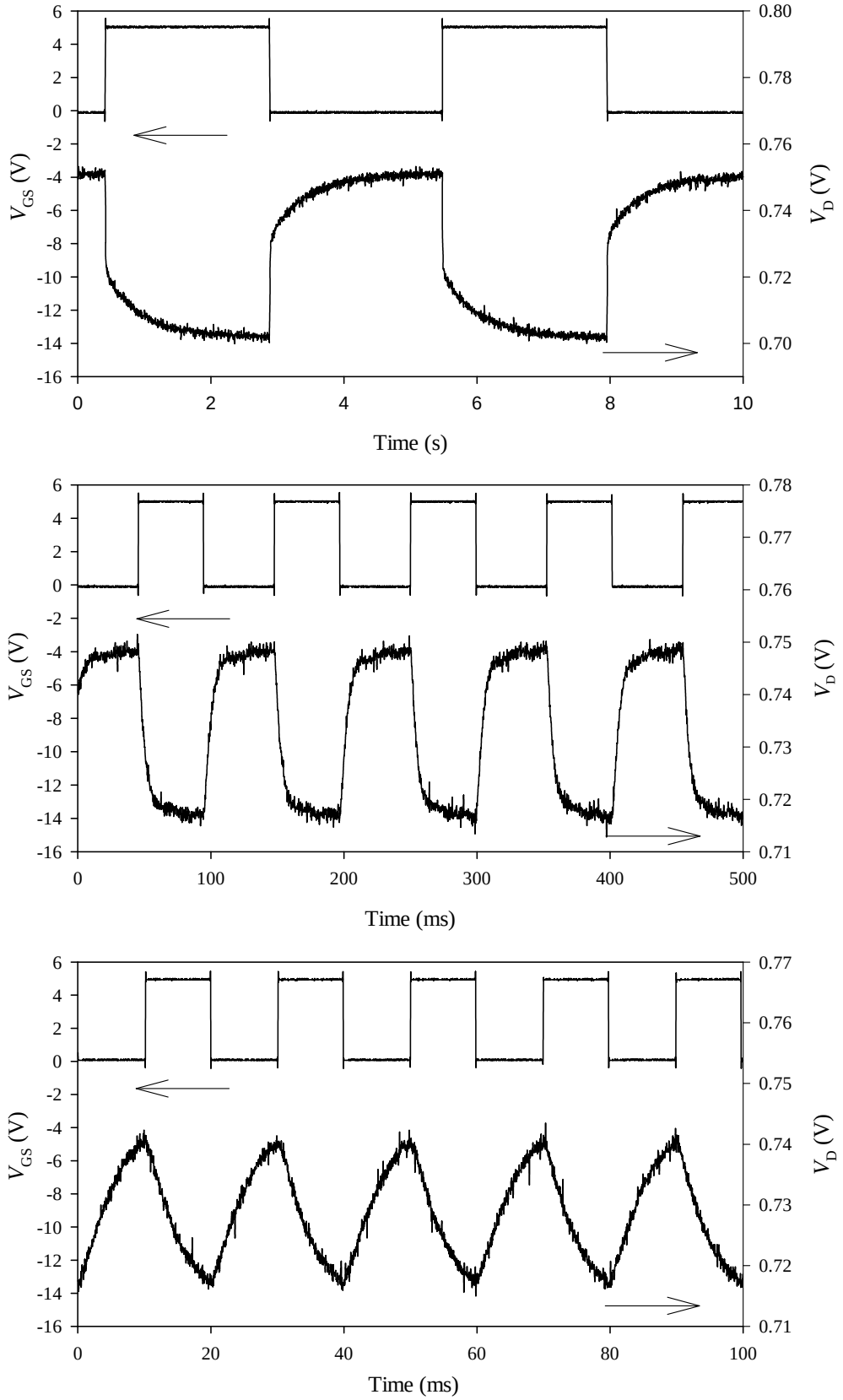

Figure 8.11: The dynamic output characteristics of a diode temperature sensor to a modulated MOSFET heater input.

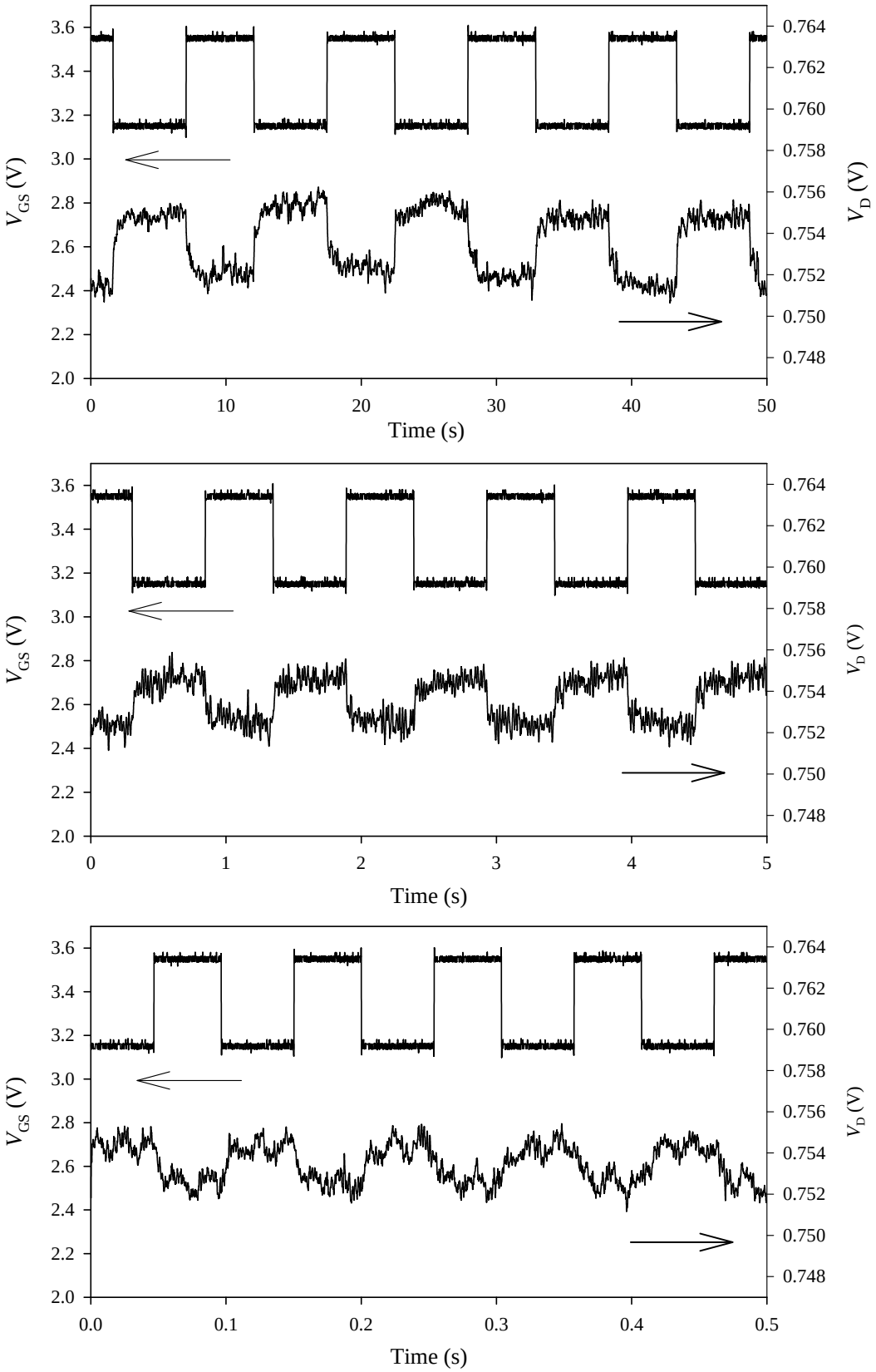

Figure 8.12: The dynamic output characteristics of a diode temperature sensor to a modulated MOSFET heater input at a fixed bias.

The results from these experiments show that it is possible to modulate the heater output to vary the temperature of the membrane and so the output of the diode temperature sensor. Results also show this dual exponential characteristic, where the membrane reaches equilibrium first followed by the bulk. When the input modulation of the gate voltage is low (0.4 Hz) the membrane and the bulk reaches a steady state at a maximum membrane temperature between 60 ^{o}C to 70 ^{o}C, with this characteristic dual exponential. As the gate voltage frequency is increased (20 Hz) the membrane component reaches near equilibrium after 50 ms, though the maximum membrane temperature has now fallen to between 50^{o}C and 60 ^{o}C. Finally, at high gate frequencies (100 Hz) even the membrane does not have sufficient time to reach equilibrium at that the maximum modulated membrane temperature has significantly fallen to 40 ^{o}C to 50 ^{o}C. These results show that rapid thermal modulation, of more than 100 Hz, of the heater is possible, though at the cost of reduced maximum operating temperature. By reducing the heat loss to the bulk though the use of a thinner membrane or trench isolation it should be possible to improve the performance (higher operating temperature, faster thermal modulation). Thermal modulation can be used to reduce the power consumption of the heater/ sensor structure, where the heater is only powered when a measurement is to be taken. In addition it can give further dynamic information from any gas sensitive material used, which could assist in the detection/separation of complex mixtures of gases or odours.

The second series of tests were used to investigate the temperature control of the MOSFET heater/temperature sensor combination. In an application it is likely that the diode and MOSFET heater would be used in a closed loop control to maintain the membrane temperature with different environmental conditions. When the input frequency is low the variation in temperature is 2.6 ^{o}C to 2.8 ^{o}C. This temperature variation falls to 1.9 ^{o}C to 2.1 ^{o}C and 1.6 ^{o}C to 1.7 ^{o}C as the frequency is increased to 1 Hz and 10 Hz. The output shows the characteristic dual exponential as described earlier with similar time constants. These results show that a temperature control of less than 1 ^{o}C are achievable at reasonable high heater frequency ($\approx$ 10 Hz). At lower frequencies and careful circuitry design it should be possible to attain a temperature control of $\pm$ 0.1 Hz. From these results we can consider a lumped model for the thermal diffusion through the membrane and the substrate as shown in figure 8.13.

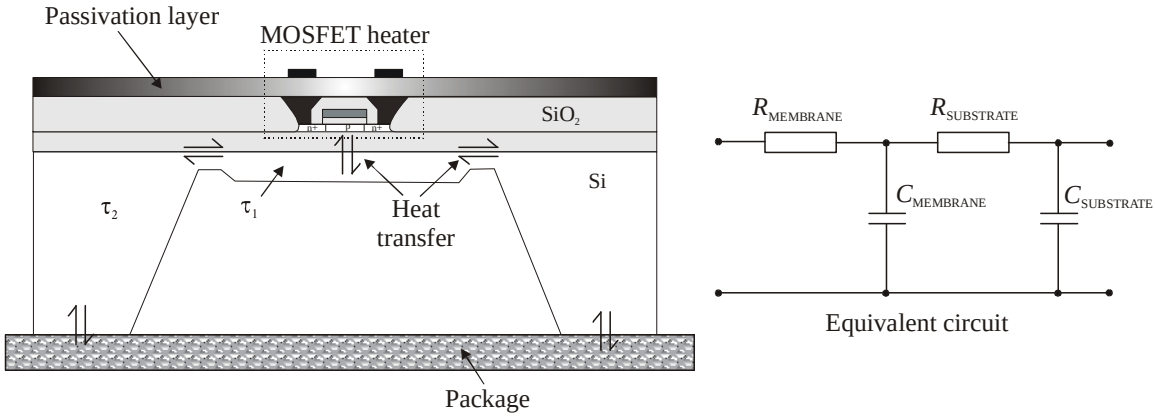

Figure 8.13: Layout of the SOI structure and an equivalent circuit of the lumped model.

Figure 8.13 shows a SOI device with a partial SOI membrane with a silicon plug in the centre of the membrane. This is the structure that has been created by the back etching process. Here thermal transfer occurs from the heater to the silicon plug, with time constant τ_1, and then from the silicon plug to the bulk and the package, with time constant τ_2. If we consider the electrical equivalent circuit of this structure, as also shown in figure 8.13, then the heating of the membrane and then the bulk can be modelled by two RC networks (one for the membrane and one for the substrate), where τ is equal to the RC time constant.

8.3.3 Thermal imaging of SOI device

To investigate the thermal profile of these SOI devices, infrared images, were taken using the Insight Vision System 80 series thermal imager. This camera measures in the mid-infrared region, 8 to 14 micron wavelength, using an array of pyro-electric detectors accessed by an electron beam. This removes the need for any mechanical scanning or liquid nitrogen cooled photon detectors. The resolution is approximately 300 lines vertically, with a maximum temperature sensitivity of approximately ± 0.5°C and at the minimum measurable temperature range (for a 0 ^{o}C to 1000 ^{o}C range) a sensitivity of 40° C. The picture is encoded in 8 different colours so that at maximum sensitivity of one colour represents 0.5° C. The Insight Thermal Imager is used to give an idea of the temperature profile over a surface but cannot give the absolute temperature. The camera output is recorded on video and then captured from videotape using a Matrox Rainbow Runner image capture card.

The resolution of the camera was not sufficient to detect individual heaters. Figure 8.14 shows a device with 2 MOSFETs powered (V_{DS} = 5 volts, V_{GS} = 4 volts, I_{DS} = 16.3 mA), as can be seen, there is a thermal gradient from heated end of the device to the non-heated end. It may also be observed that there are two hot spots on the image, which correspond to the two membranes of the heater.

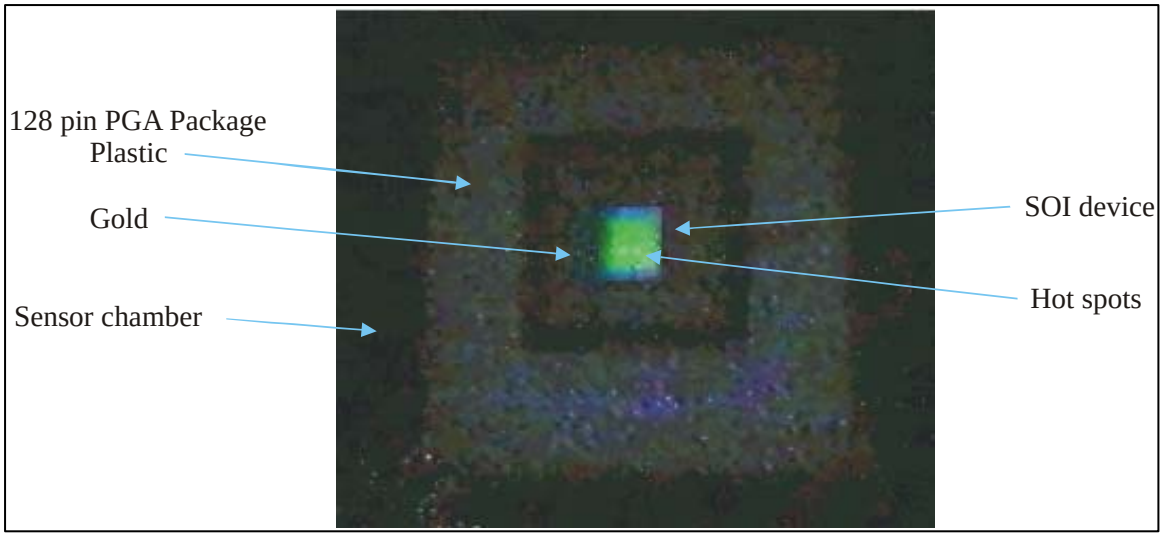

Figure 8.14: Thermal image of SOI device with two MOSFET heaters in operation.

In addition to images taken at steady state, the dynamic characteristics of the heater were examined using the infrared camera. The device was given a step input of V_{DS} = 5 volts and V_{GS} = 4 volts and the resulting thermal profiles were recorded till steady state was achieved. Images from this thermal transient are shown in figure 8.15 from time = 0 seconds to time = 1.3 seconds. From figure 8.15 it is possible to see that as the pulse input is applied to the device the thermal profile changes with the heater/membrane area getting hot first which then spreads to the bulk. Some heat loss to the membrane clearly occurs rapidly, though this does not reach equilibrium for 1 to 2 seconds.

Results from a number of devices were taken and an estimated stabilisation time of 1.3 seconds to 1.5 seconds was measured. This value is not inconsistent with the results from the dynamic characteristics of the MOSFET and of the thermal modulation of the heater. By 1.3 seconds any further increase in temperature was not distinguishable using this infrared camera so any further increase in membrane temperature can be considered to be minor.

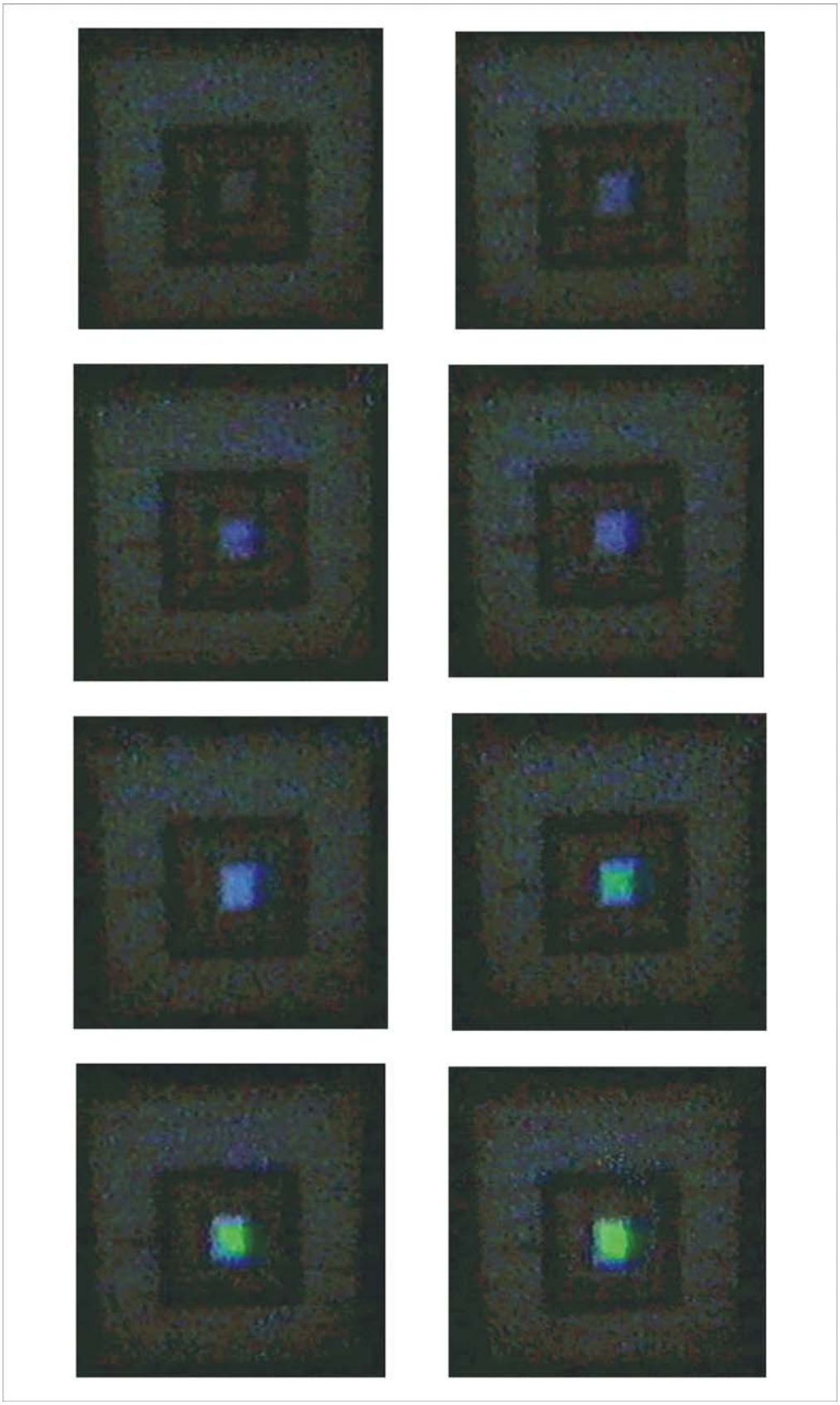

Figure 8.15: Thermal images of powering up of two SOI MOSFET heaters (at time intervals of 0.15 seconds).

8.4 Response of SOI sensors to organic vapours

As a last part of this SOI work a number of sensors were sprayed with a composite polymer (poly(sytrene-co-butadiene)). This was to investigate the operation of the sensor. A conducting polymer was used instead of a metal oxide sensing film as the operating temperature was not high enough. A full analysis with many different polymers was not undertaken, as there was not sufficient device numbers.

The MATRA sensor structure was a chemoresistor, using a pair of interdigited aluminium electrodes 21.5 μm apart and 300 μm long. The composite polymer poly(styrene-co-butadiene) was sprayed over the electrodes, performed at Warwick University, with the resulting sensor placed in a DRI-BLOCK^{TM} heater at a temperature of 35 ^{o}C. The sensors were exposed to six pulses of toluene (1316, 1843, 2633, 5793, 8690 and 12378 PPM) and ethanol vapour (2665, 3732, 11729, 17593, 25058 PPM) in air. The chemoresistors were driven at a constant current of 10 μA and the potential drop measured. The sensors were exposed to a particular water concentration for 60 minutes to create a stable baseline, then given a pulse of analyte 25 minutes in duration followed by 25 minutes recovery period. Examples of the dynamic responses are shown in figure 8.16.

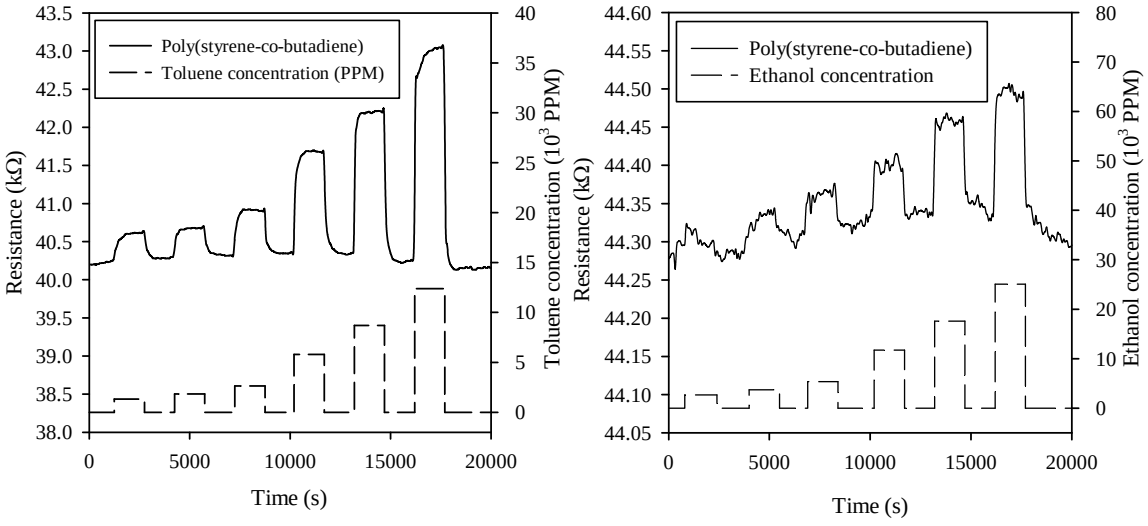

Figure 8.16: Dynamic characteristics of SOI chemoresistors to toluene and ethanol vapour in air at 35 ^{o}C.

These results can be converted into a static response as shown in figure 8.16. Here the results have been fitted to a power model associated with these sensors as described in chapter 7.

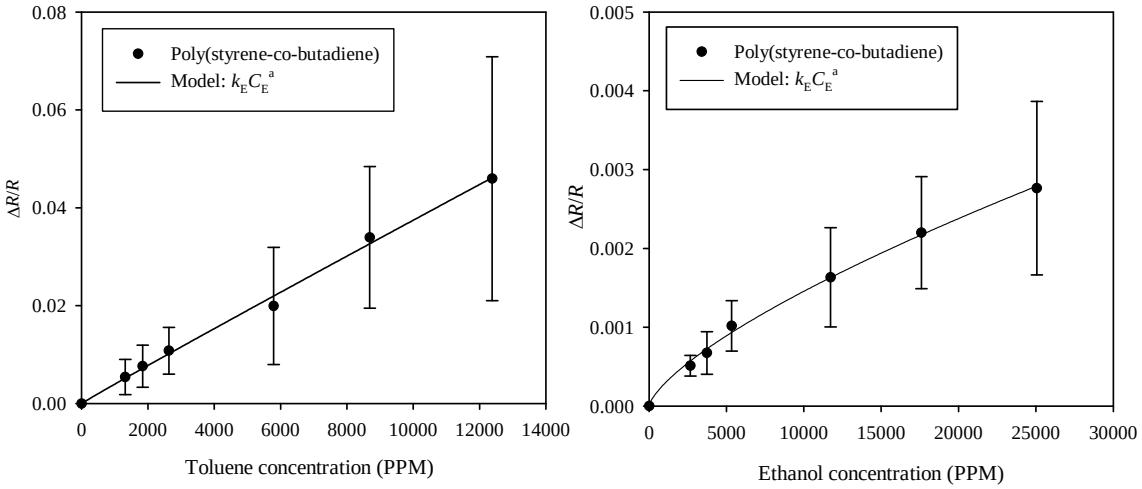

Figure 8.17: Static characteristics of SOI chemoresistors with poly(styrene-co-butadiene) coating to toluene and ethanol vapour in air.

In figure 8.17 the sensitivity (defined as $\Delta R/R_0$, with R_0 being the initial resistance) was used instead of the change in resistance. This was done, as there were significant differences in the initial resistance between 170 kΩ to 4.3 MΩ. This variation in resistance is probably due to the polymer being a different thickness and irregularities in the carbon loading. Table 8.5 gives the average sensitivity of these sensors to toluene and ethanol vapour in air.

Vapour	$\Delta R/R \times 10^{-6}$ PPM^{-1}	Standard deviation 10^{-6} PPM^{-1}
Toluene	3.89	0.28
Ethanol	0.16	0.04

Table 8.5: Typical sensitivity values for SOI chemoresistors.

A limitation of using this polymer is that the actual chemoresistor structure itself is small compared to the minimum resolution of the spray system and so thermal losses would be increased as the thickness of the membrane is expanded. These results do show however that the sensing structure of the SOI device can be used for the detection of an active gas or vapour and in the future it is hoped that by applying an alternative material a high temperature heater/sensor can be formed using the MOSFET heater to control the temperature instead of an external source.

8.5 Conclusions

In this chapter the electrical and thermal characteristics of the SOI MOSFET heaters have been presented. These experiments have been based solely on the devices fabricated through Europractice as the SUMC devices were not completed by the end of this research period. I-V and C-V analysis of the MOSFET heaters have been performed and this has shown that one of the MOSFET heaters did not operate correctly (short circuit) while the remaining MOSFET showed typical characteristics and that the gate capacitance is very small (≈ 28fF). Furthermore, I-V characterisations have been performed for transistors with and without membranes. This has shown a significant reduction in drain current at the same gate and drain voltage for a membrane device in comparison to a non-membrane device. It is proposed that this change in MOSFET characteristics is due to an increase in temperature of the MOSFET heater and of the membrane. This increase in temperature results in the degradation in the carrier mobility, which reduces the drain current. Also, on chip temperature sensors have also been calibrated and show that both diode and resistive sensors can be used to monitor the membrane. Membrane temperature measurements of the membrane show a heater/membrane coefficient of 8 mW/^{o}C. The dynamic characterisation of these MOSFET heaters has been performed and shows that this response follows a double exponential, which is composed of three components. Firstly, the MOSFET switching time, occurring in pico-seconds. Secondly the time for the membrane to reach thermal equilibrium, occurring in approximately 150 ms to 300 ms, and lastly, the time for the bulk to reach thermal equilibrium, occurring in 2 seconds to 3 seconds.

Temperature coefficients of –1.49 mV/^{o}C to –1.57 mV/^{o}C for the diodes and 305 Ω/^{o}C for the spreading resistors have been measured to a resolution of less than ± 0.01 ^{o}C (after calibration). Thermal modulation of a MOSFET heater, by applying square wave input to the gate, has been performed with the membrane temperature monitored with a *pn* junction diode. The results show that at a slow gate (0.4 Hz) modulation the output of the diode temperature sensor follows this characteristic dual exponential. At higher frequencies (20 Hz) only the membrane equilibrium is achieved, though as the bulk has not reached steady state the membrane temperature is lower. Lastly, at much higher frequencies (100 Hz) neither the bulk nor the membrane has reached equilibrium and so the variation in temperature is significantly reduced. These

results do show that it is possible to modulate the heater at frequencies in the tens of Hz, which could reduce the power consumption of the heater/membrane and possible to gain further dynamic information from the gas sensor. Temperature resolution experiments were performed by modulating the gate voltage at a fixed bias. The results show that a temperature control of less than 1 ^{o}C can be achieved and could be applied in a closed loop control to maintain the temperature of the membrane.

In addition to these experiments, further measurements were performed using an infrared camera (Insight 80). This camera was used to measure the thermal profile of the device, though the image did not have the resolution to pick out individual heaters or could give an absolute temperature measurement. Here two MOSFET heaters were switched with the resulting image showing a thermal gradient from the active heaters to the non-active. Also that the membranes are at a higher temperature than the bulk. Lastly, the dynamic characteristics were measured that showed the bulk reaching equilibrium in 1.3 seconds to 1.5 seconds.

Finally, the sensor section of the device was tested. As the operating temperature was below 100 ^{o}C and for ease of deposition, the composite polymer poly(styrene-co-butadiene) was used. Experiments showed a sensitivity to toluene and ethanol vapour in air at 30 ^{o}C, which followed a power model. These results are similar to those observed in chapter 7 also with discrete resistive sensors.

Here the characterisation of these new SOI MOSFET heaters has been performed. It has been found that these results are not the same as the simulated results shown in chapter 3. We believe this was due the membrane structure not being completely formed. This was due to inconsistencies of the back of the device, concerns over the stresses applied by the mechanical machining, the low number of devices and the non-uniform etching rate. As a result the thermal losses to the bulk are higher than would be expected and so a lower operating temperature is achieved for the same input power. These results are not ideal and it is hoped that once the SUMC devices have been completed the device characteristics would be similar to the simulated results.

8.6 References

8.1 Y. Taur, T. H. Ning, Fundamentals of modern VLSI devices, Cambridge University Press, 1998.

8.2 J.W. Gardner, Microsensors: Principles and Applications, Wiley, 1994.

8.3 N.H.E. Weste, K. Eshragian, Principles of CMOS VLSI designL A system perspective, 2nd edition, Addison-Wesley, 1993.

8.4 R.L. Geiger, P.E. Allen, N.R. Starder, VLSI: Design techniques for analogue and digital circuits, McGraw-Hill, 1990.

8.5 E.S. Yang, Microelectronic Devices, McGraw-Hill, 1988

8.6 S.M. Sze, Semiconductor devices: Physics and Technology, Wiley, 1985.

CHAPTER 9

Conclusions and further work

9.1 Aims and conclusions

In recent years there has been significant interest in the development of a portable hand-held electronic nose for both environmental monitoring and in medical applications. There is also renewed demand for gas monitors in the automotive industry which requires not only the manufacture of a large number of sensors (*ca* 10 million/year) but at very low cost with good reproducibility. Most existing commercial solid-state gas sensors suffer from high power consumption and/or reduced sensitivity and reliability. In addition, they are partially or totally incompatible with standard CMOS making transducer integration impractical. The current and most popular gas sensor technology is based on metal oxides (Taguchi type). However these operate at high temperatures (300 ^{o}C to 700 ^{o}C) and have high power consumption (500 mW – 800 mW) [9.1, 9.2]. Furthermore, they are labour intensive to fabricate and suffer from significant batch to batch variations.

The aim of this study has been the development and characterisation of new CMOS compatible gas/vapour sensors. Such a combination will allow the integration of the sensors and transducer circuitry on chip to produce a low cost, low power sensor that could supplement present technologies and be applied in a hand held instrument. Bulk CMOS and SOI CMOS processes have been adopted with the MOSFET being the predominant device structure. The study is divided into two sections: the development of room temperature (<100 ^{o}C) chemFET sensors employing conducting polymer films; and higher temperature (< 300 ^{o}C) SOI based sensors, utilising the self-heating effects

of the MOSFET on a thin SOI membrane with a chemoresistive or chemFET sensing structure. **This is the first time SOI technology has been used to create a gas sensor**. The characterisation of the room temperature chemFET sensors has been performed, investigating the effects of analyte concentration on the static and dynamic response. Also considered has been the effect water concentration and temperature on the static response and relative baseline. This is the first time a full device characterisation has been performed on chemFET sensors employing conducting polymer films. **This has resulted in final models for chemFET sensors that combine these three variables**. Electro-thermal analysis of the SOI devices has been performed to analyse the effectiveness of the heater/sensor combination. SOI is ideal for high temperature smart CMOS compatible sensors since it allows higher junction temperatures. Furthermore, the buried oxide combined with LOCOS isolation in the membrane area offer excellent thermal insulation, thus reducing the thermal conduction losses to a negligible level. The only remaining thermal losses are from conduction/convection to air and radiation, the latter term being negligible below 400°C. In addition, the buried oxide layer acts as an effective etch-stop. Electro-thermal, I-V and thermo-mechanical simulations have been performed to analyse these new MOSFET heater structures, as well as I-V and C-V analyses of the devices, including characterisation of the temperature sensors used to monitor the membrane. Lastly, the sensing section of the device has been used as chemoresistors to show that this structure can be used to detect a gas or vapour.

9.1.1 Room temperature chemFET sensors with a conducting polymer films

The design of the device itself was a critical consideration, as this defines the operation of the sensor. For a room temperature chemFETs a constant current mode of operation has many advantages over a constant voltage mode. Specifically, the device is now independent of process variations (e.g. transconductance terms at constant temperature) and constant current sources are easier to generate in CMOS than constant voltage sources. Furthermore, if the sensors are operated in the saturated regime the sensitivity is the same as in the linear, but now I_{DS} is independent of V_{DS}, simplifying the operation further, whilst improving noise rejection. The main room temperature device was designed and fabricated in collaboration with the Institute of Microtechnology at the University of Neuchatel. This was an array device of 4 *n*-channel enhanced MOSFETs with a meandered channel with a common gate and drain, so operating in the saturated

regime. Here the gate is either etched to expose the gate oxide or left intact, so the polymer is either in contact with the gate oxide or insulated by the gold film. Though not normally used in a standard CMOS process, gold allows many different active sensing materials to be used. For standard CMOS, doped polysilicon can replace the gold, though there are limitations as it is difficult to deposit some types of polymers on to it.

A full analysis with a range of conducting polymers was not undertaken in this study. Instead three different types of polymer were used, electrochemically deposited, composite, and chemically prepared electrochemically doped polymers, with a number of examples of each type. The electrochemically deposited polymers used two monomers: bithiophene and pyrrole, with the counter ions tetrabutylammonium tetrafluorborate and butane sulfonic acid, respectively. Further experiments used carbon black composite polymers, this is the **first time these polymers have been applied to chemFET sensors**. These materials combine an insulating polymer (usually used in gas chromatography) with carbon black nano spheres endowing electrical properties to the composite material. Three polymers were used poly(ethylene-co-vinyl acetate), poly(styrene-co-butadiene) and poly(9-vinylcarbazole) mixed with a 20% carbon loading (by weight). Lastly, a spun-coated/electrochemically doped polymer, poly(pyrrole), was used. Chemically prepared/electrochemically doped polymers and electrochemically deposited polymers give accurate control over the growth area, though the deposition process is more complex. The electrochemical process cannot be performed on types of metal electrodes e.g. aluminium. In contrast, composite polymers are chemically prepared and sprayed onto any type of metal electrode. This is the easiest process, though definition over the deposition area is poor and the minimum spacing between devices with different polymers is 300 μm to 500 μm.

To test systematically and characterise these sensors a Flow Injection Analysis test station was developed. This system was designed to the expose sensors to a variety of vapours at specific concentrations, humidities and temperatures. Furthermore, instrumentation was developed to measure and characterise (I-V) the response of the sensors, all controlled using LabVIEW^{TM} software.

9.1.2 Static and dynamic analysis of room temperature chemFET sensors response to organic vapours

Testing of the room temperature chemFET sensors to a broad range of vapours was beyond the scope of this research. Instead, two vapours were used with different properties. An in-depth characterisation with many gases and vapours may be envisaged if there was a full implementation of these sensors and this may form part of future work. The analytes ethanol and toluene were chosen for two reasons, firstly both have demonstrated rapid reversible responses to resistive conducting polymers sensors [9.3, 9.4, 9.5]. Furthermore, ethanol as an alcohol (a polar molecule with H- bonding) so may demonstrate a strong water dependency, unlike toluene, an aromatic, (a non-polar molecule). A summary of the sensor numbers and types is given in table 9.1.

Polymer	Ethanol (Static)	Toluene (Static)	Ethanol (Dynamic)	Toluene (Dynamic)	Ethanol/ Toluene (Humidity)	Ethanol/ Toluene (Temp.)
Polypyrrole	4 off	-	-	-	-	-
Polypyrrole/BSA	5 off	5 off	5 off	5 off	5 off	5 off
Polybithiophene/TBATFB	5 off	5 off	5 off	5 off	5 off	5 off
Poly(ethylene-co-vinyl acetate)	5 off	5 off	5 off	5 off	5 off	5 off
Poly(styrene-co-butadiene)	5 off	5 off	5 off	5 off	5 off	5 off
Poly(9-vinylcarbazole)	5 off	5 off	5 off	5 off	5 off	5 off

Table 9.1: A summary of the numbers and types of polymers used for each of the experiments carried out in this research.

A static and dynamic evaluation of these room temperature chemFET sensors to analyte concentration was performed and models developed. The initial models neglected the effects of water concentration and temperature. The sensors were operated at a constant current so any response of the sensor can be directly related to the shift in the threshold voltage. Here models were developed using a differential signal taken before and after exposure to an analyte. A steady-state model for chemFET sensors with spun coated/electrochemically doped and electrochemically deposited polymers was also developed based on a Langmuir isotherm or modified Langmuir isotherm. The chemFET sensors, with composite polymer films, response was modelled with a power law, though previous studies have shown that the response of chemoresistor sensors with these polymers typically follow a linear model (Henry's law) [9.5].

It is proposed that the observed shift in threshold voltage is a result of a modulation of the work function between the polymer and the semiconductor. In these models it is assumed that the shift in work function is directly related to the concentration of analyte within the polymer. This shift could be due to two mechanisms firstly, a charge transfer where the polymer is behaving as an acceptor or donor of electrons to the analyte. Secondly a swelling effect, where the polymer swells as the analyte diffuses through, either altering the polymer to carbon ratio, for composite polymers, or the polymer to air ratio for electrochemically deposited polymers. It is likely that some combination of these two effects is occurring. From these experiments the sensitivity of these sensors and the detection limits can be calculated, as given in table 9.2.

Dynamic modelling of these sensors was also performed, showing a double exponential response. This describes an event were two different kinetic reactions are occurring. It was found that the time constant of this expression followed a reaction limited response and reduced with increasing analyte concentration, defined by the forward and backward reaction rates as the analyte is absorbed/deabsorbs from the polymer. This suggests that this dynamic information could also be used for detecting and separating simple chemicals. It was also found that for the chemFET sensors with composite polymers (except for poly(9-vinylcarbazole) typically showed a faster response and recovery time to the test analytes than the sensor with electrochemically deposited polymers. Table 9.2 gives typical response times of these chemFET sensors employing conducting polymer films. The response and recovery periods were similar for the chemFET sensors with composite polymer films though the sensors with electrochemically deposited polymers and poly(9-vinylcarbzole) showed significantly longer response and recovery periods. **It is proposed, that these longer response and recovery periods may be due to the analyte being in competition with water vapour, so the response of the sensors is not simply controlled by the reaction of the analyte within the polymer but the time for the water vapour to deabsorb**.

The effect of film thickness was also investigated. This was limited to the composite polymers, as accurate control over the deposition depth for the electrochemical polymers was not sufficiently achieved. When tested to toluene vapour an increase in the sensor response was observed with an increase in polymer thickness. This suggests a bulk effect occurs within the polymer, where the observed reaction is

evenly distributed throughout the polymer and is related to the quantity of deposited polymer. With ethanol vapour, once a threshold thickness had been achieved, the response of the remained similar, which would suggest an interface reaction. Ethanol being a polar molecule may have some bearing on this as interactions maybe occurring between the ethanol and the gate oxide.

9.1.3 The effect of water concentration on the response and relative baseline of room temperature chemFET sensors

An important environmental factor for any sensor is the effect of water vapour on its response and relative baseline. Here it was found that for the *n*-channel MOSFET chemFET sensors with composite and electrochemically deposited polymers there was a significant water dependence on the baseline, where increasing water concentration reduced the relative baseline (up to 4 μV/PPM). **It is proposed that the water vapour is forming a dipole layer at the gate oxide, shifting work function and possibly the capacitance of the sensors**. For the chemFET sensors with composite polymer films, the effect of water concentration on the response was negligible. The chemFET sensors with electrochemically deposited or spun-coated polymer films had a significant water dependence on the response. The chemFET sensors with spun-coated polymers showed a reduction in sensor response with increasing water concentration and the chemFET electrochemically deposited polymers showed an increase in response with increasing water concentration. This increase in response was unexpected as resistive devices, with similar polymers, show a reduction in response with increasing water concentration [9.6]. A possible explanation for these observed results is that there is competition between the polymer and the analyte, where the water is being preferentially replaced with the analyte. The removal of water within the polymer may cause the removal of water molecules from the gate oxide shifting the differential result. The outcome of this is that the response is an addition of the analyte concentration and the shift in the relative baseline, as water is removed from the gate oxide. As the analyte is expelled, the water molecules re-attach themselves to the gate oxide hence shifting the device characteristics back to their original level. Supporting evidence for this explanation is given by the *p*-channel (MISFET) chemFET sensors with a spun-coated/electrochemically doped polymer film. These devices have a thin silicon nitride layer over the gate oxide and showed a reduction in response with

increasing water concentration, though this may be a material dependence. Further research into this problem is required, examining the effect of an alternative or layered gate insulator (i.e. silicon dioxide with a thin nitride coating).

9.1.4 The effect of temperature on the response and relative baseline of room temperature chemFET sensors

These models were expanded to account for the effect of temperature. The *n*-channel chemFET sensors with composite polymer films showed a logarithmic reduction and the electrochemical polymers a linear/log reduction in the magnitude of the response. **It is proposed that this temperature dependence can be explained by the analyte boiling point model.** In this model a partition coefficient, which describes the partition of analyte concentration within the polymer to the vapour phase (bulk solubility), is related to the boiling point of the analyte. This partition coefficient has a log dependence to temperature which fits the observed results. A limitation of this model is that it is purely thermodynamic, which is adequate for the composite polymers, though for the electrochemically deposited polymers further interactions may be occurring between the counterion and the analyte. Lastly, the effect of temperature on the baseline was examined. It was found that an increase in temperature caused a fall in relative baseline for all the chemFET sensors with open and the solid gate MOSFETs with composite and electrochemically deposited polymer films. The exception was those devices with a solid gate and composite polymer film, which showed a rise in relative baseline with increasing temperature. For a normal *n*-type MOSFET we would expect this increase in the relative baseline at higher temperature due to a degradation in the carrier mobility. As in most cases the opposite is occurring, another mechanism must be involved. **It is proposed that this shift in relative baseline is due to a thermal expansion of the polymer where increasing temperature swells the polymer altering the polymer to carbon ratio, for the composite polymers, or polymer to air ratio for the electrochemically deposited polymers**. A summary of all the results from these room temperature chemFET sensors with conducting polymer films is given in table 9.2.

Polymer	$\left.\frac{\partial V_{GDS}}{\partial C_T}\right\|_{C_W,T}$ (μV/PPM)	Standard deviation (μV/PPM)	$\left.\frac{\partial V_{GDS}}{\partial C_E}\right\|_{C_W,T}$ (μV/PPM)	Standard deviation (μV/PPM)	Toluene detection limit (PPM)	Ethanol detection limit (PPM)
PPY	-	-	-0.5 nA/PPM	0.2 nA/PPM	-	-
PPY/BSA	-1.03	±0.46	1.09	±0.99	10 - 20	< 20
PBT/TBATFB	-1.13	±0.40	0.54	±0.41	30 - 40	< 20
CP1	-0.6	±0.1	8.0×10^{-2}	$\pm 1.4 \times 10^{-2}$	10 – 20	10 – 50
CP2	3.1	±0.75	0.39	±0.21	< 10	10 – 50
CP3	4.0	±0.61	0.29	$\pm 6.5 \times 10^{-2}$	< 10	10 – 50
Polymer	Toluene on time response (s)	Standard deviation (s)	Ethanol on time response (s)	Standard deviation (s)		
PPY/BSA	330	±257	772	±845		
PBT/TBATFB	251	±78	572	±366		
CP1	304	±175	237	±250		
CP2	472	±300	212	± 87		
CP3	1397	±993	136	± 150		
Polymer	Toluene off time response (s)	Standard deviation (s)	Ethanol off time response (s)	Standard deviation (s)		
PPY/BSA	649	±403	1263	±7345		
PBT/TBATFB	1020	±852	1251	±881		
CP1	299	±298	360	±558		
CP2	412	±352	145	±60		
CP3	698	±383	2174	±3393		
Polymer	$\left.\frac{\partial V_{GDS}}{\partial C_W}\right\|_{C_E}$ (μV/PPM)	Standard deviation (μV/PPM)	$\left.\frac{\partial V_{GDS}}{\partial C_W}\right\|_{C_T}$ (μV/PPM)	Standard deviation (μV/PPM)	$\left.\frac{\partial V_{GDS}}{\partial C_W}\right\|_{C_T=0}$ (mV/PPM)	Standard deviation (mV/PPM)
PPY/BSA	656.2	±392.3	-447.1	±242.3	-4.2	±1.5
PBT/TBATFB	361.6	±71.5	-399.7	±69.8	-3.9	±1.6
CP1	5.8	±1.1	-14.3	±5.3	-3.6	±0.2
CP2	6.2	±5.0	46.0	±25.9	-4.5	±0.6
CP3	7.6	±3.9	74.2	±42.7	-1.1	±0.2
CP solid	-	-	-	-	0.0094	±0.00063
	$\left.\frac{\partial R}{\partial C_E}\right\|_{T=const}$ (Ω/PPM)	Standard Deviation (Ω/PPM)	$\left.\frac{\partial R}{\partial C_T}\right\|_{T=const}$ (Ω/PPM)	Standard deviation (Ω/PPM)		
Resistive	1.0	±0.1	14.4	±6.0		

	$\left.\frac{\partial R}{\partial T}\right\|_{C_E=\text{const}}$ ($\Omega/^{o}C$)	Standard deviation ($\Omega/^{o}C$)	$\left.\frac{\partial R}{\partial T}\right\|_{C_T=\text{const}}$ ($\Omega/^{o}C$)	Standard deviation ($\Omega/^{o}C$)	$\left.\frac{\partial R}{\partial T}\right\|_{C_T=0}$ ($\Omega/^{o}C$)	Standard Deviation ($\Omega/^{o}C$)
Resistive	0.0014	±0.0002	0.037	±0.013	-2.3	±0.7

Table 9.2: Summary of results for chemFET and resistive sensors employing conducting polymer films. (PPY/BSA – Poly(pyrrole)/BSA, PBT/TBATFB – Poly(bithiophene)/TBATFB, CP1 – Poly(ethylene-co-vinyl acetate), CP2 – Poly(styrene-co-butadiene), CP3 –Poly(9-vinylcarbzole).

9.1.5 The development of micro-hot plate gas sensors based in SOI technology

A number of designs based on SOI technology were produced throughout this research period in collaboration with the Department of Engineering, University of Cambridge. As stated earlier, these new SOI designs have the advantage of higher operating temperatures, whilst still being fabricated with a standard process giving rise to the possibility of transducer integration. Only two post-processing steps are necessary to complete the sensors after standard processing has been completed, the back-etching of the device silicon to form the SOI membrane and the deposition of a gas sensitive material. Here a simple composite polymer film was used to test the sensor structure, as the focus of this research is not on the gas sensitive materials, but the novel heater/sensor structure. The FET heater structure was laid out in three basic configurations, an interdigitated design with five/six *n*-type enhanced MOSFETs in parallel, interdigitated design with a gap for a spreading resistive or a diode temperature sensor and a square design for a lateral temperature or gas sensor. The gas sensors were either a chemoresistive sensor using a gold or an aluminium interdigitated electrode, or a chemFET sensor with the polysilicon gate partially removed. A number of different designs have been/are being produced fabricated through Europractice (Matra) and SUMC foundries. The Matra design contained four membranes with one simple interdigitated and three interdigitated with gap designs. The SUMC had two membranes within their standard frame using a number of different heater structures. Unfortunately, the SUMC devices were still not ready at the end of this research period (two years about design submission), furthermore one of the MATRA FET heaters did not operate correctly (short circuit). A summary of the design is given in table 9.3 below. Each membrane was 500 μm × 500 μm with a 150 μm × 150 μm active heater area. The Matra designs used a 3 arm interdigitated electrode structure of Al (aspect ratio 13.3) and the SUMC process an 11 arm interdigitated electrode structure of Au (aspect ratio 233).

MATRA design	Description	Dimensions (μm)
Device 1	4 × interdigitated heater with 25 μm gap	132 × 12
Bipolar 1 & 2	1 × central bipolar, 1 × on membrane	
Diode 1 & 2	2 × diodes on membrane (*p*-*n* junction)	26 & 22
Device 2	6 × interdigitated heater with 30 μm gap (larger heater area 300 μm × 300 μm)	275 × 25
Diode 3 – 5	1 × central diode, 2 × on membrane	26 & 22

Resistor 1 & 2	2 × resistive sensors on membrane	200 × 7
Device 3	6 × interdigitated heater with 25 μm gap	126 × 9
Bipolar 3 & 4	2 × bipolar on membrane	
Resistor 3 & 4	2 × resistive sensors on membrane	200 × 7
Device 4	5 × interdigitated heater without gap	132 × 12
Bipolar 5 & 6	2 × bipolar on membrane	
Device 5	Copy of device 4 off membrane for comparison	
SUMC designs	Description	Dimensions (μm)
Cell 1	**Chemoresistive sensors**	
Device 1	6 × interdigitated heater without gap	128 × 12
Resistive 1	1 × Channel spreading resistor	175 × 10
Diode 1	Vertical *p-n* junction diode	25
Device 2	1 × square heater with gap	424 × 12
Diode 3 & 4	1 × central diode (horizontal) 1 × on membrane (vertical)	36 × 36 & 25
Resistive 2	1 × Channel spreading resistor	175 × 10
Resistive 3 – 6	4 × spreading resistors off membrane	100, 150 and 200
Cell 2	**Chemoresistive/microcalorimeter**	
Device 1	4 × interdigitated heater with 30 μm gap	132 × 12
Diode 1 & 2	1 × central diode (vertical) 1 × on membrane (horizontal)	25 & 36 × 36
Device 2	Copy of device 1	
Device 3	Copy of device 1 without membrane	
Resistor 1 & 2	2 × off membrane spreading resistors	100 × 10
Cell 3	**Narrow chemFET sensors**	
Device 1	1 × square heater with gap	404 × 12
Diode 1	1 × vertical diode on membrane	25
Device 2	Copy of device 1	
Device 3	Copy of device 1	
Resistor 1-2	2 × spreading resistors off membrane	100 & 200
Diode 4 & 5	2 × diodes off membrane (1 vertical/1 horizontal)	36 × 36 100
ChemFET 1 & 2	FETs with 15 μm gap in polysilicon	36 × 50
Cell 4	**Wide chemFET sensors**	
Device 1	1 × square heater with gap	404 × 12
Device 2	Copy of device 1 off membrane	
Device 3	Copy of device 1 off membrane	
Device 4	Copy of device 1 off membrane	
ChemFET 1 & 2	FETs with 30 μm gap in polysilicon	50 × 50

Table 9.3: Summary of different SOI designs

9.1.6 Thermal and electrical characterisation of SOI heaters

Simulations obtained from the SOLIDIS-ISE package showed that, for these MOSFET heaters, the lattice temperature increased almost linearly with applied gate voltage once a threshold voltage had been achieved. 3D electro-thermal simulations were performed to calculate the heat loss by conduction and convection. It was shown that a temperature of 350 ^{o}C could be achieved for only 35 mW power consumption. Also that the maximum temperature variation between the core of the heater and the sensing

material was 27 ^{o}C with only a 4 ^{o}C variation over the sensing element. Furthermore, the interdigitated heater with gap design did not cause a significant temperature variation over the heater area and that the remaining bulk silicon was at ambient and so any additional circuitry would operate as normal. Thermo-mechanical simulations were also performed and showed that the maximum stress for the membrane increased from 65 MPa at room temperature to 255 MPa at 400 ^{o}C.

In the MATRA design diode and resistive temperature sensors were used to monitor the temperature of the membrane. Typical initial values at room temperature (30 ^{o}C) and temperature coefficients are given in table 9.4. Resolution measurements were also performed and showed that a change in temperature of less than 0.01 ^{o}C could be observed. This resolution could only be achieved after calibration of the sensors because of small variations in fabrication exist.

Sensor	Initial value	Standard deviation	Temperature coefficient	Standard deviation
Diode 1	0.751 V	± 0.6 mV	-1.57 mV/^{o}C	± 7 μV/^{o}C
Diode 2	0.729 V	± 0.2 mV	-1.49 mV/^{o}C	± 49 μV/^{o}C
Resistor	115.4 kΩ	± 291 Ω	305 Ω/^{o}C	± 5 Ω

Table 9.4: Characteristics of the temperature sensors used in the MATRA SOI designs.

I-V characterisation of the MOSFET heaters was performed on devices that showed a decrease in drain current after the formation of a membrane (at fixed drain and gate voltages). This reduction is due to the self-heating effect of the MOSFET, where increasing temperature decreases the effective carrier mobility of the channel and so reduces the transconductance of the transistor. The resulting temperature coefficient of 8 mW/^{o}C was lower than expected from simulation. This was due to the membrane only being partially formed, which results in higher thermal losses to the bulk silicon and the (gold) package. The reasons why the membrane was not completely formed are:

- Significant surface roughness on the back of the device
- Mechanical stresses of the machining process may have resulted in membrane failure

- Differential etching resulted in partial contact with the buried oxide, as oxide is very thin (400 nm) further etching would have removed the oxide and the MOSFET heater within the device silicon

These experiments highlight a limitation of this design. Specifically, if devices with only a partial membrane are used, then the MOSFET requires re-designed to allow additional power to be supplied to the transistor whilst still operating in the standard ± 5 volt regime. To achieve such a result the W/L ratio of the heater could be altered by increasing the channel width.

The dynamic characterisation of the MOSFET heaters was performed and showed that the response followed a double exponential, composed of three components. Firstly, the MOSFET switching time, occurring in picoseconds. Secondly, the time for the membrane to reach thermal equilibrium, occurring in approximately 150 ms to 300 ms. Lastly, the time for the bulk to reach thermal equilibrium, taking 2 seconds to 3 seconds. Thermal modulation of a MOSFET heater, by applying square wave input to the gate, was performed with the membrane temperature monitored (diode temperature sensor). Results showed that as the input frequency was increased (0.4 Hz to 100 Hz) the amplitude of the resulting temperature variation of the membrane reduced. This is a consequence of the bulk and then the membrane not having sufficient time to reach equilibrium. Further tests were used to investigate the temperature control of the MOSFET heater/temperature sensor combination. In any application, it is likely that the diode and MOSFET heater would be used in a closed loop control to maintain the membrane temperature as the device is exposed to different environmental conditions. Thermal modulation can also be used to reduce the power consumption of the heater/membrane and possible to gain further dynamic information from the gas sensor. In these tests, the gate voltage was modulated at a fixed bias to investigate the temperature resolution heater/membrane. Results showed that the membrane temperature could be controlled to a resolution of less than 1 ^{o}C.

Thermal imaging of the SOI heater was also performed. Unfortunately, the infrared camera used for these measurements did not have the resolution required to give the profile of a heater, though did show that the device was thermally elevated above ambient, also that the membranes were hotter than the bulk and the time constant to reach a stable temperature (including the bulk) was 1.3 to 1.5 seconds. Clearly, the

time for the membrane to reach a stabilised temperature will be quicker as the heater and the membrane will reach operating temperature before the bulk.

Lastly, the SOI devices were operated as chemoresistive vapour sensors to detect ethanol and toluene vapour. Here a simple composite polymer (poly(styrene-co-butadiene) was used to detect these vapours and showed a typical sensitivity of 0.25 Ω/PPM and 0.01 Ω/PPM for toluene and ethanol vapour, respectively, following a power model described earlier. These experiments simply prove that these sensors can be used to detected gas/vapours.

9.1.7 Project objectives

Many of the objectives of this study have been realised, these are summarised below:

- CMOS compatible gas/vapour sensors have been designed and developed, based predominately on the MOSFETs, using bulk CMOS and SOI CMOS.
- The static and dynamic response of room temperature chemFET sensors has been characterised to analyte concentration.
- The effect of environmental conditions (temperature and humidity) on the static response and relative baseline of room temperature chemFET sensor have been determined.
- Theoretical and empirical models have been developed for the static and dynamic response of these room temperature sensors and where possible by chemical interactions between the analyte/water vapour, conducting polymer and the device.
- Lastly, SOI based gas sensors have been designed, developed and simulated and where possible characterised as a heater/sensor combination.

9.2 Application of CMOS sensors

Clearly, the outcome of this research is to create a commercial sensor for the electronic nose industry. Any such instrument would contain an array of these sensors in order to detect and identify vapours, gases and odours. The question is whether these sensors are superior in some way to present commercial sensors or give a significant advantage for an electronic nose instrument. On the positive side these sensors are low power and have the advantage of possible circuit integration reducing noise and improving

sensitivity. In addition, the application of CMOS technology should lead to reproducible devices and a reduction in the fabrication cost. The main limitations of these room temperature sensors, highlighted in these experiments, is the variation in response and the environmental dependence of the baseline. Though the repeatability of the device itself is much improved because of the fabrication process, small variations in film thickness and constitution can produce a sensor with radically different properties. Furthermore, the temperature and water vapour dependence are still an issue, where small variations in environment can cause a shift equivalent to ten's of PPM of an analyte. Clearly, some limitations can be removed with careful control of the sampling environment, where the delivery of the gases and vapours is always at the same temperature and humidity. However, this control may not always be possible for a portable instrument, as the target sample is rarely delivered in such a regulated manner. Secondly, it could be possible to reduce the effect with meticulous sensor design (i.e. using layered gate insulator composed of silicon dioxide with a thin coating of silicon nitride). A clear advantage for these sensors over standard resistive types is that no current flows through the active material. This should improve the long term stability of the sensor and for electrochemically deposited polymers reduce unwanted ion movement through the films. By applying the models developed in this thesis it maybe possible to compensate for some of these environmental problems, with the integrating circuitry to perform some of this role directly.

For the SOI devices, clearly the yield and life span/stability of the heater/membrane structure is critical, as the designs have large membrane areas that can easily be compromised. In addition, thermal cycling of the device will also reduce the life span of the membrane by applying different stresses to the membrane. A good property of these sensors however, is the ability to linearly control the temperature of the heater though the gate voltage. This coupled with its low power operation and reasonably high operating temperature makes these devices ideal for a number of different gas sensing materials.

9.3 Smart CMOS gas sensors

The smart gas sensor is still some way off, though some early efforts have been made in this research to develop such a sensor. Before the completion of this thesis, a third SOI sensor design was implemented. This design may not be classed as smart but could

be thought of as an integrated sensor, which describes a low-level smart sensor in which some of the pre-processing is integrated. If these designs and additional circuitry operate as expected, it should be possible to create a smart sensor based on SOI technology.

The design has a number of improvements from the previous work in this report, specifically, the use of *p*-channel MOSFET heaters, the integration of transducer circuitry, the addition of trench isolation and the use of polysilicon as well as FET heaters. It has been found, through simulations, that the operating temperature for a *p*-type devices is higher than for an *n*-channel before device instability occurs, due to the lower carrier mobility for holes in comparison to electrons [9.7]. In this design, the sensing structure can be used as either a calorimetric or chemoresistive sensor with an operating temperature of up to 350°C. In the case of a microcalorimeter, a thin layer of catalyst coats the active (hot) region of the SOI membrane. The sensors are in a normal configuration operated as a pair with a sensor and reference. An amplifier circuit has been integrated within the design, which produces a linear differential output between the sensors and the reference for a differential temperature of up to 80°C, after which the circuit becomes saturated. A voltage sensitivity of 50 mV/K should permit precise measurement of the combustion process.

This third design has been fabricated through Europractice using the 0.8 μm DMILL-MATRA process. The dimensions and layout are similar to the previous design outlined here, with a die size of 4 mm × 5 mm and four membranes (membrane size 500 μm × 500 μm, active area 150 μm × 150 μm). In addition, to the two *p*-type MOSFET heaters there are two polysilicon resistive heaters. It has been found, through simulation, that the polysilicon heaters on an SOI wafer do not exhibit the usual limitations associated with their use, typically short life span and variations in resistance. Also included are off-membrane resistive and MOSFET heaters for comparison. Furthermore, eight trenches 10 μm wide, 10 μm apart are included for additional lateral thermal isolation of the transducer IC area. This has been shown to reduce the thermal loss through the membrane and improve mechanical stability. Here both *n*-*p* diodes and spreading resistors have been used to monitor the temperature of the membrane. A schematic of the design is shown in figure 9.1 with a magnified section of two of the active regions. The resistive heaters are 12 μm × 1250 μm with a

Comment [JWG1]: What about the other two cells?

typical resistance (at room temperature) of 232 Ω. The resistive spreading temperature sensor has a resistance of 20 kΩ at room temperature, with a temperature coefficient of –3.26 mΩ/K, though in normal operation this will be driven at a constant current of 40 μA, giving a –2.6 mV/K temperature coefficient. The thermodiodes are supplied at the same current and have voltage temperature coefficients of –2 mV/K. The MOSFET heaters are in an interdigitated configuration with gap. The MOSFET channel dimensions were 640 μm × 12 μm, in four arms, with a *W*/*L* ratio of 53.3. On both of these designs a 18 μm gap has been included for a temperature sensor. Further integrated circuitry has been added to amplify the signals from the temperature sensors. The op-amp has a differential input from the two sensors, where one input is from an active sensors and the second a reference, with a voltage gain of 40. A second op-amp has been included to measure the absolute temperature from the sensors. The circuit diagrams for each individual op-amp and the final circuit is given in figure 9.1. This design contains a number of components of a smart system and is one of the first designs to integrate circuitry with the gas sensing structures.

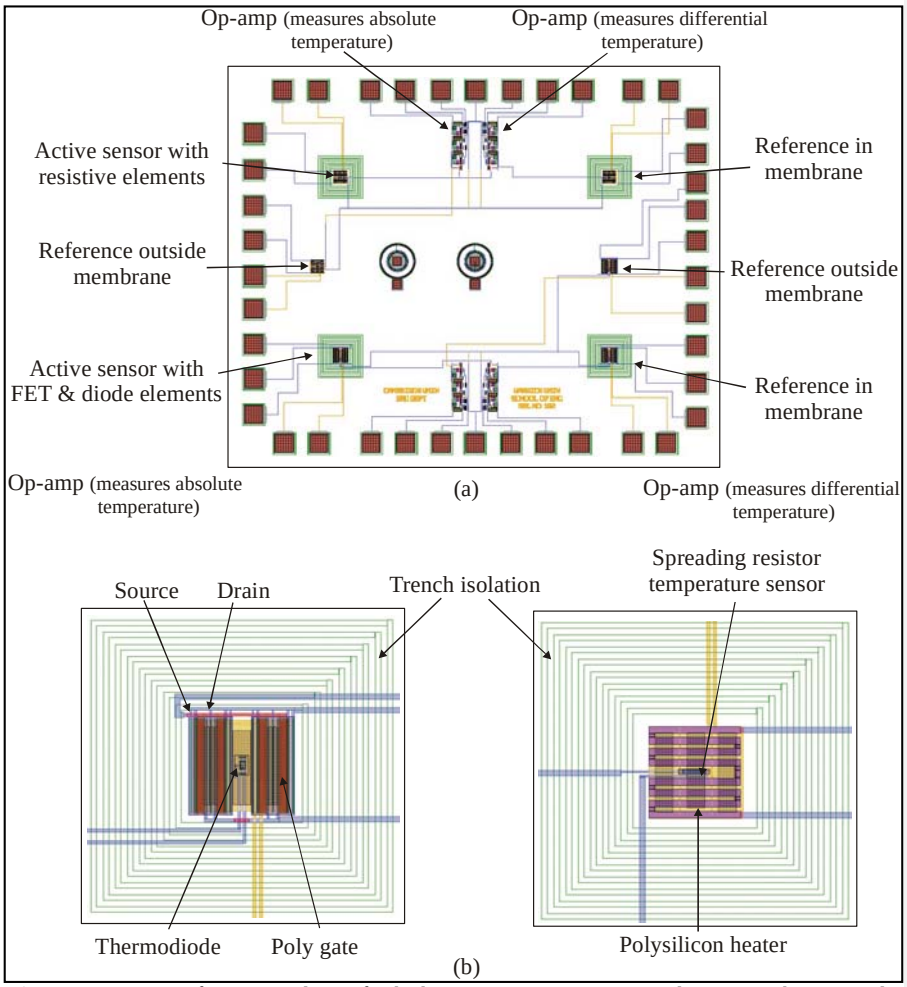

Figure 9.1: Design of new SOI device for high temperature gas sensor applications with integrated transducer circuitry.

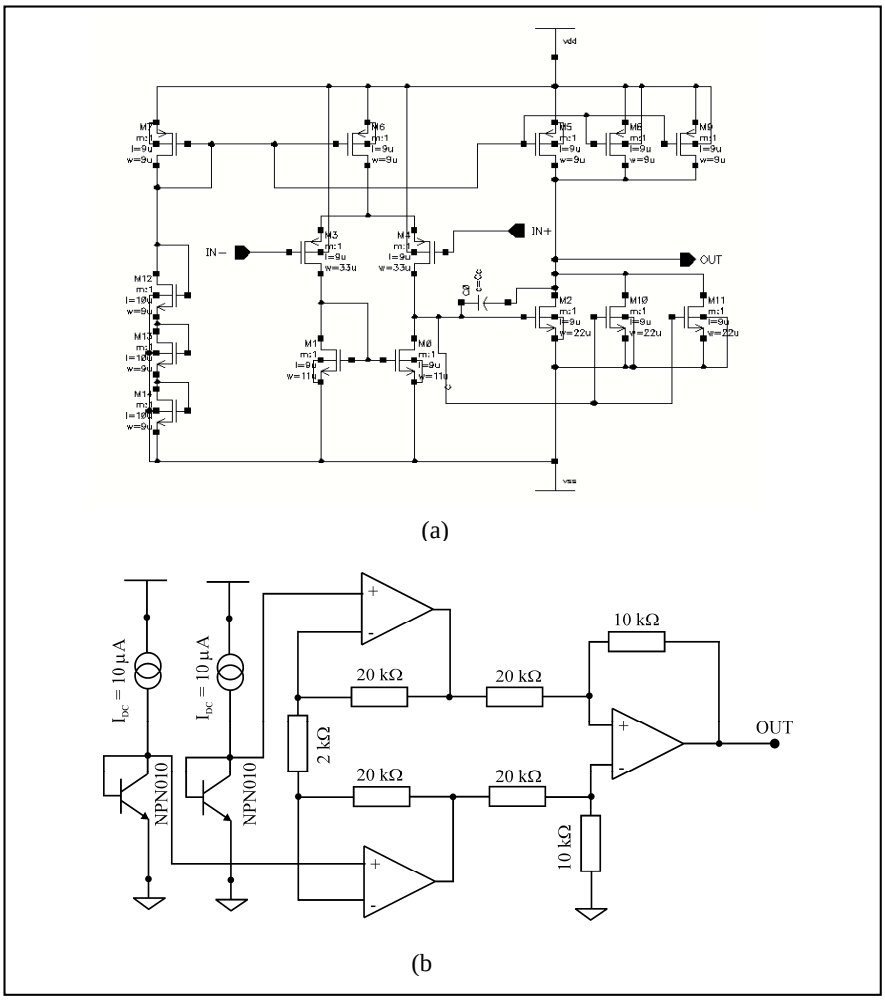
vdd
vss
IN−
IN+
OUT
M1
M2
M3
M4
M5
M6
M7
M8
M9
M10
M11
M12
M13
M14
M15
M16
M17
M18
M19
M20
M21
M22
M23
M24
M25
M26
M27
M28
M29
M30
M31
M32
M33
M34
M35
M36
M37
M38
M39
M40

Furthermore, to investigate different gate materials, specifically the use of *n*-type polysilicon as the gate material and how the electrochemical process can be altered to allow deposition of these materials. In addition, a method of depositing composite polymers more accurately is required to form array devices, producing multi-polymer chemFET arrays with higher packing densities. This would have to include additional testing for a range of composite polymers, as present commercial electronic noses using composite polymers use 32 different polymers [9.8].

The completion of heater/sensor characterisation of the SOI designs is a crucial step as only preliminary results have been taken. A full characterisation of the SUMC devices should be completed. In addition, this research has concentrated on the device more than the material technology and so further research into developing accurate methods of active material deposition is required. Furthermore, it may be of interest to fine tune materials, such as catalytic metals or metal oxides, to operate at these lower temperatures. There are still a number of advancements which still be could achieved, most notable the further integration of circuitry to create the first true high temperature smart gas sensors. Clearly, either of these technologies could lead to the development of what could be called a “nose on a chip”, where all the associated electronics and signal processing is on-board and the output can simply be monitored for a final result. This can be considered as the long-term goal of this research and possibly one of the final goals for the electronic nose industry.

9.5 References

9.1 J.W. Gardner, P.N. Bartlett, Electronic Noses: Principles and Applications, Oxford University Press, 1999.

9.2 J.W. Gardner, Microsensors: Principles and Applications, Wiley, 1994.

9.3 R.A. Bisell, F-B Li, P. Travers, K.C. Persaud, A boiling point model to describe conducting polymer gas sensor responses, Electronic Noses and Olfaction 2000 (ed. J.W. Gardner, K.C. Persaud), (2000), IOP Publishing Ltd, Bristol, 23-34.

9.4 P.N. Bartlett, P.B.M. Archer, S.K. Ling-Chung, Conducting polymer gas sensors: Part 1 and 2, *Sensors and Actuators*, **19**, (1989), 125-150.

9.5 M.C. Lonergan, E.J. Severin, B.J. Doleman, S. A. Beaber, R. H. Grubbs, N. S. Lewis, Array-based vapour sensing using chemically sensitive carbon black-polymer resistors, *Chem. Mater*. 8, (1996), 2298-2313.

9.6 P. Ingelby, PhD Thesis, University of Warwick, Coventry, CV4 7AL.

9.7 S. M. Sze, Physics of semiconductor devices, 2nd Edition, 1981.

9.8 Cyrano 320 Electronic Nose leaflet, Cyrano Sciences Inc. USA, 2000.

APPENDIX A

Circuit diagrams

This first appendix contains circuit diagrams for the following instruments:

1. Flow injection analysis test station
2. I-V characterisation instrument
3. Constant current measurement instrument

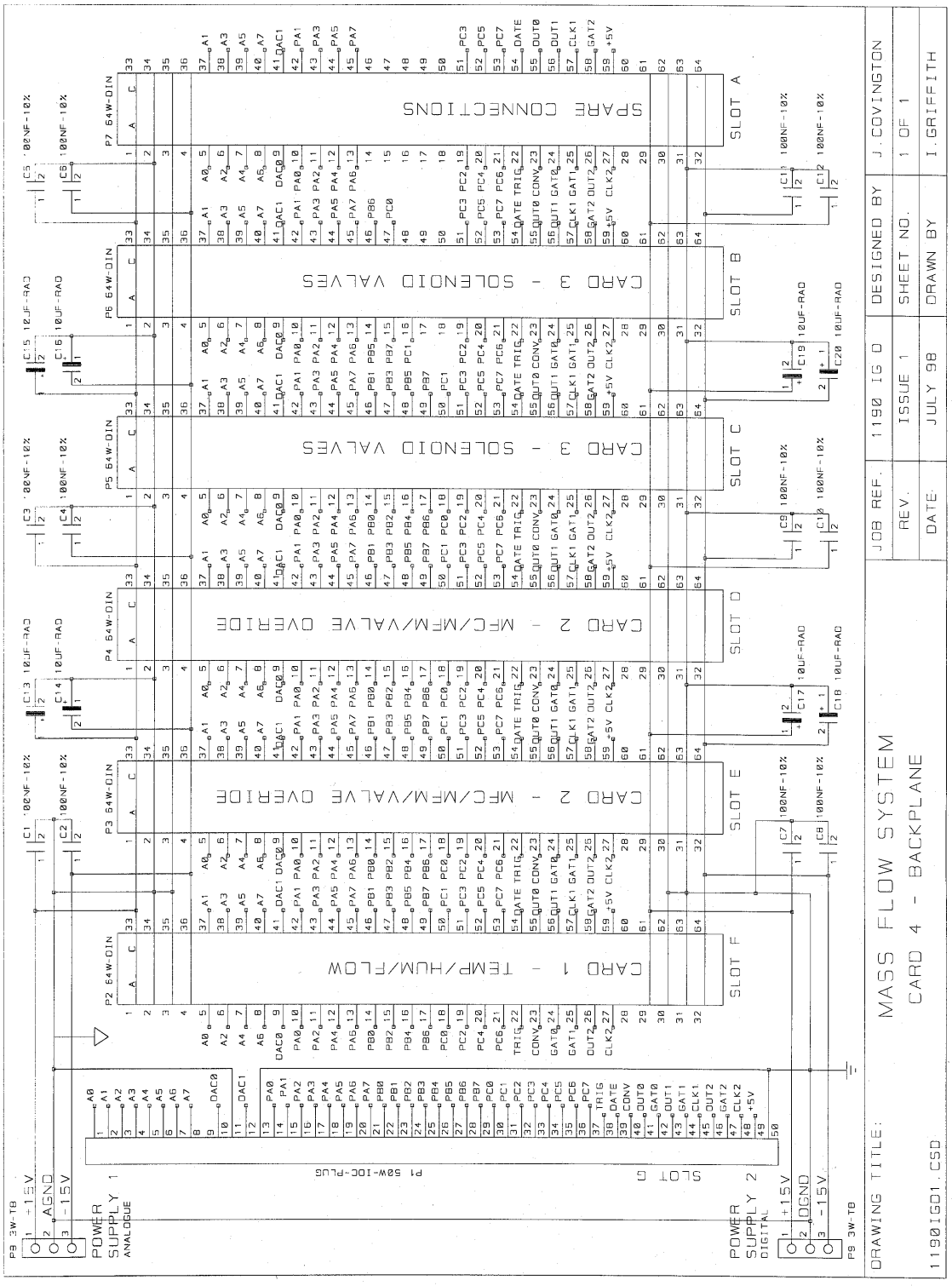
MASS FLOW SYSTEM
CARD 4 - BACKPLANE
1190IG01.CSD
JOB REF. 1190 IG 0
REV. ISSUE 1
DATE JULY 98
DESIGNED BY J.COVINGTON
SHEET NO. 1 OF 1
DRAWN BY I.GRIFFITH
SLOT A
SLOT B
SLOT C
SLOT D
SLOT E
SLOT F
SPARE CONNECTIONS
SOLENOID VALVES
TEMP/HUM/FLOW
MFC/MFM/VALVE OVERIDE
POWER SUPPLY 1 ANALOGUE
POWER SUPPLY 2 DIGITAL
SLOT 0

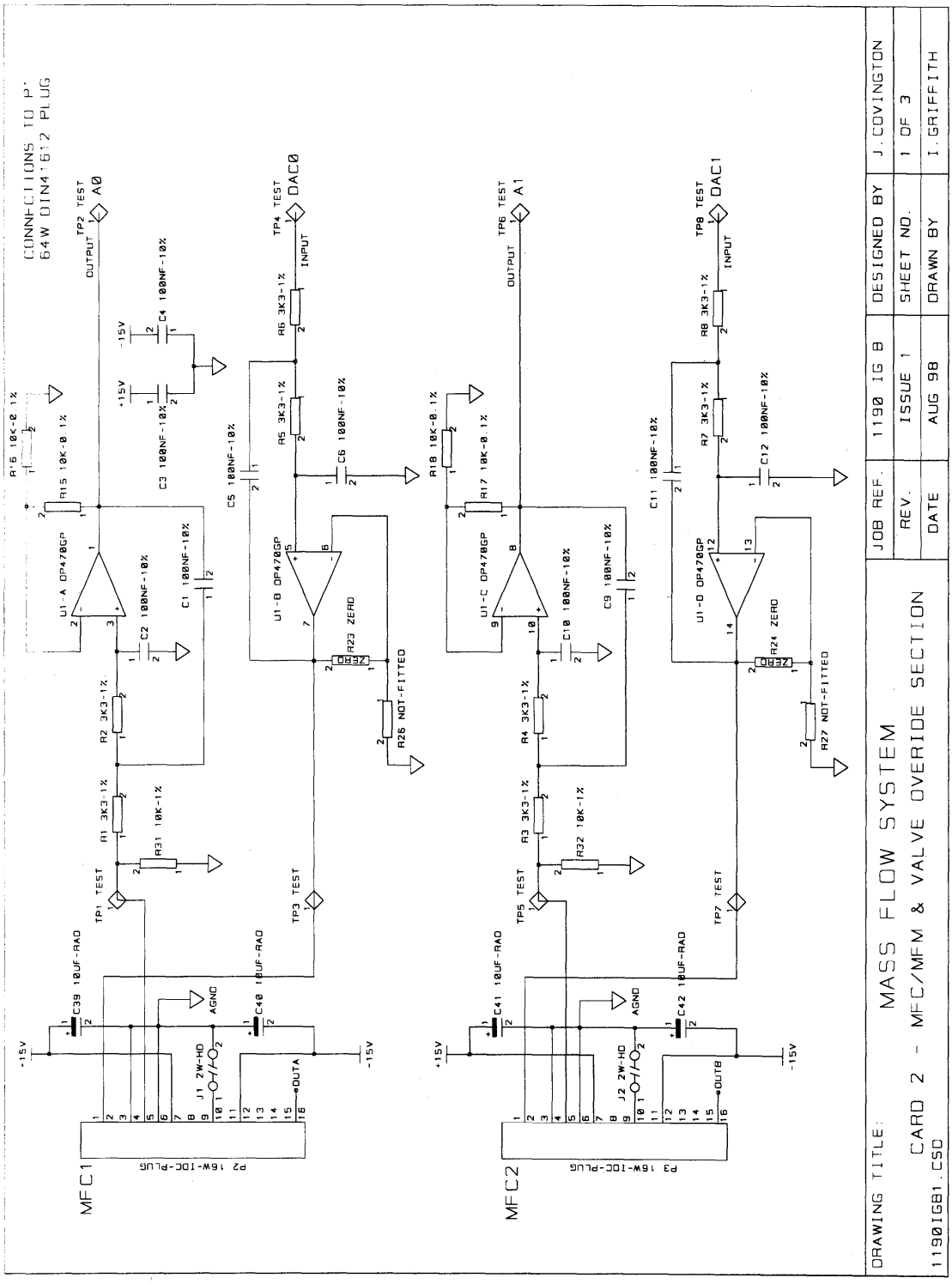
CONNECTIONS TO P1
64W DIN41612 PLUG
MFC1
MFC2
MASS FLOW SYSTEM
CARD 2 - MFC/MFM & VALVE OVERIDE SECTION
1190IGB1.CSD
JOB REF. 1190 IG B
REV. ISSUE 1
DATE AUG 98
DESIGNED BY J.COVINGTON
SHEET NO. 1 OF 3
DRAWN BY I.GRIFFITH
DRAWING TITLE:

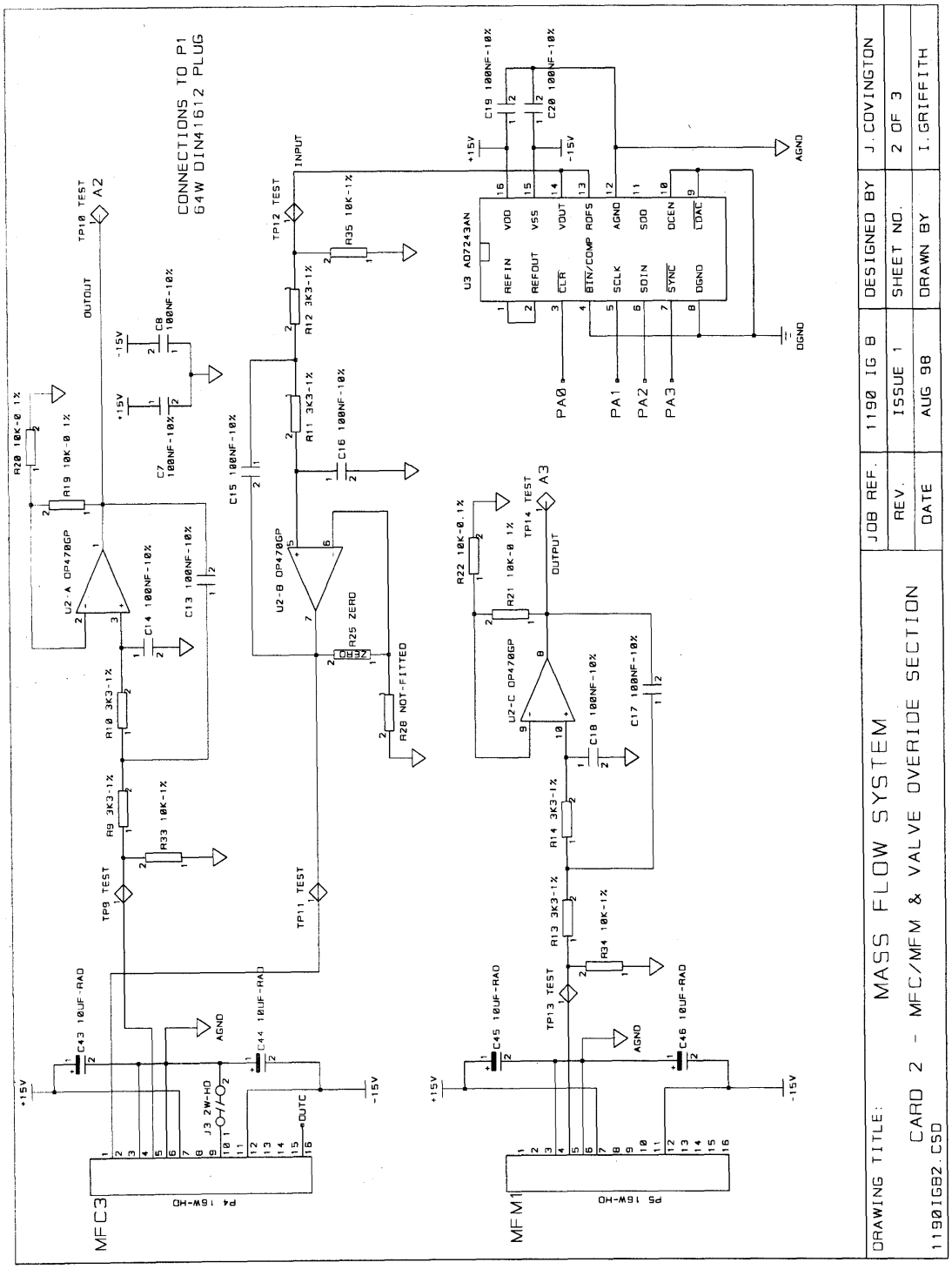
CONNECTIONS TO P1
64W DIN41612 PLUG
MASS FLOW SYSTEM
CARD 2 - MFC/MFM & VALVE OVERIDE SECTION
11901GB2.CSD
DRAWING TITLE:
JOB REF. 1190 IG B
REV.
DATE AUG 98
DESIGNED BY J.COVINGTON
SHEET NO. 2 OF 3
ISSUE 1
DRAWN BY I.GRIFFITH
MFC3
MFM1
U2-A OP470GP
U2-B OP470GP
U2-C OP470GP
U3 AD7243AN
TP10 TEST A2
TP12 TEST INPUT
TP9 TEST
TP11 TEST
TP13 TEST
TP14 TEST A3
OUTOUT
OUTPUT
R20 10K-0.1%
R19 10K-0.1%
R10 3K3-1%
R9 3K3-1%
R33 10K-1%
R11 3K3-1%
R12 3K3-1%
R35 10K-1%
R25 ZERO
R28 NOT-FITTED
R22 10K-0.1%
R21 10K-0.1%
R14 3K3-1%
R13 3K3-1%
R34 10K-1%
C7 100NF-10%
C8 100NF-10%
C13 100NF-10%
C14 100NF-10%
C15 100NF-10%
C16 100NF-10%
C17 100NF-10%
C18 100NF-10%
C19 100NF-10%
C20 100NF-10%
C43 10UF-RAD
C44 10UF-RAD
C45 10UF-RAD
C46 10UF-RAD
+15V
-15V
AGND
DGND
PA0
PA1
PA2
PA3
J3 2W-HD
P4 15W-HD
P5 15W-HD
OUTC

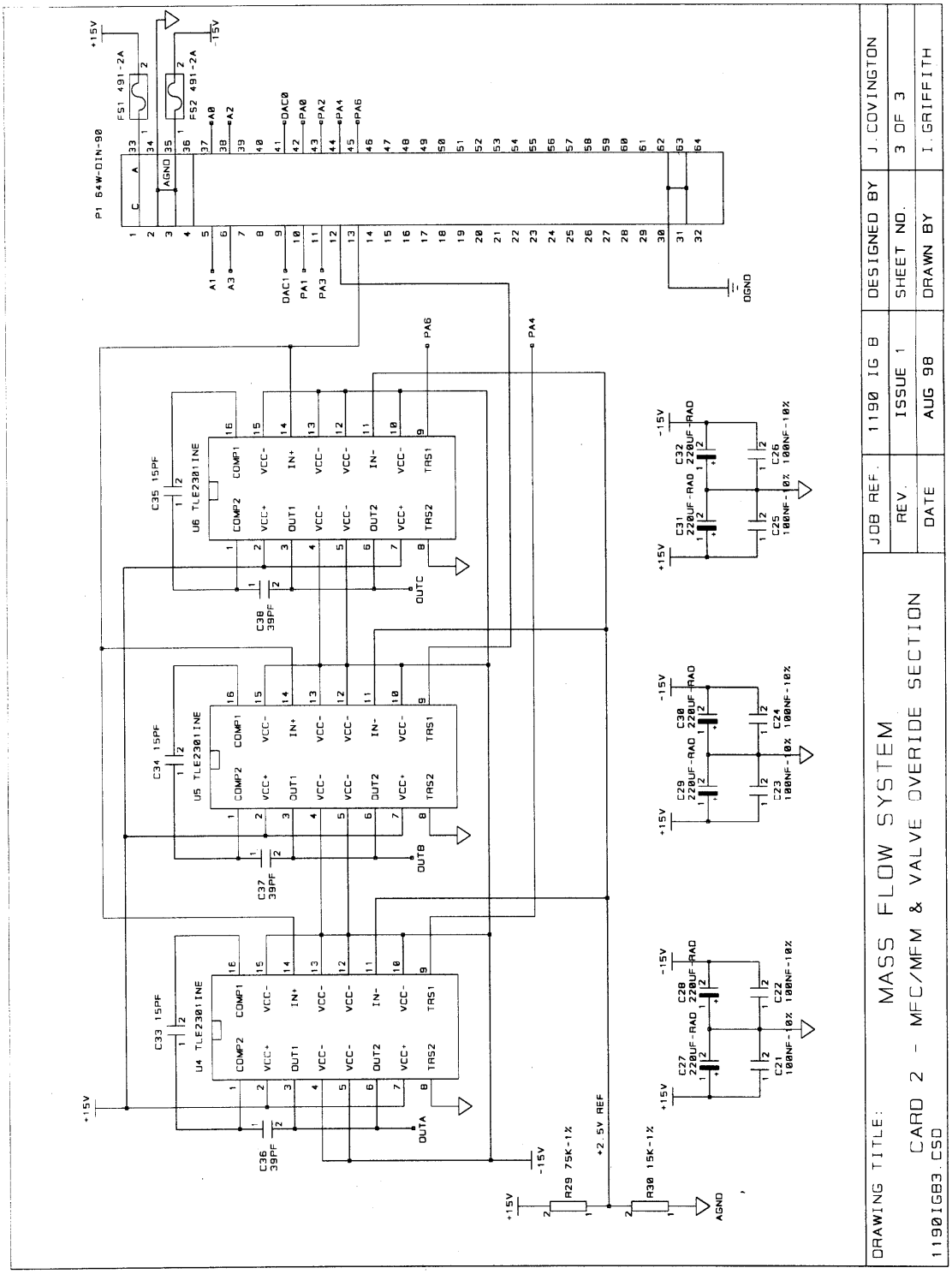
DRAWING TITLE:
MASS FLOW SYSTEM
CARD 2 - MFC/MFM & VALVE OVERIDE SECTION
1190IGB3.CSD
JOB REF. 1190 IG B
REV. ISSUE 1
DATE AUG 98
DESIGNED BY J.COVINGTON
SHEET NO. 3 OF 3
DRAWN BY I.GRIFFITH
P1 64W-DIN-90
FS1 491-2A
FS2 491-2A
+15V
-15V
AGND
DGND
DAC0
PA0
PA2
PA4
PA6
A0
A2
A1
A3
DAC1
PA1
PA3
U4 TLE2301INE
U5 TLE2301INE
U6 TLE2301INE
C33 15PF
C34 15PF
C35 15PF
C36 39PF
C37 39PF
C38 39PF
OUTA
OUTB
OUTC
C20 220UF-RAD
C21 100NF-10%
C22 100NF-10%
C23 100NF-10%
C24 100NF-10%
C25 100NF-10%
C26 100NF-10%
C27 220UF-RAD
C29 220UF-RAD
C30 220UF-RAD
C31 220UF-RAD
C32 220UF-RAD
R29 75K-1%
R30 15K-1%
+2.5V REF

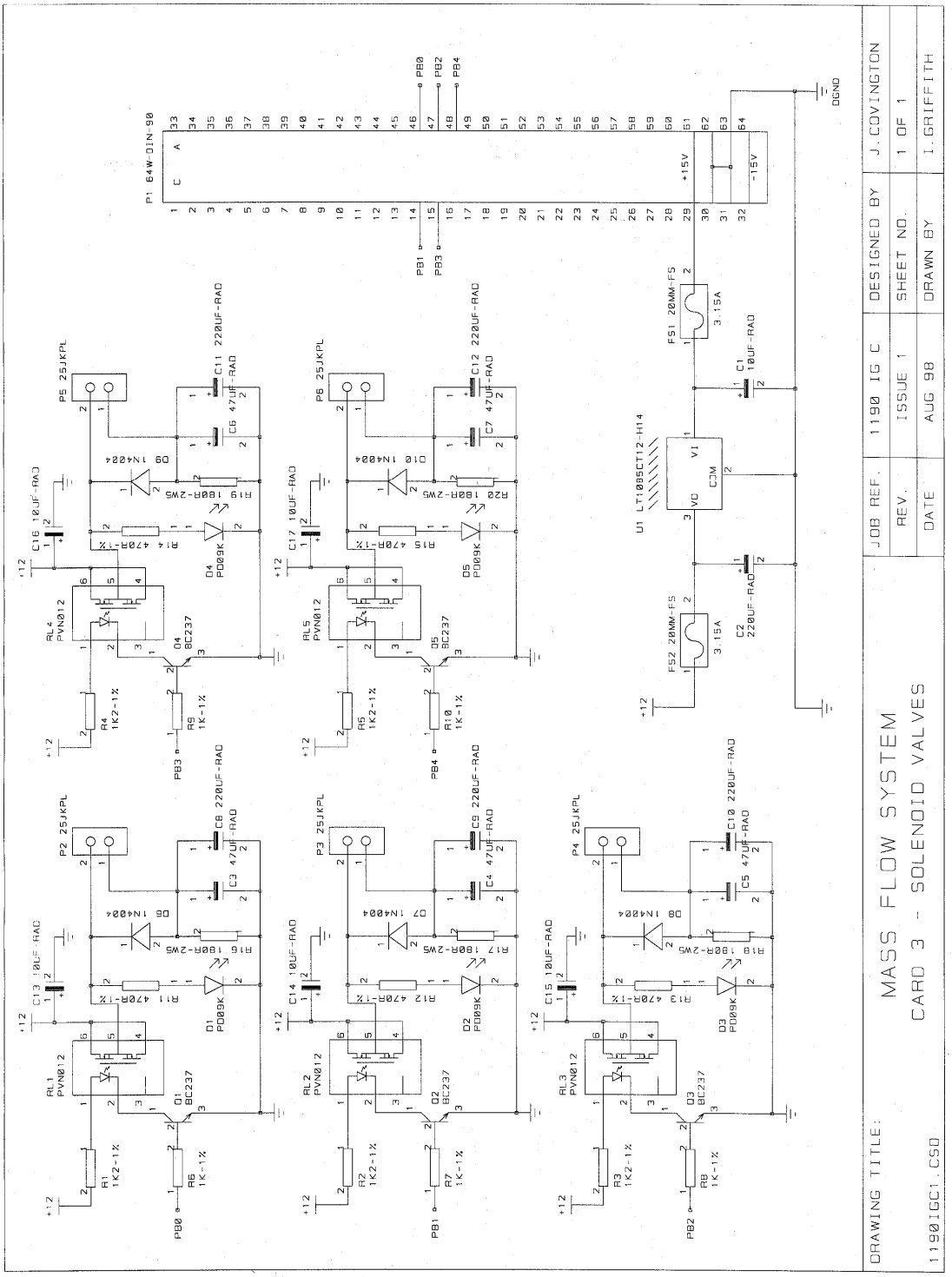
DRAWING TITLE:
MASS FLOW SYSTEM
CARD 3 - SOLENOID VALVES
1190IGC1.CSD
JOB REF. 1190 IG C
REV. ISSUE 1
DATE AUG 98
DESIGNED BY J.COVINGTON
SHEET NO. 1 OF 1
DRAWN BY I.GRIFFITH
P1 64W-DIN-90
U1 LT1085CT12-H14
FS1 20MM-FS 3.15A
FS2 20MM-FS 3.15A
C1 10UF-RAD
C2 220UF-RAD
RL1 PVN012
RL2 PVN012
RL3 PVN012
RL4 PVN012
RL5 PVN012
Q1 BC237
Q2 BC237
Q3 BC237
Q4 BC237
Q5 BC237
D1 PD09K
D2 PD09K
D3 PD09K
D4 PD09K
D5 PD09K
D6 1N4004
D7 1N4004
D8 1N4004
D9 1N4004
D10 1N4004
P2 25JKPL
P3 25JKPL
P4 25JKPL
P5 25JKPL
P6 25JKPL
C3 47UF-RAD
C4 47UF-RAD
C5 47UF-RAD
C6 47UF-RAD
C7 47UF-RAD
C8 220UF-RAD
C9 220UF-RAD
C10 220UF-RAD
C11 220UF-RAD
C12 220UF-RAD
C13 10UF-RAD
C14 10UF-RAD
C15 10UF-RAD
C16 10UF-RAD
C17 10UF-RAD
R1 1K2-1%
R2 1K2-1%
R3 1K2-1%
R4 1K2-1%
R5 1K2-1%
R6 1K-1%
R7 1K-1%
R8 1K-1%
R9 1K-1%
R10 1K-1%
R11 470R-1%
R12 470R-1%
R13 470R-1%
R14 470R-1%
R15 470R-1%
R16 180R-2W5
R17 180R-2W5
R18 180R-2W5
R19 180R-2W5
R20 180R-2W5
+12
+15V
-15V
DGND
PB0
PB1
PB2
PB3
PB4

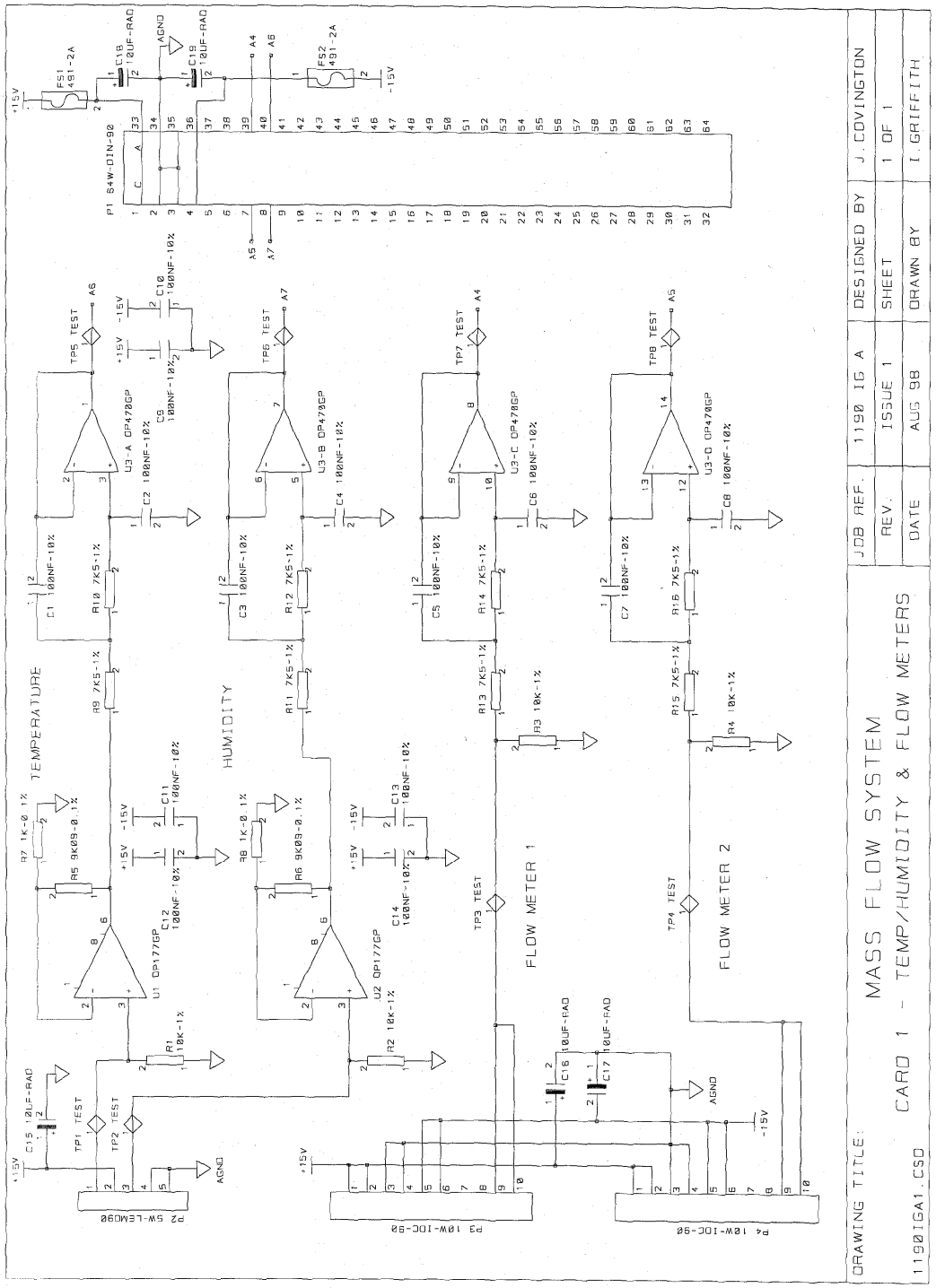
MASS FLOW SYSTEM
CARD 1 - TEMP/HUMIDITY & FLOW METERS
TEMPERATURE
HUMIDITY
FLOW METER 1
FLOW METER 2
DESIGNED BY J.COVINGTON
DRAWN BY I.GRIFFITH
SHEET 1 OF 1
ISSUE 1
AUG 98
1190 IG A
1190IGA1.CSD

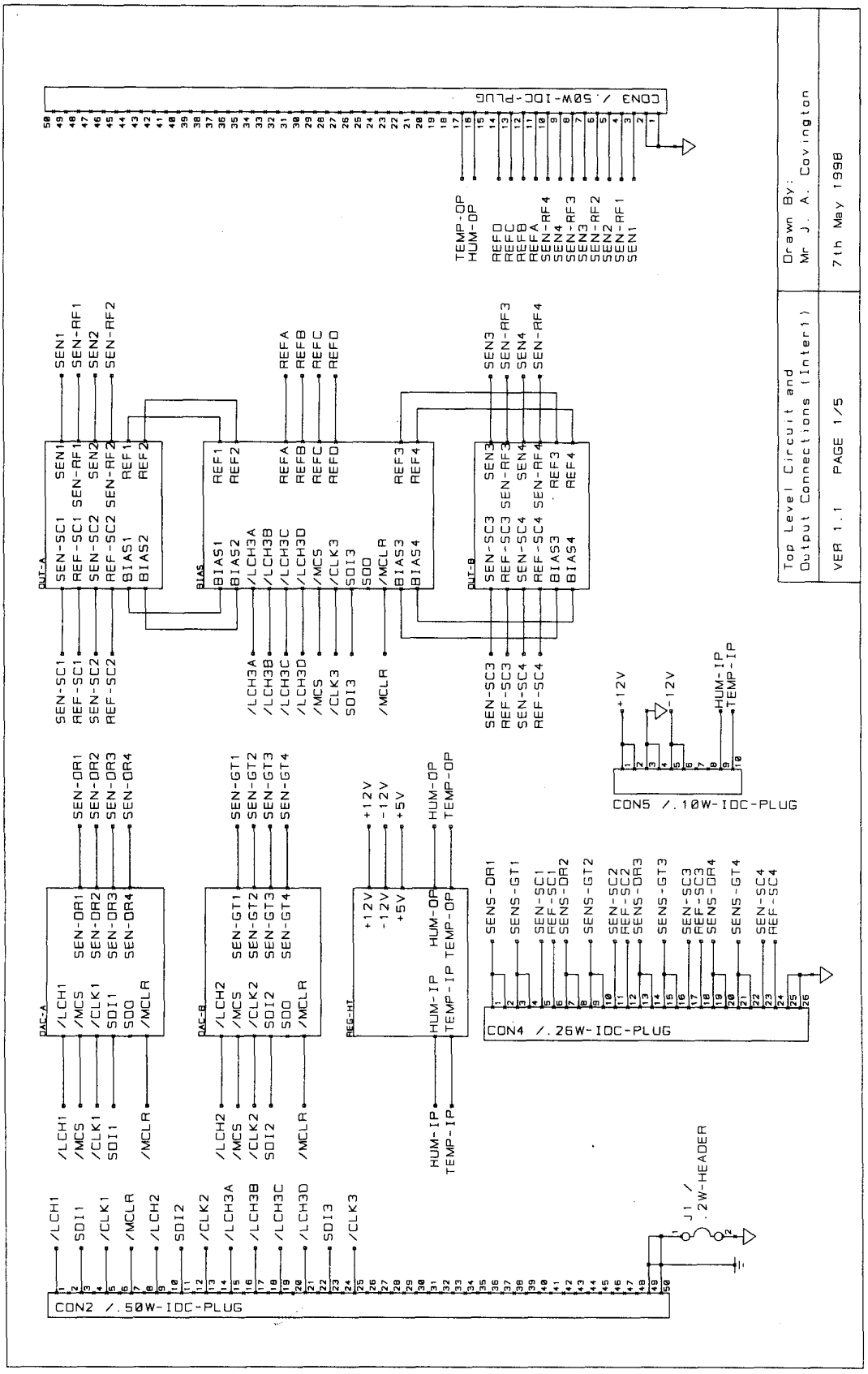
Top Level Circuit and Output Connections (Inter1)
VER 1.1 PAGE 1/5
Drawn By: Mr J. A. Covington
7th May 1998
CON3 /.50W-IDC-PLUG
CON2 /.50W-IDC-PLUG
CON4 /.26W-IDC-PLUG
CON5 /.10W-IDC-PLUG
J1 /.2W-HEADER
DAC-A
DAC-B
REG-HI
OUT-A
BIAS
OUT-B
SEN-SC1
REF-SC1
SEN-SC2
REF-SC2
SEN-SC3
REF-SC3
SEN-SC4
REF-SC4
/LCH1
/LCH2
/LCH3A
/LCH3B
/LCH3C
/LCH3D
/MCS
/CLK1
/CLK2
/CLK3
SDI1
SDI2
SDI3
SDO
/MCLR
SEN-DR1
SEN-DR2
SEN-DR3
SEN-DR4
SEN-GT1
SEN-GT2
SEN-GT3
SEN-GT4
+12V
-12V
+5V
HUM-IP
TEMP-IP
HUM-OP
TEMP-OP
SEN1
SEN2
SEN3
SEN4
SEN-RF1
SEN-RF2
SEN-RF3
SEN-RF4
REF1
REF2
REF3
REF4
BIAS1
BIAS2
BIAS3
BIAS4
REFA
REFB
REFC
REFD

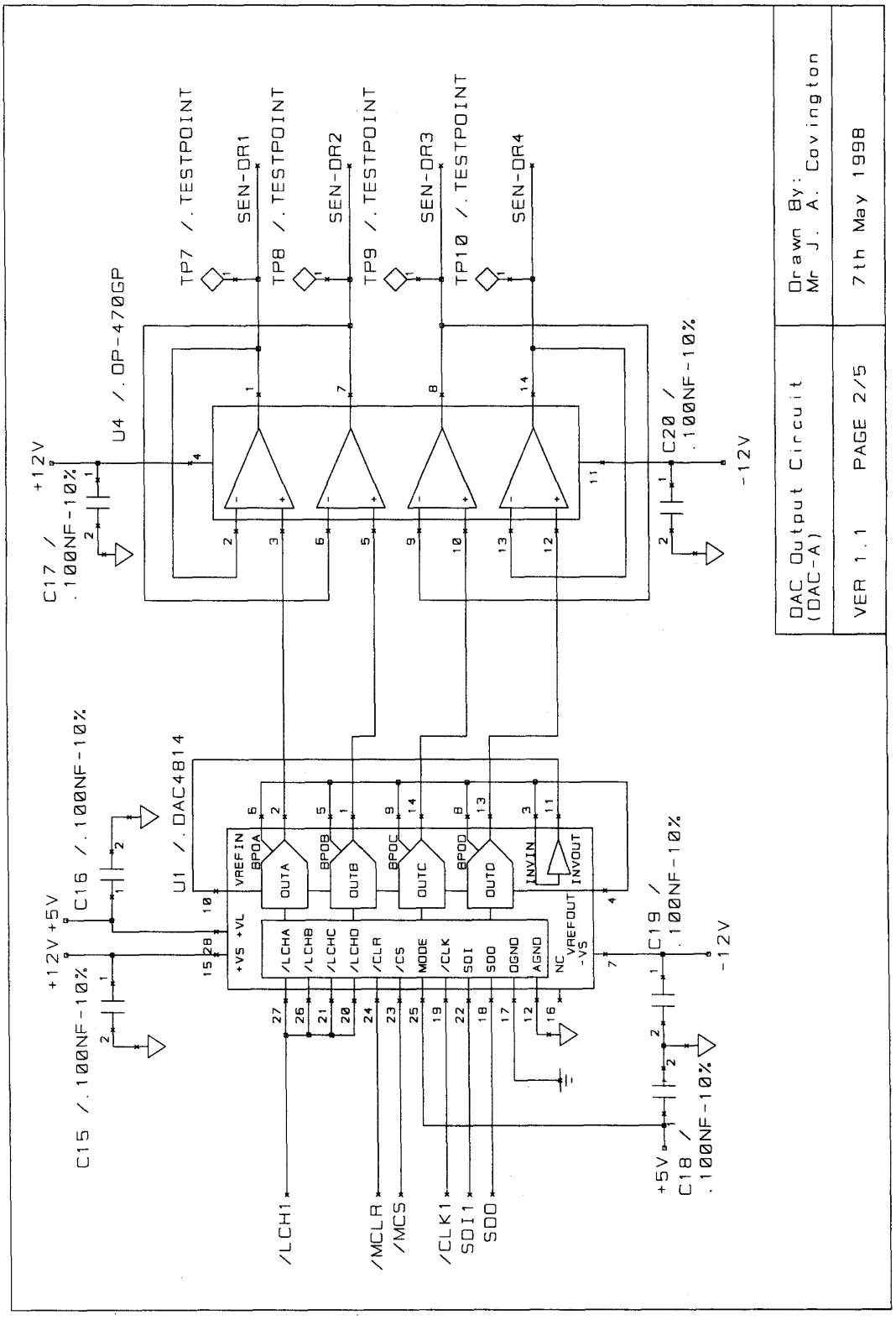
DAC Output Circuit
(DAC-A)
Drawn By:
Mr J. A. Covington
VER 1.1
PAGE 2/5
7th May 1998
U4 /.OP-470GP
U1 /.DAC4814
TP7 /.TESTPOINT
TP8 /.TESTPOINT
TP9 /.TESTPOINT
TP10 /.TESTPOINT
SEN-OR1
SEN-OR2
SEN-OR3
SEN-OR4
+12V
-12V
+5V
C15 /.100NF-10%
C16 /.100NF-10%
C17 /.100NF-10%
C18 /.100NF-10%
C19 /.100NF-10%
C20 /.100NF-10%
VREFIN
BPDA
BPDB
BPDC
BPDD
INVIN
OUTA
OUTB
OUTC
OUTD
INVOUT
+VS +VL
/LCHA
/LCHB
/LCHC
/LCHD
/CLR
/CS
MODE
/CLK
SDI
SDO
DGND
AGND
NC
VREFOUT
-VS
/LCH1
/MCLR
/MCS
/CLK1
SDI1
SDO

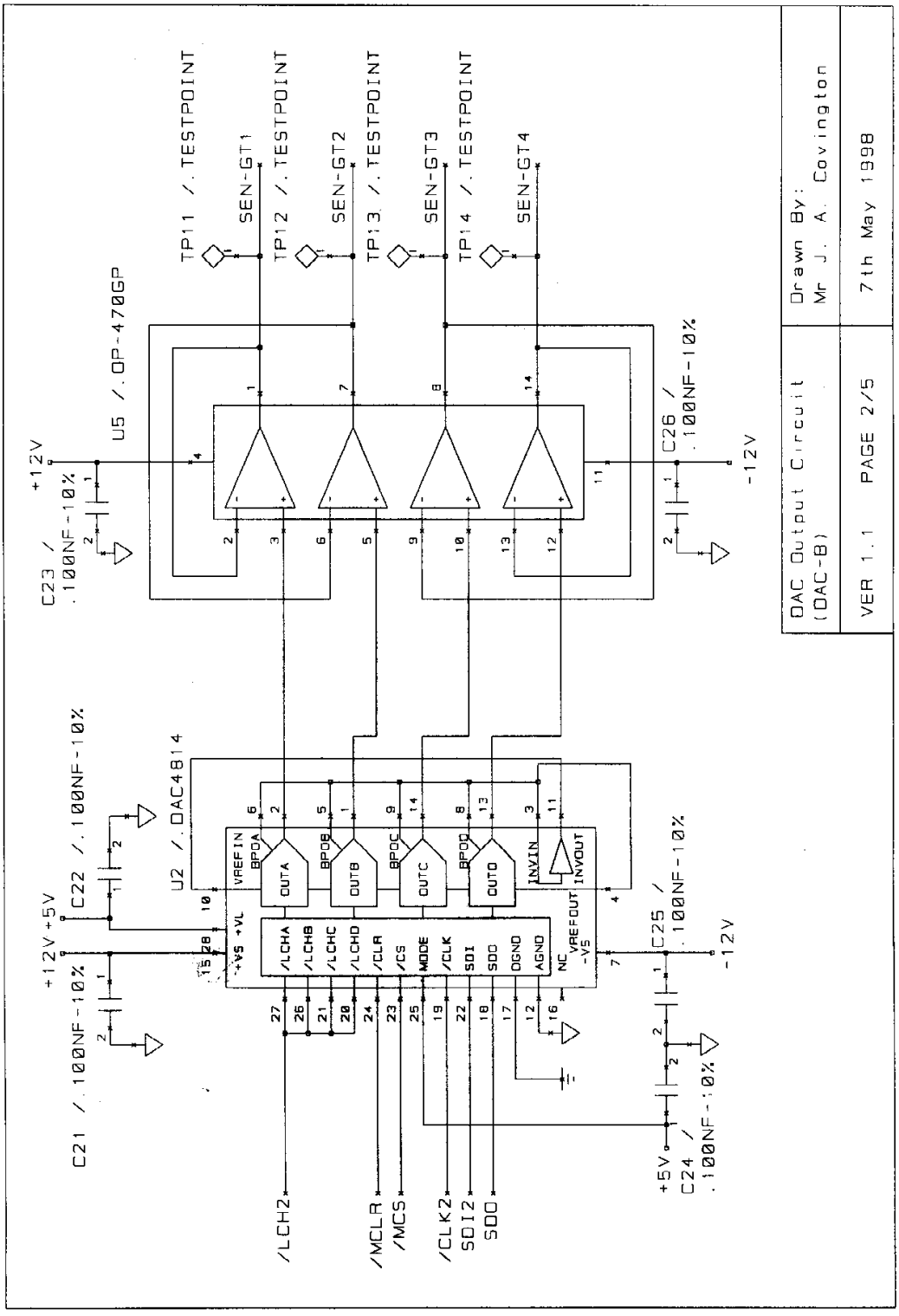
DAC Output Circuit
(DAC-B)
Drawn By:
Mr J. A. Covington
VER 1.1
PAGE 2/5
7th May 1998
U5 /.OP-470GP
U2 /.DAC8814
TP11 /.TESTPOINT
TP12 /.TESTPOINT
TP13 /.TESTPOINT
TP14 /.TESTPOINT
SEN-GT1
SEN-GT2
SEN-GT3
SEN-GT4
+12V
-12V
+5V
+12V+5V
C21 /.100NF-10%
C22 /.100NF-10%
C23 /.100NF-10%
C24 /.100NF-10%
C25 /.100NF-10%
C26 /.100NF-10%
/LCH2
/MCLR
/MCS
/CLK2
SDI2
SDO

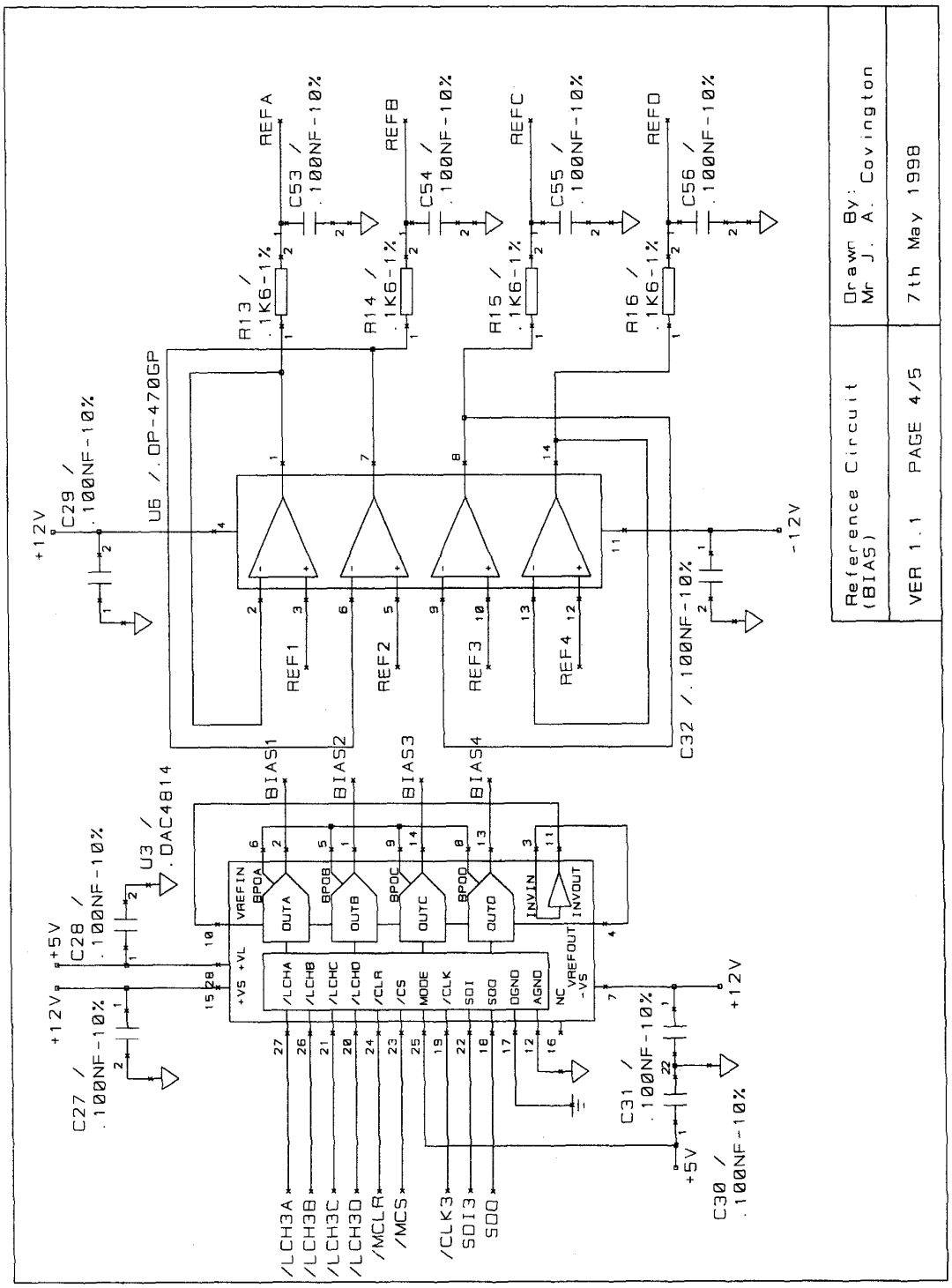
Reference Circuit (BIAS)
Drawn By: Mr J. A. Covington
VER 1.1 PAGE 4/5
7th May 1998
U6 / .OP-470GP
U3 / .DAC4814
C32 / .100NF-10%
C27 / .100NF-10%
C28 / .100NF-10%
C29 / .100NF-10%
C30 / .100NF-10%
C31 / .100NF-10%
C53 / .100NF-10%
C54 / .100NF-10%
C55 / .100NF-10%
C56 / .100NF-10%
R13 / .1K6-1%
R14 / .1K6-1%
R15 / .1K6-1%
R16 / .1K6-1%
REFA
REFB
REFC
REFD
REF1
REF2
REF3
REF4
BIAS1
BIAS2
BIAS3
BIAS4
+12V
-12V
+5V
/LCH3A
/LCH3B
/LCH3C
/LCH3D
/MCLR
/MCS
/CLK3
SDI3
SDO

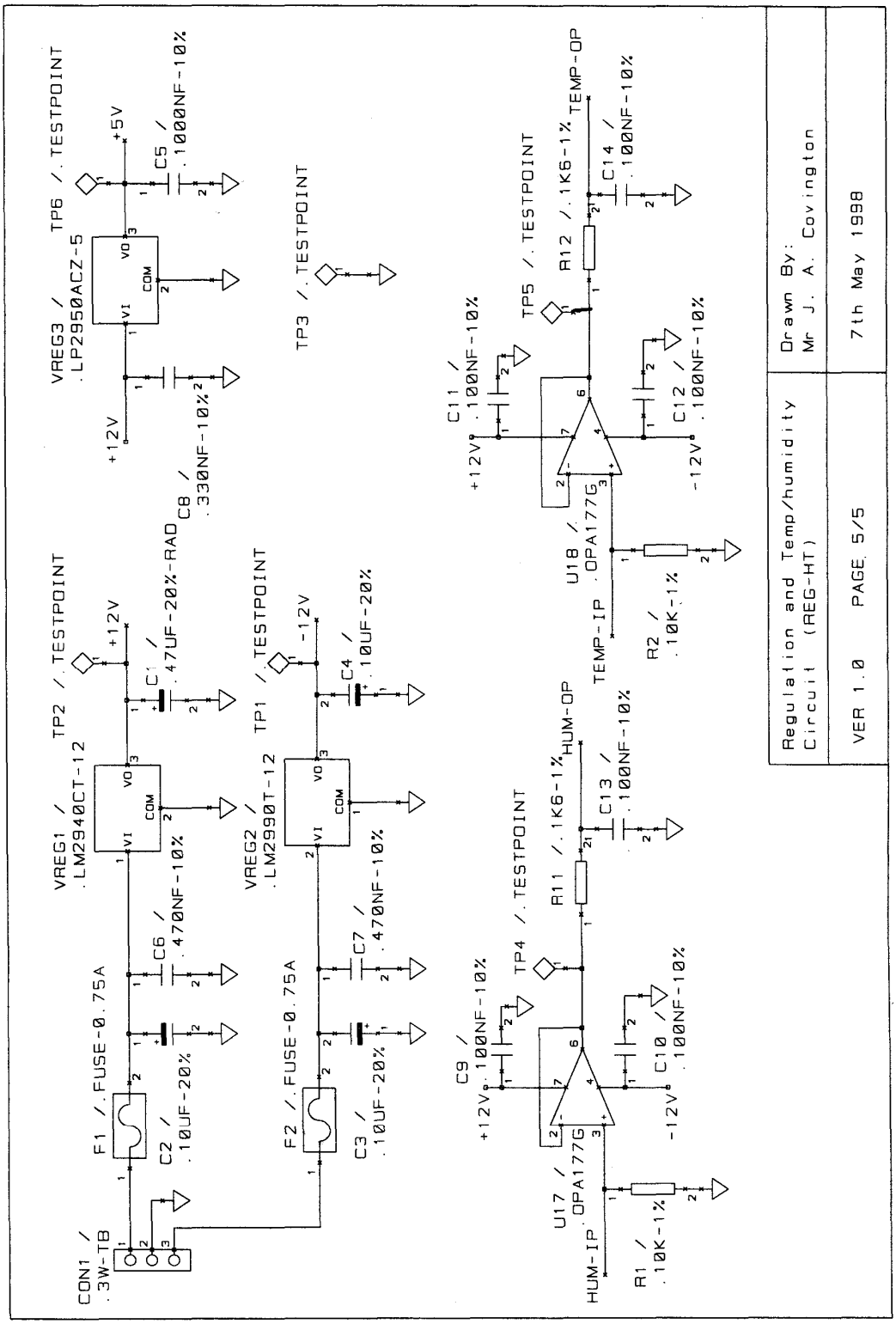
CON1 / .3W-TB
F1 / .FUSE-0.75A
F2 / .FUSE-0.75A
C2 / .10UF-20%
C3 / .10UF-20%
C6 / .470NF-10%
C7 / .470NF-10%
VREG1 / .LM2940CT-12
VREG2 / .LM2990T-12
VREG3 / .LP2950ACZ-5
TP1 / .TESTPOINT
TP2 / .TESTPOINT
TP3 / .TESTPOINT
TP4 / .TESTPOINT
TP5 / .TESTPOINT
TP6 / .TESTPOINT
C1 / .47UF-20%-RAD
C4 / .10UF-20%
C5 / .1000NF-10%
C8 / .330NF-10%
+12V
-12V
+5V
C9 / .100NF-10%
C10 / .100NF-10%
C11 / .100NF-10%
C12 / .100NF-10%
C13 / .100NF-10%
C14 / .100NF-10%
R1 / .10K-1%
R2 / .10K-1%
R11 / .1K6-1%
R12 / .1K6-1%
U17 / OPA177G
U18 / OPA177G
HUM-IP
HUM-OP
TEMP-IP
TEMP-OP
Regulation and Temp/humidity Circuit (REG-HT)
Drawn By: Mr J. A. Covington
VER 1.0
PAGE 5/5
7th May 1998

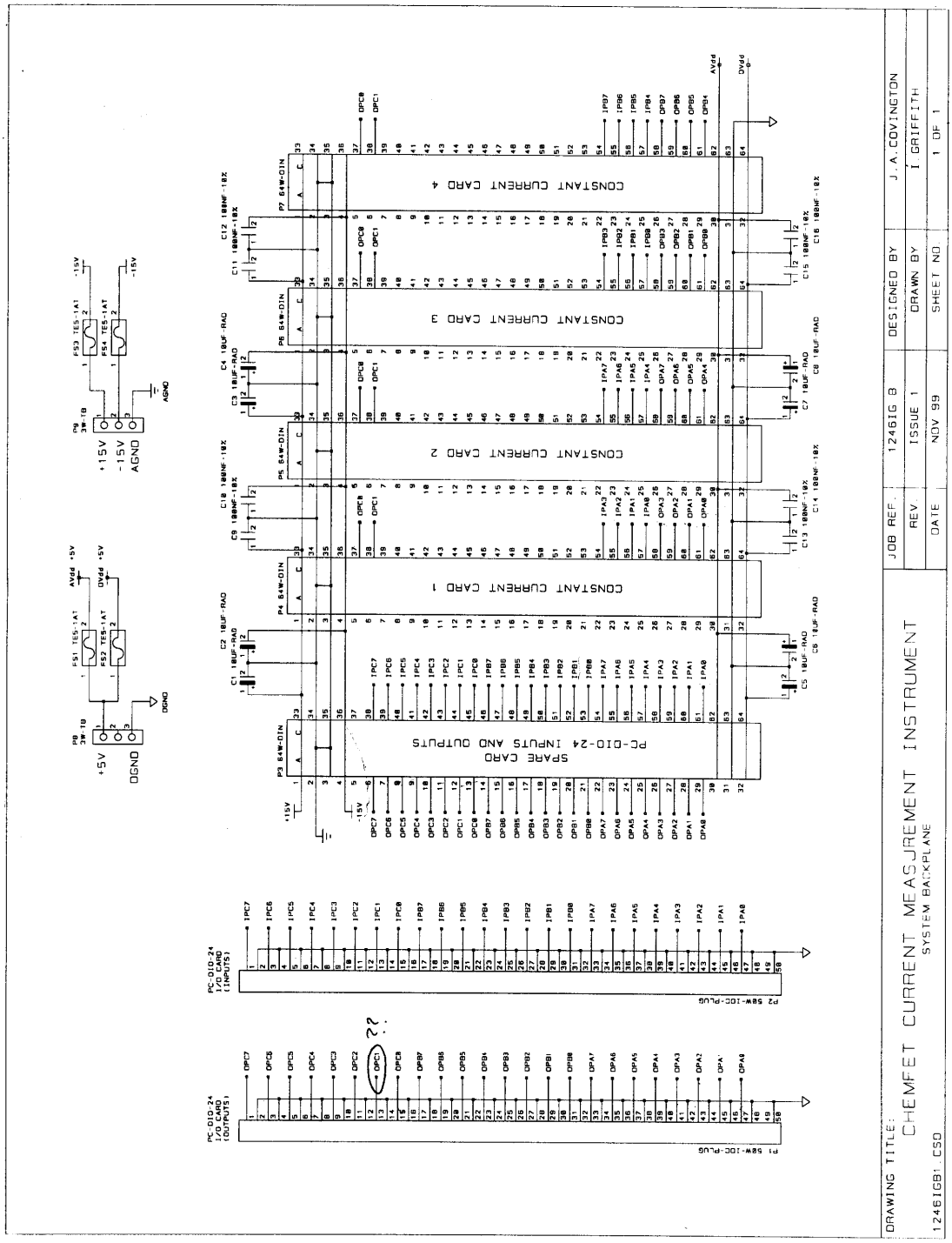
SPARE CARD
PC-DIO-24 INPUTS AND OUTPUTS
CONSTANT CURRENT CARD 1
CONSTANT CURRENT CARD 2
CONSTANT CURRENT CARD 3
CONSTANT CURRENT CARD 4
+15V
-15V
AGND
+5V
DGND
DRAWING TITLE:
CHEMFET CURRENT MEASUREMENT INSTRUMENT
SYSTEM BACKPLANE
12461GB1.CSD
JOB REF. 12461G B
REV ISSUE 1
DATE NOV 99
DESIGNED BY J.A.COVINGTON
DRAWN BY I.GRIFFITH
SHEET NO 1 OF 1

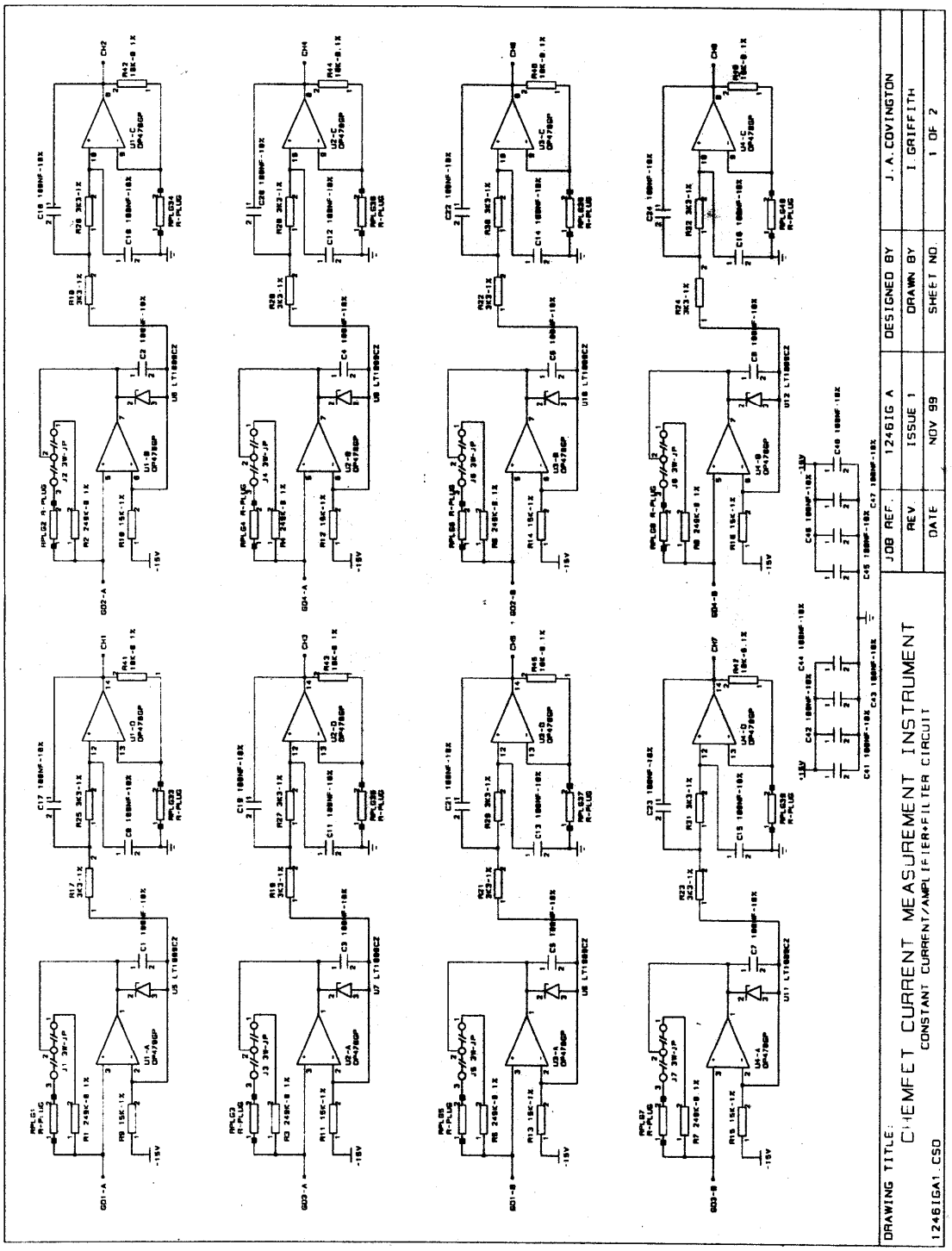
DRAWING TITLE:
CHEMFET CURRENT MEASUREMENT INSTRUMENT
CONSTANT CURRENT/AMPLIFIER+FILTER CIRCUIT
1246IGA1.CSD
JOB REF. 1246IG A
REV ISSUE 1
DATE NOV 99
DESIGNED BY J.A.COVINGTON
DRAWN BY I.GRIFFITH
SHEET NO. 1 OF 2

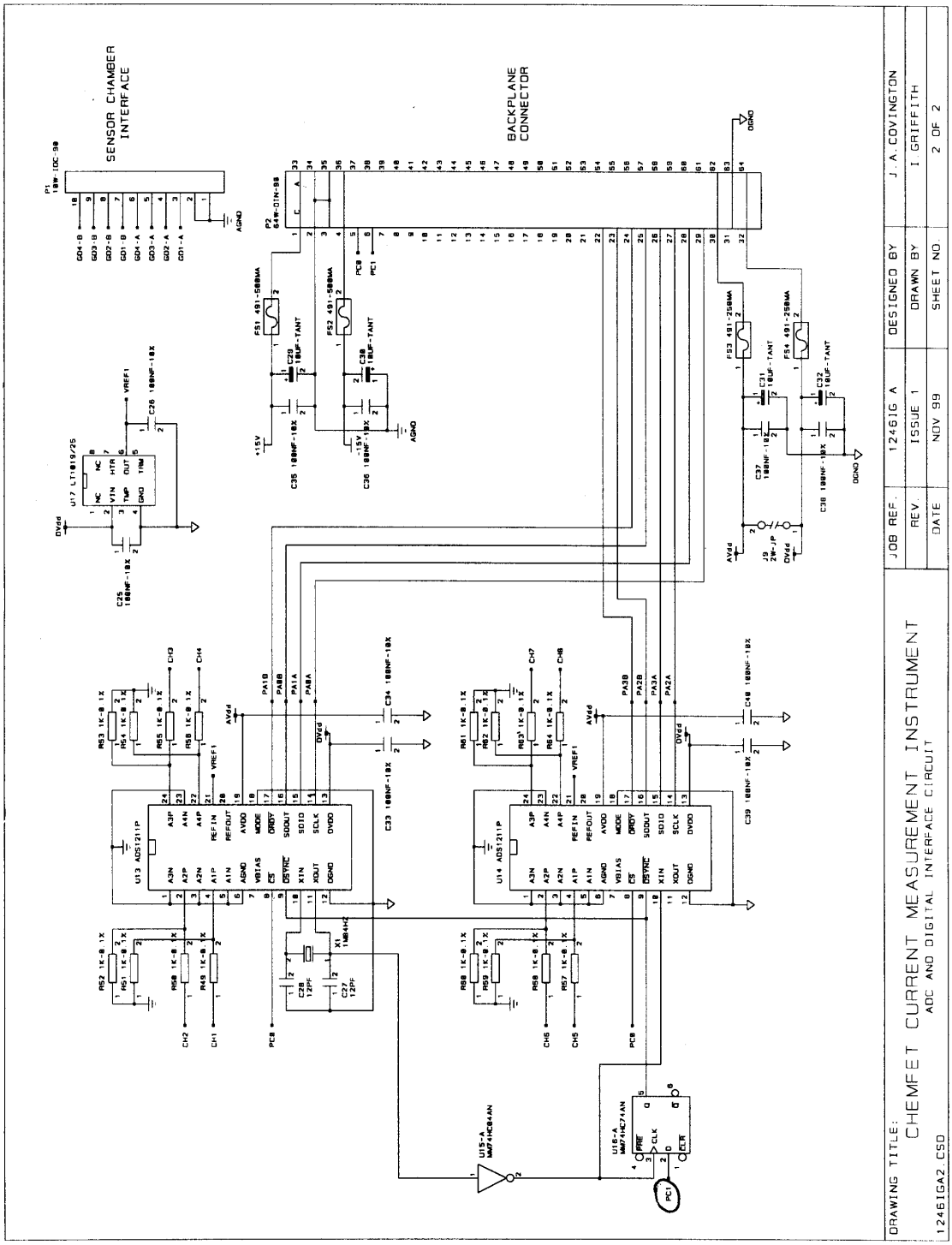
SENSOR CHAMBER INTERFACE
BACKPLANE CONNECTOR
DRAWING TITLE:
CHEMFET CURRENT MEASUREMENT INSTRUMENT
ADC AND DIGITAL INTERFACE CIRCUIT
12461GA2.CSD
JOB REF. 12461G A
REV. ISSUE 1
DATE NOV 99
DESIGNED BY J.A.COVINGTON
DRAWN BY I.GRIFFITH
SHEET NO 2 OF 2

APPENDIX B

Software programs

This appendix contains flow diagrams and the software for the top level routines for:

1. FIA test station
2. I-V characterisation instrument
3. Constant current characterisation instrument

1. Flow diagram of FIA control software

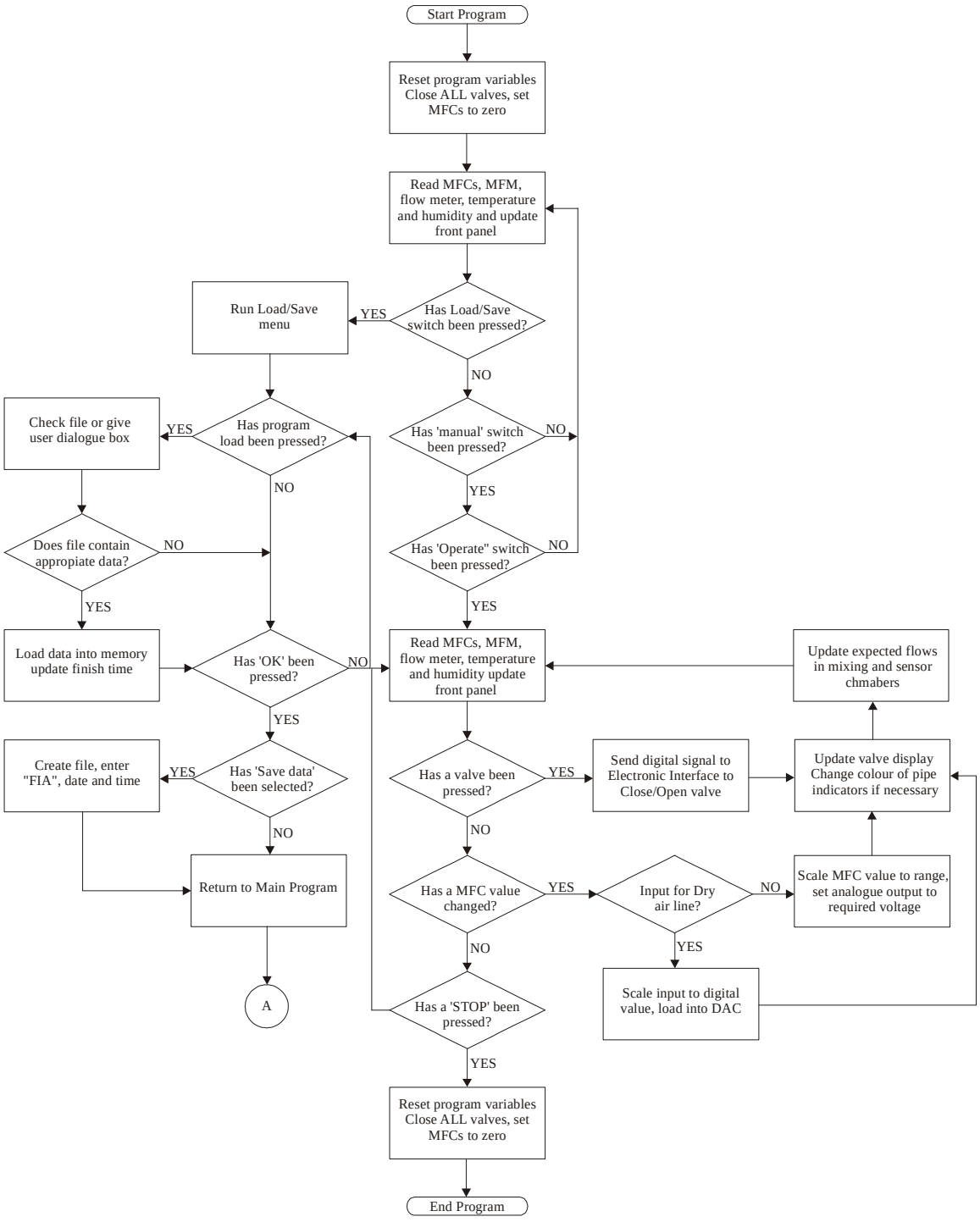

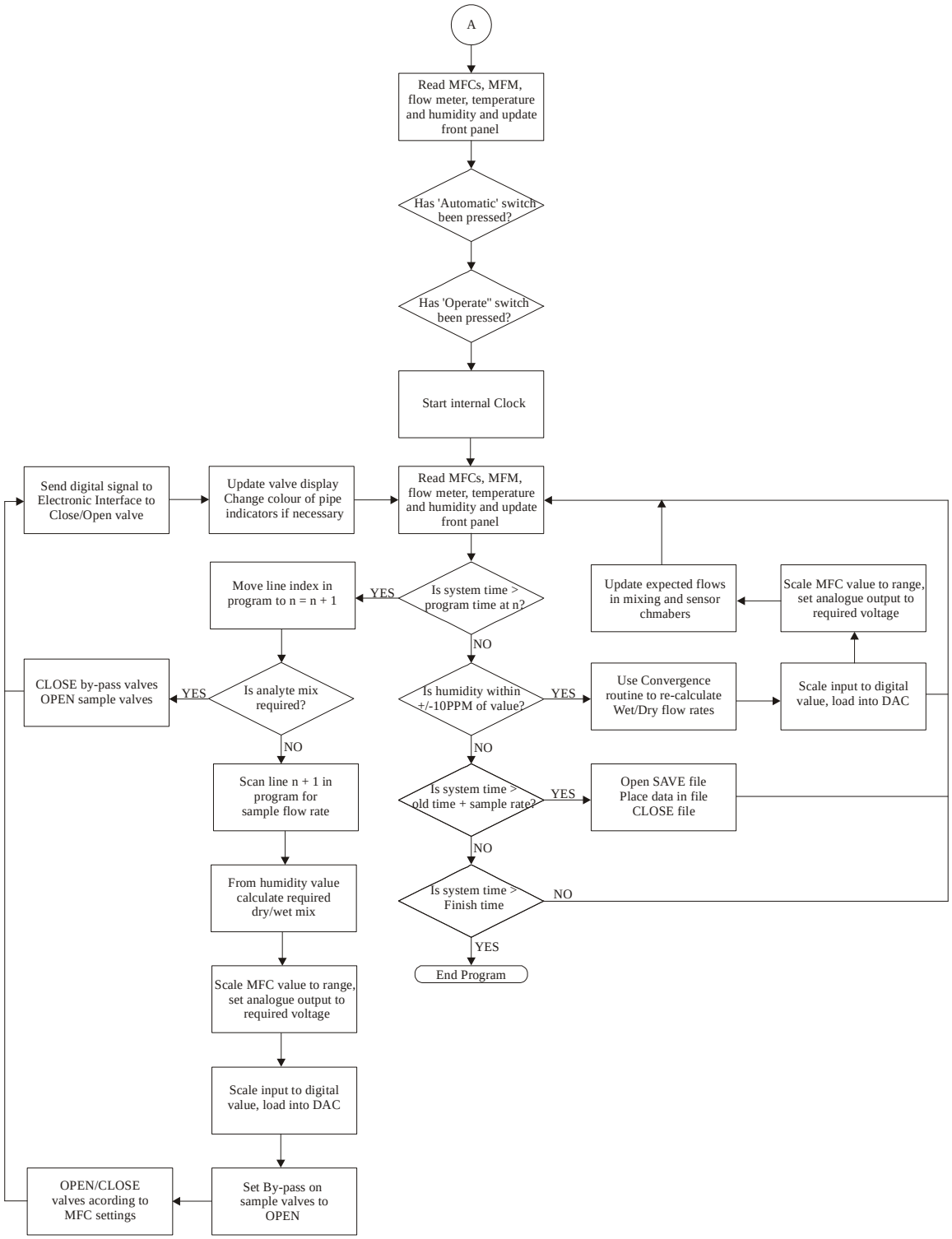
A
Read MFCs, MFM, flow meter, temperature and humidity and update front panel
Has 'Automatic' switch been pressed?
Has 'Operate" switch been pressed?
Start internal Clock
Send digital signal to Electronic Interface to Close/Open valve
Update valve display Change colour of pipe indicators if necessary
Read MFCs, MFM, flow meter, temperature and humidity and update front panel
Move line index in program to n = n + 1
YES
Is system time > program time at n?
Update expected flows in mixing and sensor chmabers
Scale MFC value to range, set analogue output to required voltage
NO
CLOSE by-pass valves OPEN sample valves
YES
Is analyte mix required?
Is humidity within +/-10PPM of value?
YES
Use Convergence routine to re-calculate Wet/Dry flow rates
Scale input to digital value, load into DAC
NO
NO
Scan line n + 1 in program for sample flow rate
Is system time > old time + sample rate?
YES
Open SAVE file Place data in file CLOSE file
NO
From humidity value calculate required dry/wet mix
Is system time > Finish time
NO
YES
End Program
Scale MFC value to range, set analogue output to required voltage
Scale input to digital value, load into DAC
OPEN/CLOSE valves acording to MFC settings
Set By-pass on sample valves to OPEN

Front panel of FIA test station control software

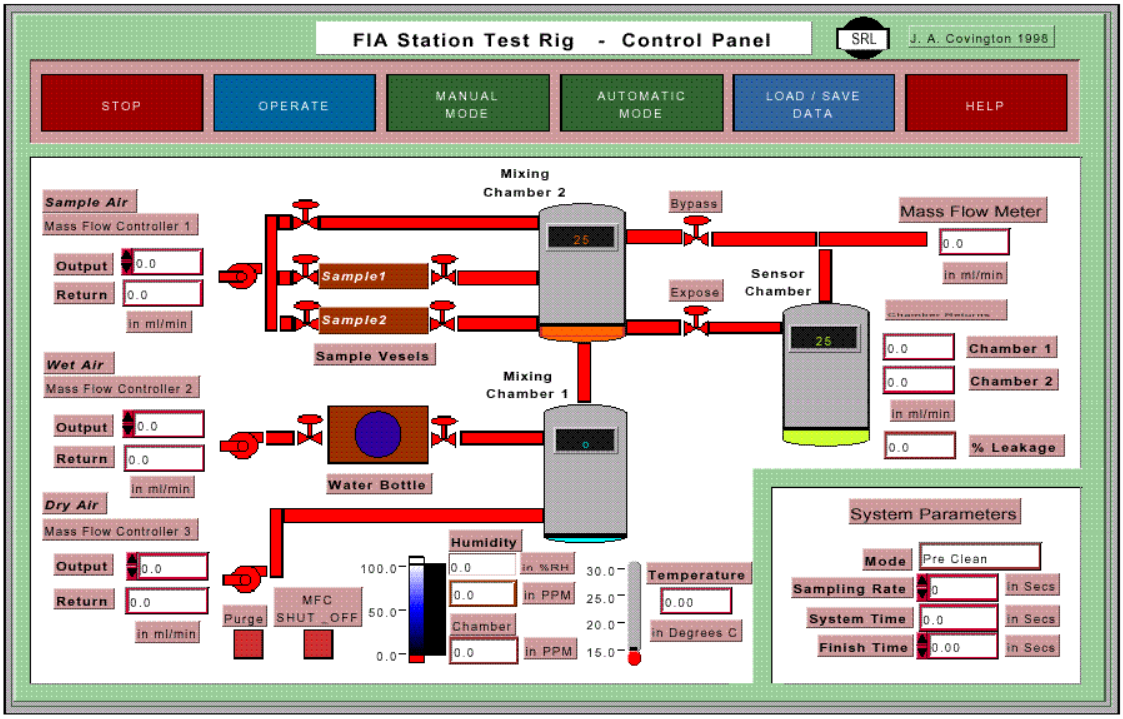

Block diagram of FIA test station control software

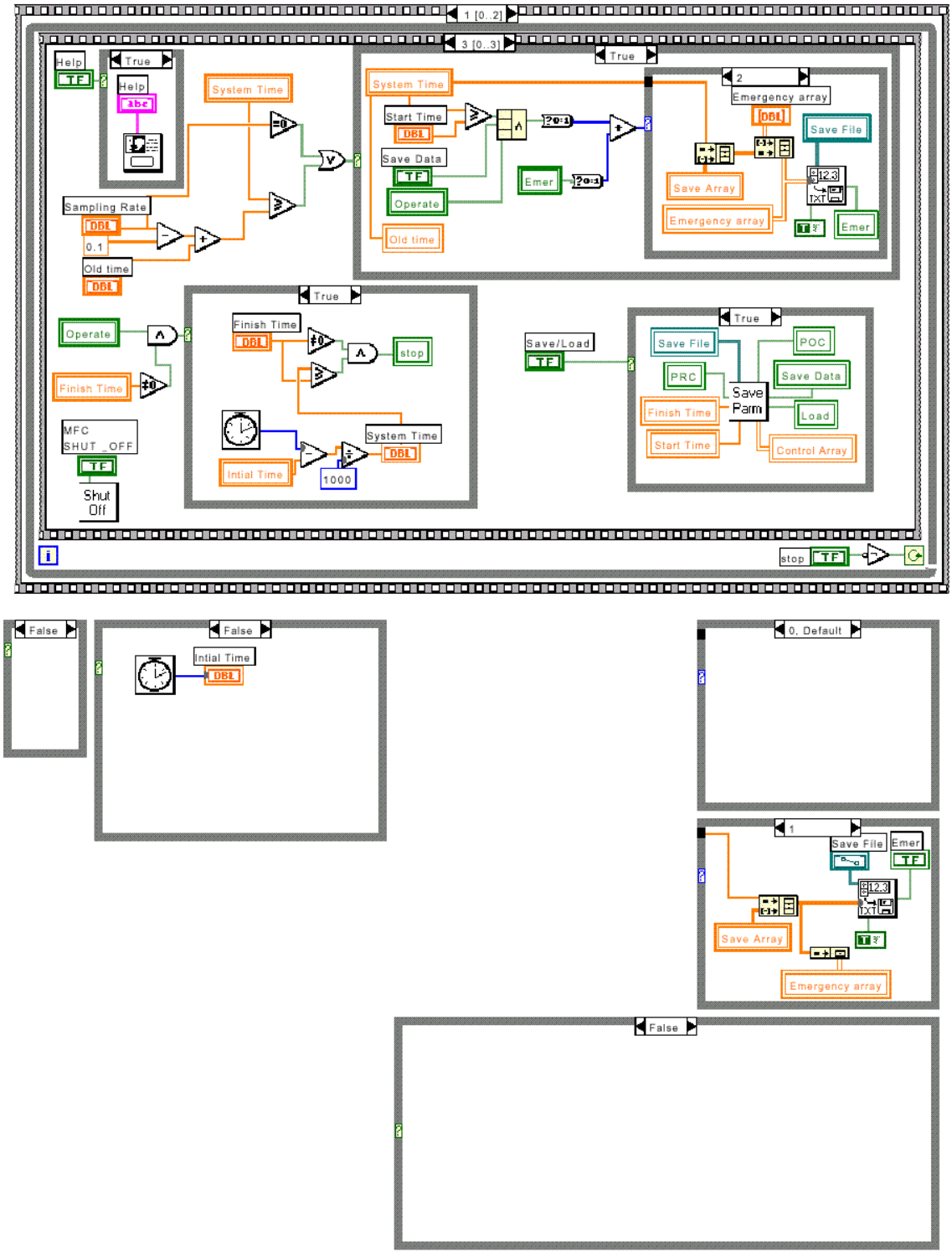

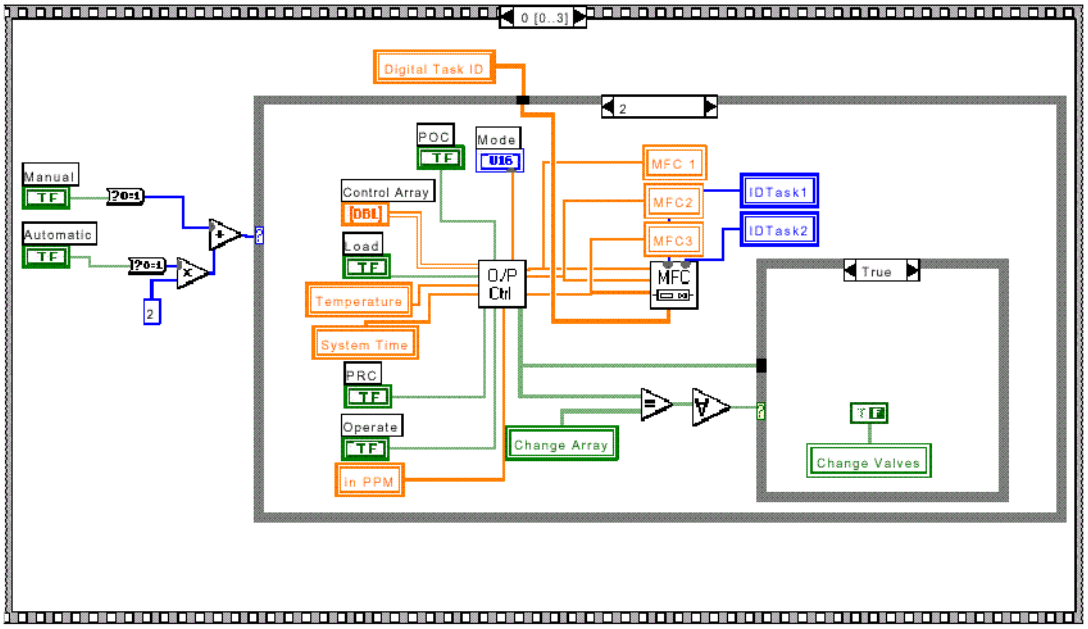
0 [0..3]
Digital Task ID
2
POC
TF
Mode
U16
Manual
TF
Automatic
TF
Control Array
DBL
Load
TF
Temperature
System Time
PRC
TF
Operate
TF
In PPM
O./P
Ctrl
MFC 1
MFC2
MFC3
MFC
IDTask1
IDTask2
Change Array
True
Change Valves

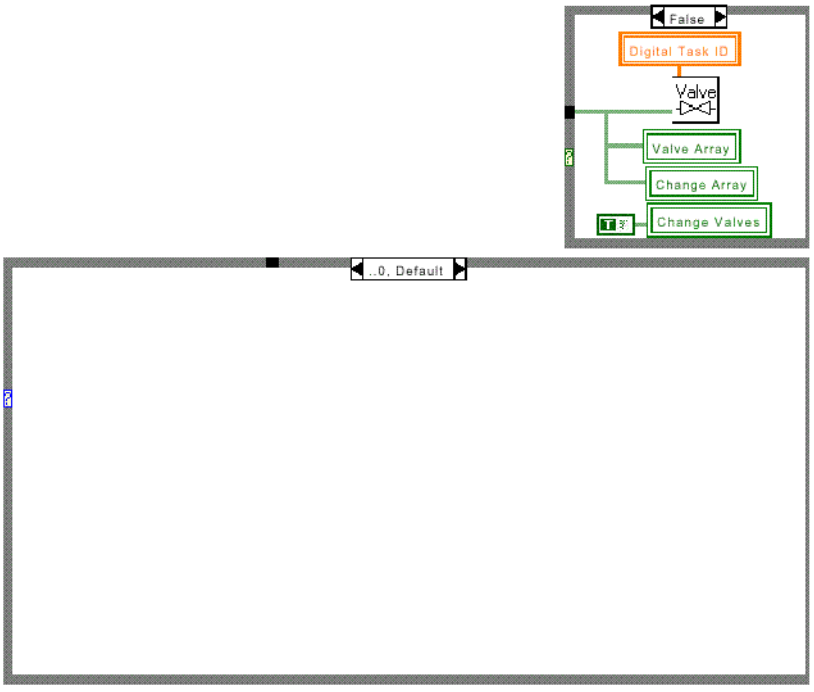
False
Digital Task ID
Valve
Valve Array
Change Array
Change Valves
..0, Default

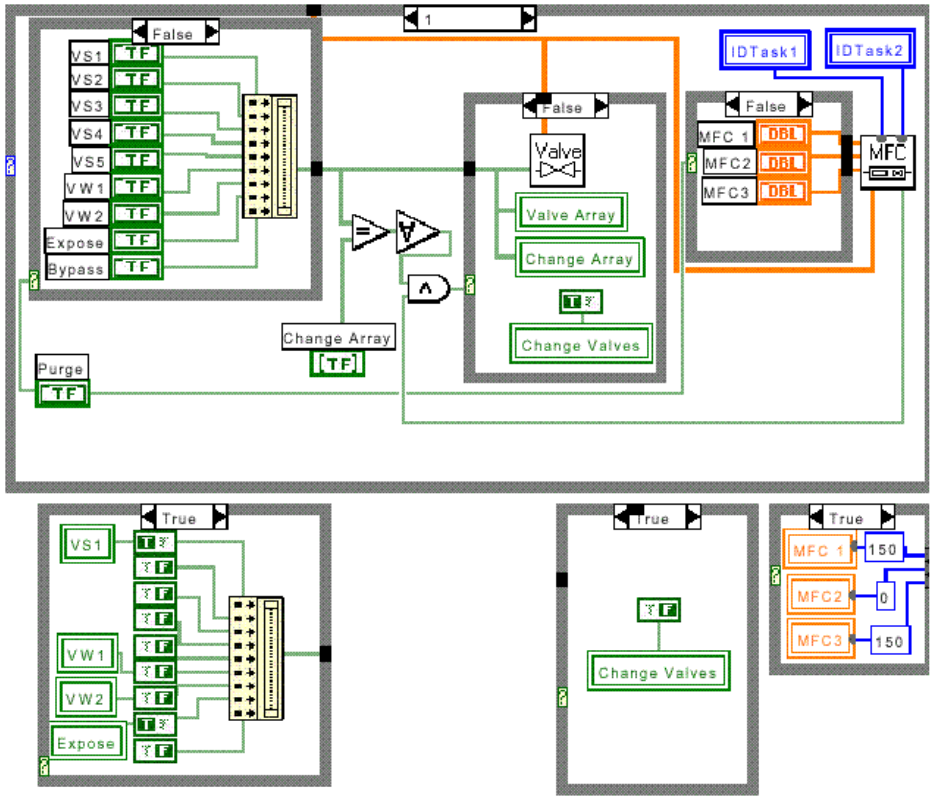
False
VS1
VS2
VS3
VS4
VS5
VW1
VW2
Expose
Bypass
TF
1
Change Array
[TF]
Purge
False
Valve
Valve Array
Change Array
Change Valves
IDTask1
IDTask2
False
MFC 1
MFC2
MFC3
DBL
MFC
True
VS1
VW1
VW2
Expose
True
Change Valves
True
MFC 1
MFC2
MFC3
150
0
150

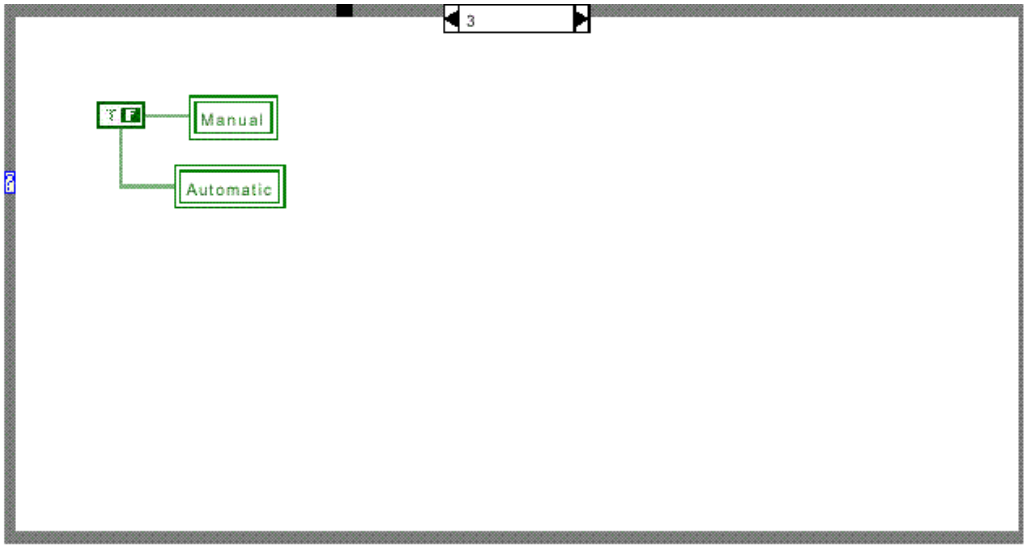
3
Manual
Automatic

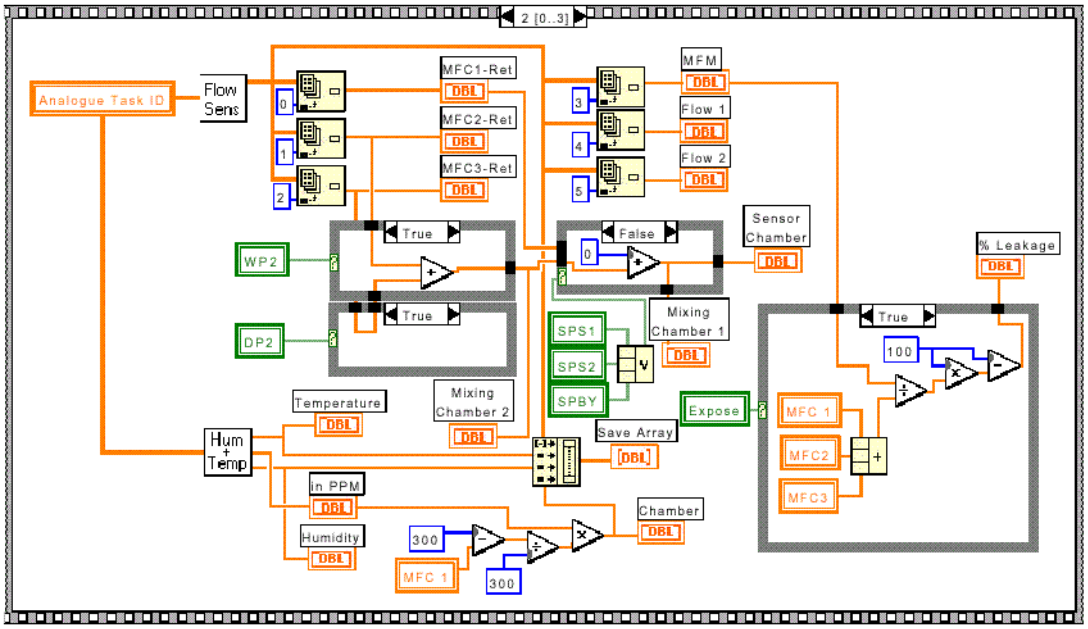

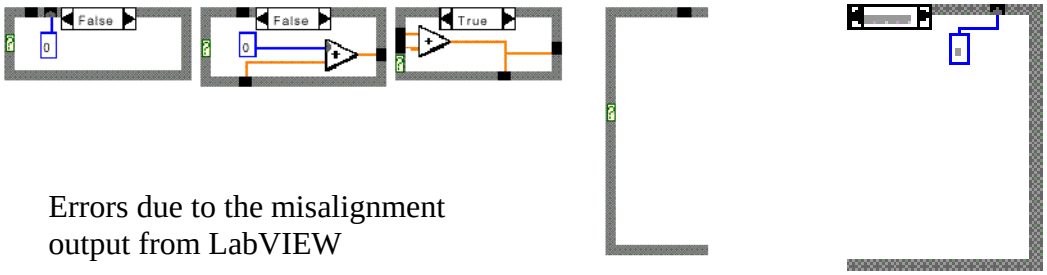

Errors due to the misalignment output from LabVIEW

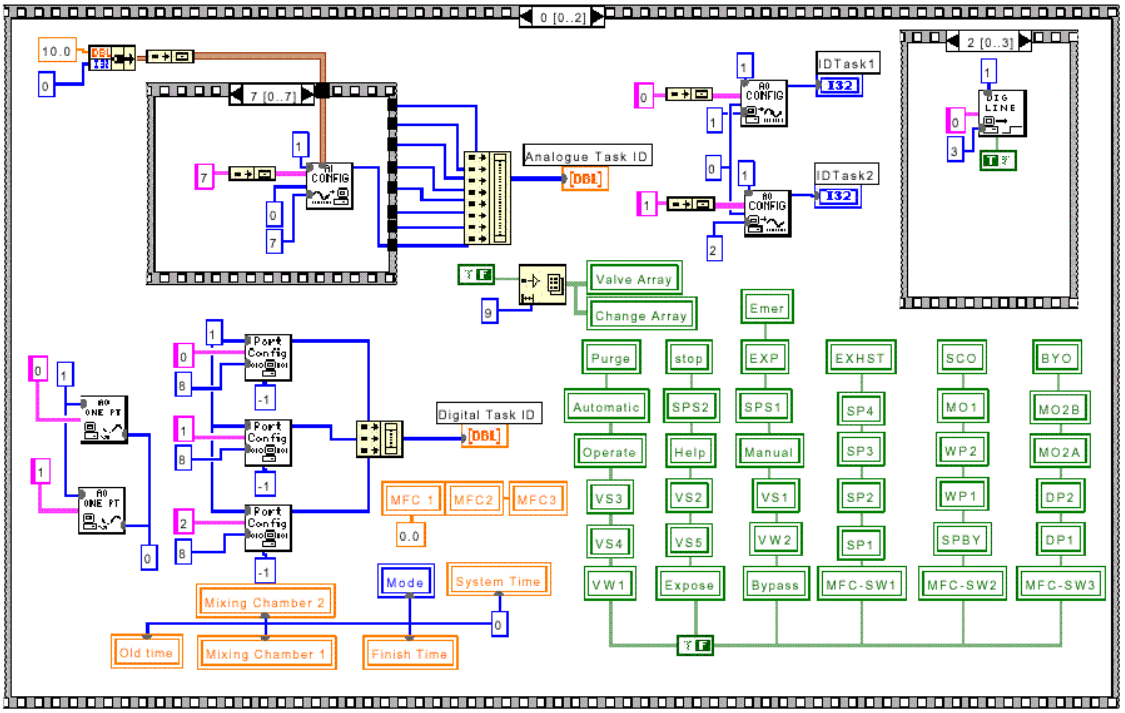

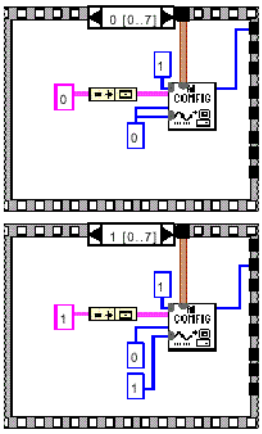
0 [0..7]
CONFIG
1 [0..7]
CONFIG

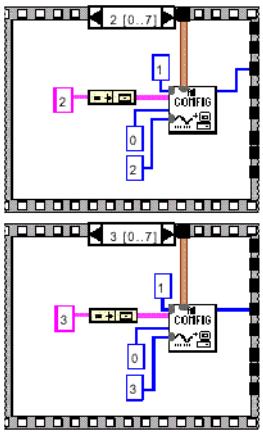
2 [0..7]
CONFIG
3 [0..7]
CONFIG

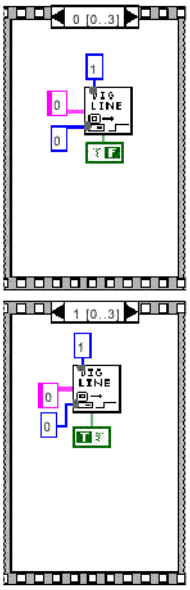
0 [0..3]
DIG LINE
1 [0..3]
DIG LINE

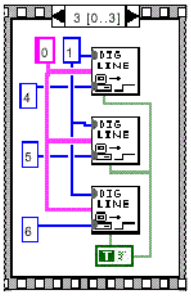
3 [0..3]
DIG LINE
DIG LINE
DIG LINE

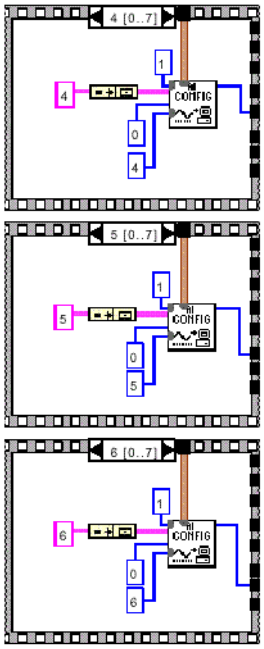
4 [0..7]
CONFIG
5 [0..7]
CONFIG
6 [0..7]
CONFIG

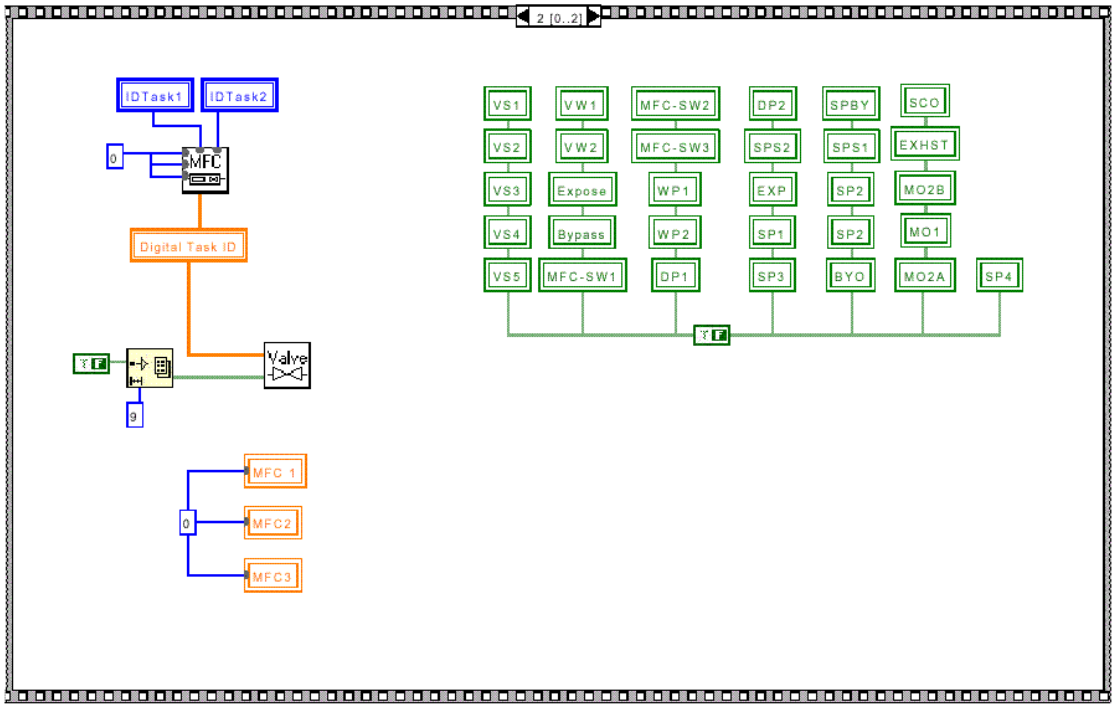
2 [0..2]
IDTask1
IDTask2
MFC
Digital Task ID
Valve
MFC 1
MFC2
MFC3
VS1
VW1
MFC-SW2
DP2
SPBY
SCO
VS2
VW2
MFC-SW3
SPS2
SPS1
EXHST
VS3
Expose
WP1
EXP
SP2
MO2B
VS4
Bypass
WP2
SP1
SP2
MO1
VS5
MFC-SW1
DP1
SP3
BYO
MO2A
SP4

List of sub-vi's

AI Config.vi
C:\LABVIEW\vi.lib\DAQ\AI.LLB\AI Config.vi

DIO Port Config.vi
C:\LABVIEW\vi.lib\DAQ\ZADVD.LLB\DIO Port Config.vi

AO Config.vi
C:\LABVIEW\vi.lib\DAQ\AO.LLB\AO Config.vi

Save/Load.vi
D:\PhD Documents\LabVIEW\fia2.llb\Save/Load.vi

Valve Control.vi
D:\PhD Documents\LabVIEW\fia2.llb\Valve Control.vi

MFC O/P.vi
D:\PhD Documents\LabVIEW\fia2.llb\MFC O/P.vi

Temp & Hum.vi
D:\PhD Documents\LabVIEW\fia2.llb\Temp & Hum.vi

Flow Returns.vi
D:\PhD Documents\LabVIEW\fia2.llb\Flow Returns.vi

Control.vi
D:\PhD Documents\LabVIEW\fia2.llb\Control.vi

Write to Digital Line.vi
C:\LABVIEW\vi.lib\DAQ\1EASYIO.LLB\Write to Digital Line.vi

Shut Off.vi
D:\PhD Documents\LabVIEW\fia2.llb\Shut Off.vi

AO Update Channel.vi
C:\LABVIEW\vi.lib\DAQ\1EASYIO.LLB\AO Update Channel.vi

Write To Spreadsheet File 2.vi
D:\PhD Documents\LabVIEW\fia2.llb\Write To Spreadsheet File 2.vi

2. Flow diagrams for I-V characterisation instrument

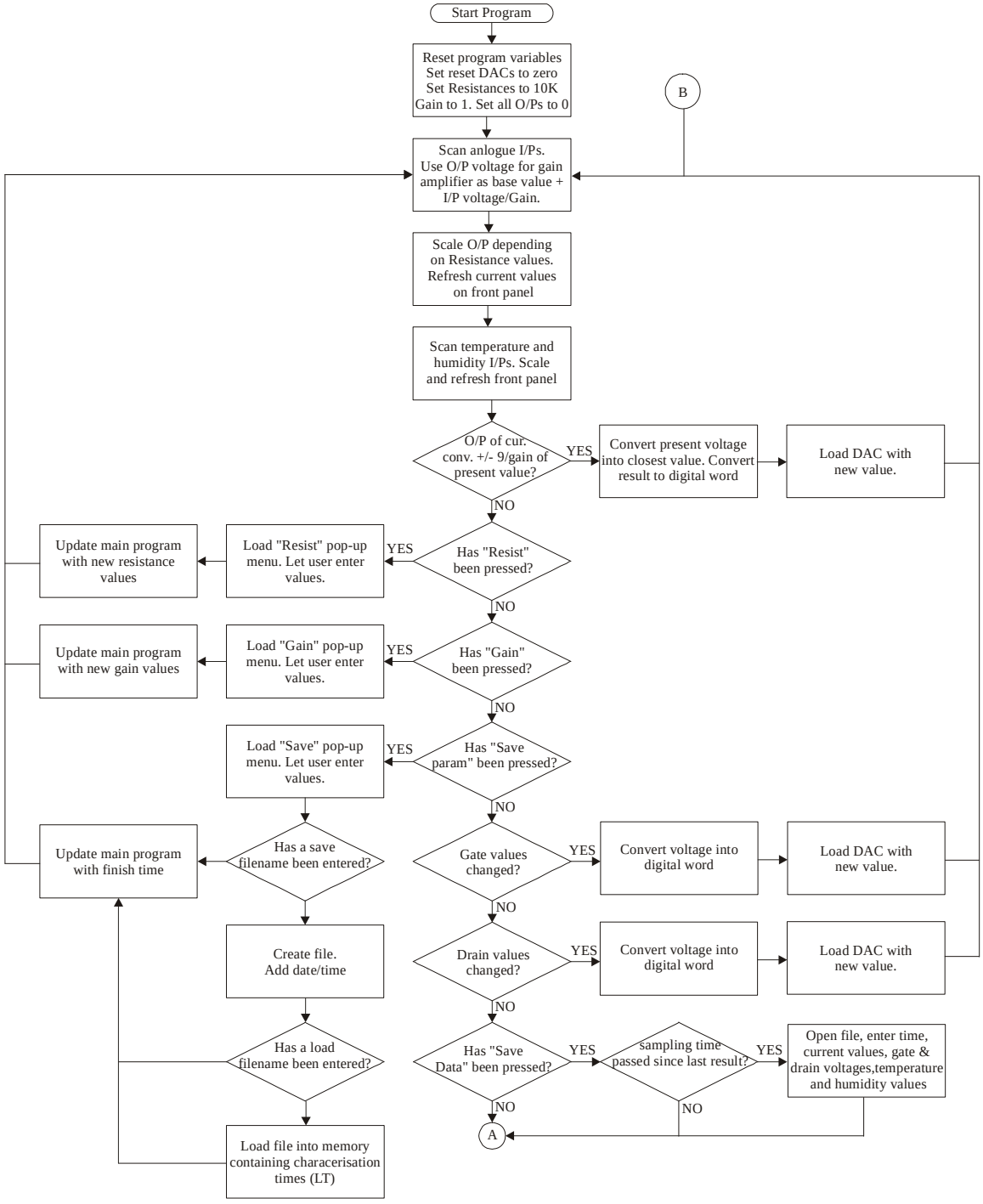

Front panel **of I-V characterisation instrument**

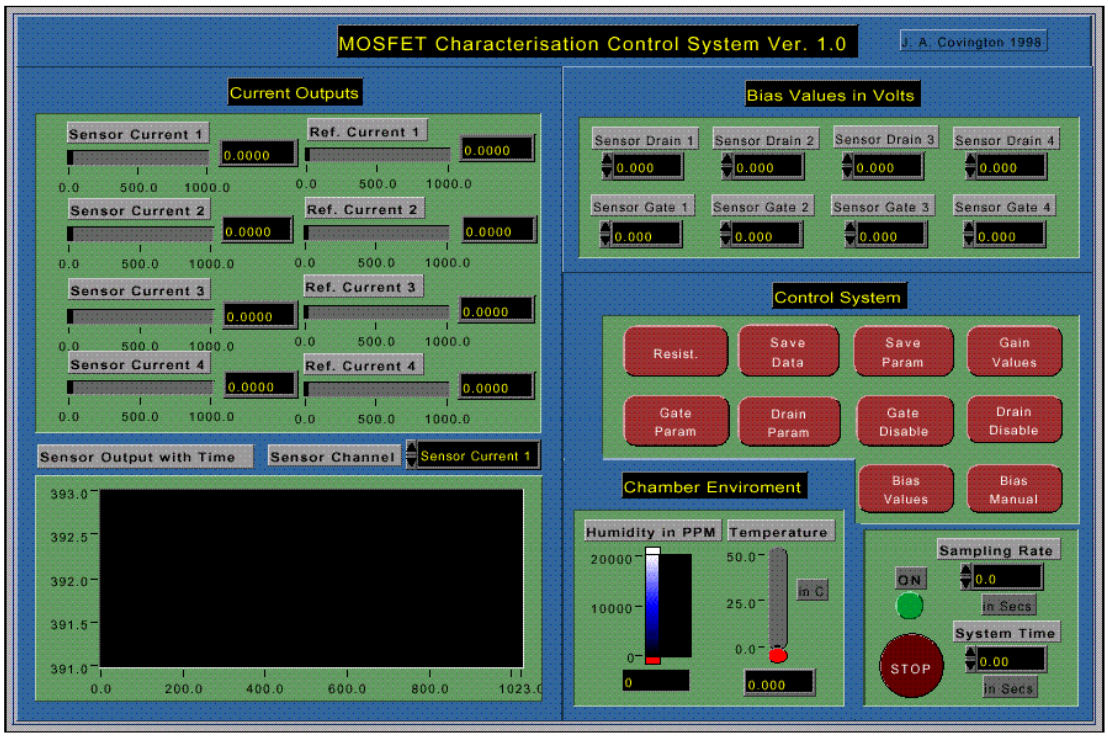

Block diagram of I-V characterisation instrument

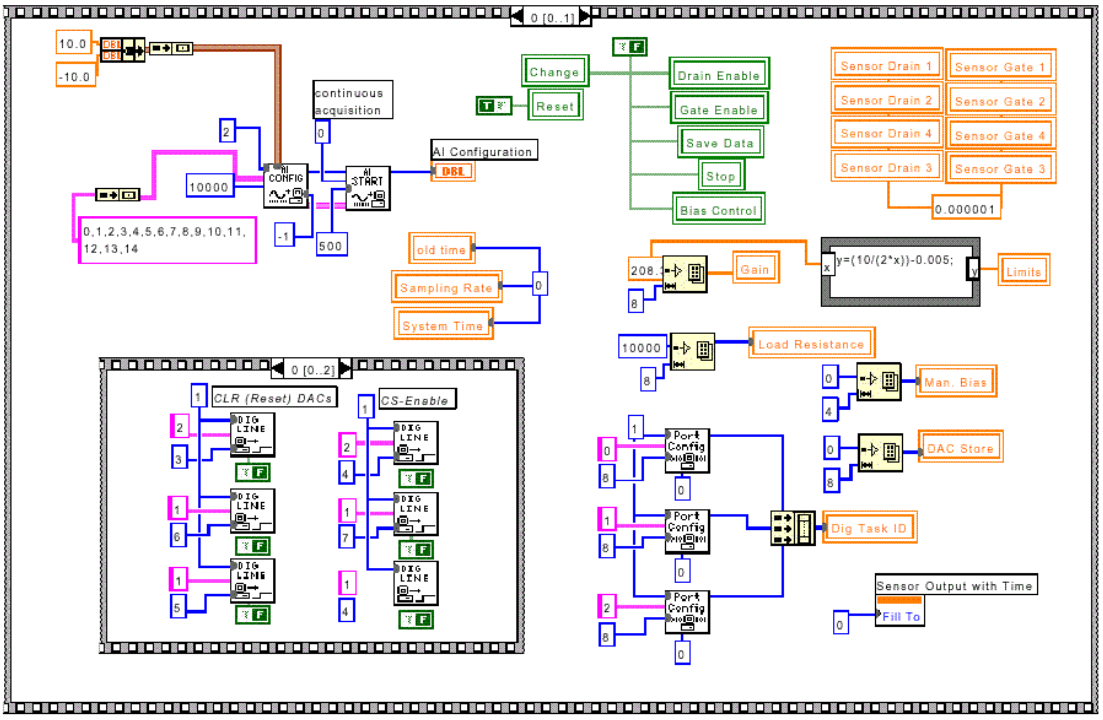

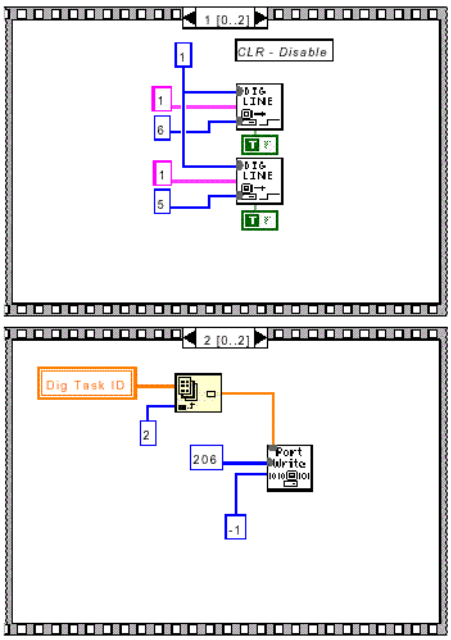

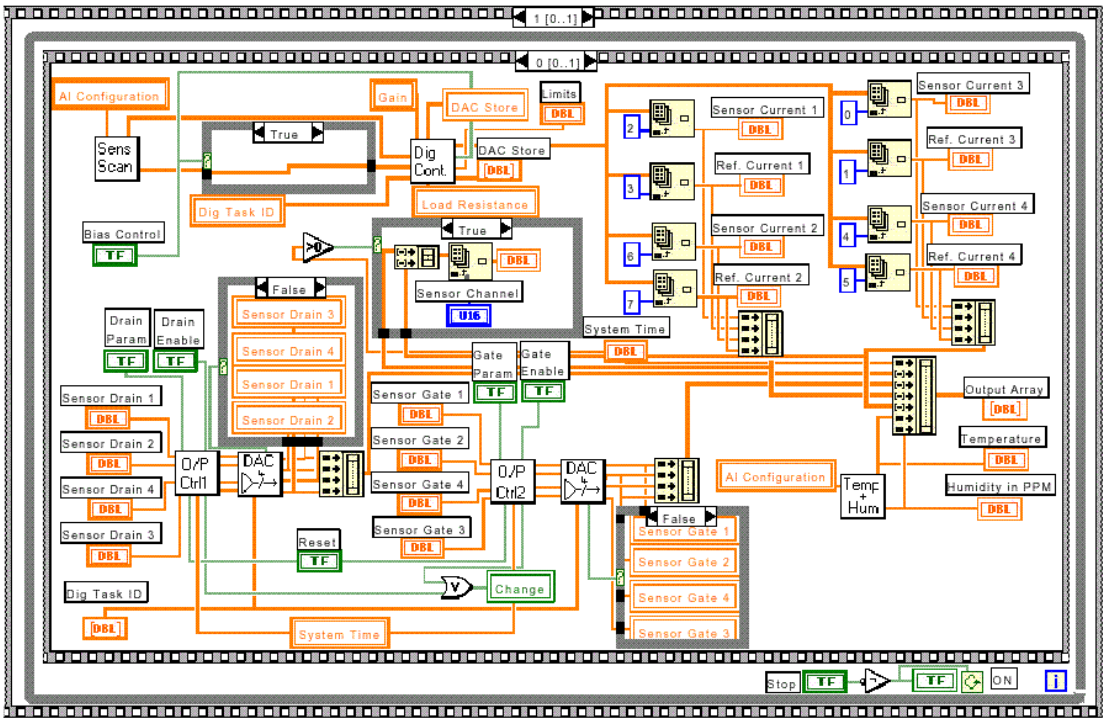
1 [0..1]
0 [0..1]
AI Configuration
Gain
DAC Store
Limits
Sens Scan
True
Dig Cont.
DAC Store
Sensor Current 1
Sensor Current 3
Ref. Current 1
Ref. Current 3
Dig Task ID
Load Resistance
Sensor Current 2
Sensor Current 4
Bias Control
Ref. Current 2
Ref. Current 4
False
Sensor Channel
Drain Param
Drain Enable
Sensor Drain 3
Sensor Drain 4
Sensor Drain 1
Sensor Drain 2
System Time
Gate Param
Gate Enable
Sensor Gate 1
Output Array
Sensor Drain 1
Sensor Gate 2
Temperature
Sensor Drain 2
O/P Ctrl1
DAC
Sensor Gate 4
O/P Ctrl2
Humidity in PPM
Sensor Drain 4
Sensor Drain 3
Sensor Gate 3
Reset
Temp + Hum
Change
Dig Task ID
System Time
Stop
ON

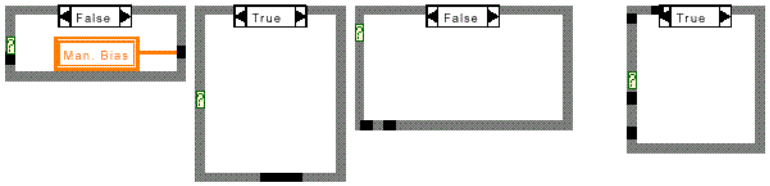
False
Man. Bias
True
False
True

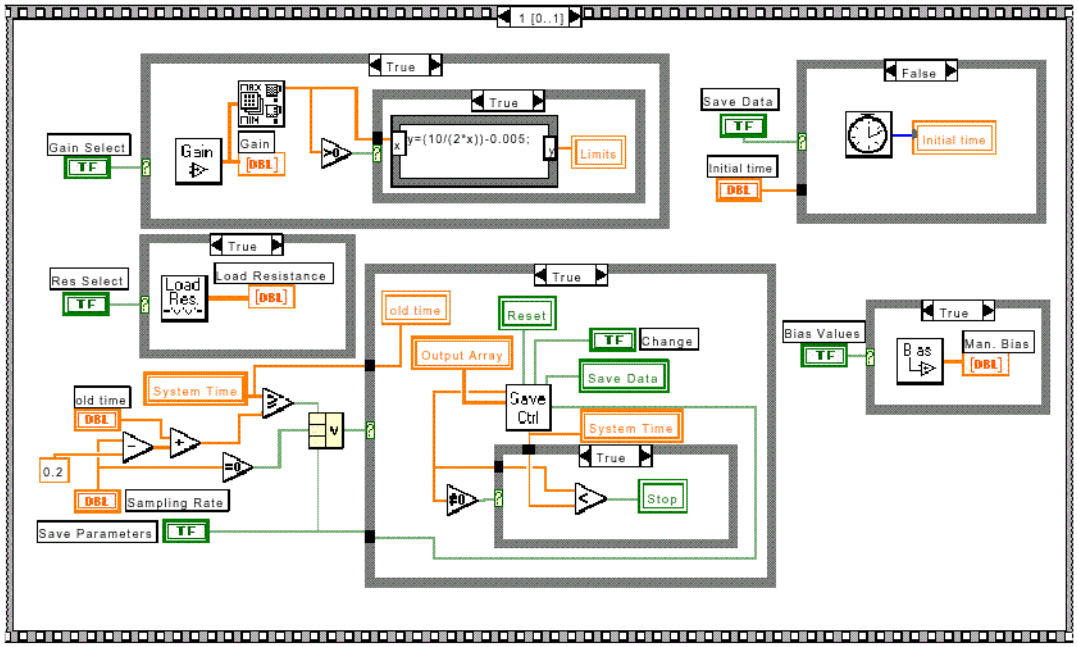
1 [0..1]
True
Gain Select
Gain
Limits
y=(10/(2*x))-0.005;
Save Data
False
Initial time
Res Select
Load Res.
Load Resistance
old time
Reset
Output Array
Change
Save Data
Save Ctrl
System Time
Bias Values
Bias
Man. Bias
0.2
Sampling Rate
Save Parameters
Stop

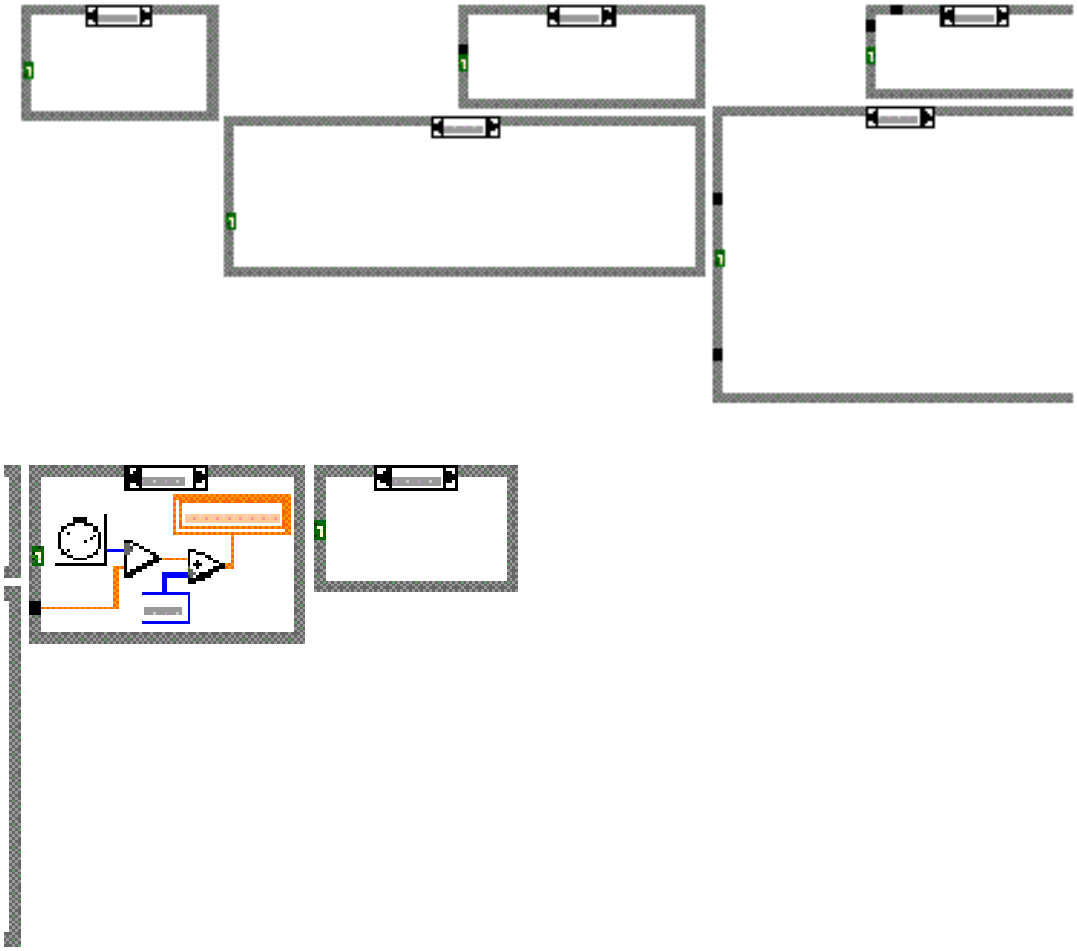

List of sub-vi's

Sensors Output.vi
D:\PhD Documents\LabVIEW\continous polyfet1.llb\Sensors Output.vi

Dig Control and Proc.vi
D:\PhD Documents\LabVIEW\continous polyfet1.llb\Dig Control and Proc.vi

Gain Select.vi
D:\PhD Documents\LabVIEW\continous polyfet1.llb\Gain Select.vi

Load Resistances.vi
D:\PhD Documents\LabVIEW\continous polyfet1.llb\Load Resistances.vi

Temp & Hum.vi
D:\PhD Documents\LabVIEW\continous polyfet1.llb\Temp & Hum.vi

Save Control.vi
D:\PhD Documents\LabVIEW\continous polyfet1.llb\Save Control.vi

Write to Digital Line.vi
C:\LABVIEW\vi.lib\DAQ\1EASYIO.LLB\Write to Digital Line.vi

DIO Port Config.vi
C:\LABVIEW\vi.lib\DAQ\ZADVD.LLB\DIO Port Config.vi

Output Ctrl1.vi
D:\PhD Documents\LabVIEW\continous polyfet1.llb\Output Ctrl1.vi

DAC Upadate 3.vi
D:\PhD Documents\LabVIEW\continous polyfet1.llb\DAC Upadate 3.vi

Bias Input.vi
D:\PhD Documents\LabVIEW\continous polyfet1.llb\Bias Input.vi

DAC Upadate 2.vi
D:\PhD Documents\LabVIEW\continous polyfet1.llb\DAC Upadate 2.vi

DIO Port Write.vi
C:\LABVIEW\vi.lib\DAQ\ZADVD.LLB\DIO Port Write.vi

Output Ctrl2.vi
D:\PhD Documents\LabVIEW\continous polyfet1.llb\Output Ctrl2.vi

AI Config.vi
C:\LABVIEW\vi.lib\daq\ai.llb\AI Config.vi

AI Start.vi
C:\LABVIEW\vi.lib\daq\ai.llb\AI Start.vi

3. Flow diagrams for current characterisation instrument

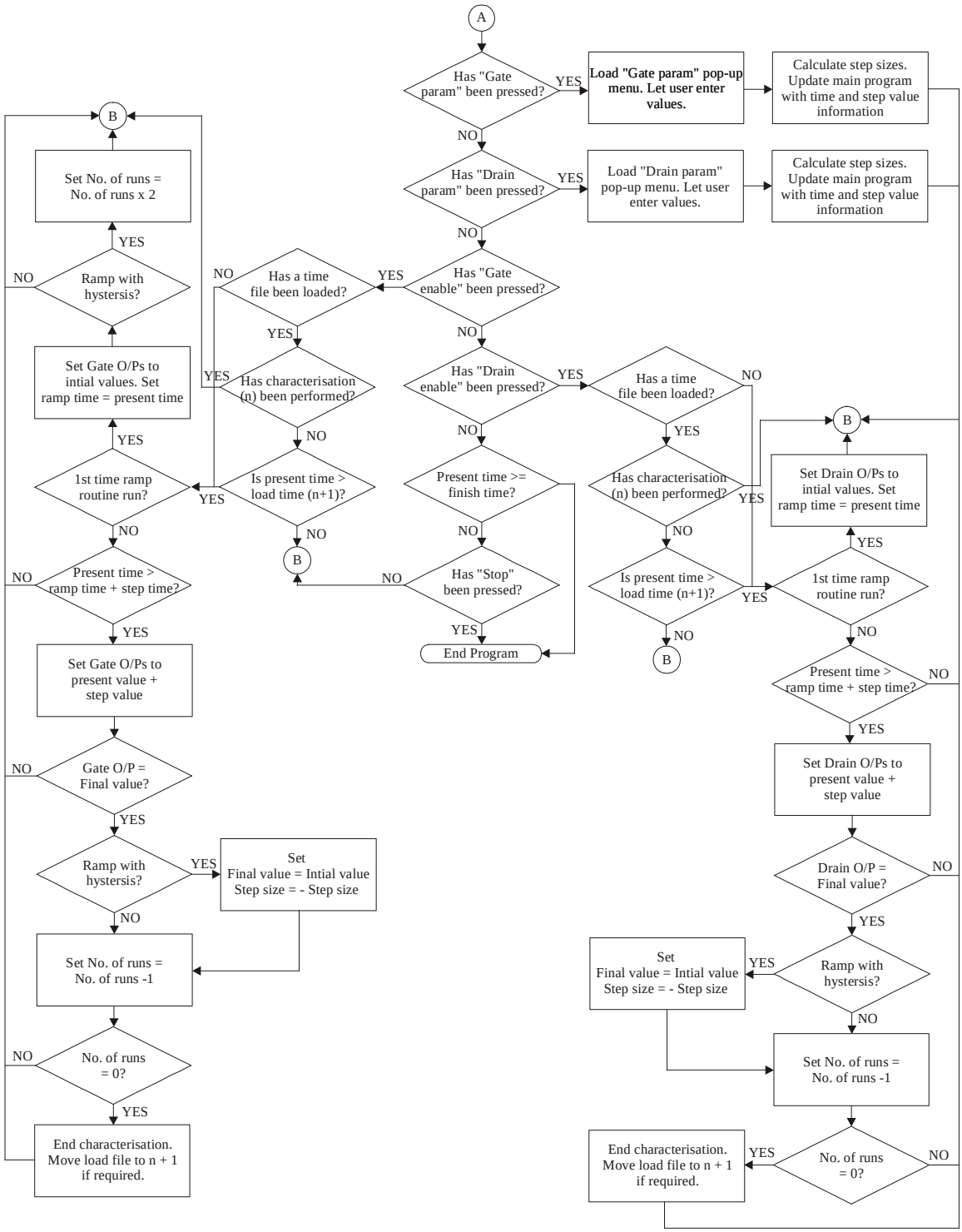

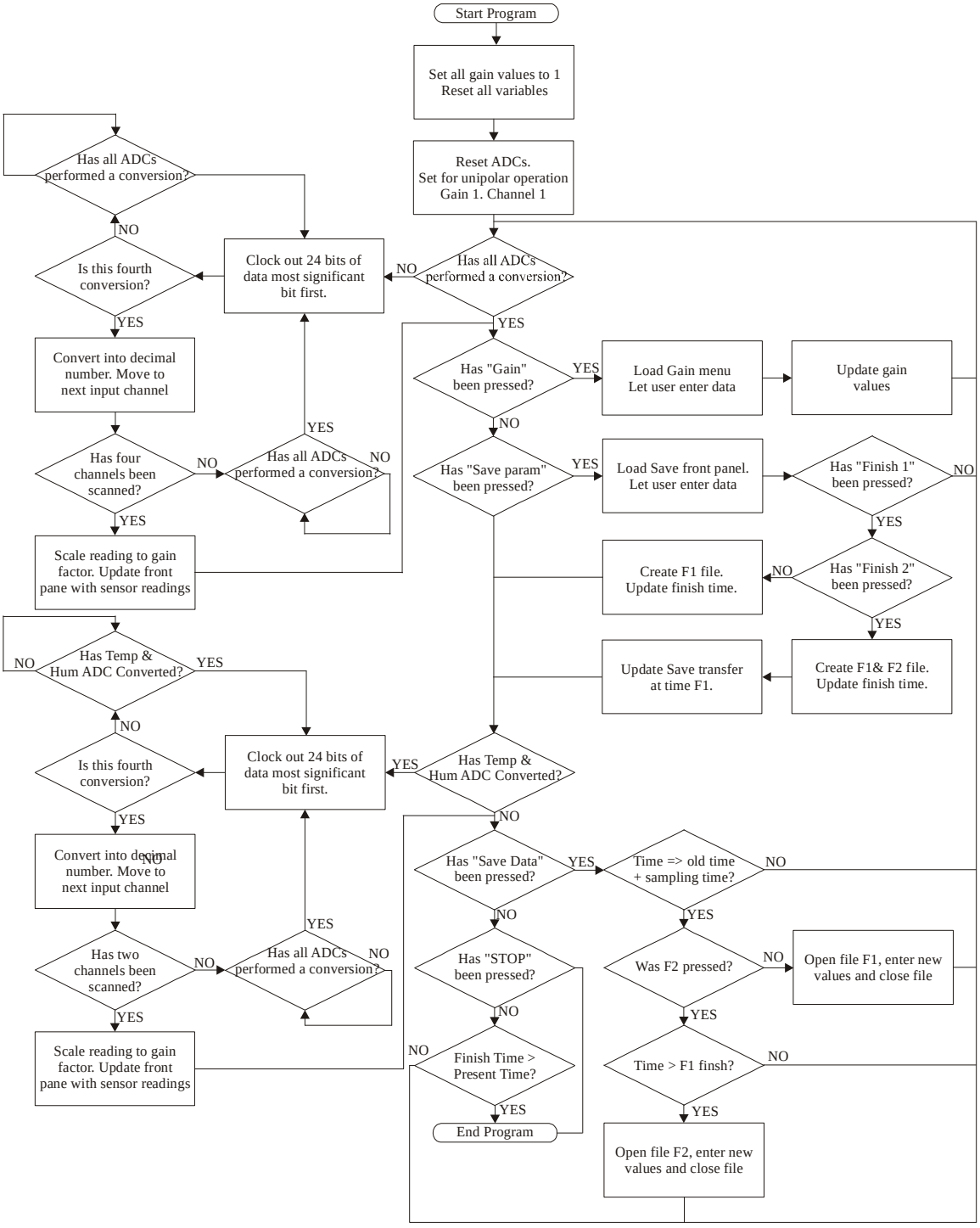
Start Program
Set all gain values to 1
Reset all variables
Reset ADCs.
Set for unipolar operation
Gain 1. Channel 1
Has all ADCs performed a conversion?
NO
YES
Clock out 24 bits of data most significant bit first.
Is this fourth conversion?
Convert into decimal number. Move to next input channel
Has four channels been scanned?
Has all ADCs performed a conversion?
Scale reading to gain factor. Update front pane with sensor readings
Has "Gain" been pressed?
Load Gain menu
Let user enter data
Update gain values
Has "Save param" been pressed?
Load Save front panel.
Let user enter data
Has "Finish 1" been pressed?
Has "Finish 2" been pressed?
Create F1 file.
Update finish time.
Create F1& F2 file.
Update finish time.
Update Save transfer at time F1.
Has Temp & Hum ADC Converted?
Has "Save Data" been pressed?
Time => old time + sampling time?
Has "STOP" been pressed?
Was F2 pressed?
Open file F1, enter new values and close file
Finish Time > Present Time?
Time > F1 finsh?
End Program
Open file F2, enter new values and close file

Front panel of constant current characterisation instrument

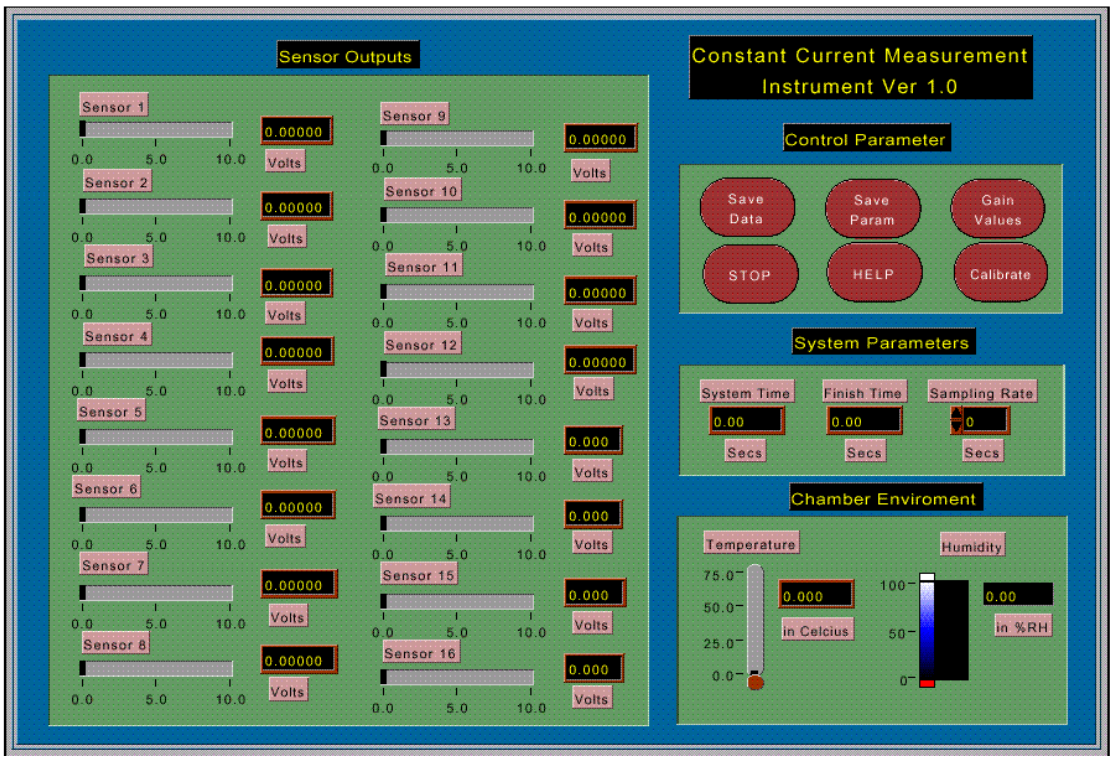

Block diagram of constant current characterisation instrument

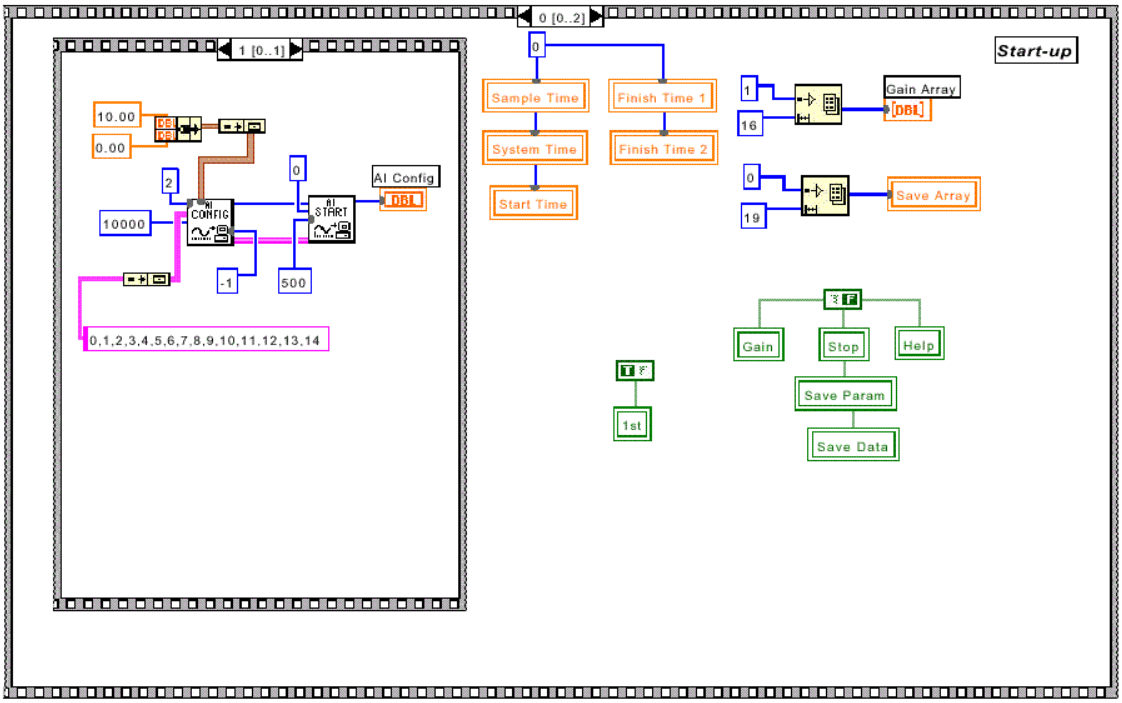

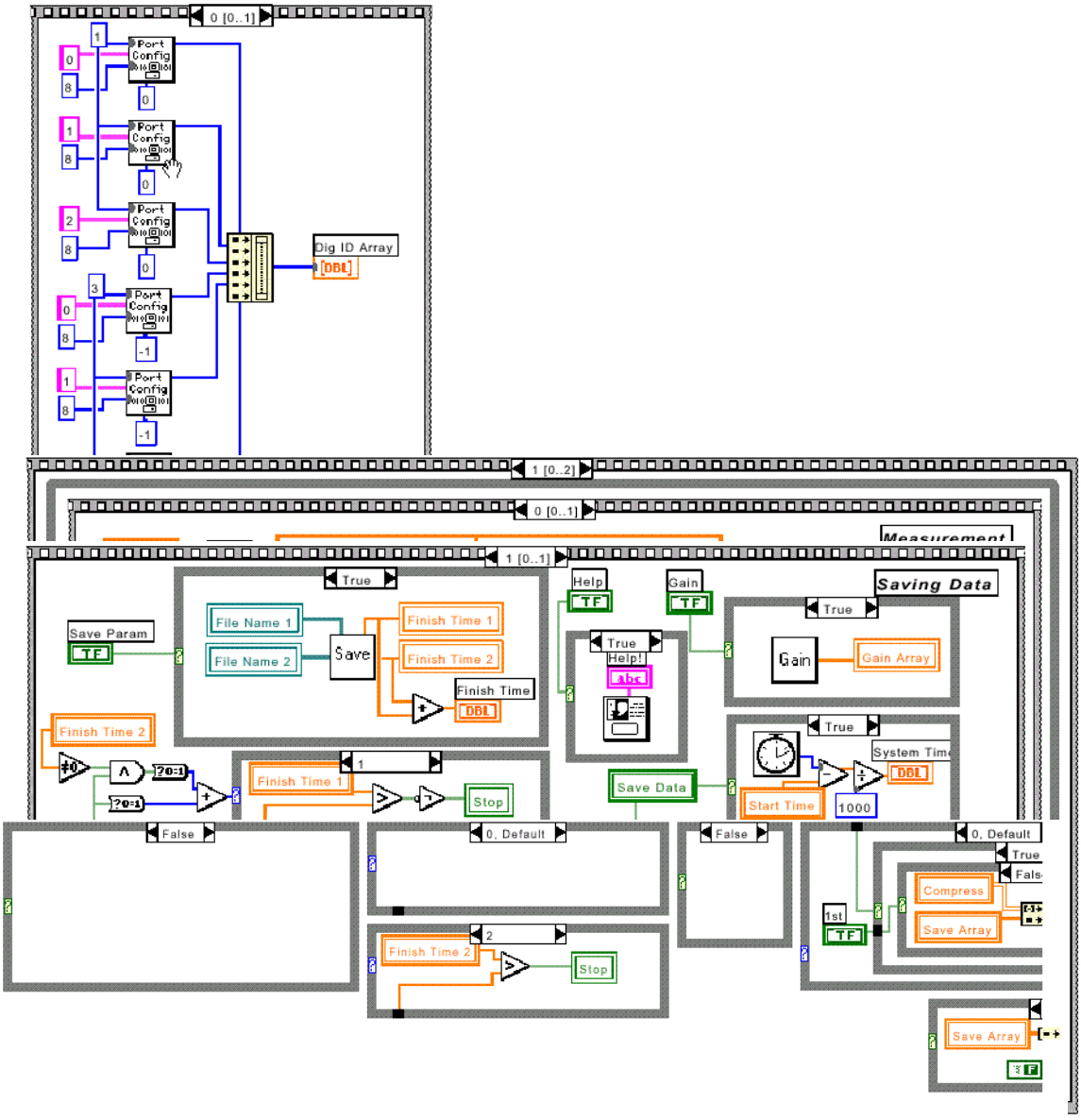

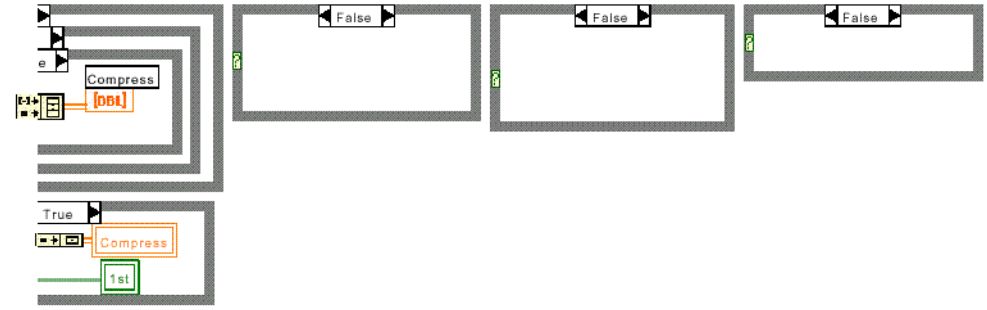

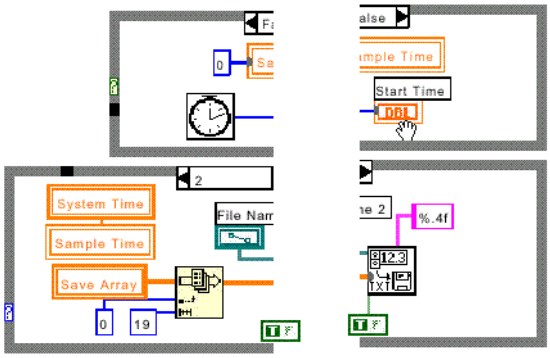

Errors due to the misalignment output from LabVIEW

List of Sub-vi's

Write To Spreadsheet File.vi
C:\LABVIEW\vi.lib\Utility\file.llb\Write To Spreadsheet File.vi

DIO Port Config.vi
C:\LABVIEW\vi.lib\DAQ\ZADVD.LLB\DIO Port Config.vi

Gain.vi
D:\PhD Documents\LabVIEW\ccs4.llb\Gain.vi

Save Parameters.vi
D:\PhD Documents\LabVIEW\ccs4.llb\Save Parameters.vi

Calibrate.vi
D:\PhD Documents\LabVIEW\ccs4.llb\Calibrate.vi

Sensors Output.vi
D:\PhD Documents\LabVIEW\ccs4.llb\Sensors Output.vi

AI Config.vi
C:\LABVIEW\vi.lib\DAQ\AI.LLB\AI Config.vi

AI Start.vi
C:\LABVIEW\vi.lib\DAQ\AI.LLB\AI Start.vi

Compress.vi
D:\PhD Documents\LabVIEW\ccs4.llb\Compress.vi